

AD-A165 303

A STUDY OF SEA ICE KINEMATICS AND THEIR RELATIONSHIP TO

1/4

ARCTIC AMBIENT NO. (U) SCIENCE APPLICATIONS

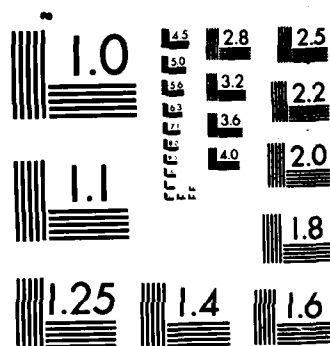
INTERNATIONAL CORP COLLEGE STATION TX J K LEWIS ET AL.

UNCLASSIFIED

FEB 86 SAIC-85/1950-PT-1/2 N00014-85-C-0531 F/G 8/12

NL





MICROCOPY RESOLUTION TEST CHART
NATIONAL BUREAU OF STANDARDS-1963-A

AD-A165 303

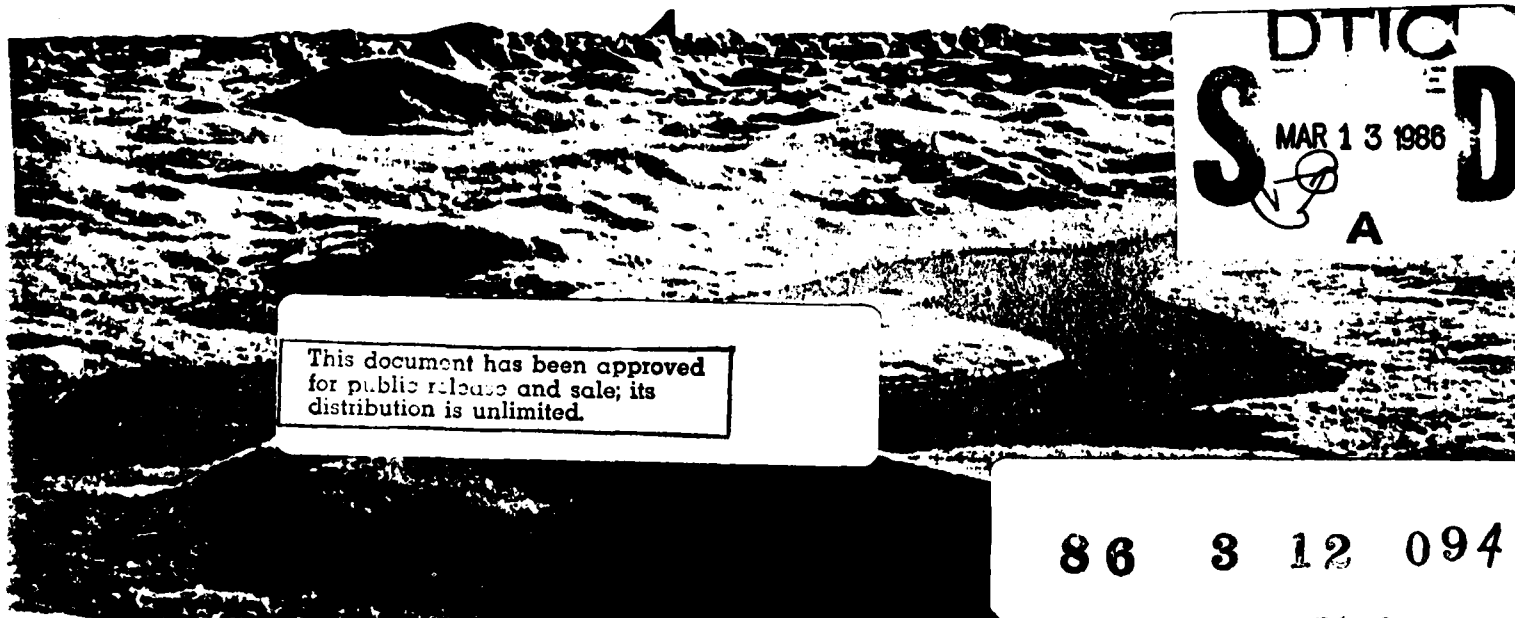
A Study of Sea Ice Kinematics and Their Relationships to Arctic Ambient Noise

Part 1 Technical Papers

Part 2 Ice and Atmospheric Parameters

Science Applications International Corp.

SAIC



86 3 12 094

2



Science Applications International Corporation

DTIC
ELECTE
MAR 13 1986
S A D

Unclassified

SECURITY CLASSIFICATION OF THIS PAGE (When Data Entered)

REPORT DOCUMENTATION PAGE		READ INSTRUCTIONS BEFORE COMPLETING FORM
1. REPORT NUMBER SAIC - 85/1950	2. GOVT ACCESSION NO. AD-A1165303	3. RECIPIENT'S CATALOG NUMBER
4. TITLE (and Subtitle) A Study of Sea Ice Kinematics and Their Relationships to Arctic Ambient Noise	5. TYPE OF REPORT & PERIOD COVERED Final Report March 1985-February 1986	
	6. PERFORMING ORG. REPORT NUMBER SAIC 1-425-07-356-10	
7. AUTHOR(s) James K. Lewis Warren W. Denner	8. CONTRACT OR GRANT NUMBER(s) N00014-85-C-0531	
9. PERFORMING ORGANIZATION NAME AND ADDRESS Science Applications International Corporation 1304 Deacon College Station, Texas 77840	10. PROGRAM ELEMENT, PROJECT, TASK AREA & WORK UNIT NUMBERS	
11. CONTROLLING OFFICE NAME AND ADDRESS Office of Naval Research Department of the Navy Arlington, Virginia 22217	12. REPORT DATE February 1986	
	13. NUMBER OF PAGES 770	
14. MONITORING AGENCY NAME & ADDRESS (if different from Controlling Office)	15. SECURITY CLASS. (of this report) Unclassified	
	15a. DECLASSIFICATION/DOWNGRADING SCHEDULE	
16. DISTRIBUTION STATEMENT (of this Report) Approved for public release; distribution unlimited.		
17. DISTRIBUTION STATEMENT (of the abstract entered in Block 20, if different from Report)		
18. SUPPLEMENTARY NOTES		
19. KEY WORDS (Continue on reverse side if necessary and identify by block number) sea ice processes arctic ambient noise Lagrangian data ice kinematics thermal cracking		
20. ABSTRACT (Continue on reverse side if necessary and identify by block number) This report details the kinematic analysis of sea ice motion data collected during the Arctic Ice Dynamics Joint Experiment (AIDJEX) in the Beaufort Sea. In addition, relationships between the ice kinematic parameters and associated ambient noise are presented. These relationships were determined by an extensive correlation process between the noise and ice motion time histories. Time scales of the various modes of ice motion were calculated by season. Also, seasonal time and space scales were calculated for ambient noise at 10 Hz, 32 Hz, and 1000 Hz.		

DTIC
ELECTE
MAR 13 1986
S A

DD FORM 1 JAN 73 1473

EDITION OF 1 NOV 65 IS OBSOLETE
S/N 0102-LF-014-6601

Unclassified
SECURITY CLASSIFICATION OF THIS PAGE (When Data Entered)

1

A STUDY OF SEA ICE KINEMATICS
AND THEIR RELATIONSHIPS
TO ARCTIC AMBIENT NOISE

A Report to the Office of Naval Research
Department of the Navy
Arlington, Virginia 22217
Contract N00014-85-C-0531

February 1986

James K. Lewis
Warren W. Denner

Science Applications International Corp.
1304 Deacon
College Station, Texas 77840

DTIC
ELECTE
MAR 13 1986
A

SAIC
Science Applications
International Corporation

Table of Contents

	<u>Page</u>
Part 1 - Technical Papers	
Executive Summary	1-1
Calculation of an Effective Ice Thickness Term for Pack Ice Using Lagrangian Data	1-7
Seasonal Variability of the Principle Modes of Ice Movement in the Beaufort Sea	1-23
Arctic Ambient Noise in the Beaufort Sea and Its Relationship to Sea Ice Kinematics	1-53
Part 2 - Ice and Atmospheric Parameters	
Appendices A through K	2-1
Part 3, Section 1 - Ambient Noise	
Appendices A through C	3.1
Part 3, Section 2 - Ambient Noise	
Appendices D through F	3.2
Part 3, Section 3 - Ambient Noise	
Appendices G through I	3.3

Accession For	
NTIS - GRA&I	<input checked="" type="checkbox"/>
DTIC TAB	<input type="checkbox"/>
Unannounced	<input type="checkbox"/>
Justification	
By	
Distribution/	
Availability Codes	
Dist	Avail and/or Special
A-1	



EXECUTIVE SUMMARY

This report details a study of sea ice processes and ambient noise variations from data sets collected during the Arctic Ice Dynamics Joint Experiment (AIDJEX) in 1975 and 1976. The data, which come from buoys drifting with the ice for a period of over one year in the Beaufort Sea, consist of ambient noise, position, atmospheric temperature and pressure, and a number of other parameters. This report consists of three parts pertaining to data presentation and analysis: *Volume 1 contains technical papers on*

Part 1 - Technical Papers

Part 2 - Ice and Atmospheric Parameters

Part 3 - Ambient Noise.

Part 1 contains the technical papers generated from the study of the AIDJEX data. The first is a paper dealing with dynamics and is entitled "Calculation of an Effective Ice Thickness Term for Pack Ice Using Lagrangian Data." The second paper deals with ice kinematics and is entitled "Seasonal Variability of the Principle Modes of Ice Movement in the Beaufort Sea." The reader will note that some of the dynamic processes discussed in the first paper are used to explain some interesting kinematics presented in the second paper. The last technical paper is entitled "Arctic Ambient Noise in the Beaufort Sea and Its Relationship to Sea Ice Kinematics." This paper presents the results of correlations between ambient noise and various processes such as ice deformation, convergence, and translation. *Also included are*

Part 2 of the report contains a number of appendices that present most of the ice and atmospheric data used in this study in graphical format. Part 3 is similar to Part 2 in that its appendices present graphically various aspects of the ambient noise data. However, Part 3 has been divided into three sections for

convenience. The first section shows the noise time histories used in this study at each acoustic station. In addition, this first section presents some of the two-dimensional contour maps of noise at three hour intervals. These contour maps are continued in the second section of Part 3. Finally, the third section of Part 3 shows the ambient noise temporal and spatial autocorrelation curves. Moreover, this last section presents ambient noise spectra at a particular station for the four seasons.

The figures generated for Parts 2 and 3 were made such that one may overlay figures for a given period in time in order to make comparisons and visually study relationships between variables. In addition, the tracks of the two ice stations with which the acoustical correlations were performed (Stations 10 and 66) are presented in Figs. 1 and 2 of this summary and may be overlaid. In Fig. 3 we present the track of one of the ice stations which was used in calculating the ice kinematic parameters, and this figure may be overlaid with the first two. This allows one to study the relative distance and motion of the stations for various seasons.

This analysis of the AIDJEX noise and ice movement data is by no means exhaustive. Although we were able to answer many of the questions that we set out to study, a number of intriguing relationships have resulted from our work. The most important of these is the relationship between air temperature and noise variations at the kilohertz range. We present an example of what appears to be strong noise variations at 1000 Hz induced by air temperature fluctuations, yet our correlations indicate that no significant correlation exists between noise at 1000 Hz and a calculated thermal cracking parameter based on air temperature rate of change. Moreover, we show that the same temperature variation can apparently cause a tremendous amount of noise in one

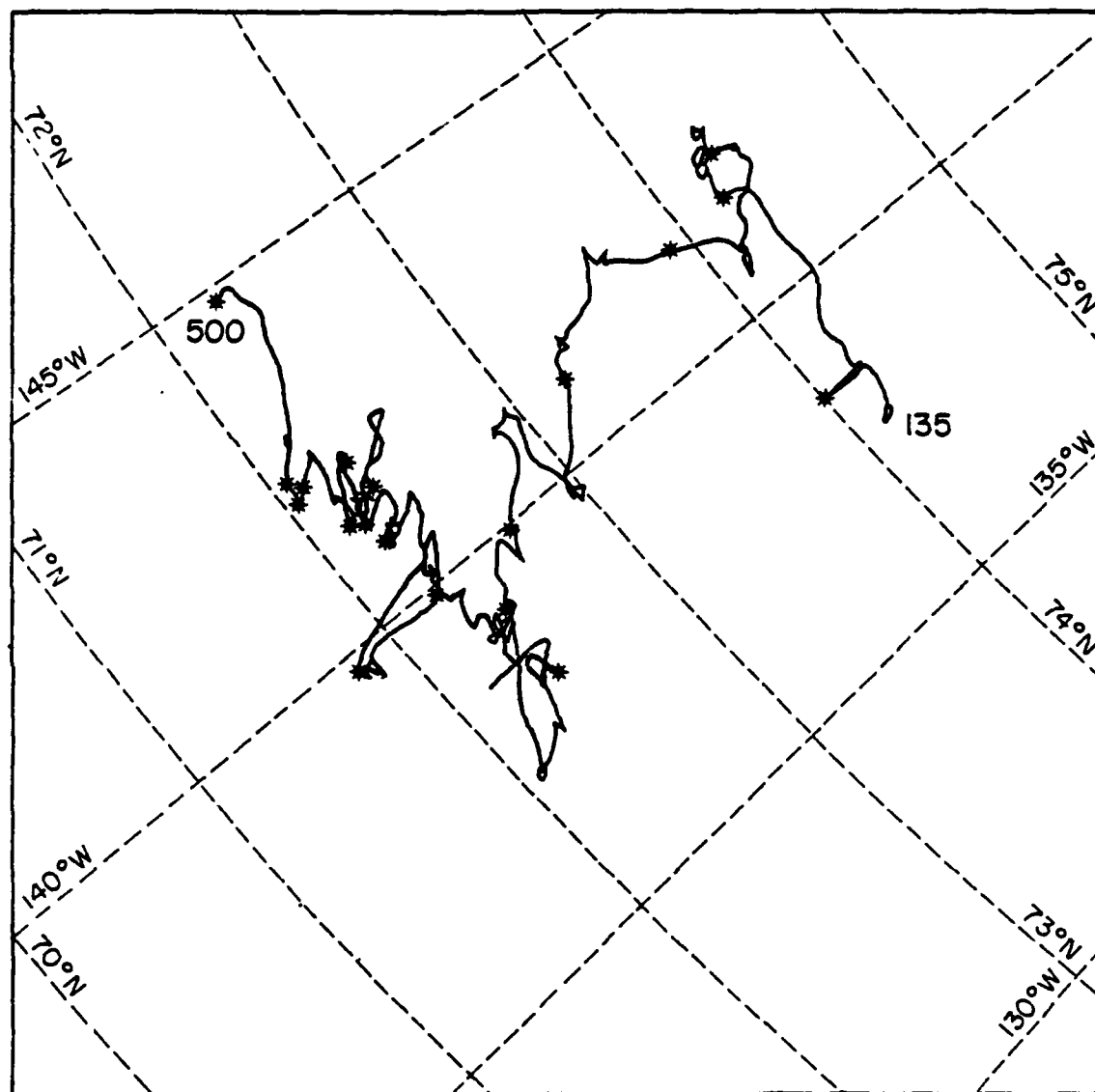


Fig. 1. Time history of the position of AIDJEX Station 10 starting at Julian day 135, 1975, and ending at Julian day 500. The asterics denote the position of the station at 20 day intervals.

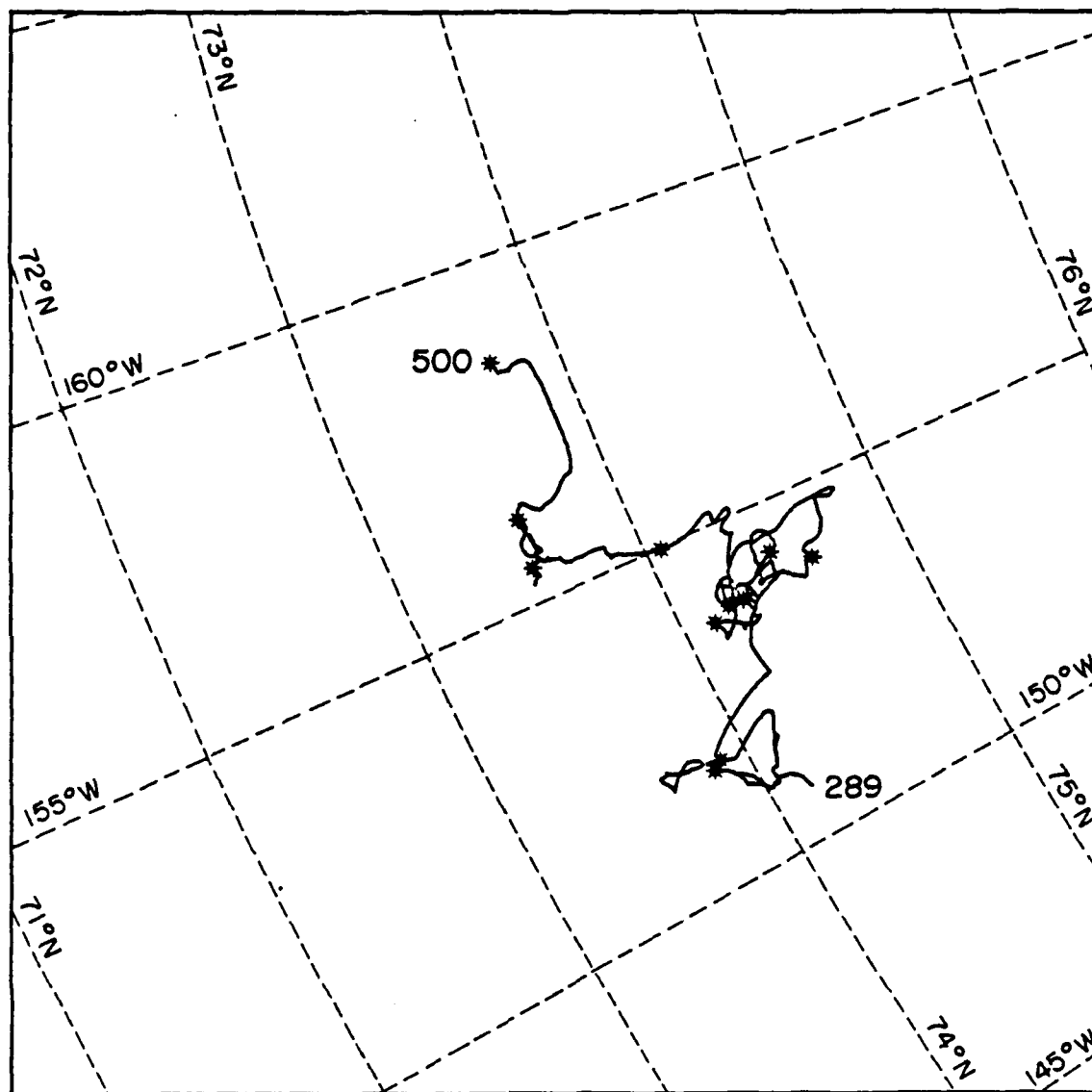


Fig. 2. Time history of the position of AIDJEX Station 66 starting at Julian day 289, 1975, and ending at Julian day 500. The asterics denote the position of the station at 20 day intervals.

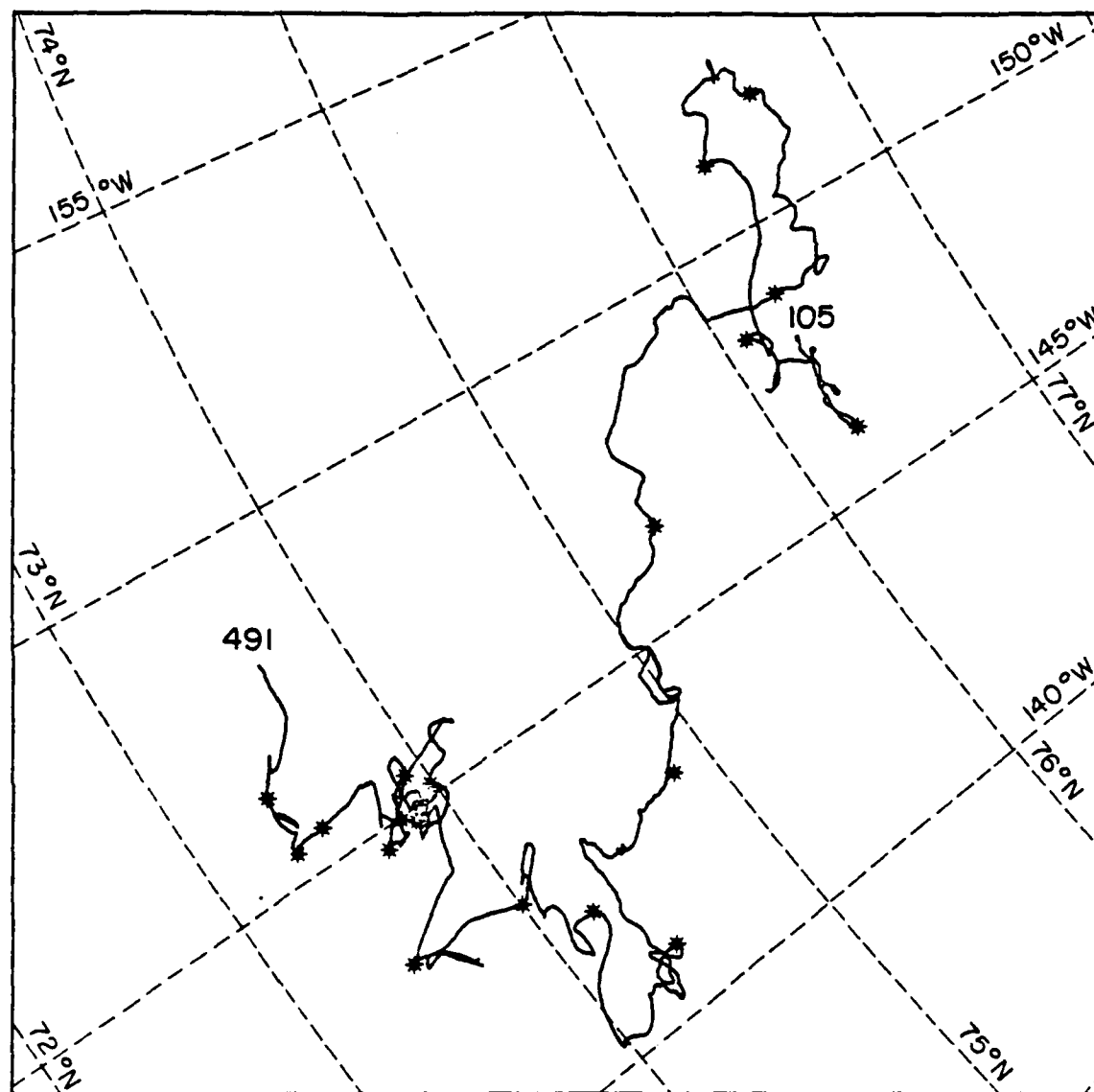


Fig. 3. Time history of the position of AIDJEX Station 3 starting at Julian day 105, 1975, and ending at Julian day 491. The asterisks denote the position of the station at 20 day intervals.

region of the Beaufort Sea (increases of up to 30 dB at 1000 Hz) but have no effect in another region. These results seem to warrant further research into the process of thermal microfracturing.

CALCULATING AN EFFECTIVE THICKNESS
TERM FOR PACK ICE USING
LAGRANGIAN DATA

ABSTRACT

A methodology is presented which allows one to calculate an ice thickness term using observed ice motion and wind data. Since the wind data can come from atmospheric pressure fields or numerical models, the methodology is in fact a remote-sensing capability which relies on ice motion data from satellite imagery, buoys drifting on the ice, etc. The thickness term is shown to be an effective ice thickness which reflects the strength of the ice as a result of the true ice thickness plus the added mass effect of the horizontal gradients of pressure and internal ice stresses. Examples of the temporal variations of the effective ice thickness in the Beaufort Sea are presented. These variations are explained in terms of the compactness of the ice field as the motion is toward or away from the ice pack.

1. INTRODUCTION

Consider a parcel of pack ice which consists of a number of individual floes plus a variable percent of open water. As wind blows over the ice parcel, the energy of the wind is transferred to and through the ice, and the ice moves according to the geophysical balance of forces. In other words, force is balanced by acceleration times the mass, which implies that an ice parcel of greater thickness (mass) is accelerated less for a given wind stress. However, this concept of the relationship between wind forcing and ice thickness is complicated by the fact that the internal stresses and pressures within the ice pack can be considerable, and an ice parcel under greater compression is also accelerated less for a given wind stress. In this case, the internal ice stresses make the ice parcel appear thicker than it actually is.

The balance of forces within an ice parcel can be determined directly from wind and current data, ice thickness measurements, and a time history of the position of the ice. Internal ice stresses are then calculated as a residual. In lieu of an abundance of such data, several methods have been used to estimate pack ice force balances, including statistical models (e.g. Thorndike and Colony, 1982) and more sophisticated dynamic/thermodynamic models (e.g. McPhee, 1978; Hibler, 1979). In this note, we present a method for determining sea ice force balances using observed ice motion and wind data. This methodology provides a basis for calculating an effective ice thickness, which is the summation of the true ice thickness plus the added mass effect of the internal ice stresses. In essence, we take the wind forcing and the observed ice response and force the equation of motion to balance. The resulting mass parameter, \tilde{H}_e , is the

effective ice thickness, a vector as a consequence of the internal ice stresses.

Our technique is based upon observations of ice velocity \vec{U} , corresponding wind stress $\vec{\tau}$, and the analytical solutions to the appropriate equations of motion. Ice motion data derived from buoys drifting on the ice, synthetic aperture radar (SAR) imagery, or repetitive satellite imagery can be used with wind stress values determined from atmospheric pressure fields or numerical models to calculate \vec{H}_e . The fit of the various parameters is accomplished using statistical methods.

2. THEORETICAL AND TECHNICAL CONSIDERATIONS

The governing equations for motion of a parcel of ice can be expressed as

$$d\vec{U}/dt + f\vec{k} \times \vec{U} = (\vec{\tau} - KR\vec{U} + \vec{I})/H\rho \quad (1)$$

where f is the Coriolis parameter, \vec{I} represents the horizontal gradients of pressure and internal stresses, H is the ice thickness, ρ is the ice density, and $KR\vec{U}$ represents the drag between the ice and the underlying water, with K being a drag coefficient,

$$R_x = 1 - V_x/U_x,$$

$$R_y = 1 - V_y/U_y,$$

and \vec{V} is the speed of water. Consider the situation in which $\vec{I}=\vec{U}=0$ at $t=0$. In this case, the solutions to (1) are (Lewis and Denner, 1984):

$$U_{x,t} = \int_0^t e^{-\Gamma_x \delta} (\tau_x + I_x) \Big|_{t-\delta} \cos f\delta + (\tau_y + I_y) \Big|_{t-\delta} \sin f\delta \, d\delta / (H\rho) \quad (2)$$

$$U_{y,t} = \int_0^t e^{-\Gamma_y \delta} (\tau_y + I_y) \Big|_{t-\delta} \cos f\delta - (\tau_x + I_x) \Big|_{t-\delta} \sin f\delta \, d\delta / (H\rho)$$

where

$$\vec{\Gamma} = (\Gamma_x, \Gamma_y) = K(R_x, R_y)/(H\rho).$$

These expressions are obtained by assuming Γ is relatively constant over the period of integration and that $\vec{\tau}$ and \vec{I} are not

functions of the velocity of the ice parcel \vec{U} . The most questionable of these assumptions is the independence of \vec{I} with respect to \vec{U} . For compact ice, the internal ice stresses are typically formulated in terms of the spatial gradients of the ice velocity field. However, this does not explicitly imply that \vec{I} is a well defined function of the velocity time history of an individual ice parcel. We will return to this point later.

Equations (2) express wind-induced ice motion as the summation of inertial oscillations that are modified by a) the water stress under the ice (\vec{T}) and by b) the gradients of the horizontal pressure and internal ice stresses (\vec{I}). Lagrangian ice data can be used to estimate $U_{x,t}$ and $U_{y,t}$ on the LHS of (2), and wind data can be used to estimate \vec{T} . Thus, we have two equations in five unknowns: H , Γ_x , Γ_y , I_x , and I_y . We now rewrite the expressions in (2) to combine the H and \vec{I} terms to give two equations in four unknowns: Γ_x , Γ_y , and an effective ice thickness $\vec{H}_e = (H_u, H_v)$. Consider the x-directed equation of (2) in the form of:

$$\begin{aligned} U_{x,t} &= \text{Transport}/H \\ &= T_{\vec{T}}(1 + T_{\vec{I}}/T_{\vec{T}})/H \\ &= T_{\vec{T}}/H_u \end{aligned}$$

where $T_{\vec{T}}$ is the wind-induced ice transport in the x direction, $T_{\vec{I}}$ is the ice transport in the x direction resulting from \vec{I} , and

$$H_u = H/(1 + T_{\vec{I}}/T_{\vec{T}}).$$

Thus, we have

$$U_{x,t} = \int_0^t e^{-\Gamma_x \delta} \left[\tau_x \Big|_{t-\delta} \cos f\delta + \tau_y \Big|_{t-\delta} \sin f\delta \right] d\delta / H_u \rho.$$

Similarly, in the y direction we have

$$U_{y,t} = \int_0^t e^{-\Gamma_y \delta} \left[\tau_y \Big|_{t-\delta} \cos f\delta - \tau_x \Big|_{t-\delta} \sin f\delta \right] d\delta / H_v \rho$$

where H_v is a function similar to H_u except for transports in the y direction. We see that the effective ice thickness reflects the added mass effects of \vec{I} relative to wind-generated motion. As the effect of the internal ice stresses decreases ($\vec{I} \rightarrow 0$), \vec{H}_e approaches the true ice thickness H .

Our analytical solutions are used to determine \vec{H}_e as a residual. The variables \vec{U} and $\vec{\tau}$ are calculated using measured ice motion and wind data. However, we still must determine \vec{I} , and this is done empirically as outlined in Fig. 1. Over a given time interval of n hours, various values of Γ_x and Γ_y are used to calculate series of theoretical ice transports using $\vec{\tau}$ in the RHS of equations (2) after multiplying by \vec{H}_e (Lewis and Denner, 1984). Each series of theoretical transports for each Γ are then correlated with the corresponding observed ice speeds. The Γ 's of the series which give the highest correlations between the observed speeds and the theoretical transports are used as estimators of the true Γ 's. The \vec{H}_e terms are then calculated by determining the

Start With the Analytical Solution:

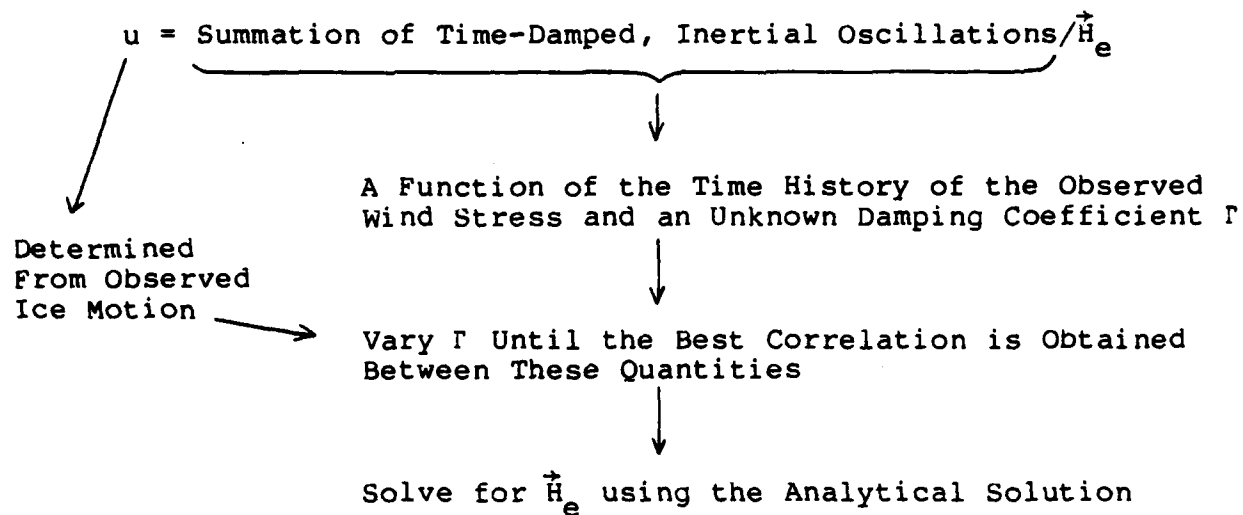


Fig. 1. Method for calculating \vec{H}_e .

least squares slope of the theoretical transports versus \vec{U} (see Fig. 2).

This method results in an average effective ice thickness over the n hour period. Fluctuations in \vec{H}_e can be a result of variations of \vec{I} or H . However, one would expect that the true ice thickness H would vary over a considerably longer time scale than that of \vec{I} . Thus, the shorter term fluctuations in \vec{H}_e will most likely be the result of variations in \vec{I} , and this information can be used to calculate the variations in the forces which result from horizontal pressure gradients and internal ice stresses. Moreover, minimum values of \vec{H}_e will tend to reflect the actual ice thickness H since the tensile strength of pack ice is relatively small with respect to its compressive strength (Mellor, 1983).

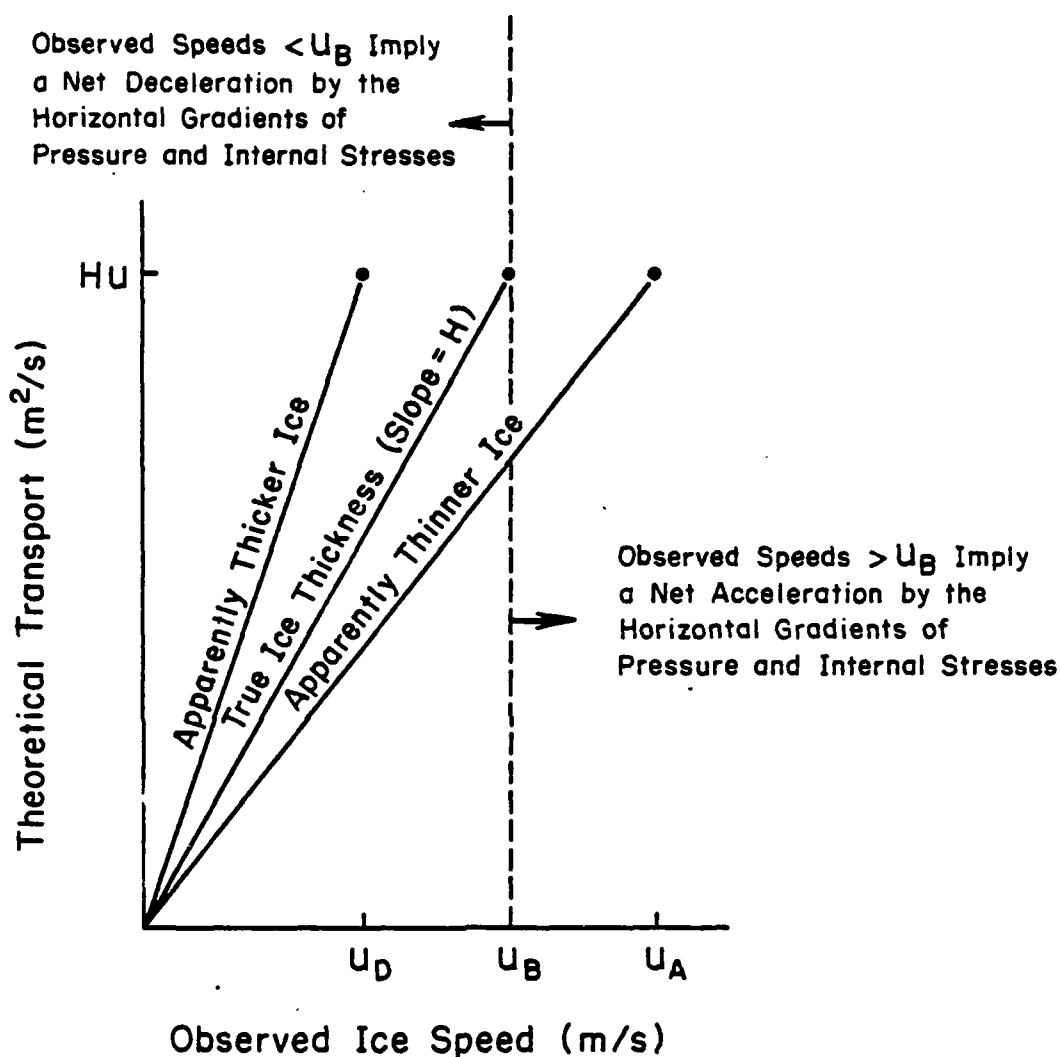


Fig. 2. The effect of the horizontal gradients of pressure and stress on the determination of the effective ice thickness. For the observed ice speed U_D (U_A), the effect is a net deceleration (acceleration) which makes the ice appear thicker (thinner) than it actually is.

3. EFFECTIVE ICE THICKNESSES IN THE BEAUFORT SEA

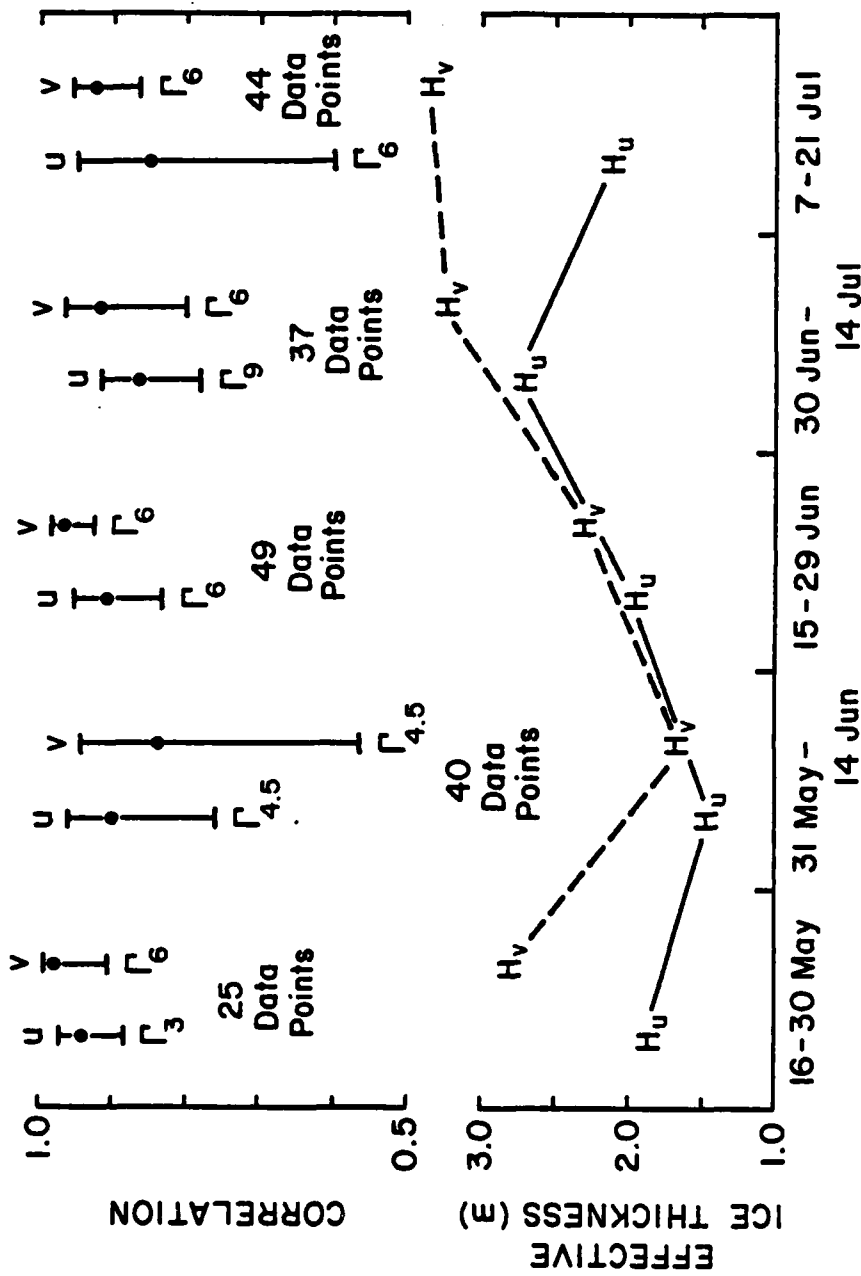
Wind speed and ice motion data from the manned camps of the Arctic Ice Dynamics Joint Experiment (AIDJEX) were used to calculate \vec{H}_e in the Beaufort Sea during May-September 1975. Wind stress was calculated following Amorochio and DeVries (1981). Six hour averages of the observed ice speeds and theoretical ice transports were correlated over 15 day periods by varying Γ such that

$$e^{-\Gamma t} = 0.1 \text{ for } \left\{ \begin{array}{l} t=3 \text{ hr} \\ t=4.5 \text{ hr} \\ t=6 \text{ hr} \\ t=9 \text{ hr} \end{array} \right.$$

These values of Γ will be referred to as Γ_3 , $\Gamma_{4.5}$, Γ_6 , and Γ_9 , respectively.

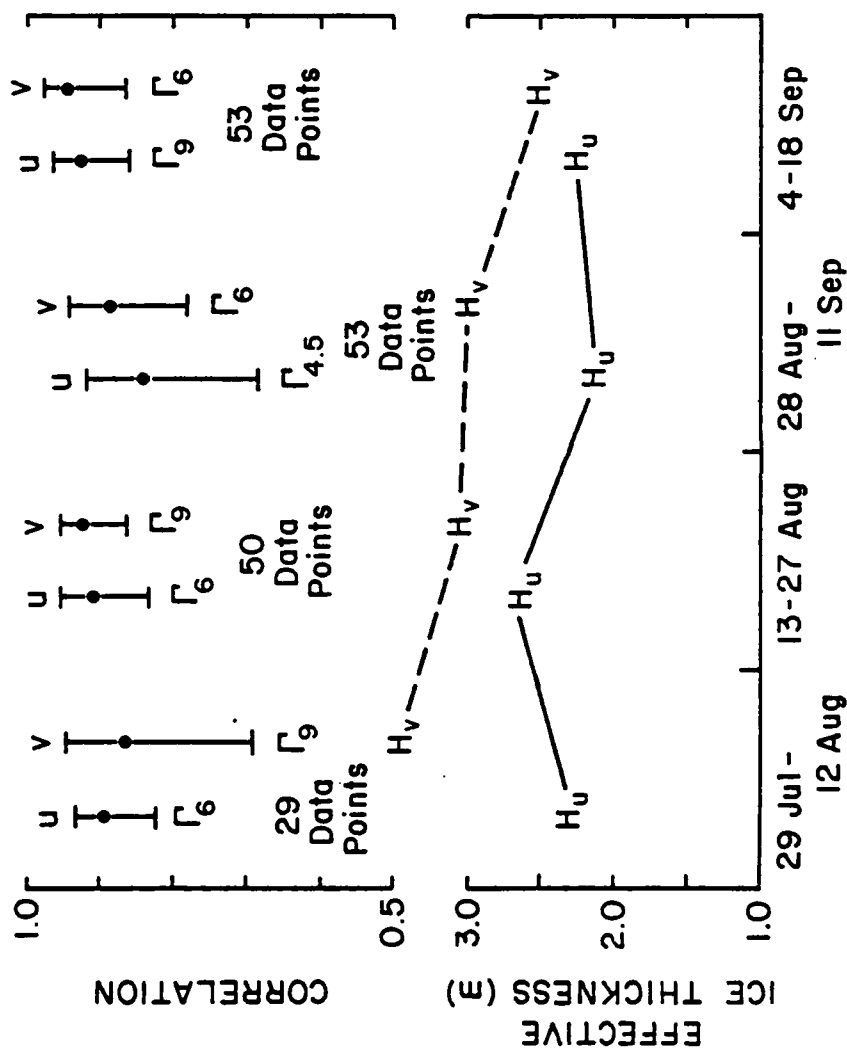
The maximum linear correlations for 16 May-21 July 1975 at 15 day intervals are shown in Fig. 3. All the correlations are ~ 0.85 or greater. The corresponding \vec{H}_e are also shown in Fig. 3. During 16-30 May and 7-21 July, H_v is significantly greater than H_u , the implication being that the y component of \vec{I} had a greater decelerating effect than the x component of \vec{I} . Thus, the ice appears thicker in the y direction during the 16-30 May and 7-21 July periods.

The linear correlations for 24 July-18 September 1975 at 15 day intervals are shown in Fig. 4. Once again, the correlations are ~ 0.85 or greater. Also, during this period H_v is larger than H_u . These and the May-July variations of \vec{H}_e can be associated with the direction of movement of the ice. During 16 May-21 July 1975, most of the motion was in the y direction (approximately east/west). This motion of the ice was most likely restricted by



TIME PERIODS, 1975

Fig. 3. Linear correlations (top) between observed ice speeds and theoretical ice transports, $\pm 90\%$ confidence limits. The r factor which gave the best correlation and the number of data points (at 6 hr intervals) used to calculate the correlation are also given. Effective ice thickness components (bottom) were determined using a least squares fit.



TIME PERIODS, 1975

Fig. 4. Linear correlations (top) between observed ice speeds and theoretical ice transports, $\pm 90\%$ confidence limits. The Γ factor which gave the best correlation and the number of data points (at 6 hr intervals) used to calculate the correlation are also given. Effective ice thickness components (bottom) were determined using a least squares fit.

adjacent ice in the pack (Fig. 5). This would lead to a general increase in \vec{H}_e , especially in the y direction.

For the period of 29 July-18 September 1975, the motion was primarily southeastward toward coastal regions which are typically ice free during the summer (Fig. 5). Thus, one would expect less internal ice stresses, and \vec{H}_e does tend to decrease during the 29 July-18 September period (Fig. 4), especially the H_v term. By the end of August, H_u is calculated at 2.2 m, which is in good agreement with the average ice thickness of 2.3 m measured during August 1975 at the most centrally located AIDJEX manned camp. This would imply that $I_x \approx 0$ during the end of August.

The high correlations between the six hour averages of actual ice velocities and theoretical ice transports indicate that our expressions do a good job in reproducing the general physics of the true motion of the ice parcel. This brings us back to the point of whether \vec{I} can be associated with the Lagrangian velocity \vec{U} . The ability to obtain high correlations over a four month period seems to imply that \vec{I} can be considered independent of \vec{U} for these mathematical calculations. Also, the values of \vec{H}_e are reasonable, and this too indicates $\vec{I} \neq f(\vec{U})$. It appears that the velocity following a parcel of ice is not strongly related to the horizontal gradients of pressure and internal stresses that the ice parcel encounters along its path. A simple example of such a situation is $\vec{U} \rightarrow 0$ for either a) $\vec{\tau} = 0$ or for b) the effect of \vec{I} as the ice compacts under a given wind stress. Similarly, $\vec{U} = 0$ for either a) wind-induced motion or for b) $\vec{\tau} = 0$ and the ice pack relieves its built-up compression. Thus, the fact that \vec{I} may be related to the horizontal velocity gradients of the ice pack does not seem to hamper our ability in making the above calculations using Lagrangian data.

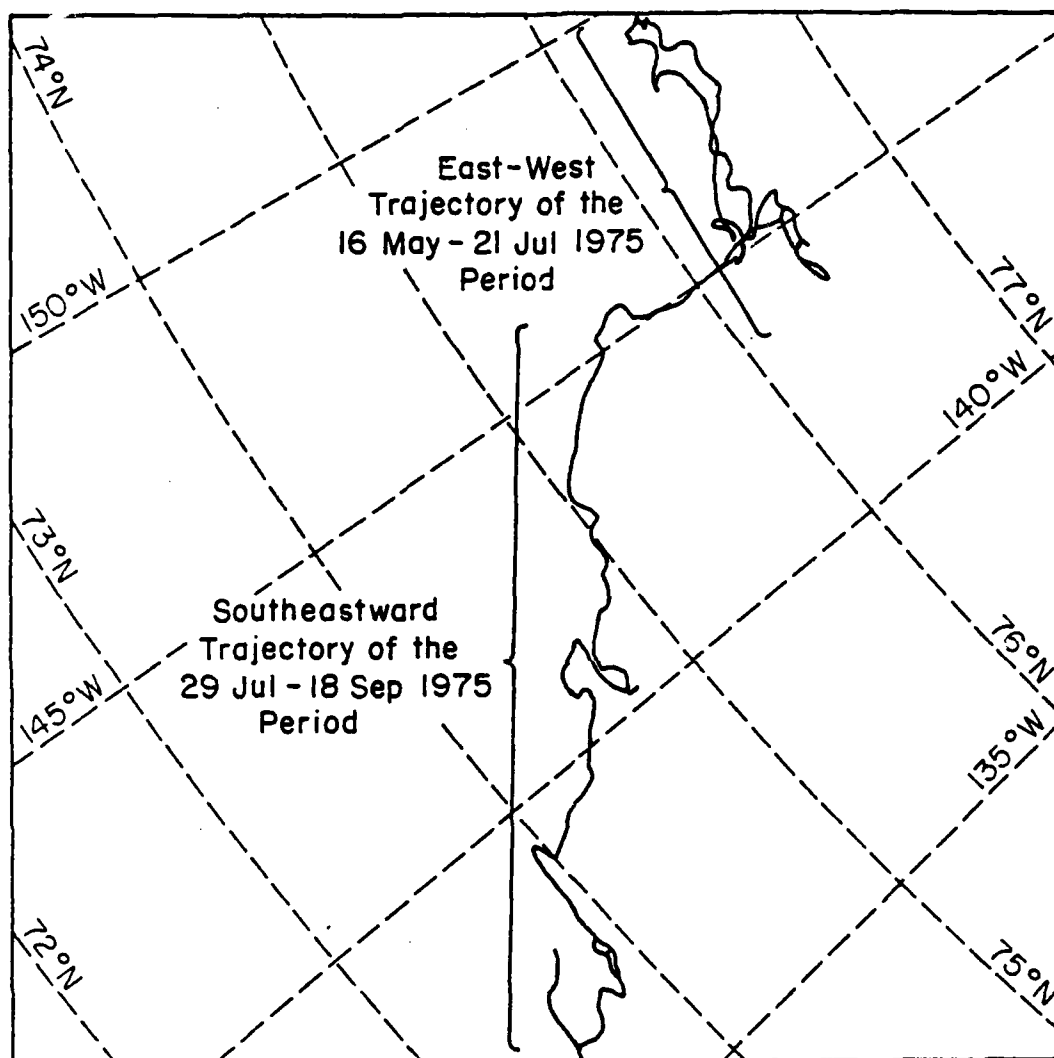


Fig. 5. Motion of the AIDJEX manned camp "Big Bear" for the period of 16 May-18 September 1975.

REFERENCES

- Amorocho, J., and J.J. DeVries; Reply to "Comment on a New Evaluation of the Wind Stress Coefficient Over Water Surfaces." J. Geophys. Res., 86(C5), 1981, 4308.
- Hibler, W.D., III, 1979: A dynamic thermodynamic sea ice model. J. Phys. Oceanogr., 9, 815-846.
- Lewis, J.K., and W.W. Denner, 1984: A theoretical response of a wind-driven oceanic surface layer and its application to the analysis of Lagrangian measurements. J. Geophys. Res., 89 (C2), 2101-2103.
- McPhee, M.G., 1978: A simulation of inertial oscillations in drifting pack ice. Dyn. Atmos. Oceans, 2, 107-122.
- Mellor, M., 1983: Mechanical behavior of sea ice. Cold Regions Res. and Eng. Lab., Monograph 83- 1, U.S. Army Corps Eng., Hanover, NH, 105 pp.
- Thorndike, A.S., and R. Colony, 1982: Sea ice motion in response to geostrophic winds. J. Geophys. Res., 87(C8), 5845-5852.

SEASONAL VARIABILITY OF THE
PRINCIPLE MODES OF ICE
MOVEMENT IN THE BEAUFORT SEA

ABSTRACT

Sea ice kinematics in the Beaufort Sea are considered in terms of the seasonal variability of the principle modes of movement and the e-folding scales of the time variations of ice translation, divergence, vorticity, and deformation. We find two basic states of movement: a free (inertial) state and a forced state driven by synoptic winds. The free state is the more energetic mode during summer, and this results in relatively small e-folding time scales (of the order of 5 hrs for differential motion). However, it is shown that this summer-time free state leads to a misrepresentation in the calculated ice vorticity and shear deformation. The forced mode of ice motion during summer is seen to differ in character from that of fall, winter, and spring. The differences are shown to follow previous analytical results and can be attributed to the greater effects of internal ice stresses for shorter wavelength atmospheric forcing. Time scales of variations for all but two of the ice kinematic parameters are shown to increase during the non-summer periods.

1. INTRODUCTION

The kinematics of pack ice are in many ways distinctively different from those kinematics of other sea surface phenomena. During the polar summers, when the pack ice has a greater percent of open water, the effect of internal ice stresses is lessened. It is during this summer season that the kinematics of sea ice is most similar to the rest of the world's ocean surfaces. Most notably, summer sea ice movement exhibits inertial oscillations (amplitudes of up to 30 cm/s) imposed onto the mean motion of the ice (McPhee, 1978a; Khandekar, 1980). However, the internal ice stress is still an important factor. MCPhee (1978a) found that the summer inertial oscillations were not reproduced unless a damping factor was incorporated which suppressed movement as a result of the stiffness or compactness of the ice. Considering the spatial variability of summer ice movement, Colony and Thorndike (1980) found that synoptic ice motion on the scale of ~ 100 km is highly coherent (squared coherency of ~ 0.9) while the coherency of inertial ice motion was of the order of 0.65. This is as one would expect for the open oceans, with the variability at the higher frequencies (inertial periods) being induced by spatial variations in the synoptic wind pattern.

The movement of sea ice during the polar winter reflects a situation of almost zero percent open water and a maximum effect of internal ice stresses. In this situation, movement of the pack ice is much more restricted and is least like that of the surfaces of the rest of the world's oceans. In particular, the coherency of the ice pack motion at almost all frequencies can be expected to be quite high. Moreover, the response of the ice to forces which cause divergence is changed. Hibler (1974) showed analytically that, as a result of internal ice stresses, atmospheric lows would be expected to cause ice convergence in winter while lows during summer would cause ice divergence.

In this paper, we consider sea ice kinematics in the Beaufort Sea in terms of the seasonal variability of 1) the principle modes of movement, 2) the time scales of variations of the various ice kinematic parameters, and 3) the effects of internal ice stresses. We consider the translation and differential motion of pack ice, and we find two basic states of movement: a) a free (inertial) state and b) a forced state driven by the synoptic winds. The free state is the more energetic mode of motion during summer, and this results in relatively small e-folding time scales of the various ice kinematic parameters. However, the summer-time free state can also lead to a misrepresentation in some of the calculated differential motion parameters.

The summer-time forced state is seen to differ in character from that of the fall, winter, and spring. The differences follow the theoretical findings of Hibler (1974) and can be attributed directly to the greater effects of internal ice stresses for shorter wavelength atmospheric forcing. Time scales of variations for all but two of the ice kinematic parameters increase during these non-summer periods.

2. ICE POSITION DATA

The data used in this study were from the Arctic Ice Dynamics Joint Experiment (AIDJEX) which began in March 1975 and ended in May 1976 (Fig. 1). Four sites on the Beaufort Sea pack ice were initially manned, and were tracked by the Navy Navigation Satellite System (± 60 m). In addition, an array of self-tending buoys were placed around the four manned sites. Ice kinematics were determined for periods during which at least three of the four manned camps were providing position data (Thorndike and Cheung, 1977):

25 Apr - 22 Jul 1975 (all four sites)
29 Jul - 7 Oct 1975 (all four sites)
7 Oct - 29 Dec 1975 (3 sites)
1 Jan - 7 Mar 1976 (3 sites)
13 Mar - 2 May 1976 (3 sites)

During the winter, station 3 (radio call name Snow Bird) was split by cracks and the antennas were moved short distances several times. These moves, however, were of the order of 10 m, well within the 60 m rms fix error of the positioning system (personal communication, Dr. A. S. Thorndike). The region of ice delineated by the manned camps was of the order of a hundred kilometers. The position data were at three hour intervals, and the coordinate system was centered at the north pole with the positive x direction being approximately northward and the positive y direction being approximately westward.

In this paper we will concentrate on four subsets of the ice kinematic data:

May 1975 - Spring
August 1975 - Summer

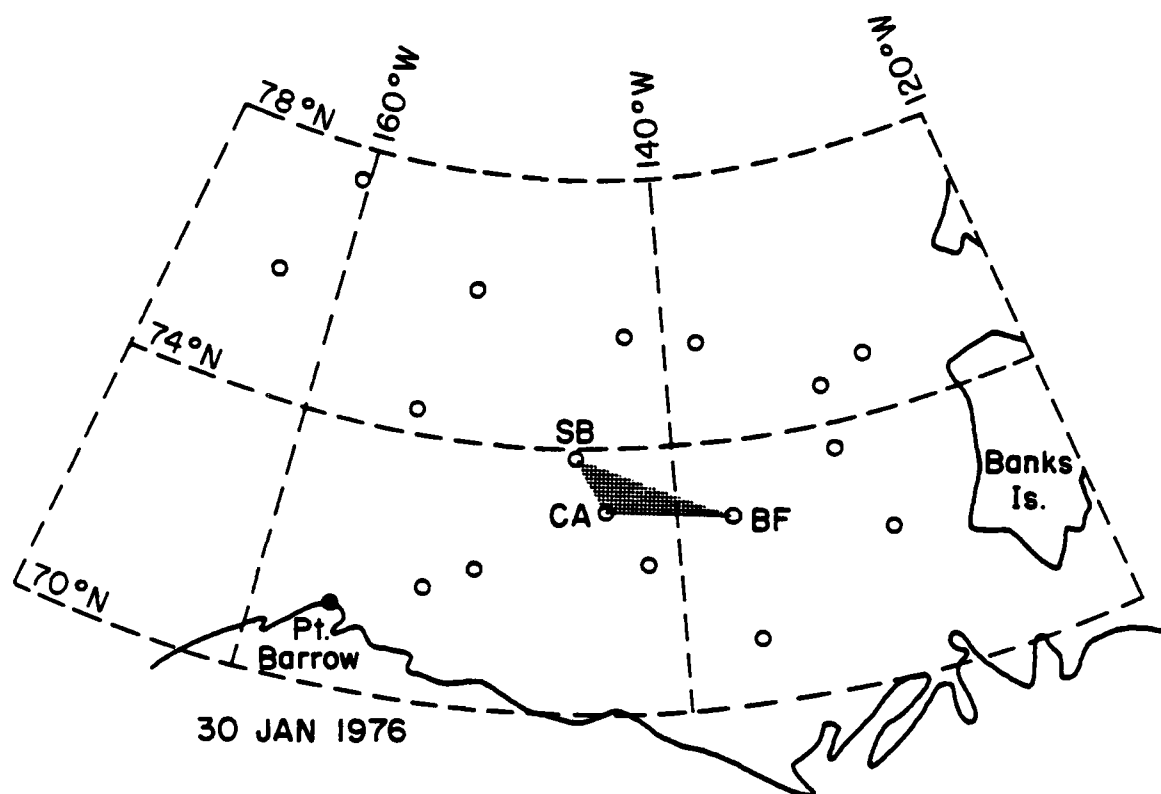


Fig. 1.

Locations of a number of AIDJEX data buoys and manned camps for 30 January 1976. The Big Bear manned camp, originally located at approximately the center of the shaded region, was abandoned in October 1975.

November 1975 - Fall
February 1976 - Winter.

Moreover, we consider fluctuations at all frequencies. In a previous calculation of the ice kinematics using the same position data, McPhee (1978b) considered steady-state conditions by low-pass filtering the data. This effectively removed the energy at periods which included inertial oscillations. As we shall show, inertial oscillations dominate all the kinematic parameters of the ice during summer, and additional short-term oscillations still occur during other seasons.

3. ICE KINEMATICS

As opposed to defining ice kinematics based on the motion of each individual station on the ice, the stations are considered to delineate a parcel of ice. The kinematics are then defined as the translation of that ice parcel as well as any rotation, area change, or deformation that occurs during the translation (Fig. 2): The motion of the ice parcel is decomposed into five independent components: translation (\vec{U}), vorticity (ζ) (rotation rate), divergence (D), normal deformation rate (N), and shear deformation rate (S). The last four of these parameters describe relative motion within the ice parcel as it translates:

- ζ - the change in the orientation of the parcel (without a shape or size change),
- D - the change in the size of the parcel (without an orientation or shape change).
- N - the change in the shape of the parcel due to forces acting normal to the sides of the parcel (without a size or orientation change), and
- S - the change in the shape of the parcel due to forces acting parallel to the sides of the parcel (without a size or orientation change).

We will refer to the above four parameters as the differential kinematic parameters (DKP).

The ice parcel dealt with in this study was that delineated by the AIDJEX manned camps. The three hour position data of these manned camps were used to calculate the time histories of \vec{U} and the

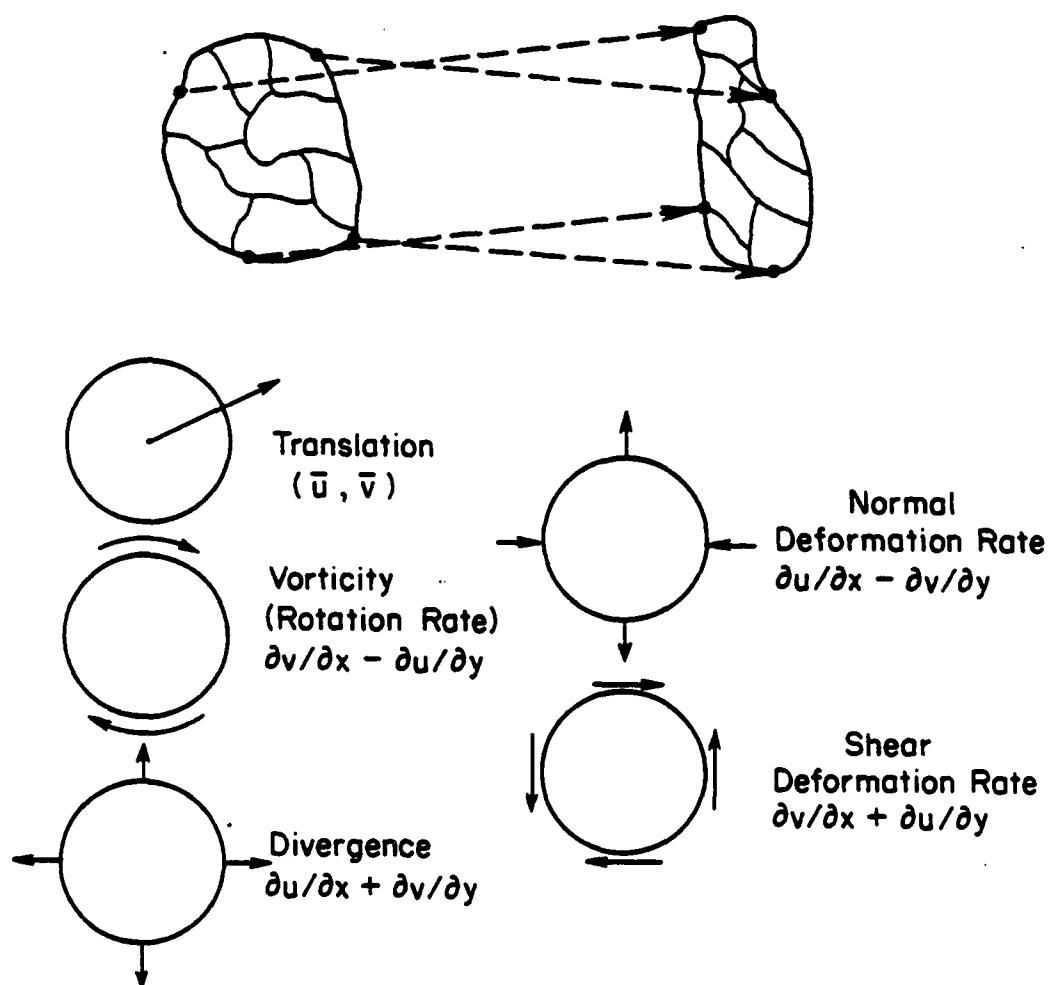


Fig. 2. Mathematical and physical definitions of the five basic components of the motion of a parcel of ice.

DKP based on the solution technique of Kirwan et al. (1984). This technique is based on the analytical solutions to the model equations

$$u = \frac{\partial u}{\partial x} x + \frac{\partial u}{\partial y} y + f$$

$$v = \frac{\partial v}{\partial x} x + \frac{\partial v}{\partial y} y + g$$

where (u,v) are the relative velocity components of a drifter, (x,y) are the position coordinates of the drifter relative to the center of expansion of the Taylor's series, and (f,g) represent higher-order terms and variations from the model. Although the analytical solutions are non-linear, it can be shown that they may be approximated by linear expressions if the time interval T between successive position fixes for the camps is such that $T \ll 2/D$ and $T \ll 2/[N^2 + S^2 - \zeta^2]^{1/2}$. For these small time intervals, the non-linearity resulting from differential motion within the parcel is negligible, and the linear form of the analytical solutions may be used to calculate the DKP. To insure that the three hour position interval fulfills this requirement, $2/D$ and $2/[N^2 + S^2 - \zeta^2]^{1/2}$ are calculated for each set of DKP parameters at each three hour interval.

Examples of time series of the ice translation speed, vorticity, and divergence are given in Figs. 3-6. Normal and shear deformation rates showed fluctuations similar to the vorticity and divergence at about the same amplitudes. The data show that, during early summer 1975, the oscillations of the ice kinematics became higher in frequency and larger in amplitude (Figs. 3 and 4), with motion of the inertial frequency being very energetic. These high frequency fluctuations continued through early fall of 1975 but were damped out during early October. The kinematics for the fall of 1975 (Fig. 5) were longer in period with smaller amplitude oscillations. The ice

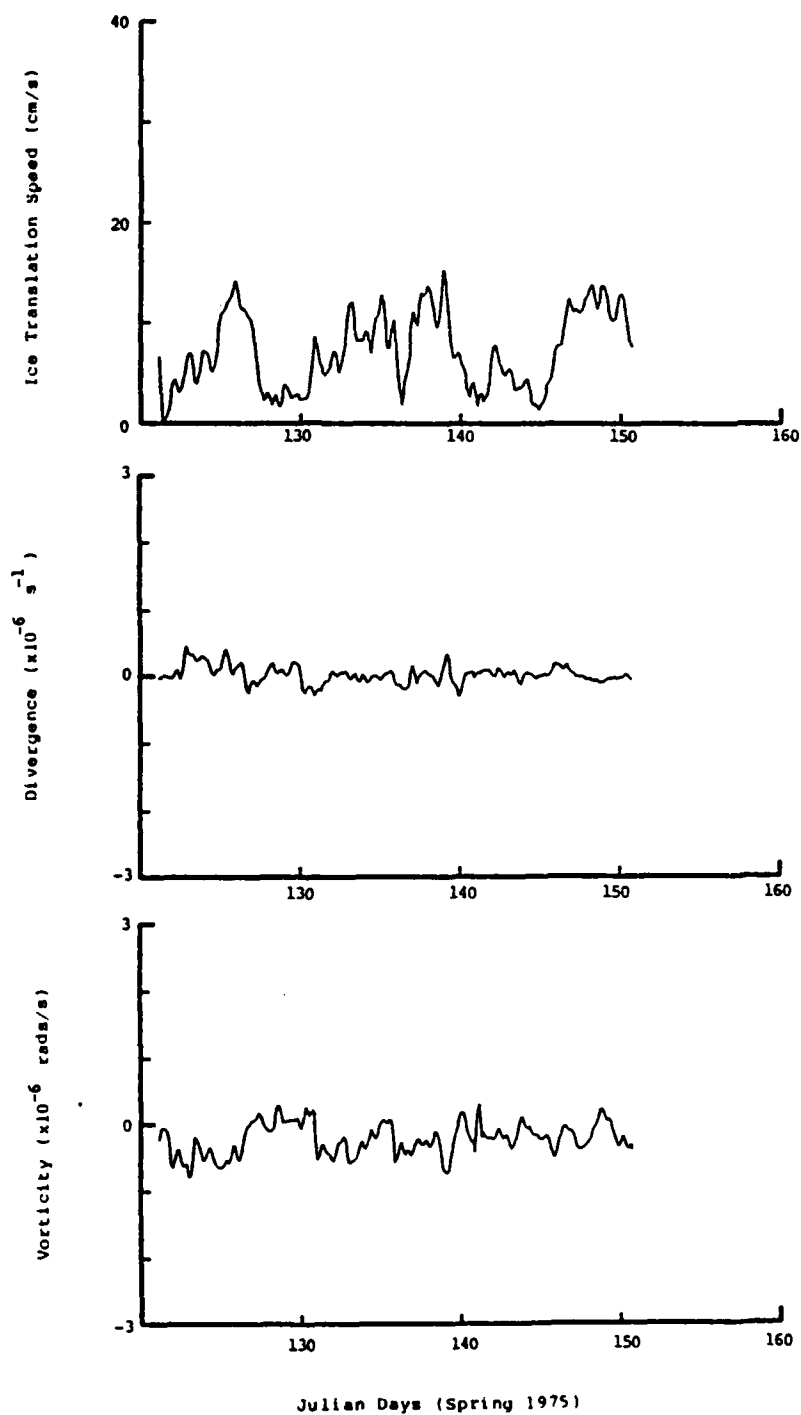


Fig. 3. Variations in the a) speed, b) divergence, and c) vorticity of the AIDJEX manned camp array during May 1975.

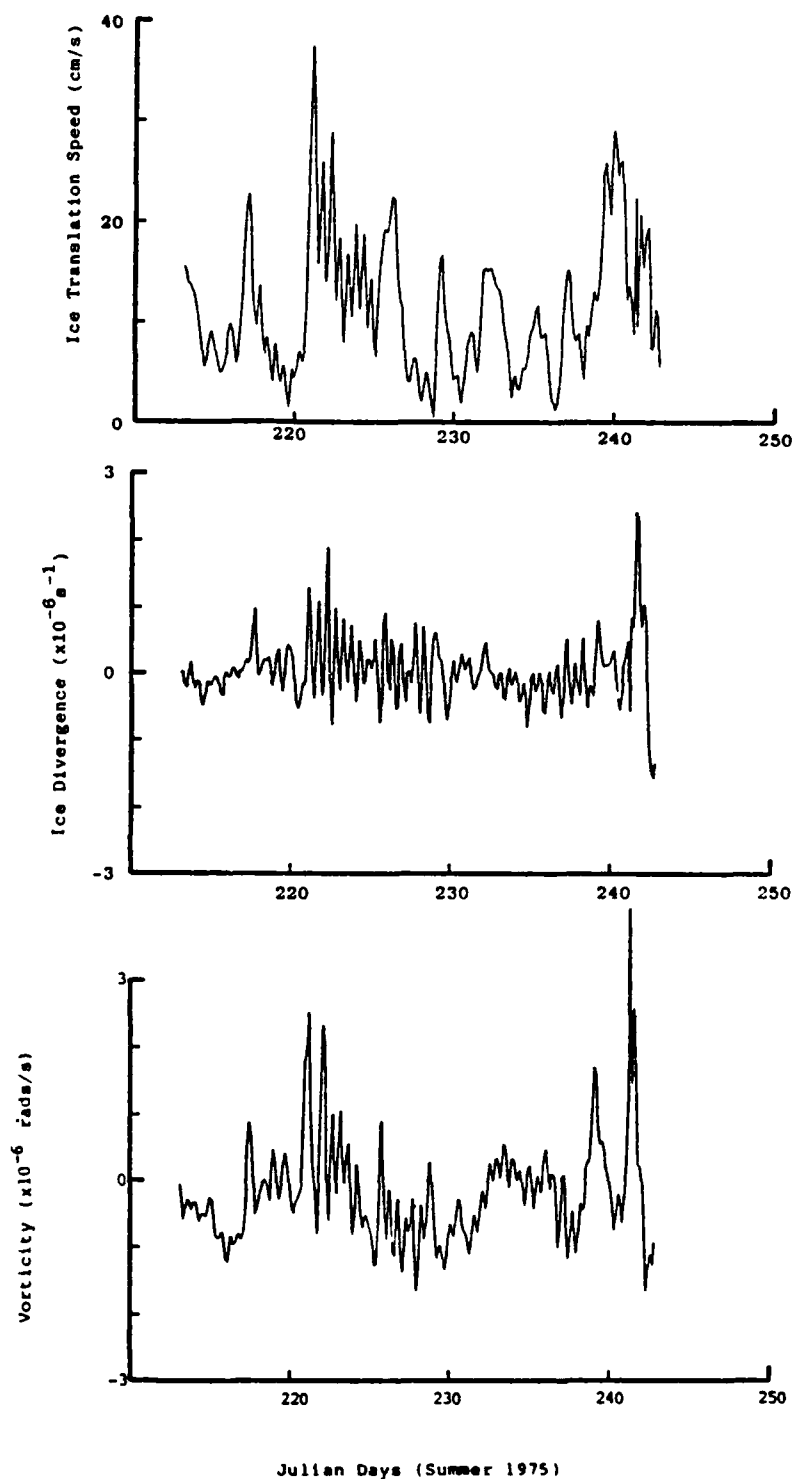


Fig. 4.

Variations in the a) speed, b) divergence, and c) vorticity of the AIDJEX manned camp array during August 1975.

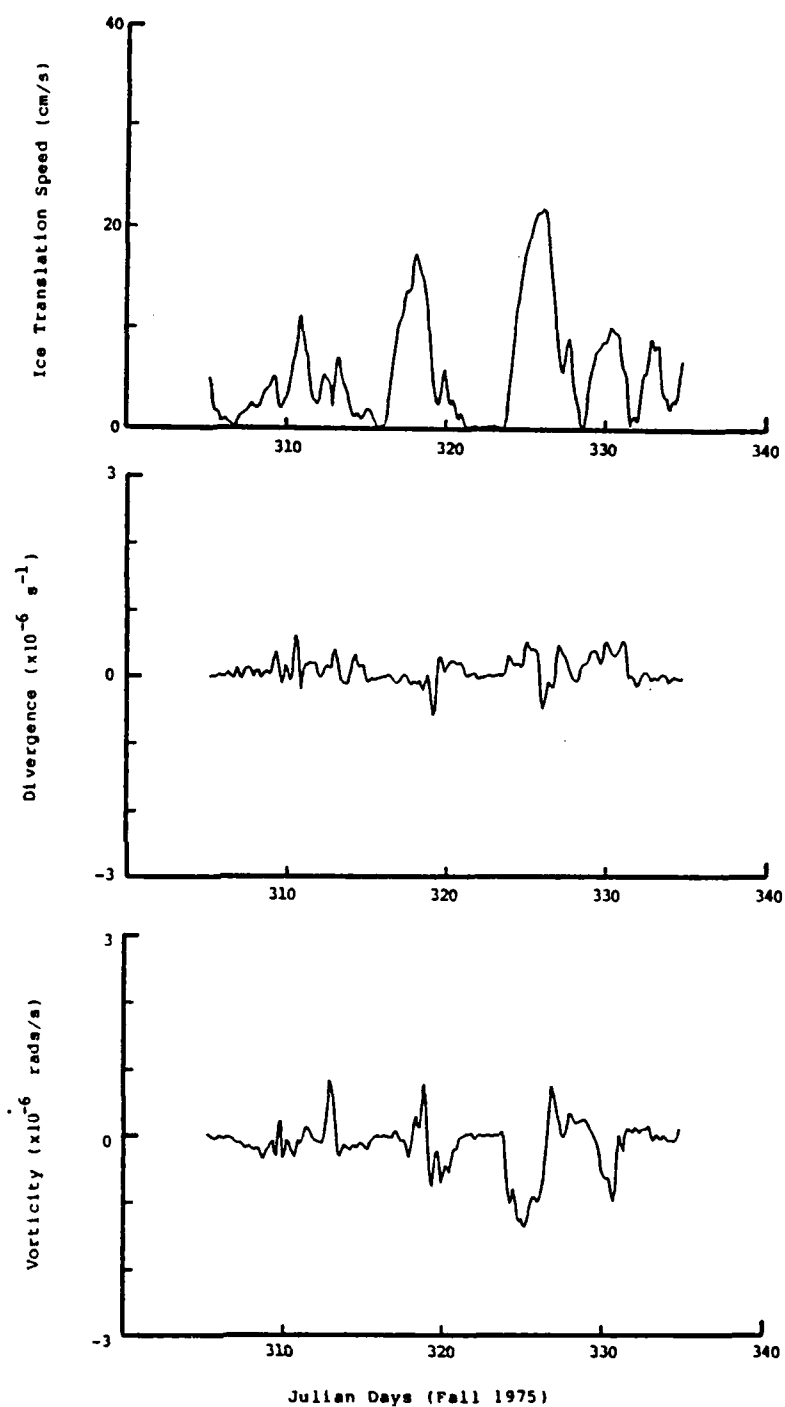


Fig. 5. Variations in the a) speed, b) divergence, and c) vorticity of the AIDJEX manned camp array during November 1975.

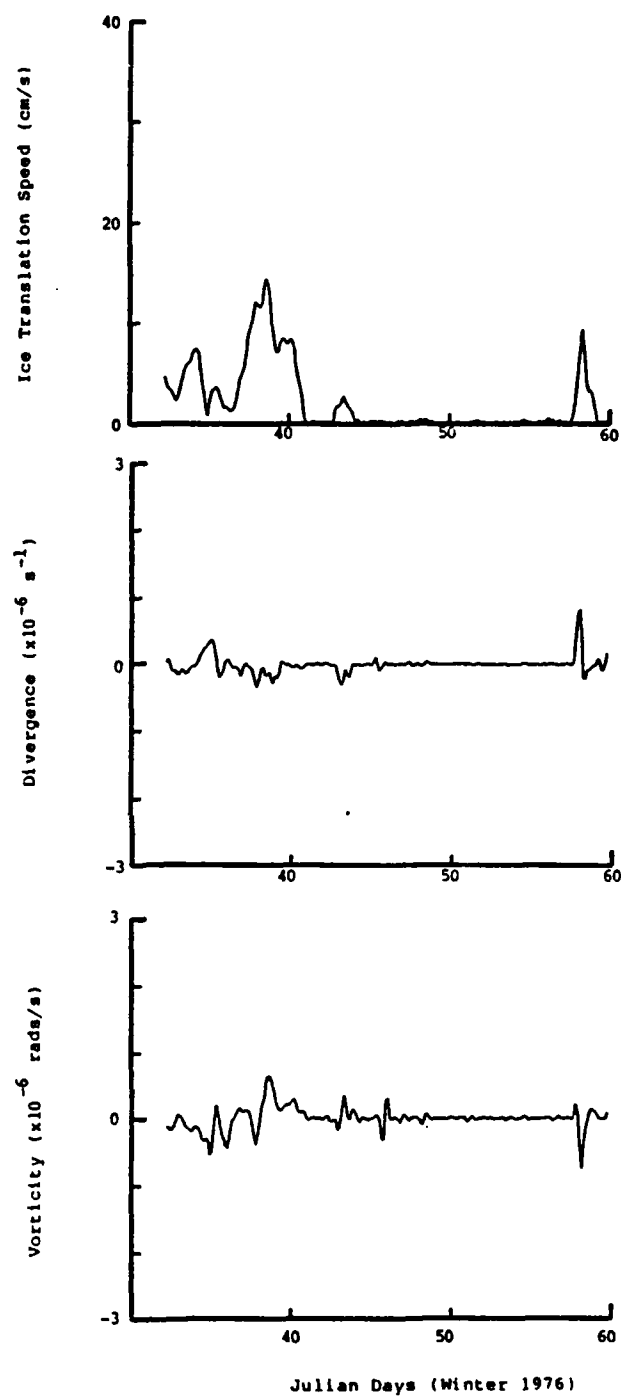


Fig. 6. Variations in the a) speed, b) divergence, and c) vorticity of the AIDJEX manned camp array during February 1976.

kinematics for the first two months in 1976 showed a continued decrease in variation amplitudes, with February 1976 (Fig. 6) having a long period of relatively little motion. Several individual events can be delineated during this period, as well as in the kinematic time histories for March 1976 (not shown). After March, the amplitudes of the oscillations of the ice kinematics became larger, similar to those of May 1975 and October through December 1975.

The DKP were used to calculate T , the time period between position fixes such that $T \ll 2/D$ and $T \ll 2/[N^2 + S^2 - \zeta^2]^{1/2}$. The results are shown in Table 1. For those periods of relatively little differential motion (1 January - 24 April 1976), the time period restriction was over 5 days. The shortest time period restriction (0.8 days) occurred during the period of relatively large DKP variations (19 July - 7 October 1975.)

TABLE 1. Time interval restriction between position fixes based on the calculated DKP.

<u>Period</u>	<u>T (Days)</u>
25 Apr-22 Jul 1975	1.5
29 Jul-7 Oct 1975	0.8
7 Oct-29 Dec 1975	2.9
1 Jan-7 Mar 1976	5.3
13 Mar-2 May 1976	5.7

4. DISCUSSION

Summer Time Conditions

We will first take up the motion seen during the summer (Fig. 4). This time period is characterized by oscillations at the inertial frequency (~ 12.5 hr) superimposed upon background variations. However, a closer examination of the individual drift tracks shows that the inertial oscillations seen in the vorticity (often with changes in sign) is not a true indication of the ice parcel vorticity. Rather, this is an artifact of the calculations when dealing with nearly free-drift conditions (with relatively small internal ice stress effects) and determining variations of velocity in a direction normal to the velocity (i.e. $\partial u/\partial y$ and $\partial v/\partial x$). A schematic of this summer free drift state is shown in Fig. 7. The trajectories of the individual stations show each undergoing inertial oscillations (anticyclonic motion) but with slightly different phases and/or amplitudes. At any instant in time, these spatial variations can give a calculated $\partial u/\partial y$ and $\partial v/\partial x$ which is not a true indication of the ice parcel motion (Fig. 7). On the other hand, the calculated $\partial u/\partial x$ and $\partial v/\partial y$ are valid representations of the ice kinematics. Thus, while there is actual diverging and converging within the ice parcel at an inertial period, the variation in vorticity is only a result of the calculation technique (actually ζ could be zero at all times for each element of the ice parcel).

One of the interesting effects of the divergence/convergence process is the variation of the translation speed U of the ice (Fig. 4). The data show that U increases for $D > 0$ and decreases for $D < 0$. Thus, the free state motion typically consists of a translating ice parcel whose elements are circling anticyclonically, with the amplitude of rotation increasing during the period of divergence but decreasing during the period of convergence.

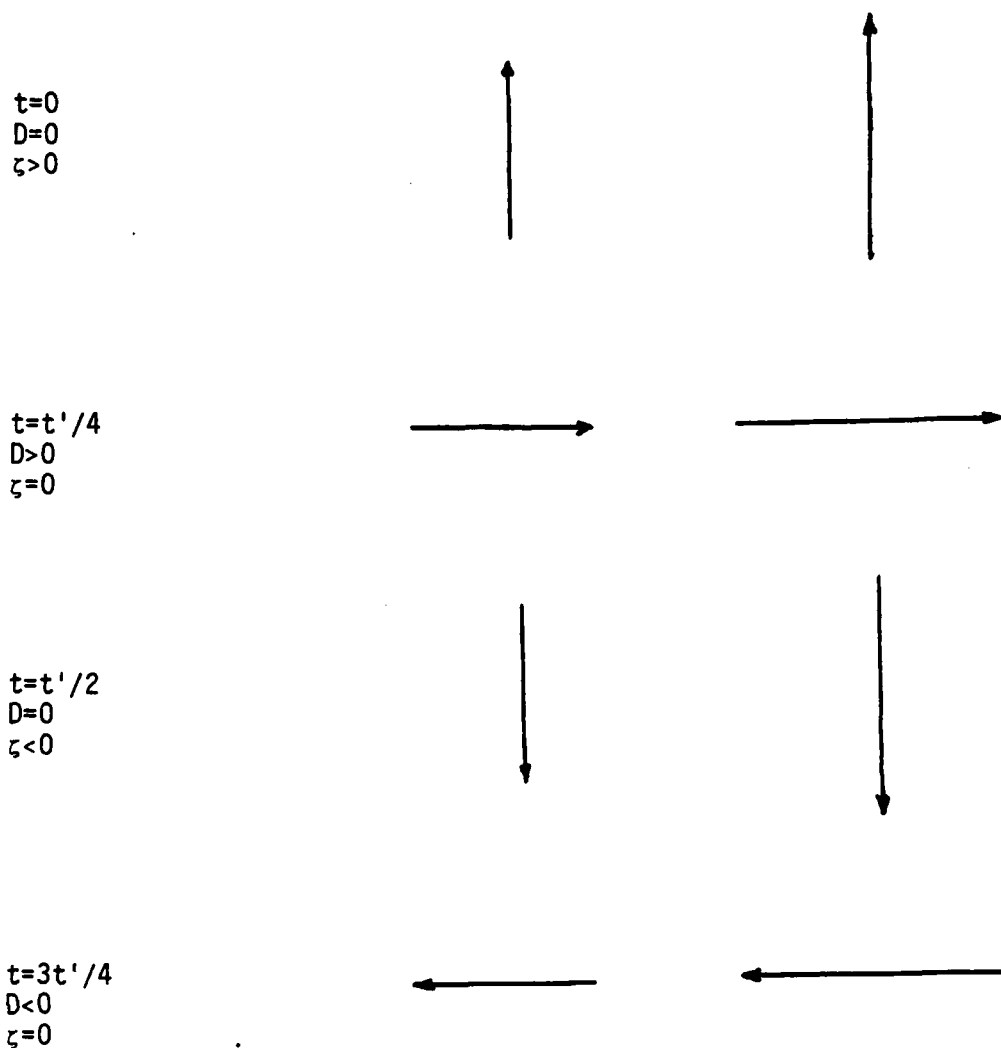


Fig. 7.

Schematic of the summer free drift state composed of inertial oscillations of varying magnitude. The inertial period is t' .

Analytically, the free drift state can be modeled by the expression

$$d\vec{U}/dt + f\vec{k} \times \vec{U} = \vec{\tau}/H\rho \quad (1)$$

where \vec{U} is the ice velocity, f is the Coriolis parameter, $\vec{\tau}$ is the wind stress, H is the ice thickness, and ρ is the ice density. For $\vec{U}=0$ at $t=0$, the analytical solution to (1) can be formulated in terms of D and ζ as

$$\zeta_t = \int_0^t [\text{curl}_z \vec{\tau}|_{t-\gamma} \cos f\gamma - \nabla \vec{\tau}|_{t-\gamma} \sin f\gamma] d\gamma / H\rho \quad (2)$$

$$D_t = \int_0^t [\nabla \vec{\tau}|_{t-\gamma} \cos f\gamma + \text{curl}_z \vec{\tau}|_{t-\gamma} \sin f\gamma] d\gamma / H\rho.$$

The expressions in (2) show the inertial variations in ζ and D ($\cos f\gamma$ and $\sin f\gamma$) which are a result of the Coriolis effect in conjunction with the spatial variations of the driving force $\vec{\tau}$. We note that inertial oscillations of ζ and D can be caused by both the curl of the wind stress as well as the horizontal divergence of the wind stress.

We now focus on the lower frequency (background) variations of the summer time ice kinematic parameters. Using the above expressions, Lewis and Denner (1984) obtained expressions for a constant wind stress, and these give

$$D = \text{curl}_z \vec{\tau} / fH\rho$$

$$\zeta = -\nabla \vec{\tau} / fH\rho.$$

These expressions would imply that ζ and D of the ice take on the sign of the curl of the wind stress:

ζ and $D < 0$ for atmospheric highs

(3)

ζ and $D > 0$ for atmospheric lows.

In order to verify this result, we consider the atmospheric pressure in the vicinity of the manned camps. Fig. 8 shows two distinct low pressure periods centered on days 222 and 239. For a 3 to 4 day period after these lows, the means of ζ and D (Fig. 4) are seen to be both positive. In addition, during the high pressure period before day 215, both ζ and D tended to be negative. However, for the period of days 225-239, ζ and D tended to be opposite in sign. Thus, this simplified concept of summer time ice kinematics is not totally correct. The additional complexity arises as a result of the internal ice stresses. In a steady-state situation (our background variations approach this condition), Hibler (1974) showed analytically that the internal ice stresses and the spatial gradients of the wind can determine whether the ice responds by converging or diverging. For relatively weak spatial gradients of the wind, the internal ice stresses become unimportant, and one obtains relationships similar to those in (3). However, for relatively strong spatial gradients in the wind stress, Hibler's expressions show that the internal ice stress becomes critical, with the results being:

$\zeta < 0$ and $D > 0$ for atmospheric highs

(4)

$\zeta > 0$ and $D < 0$ for atmospheric lows.

This is as we found during days 225-239. Thus, the overall summer background variations can be represented by a forced state, driven by the synoptic winds, in which the importance of internal ice stresses varies.

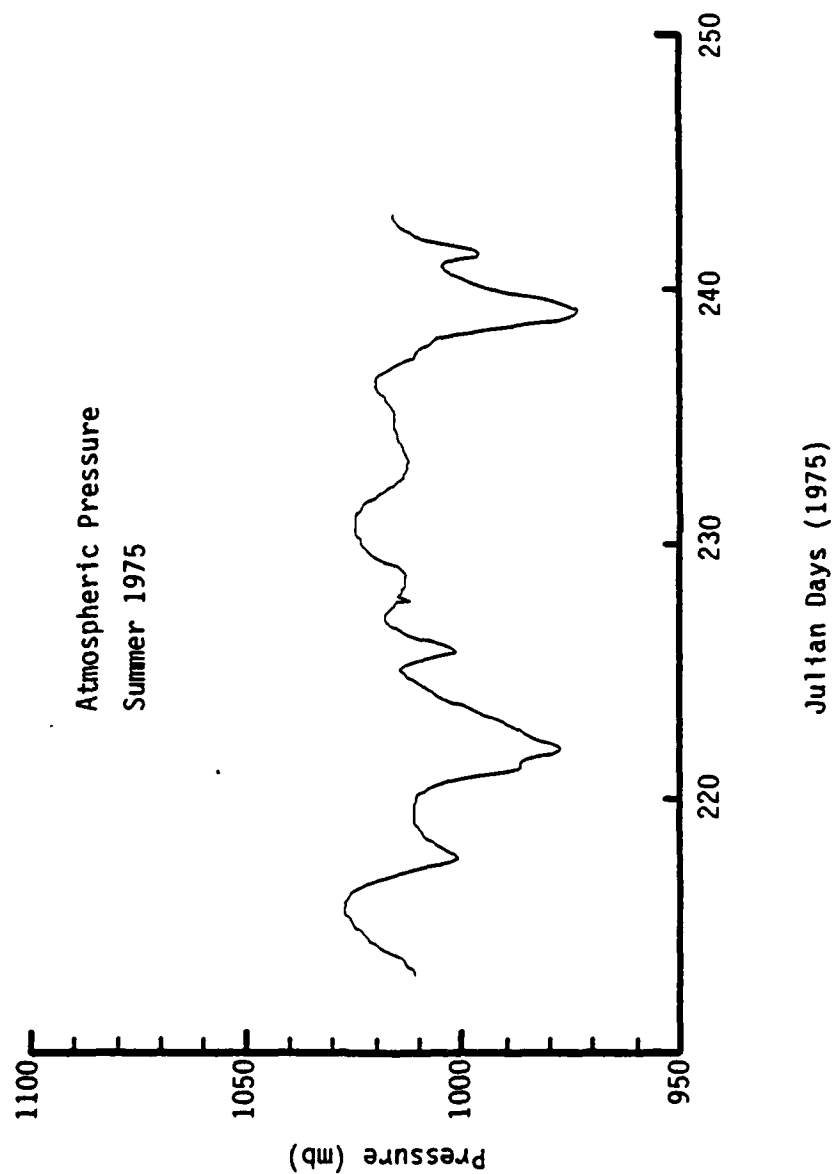


Fig. 8. Variations of the atmospheric pressure in the vicinity of the manned camps during August 1975.

Non-Summer Time Ice Kinematics

We now consider the ice kinematics for the spring, fall, and winter (Figs. 3, 5, and 6). One first notes that the inertial variations of the kinematic parameters are still detectable, but these variations have been greatly reduced. One might suppose that this free state of motion has been practically eliminated, but this is not entirely true. Analysis of the trajectories of the individual ice stations shows that the ice parcel can still undergo inertial oscillations (although with reduced amplitudes of 5 to 10 cm/s), but the compactness and rigidity of the pack ice results in near solid-body movement. Thus, the inertial variations seen during the summer (especially in the DKP) are absent, indicating high coherency of motion over large horizontal scales even at higher frequencies.

The majority of the motion during spring, fall, and winter appears to be that of the forced state of movement in response to regional atmospheric systems. In considering the vorticity and divergence, we find a strong tendency for these terms to be opposite in sign, similar to days 225-239 during the summer. Based on the previously cited results of Hibler, this tendency would indicate that the short wave-length variations in the wind stress dominate the fall, winter, and spring atmospheric forcing. Thus, the internal ice stresses become important and we have the results given in (4). Overall, the ice kinematic data indicate stronger spatial gradients of wind during non-summer months than during summer months. However, the AIDJEX summer and winter surface pressure levels do not support this conclusion. As we will now show, the effect of the spatial pressure gradients can be enhanced or suppressed by a particular multiplier, and this enhancement/suppression can also cause a change in whether the ice diverges or converges.

Lewis and Denner (1984) give the analytical solutions to the equations of steady-state Lagrangian ice motion as

$$\vec{U} = Q \tilde{A} \vec{\tau}_s$$

where

$$\tilde{A} = \begin{bmatrix} \Gamma & f \\ -f & \Gamma \end{bmatrix}$$

$$Q = [(\Gamma^2 + f^2)_{\rho H}]^{-1}.$$

In the above expression, Γ is that factor that represents the dampening of movement with time. In most cases, the Γ (damping) in the x direction will differ from the Γ (damping) in the y direction. Also, Lewis et al. (1985) have shown that the H in the x and y directions are actually the sums of the true ice thickness plus the added mass effects in the x and y directions of the gradients of pressure and internal ice stresses. Thus, H in the x direction will not necessarily equal H in the y direction for these expressions. However, for the development of our argument, we assume Γ and H constant. This allows us to write the vorticity and divergence of the ice as

$$\zeta = [\Gamma \text{curl}_z \vec{\tau} - f \nabla \vec{\tau}] Q$$

$$D = [\Gamma \nabla \vec{\tau} + f \text{curl}_z \vec{\tau}] Q.$$

Thus, we now see that the background ζ and D of the ice is a result of both the curl and the divergence of the wind stress. For wind-driven motion, $\Gamma > 0$ (Lewis and Denner, 1984). Thus, the above expressions show us that the ice vorticity will always have the sign of $\text{curl}_z \vec{\tau}$ but that ice divergence varies:

$$D > 0 \text{ if } \text{curl}_z \vec{\tau} > -\Gamma \nabla \vec{\tau} / f$$

(5)

$$D < 0 \text{ if } \text{curl}_z \vec{\tau} < -\Gamma \nabla \vec{\tau} / f.$$

As indicated by Hibler's work, our expressions show that stronger spatial gradients of the wind stress ($\nabla \vec{\tau}$) can cause ice convergence as opposed to ice divergence. But we also note that $\nabla \vec{\tau}$ is multiplied in (5) by Γ/f . For typical values of Γ (Lewis et al., 1985) and for $f=1.4 \cdot 10^{-4}/s$, Γ/f ranges from 0.5 to 1.5. Thus, the effects of the spatial gradients of the wind stress can be enhanced ($\Gamma/f > 1$) or suppressed ($\Gamma/f < 1$). Therefore, even though the AIDJEX summer and non-summer atmospheric fields have spatial gradients of the same order, it appears that the effects of these gradients tend to be enhanced for low pressure systems during the non-summer periods. This implies larger values of Γ , and the work of Lewis et al. (1985) shows that larger Γ 's typically coincide with greater effects of the horizontal gradients of pressure and internal ice stresses. This is the pattern that one would expect during non-summer periods.

Time Scales of Variations

The results of our ice kinematic calculations and those of others (e.g. Hibler, 1974; McPhee, 1978b; Colony and Thorndike, 1981; Popelar and Kouba, 1983) indicate higher frequency fluctuations during the summer and smaller amplitude, lower frequency fluctuations during the fall, winter, and spring. However, the non-summer conditions still have significant short-term (<24 hrs) variations of the sea ice kinematics. One set of time scales of these variations are given in Table 1. These time scales indicate the effects of the non-linearity of the motion in calculating the kinematic parameters. The results imply that non-linear effects during winter would be negligible for position fixes of approximately every 5 days. However, one would miss major events if a Δt of 5 days were used. To obtain a time scale of how rapidly the ice kinematic parameters vary,

we use a temporal autocorrelation function (see Thorndike, 1985, for an in-depth discussion of sea ice kinematic correlations in time).

We consider seasonal variations by calculating the autocorrelations of \vec{U} and the DKP using the spring, summer, winter, and fall data. We define the time scale of variations as that time lag at which the autocorrelation drops to e^{-1} (e-folding scale). The results are shown in Table 2. These e-folding scales (e_T) can be thought of in terms of persistence, with longer e-folding times implying a slower rate of change in the variable.

For the approximately north/south translation speed u , we see a bimodal structure with maximums in the fall and spring and minimums during the summer and winter ($e_T \sim 12$ hrs). In the approximately east/west direction, the translation speed v has its maximum e-folding times during winter and spring and a minimum e-folding time of 27 hrs in summer. The vorticity of the ice has a bimodal distribution of e_T times similar to the north/south translation speed, with the maximum times being 15-20 hrs and the minimum times being of the order of 10 hrs (summer and winter). The rest of the DKP appear to be quite different than u , v , and ζ . The minimum for D , N , and S all occur during the summer and are about 4 hrs, close to the 3 hr time interval of the position data. Moreover, e_T for N occurs in spring (33 hrs) while $e_{T_{\max}}$ for S occurs in the fall (31.5 hrs). Finally, the e-folding time scales for the divergence D are relatively small for all seasons (maximum of only 12 hrs).

Although the e-folding times are valuable pieces of information when considering the response of sea ice to forcing and when planning experiments, it is tempting to associate particular physical processes with the magnitudes and variability of these times. For example, the larger e_T times for v are likely associated with the

TABLE 2. Seasonal e-folding scales (hrs) for the various ice kinematic parameters calculated using the AIDJEX ice position data.

	<u>Spring</u>	<u>Summer</u>	<u>Fall</u>	<u>Winter</u>
<u>u(\simNorth)</u>	24	16.5	33.5	12.5
<u>v(\simWest)</u>	44	27	34	43.5
<u>ζ</u>	15	9	19.5	8
<u>D</u>	12	4.5	9	7.5
<u>N</u>	33	4	14	10
<u>S</u>	14	4.5	31.5	7.5

predominate east/west winds of the region. We note that u becomes more persistent during fall and spring, the times of seasonal change in the Arctic along with the north/south movements of warm and cold fronts. One interesting aspect of the DKP e_T times is the maximum e_T 's: only 12 hrs for divergence, up to ~20 hrs for vorticity, and of the order of 30 hrs for the two deformation rates. The reason for the divergence always having a relatively small e_T scale is likely a product of not only variations in $r\vec{v}_T/f$ but also the internal ice stresses. In our definitions of the DKP (Fig. 2), we see that only D involves the change in area of the ice parcel. Thus, the tensile and compressive strengths of ice come into play during divergence, with compression opposing convergence and tension opposing divergence. These forces (and the failure of the ice structure upon surpassing critical limits of these forces) will introduce additional variations in D not seen in the other DKP. This plus fluctuations induced by variations in $r\vec{v}_T/f$ would tend to lower e_T for D .

The minimum e_T 's of the DKP during the summer are obviously a result of the energetic inertial variations. The e_T 's are longer during spring and fall, seasons in which there can still be substantial motion but there is little energy at the inertial period. Secondary e_T minimums occur for all the DKP during winter, but this appears to be mostly the result of erratic, small scale motion, possibly introduced by errors in the position fixes.

The longest e_T times for ζ occur during the spring (15 hrs) and fall (19.5 hrs). As previously indicated, ζ during these seasons tends to be driven by the curl of the wind stress. It would appear that $\text{curl}_z \vec{v}_T$ becomes more persistent during spring and fall, a factor indicated by the higher e_T 's of u (north/south) during these seasons along with the high e_T values of v (east/west).

Of all the DKP e_T values, the 33 hr spring value for N and the 31.5 hr fall value for S are the most anomalous. The magnitude of each of these parameters for these seasons are of the same order as the other DKP. Yet, during spring there is a persistence of east-west or north-south elongation of the ice parcel while during fall there is a persistence of northeast-southwest or northwest-southeast elongation. Since N and S are related to the strain rates of the ice, further investigation into the variations of their e_T values is warranted.

We re-emphasize the fact that these e-folding time scales were calculated using position data from the Beaufort Sea. One could expect different time scales in other regions of the Arctic as a result of slightly different governing processes. For example, Popelar and Kouba (1983) monitored the positions of ice camps in the central Arctic and found major changes in the pattern of pack ice deformation as the camps passed over the Lomonosov Ridge. This is an example of topographic influences, the space and time scales of which can be quite different than atmospheric influences.

Finally, we wish to comment on an interesting feature found in some of the spring and winter autocorrelations. This feature is an oscillation with a period of ~ 24 hrs. Fig. 11 shows an example of this phenomena in the autocorrelation function for S during the winter. Such a 24 hr fluctuation was found in the winter D and τ autocorrelations and the spring translation speed and D autocorrelations. The question arises as to what driving force produces these daily fluctuations. Whatever the force may be, it would appear to be associated with the rigidity and compactness of the winter and spring ice conditions.

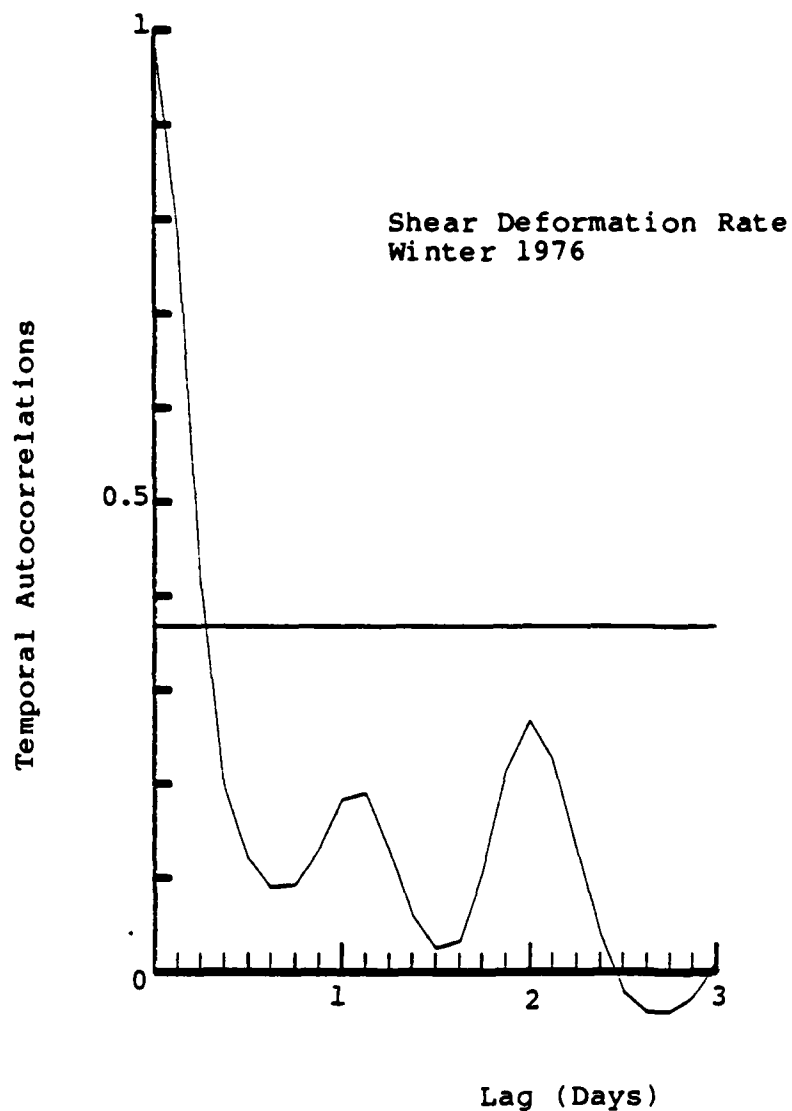


Fig. 9.

Autocorrelation in time of the shear deformation rate during February 1976. Lag interval is 3 hrs. Note the strong diurnal oscillations.

REFERENCES

- Colony, R., and A.S. Thorndike, 1980: The horizontal coherency of the motion of summer Arctic sea ice. *J. Phys. Oceanogra.*, 10, 1281-1289.
- Colony, R., and A.S. Thorndike, 1981: Sea ice strains during 1979. *Proceedings, 6th Int'l Conf. on Port and Ocean Engineering Under Arctic Conditions*, July 1981. Quebec City, Quebec, 27-31.
- Hibler, W.D., III, 1974: Differential sea ice drift. II. Comparison of mesoscale strain measurements to linear drift theory predictions. *J. Glaciology*, 13, 457-471.
- Khandekar, M.L., 1980: Inertial oscillations in floe motion over the Beaufort Sea - observations and analysis. *Atmosphere-Ocean*, 18 (1), 1-14.
- Kirwan, A.D., W.J. Merrell, Jr., J.K. Lewis, R.E. Whitaker, and R. Legeckis, 1984: A model for the analysis of drifter data with an application to a warm core ring in the Gulf of Mexico. *J. Geophys. Res.*, 89 (C3), 3425-3438.
- Lewis, J.K., R.D. Crissman, and W.W. Denner, 1985: Calculation of an effective thickness term for pack ice using Lagrangian data. Submitted, *J. Geophys. Res.*
- Lewis, J.K., and W.W. Denner, 1984: A theoretical response of a wind-driven oceanic surface layer and its application to the analysis of Lagrangian measurements. *J. Geophys. Res.*, 89 (C2), 2101-2103.
- McPhee, M.G., 1978a: A simulation of inertial oscillations in drifting pack ice. *Dynamics of Atmos. and Oceans*, 2, 107-122.
- McPhee, M.G., 1978b: The free drift velocity field across the AIDJEX manned camp array. *AIDJEX Bulletin No. 38*, Univ. of Washington, Seattle, 158-170.
- Popelar, J., and J. Kouba, 1983: Satellite Doppler determination of differential sea ice motion in the vicinity of the North Pole. *Marine Geodesy*, 7, 171-198.
- Thorndike, A.S., 1985: Kinematics of sea ice. In *Sea Ice Geophysics* (Untersteiner, ed.), NATO Adv. Study Inst., Ser. C, Math. Phys. Sci., D. Reidel, Hingham, Mass., in press.
- Thorndike, A.S., and J.Y. Cheung, 1977: AIDJEX measurements of sea ice motion 11 April 1975 to 14 May 1976. *AIDJEX Bulletin No. 35*, Univ. of Washington, Seattle, 149 pp.

ARCTIC AMBIENT NOISE IN
THE BEAUFORT SEA AND
ITS RELATIONSHIP TO SEA
ICE KINEMATICS

ABSTRACT

The generation of Arctic ambient noise is studied in terms of sea ice motion and air temperature fluctuations. Results are presented for three seasons in the Beaufort Sea: summer, fall, and winter. During the summer, the correlations indicate that low frequency (10-32 Hz) ambient noise is primarily a response to the ice rushing through the water. During the fall, low frequency noise fluctuations correlate best with a linear combination of the speed of the ice parcel plus the total deformation rate (shape change) of the ice parcel. This latter factor is an indication of noise generated as individual floes move past one another as they rearrange into a new shape. It is only during winter that the correlations indicate differential motion of other forms (primarily ice convergence) becomes important in generating under-ice noise.

At 1000 Hz during the summer, the data again show that the speed of the ice is best correlated with the noise. For the fall the 1000 Hz e-folding scale is at its minimum of 170 km, and this results in low correlations (of the order of 0.5). The fall data from the southern Beaufort indicate that ice speed and ice deformation are the most important parameters in generating higher frequency noise, while in the northern Beaufort the absolute value of divergence seems to be the most important parameter. This dichotomy of processes is likely the cause of the low spatial coherence and correlations during the fall. The winter results for 1000 Hz are ambiguous, and it is not clear as to whether the ice rushing through the water or differential motion is the primary source for under-ice noise. However, the winter results do show that air/ice heat fluxes are poorly correlated with the noise, even though we present an example of strong high-frequency noise variations that are apparently induced by air temperature variations. The data indicate that thermal-cracking noise intensity can remain high while the air temperature is low, and then decrease as the air temperature rises.

1. INTRODUCTION

As sea ice moves or is put under stress, a considerable amount of noise can be generated within the water column. The frequency of this under-ice ambient noise is dependent upon the length scale of the response of the ice to the forcing, with longer scale lengths generating lower frequency noise. Dyer (1984) classifies Arctic ambient noise into four major categories. The first category ranges between 10^{-2} to 10^{-1} Hz and is attributed by Dyer to quasistatic velocity fluctuations of ocean currents past the hydrophone. The second category is strum (0.5 to 10 Hz), a result of transverse oscillations of hydrophone cables that is induced by the interaction of a cable with ocean currents. These first two categories have not been of much interest to those investigating the relationships between sea ice and under-ice noise. However, Dyer (1984) pointed out that under-ice eddies (Manley and Hunkins, 1985) may have some signature in cable strum.

The third category of Dyer ranges from ~ 1 to ~ 100 Hz with a peak at about 10 to 20 Hz. Dyer indicates that this broad spectrum is caused by ice action of different types. Various studies have been conducted that have related the noise variations at these frequencies to wind blowing over sea ice, the ridging of sea ice, the internal fracturing of sea ice, and internal stresses and bending moments (e.g., Greene and Buck, 1978; Pritchard, 1984; Dyer, 1984; Makris and Dyer, 1985).

The final category of Arctic ambient noise is a second broadly peaked spectrum which ranges from ~ 150 to 5000 Hz. These high frequency oscillations (approaching the order of micro-scales in space) were related by Milne (1972) to the thermal cracking of ice.

This typically occurs at the low air temperatures of a polar winter or spring, but only when the air temperature drops.

In a study of the relationships between ambient noise in the various frequencies bands and the factors related to the cause of the noise, one may consider temporal and spatial scales of the variations of the noise. These scales can offer clues as to the forcing mechanism and to the response of the ice to the forcing. In this paper, we investigate these scales for the Beaufort Sea at several different frequency categories. We realize that the variability of the percent of open water and ice strength (temperature and thickness) must be considered in such an investigation. Based on the seasonal differences observed in mean Arctic ambient noise levels (Greene and Buck, 1977), we have calculated space and time scales of three frequency bands for four seasons:

Summer (using acoustic data from August 1975),

Fall (using acoustic data from November 1975),

Winter (using acoustic data from February 1976), and

Spring (using acoustic data from May 1976).

These space and time scales are then used in interpreting relationships between the ambient noise (1/3 octave bands centered at 10, 32, and 1000 Hz) and observed ice motion and air temperature fluctuations.

Numerous methods have been used to relate Arctic ambient noise levels to sea ice phenomena. Analytical methods include the use of a dynamic ice model to calculate ice strain fields (Denner, personal communication) and the use of a ridging model to calculate energy dissipation (Pritchard, 1984). Denner found no apparent relationship between simulated strain fields and Arctic ambient noise, possibly a

result of the temporal and spatial integration of the model. Pritchard (1984) was more successful, with his method accounting for up to 64% of the noise intensity at 10 Hz and 32 Hz for several 20 day periods during the 1975-76 winter in the Beaufort Sea.

Makris and Dyer (1985) used current, wind, and ice movement data to calculate internal ice stresses and bending moments using the steady-state equations of motion. The internal ice stresses and bending moments were then correlated with ambient noise at low frequencies (10-20 Hz). The correlations were 0.81 and 0.87 with an approximately zero time lag.

Greene and Buck (1978) correlated atmospheric pressure gradients with ambient noise levels in the Beaufort Sea, obtaining correlations of the order of 0.6. This is a reasonable result seeing that wind is the primary forcing of sea ice.

In this paper we also use a statistical model, but we take a different approach than previous researchers in that we use only observed ice motion as determined by satellite-tracked drifters on the ice. This approach eliminates the need to formulate how the ice responds to forcing given its thickness, inertia, rheology, etc. Moreover, in this study we consider the observed ice motion not only in terms of speed, but also in terms of divergence (spreading rate), vorticity (rotation rate), and deformation. In addition, air temperature fluctuations are included in the model, and the statistical relationships are calculated by season. These relationships are determined for 10 Hz, (categories 2 and 3 of Dyer's classification), 32 Hz (category 3), and for 1000 Hz (category 4).

2. THE DATA

During the Arctic Ice Dynamics Joint Experiment (AIDJEX) in 1975-76, approximately 40 satellite-tracked drifters were deployed on the pack ice in the Beaufort Sea (Fig. 1). The movement of the area covered by the manned camp stations (shaded area, Fig. 1) is known relatively accurately (± 60 m), and it is the motion of that ice parcel that is used in this study. Noise data were collected at eight other stations around the manned camp array during various periods from the spring of 1975 to the spring of 1976. The noise data are at 1/3 octave bands centered at 3.2 Hz, 10 Hz, 32 Hz, and 1000 Hz. These data are 45 s averages sampled at 3 hr intervals. Greene and Buck (1977) indicated that the 3.2 Hz signal was likely contaminated by strum, and these data are not presented in detail here. Also, our statistical analyses use the noise data in terms of pressure amplitudes (relative to 1 μ Pa) as opposed to decibells.

Air temperature data were also collected at the eight acoustic stations, and these data were used in the following manner. The heat flux between the air and sea ice is proportional to $\Delta = T_a - T_i$, where T_a is the air temperature and T_i is the ice temperature. Microfracturing of the ice occurs only if $\Delta < 0$, and we assume that the ice temperature takes approximately 3 hrs to adjust to the air temperature. Therefore, we use

$$T_i \Big|_{t=0} = T_a \Big|_{t=-3 \text{ hrs}}$$

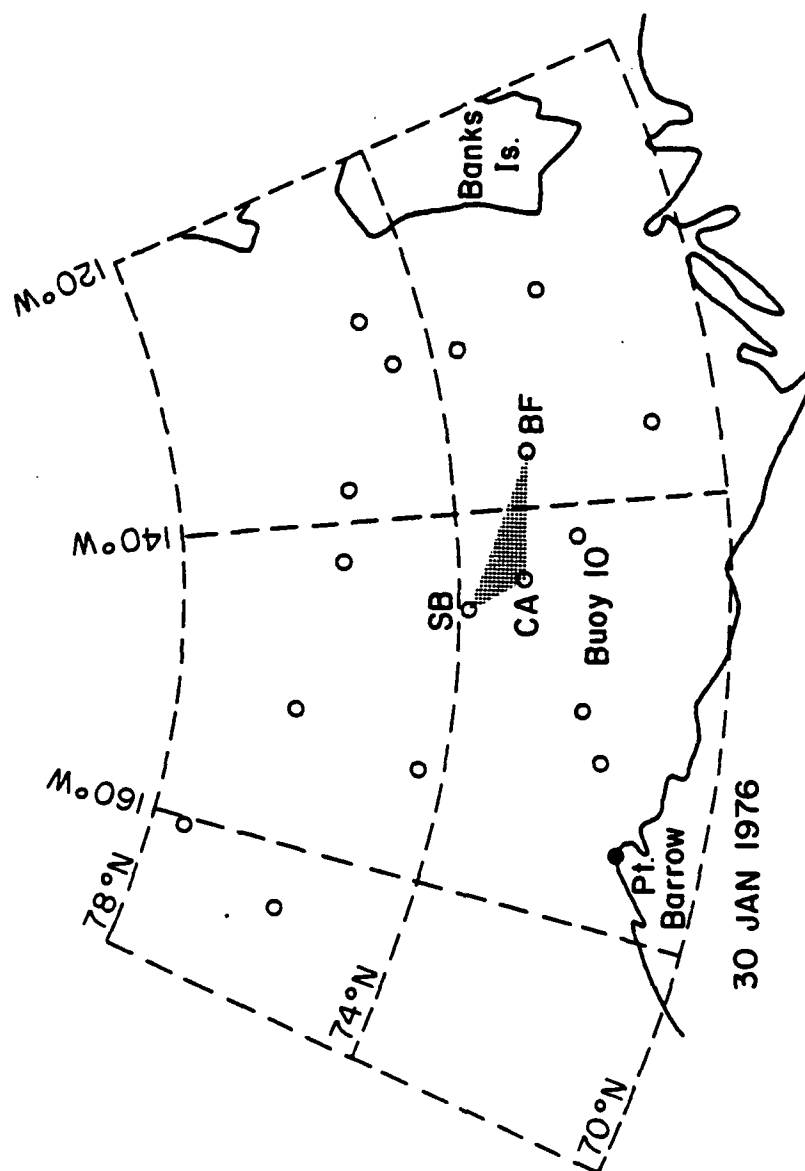


Fig. 1. Locations of a number of AIDJEX data buoys and manned camps (SB, CA, and BF) for 30 January 1976. Station 10 acoustic data discussed in this paper were collected at Buoy 10.

and so $\Delta = T_{a|t} - T_{a|t-3 \text{ hrs}}$. Since $\Delta \geq 0$ should not result in any thermal cracking, we correlate the ambient noise with the time series

$$\Delta = \begin{cases} 0 & \text{for } T_{a|t} - T_{a|t-3 \text{ hrs}} \geq 0 \\ T_{a|t} - T_{a|t-3 \text{ hrs}} & \text{otherwise.} \end{cases}$$

The ice kinematic data used in this study are discussed in a companion paper by Lewis et al. (1985). In essence, we treat our region of ice as an ice parcel which not only translates, but rotates, changes in area, and changes in shape (Fig. 2). The movement of the ice parcel is described in terms of a combination of the five basic modes of motion: translation (\vec{U}), vorticity (ζ) (rotation rate), divergence (D), normal deformation rate (N), and shear deformation rate (S). The last four of these parameters describe relative motion within the ice parcel as it translates. Kirwan (1975) has provided the physical interpretations of these differential kinematic parameters (DKP):

- ζ - the change in the orientation of the parcel (without a shape or size change),
- D - the change in the size of the parcel (without an orientation or shape change),
- N - the change in the shape of the parcel due to forces acting normal to the sides of the parcel (without a size or orientation change), and
- S - the change in the shape of the parcel due to forces acting parallel to the sides of the parcel (without a size or orientation change).

The ice parcel dealt with in this study was that delineated by the AIDJEX manned camps. The three hour position data of these

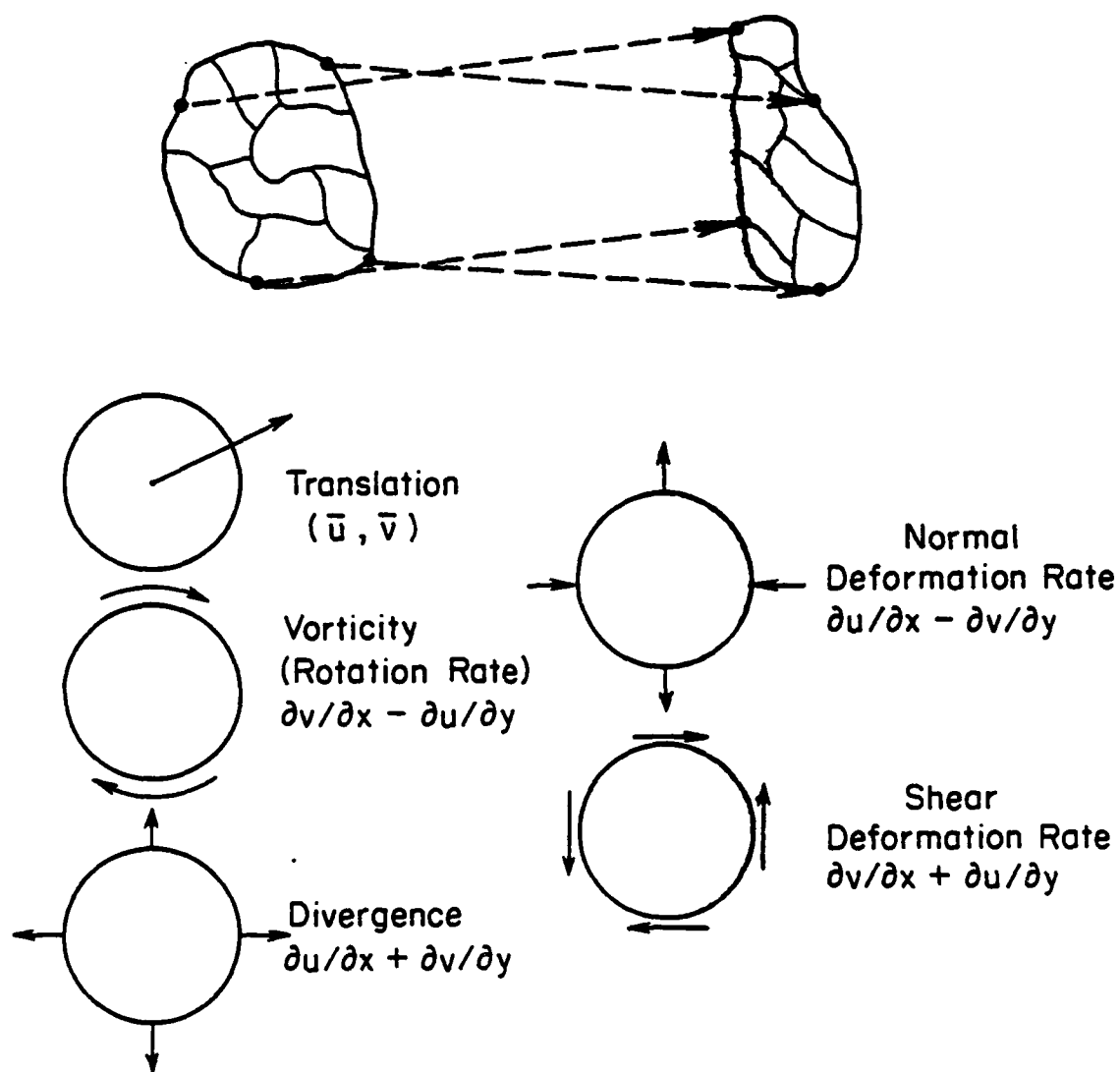


Fig. 2. Mathematical and physical definitions of the five basic components of the motion of a parcel of ice.

manned camps were used to calculate the time histories of \vec{U} and the DKP. The utility of this type of analysis is that each mode of motion has a specific physical interpretation. For example, noise generated by lead and ridge formation is related to the divergence D . Also, the magnitude of \vec{U} is related to the ice rushing through the water. It may also be related to kinetic energy and, thus, floe/floe interaction through turbulent kinetic energy. Finally, shape changes caused by deformation (N and S) can be considered in terms of simply a rearrangement of individual floes within the ice parcel (no area change). Thus, N and S represent the degree to which the floes are moving (rubbing) past one another in the rearrangement process. Besides air temperature, the acoustic stations also collected atmospheric pressure data at three hour intervals. Although these data are not used in our evaluation of the relationships between ambient noise and other phenomena, we do present some of the pressure data when considering the spatial structure of the noise.

3. SEASONAL VARIATIONS OF NOISE AND ICE PARAMETERS

Ambient Noise Variations

We first present ambient noise data that is representative of the various seasons. Fig. 3 shows the time histories of the 10 Hz, 32 Hz, and 1000 Hz signals during August 1975 (Summer) collected ~200 km south of the manned camps (Buoy 10, Fig. 1). We see that the trends at all 3 frequencies are similar and that the 10 Hz signal has a very strong component which fluctuates at about the inertial period (~12.5 hrs). Data during November 1975 are used to represent fall conditions (Fig. 4) at the same station, and these data show that the strong inertial oscillations in the 10 Hz signal are gone. In this case, the 10 Hz and 32 Hz signals are almost identical. Also, we see shorter term fluctuations in the 1000 Hz signal that appears more energetic than similar fluctuations in the 10 Hz and 32 Hz signals.

Data for the winter of 1976 (February, Fig. 5) indicate that the 10 Hz and 32 Hz signals are still quite similar. Also, the higher frequency fluctuations with the greatest energy are still found in the 1000 Hz data. One feature that was noted at all the acoustic stations during the winter was the period of relatively low noise levels during days 52 and 53 (Fig. 5). We will consider this period in greater detail later.

During the spring of 1976 (May, Fig. 6) the data from most of the acoustic stations showed that the 10 Hz and 32 Hz signals were still somewhat similar. Also, the higher frequency fluctuations in the 1000 Hz signals decreased substantially at 3 of the 5 operational acoustic stations.

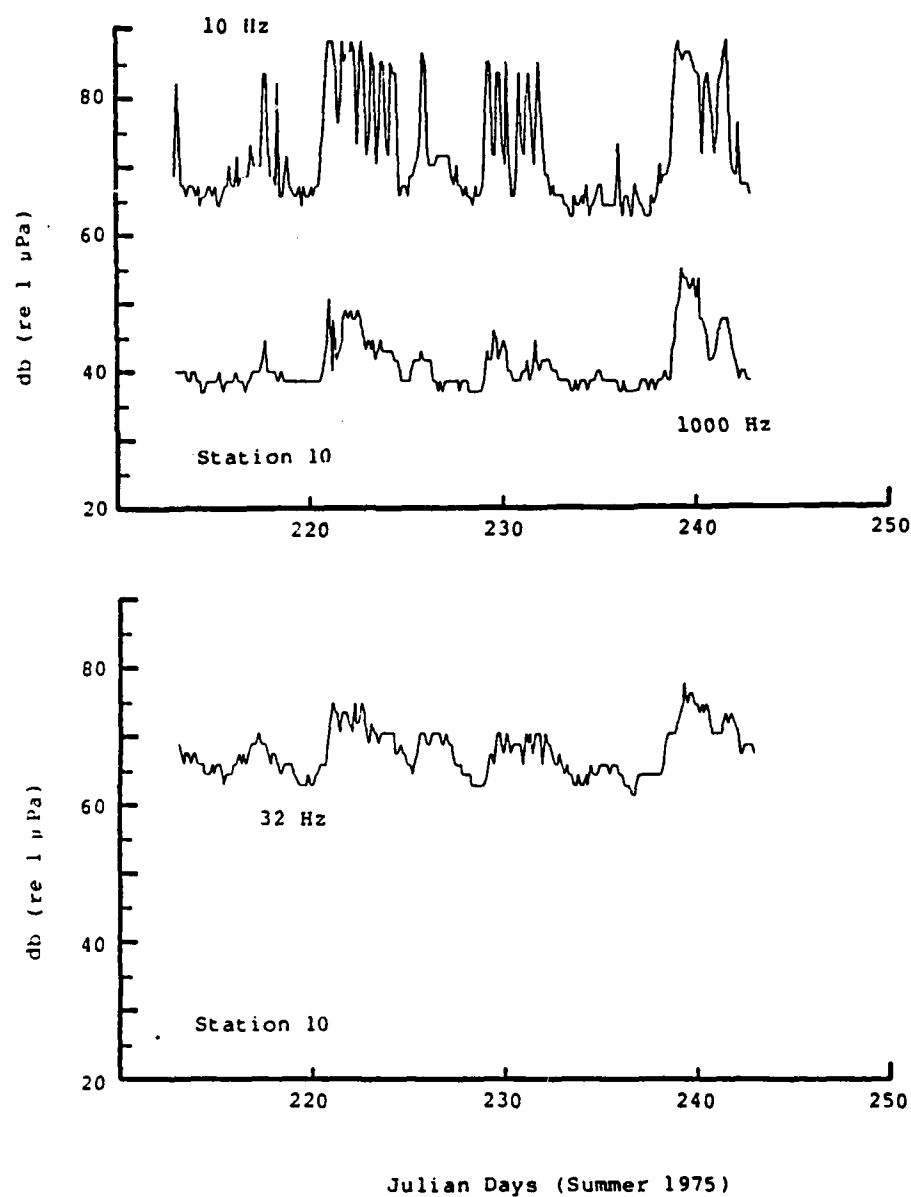


Fig. 3. Ambient noise variations at 10 Hz, 32 Hz, and 1000 Hz at Station 10 during August 1975.

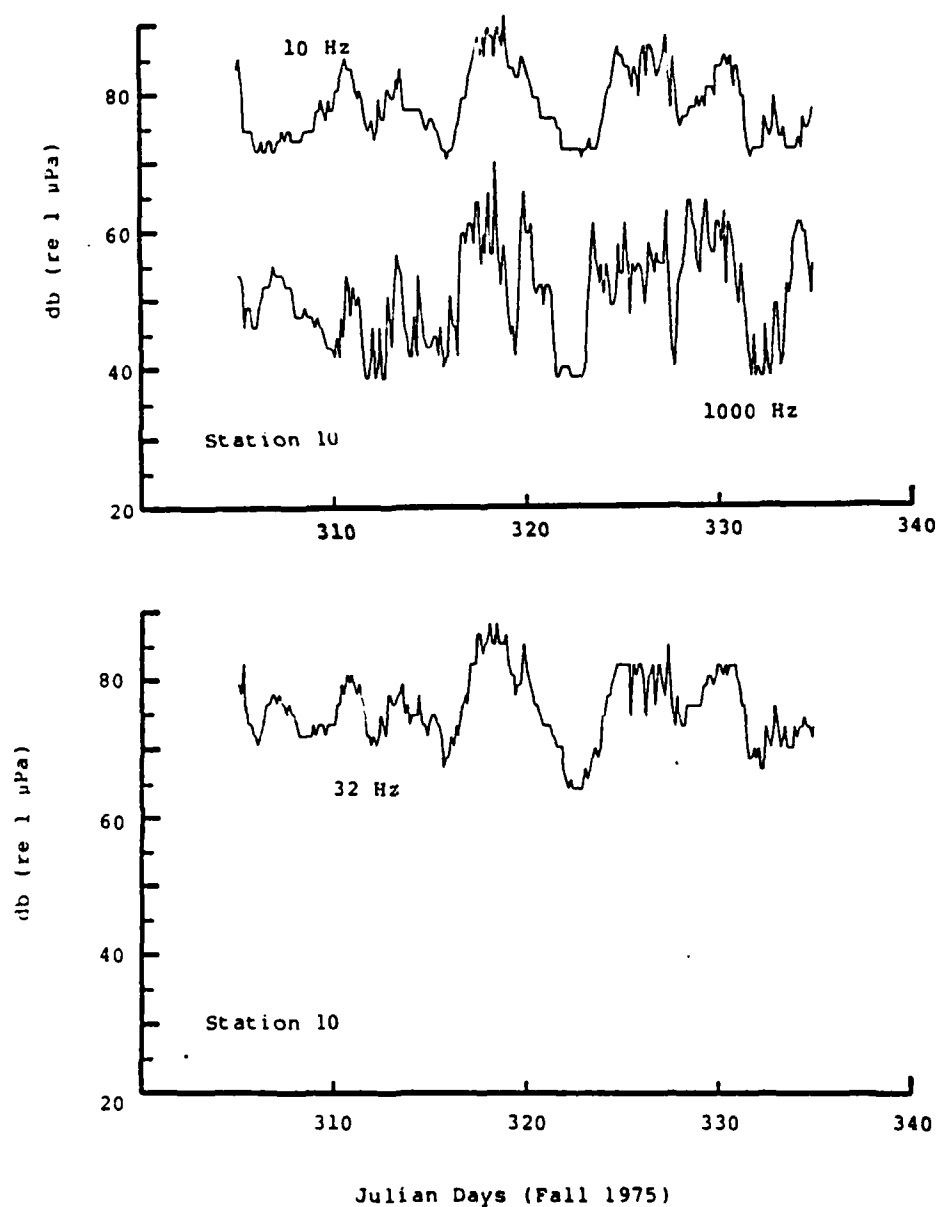


Fig. 4. Ambient noise variations at 10 Hz, 32 Hz, and 1000 Hz at Station 10 for November 1975.

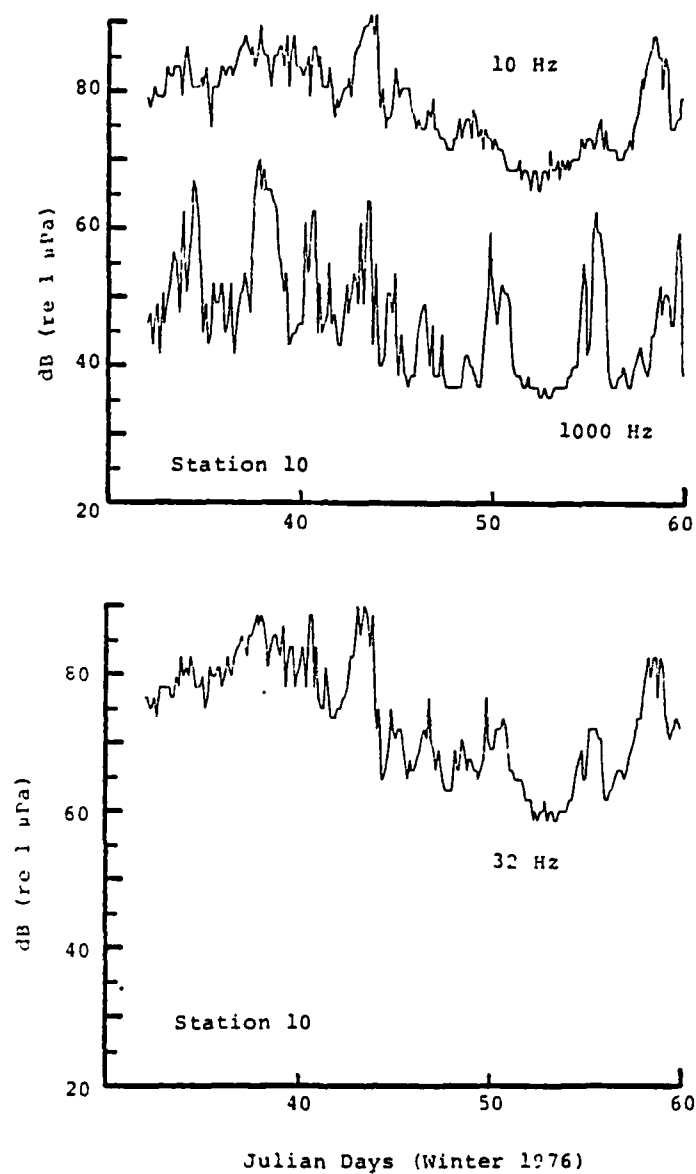


Fig. 5. Ambient noise variations at 10 Hz, 32 Hz, and 1000 Hz at Station 10 during February 1976.

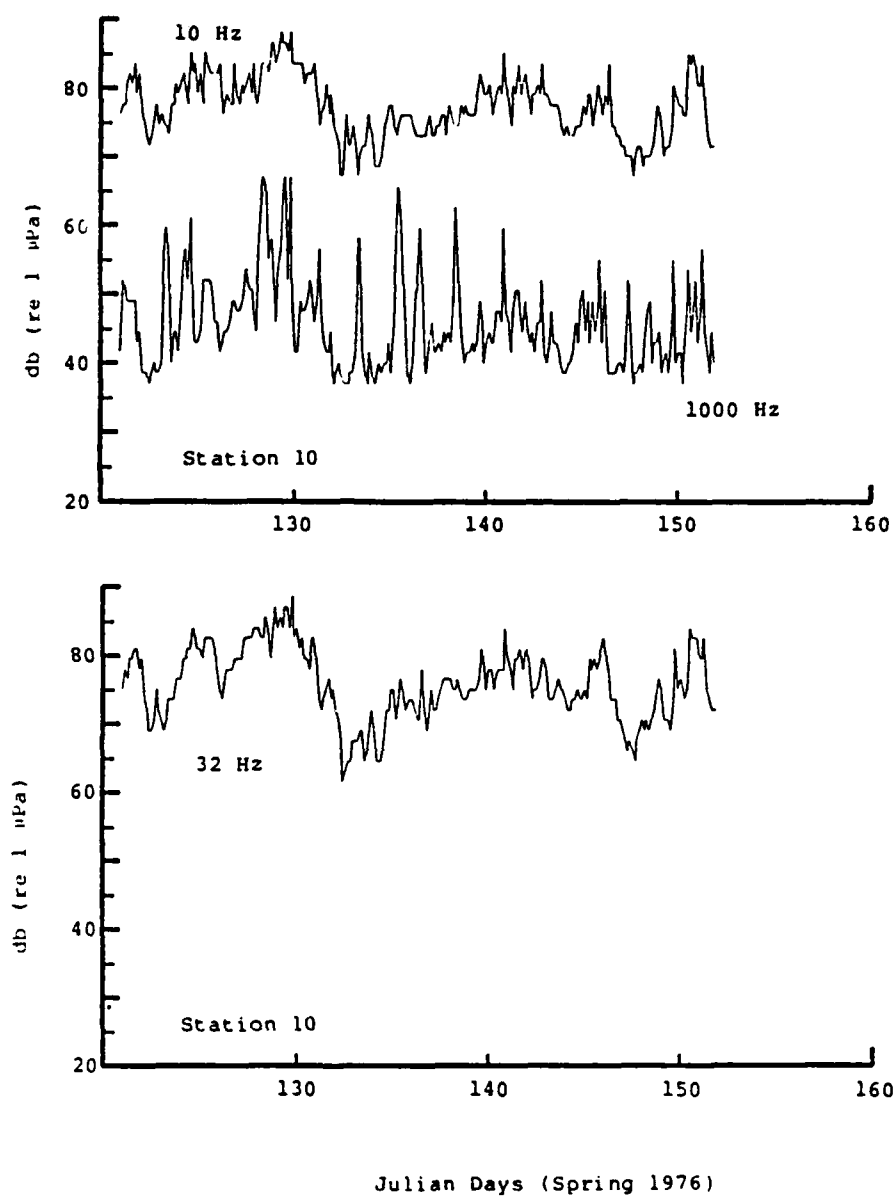


Fig. 6. Ambient noise variations at 10 Hz, 32 Hz, and 1000 Hz at Station 10 during May 1976.

An intriguing aspect of all the above acoustic data is the large degree of differences seen between the 10 Hz and 32 Hz signals during the summer. It is difficult to describe a particular sea ice process that strongly magnifies the summer 10 Hz signal but is not detectable in the 32 Hz signal. We note that the large amplitude variations of the 10 Hz signal have a strong periodicity at the inertial frequency. This implies that the horizontal movement of the inertial motion of the ice is in some way responsible for the differences between the 10 Hz and 32 Hz signals. However, the inertial movement of summer pack ice has horizontal scales of the order of kilometers, and one is hard pressed to describe the physics of how a process of such a scale generates noise that can be detected at the 10 Hz level (scale length of $\sim 150\text{m}$) but not at the 32 Hz level (scale length of $\sim 50\text{m}$).

An indication of the cause of this 10 Hz/32 Hz paradox is seen in the 3.2 Hz data. The 3.2 Hz summer data is shown in Fig. 7, and we see that this signal also has large amplitude variations that oscillate at the inertial period. Indeed, most of the 3.2 Hz oscillations are exactly in phase with the 10 Hz oscillations. Greene and Buck (1977) found that the 3.2 Hz signal was poorly correlated with the other AIDJEX noise data, and this poor correlation was interpreted as contamination of the 3.2 Hz data by strum or seismic activity. Since oscillations at the inertial period are obviously not seismic, we assume that the 3.2 Hz summer data is contaminated by strum. Thus, the similarities between the 3.2 Hz and 10 Hz data imply that the 10 Hz summer data is also contaminated by the cable strum. Our research shows that most of the AIDJEX summer acoustic data at 10 Hz is contaminated by strum, with only occasional contaminations seen during the spring and none during fall and winter. Other 10 Hz data collected since AIDJEX also show large amplitude oscillations at the inertial period during the summer but the associated 20 Hz data do not (Buck and Jaekis, 1984). It appears that

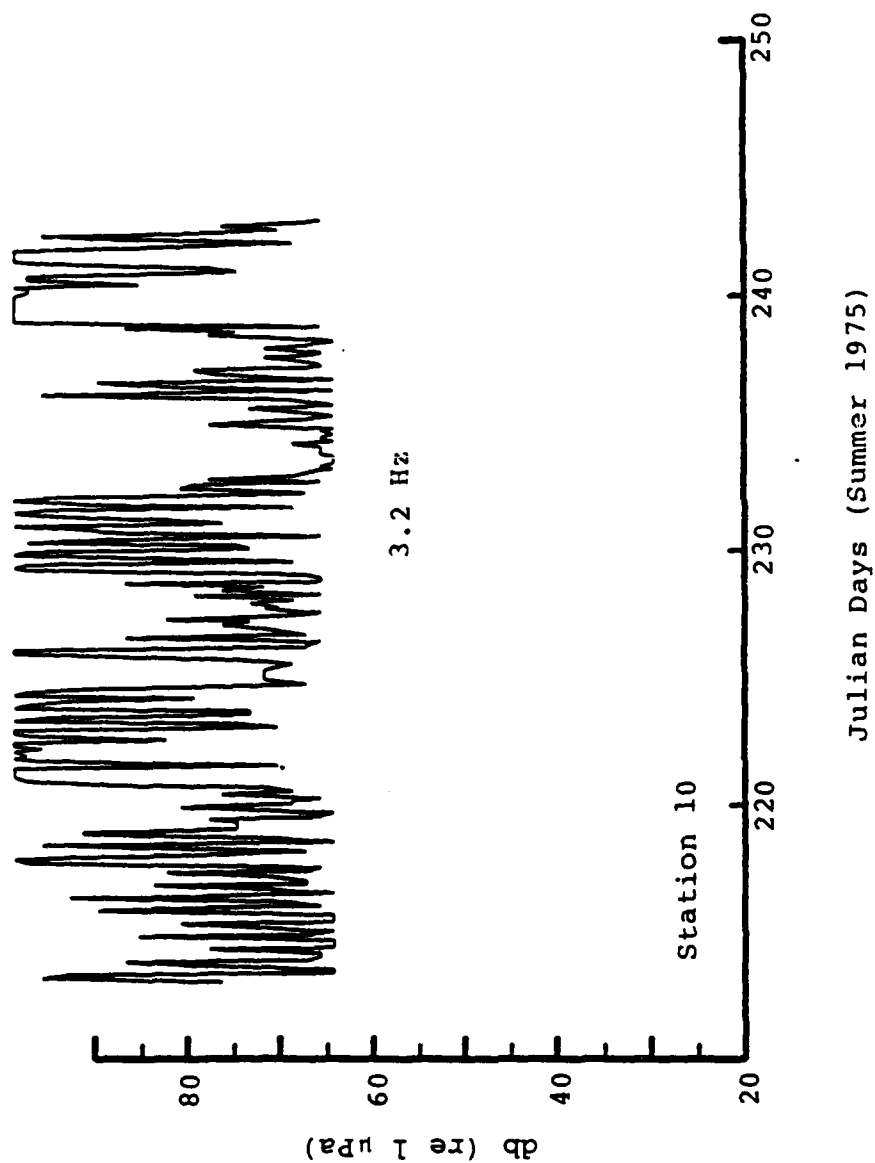


Fig. 7. Ambient noise variations at 3.2 Hz at Station 10 during August 1975.

it is the higher velocities of summer-time inertial ice motion that are directly responsible for triggering the particular cable harmonics that can contaminate the 10 Hz as well as the 3.2 Hz signals (but not the higher frequencies such as 20 Hz or 32 Hz). Although inertial oscillations in Arctic acoustic data have been documented during non-summer periods (Buck and Jaekis, 1984), these oscillations are of much lower amplitude (~ 5 dB), are broad banded, and are best defined at higher frequencies (~ 100 Hz). Such acoustic signal variations are likely the true signatures of the inertial motion of ice.

Ice Kinematic Parameter Variations

The kinematics of the ice parcel used in this study are discussed in detail by Lewis et al. (1985). The translation speed U , divergence D , and vorticity ζ for the summer of 1975 are shown in Fig. 8. We note that all of these parameters often show strong inertial oscillations, the cause of the strum that contaminated the 10 Hz summer data. We also note that, in general, increases in U tend to coincide with noise level increases (Fig. 3). This trend is also seen in the fall ice kinematic data (Fig. 9). These fall data show the expected decrease in the energy of the ice kinematic parameters which continues into the winter (Fig. 10). The winter data shows a long time period of practically no motion beginning at about Julian day 49 and lasting until approximately Julian day 57. This coincides with the previously mentioned period of low ambient noise levels.

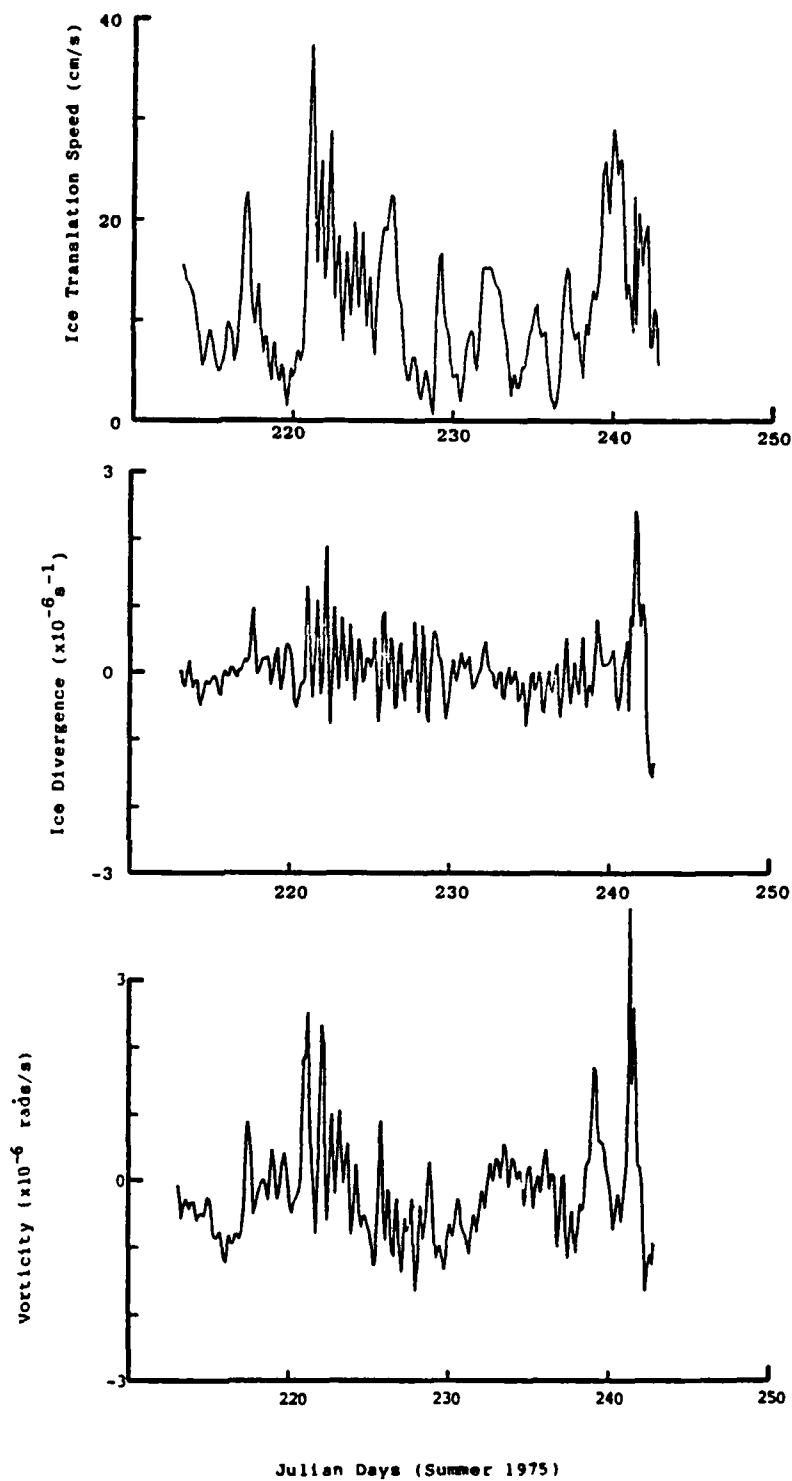


Fig. 8. Variations in the speed, divergence, and vorticity of the manned camp array during August 1975.

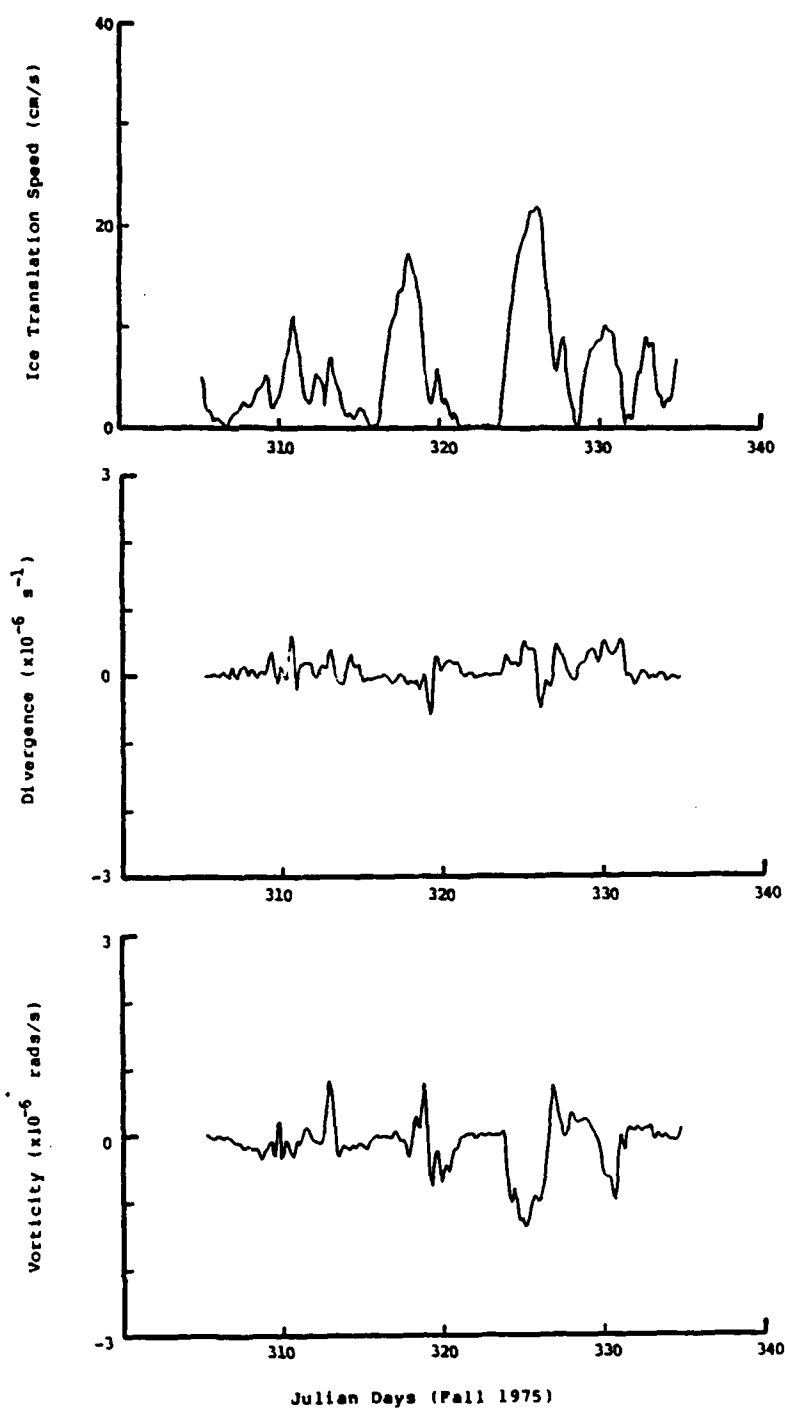


Fig. 9. Variations in the speed, divergence, and vorticity of the manned camp array during November 1975.

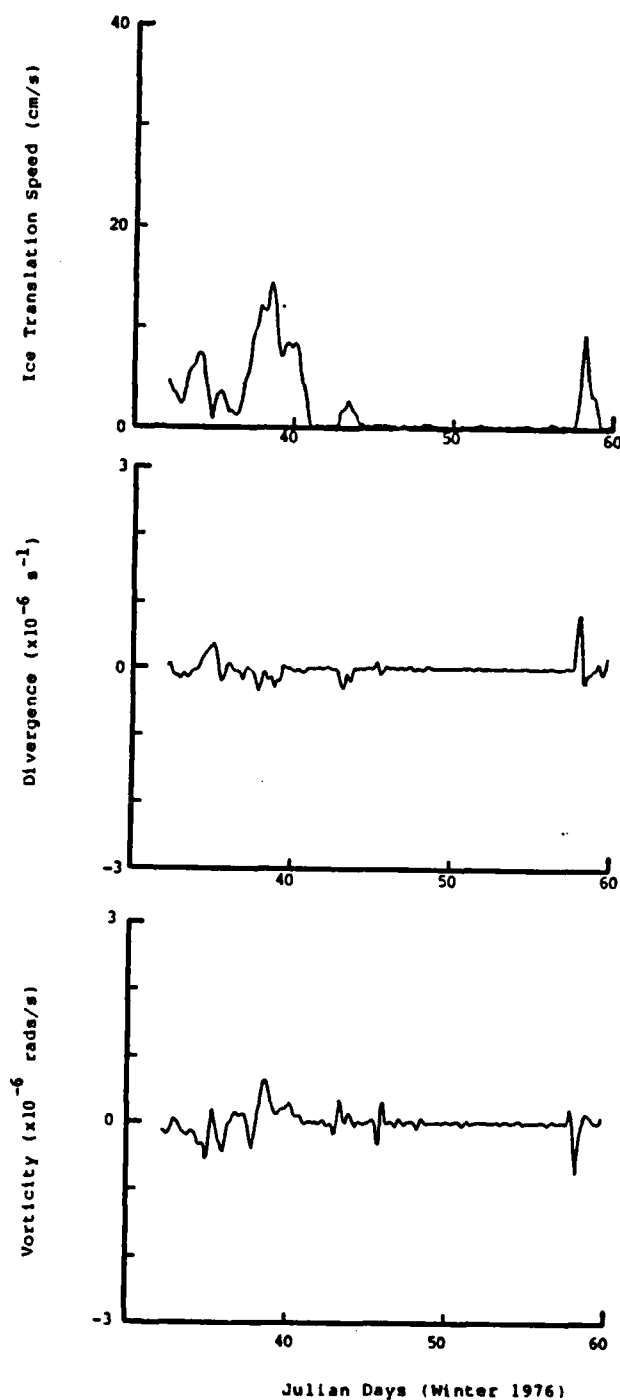


Fig. 10. Variations in the speed, divergence, and vorticity of the manned camp array during February 1976.

4. TWO-DIMENSIONAL PATTERNS

One of the most interesting aspects of the AIDJEX data sets is the ability to consider the two-dimensional patterns at small time intervals of ambient noise, atmospheric temperature, and atmospheric pressure. In this section we present several examples which indicate some relationships between the noise fields and atmospheric pressure and temperature variations. The situation of the passage of a summer-time low pressure system is depicted in Figs. 11-15. At the beginning of this time period (Julian day 220, August 1975, Fig. 11), we see that the Beaufort Sea was under the influence of an atmospheric high with highest pressures found in the eastern Beaufort. Air temperatures were relatively constant at 4.5°C. At 32 Hz (the 10 Hz signal is contaminated by strum), sound levels are approximately constant (62-63 db) with a low of 57.5 db in the eastern Beaufort. This pattern is similar to the 1000 Hz pattern which has an average of ~37 db and a low of 30.5 db in the eastern Beaufort. Twelve hours later (Fig. 12) the pressure map shows that a low pressure system had moved into the western Beaufort. Air temperatures had dropped, but only by 3-5° C. We note that the 32 Hz noise field was little affected by the incoming low pressure system, with noise levels increasing by a maximum of 4 to 5 db's in the eastern Beaufort. Similarly, the increases seen at 1000 Hz were of the order of 4 to 6 db's, again in the eastern Beaufort. Twenty-four hours after our initial time, the surface pressure data show that the atmospheric low was influencing most of the Beaufort, with the strongest pressure gradients being in the south (Fig. 13). Air temperatures had all increased to above zero. At this time, the 32 Hz noise levels in the eastern Beaufort increased again (7 to 10 db's), with the greatest increases found in the southeastern Beaufort. Variations in the 1000 Hz signals in the western Beaufort were similar, with increases of up

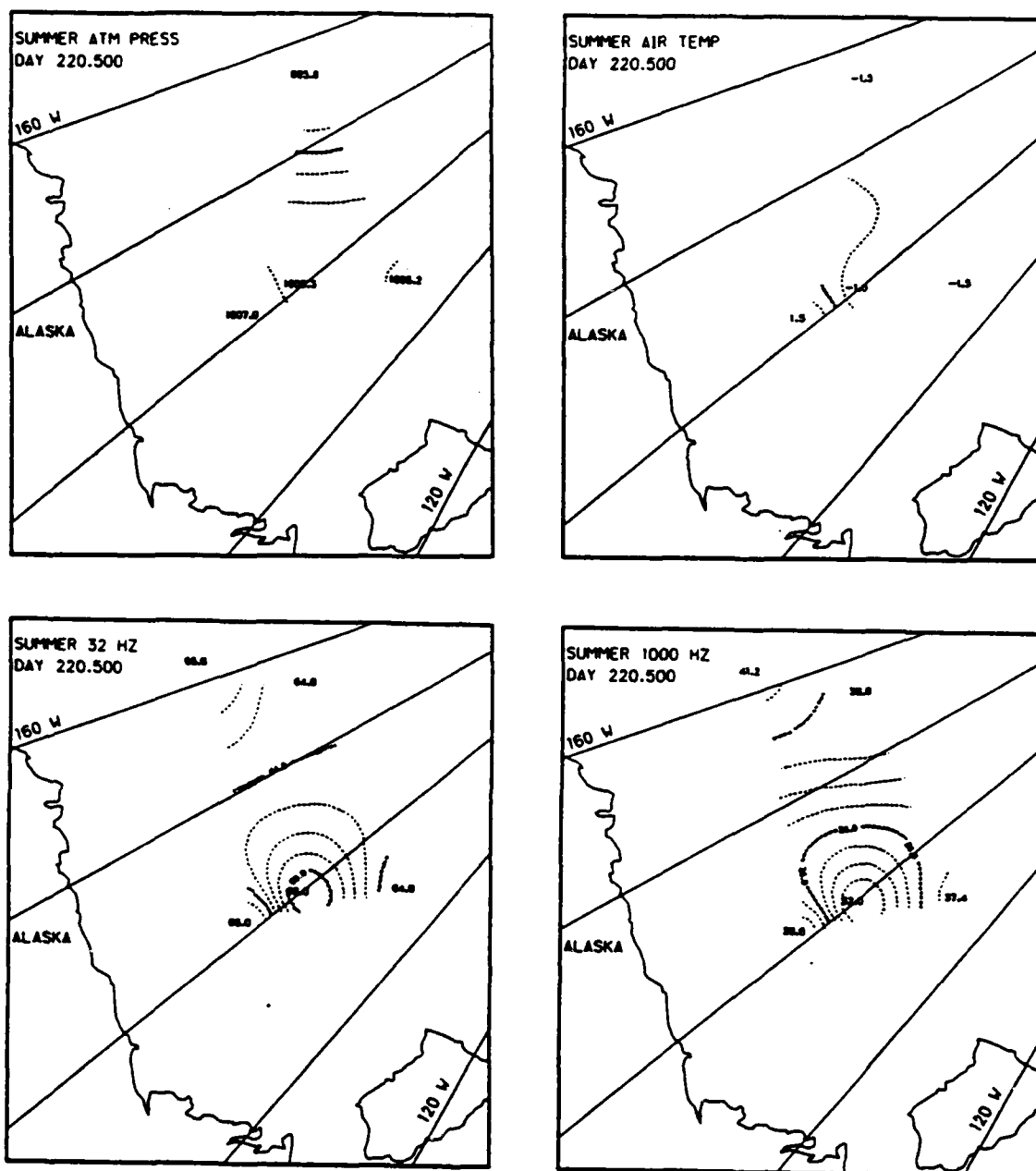


Fig. 12. Two-dimensional contour maps of atmospheric pressure, air temperature, 32 Hz ambient noise, and 1000 Hz ambient noise during August 1975, Julian day 220.5.

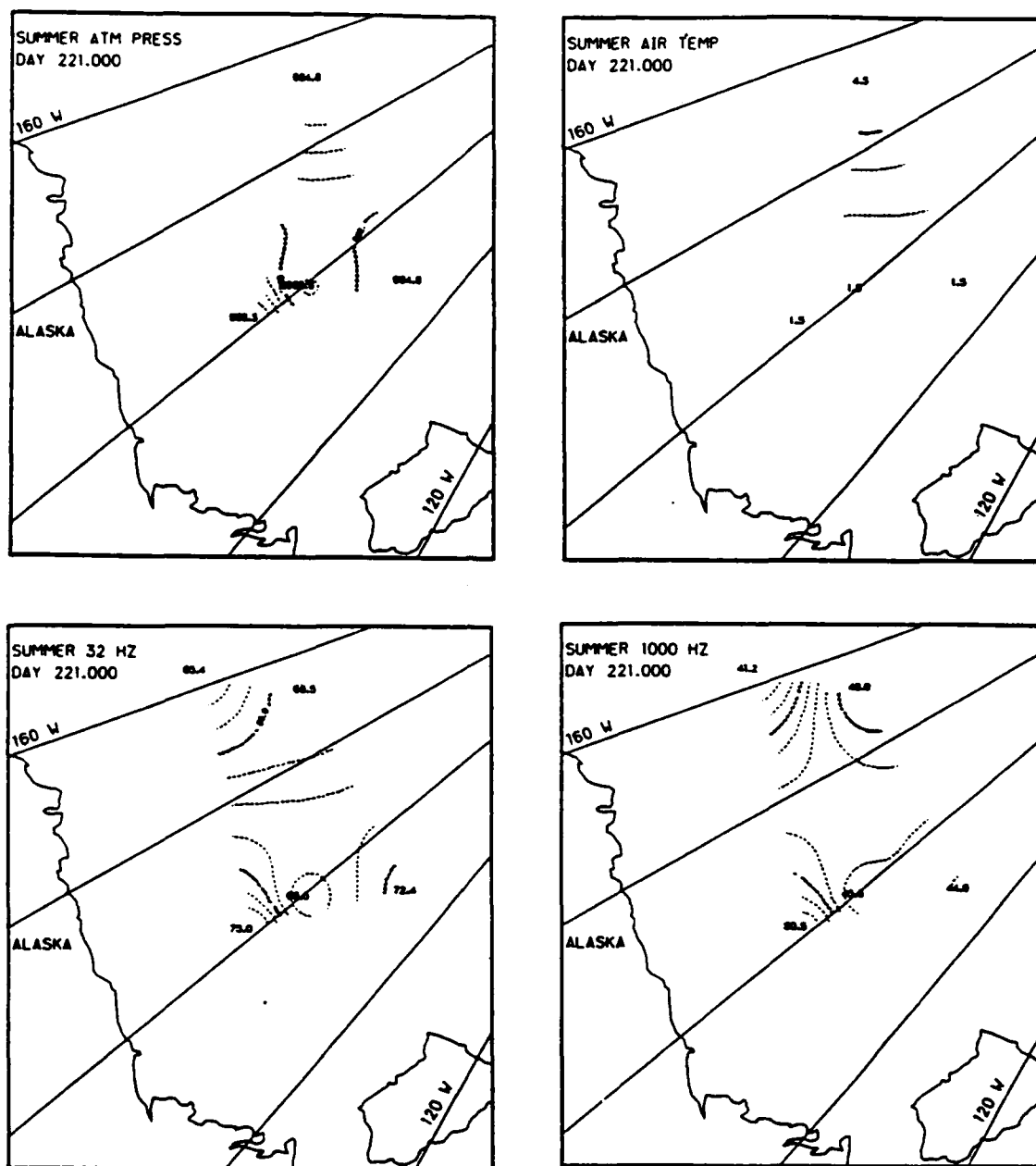


Fig. 13. Two-dimensional contour maps of atmospheric pressure, air temperature, 32 Hz ambient noise, and 1000 Hz ambient noise during August 1975, Julian day 221.0.

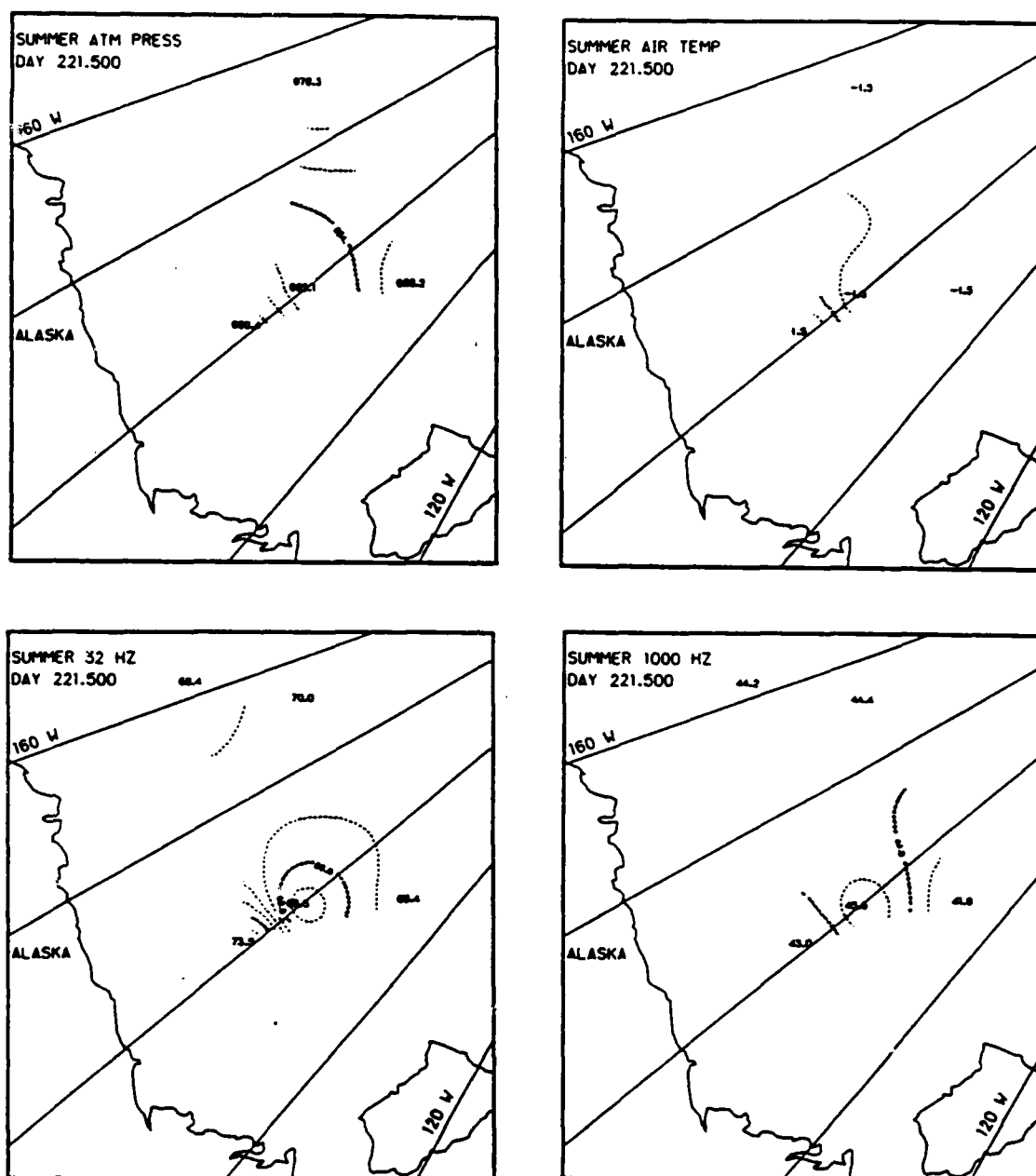


Fig. 14. Two-dimensional contour maps of atmospheric pressure, air temperature, 32 Hz ambient noise, and 1000 Hz ambient noise during August 1975, Julian day 221.5.

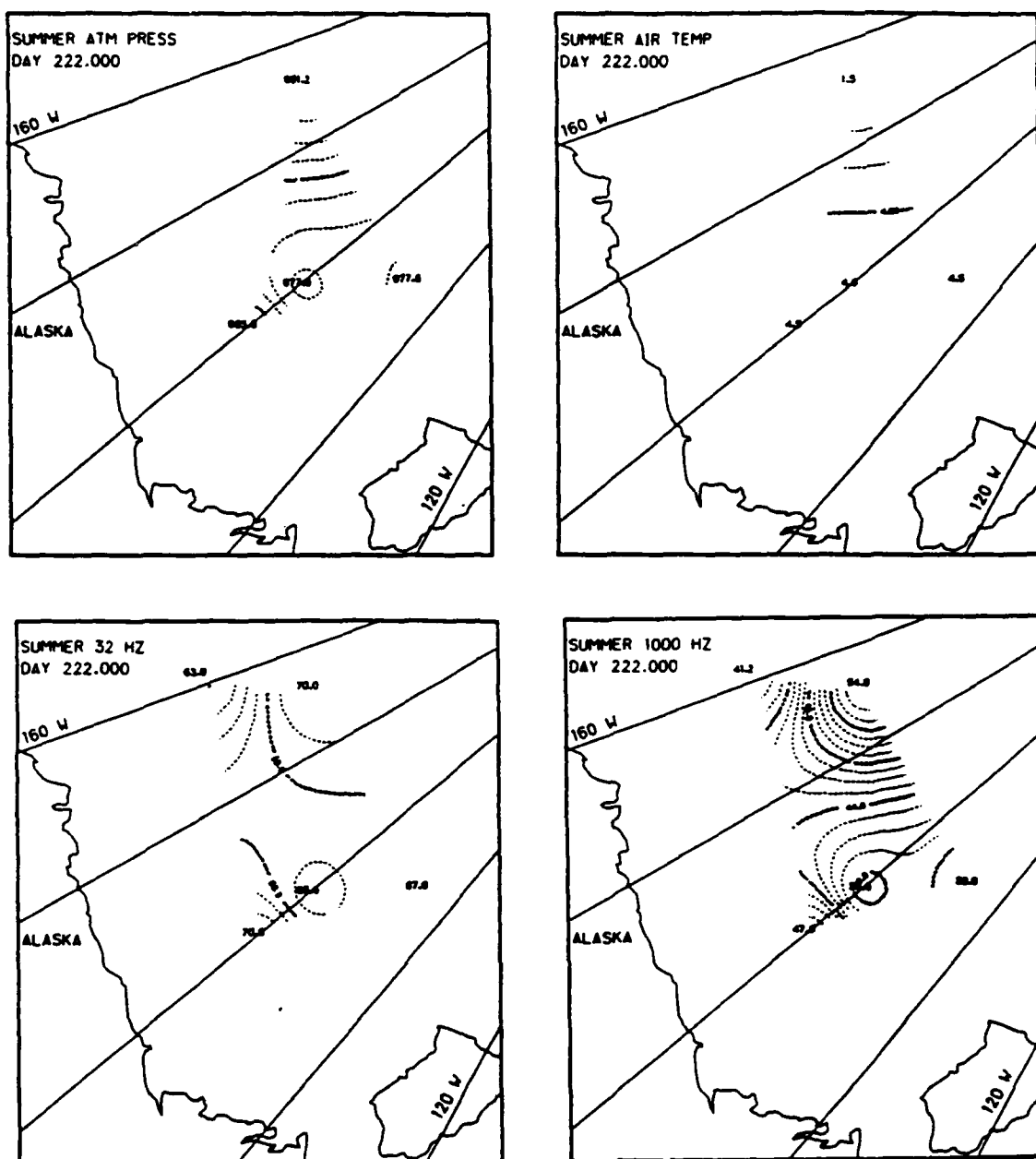


Fig. 15. Two-dimensional contour maps of atmospheric pressure, air temperature, 32 Hz ambient noise, and 1000 Hz ambient noise during August 1975, Julian day 222.0.

to 13 db. However, the 1000 Hz signal in the northeastern Beaufort also showed a substantial increase (9 db), a change not reflected in the 32 Hz data. After another 12 hours (day 221.5, Fig. 14), a low of 979.3 millibars is seen in the northwest Beaufort, and air temperatures vary from -1.5 to 1.5° C. At this point, the 32 Hz noise levels in the eastern Beaufort had begun to decrease, and this is reflected somewhat in the 1000 Hz data. For Julian day 222, the central part of the low system had moved to the northeastern Beaufort, and air temperatures were 4.5° C except in the northwestern Beaufort where it was 1.5° C. The 32 Hz noise levels at this time continued to fall, with a range of 64 to 70 db's. The 1000 Hz data show similar drops except in the northwestern Beaufort where a 10 db increase is seen.

These summer data indicate the type and scale of ambient noise variations that are a result of the response of ice to varying atmospheric conditions. Since the air was relatively warm and the temperature variations were small, we assume that the thermal cracking of the ice is negligible. This would indicate that the noise variations at 1000 Hz (category 4 of Dyer's classification) were a result of either ice motion or some other cause of micro-fracturing of sea ice. Considering the relatively good correlation between the 1000 Hz data (Fig. 3) and the speed of the manned camp ice parcel (Fig. 6), we suspect that the ice motion was the cause for most of the 1000 Hz noise variations.

Examples of the spatial characteristics of ambient noise during the fall of 1975 are shown in Figs. 16 (10 Hz) and 17 (1000 Hz). The 10 Hz signal ranges from ~ 67 db to ~ 80 db, with the western Beaufort being the quietest region. The noisiest region was the north central Beaufort Sea. This spatial characterization is also true for the 1000 Hz data (Fig. 17), with the spatial variations at this higher frequency ranging up to 25 db.

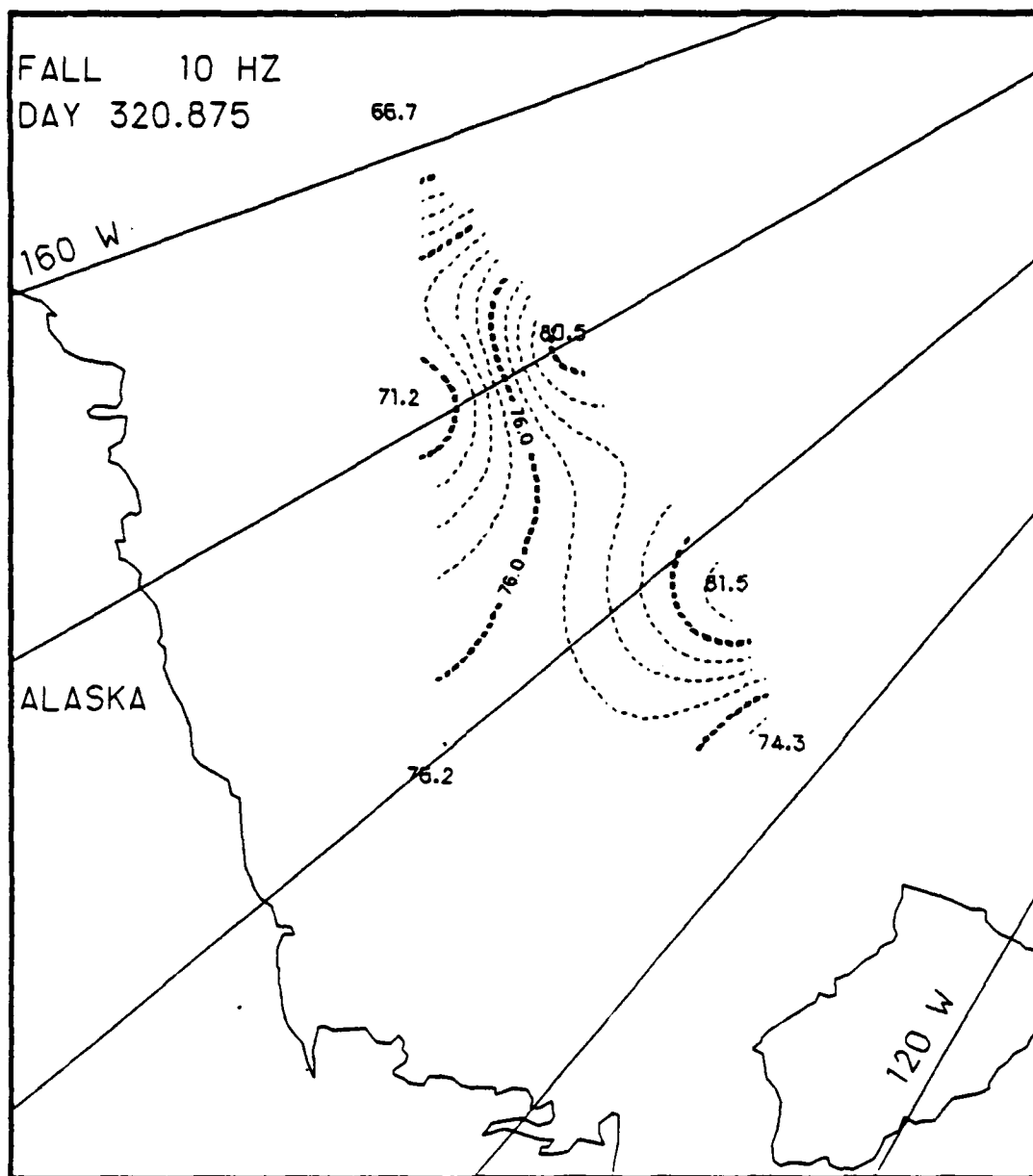


Fig. 16. Two-dimensional contour map of 10 Hz ambient noise during November 1975, Julian day 320.875.

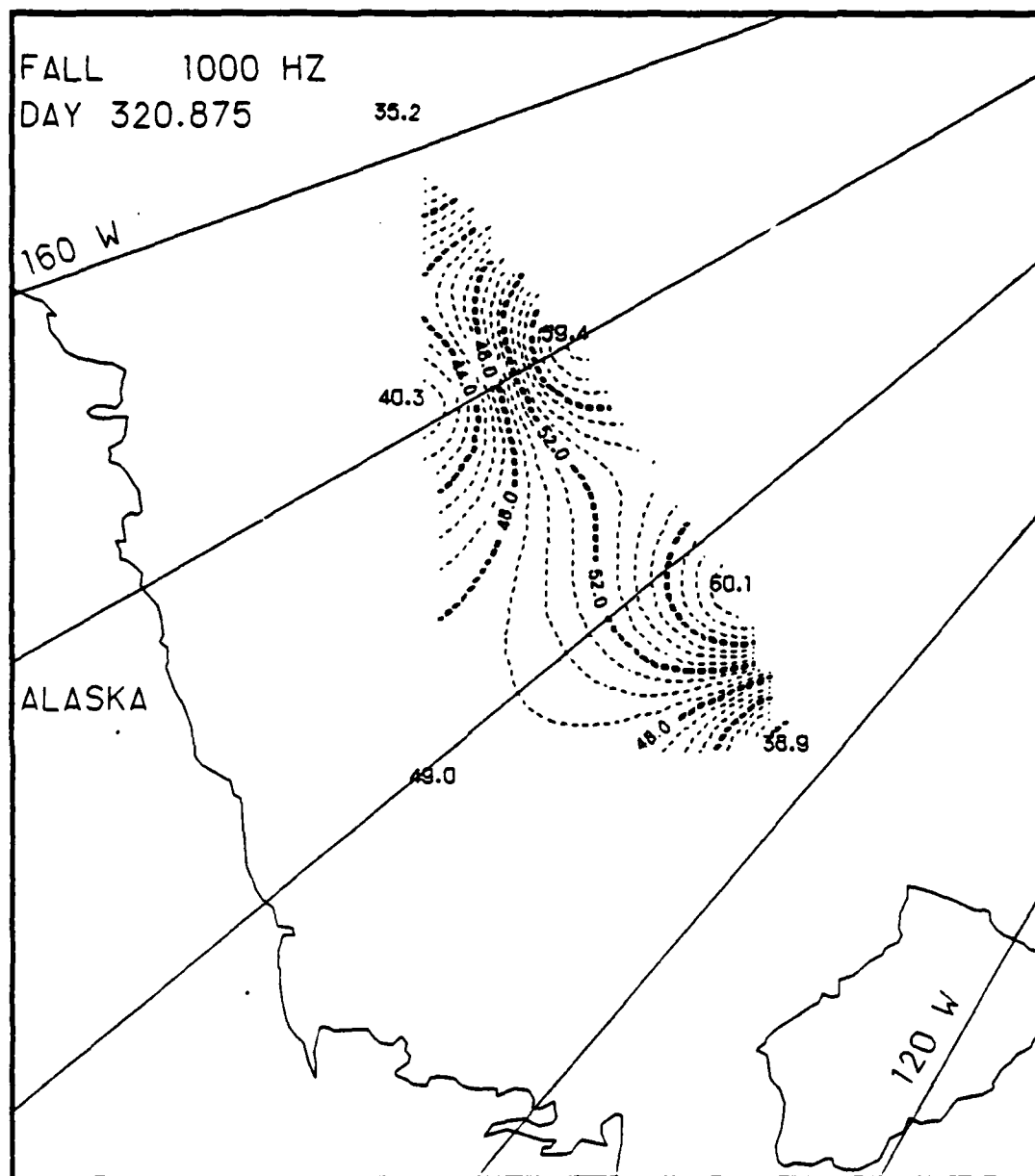


Fig. 17. Two-dimensional contour map of 1000 Hz ambient noise during November 1975, Julian day 320.875.

Winter-time acoustic characteristics are typical of those shown in Figs. 18 (10 Hz) and 19 (1000 Hz). The spatial structure of the 10 Hz winter data is similar to that of the fall, and all the noise levels tended to be slightly higher with a range of ~ 70 db to 87 db. Noise levels at 1000 Hz also tended to increase. The western Beaufort again tended to be the quietest region, and one often finds the situation as depicted in Fig. 19 in which the southern Beaufort becomes quite noisy. This results in a relatively noisy region cutting north/south across the central Beaufort.

An example of the effects of temperature variations are indicated by spring data shown in Figs. 20-25. At Julian day 135 (Fig. 20), we see the study area influenced by a high pressure system with an anticyclonic flow from the northeast to the west and the southwest. Fig. 20 also shows that the corresponding air temperatures ranged from 1.5° C in the north to -4.5 in the south-central Beaufort. At both 10 Hz and 1000 Hz, the maximum noise levels are found in the north central Beaufort, with a maximum of ~ 78 db for 10 Hz and ~ 43 db for 1000 Hz.

After a 9 hour period, we find that the atmospheric high continued to build from the northwest (Fig. 21), with the air temperature dropping 12° - 18° C. The pattern of 10 Hz ambient noise at this time is similar to the previous pattern, but the 1000 Hz pattern changed considerably as a result of a 14-25 db increase in noise levels in the southern and southwestern Beaufort. After an additional 15 hrs (Fig. 22) one finds an almost constant atmospheric pressure field, but with warmer air temperatures (-4.5° to 4.5° C). The 10 Hz noise levels increased slightly (increases up to 6 db), while the 1000 Hz noise levels decreased in the southern Beaufort (14 to 29 db) but increased in the northern Beaufort (6 to 10 db). However, after an additional 3 hrs (Fig. 23), as the air temperature begins to drop

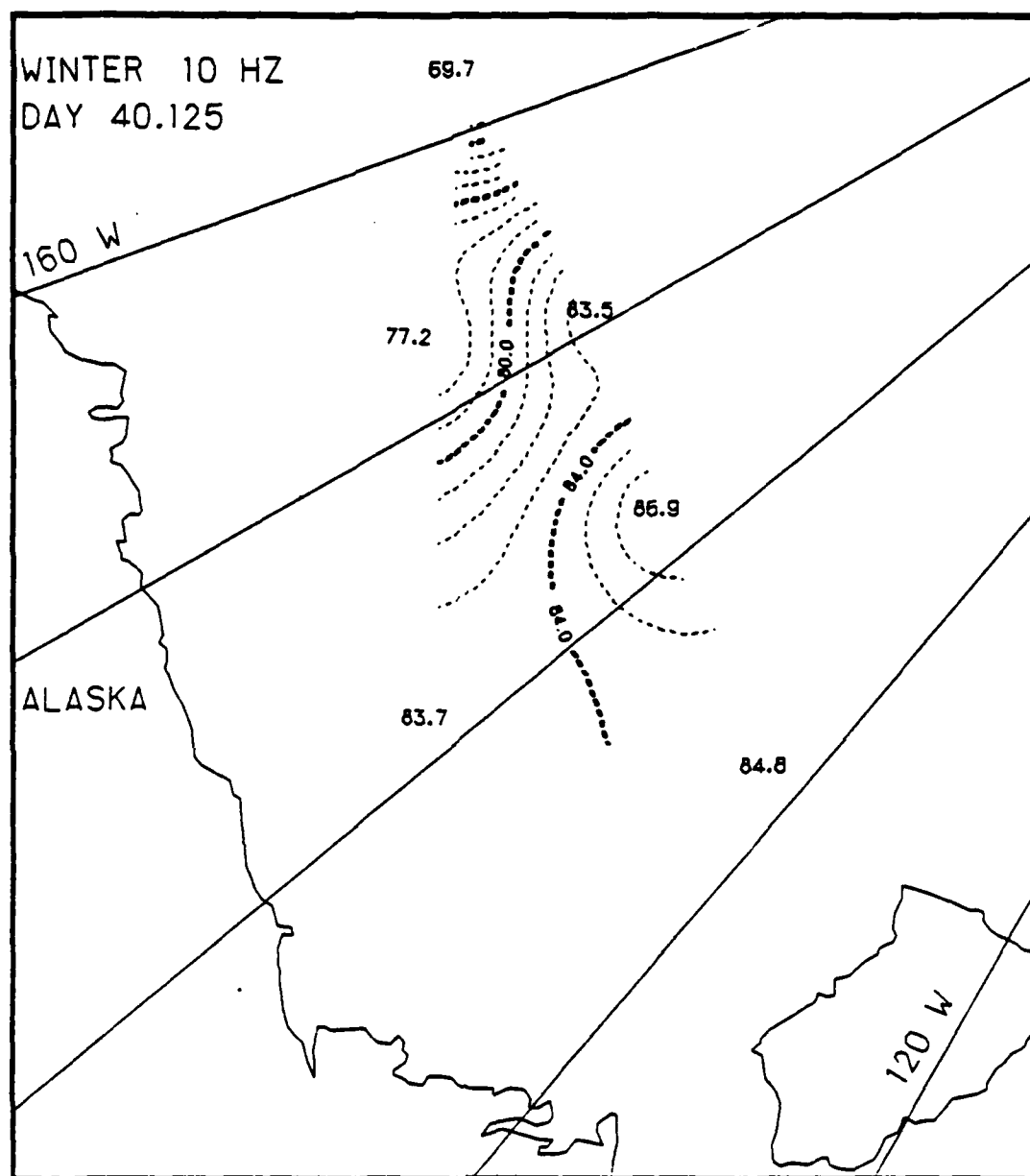


Fig. 18. Two-dimensional contour map of 10 Hz ambient noise during February 1976, Julian day 40.125.

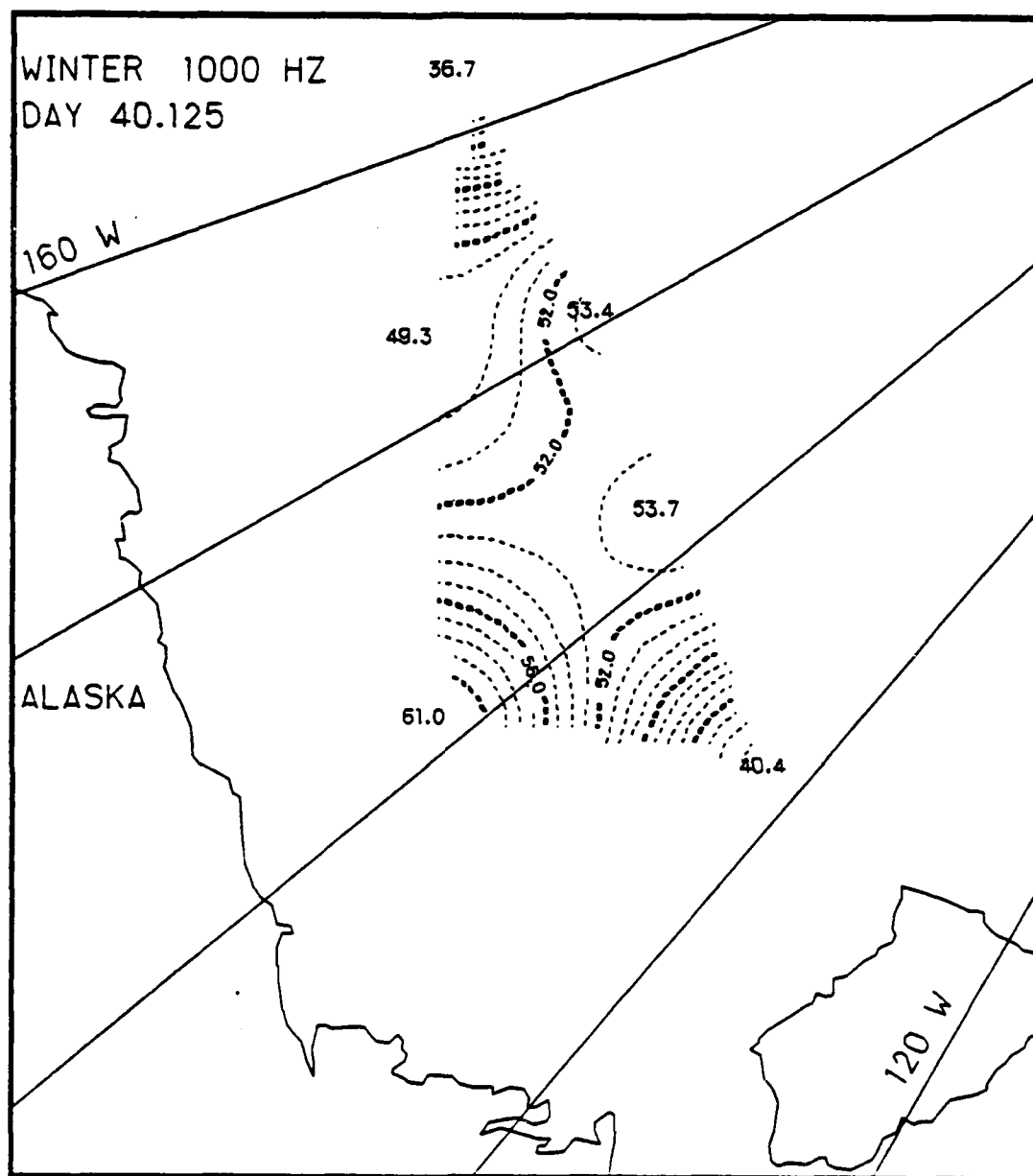


Fig. 19. Two-dimensional contour map of 1000 Hz ambient noise during February 1976, Julian day 40.125.

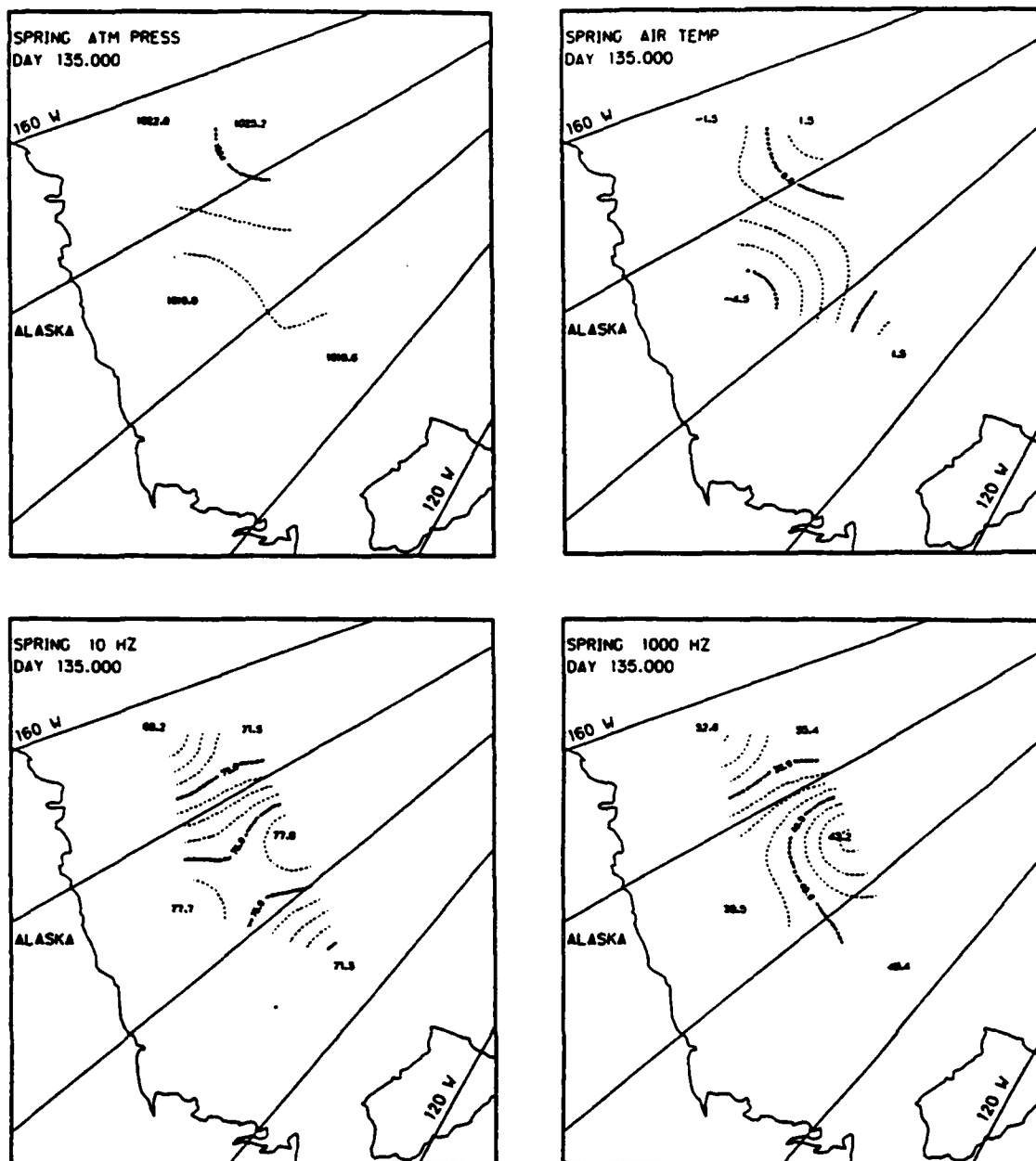


Fig. 20. Two-dimensional contour maps of atmospheric pressure, air temperature, 10 Hz ambient noise, and 1000 Hz ambient noise during spring 1976, Julian day 135.0.

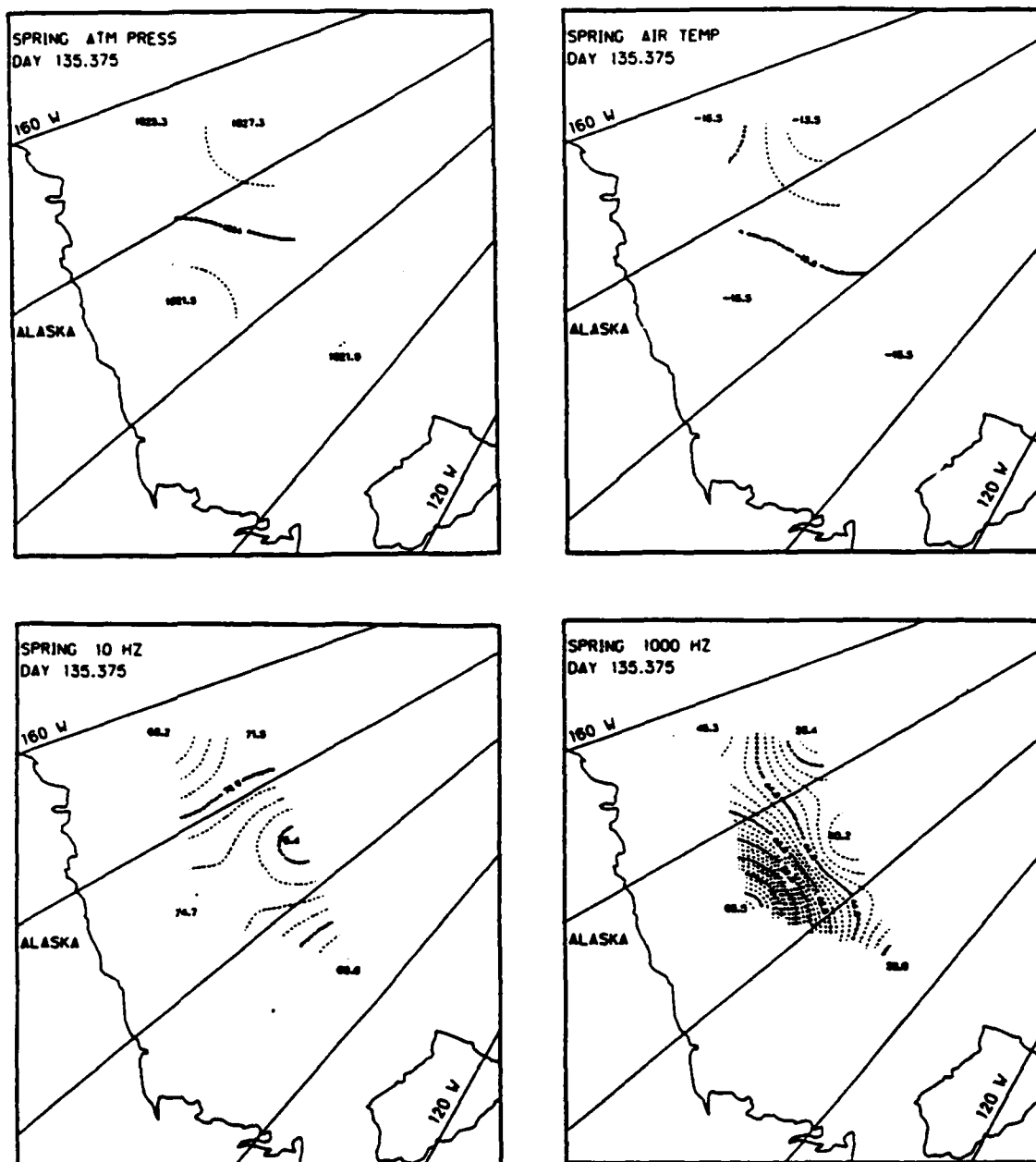


Fig. 21. Two-dimensional contour maps of atmospheric pressure, air temperature, 10 Hz ambient noise, and 1000 Hz ambient noise during spring 1976, Julian day 135.375.

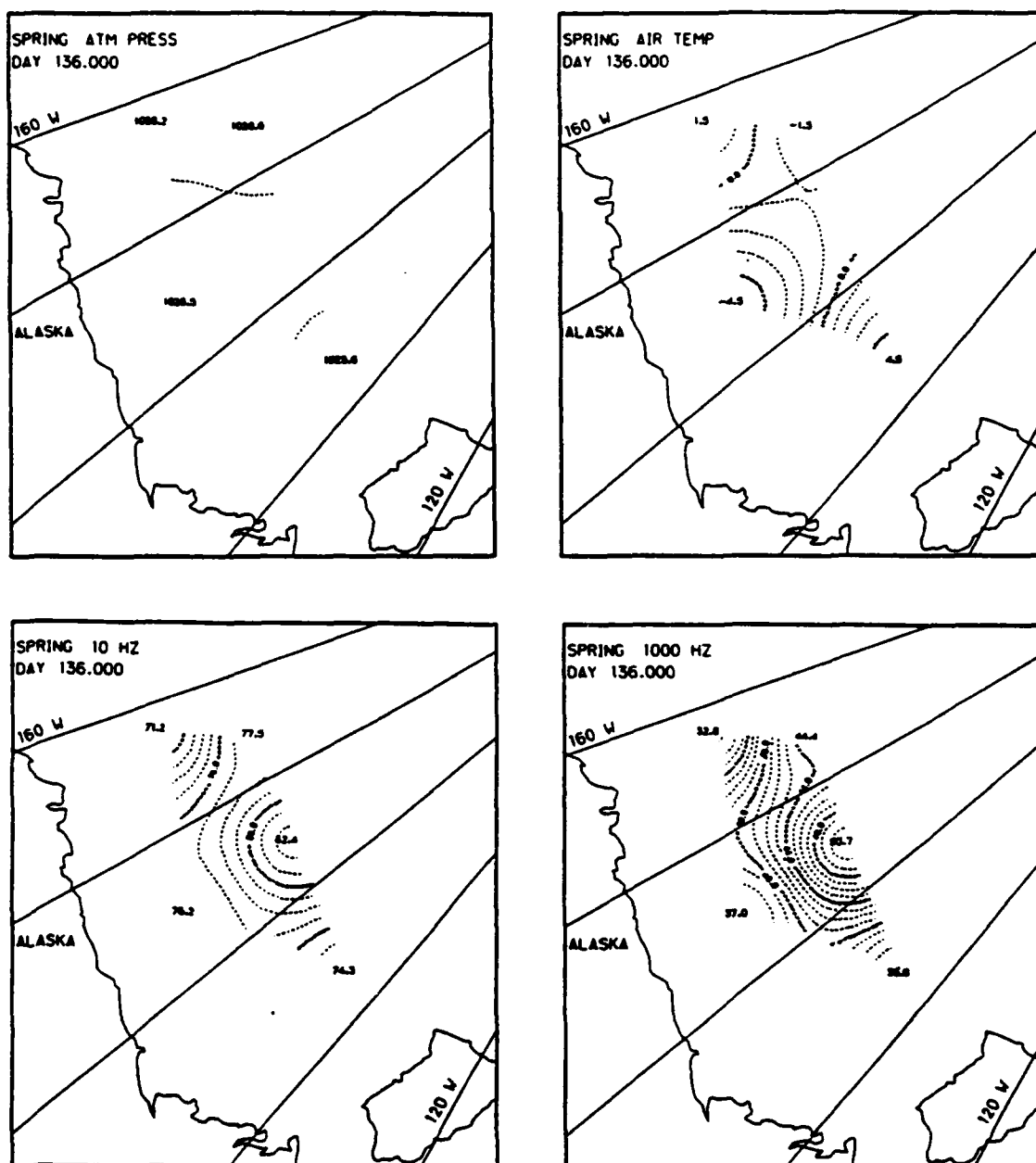


Fig. 22. Two-dimensional contour maps of atmospheric pressure, air temperature, 10 Hz ambient noise, and 1000 Hz ambient noise during spring 1976, Julian day 136.0.

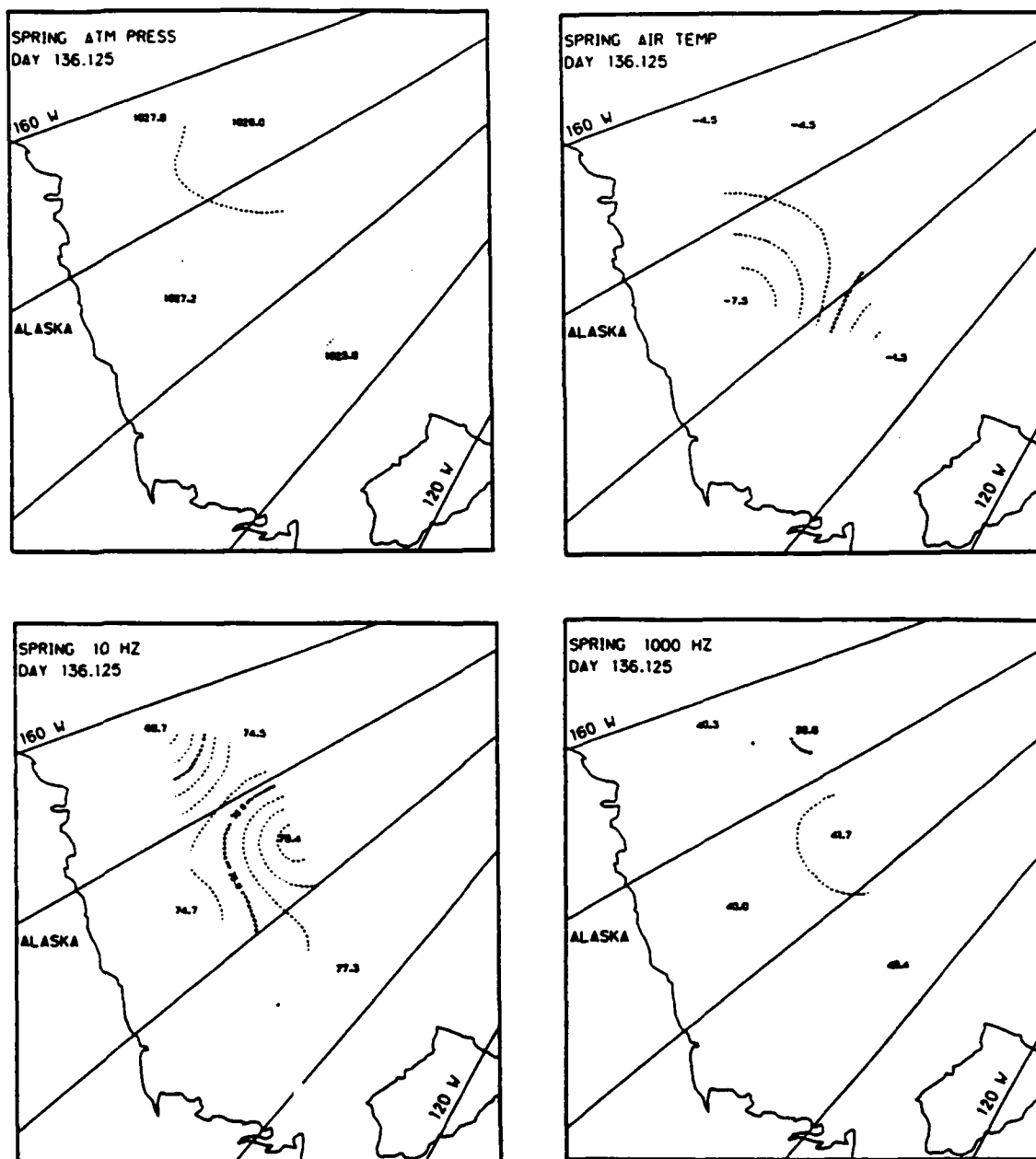


Fig. 23. Two-dimensional contour maps of atmospheric pressure, air temperature, 10 Hz ambient noise, and 1000 Hz ambient noise during spring 1976, Julian day 136.125.

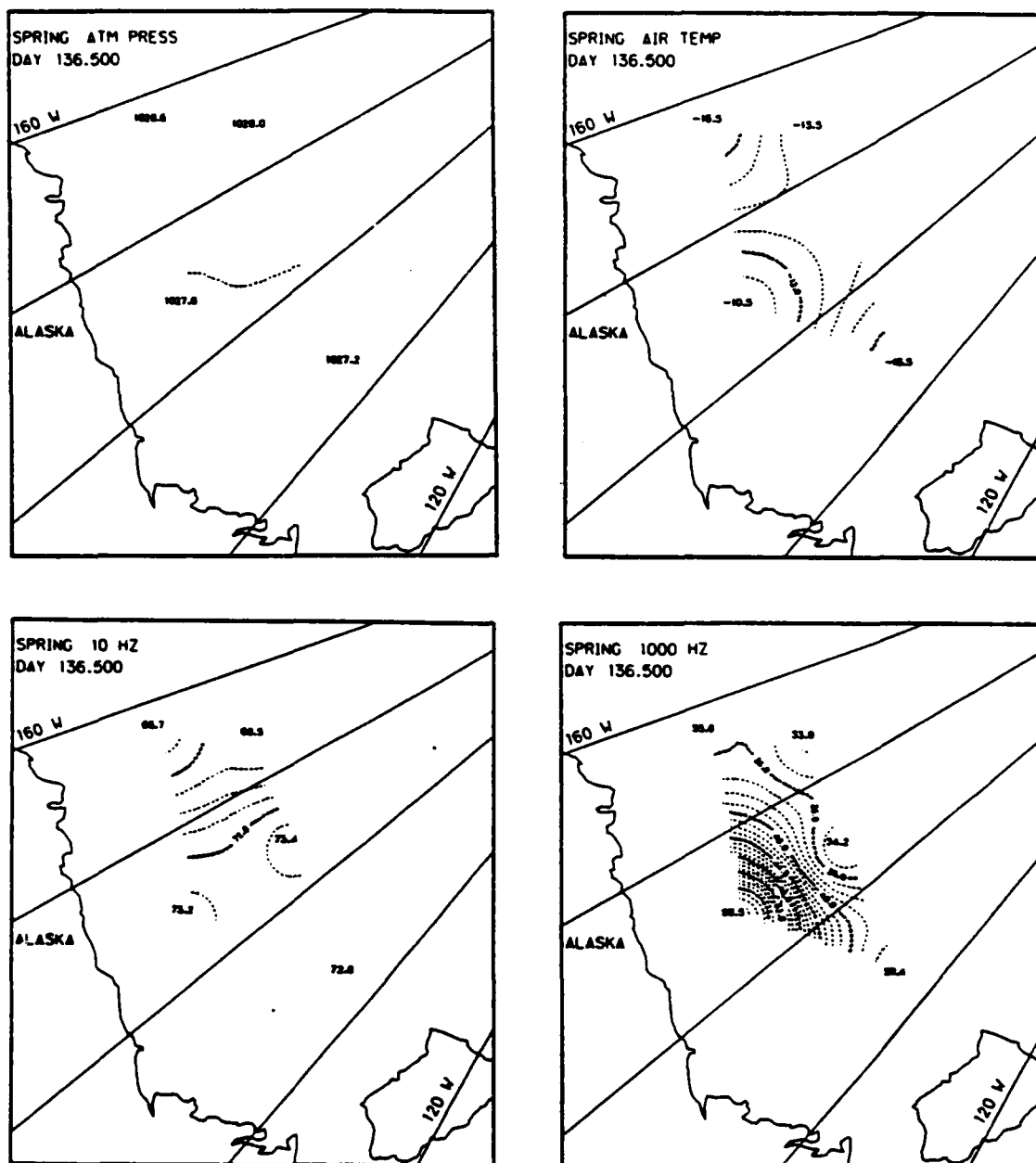


Fig. 24. Two-dimensional contour maps of atmospheric pressure, air temperature, 10 Hz ambient noise, and 1000 Hz ambient noise during spring 1976, Julian day 136.5.

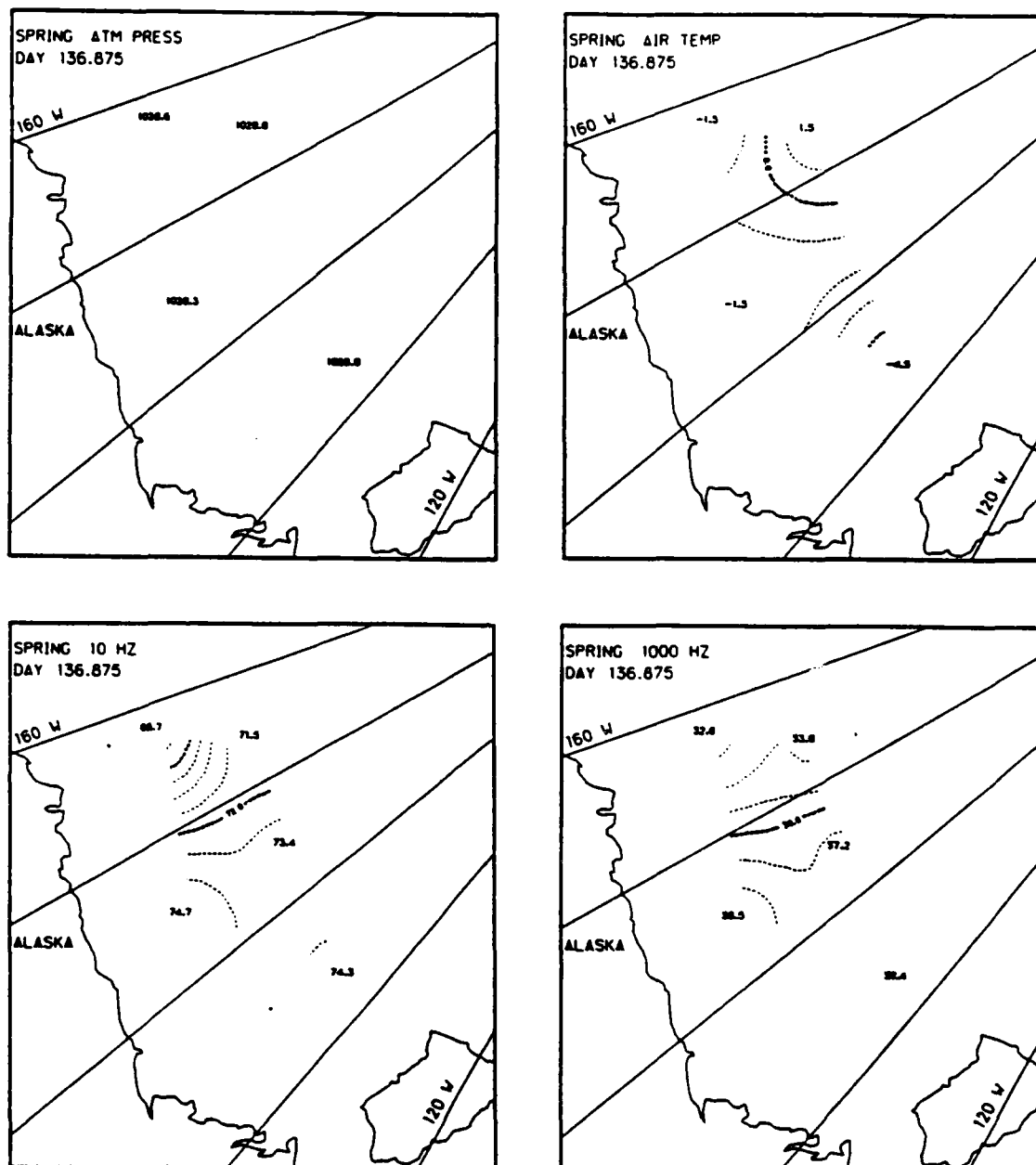


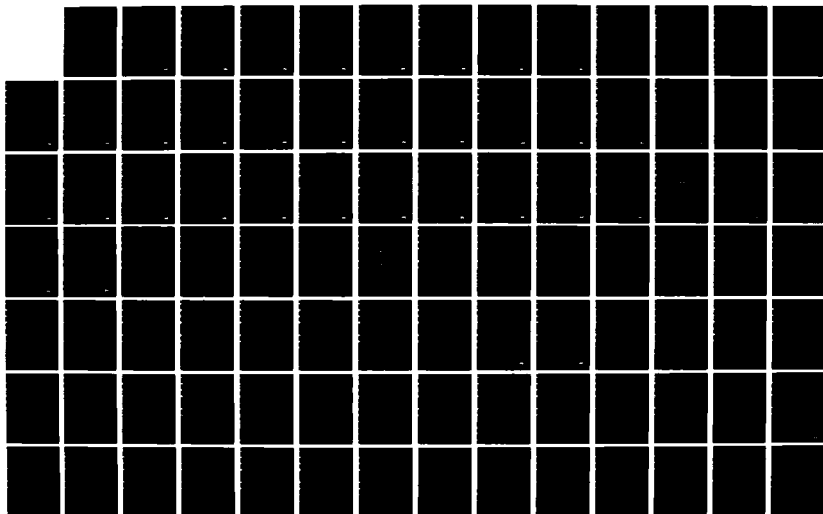
Fig. 25. Two-dimensional contour maps of atmospheric pressure, air temperature, 10 Hz ambient noise, and 1000 Hz ambient noise during spring 1976, Julian day 136.875.

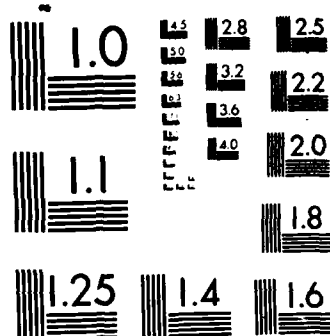
AD-A165 303

A STUDY OF SEA ICE KINEMATICS AND THEIR RELATIONSHIP TO 2/4
ARCTIC AMBIENT NO. (U) SCIENCE APPLICATIONS
INTERNATIONAL CORP COLLEGE STATION TX J K LEWIS ET AL.

UNCLASSIFIED

FEB 86 SAIC-85/1950-PT-1/2 N00014-85-C-0531 F/G 8/12 NL





MICROCOPY RESOLUTION TEST CHART
NATIONAL BUREAU OF STANDARDS-1963-A

again, the 1000 Hz noise level was almost spatially constant at 40 db. Thus, in a 27 hr period we see a diurnal fluctuation in the air temperature and the 1000 Hz signal.

This pattern is continued over the next 21 hrs as shown in Figs. 24 and 25. The atmospheric pressure field appears to be relatively constant, but the air temperature once again reaches a minimum (Fig. 24) and then increases (Fig. 25). The 10 Hz ambient noise levels are not greatly affected by this temperature fluctuation, but the 1000 Hz signal in the southern Beaufort once again increases by almost 10 db (Fig. 24) and then decreases by 20 db (Fig. 25).

It is curious to note that the apparent effects of these temperature fluctuations were enhanced in the southern Beaufort Sea. If the variations in the 1000 Hz signal were truly a result of heat fluxes, the spatial structure of the 1000 Hz data would indicate greater heat fluxes in the southern Beaufort. We can only speculate as to the factors that could enhance heat flux in this southern region, but the data distinctly indicate that the degree of thermal microfracturing for a given air temperature fluctuation can be highly regionally dependent.

Finally, this spring data set seems to indicate that high frequency noise levels tend to fall with increasing air temperature. This is opposed to the accepted concept that the noise level falls as the air temperature reaches its minimum, with no noise intensity variations during periods of increasing air temperatures.

5. SPACE AND TIME SCALES

Space Scales

In order to consider scales of spatial variations, we calculate the spatial autocorrelations of the 10 Hz, 32 Hz, and 1000 Hz signals for all four seasons. We then define the e-folding length scale e_L as that distance at which the correlation first drops below e^{-1} . We use $e_L=1000$ km if the correlation never drops below e^{-1} . Thus, our e-folding scale indicates the distance at which one would expect, on the average, significant variations in the 10 Hz, 32 Hz, and 1000 Hz ambient noise signals for each season.

Our results are shown in the three-dimensional figure in Fig. 26. For the 10 Hz signal, we see a maximum e_L of 825 km during the winter and a minimum e_L of 300 km during the summer. Recall that the summer data were contaminated by strum, but the strum was apparently spatially coherent enough to produce an e_L of the same order as the uncontaminated fall 10 Hz signal ($e_L=325$ km). During the spring, the 10 Hz e-folding scale was 440 km.

The 32 Hz signal was found to have significantly larger length scales for all seasons but winter. The minimum e_L was 440 km for the summer, and the spatial correlation was never below e^{-1} for the spring ($e_L=1000$ km). During the winter, the 32 Hz space scale was essentially the same as that of the 10 Hz signal (~ 800 km). The differences between the 32 Hz and 10 Hz e_L 's for spring and fall are somewhat puzzling considering the similarities between these two signals.

Considering the 1000 Hz length scales, we find a maximum e_L of 300 km which occurs during the summer and spring. The minimum e_L

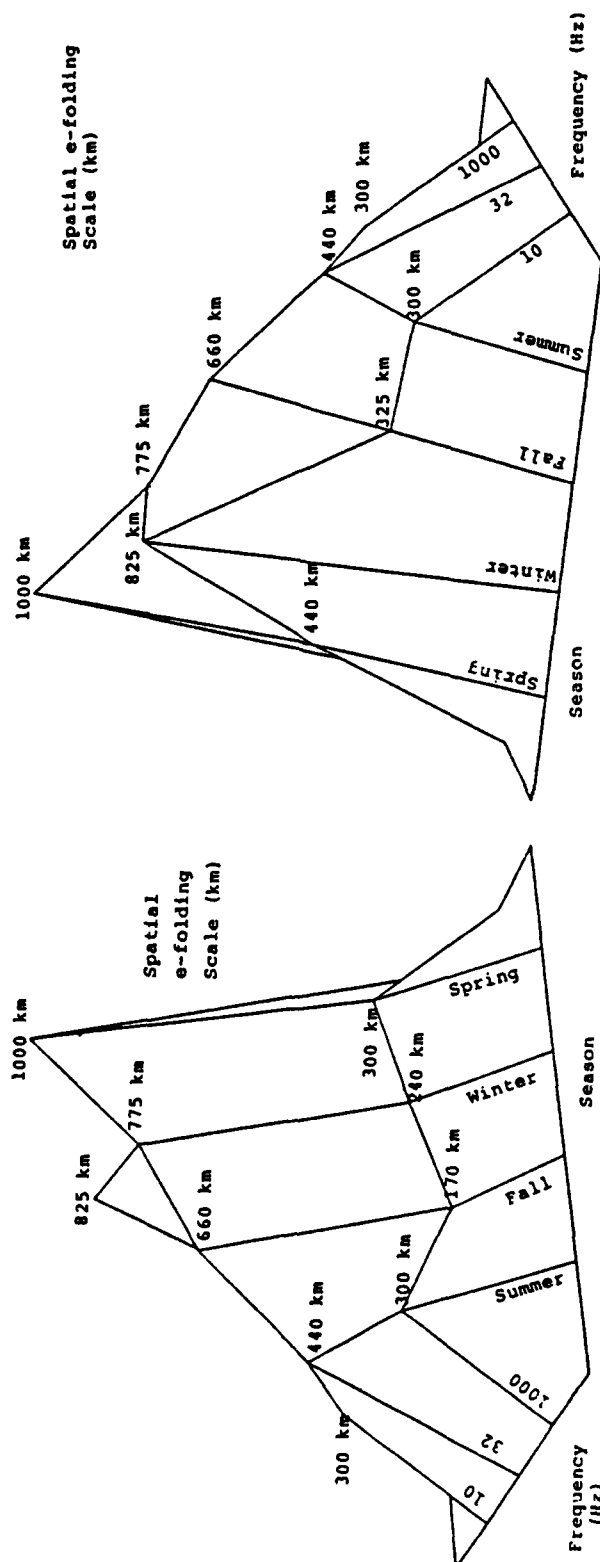


Fig. 26. Spatial e-folding scales (km) of ambient noise (pressure amplitude) as a function of season and frequency.

occurs during the fall with an e-folding scale of only 170 km. These smaller spatial scales of variations in the kHz range are most likely the effect of the more rapid decay of higher frequency noise energies with distance. The larger spatial coherences at lower frequencies can be a result of a) larger spatial scales of the forcing functions and/or b) the ability of one hydrophone to "hear" what is happening further away because of less noise energy decay with distance.

One must realize that the distances shown in Fig. 26 are the result of an arbitrary definition of a length scale. Actually, these results are somewhat misleading because of the variations of noise characteristics throughout the Beaufort Sea. Consider the following:

- 1) During the summer, the variations of noise levels at all three frequencies in the eastern Beaufort Sea are distinctly different from the rest of the Beaufort (see Figs. 11-15). Indeed, if the acoustic station in the eastern Beaufort is neglected, we would have

summer 32 Hz $e_L = 1000$ km
 summer 1000 Hz $e_L = 1000$ km

- 2) During the fall and winter, the variations of the 10 Hz and 32 Hz signals in the western Beaufort are distinctly different from the rest of the Beaufort (see Figs. 16 and 18). Neglecting the western Beaufort acoustic data gives

fall 10 Hz $e_L = 1000$ km
 fall 32 Hz $e_L = 1000$ km
 winter 10 Hz $e_L = 1000$ km
 winter 32 Hz $e_L = 1000$ km.

Thus, if we were to only consider the central portion of the Beaufort Sea, the data would indicate some length scales of variations greater than those depicted in Fig. 26.

Time Scales

We can calculate the autocorrelations of the 10 Hz, 32 Hz, and 1000 Hz signals at each acoustic station for each season. This allows us to define an e-folding time e_T at each acoustic station for each frequency. This parameter indicates the time at which one could expect significant variations in the ambient noise signals given a location and season. If our calculations did not show a correlation dropping below e^{-1} for up to 3 days time lag (at 3 hr intervals), we use $e_T=80$ hrs.

The results of the 10 Hz data are presented in Figs. 27-30. The effects of strum during the summer result in e_T 's of 7 to 20 hrs, with the shorter e-folding times found in the eastern Beaufort. During the fall (Fig. 28), we see that the e_T 's vary from 14 to 27 hrs, with scale times increasing on approaching the United States and Canadian coasts. Thus, the offshore 10 Hz noise variations were less consistent in time compared to the noise variations close to shore. By the winter (Fig. 29), the situation had reversed with the lowest e_T 's being found in the southern Beaufort (29.5 hrs) and western Beaufort (25 hrs). Winter is the most temporally consistent season at 10 Hz, but the spring (Fig. 30) still has e-folding times of the order of 30 hrs. However, the spatial structure of the spring 10 Hz e_T 's shows minimum time scales in the eastern Beaufort (23 hrs) with a gradual increase of up to $e_T=33$ hrs in the western Beaufort.

The spatial patterns of the 32 Hz e-folding times are shown in Figs. 31-34. Except for the summer data, the patterns are similar to

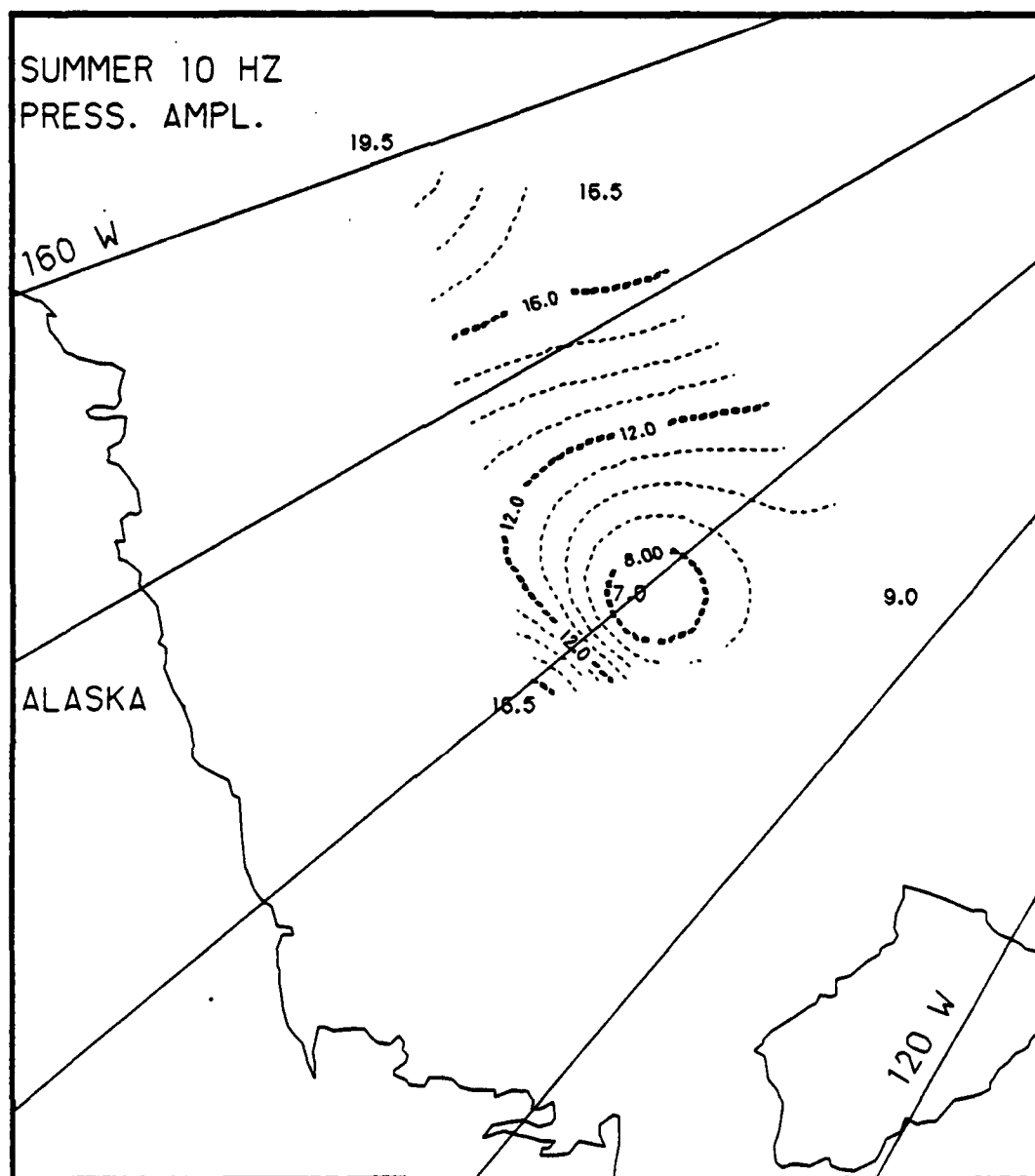


Fig. 27.

Ambient noise e-folding times (hrs) based on the AIDJEX data during summer at 10 Hz (pressure amplitude).

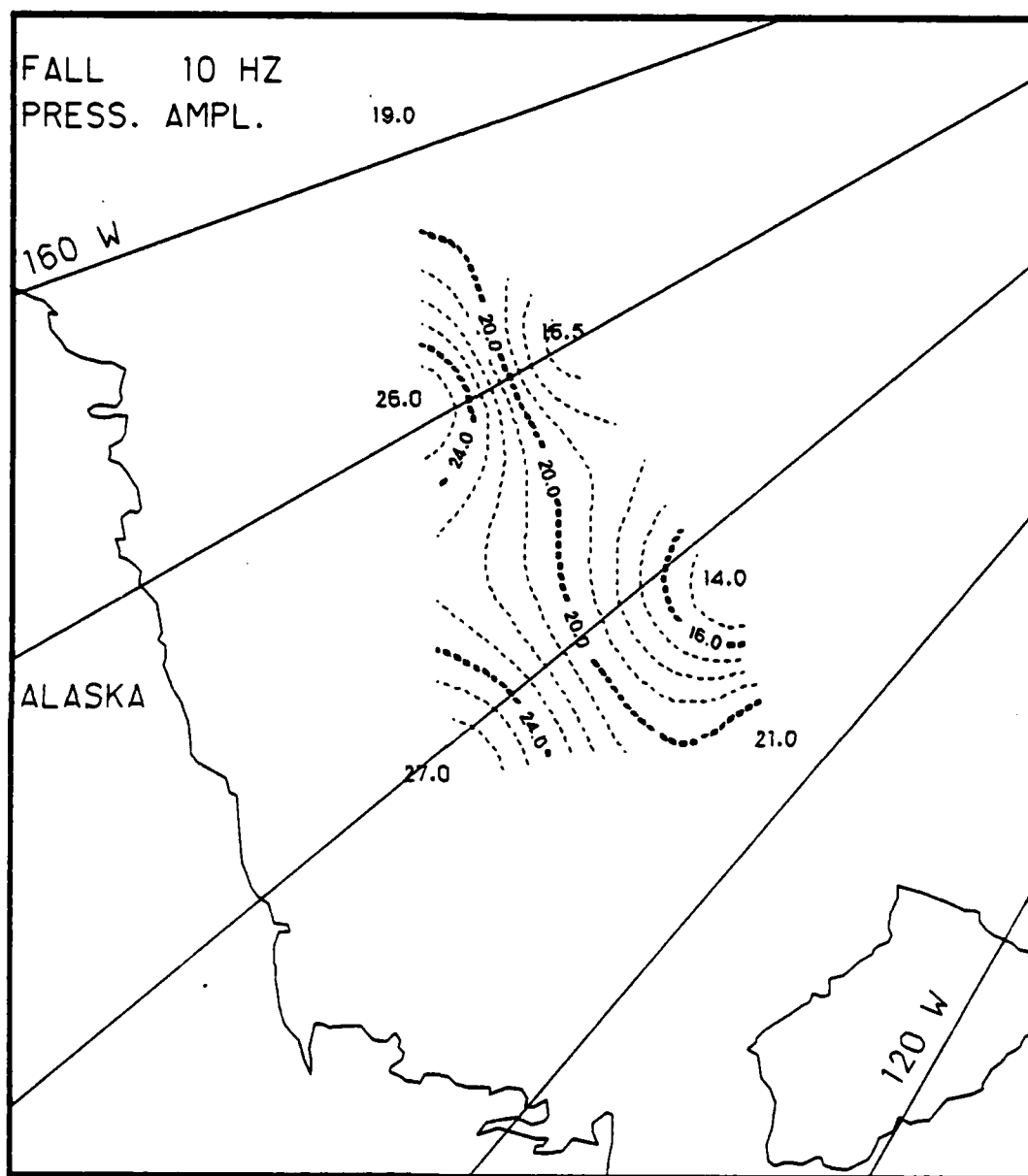


Fig. 28.

Ambient noise e-folding times (hrs) based on the AIDJEX data during fall at 10 Hz (pressure amplitude).

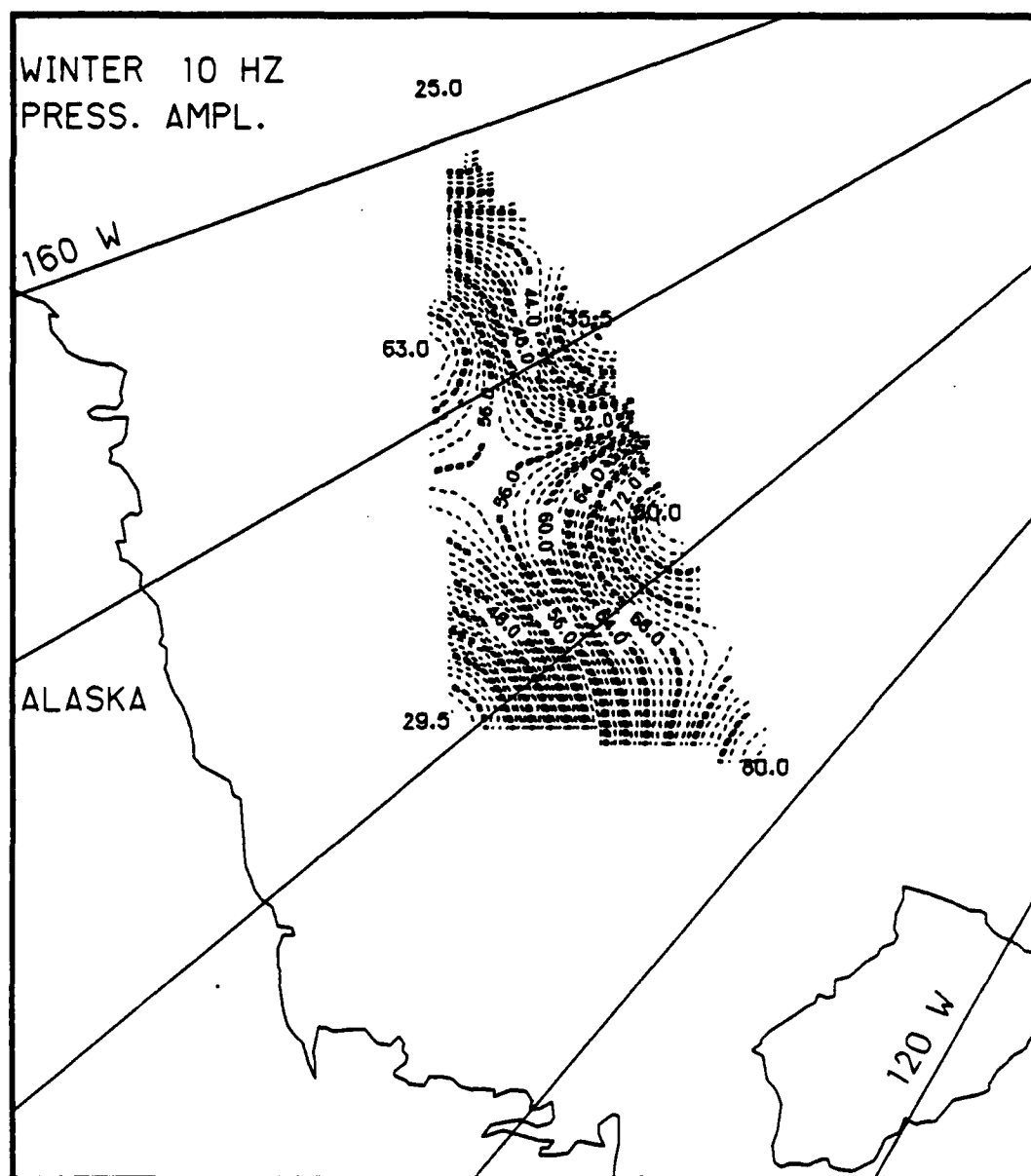


Fig. 29.

Ambient noise e-folding times (hrs) based on the AIDJEX data during winter at 10 Hz (pressure amplitude). An 80 hr e-folding time indicates that the autocorrelation did not fall below e^{-1} for any of the phase lags.

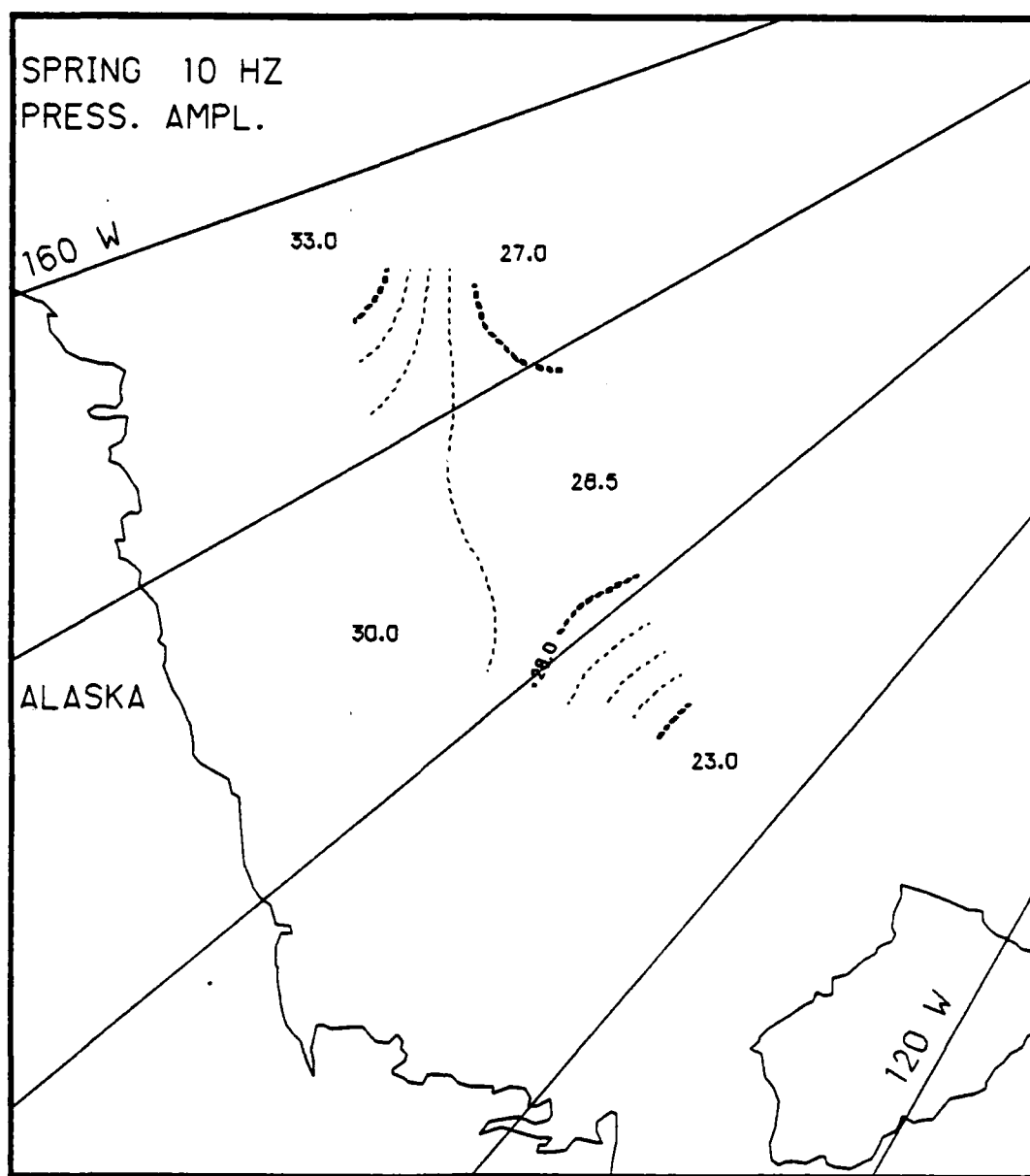


Fig. 30.

Ambient noise e-folding times (hrs) based on the AIDJEX data during spring at 10 Hz (pressure amplitude).

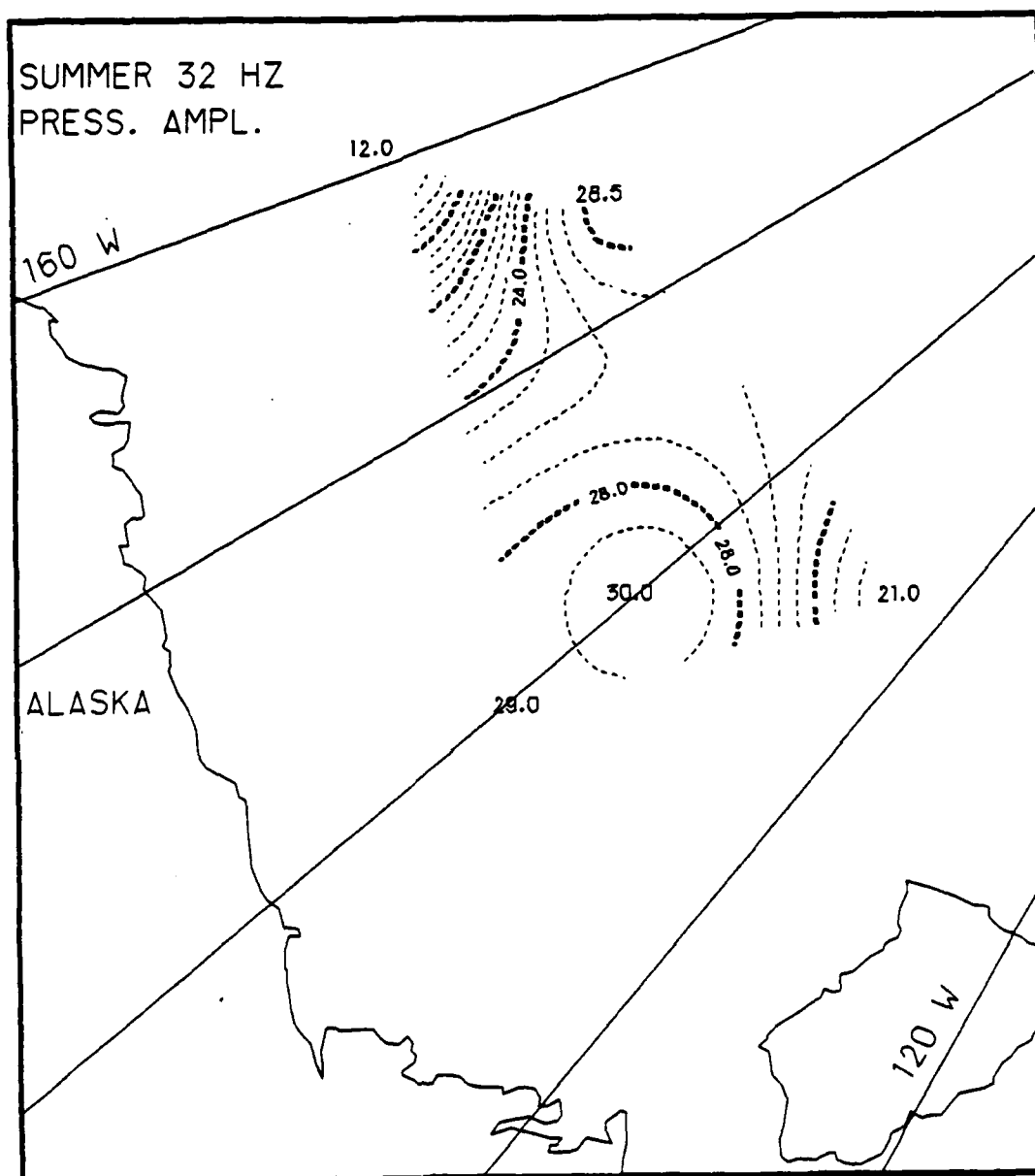


Fig. 31.

Ambient noise e-folding times (hrs) based on the AIDJEX data during summer at 32 Hz (pressure amplitude).

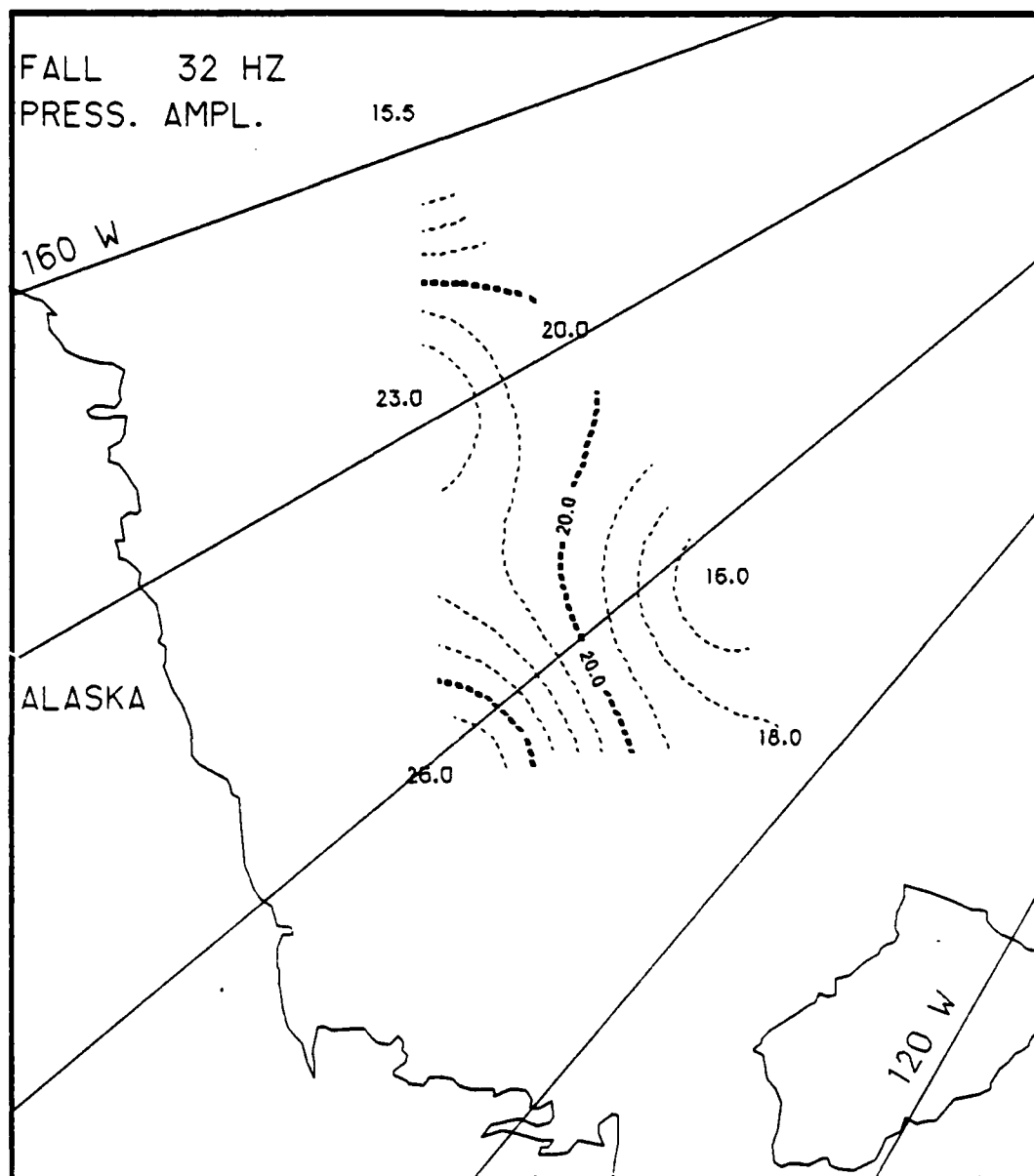


Fig. 32.

Ambient noise e-folding times (hrs) based on the AIDJEX data during fall at 32 Hz (pressure amplitude).

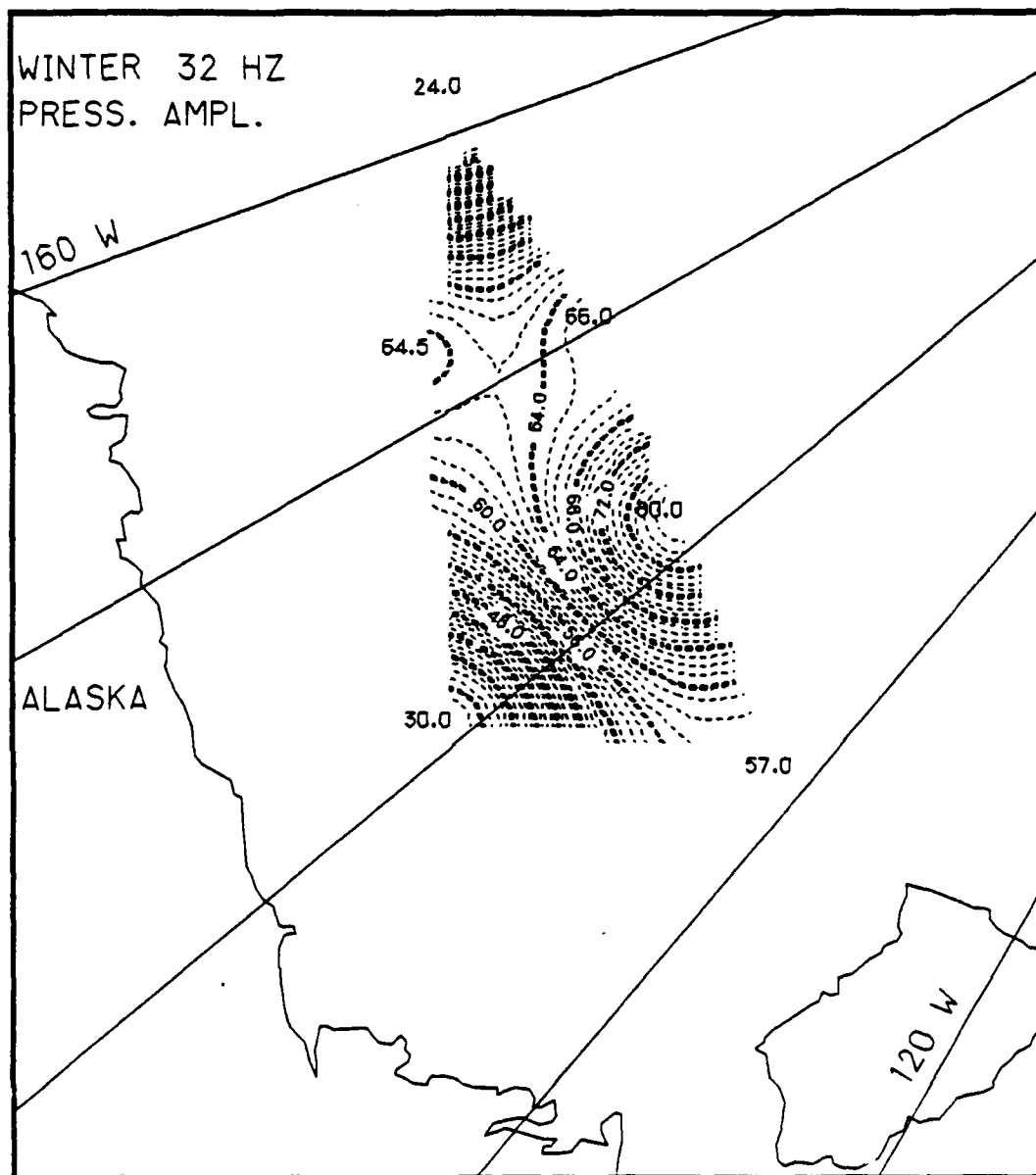


Fig. 33.

Ambient noise e-folding times (hrs) based on the AIDJEX data during winter at 32 Hz (pressure amplitude). An 80 hr e-folding time indicates that the autocorrelation did not fall below e^{-1} for any of the phase lags.

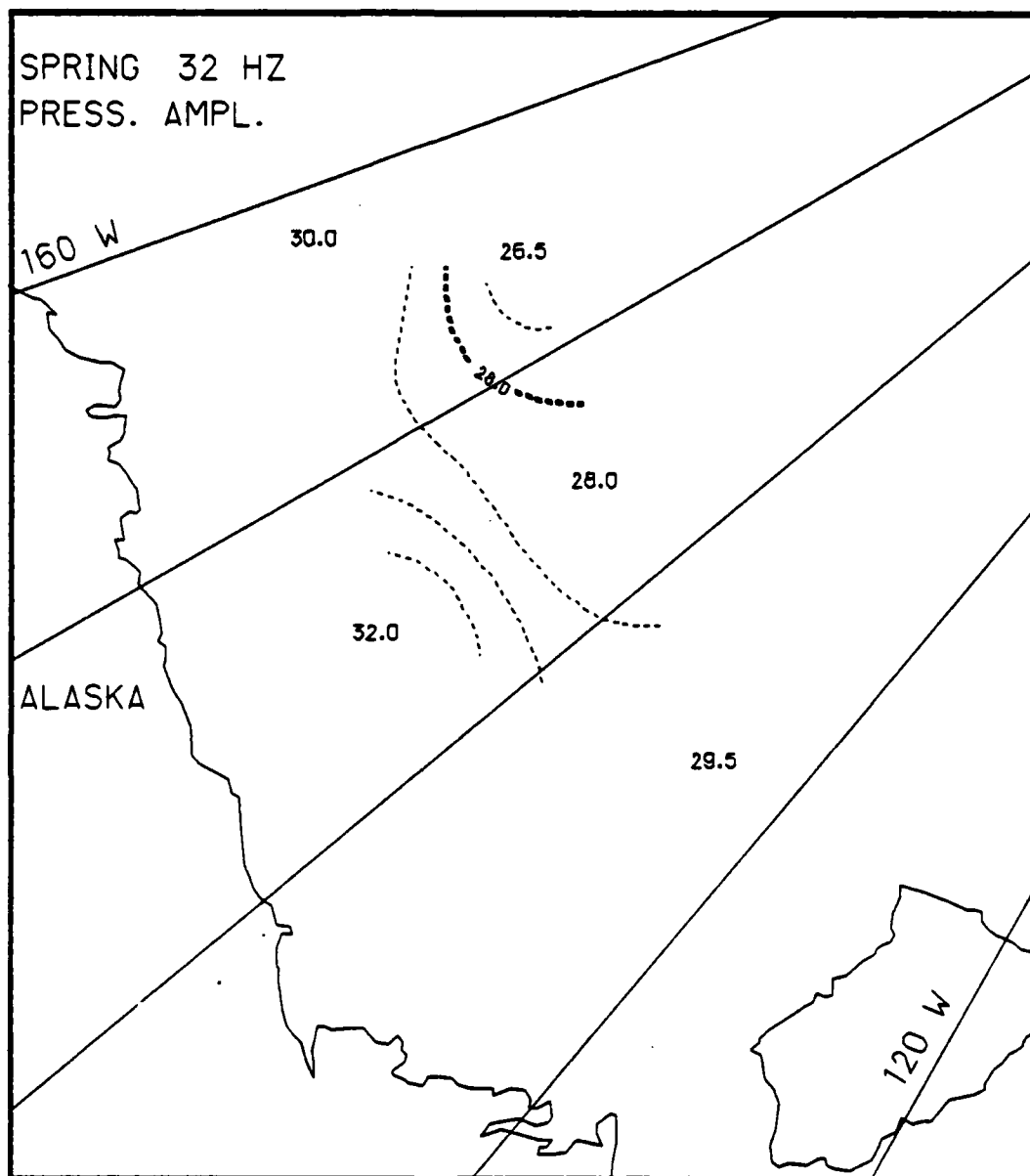


Fig. 34.

Ambient noise e-folding times (hrs) based on the AIDJEX data during spring at 32 Hz (pressure amplitude).

the 10 Hz patterns, as one would expect. During the summer, the 32 Hz e_T 's for the central Beaufort are in the range of 29 hrs, while in the eastern Beaufort $e_T=21$ hrs and in the western Beaufort e_T is even smaller at 12 hrs. Based on the poor spatial noise correlations between the eastern Beaufort and the rest of the region, one might expect a significantly different e-folding time in the east, but the western e_T of 12 hrs was not expected. The fall e_T spatial pattern at 32 Hz (Fig. 32) shows a general decrease in time scales and is very similar to the 10 Hz fall pattern (Fig. 28), with, once again, the time scales decreasing with distance offshore. The winter 32 Hz pattern (Fig. 33) shows the smallest time scales of variations in the southern Beaufort and the western Beaufort. The winter time scales range from 24 hrs to 80 hrs. By spring (Fig. 34), all time scales had dropped (less temporally coherent), with a range throughout the study area of only 26.5 to 32 hrs.

The e-folding times for the 1000 Hz data are presented in Figs. 35-38. We see that the 1000 Hz summer time scales (Fig. 35) are quite similar in magnitude and structure to the 32 Hz summer time scales (Fig. 31). However, this similarity is not seen during the rest of the seasons. As with the spatial scales, the 1000 Hz temporal scales are considerably smaller than the corresponding 10 Hz and 32 Hz scales for the fall, winter, and spring. During the fall (Fig. 36), the 1000 Hz e_T has a minimum of only 4.5 hrs in the eastern Beaufort Sea, and the e_T scales gradually increase up to 18.5 hrs going westward. During the winter (Fig. 37), we find the longest time scale in the southern Beaufort (15 hrs) with the e_T 's decreasing as one goes offshore. This is opposite of the general 10 Hz and 32 Hz patterns. The minimum 1000 Hz winter e_T was only 3 hrs (the time interval of the sampling of the noise). By the spring (Fig. 38), the offshore 1000 Hz e-folding times had increased somewhat, but the time scales for the stations closest to shore had decreased. The 6 hr e_T

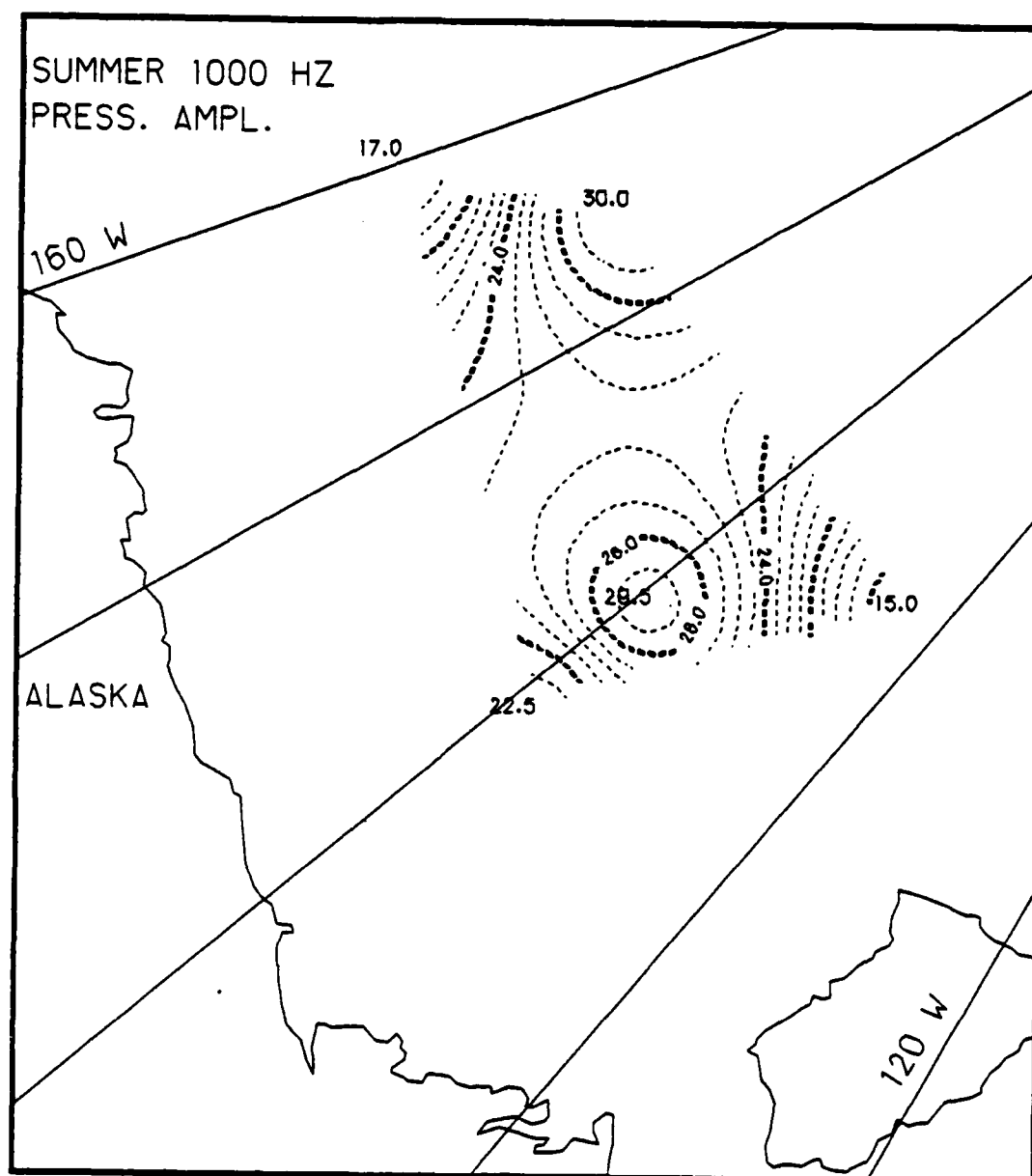


Fig. 35.

Ambient noise e-folding times (hrs) based on the AIDJEX data during summer at 1000 Hz (pressure amplitude).

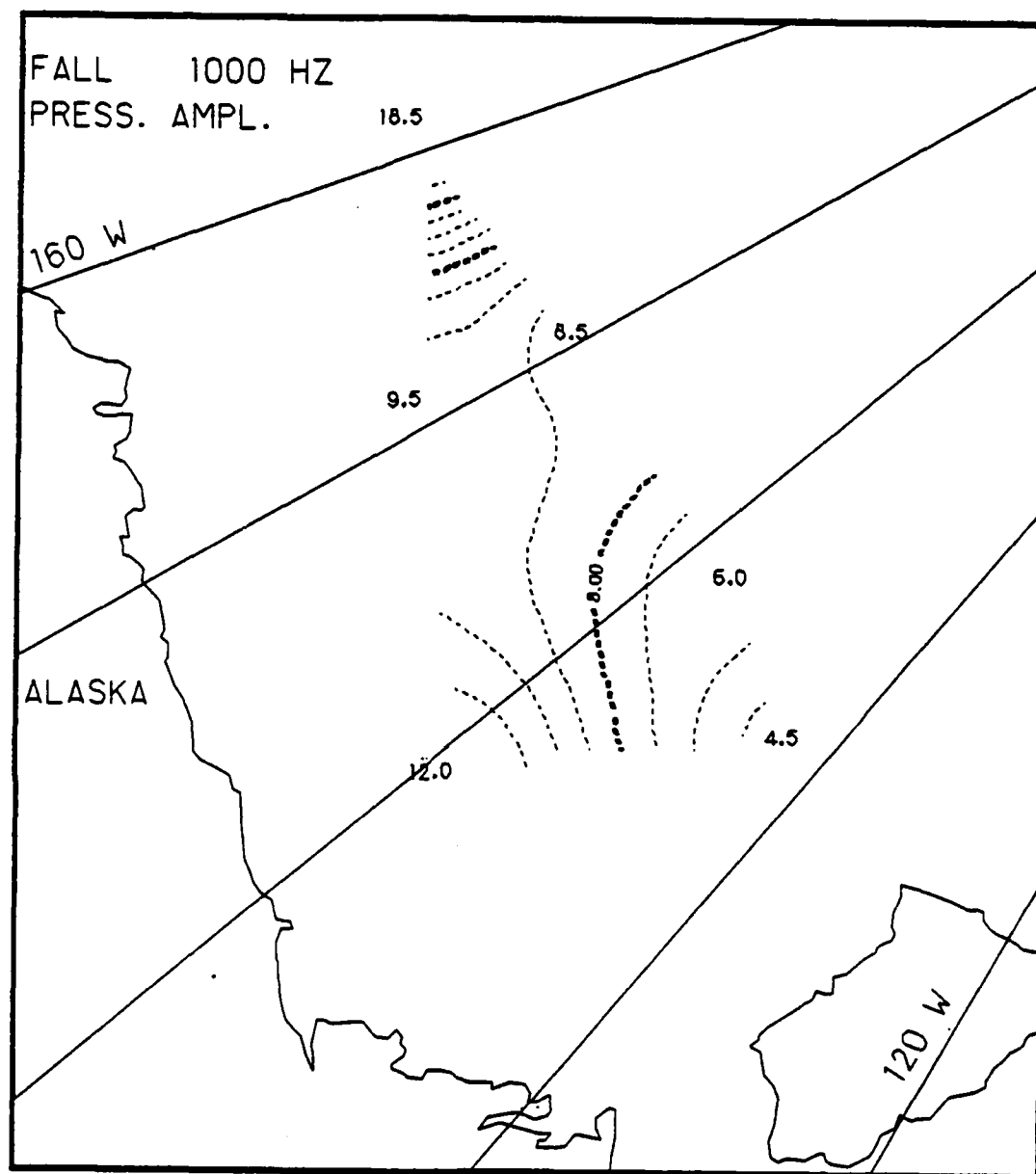


Fig. 36.

Ambient noise e-folding times (hrs) based on the AIDJEX data during fall at 1000 Hz (pressure amplitude).

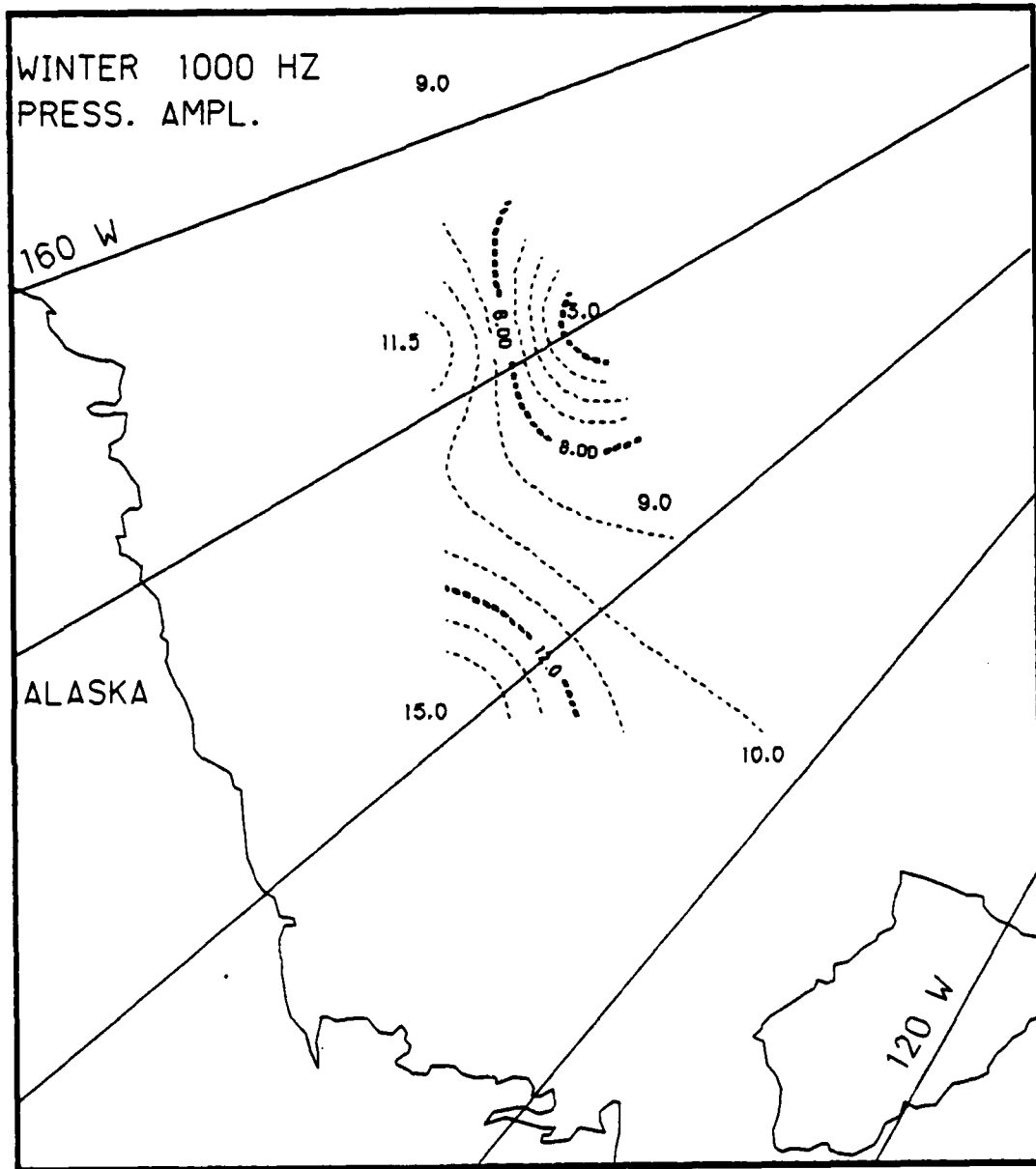


Fig. 37.

Ambient noise e-folding times (hrs) based on the AIDJEX data during winter at 1000 Hz (pressure amplitude).

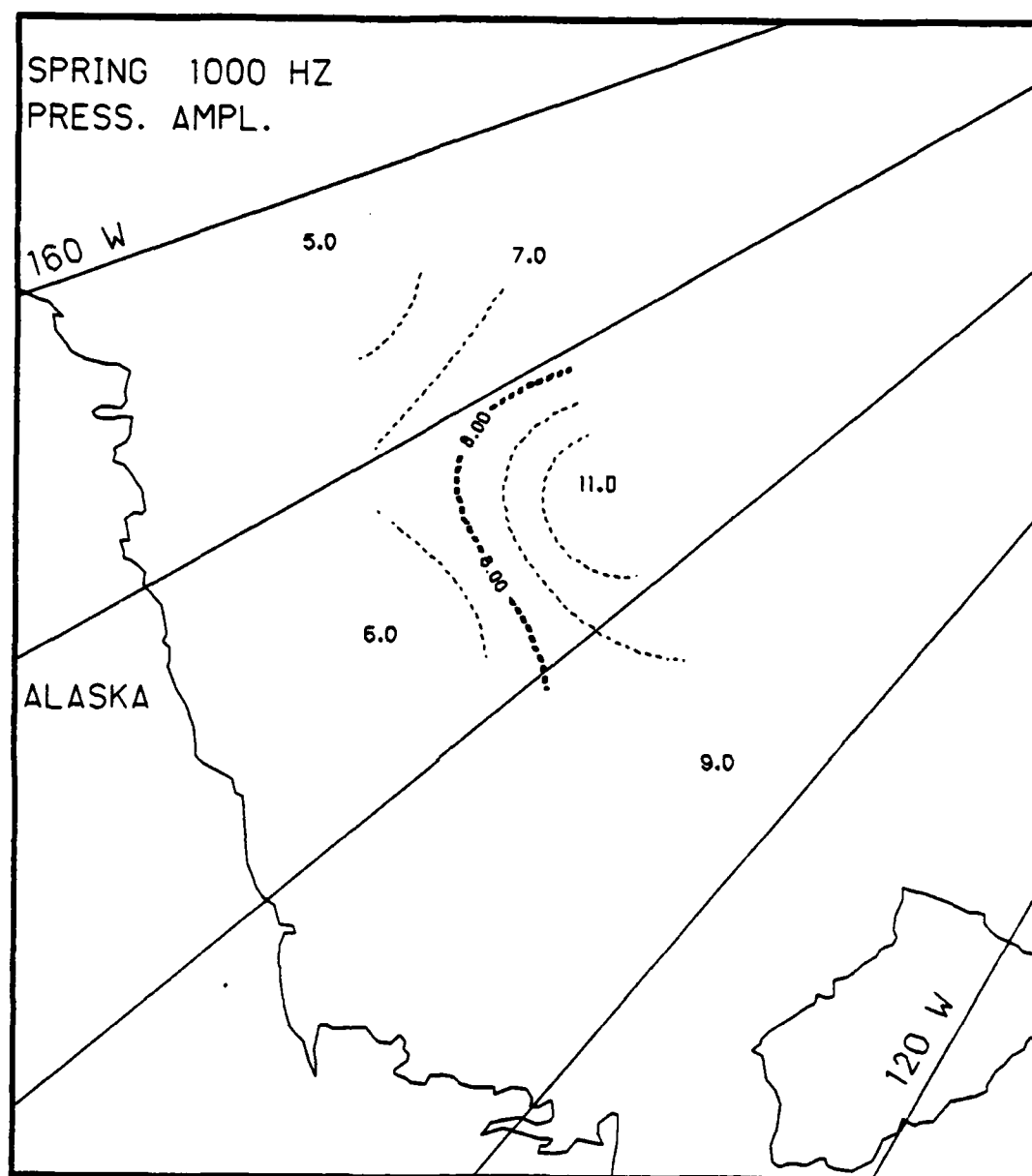


Fig. 38.

Ambient noise e-folding times (hrs) based on the AIDJEX data during spring at 1000 Hz (pressure amplitude).

found in the southern Beaufort during the spring was the lowest found in that region by a factor of 50%.

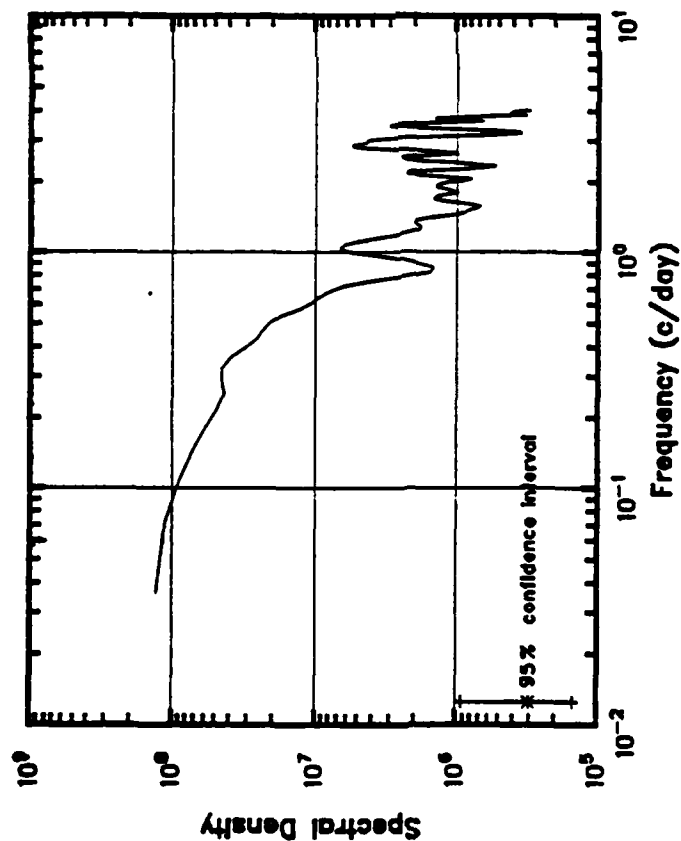
We stress once again that the results of our calculations are based on an arbitrary choice of a scaling parameter. Some of the features in Figs. 27-38 could change if other parameterizations had been used. For example, consider the winter 10 Hz time scales of 35.5 hrs (north central Beaufort) and 29.5 hrs (southern Beaufort) and the winter 32 Hz time scale of 30 hrs (southern Beaufort). In all three of these cases, the autocorrelation dipped just to the e^{-1} level and then increased. Without these dips, the e_T 's would all have been higher, sometimes by a factor of up to 2. However, the trend of having smaller e_T scales in the southern Beaufort would not have been changed.

Noise Power Spectra

In performing the above autocorrelations, some interesting fluctuations were noted. Here we discuss these fluctuations in terms of the power spectra of the ambient noise levels for all three frequencies.

First, we note an energy peak at 1 cycle per day (cpd) in the 10 Hz and 32 Hz signals during winter (Fig. 39) and spring (Fig. 40). In Dyer's classification, these frequency bands are primarily the result of ice motion. Thus, we would not expect daily temperature fluctuations to be responsible for this 1 cpd energy peak. Lewis et al. (1985) noted some daily oscillations in some of the winter and spring ice kinematic parameters, and it is possible that that daily motion causes the diurnal signal in the noise. However, it is not clear what physical process would cause a distinct daily variation in ice movement.

AMBIENT NOISE SPECTRUM
10 HZ, PRESS AMP
WINTER 1976



AMBIENT NOISE SPECTRUM
32 HZ, PRESS AMP
WINTER 1976

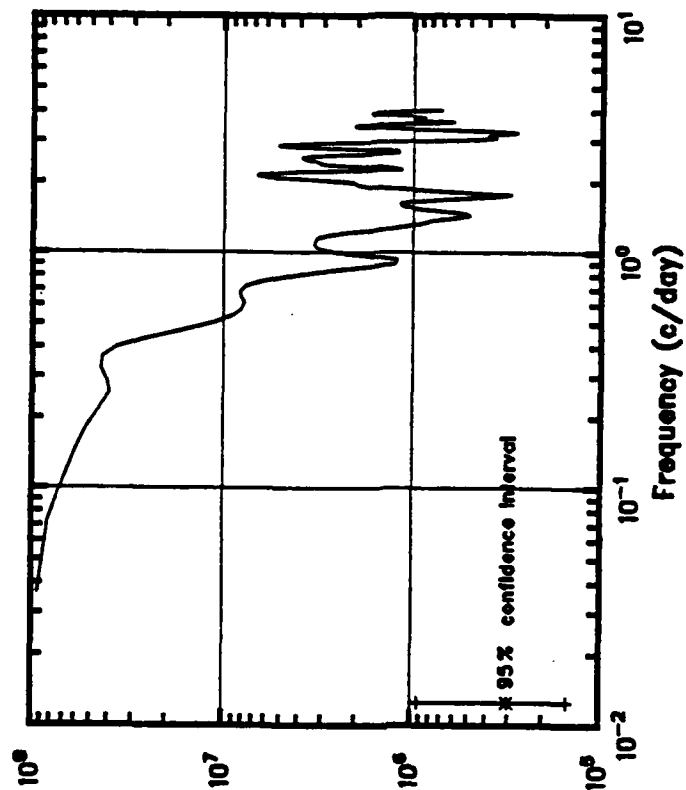
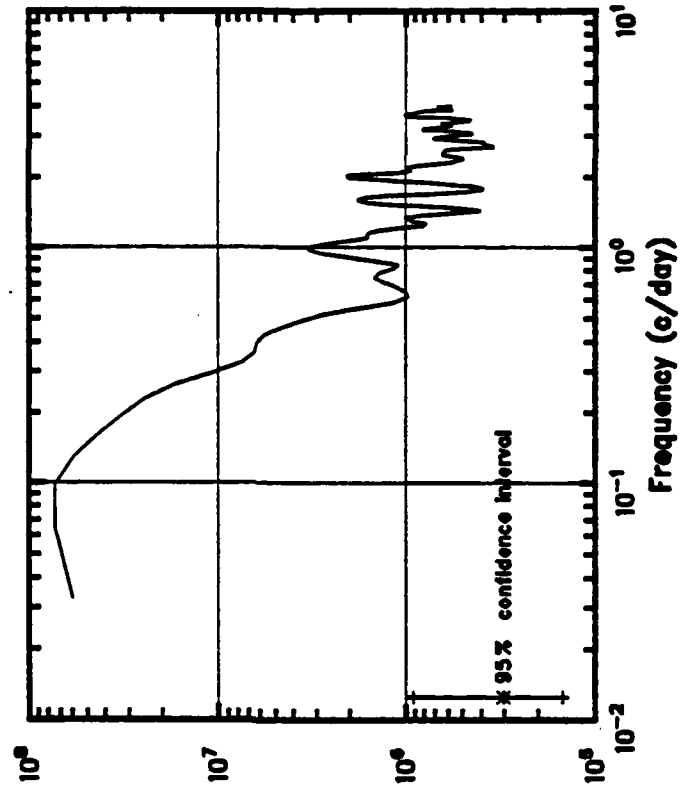


Fig. 39. Winter energy density spectra at a) 10 Hz and b) 32 Hz (pressure amplitude).

AMBIENT NOISE SPECTRUM
32 HZ, PRESS AMP
SPRING 1976



AMBIENT NOISE SPECTRUM
10 HZ, PRESS AMP
SPRING 1976

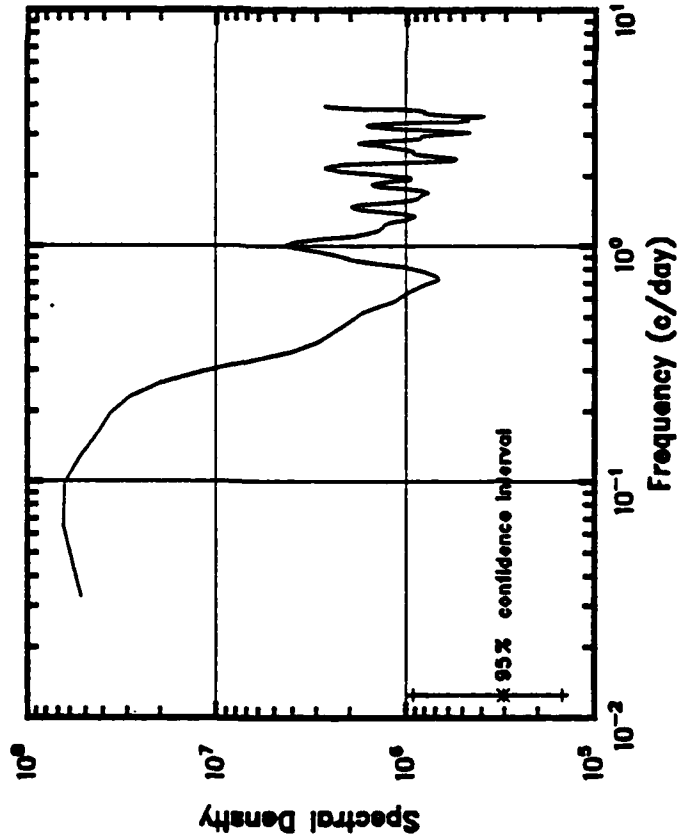
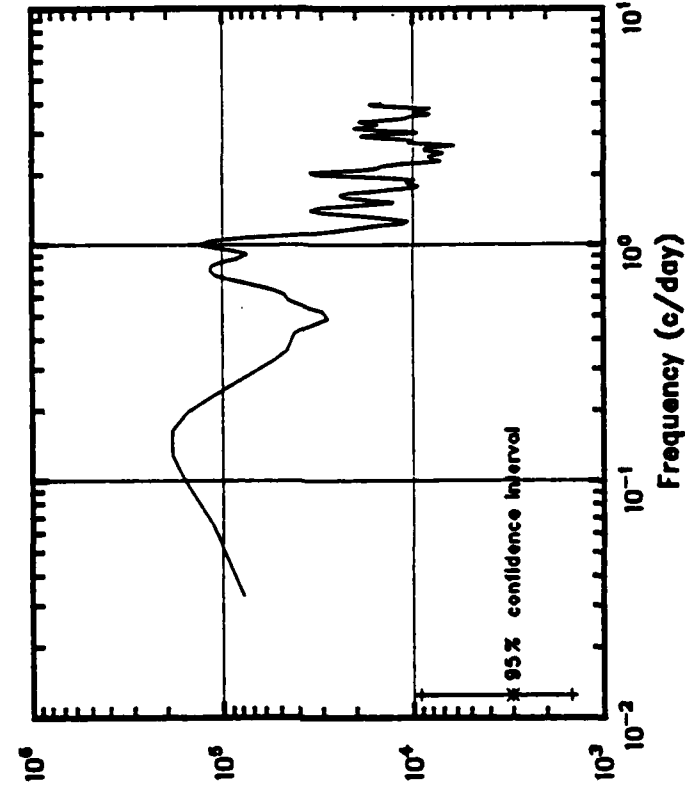


Fig. 40. Spring energy density spectra at a) 10 Hz and b) 32 Hz (pressure amplitude).

Another factor seen in the 32 Hz winter spectra (Fig. 39) is the presence of relatively strong oscillations at 2 to 3 cpd. Other energetic, higher frequency signals are seen in the 1000 Hz data during the non-summer periods (see Fig. 41). These oscillations are too high in frequency (>1 cpd) to be caused by temperature fluctuations. One would again assume that ice motion is responsible.

AMBIENT NOISE SPECTRUM
1000 HZ, PRESS AMP
SPRING 1976



AMBIENT NOISE SPECTRUM
1000 HZ, PRESS AMP
FALL 1975

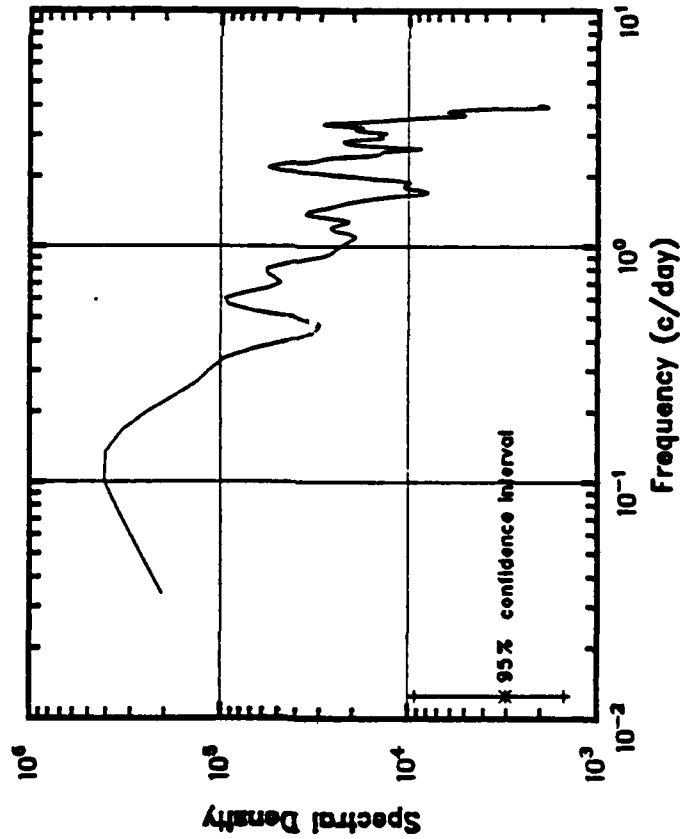


Fig. 41. Energy density spectra at 1000 Hz for a) fall and b) spring (pressure amplitude).

6. CORRELATIONS BETWEEN AMBIENT NOISE AND ICE KINEMATICS

Ambient noise levels from two acoustic stations were correlated with the variations of the ice kinematic parameters plus the air temperature fluctuations for the summer and fall of 1975. The acoustic stations were Station 10 (~100 km south of the manned camps) and Station 66 (~70 km north of the manned camps). During the winter, only Station 10 was close enough to perform the correlations. Unfortunately, coinciding noise and high resolution ice kinematic data do not exist for spring, so correlations could not be calculated for that season.

We first consider the correlations at 10 Hz and 32 Hz for the three seasons (Tables 1-3). Since these two low frequency signals are so similar for most of the year, one would expect similar results. Due to the situation of the summer 10 Hz data probably being contaminated by strum, the correlations for that data set will not be discussed.

Correlations - 10 Hz and 32 Hz

During the summer, we see that the translation speed U of the ice is well correlated with the 32 Hz ambient noise signals for both stations (Station 10 in the southern Beaufort Sea and Station 66 in the central Beaufort Sea). Of course, this is not a surprising result since, in most cases, the ice pack will try to move as it is put under stress. We may test the hypothesis that differential motion is the true cause of the noise by eliminating U in the correlation calculation. If this is done, the correlations between the DKP and Δ and the noise are only 0.48 for Station 10 and 0.59 for Station 66. These correlations imply that the 32 Hz signal is indeed

Correlations (% Variances)

	10 Hz		32 Hz		1000 Hz	
	Stat. 10	Stat. 66	Stat. 10	Stat. 66	Stat. 10	Stat. 66
U	—	—	0.74 (54.6)	0.82 (67.3)	0.63 (40.3)	—
U ²	0.65 (42.4)	0.70 (48.9)	0.72 (52.3)	0.80 (63.6)	0.65 (41.7)	0.76 (58.1)
D	0.48 (23.2)	0.41 (16.8)	0.28 (8.1)	0.40 (15.7)	0.30 (8.7)	0.23 (5.3)
ζ	0.47 (22.5)	0.31 (9.7)	0.41 (16.5)	0.37 (13.6)	0.44 (19.0)	0.27 (7.1)
N	-0.04 (0.2)	-0.11 (1.2)	0.01 (0.0)	0.0 (0.0)	-0.09 (0.8)	0.0 (0.0)
S	0.09 (0.9)	-0.02 (0.0)	0.06 (0.3)	0.09 (0.8)	0.08 (0.6)	-0.07 (0.5)
Δ	0.02 (0.0)	0.06 (0.4)	0.03 (0.1)	0.05 (0.2)	0.0 (0.0)	0.07 (0.5)
D	0.40 (15.9)	0.50 (25.1)	0.27 (7.2)	0.40 (16.3)	0.20 (3.9)	0.19 (3.8)
ζ	0.39 (15.2)	0.31 (9.5)	0.33 (10.8)	0.35 (12.5)	0.23 (5.5)	0.13 (1.7)
(N ² +S ²) ^{1/2}	0.23 (5.3)	0.38 (14.3)	0.30 (8.7)	0.42 (17.4)	0.14 (1.9)	0.32 (10.1)
Maximum Correlation	0.73	0.74	0.76	0.84	0.69	0.81

Table 1. Linear correlation coefficients between the summer AIDJEX ambient noise data sets (Stations 10 and 66) and various ice kinematic parameters (manned camp position data). The percent variances accounted for are in parentheses. The maximum correlation is that obtained by the linear combination of various ice kinematic parameters and air temperature fluctuations.

Correlations (% Variances)

	10 Hz		32 Hz		1000 Hz	
	Stat. 10	Stat. 66	Stat. 10	Stat. 66	Stat. 10	Stat. 66
U	0.72(52.5)	0.76(58.4)	0.70(49.2)	0.70(48.7)	0.34(11.5)	0.28(7.7)
U ²	0.61(37.7)	0.74(55.4)	0.59(35.4)	0.62(38.8)	0.28(7.6)	0.20(4.0)
D	0.07(0.5)	0.23(5.5)	0.09(0.8)	0.18(3.2)	0.11(1.3)	0.26(6.6)
z	-0.21(4.4)	-0.48(22.7)	-0.21(4.3)	-0.42(17.6)	-0.08(0.6)	-0.20(3.9)
N	-0.06(0.4)	0.01(0.0)	-0.09(0.8)	-0.02(0.1)	-0.11(1.3)	0.01(0.0)
S	-0.46(21.0)	-0.40(16.2)	-0.49(24.2)	-0.34(11.8)	-0.32(10.1)	-0.06(0.4)
Δ	0.06(0.4)	0.10(1.0)	0.01(0.0)	0.07(0.4)	-0.08(0.6)	0.04(0.2)
D	0.41(17.0)	0.58(33.4)	0.35(12.4)	0.55(29.9)	0.17(2.9)	0.40(16.3)
z	0.46(20.9)	0.67(44.6)	0.44(19.0)	0.59(34.4)	0.16(2.7)	0.28(7.9)
(N ² +S ²) ^{1/2}	0.63(39.4)	0.72(51.9)	0.57(32.3)	0.65(41.8)	0.11(1.3)	0.24(5.7)
Maximum Correlation	0.79	0.86	0.76	0.78	0.49	0.45

Table 2. Linear correlation coefficients between the fall AIDJEX ambient noise data sets (Stations 10 and 66) and various ice kinematic parameters (manned camp position data). The percent variances accounted for are in parentheses. The maximum correlation is that obtained by the linear combination of various ice kinematic parameters and air temperature fluctuations.

Correlations (% Variances)

	10 Hz	32 Hz	1000 Hz
U	0.60 (35.9)	0.66 (43.7)	0.60 (35.5)
U ²	0.46 (21.3)	0.56 (31.1)	0.62 (38.8)
D	-0.29 (8.4)	-0.38 (14.2)	-0.27 (7.5)
z	0.05 (0.2)	0.12 (1.4)	0.01 (0.0)
N	0.01 (0.0)	-0.04 (0.2)	-0.11 (1.3)
S	-0.10 (1.1)	-0.23 (5.3)	-0.31 (9.4)
A	0.18 (3.0)	0.13 (1.5)	-0.07 (0.1)
D	0.49 (24.0)	0.42 (18.0)	0.30 (8.8)
z	0.50 (25.4)	0.49 (23.9)	0.38 (14.1)
(N ² +S ²) ^{1/2}	0.39 (15.4)	0.38 (14.5)	0.36 (12.8)
Maximum Correlation	0.76	0.78	0.67

Table 3. Linear correlation coefficients between the winter AIDJEX ambient noise data sets (Station 10) and various ice kinematic parameters (manned camp position data). The percent variances accounted for are in parentheses. The maximum correlation is that obtained by the linear combination of various ice kinematic parameters and air temperature fluctuations.

primarily a response to the ice rushing through the water as opposed to differential motion.

The maximum correlation at Station 10 using all the summer environmental parameters is 0.76. For Station 66, the maximum correlation is 0.84. Recall that the e-folding distance for 32 Hz during the summer is 440 km. Since we are working with noise data collected on the order of 100 km from where the ice motion data were collected, one might expect that these correlations are the largest obtainable.

We note that there is little difference between the summer correlations for U and U^2 . Thus, the summer data does not allow one to interpret whether or not the lower frequency ambient noise is better related to the speed of the ice or the kinetic energy. The fall data (Table 2) seem to answer this question more clearly, with significantly higher correlations between U and both the 10 Hz and 32 Hz signals. However, during this fall season we see that differential motion becomes quite important. This is particularly true for the parameter $(N^2+S^2)^{1/2}$. Linear combinations of the DKP and Δ do not produce correlations significantly higher than by just using $(N^2+S^2)^{1/2}$. However, U and $(N^2+S^2)^{1/2}$ can be combined to obtain correlations that range from 0.72 (10 Hz at Station 10) to 0.83 (32 Hz at Station 66). Thus, the data indicate that low frequency noise during the fall is primarily a result of the ice translating through the water plus the individual ice floes moving past one another as the shape of the ice parcel changes.

During the winter (Table 3), the importance of $(N^2+S^2)^{1/2}$ decreases while other forms of differential motion become more important. We see that the best correlations are with U , the speed of the ice. However, at 10 Hz we can combine the DKP and Δ to obtain a correlation of 0.71. At 32 Hz, a combination of the DKP and Δ gives

a correlation of 0.64. This would indicate that differential motion is quite important at 10 Hz while U and the DKP are both important at 32 Hz.

During the process of correlating all the various combinations of the winter DKP and Δ shown in Table 3, it was found that only particular combinations would give relatively high correlations. For the 10 Hz signal, it was found the D, N, S, and U could be combined to obtain a correlation of 0.74. Dropping any of these parameters dropped the correlation by 0.06 or more. Divergence was the most important of the DKP, and the negative correlation implies the generation of 10 Hz noise during ice convergence. Also, the results imply that noise tends to be generated by positive normal and shear deformation.

For the 32 Hz winter signal, D, N, and U were found to give a correlation of 0.74. Once again, $D < 0$ and $N > 0$ tended to produce noise. This and the 10 Hz correlations are not as encouraging as one might have expected considering the large space scales of the 10 Hz and 32 Hz winter data (order of 800 km). This could be an indication that other processes are at work during the winter which produce low frequency noise but have no associated ice movement. For example, winter-time ice may not move under a limited forcing as a result of internal ice stresses. However, one would still expect the generation of noise due to the load put on the ice.

Correlations - 1000 Hz

The summer-time correlations between ice motion, Δ , and the 1000 Hz noise are shown in Table 1. We first point out that this higher frequency noise is best correlated with U^2 . (Indeed, at Station 66

the correlation calculation between U and 1000 Hz resulted in a negative constant in the least-squares fit. This implies a negative baseline (minimum) noise level, which is physically impossible.) The best correlations that were obtained using various combinations of the DKP and Δ (U being excluded) were 0.47 for Station 10 and 0.44 for Station 66. Thus, unlike the lower frequencies, the 1000 Hz summer signal appears to be primarily a function of the kinetic energy of the ice parcel.

The fall correlations at 1000 Hz are shown in Table 2. One immediately notices that the maximum of these correlations is considerably lower than the correlations for other frequencies and other seasons. The e-folding space scales give us a clue as to the probable reason for the low correlations. As seen in Fig. 26, the minimum e-folding length at 1000 Hz is 170 km and occurs during the fall. Thus, the problem of using noise and ice kinematic data from two different locations is enhanced during the fall. However, we will assume that the relative magnitudes of the various correlations give an indication of the relative importance of various parameters.

The fall correlations at the two stations are strikingly different. At Station 10 in the southern part of the study area, we see that the speed of the ice parcel as well as the shearing deformation are relatively important. However, at Station 66 in the central part of the study area, the absolute value of divergence is the parameter that is best correlated with the 1000 Hz signal. Thus, in the southern region, which would typically have more open water, the 1000 Hz noise appears to be generated by translation and by the types of deformation which cause elongation along a northwest/southeast axis. But farther north, where conditions may be more solidly frozen, the

opening ($D > 0$) and closing ($D < 0$) of leads and perhaps ridging ($D < 0$ for compacted ice) appears to be most responsible for generating noise.

These differences between the mechanisms which generate the 1000 Hz ambient noise may be the cause of the low e-folding scale during the fall. Spatial variations in the frozen state of the ice pack could allow for one mode of response in the south and another in the north. Thus, any given forcing of the ice could result in different noise signals at different locations. This would translate to a spatial incoherence.

The winter correlations (Table 3) show that the 1000 Hz signal goes back to being slightly more coherent with U^2 than U . The highest correlation that can be obtained using all variables except U^2 (or U) is 0.55. Thus, ice parcel translation at Station 10 still appears to be of some importance during winter. As seen in Table 3, several of the DKP have correlations of the order of 0.3-0.4. The magnitude of these correlations are relatively small with respect to that of U^2 or U . But since a combination of their effects gives a 0.55 correlation (close to 0.60 for U and 0.62 for U^2), it is difficult to speculate as to whether translation or differential motion is the true cause of the higher frequency noise.

Of particular interest at the 1000 Hz frequency is the influence of the air temperature fluctuations, Δ . The correlations indicate that the effect of thermal cracking is either a) insignificant or b) not being properly calculated. It is the latter that we believe to be true. Our previous example of 1000 Hz noise fluctuations associated with temperature variations (Figs. 20-25) seems to imply that a decrease in noise occurs for increasing air temperature. If this is the case, then our calculated Δ would be poorly correlated with the 1000 Hz ambient noise.

7. SUMMARY AND CONCLUSIONS

We have considered the seasonal characteristics of Arctic ambient noise in the Beaufort Sea and the relationships between noise variations and ice kinematics. Our ability to analyze low frequency noise during the summer has been limited to the 32 Hz data set since all indications imply that the 10 Hz summer data are contaminated by cable strum. This strum is associated with the inertial oscillations of the ice pack and is initiated during the divergence stage of this rotary motion (Lewis et al., 1985). We stress that not all ambient noise variations at the inertial period are associated with strum. Considering various data sets (e.g. Buck and Jaekis, 1984), the strum phenomena appears to occur at frequencies of ≤ 10 Hz and during the summer. The primary indicator of a strum problem seems to be noise level variations that exceed 10 or 15 dB.

The time series of the two-dimensional contour maps of noise and atmospheric temperature and pressure point out two interesting facts. First, atmospheric pressure variations can apparently induce significant fluctuations at 1000 Hz. Assuming pressure variations produce ice motion, these results indicate that Dyer's fourth classification of ambient noise (150 to 5000 Hz) is only partially a result of thermal micro-fracturing. The second point made by the contour map time series pertains to the relationship between the 1000 Hz ambient noise and air temperature fluctuations. The data tend to indicate that higher frequency noise is generated while the air temperature drops and while the air temperature is at its minimum. It is during the increase in air temperature that the higher frequency noise levels drop. An interpretation of these results is that there continues to be a flux of heat from the ice to the air during the entire period of lower air temperatures. Moreover, our data show that the response of one region (measured by the increase in the 1000 Hz intensity) may be

considerably greater than another region for the same temperature drop. This is obviously a result of different regional ice characteristics (temperature, mean thickness, etc.).

Our length scale analysis shows the 32 Hz signal to be the most highly spatially coherent noise during most of the year. However, this result is based on our arbitrary choice of a length scale. What this analysis tends to point out are distinct regions in which the noise signals are similar. During the summer, the eastern Beaufort Sea is part of one region while the rest of the Beaufort makes up another region. Perhaps the ice rubble field of the Canadian archipelago is the influential regional factor in the eastern Beaufort during summer. If so, its influence is not a factor during the fall and winter. During these periods, it is the western Beaufort region that is distinctly different from the rest of the Beaufort.

The analysis of time scales gives one an indication of the temporal variability of the Arctic ambient noise. The 1000 Hz time scales during the fall, winter, and spring tend to be small with respect to the 10 Hz and 32 Hz time scales. This is likely the result of multiple sources of higher frequency noise (e.g. fracturing due to heat fluxes as well as ice motion), with each source being relatively incoherent with another source. The spatial structure of the time scales may offer clues to the intensity of those processes which cause noise. A comparison of 10 Hz noise data sets as well as the 32 Hz data sets indicate that larger e-folding times are associated with higher noise levels for a given event. Of course, a stronger response will better mask background fluctuations in the noise, and a higher e-folding scale can result.

The correlations between noise, ice motion, and temperature changes have provided the following conceptual model for the generation of Arctic ambient noise at lower frequencies. During the summer, most of the lower frequency noise is generated by the ice rushing through the water. Differential ice motion appears to be insignificant in producing noise. This is possibly a result of the relatively large percent of open water along with the fact that the internal structure of ice weakens and decays during summer. However, this situation changes by fall when the total deformation $([N^2+S^2]^{\frac{1}{2}})$ as well as the translation of the pack ice becomes important in producing low frequency noise. The motion implied by $(N^2+S^2)^{\frac{1}{2}}$ is that of individual ice floes moving past one another during a rearrangement process. Thus, noise could be generated as the bonds between floes are broken and as the floes grind and slip past each other. It is only during winter that some of the other forms of differential motion become important. Indeed, at 10 Hz the DKP and Δ can be combined to account for a significant amount of the noise. In particular, we find that the influence of D, N, and S can be considerable. The effects of the variations of vorticity (ζ or $|\zeta|$) are apparently incorporated into other parameters. We base this statement on the fact that linear combinations of the DKP, U, and Δ that included vorticity did not have significantly higher correlations than combinations that excluded vorticity. We also found that correlations were higher when the divergence D was used as opposed to $|D|$. For winter-time conditions, the negative correlation with D would imply that ridging and rafting have become noise generating processes at lower frequencies.

The correlations using the 1000 Hz data result in a somewhat different scenario for the generation of higher frequency noise in the Arctic. First, the summer correlations imply that the kinetic energy related to the ice parcel translation is the primary factor in higher frequency noise generation. During the fall, all correlations

drop considerably. The fall correlations indicate that U and $-S$ are important parameters in the southern Beaufort while $|D|$ is the important parameter farther north. This implies a high degree of regional variability in the generation of higher frequency ambient noise. And this is likely the factor leading to the small e-folding length at 1000 Hz during fall.

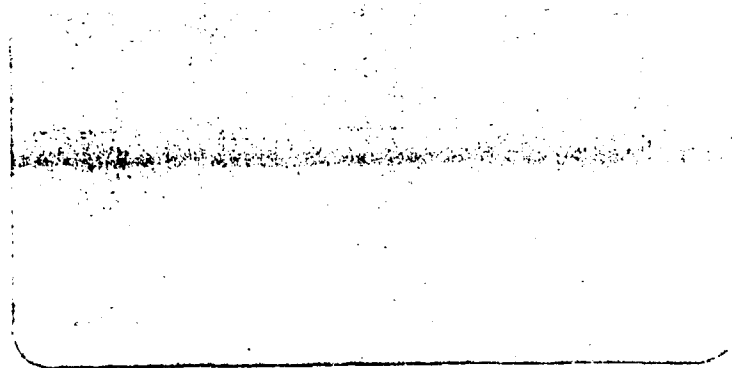
Two points should be made about the fall correlations at 1000 Hz. First of all, the effect of our parameter reflecting air temperature changes, Δ , is small. Perhaps this is a result of insignificant temperature variations, but the winter correlations also indicate that Δ is poorly correlated with the 1000 Hz noise. The second point deals with the relatively large negative correlation between S and 1000 Hz. This occurs in the southern Beaufort, a region associated with the westward flow of the Beaufort gyre (Colony and Thorndike, 1984). Moreover, fall is the season during which the pack ice within the Beaufort gyre reestablishes its connections to the northern coast of Alaska. Lewis et al. (1985), using the same AIDJEX position data, found that the fall was also the period during which the shearing deformation rate has its maximum e-folding time scale, $e_T = 31.5$ hrs. The time scales of the other DKP for fall were 14 hrs or less. All these factors suggest high frequency noise generation in the southern Beaufort as a result of lateral shearing stresses between the Beaufort gyre and the land-fast ice.

The results of our correlations using the winter 1000 Hz noise are ambiguous. The translation velocity has the highest correlation, but, as previously stated, movement is almost always associated with ice put under stress. Combinations of the DKP indicate that differential motion could be the actual cause of the noise. A disturbing aspect of the calculations is the poor correlation associated with our temperature parameter Δ . A review of the temperature data shows

sizable short-term temperature drops (up to 20° C), so one would expect some correlation. These results again point out that our understanding of temperature-induced noise fluctuations appears to be incomplete and warrants further study.

REFERENCES

- Buck, B.M. and D.W. Jaeckis, 1984: Long term statistical measurements of environmental acoustics parameters in the Arctic - AEAS Rpt. No. 1 - Ambient noise levels in the west Greenland Sea. Office of Naval Res. contract N00014-84-C-0394, Polar Res. Lab., Inc, Carpinteria, CA.
- Colony, R., and A.S. Thorndike, 1984: An estimate of the mean field of Arctic Sea ice motion. J. Geophys. Res., 86 (C6), 10623-10629.
- Dyer, I., 1984: The song of sea ice and other Arctic Ocean melodies. In Arctic Policy and Technology (I. Dyer and C. Chrystostomidis, eds.), Hemisphere Publ. Corp., New York, 11-37.
- Greene, C.R., and B.M. Buck, 1977: Arctic noise measurement experiment using Nimbus 6 data buoys. U.S. Navy J. Underwater Acoustics, 27 (4).
- Greene, C.R., and B.M. Buck, 1978: Influence of atmospheric pressure gradient on under-ice ambient noise. U.S. Navy J. Underwater Acoustics, 28 (4).
- Kirwan, A.D., 1975: Oceanic velocity gradients. J. Phys. Oceangra., 5 (4), 729-735.
- Lewis, J.K., R.D. Crissman, and W.W. Denner, 1985: Seasonal variability of the principle modes of ice movement in the Beaufort Sea. Submitted to J. Geophys. Res.
- Makris, N.C., and I. Dyer, 1985: Environmental correlates of pack ice noise. Submitted to J. Acoust. Soc. Am.
- Manley, R.O., and K. Hunkins, 1985: Mesoscale eddies of the Arctic Ocean. J. Geophys. Res., 90 (C3), 4911-4930.
- Milne, A.R., 1972: Thermal tension cracking in sea ice: a source of under-ice noise. J. Geophys. Res., 77, 2177-2192.
- Pritchard, R.S., 1984: Arctic Ocean background noise caused by ridging of sea ice. J. Acoust. Soc. Am., 75 (2), 419-427.



SAICTM

Science Applications International Corporation

A STUDY OF SEA ICE KINEMATICS
AND THEIR RELATIONSHIPS
TO ARCTIC AMBIENT NOISE

PART 2 - ICE AND ATMOSPHERIC PARAMETERS

Table of Contents

	<u>Page</u>
Appendix A - Seasonal Arctic Ice Kinematic Variations, Beaufort Sea, 1975-1976	2-1
Appendix B - Two-Dimensional Contour Maps of Arctic Atmospheric Pressure Variations, 8-9 August 1975 (Summer)	2-23
Appendix C - Two-Dimensional Contour Maps of Arctic Atmospheric Temperature Variations, 8-9 August 1975 (Summer)	2-43
Appendix D - Two-Dimensional Contour Maps of Arctic Atmospheric Pressure Variations, 16-17 November 1975 (Fall)	2-61
Appendix E - Two-Dimensional Contour Maps of Arctic Atmospheric Temperature Variations, 16-17 November 1975 (Fall)	2-80
Appendix F - Two-Dimensional Contour Maps of Arctic Atmospheric Pressure Variations, 9-10 February 1976 (Winter)	2-99
Appendix G - Two-Dimensional Contour Maps of Arctic Atmospheric Temperature Variations, 9-10 February 1976 (Winter)	2-118
Appendix H - Two-Dimensional Contour Maps of Arctic Atmospheric Pressure Variations, 21-22 February 1976 (Winter)	2-137
Appendix I - Two-Dimensional Contour Maps of Arctic Atmospheric Temperature Variations, 21-22 February 1976 (Winter)	2-156
Appendix J - Two-Dimensional Contour Maps of Arctic Atmospheric Pressure Variations, 16-17 May 1976 (Spring)	2-175
Appendix K - Two-Dimensional Contour Maps of Arctic Atmospheric Temperature Variations, 16-17 May 1976 (Spring)	2-193

Appendix A

Seasonal Arctic Ice Kinematic Variations,
Beaufort Sea, 1975-1976

This appendix presents the plots of some of the temporal variations of the ice kinematic parameters of translation speed, divergence, vorticity, normal deformation rate, and shear deformation rate as calculated using the manned camp position data (at 3 hr intervals). One month of data is plotted, and each season is represented:

Summer - ice kinematic data from August 1975,
Fall - ice kinematic data from November 1975,
Winter - ice kinematic data from February 1976, and
Spring - ice kinematic data from May 1975.

List of Figures Appendix A

<u>Summer</u>	<u>Page</u>
Fig. A.1. Variations of the centroid speed	2-3
Fig. A.2. Variations of the divergence	2-4
Fig. A.3. Variations of the vorticity	2-5
Fig. A.4. Variations of the normal deformation rate . .	2-6
Fig. A.5. Variations of the shear deformation rate . . .	2-7
<u>Fall</u>	
Fig. A.6. Variations of the centroid speed	2-8
Fig. A.7. Variations of the divergence	2-9
Fig. A.8. Variations of the vorticity	2-10
Fig. A.9. Variations of the normal deformation rate . .	2-11
Fig. A.10. Variations of the shear deformation rate . . .	2-12
<u>Winter</u>	
Fig. A.11. Variations of the centroid speed	2-13
Fig. A.12. Variations of the divergence	2-14
Fig. A.13. Variations of the vorticity	2-15
Fig. A.14. Variations of the normal deformation rate . .	2-16
Fig. A.15. Variations of the shear deformation rate . . .	2-17
<u>Spring</u>	
Fig. A.16. Variations of the centroid speed	2-18
Fig. A.17. Variations of the divergence	2-19
Fig. A.18. Variations of the vorticity	2-20
Fig. A.19. Variations of the normal deformation rate . .	2-21
Fig. A.20. Variations of the shear deformation rate . . .	2-22

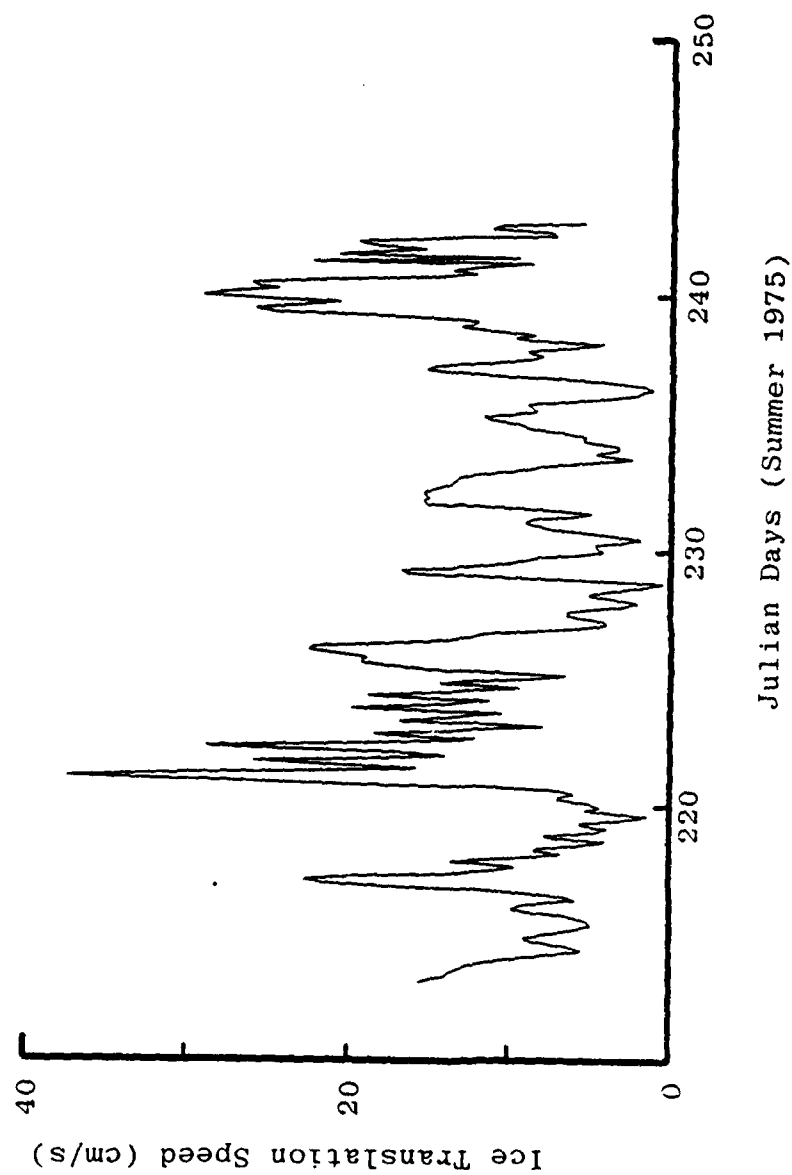


Fig. A.1. Variations of the centroid speed of the AIDJEX ice parcel defined by the manned camp array, August 1975.

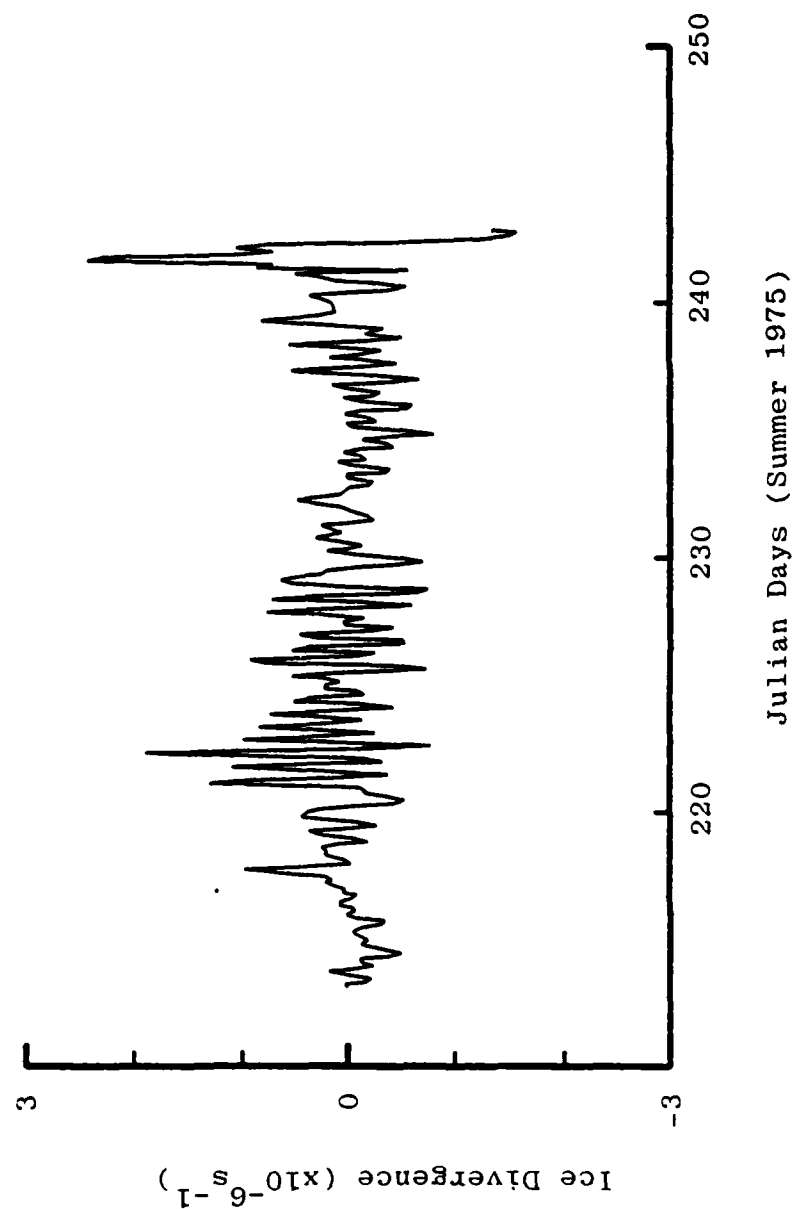
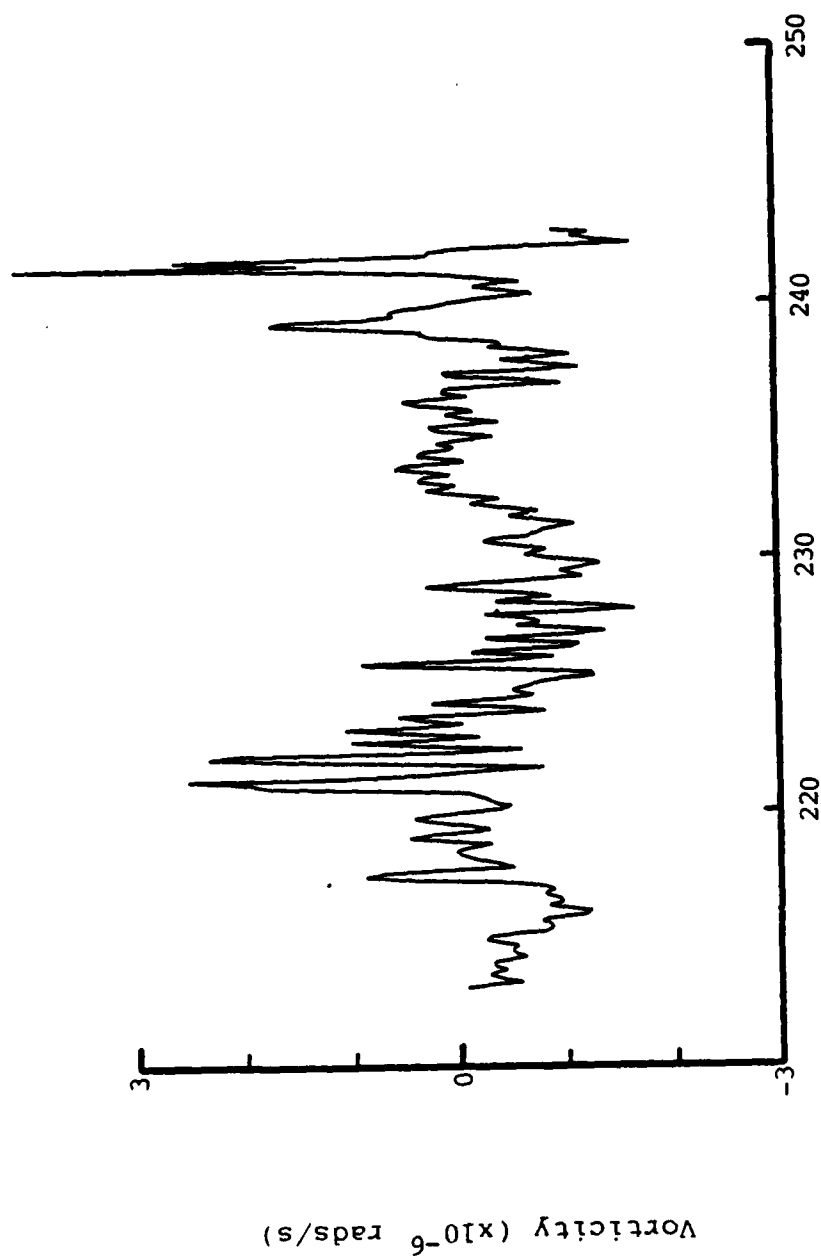


Fig. A.2. Variations of the divergence of the AIDJEX ice parcel defined by the manned camp array, August 1975.



Julian Days (Summer 1975)

Fig. A.3. Variations of the vorticity of the AIDJEX ice parcel defined by the manned camp array, August 1975.

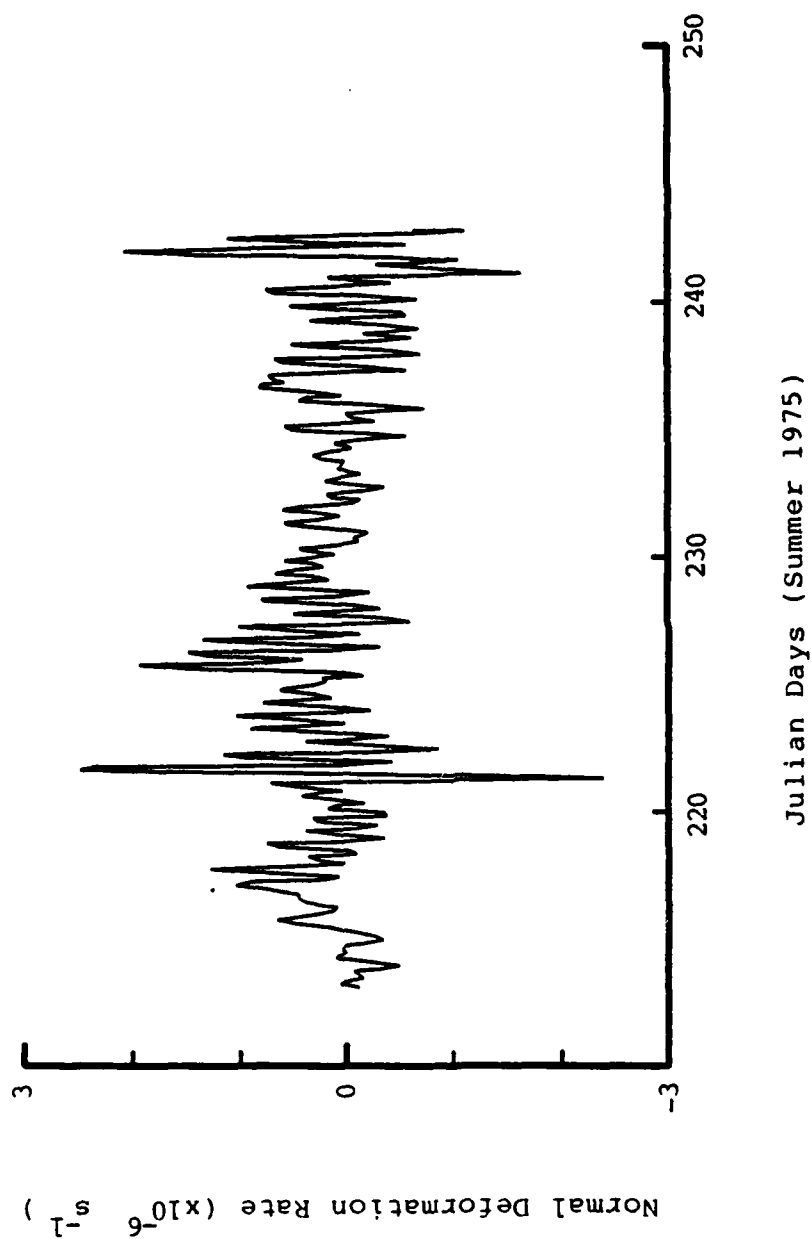


Fig. A.4. Variations of the normal deformation rate of the AIDJEX ice parcel defined by the manned camp array, August 1975.

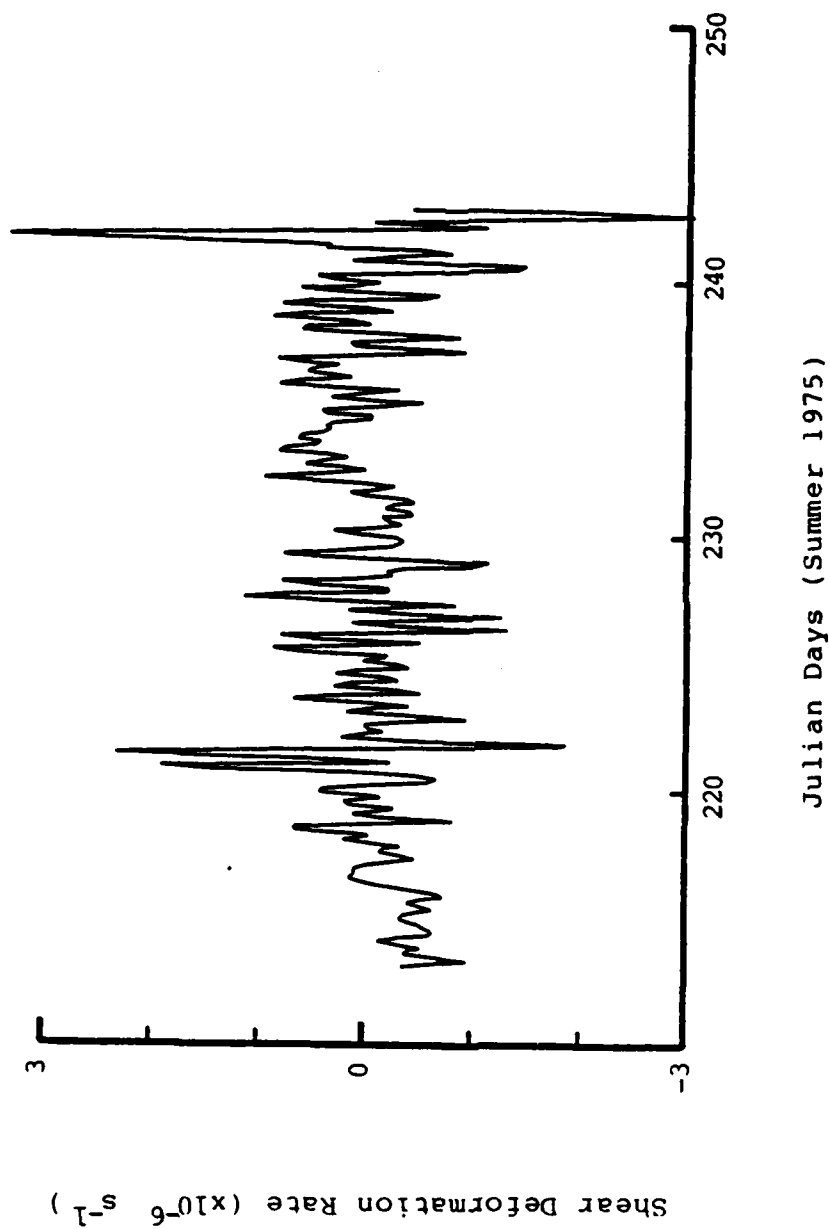


Fig. A.5. Variations of the shear deformation rate of the AIDJEX ice parcel defined by the manned camp array, August 1975.

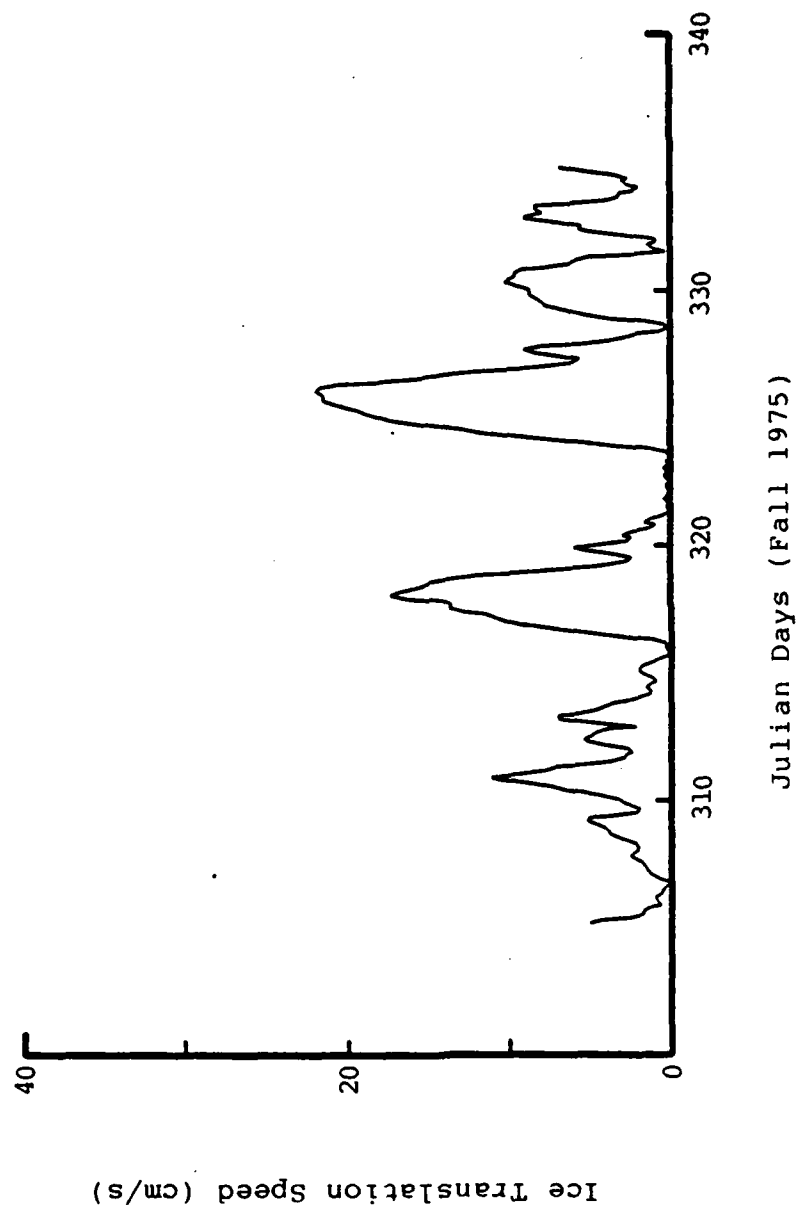


Fig. A.6. Variations of the centroid speed of the AIDJEX ice parcel defined by the manned camp array, November 1975.

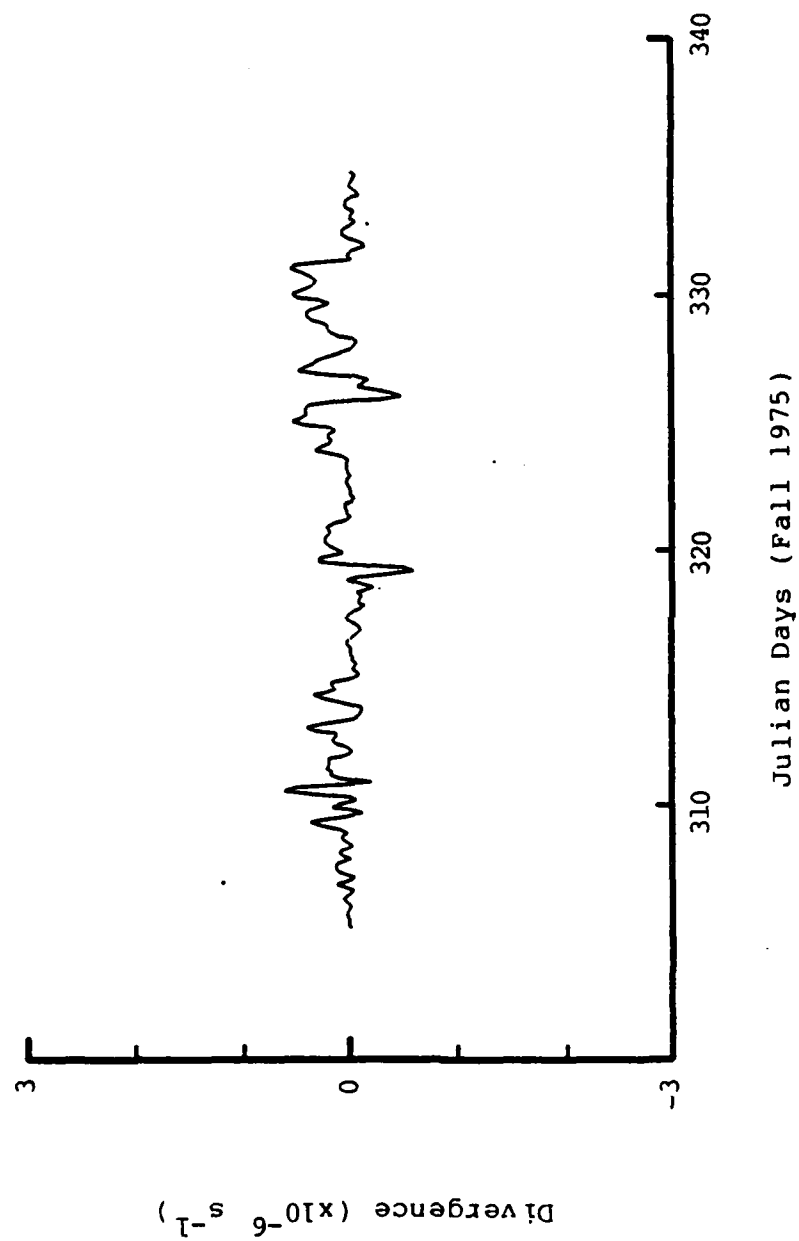


Fig. A.7. Variations of the divergence of the AIDJEX ice parcel defined by the manned camp array, November 1975.

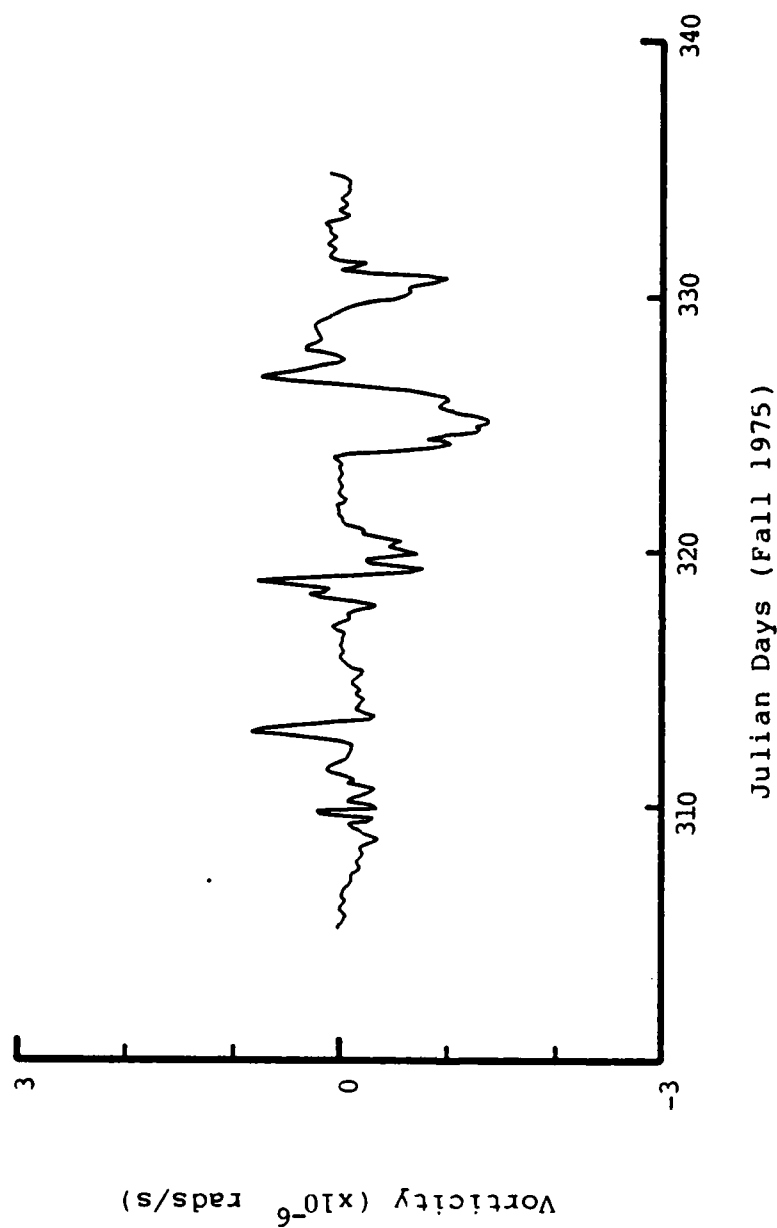


Fig. A.8. Variations of the vorticity of the AIDJEX ice parcel defined by the manned camp array, November 1975.

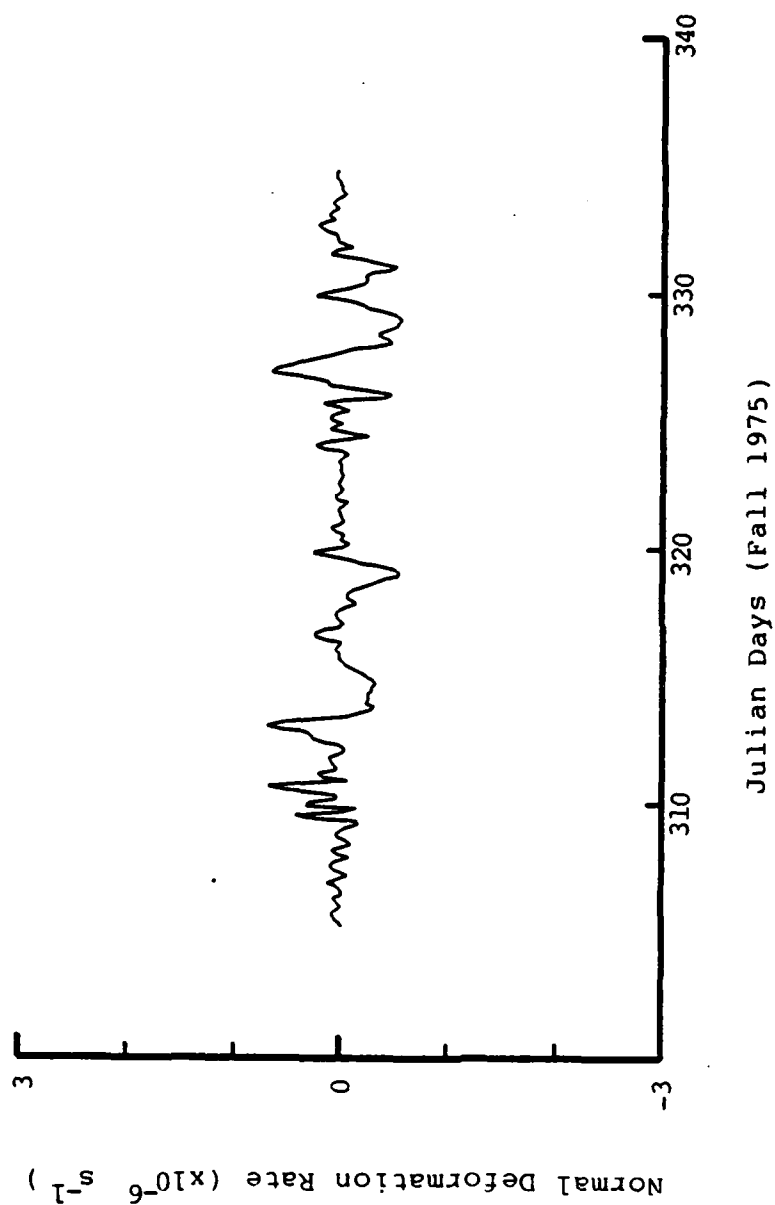
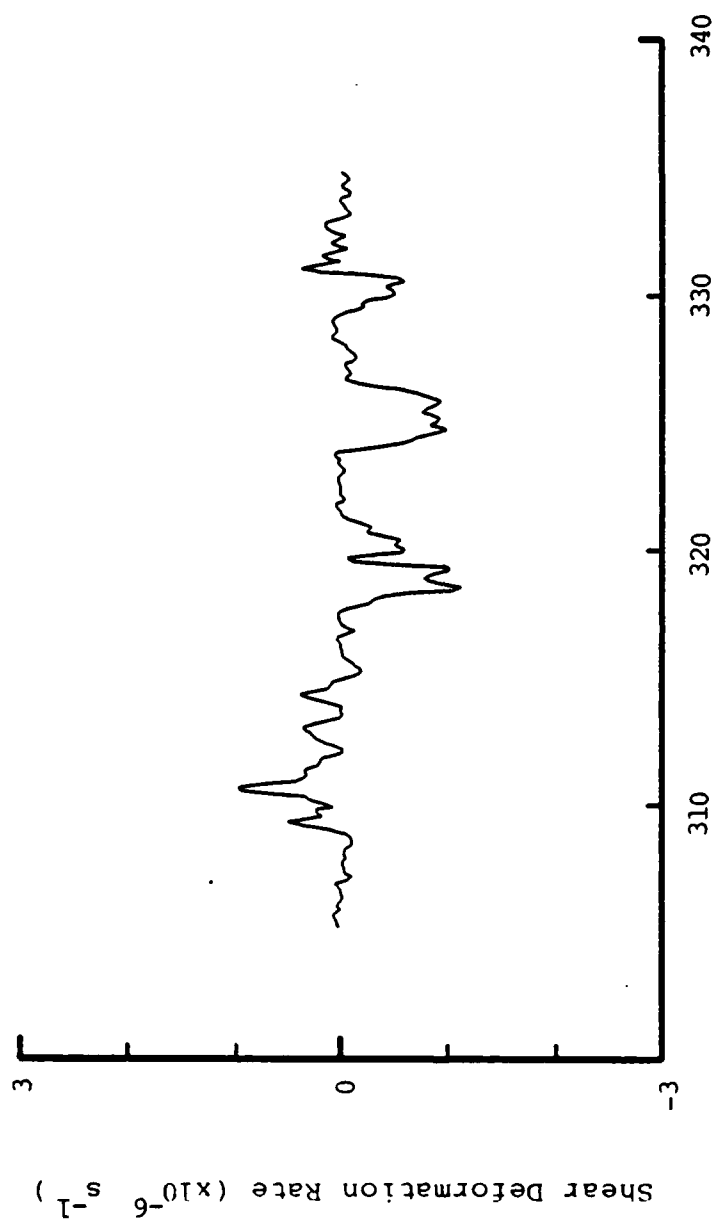


Fig. A.9. Variations of the normal deformation rate of the AIDJEX ice parcel defined by the manned camp array, November 1975.



Julian Days (Fall 1975)

Fig. A.10. Variations of the shear deformation rate of the AIDJEX ice parcel defined by the manned camp array, November 1975.

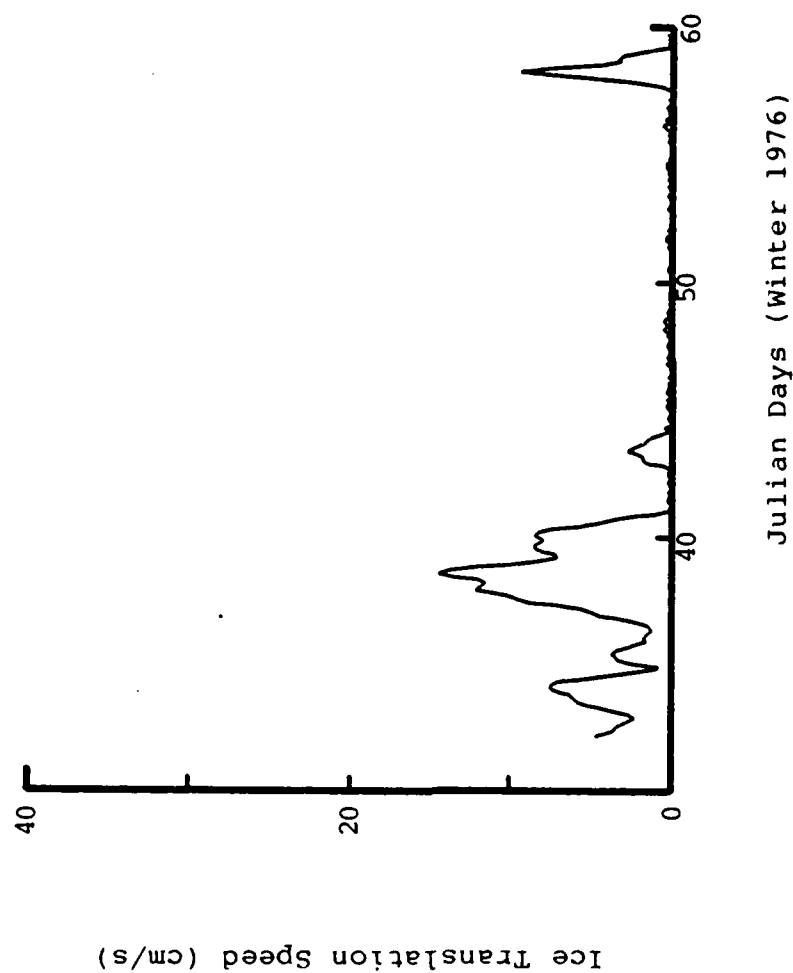
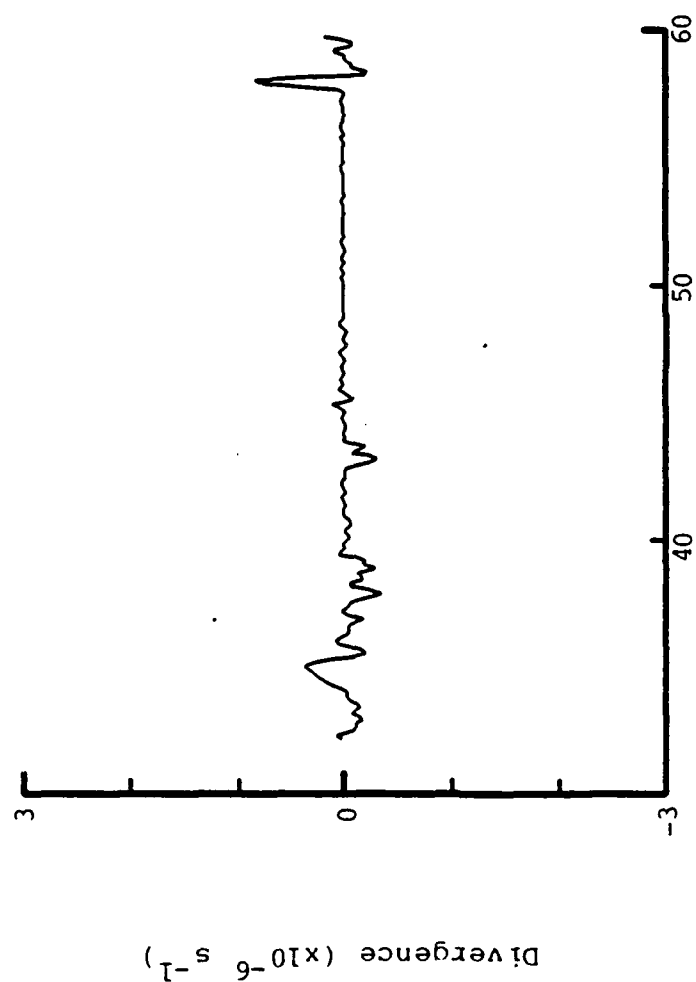


Fig. A.11. Variations of the centroid speed of the AIDJEX ice parcel defined by the manned camp array, February 1976.



Julian Days (Winter 1976)

Fig. A.12. Variations of the divergence of the AIDJEX ice parcel defined by the manned camp array, February 1976.

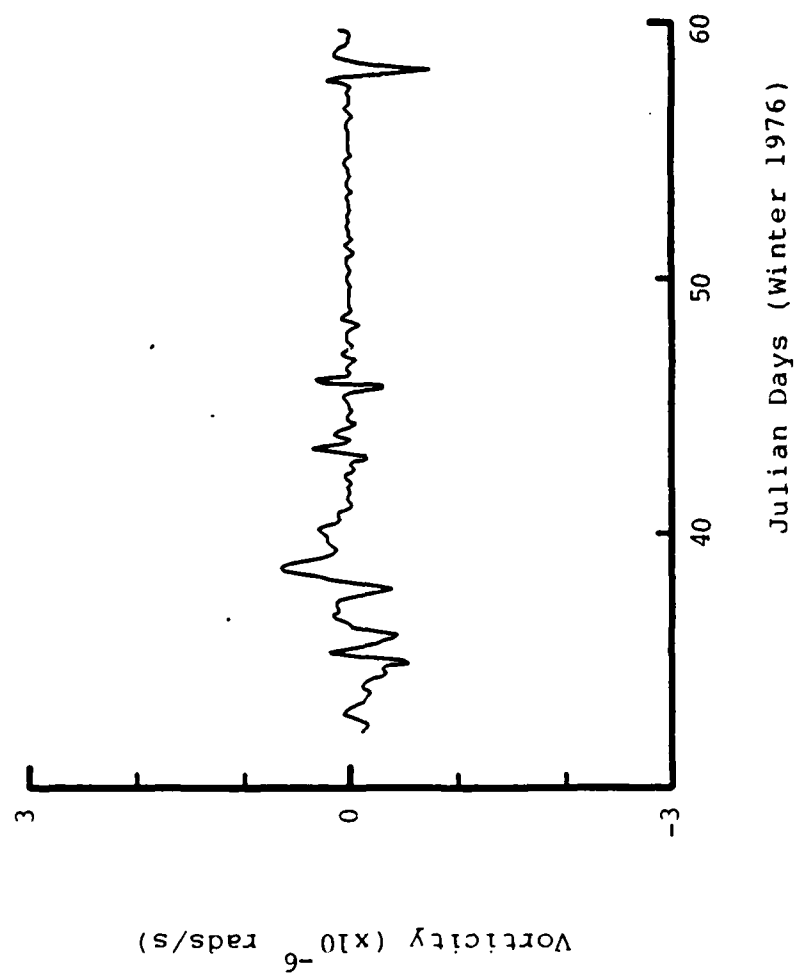
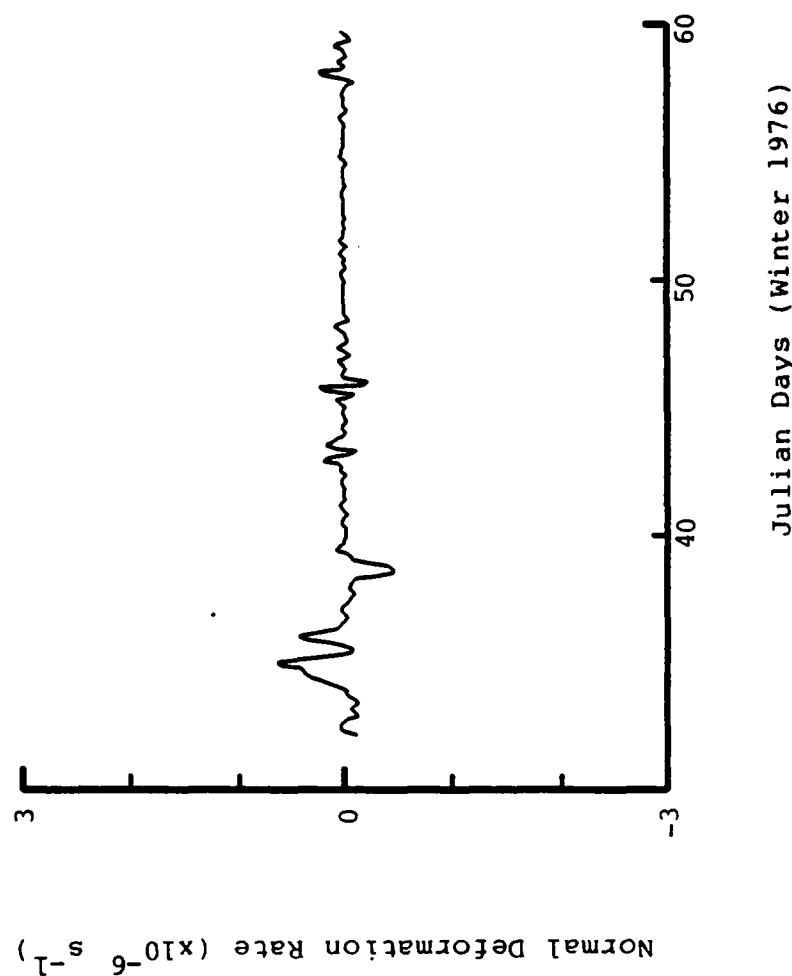


Fig. A.13. Variations of the vorticity of the AIDJEX ice parcel defined by the manned camp array, February 1976.



Julian Days (Winter 1976)

Fig. A.14. Variations of the normal deformation rate of the AIDJEX ice parcel defined by the manned camp array, February 1976.

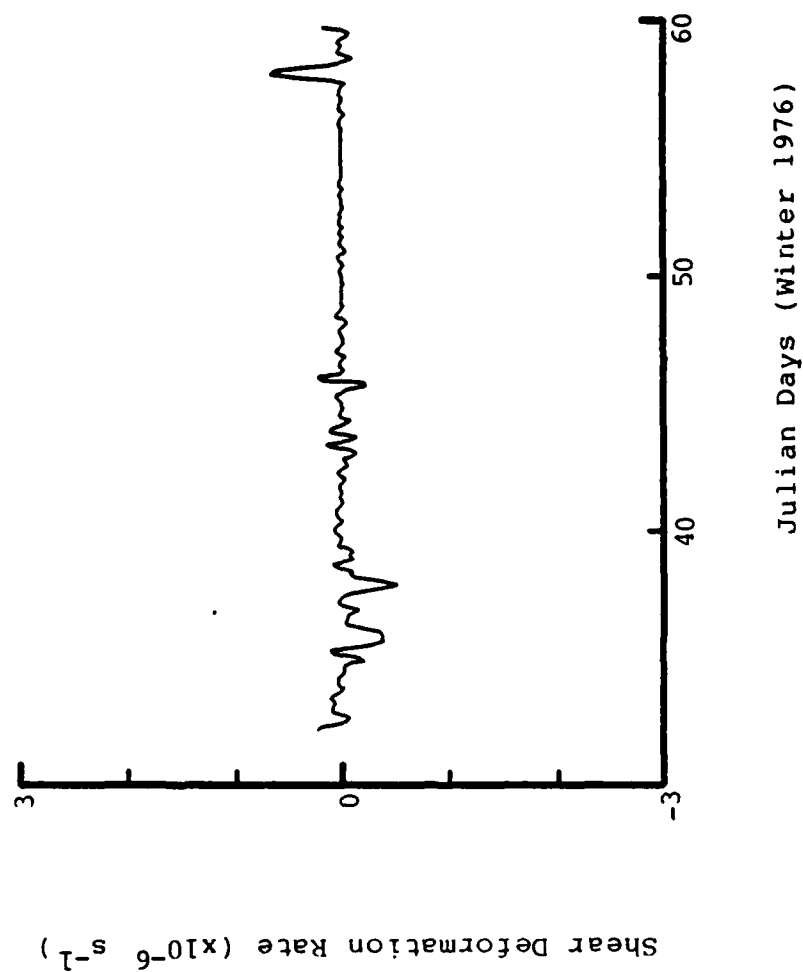


Fig. A.15. Variations of the shear deformation rate of the AIDJEX ice parcel defined by the manned camp array, February 1976.

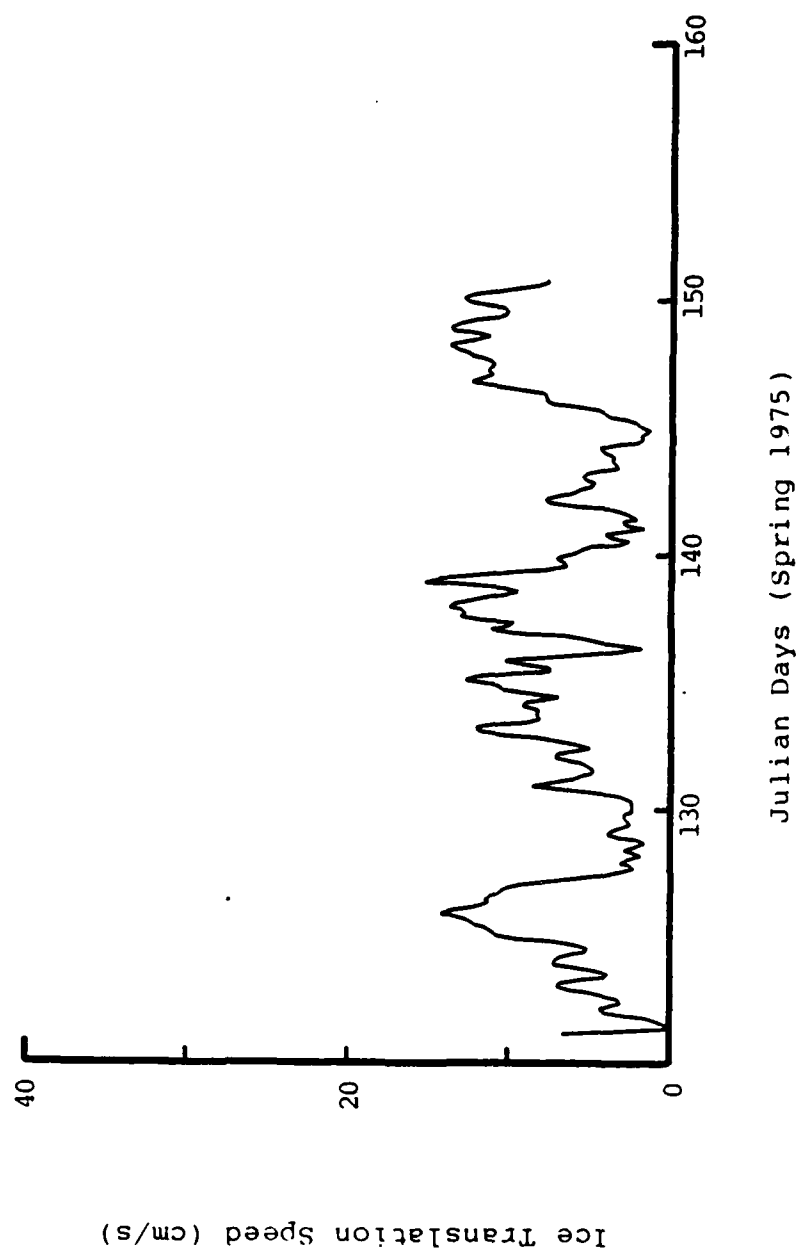


Fig. A.16. Variations of the centroid speed of the AIDJEX ice parcel defined by the manned camp array, spring 1975.

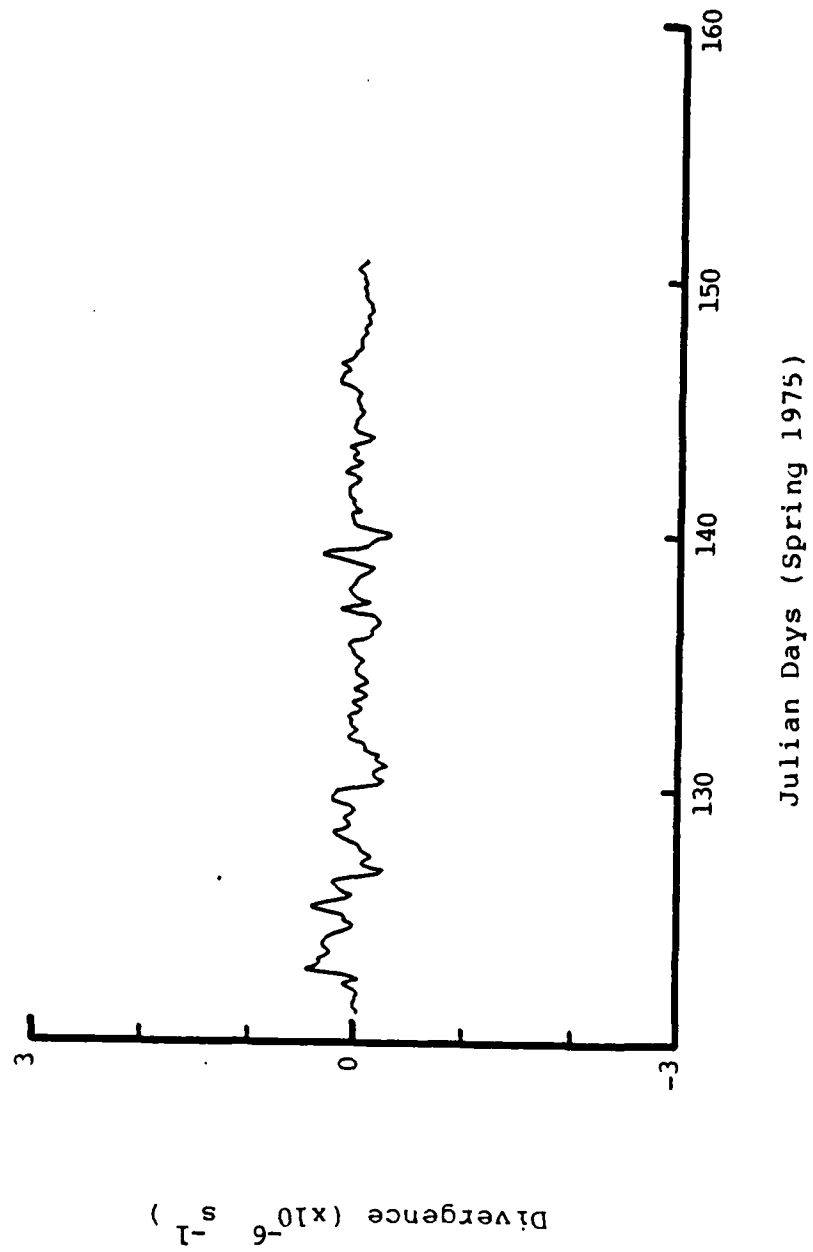


Fig. A.17. Variations of the divergence of the AIDJEX ice parcel defined by the manned camp array, spring 1975.

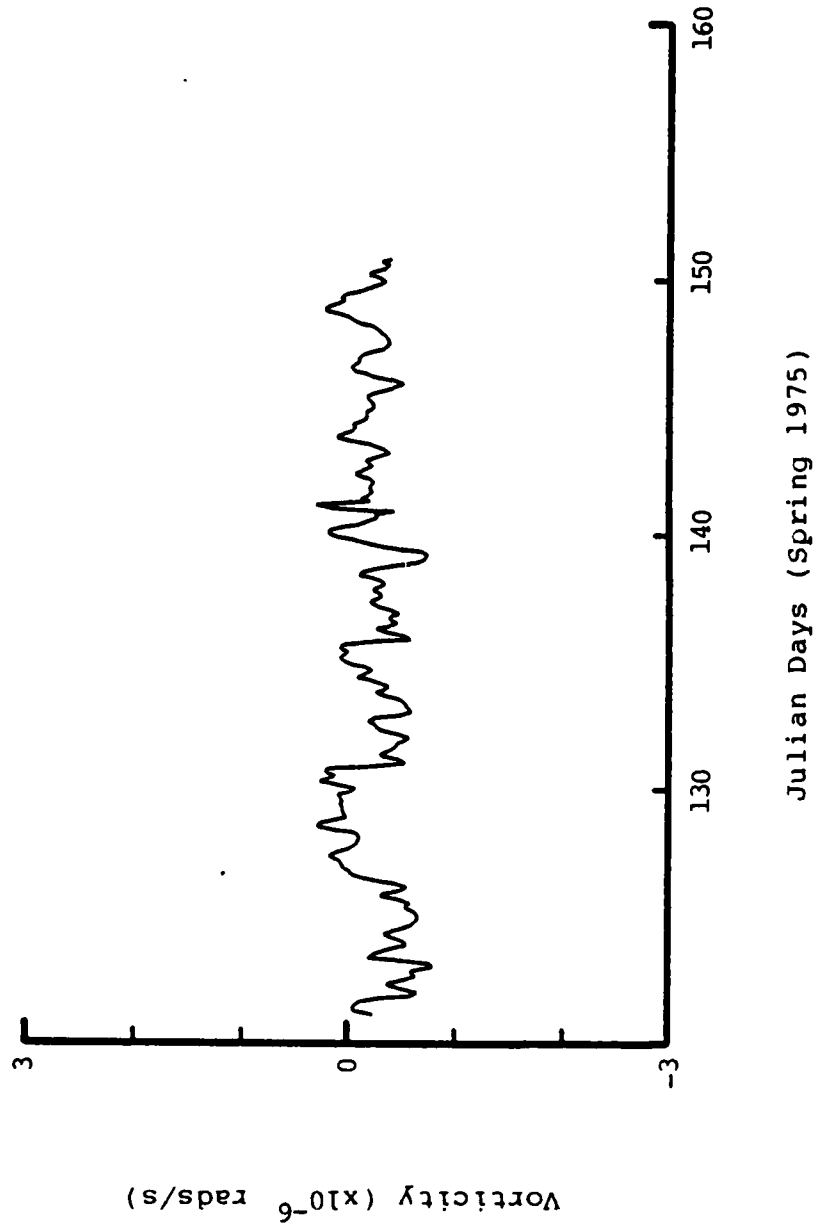


Fig. A.18. Variations of the vorticity of the AIDJEX ice parcel defined by the manned camp array, spring 1975.

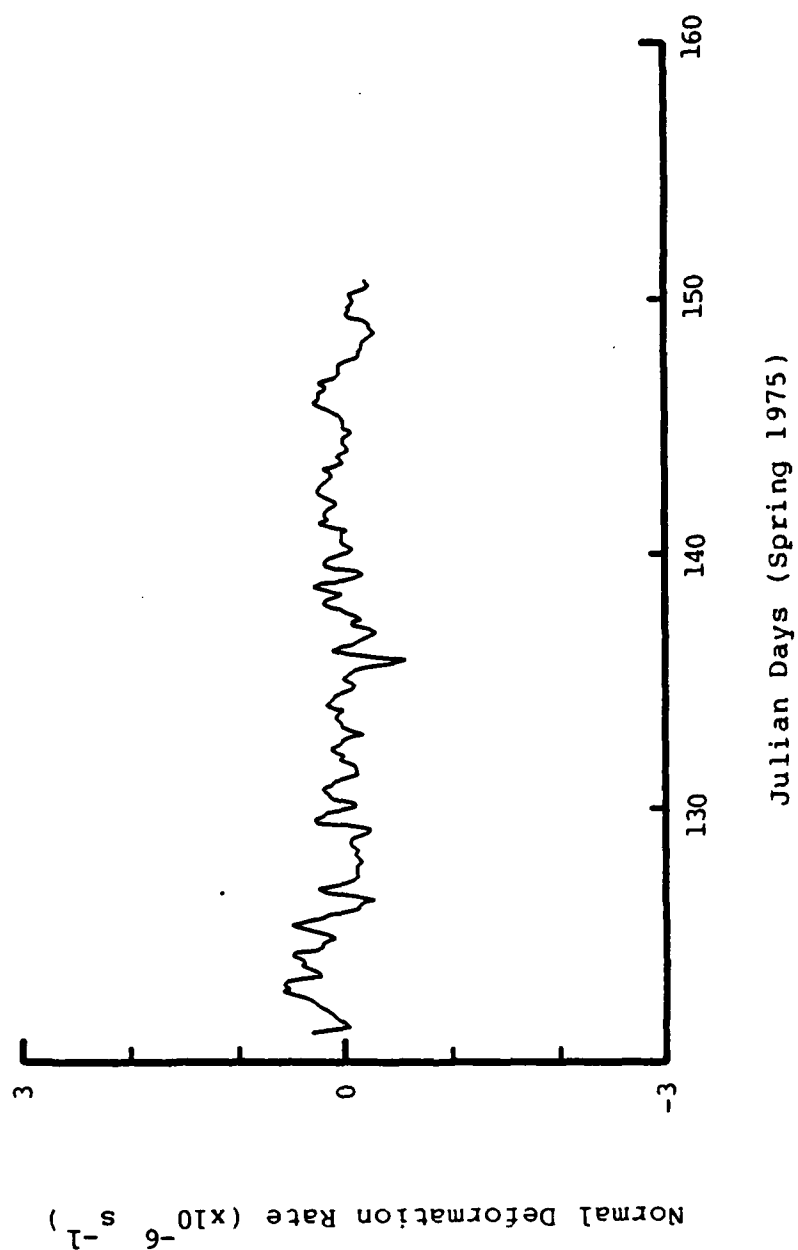


Fig. A.19. Variations of the normal deformation rate of the AIDJEX ice parcel defined by the manned camp array, spring 1975.

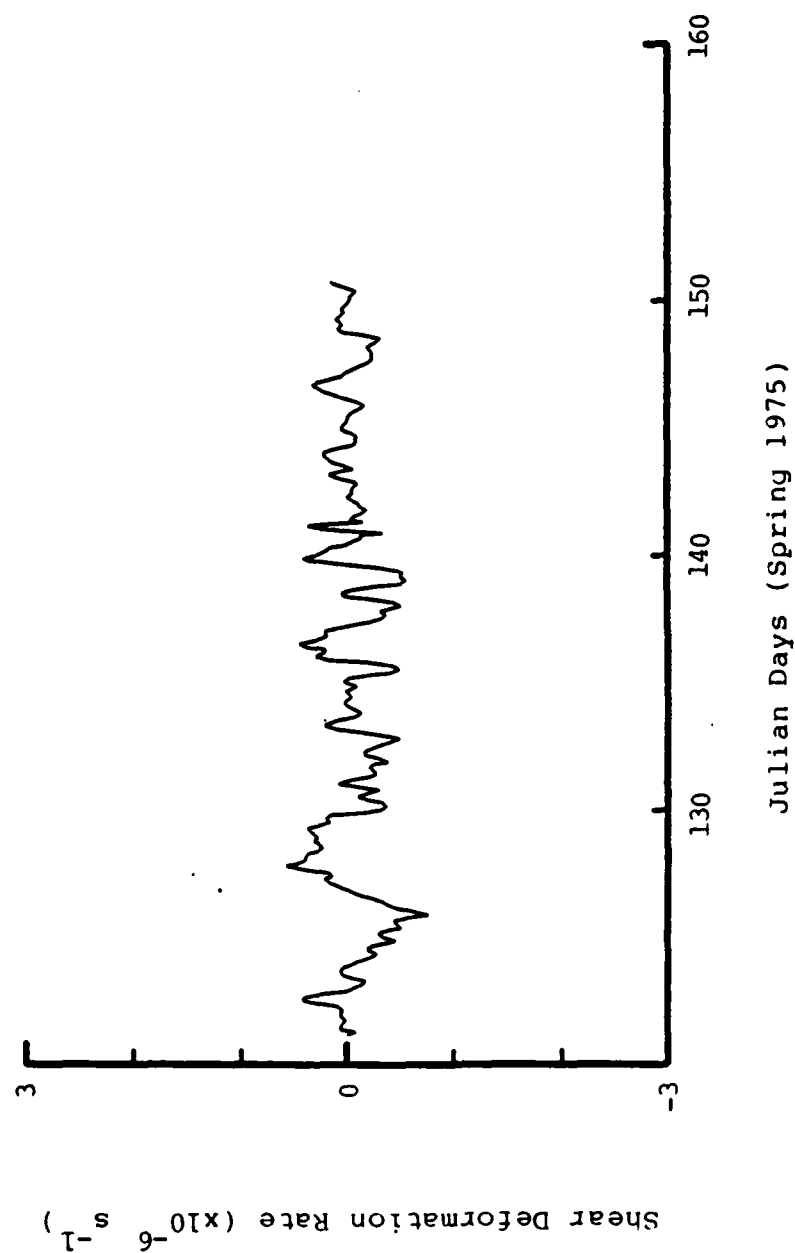


Fig. A.20. Variations of the shear deformation rate of the AIDJEX ice parcel defined by the manned camp array, spring 1975.

Appendix B

Two-Dimensional Contour Maps of Arctic Atmospheric Pressure Variations, 8-9 August 1975 (Summer)

This appendix contains the two-dimensional contour maps of the AIDJEX atmospheric pressure data collected at those stations with hydrophones during the 48 hour period of 8-9 August 1975. The contour maps show the spatial variations of atmospheric pressure (millibars) at 3 hr intervals.

List of Figures
Appendix B

	<u>Page</u>
Fig. B.1. Spatial atmospheric pressure variations, day 220.0	2-25
Fig. B.2. Spatial atmospheric pressure variations, day 220.125	2-26
Fig. B.3. Spatial atmospheric pressure variations, day 220.25	2-27
Fig. B.4. Spatial atmospheric pressure variations, day 220.375	2-28
Fig. B.5. Spatial atmospheric pressure variations, day 220.5	2-29
Fig. B.6. Spatial atmospheric pressure variations, day 220.625	2-30
Fig. B.7. Spatial atmospheric pressure variations, day 220.75	2-31
Fig. B.8. Spatial atmospheric pressure variations, day 220.875	2-32
Fig. B.9. Spatial atmospheric pressure variations, day 221.0	2-33
Fig. B.10. Spatial atmospheric pressure variations, day 221.125	2-34
Fig. B.11. Spatial atmospheric pressure variations, day 221.25	2-35
Fig. B.12. Spatial atmospheric pressure variations, day 221.375	2-36
Fig. B.13. Spatial atmospheric pressure variations, day 221.5	2-37
Fig. B.14. Spatial atmospheric pressure variations, day 221.625	2-38
Fig. B.15. Spatial atmospheric pressure variations, day 221.75	2-39
Fig. B.16. Spatial atmospheric pressure variations, day 221.875	2-40
Fig. B.17. Spatial atmospheric pressure variations, day 222.0	2-41

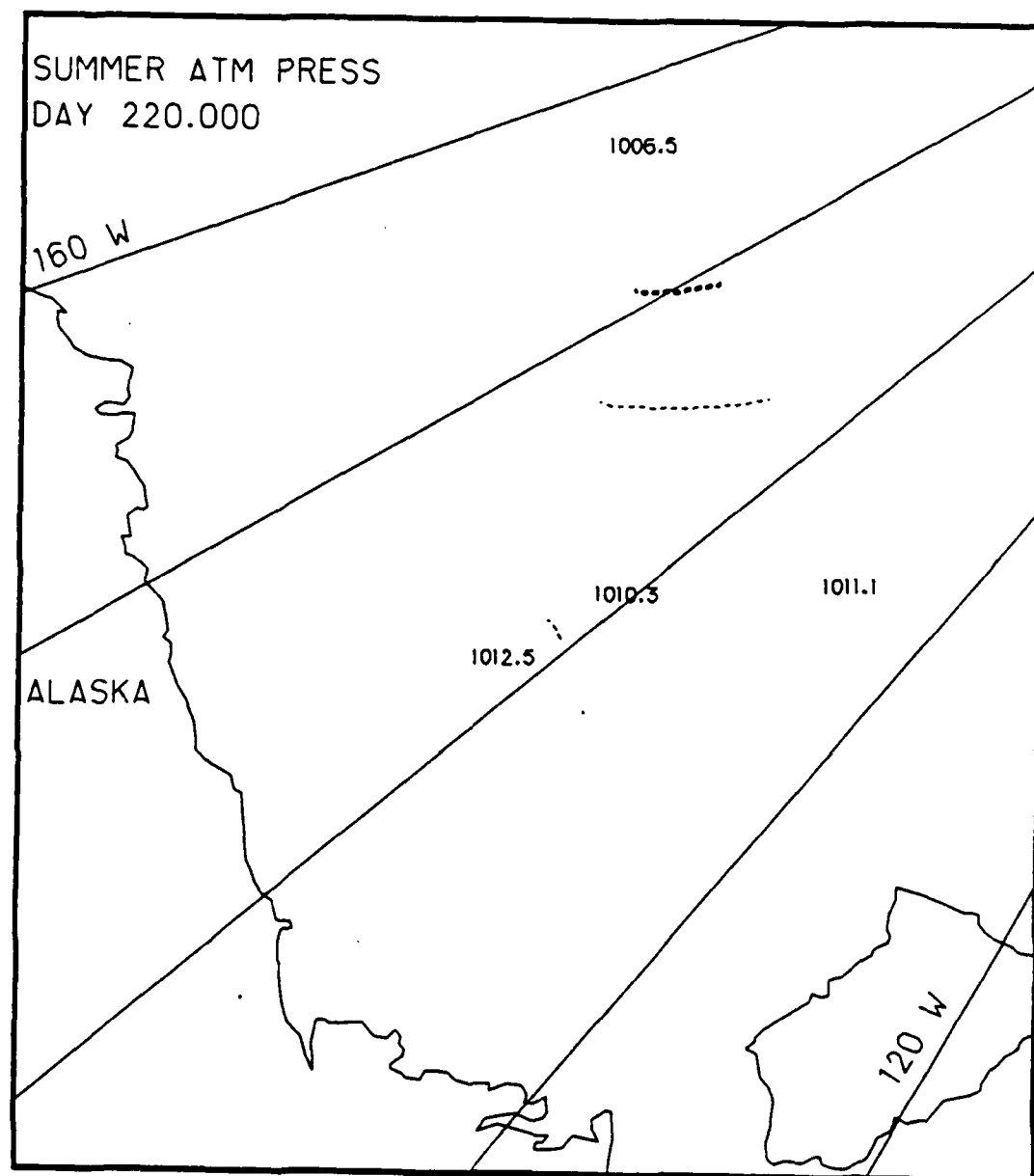


Fig. B.1. Spatial atmospheric pressure variations, day 220.0, based on the AIDJEX data from stations with hydrophones, summer 1975.

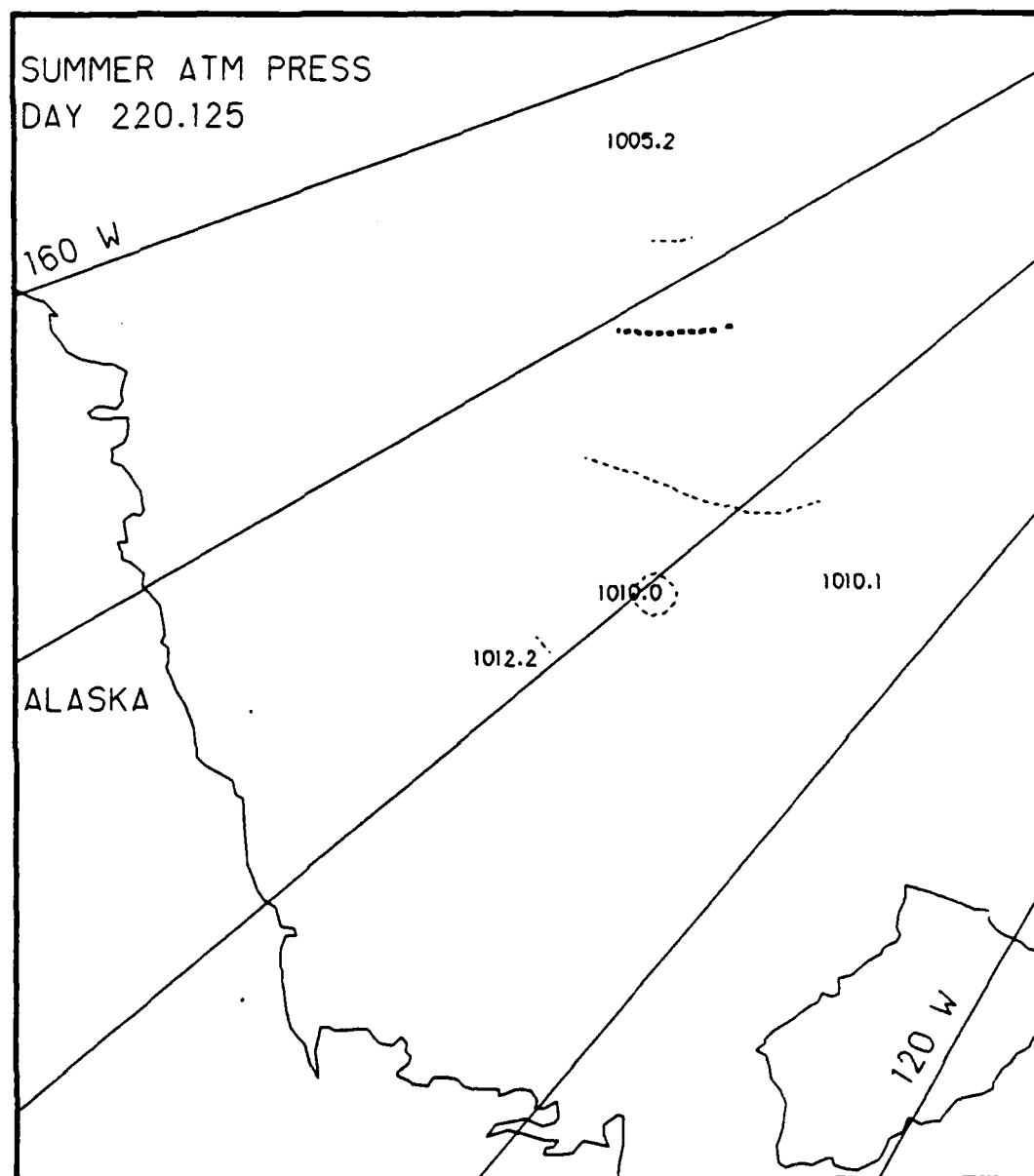


Fig. B.2. Spatial atmospheric pressure variations, day 220.125, based on the AIDJEX data from stations with hydrophones, summer 1975.

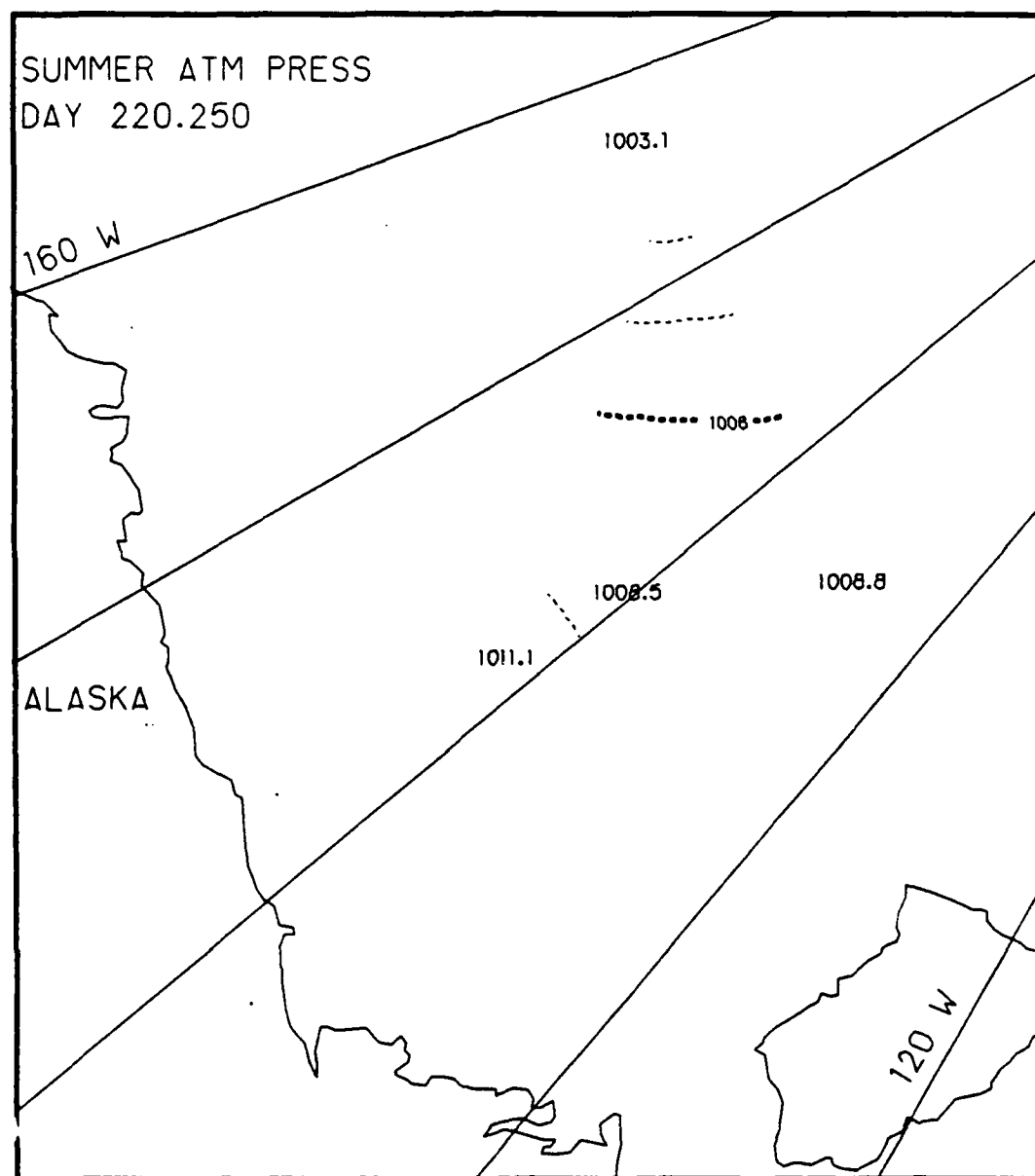


Fig. B.3. Spatial atmospheric pressure variations, day 220.25, based on the AIDJEX data from stations with hydrophones, summer 1975.

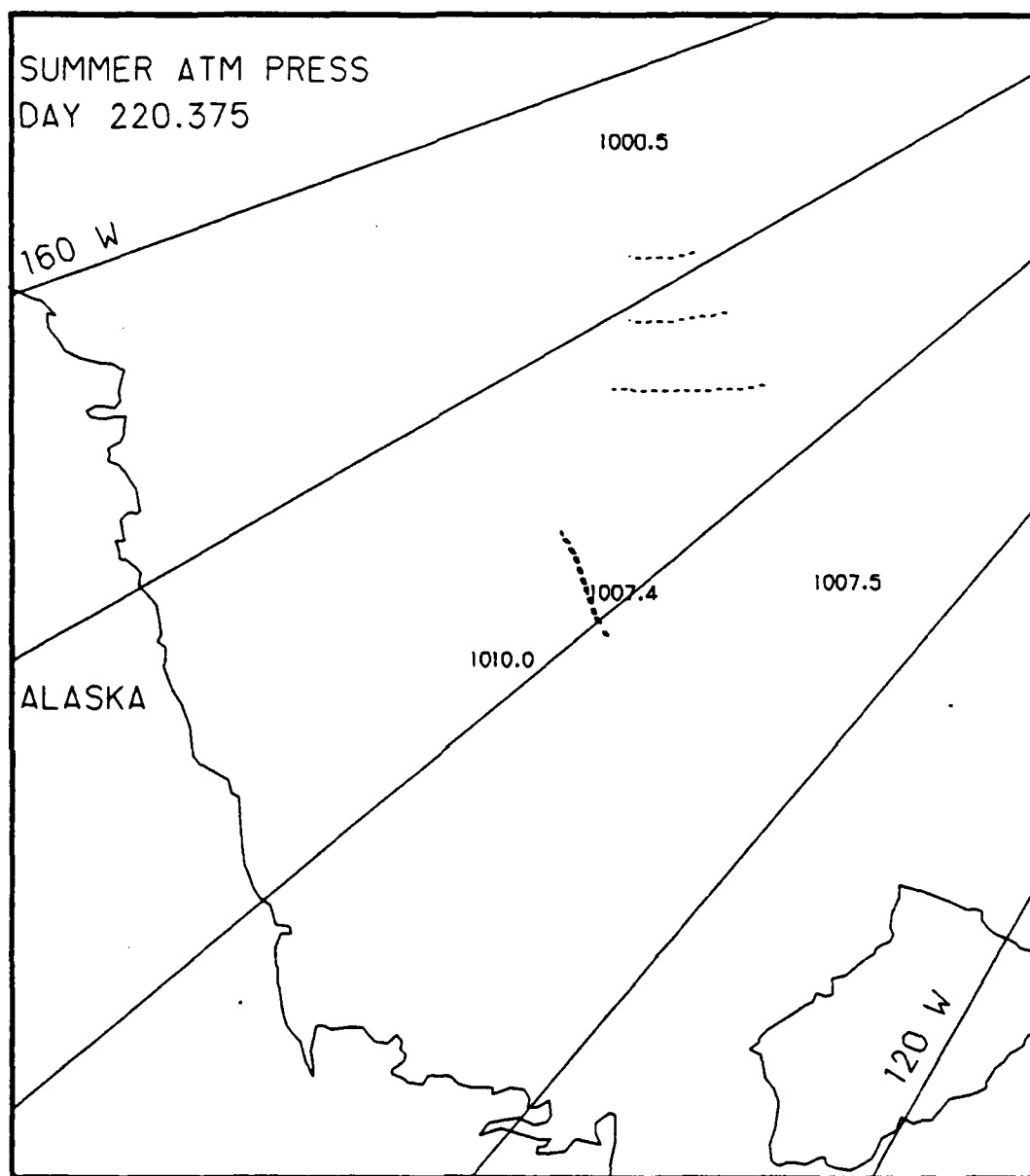


Fig. B.4. Spatial atmospheric pressure variations, day 220.375, based on the AIDJEX data from stations with hydrophones, summer 1975.

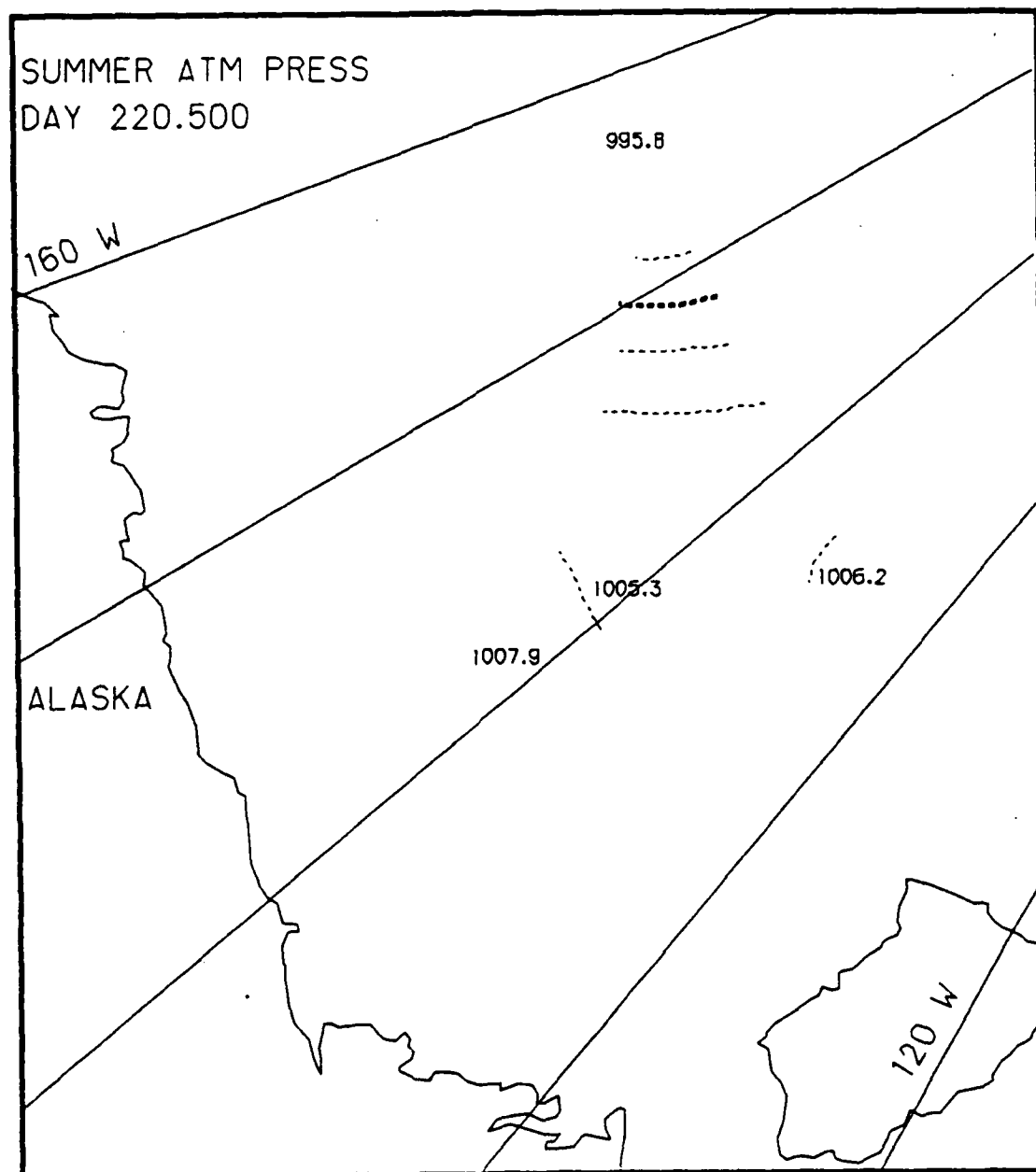


Fig. B.5. Spatial atmospheric pressure variations, day 220.5, based on the AIDJEX data from stations with hydrophones, summer 1975.

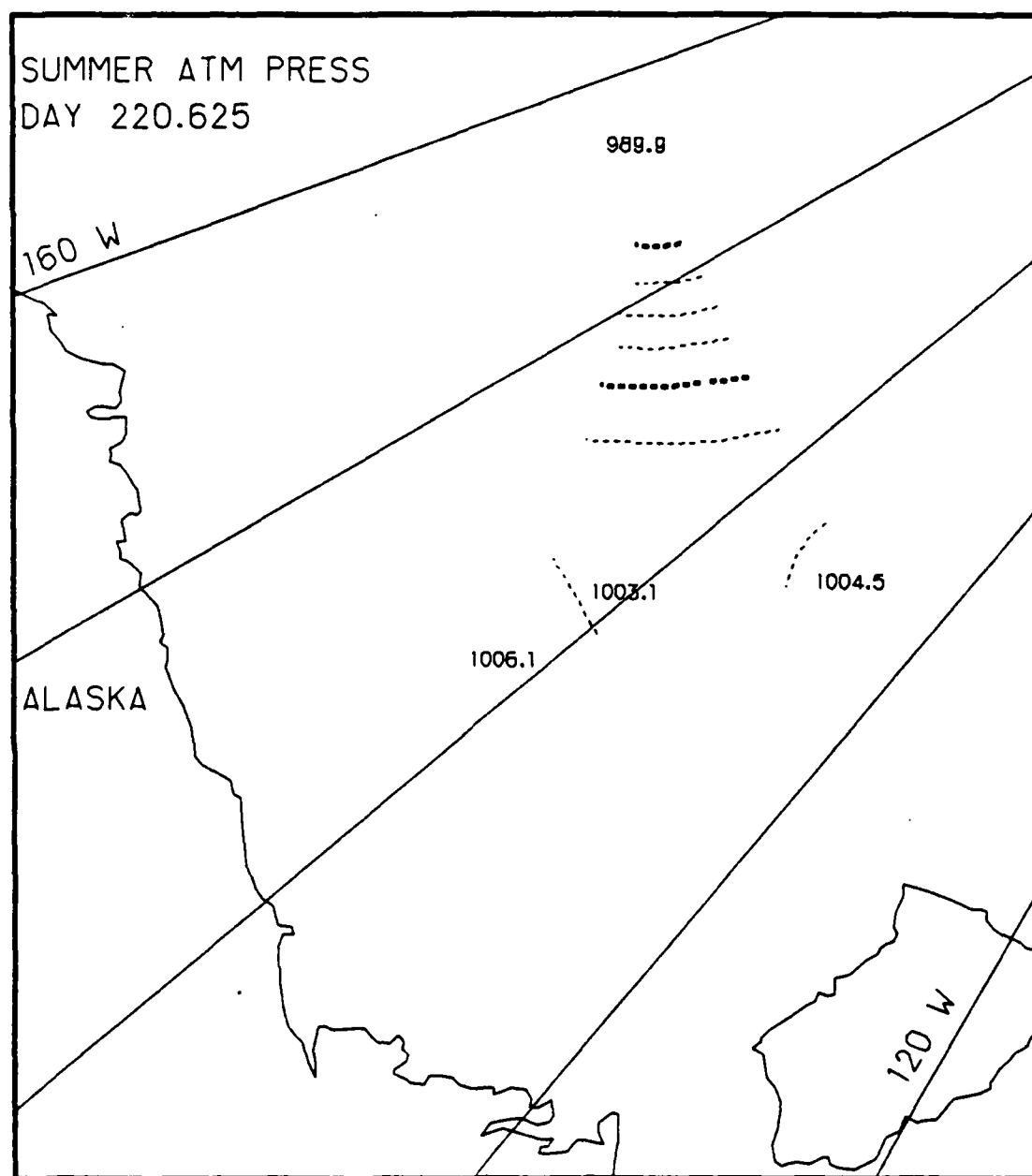


Fig. B.6. Spatial atmospheric pressure variations, day 220.625, based on the AIDJEX data from stations with hydrophones, summer 1975.

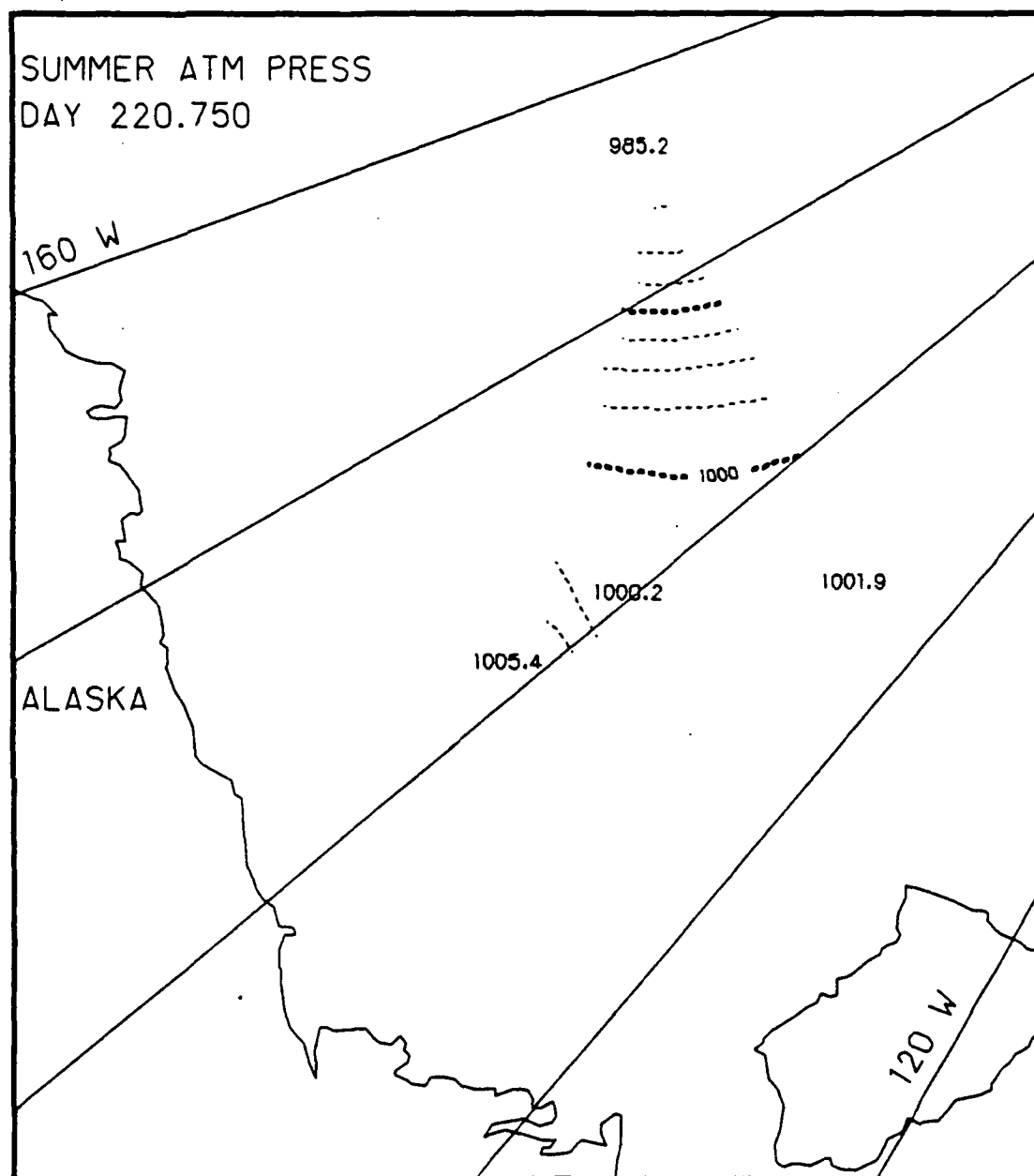


Fig. B.7. Spatial atmospheric pressure variations, day 220.75, based on the AIDJEX data from stations with hydrophones, summer 1975.

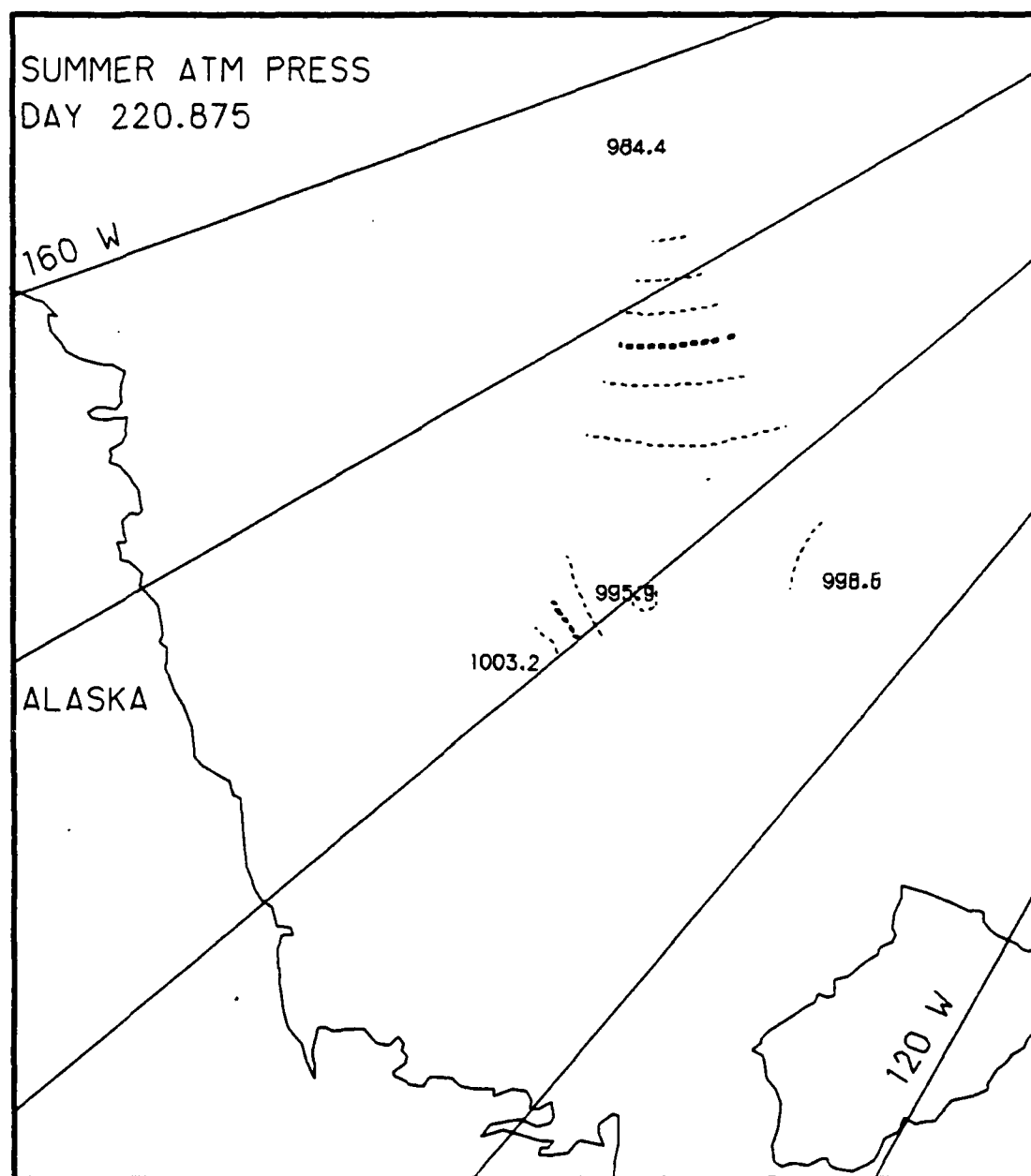


Fig. B.8. Spatial atmospheric pressure variations, day 220.875, based on the AIDJEX data from stations with hydrophones, summer 1975.

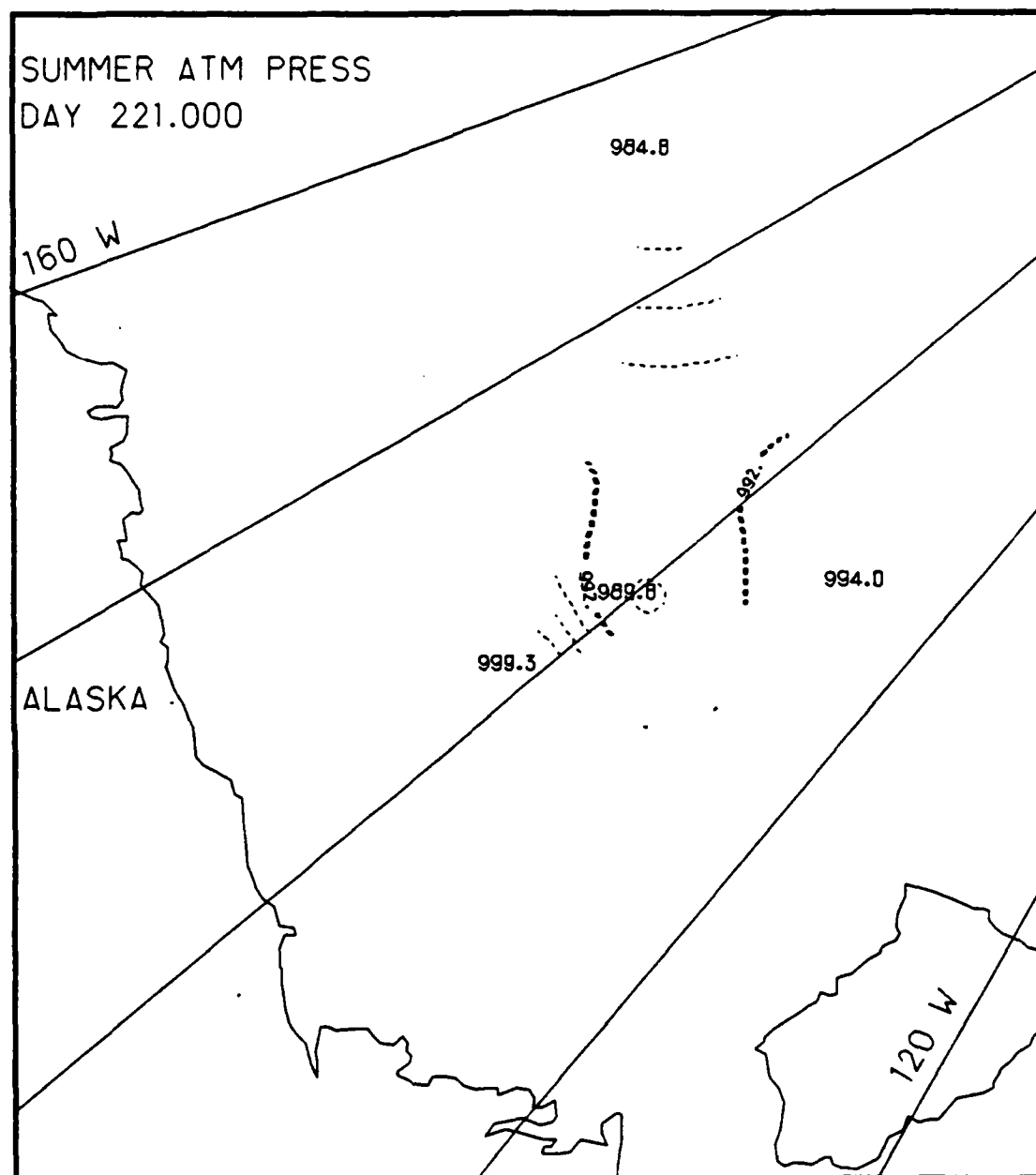


Fig. B.9. Spatial atmospheric pressure variations, day 221.0, based on the AIDJEX data from stations with hydrophones, summer 1975.

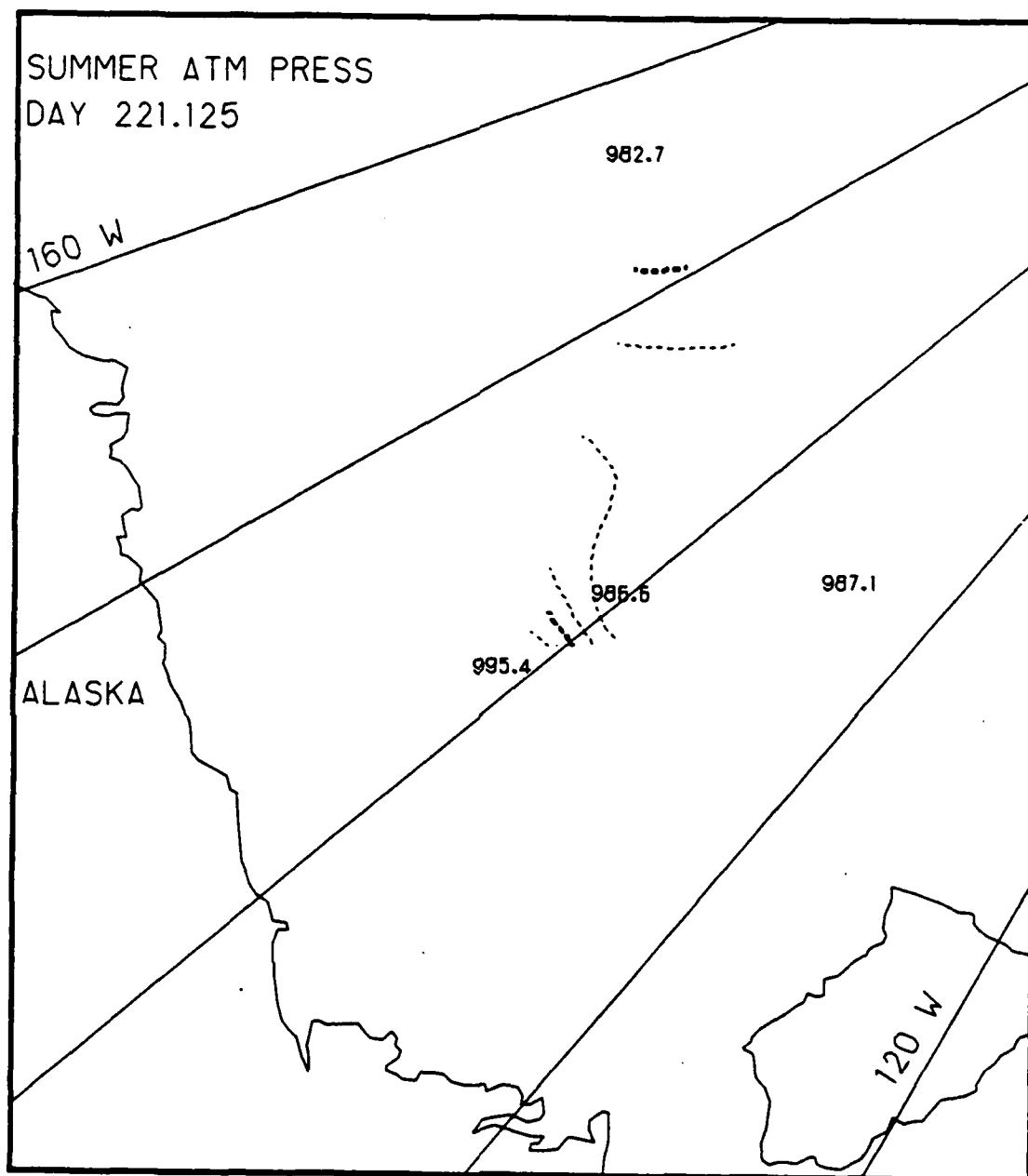


Fig. B.10. Spatial atmospheric pressure variations, day 221.125, based on the AIDJEX data from stations with hydrophones, summer 1975.

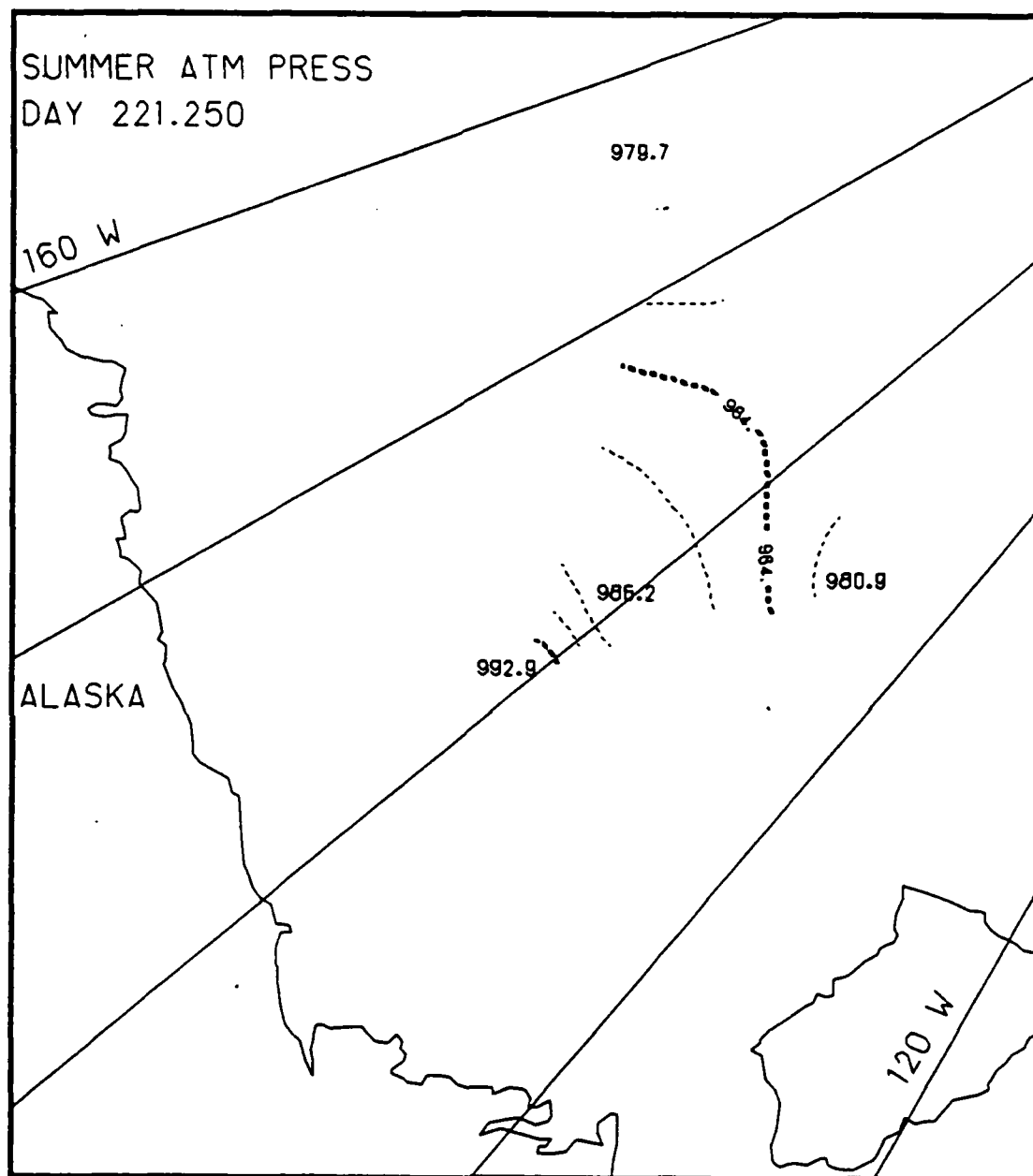


Fig. B.11. Spatial atmospheric pressure variations, day 221.25, based on the AIDJEX data from stations with hydrophones, summer 1975.

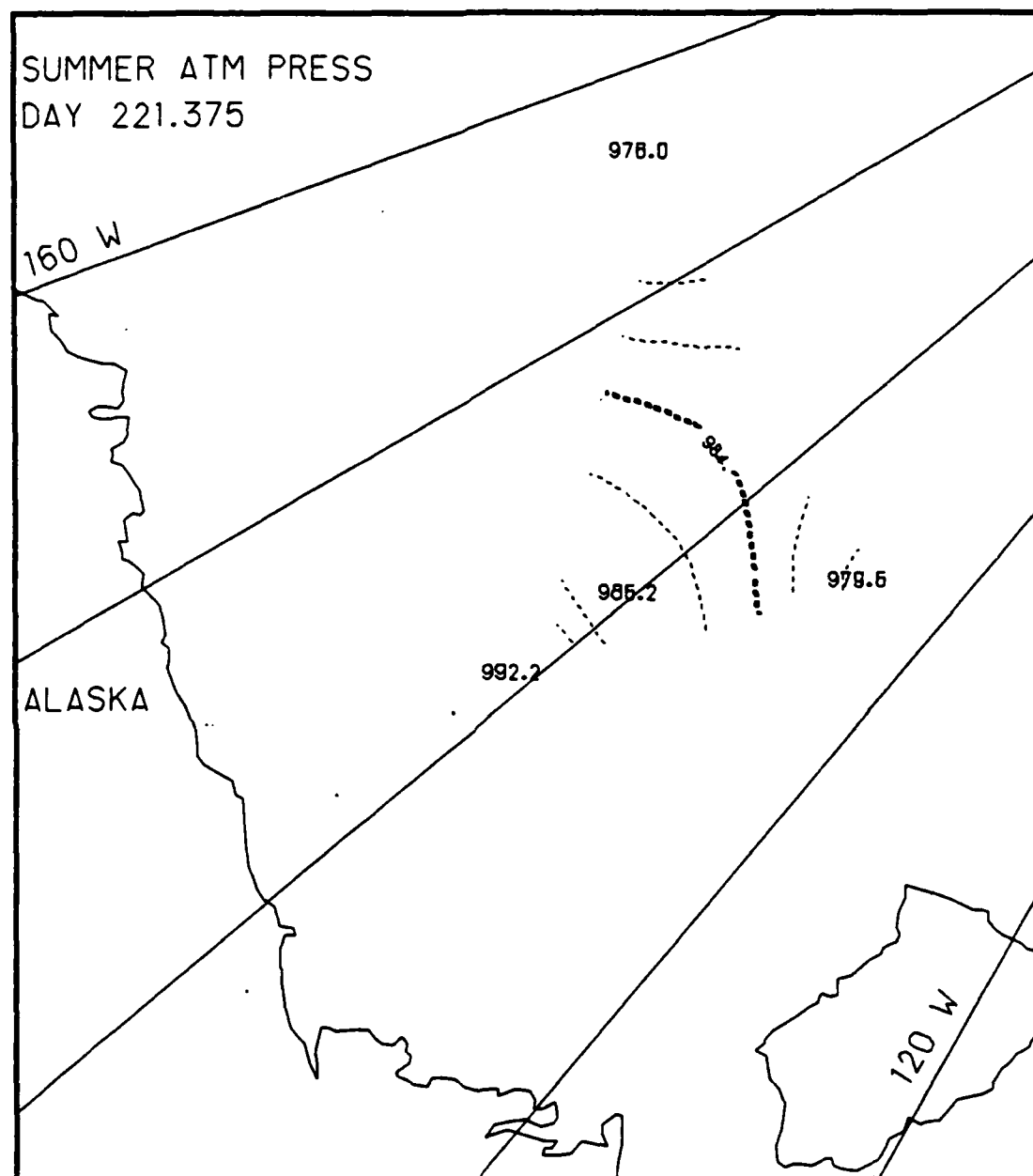


Fig. B.12. Spatial atmospheric pressure variations, day 221.375, based on the AIDJEX data from stations with hydrophones, summer 1975.

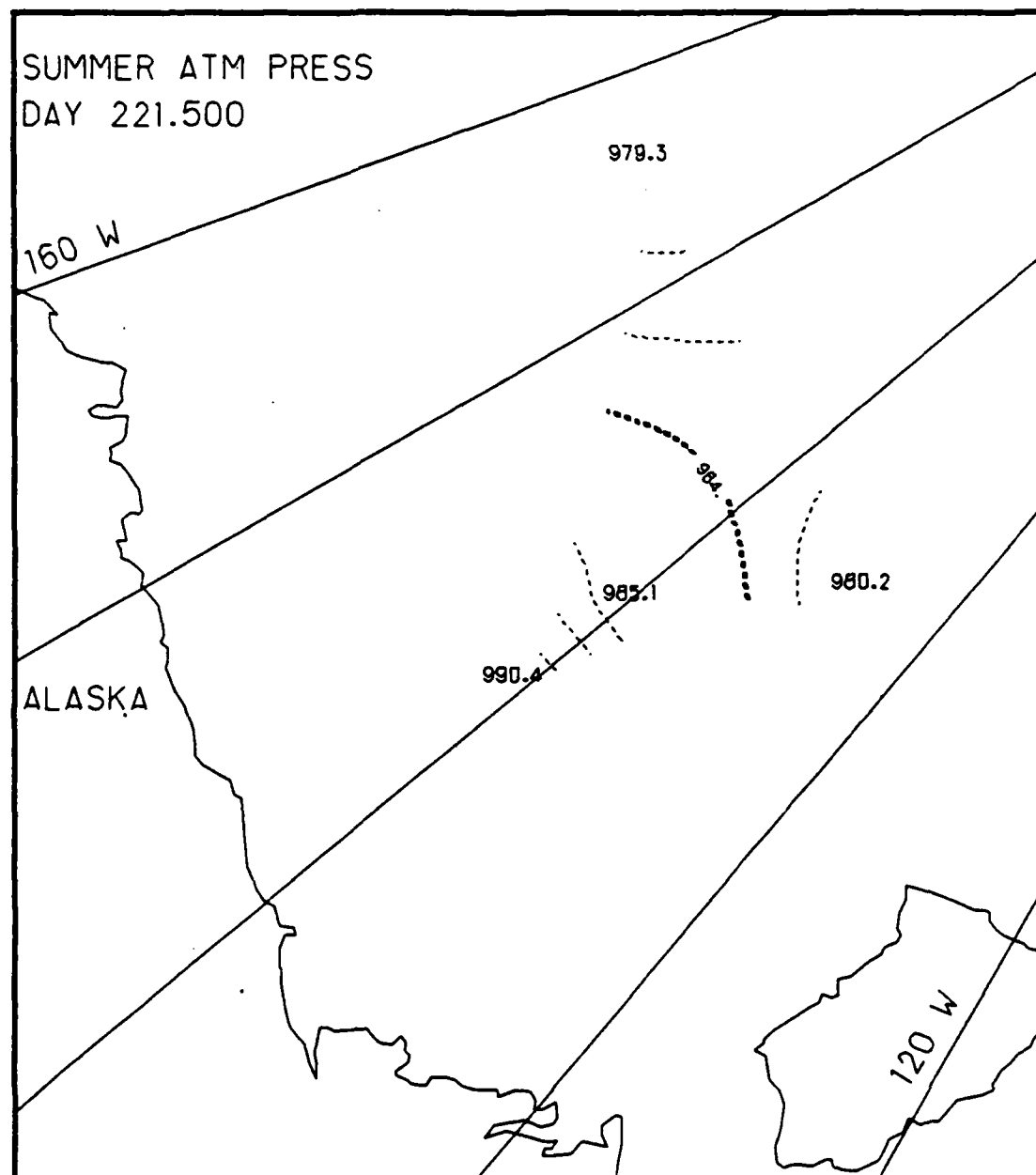


Fig. B.13. Spatial atmospheric pressure variations, day 221.5, based on the AIDJEX data from stations with hydrophones, summer 1975.

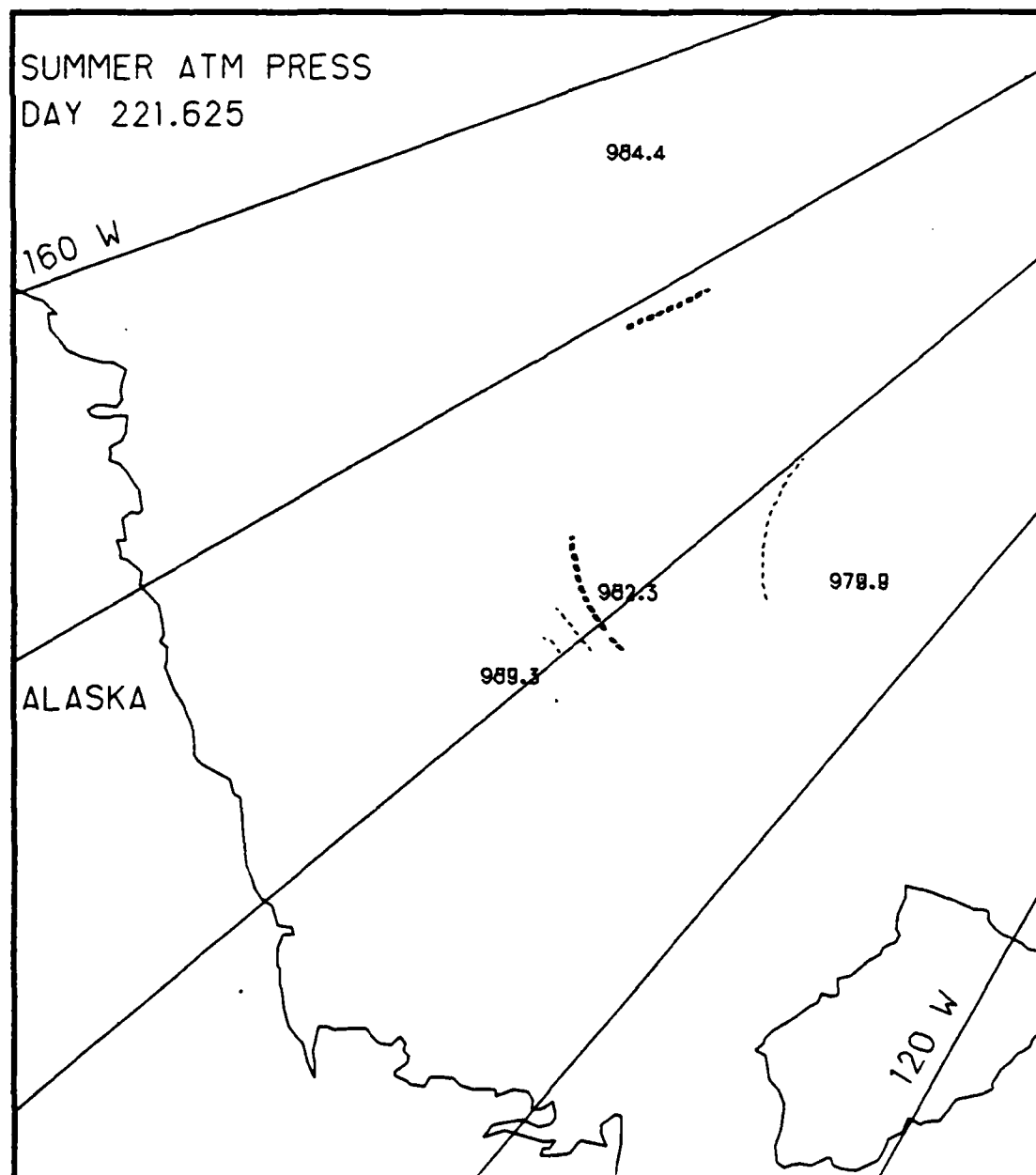


Fig. B.14. Spatial atmospheric pressure variations, day 221.625, based on the AIDJEX data from stations with hydrophones, summer 1975.

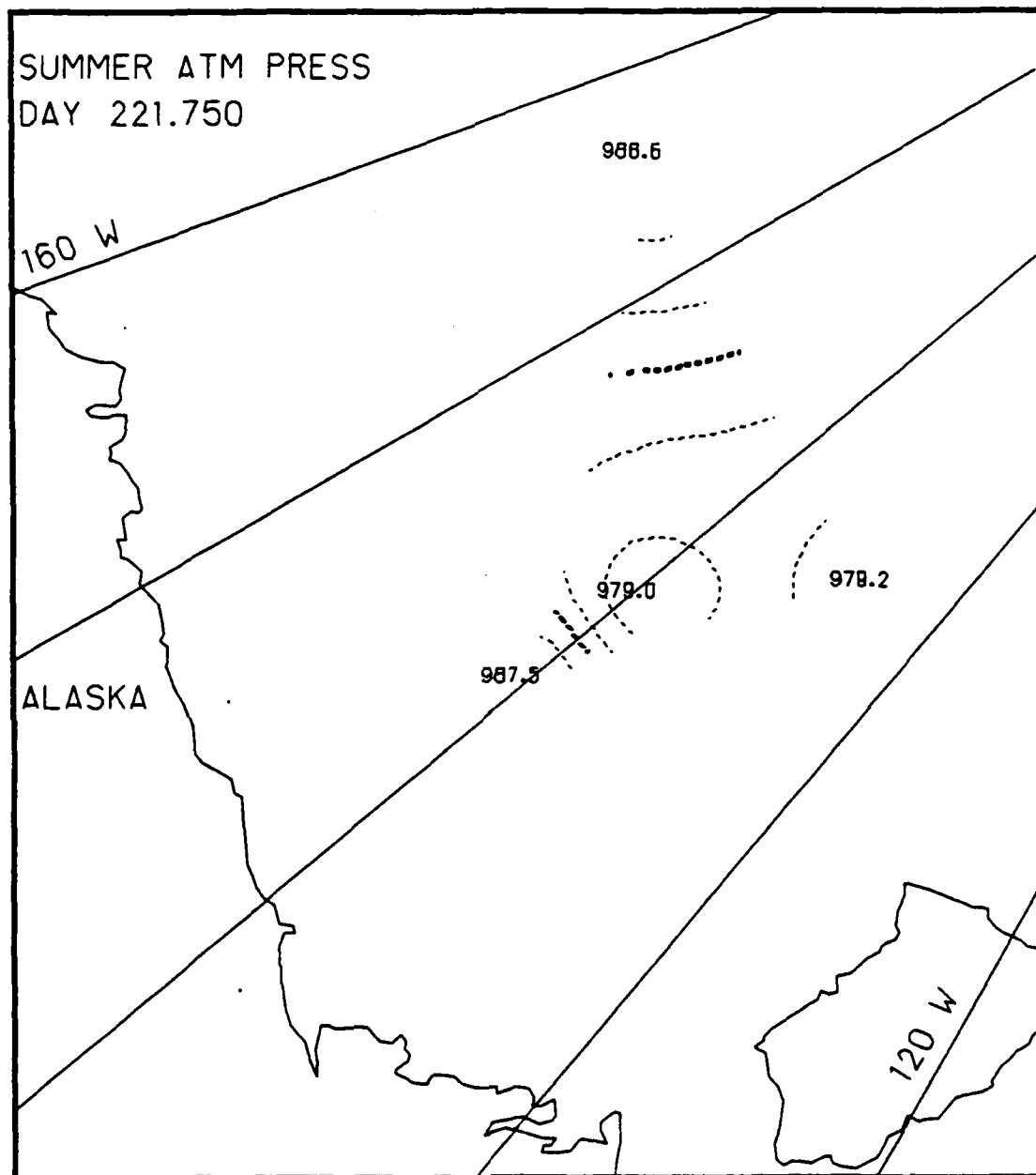


Fig. B.15. Spatial atmospheric pressure variations, day 221.75, based on the AIDJEX data from stations with hydrophones, summer 1975.

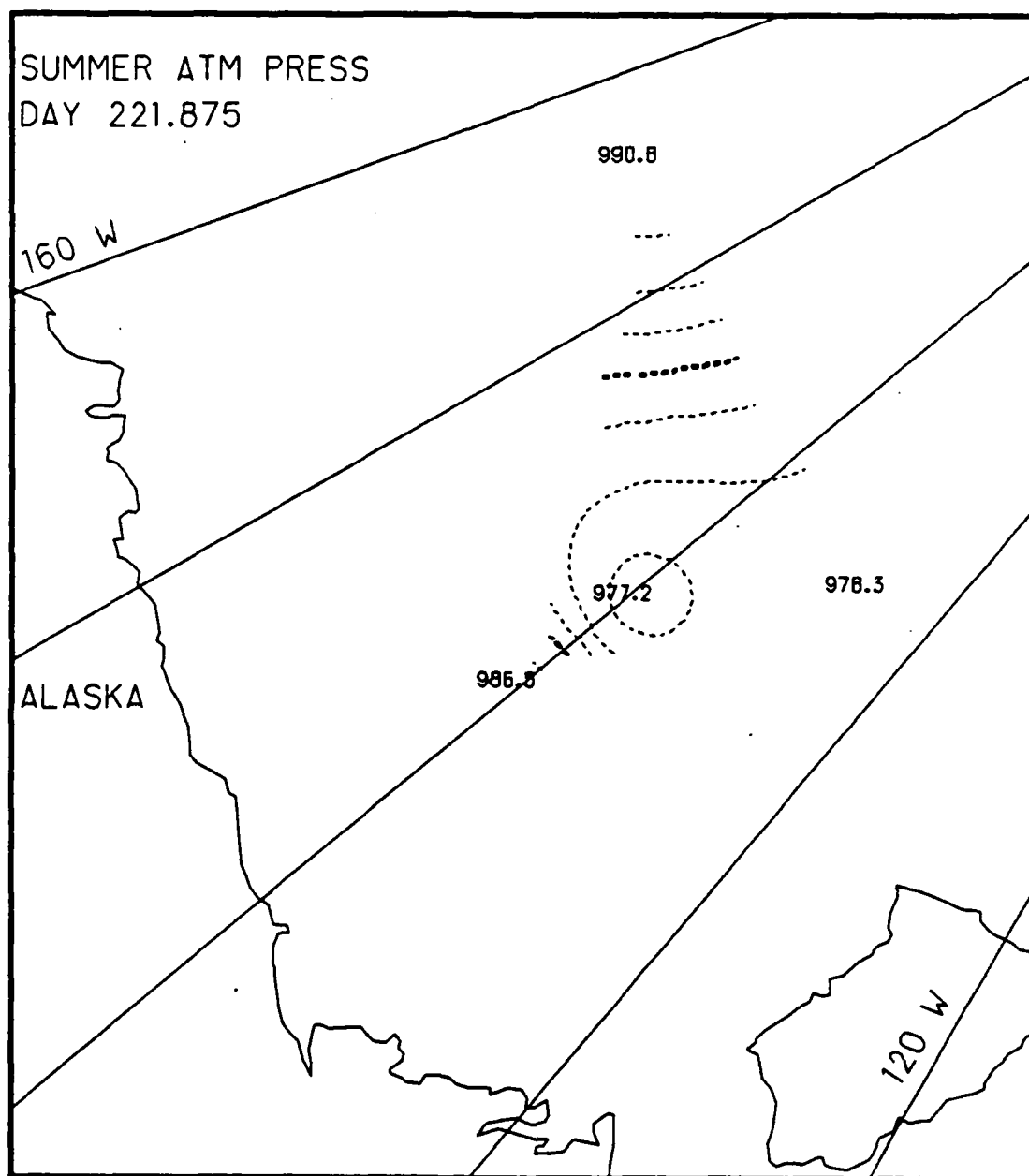


Fig. B.16. Spatial atmospheric pressure variations, day 221.875, based on the AIDJEX data from stations with hydrophones, summer 1975.

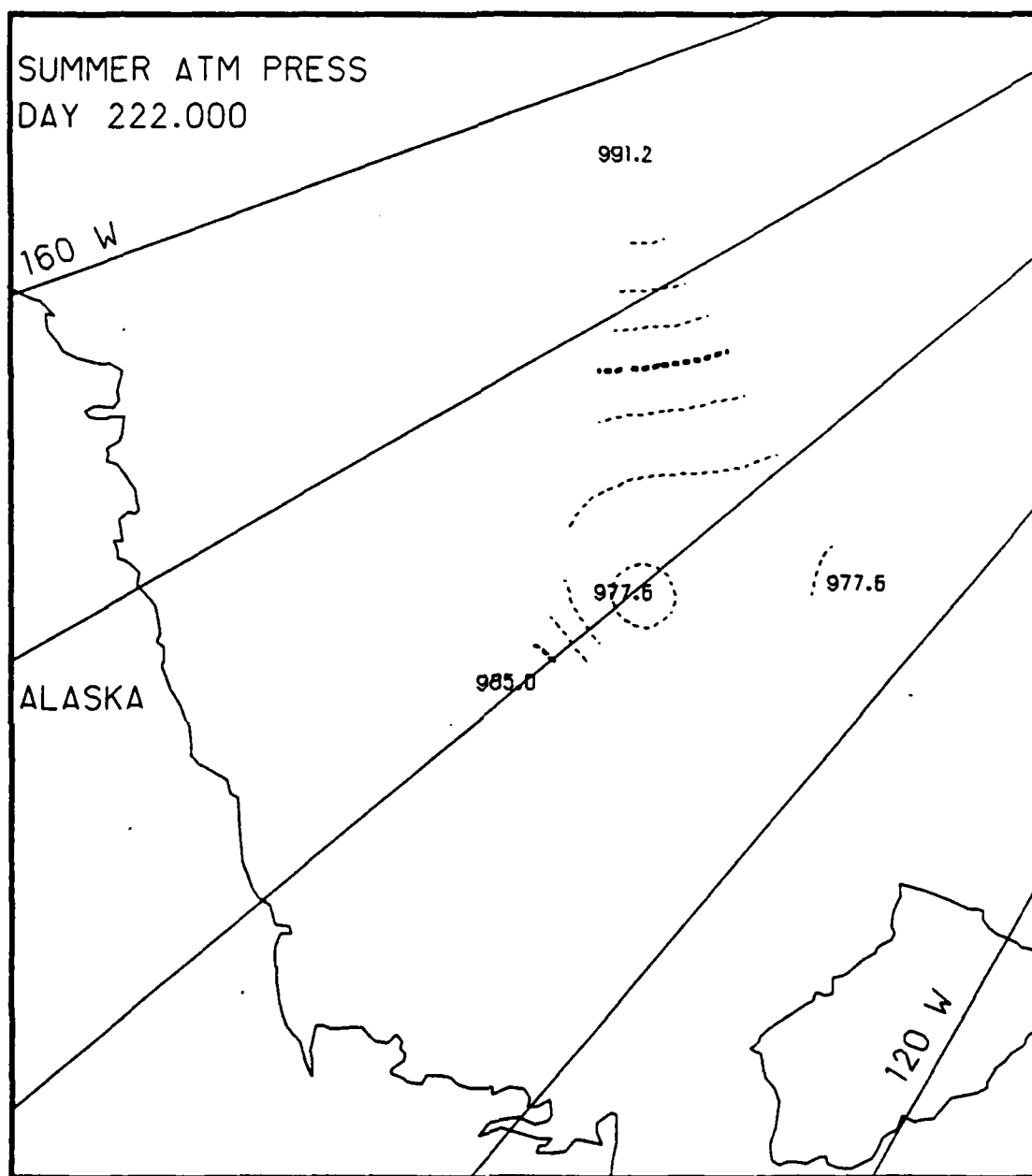


Fig. B.17. Spatial atmospheric pressure variations, day 222.0, based on the AIDJEX data from stations with hydrophones, summer 1975.

Appendix C

Two-Dimensional Contour Maps of Arctic Atmospheric Temperature Variations, 8-9 August 1975 (Summer)

This appendix contains the two-dimensional contour maps of the AIDJEX atmospheric temperature data collected at those stations with hydrophones during the 48 hour period of 8-9 August 1975. The contour maps show the spatial variations of atmospheric temperature ($^{\circ}\text{C}$) at 3 hr intervals.

List of Figures
Appendix C

2-43

	<u>Page</u>
Fig. C.1. Spatial atmospheric temperature variations, day 220.0	2-44
Fig. C.2. Spatial atmospheric temperature variations, day 220.125	2-45
Fig. C.3. Spatial atmospheric temperature variations, day 220.25	2-46
Fig. C.4. Spatial atmospheric temperature variations, day 220.375	2-47
Fig. C.5. Spatial atmospheric temperature variations, day 220.5	2-48
Fig. C.6. Spatial atmospheric temperature variations, day 220.625	2-49
Fig. C.7. Spatial atmospheric temperature variations, day 220.75	2-50
Fig. C.8. Spatial atmospheric temperature variations, day 220.875	2-51
Fig. C.9. Spatial atmospheric temperature variations, day 221.0	2-52
Fig. C.10. Spatial atmospheric temperature variations, day 221.125	2-53
Fig. C.11. Spatial atmospheric temperature variations, day 221.25	2-54
Fig. C.12. Spatial atmospheric temperature variations, day 221.375	2-55
Fig. C.13. Spatial atmospheric temperature variations, day 221.5	2-56
Fig. C.14. Spatial atmospheric temperature variations, day 221.625	2-57
Fig. C.15. Spatial atmospheric temperature variations, day 221.75	2-58
Fig. C.16. Spatial atmospheric temperature variations, day 221.875	2-59
Fig. C.17. Spatial atmospheric temperature variations, day 222.0	2-60

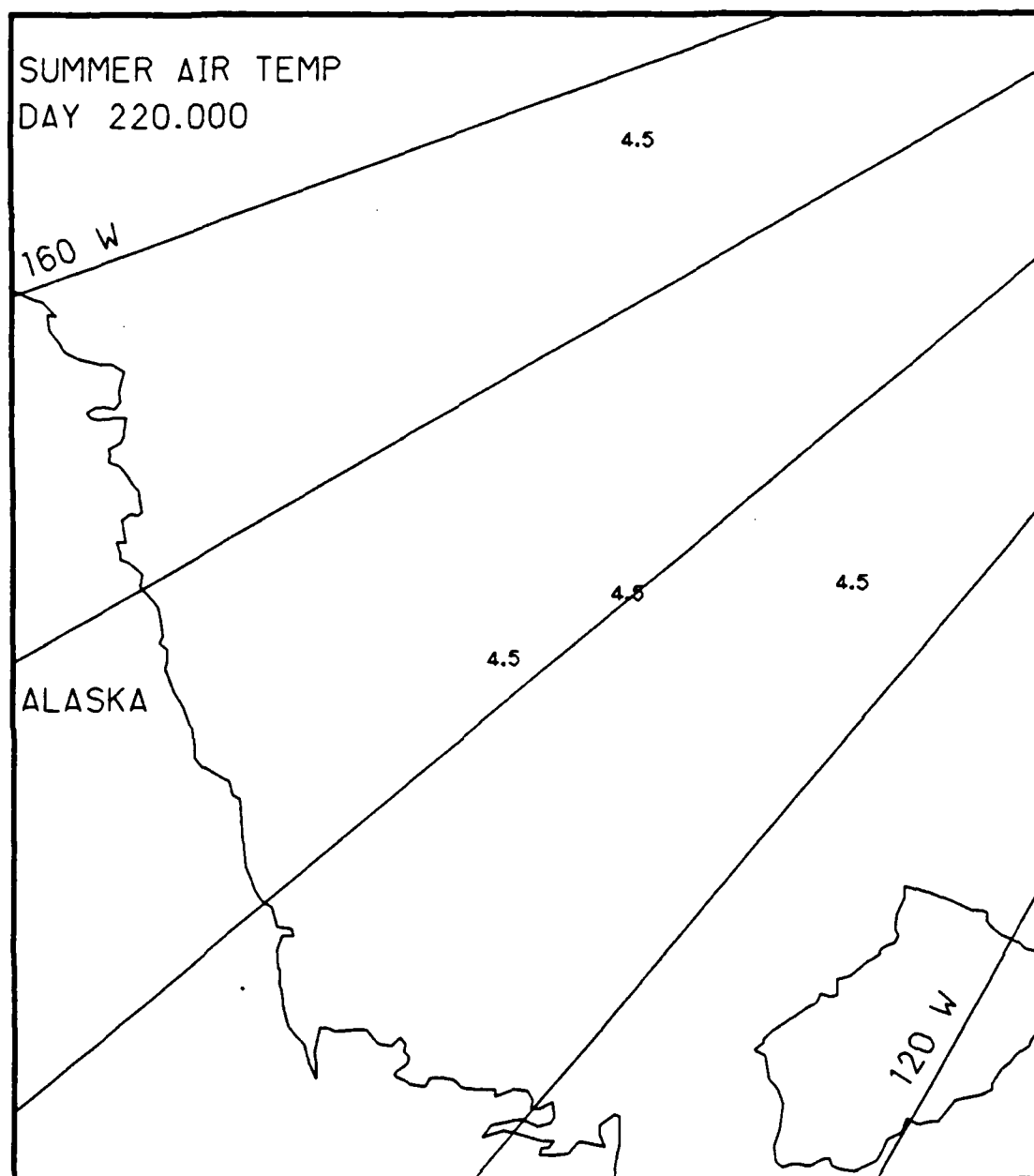


Fig. C.1. Spatial atmospheric temperature variations, day 220.0, based on the AIDJEX data from stations with hydrophones, summer 1975.

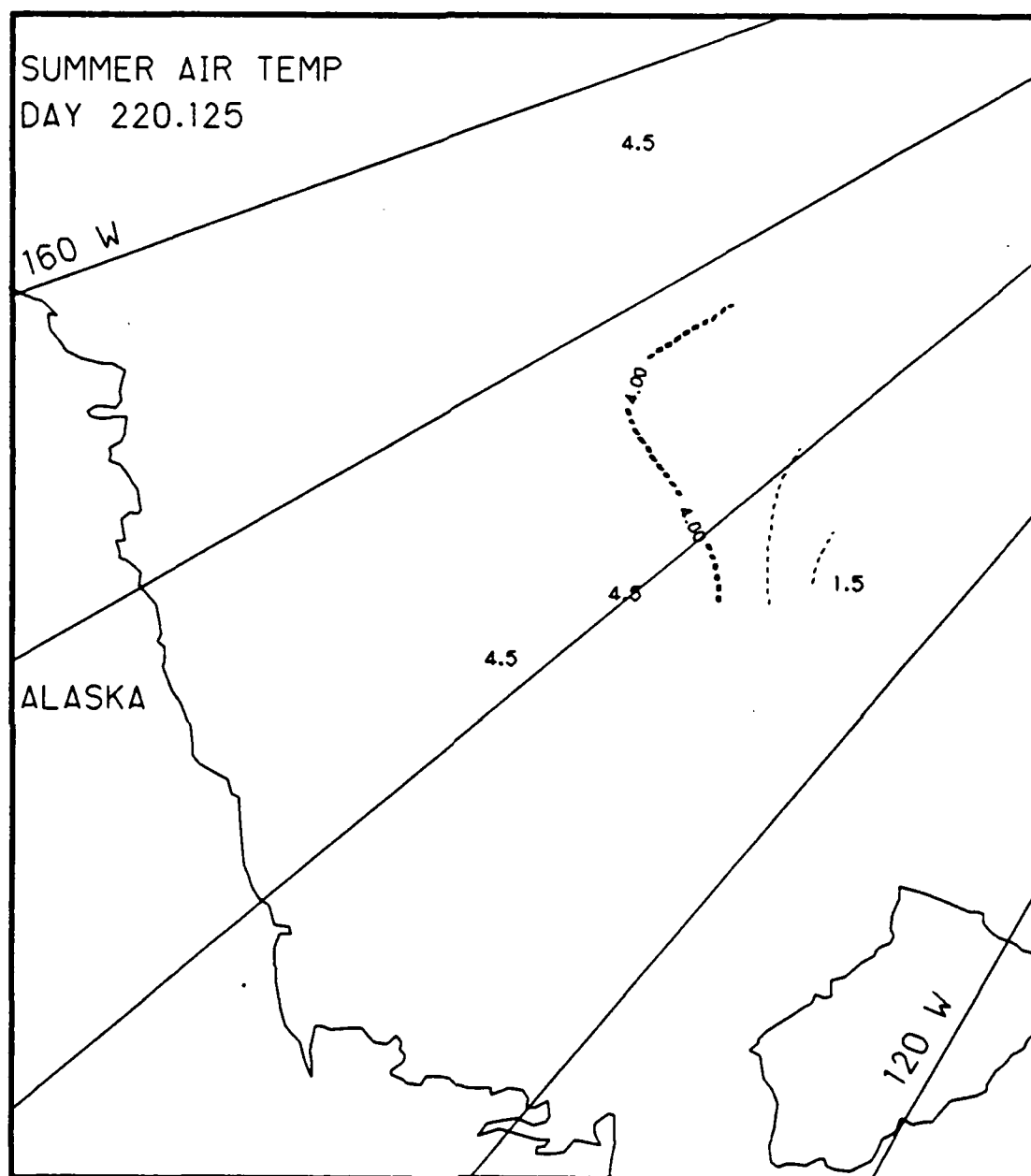


Fig. C.2. Spatial atmospheric temperature variations, day 220.125, based on the AIDJEX data from stations with hydrophones, summer 1975.

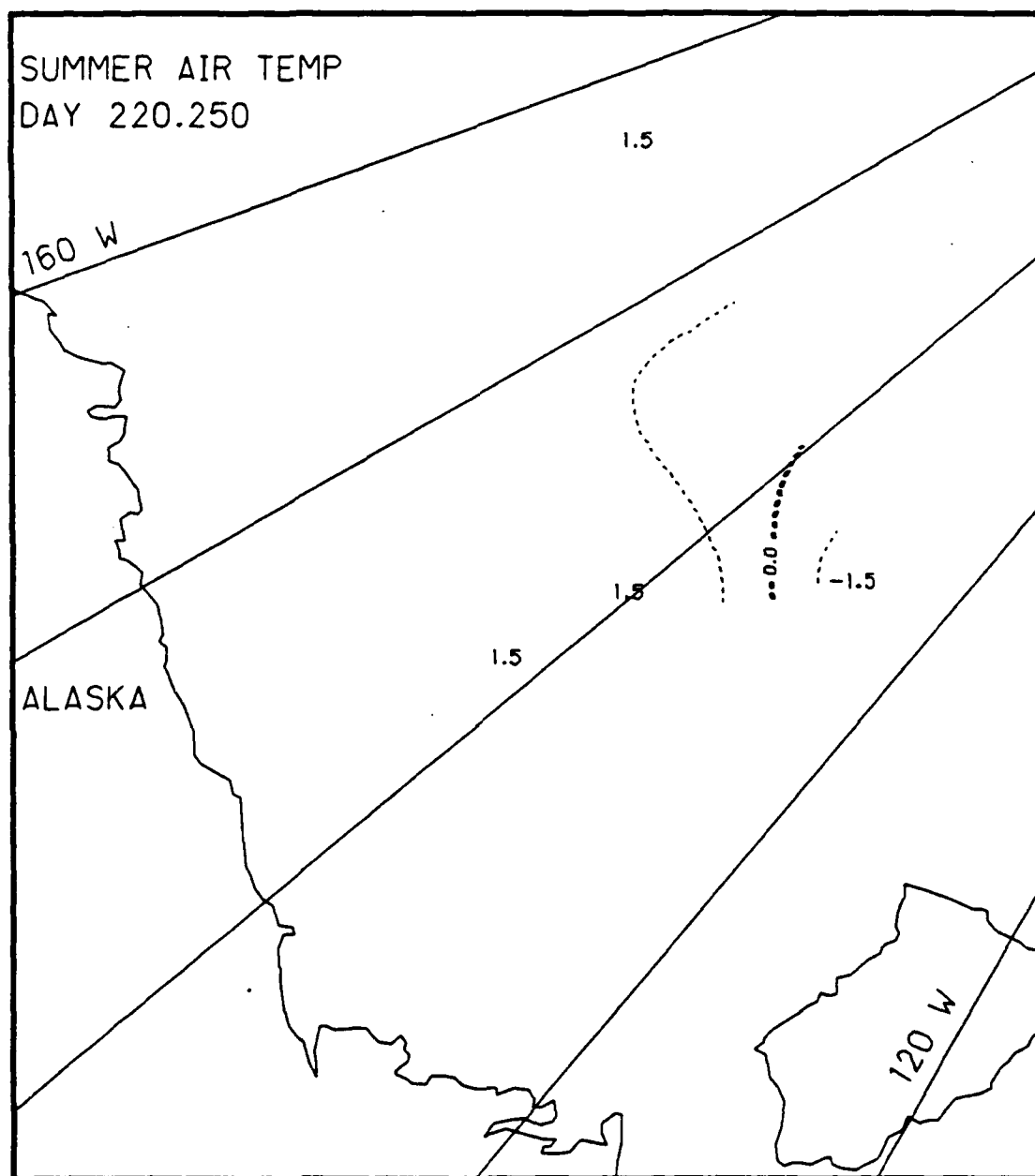


Fig. C.3. Spatial atmospheric temperature variations, day 220.25, based on the AIDJEX data from stations with hydrophones, summer 1975.

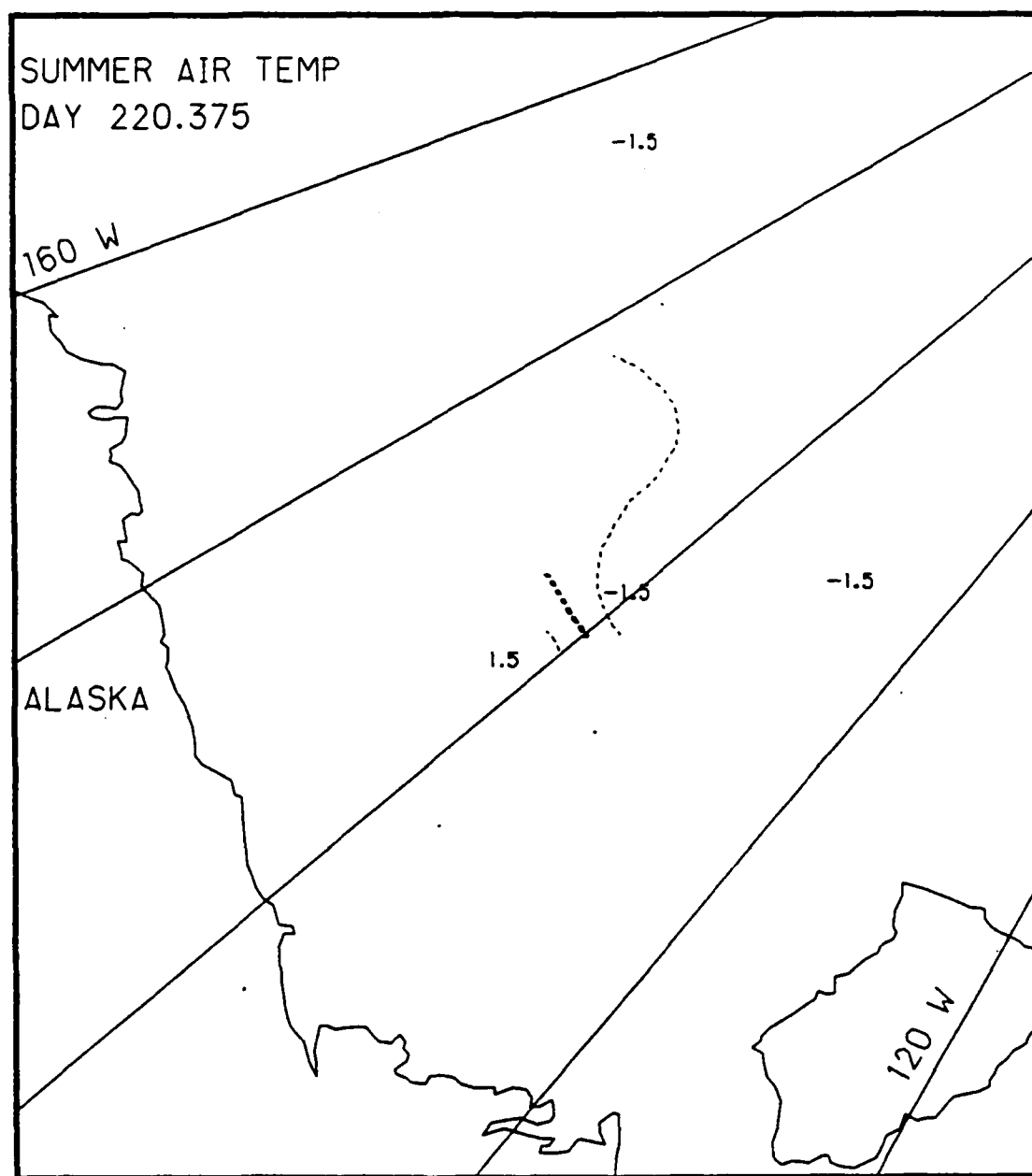


Fig. C.4. Spatial atmospheric temperature variations, day 220.375, based on the AIDJEX data from stations with hydrophones, summer 1975.

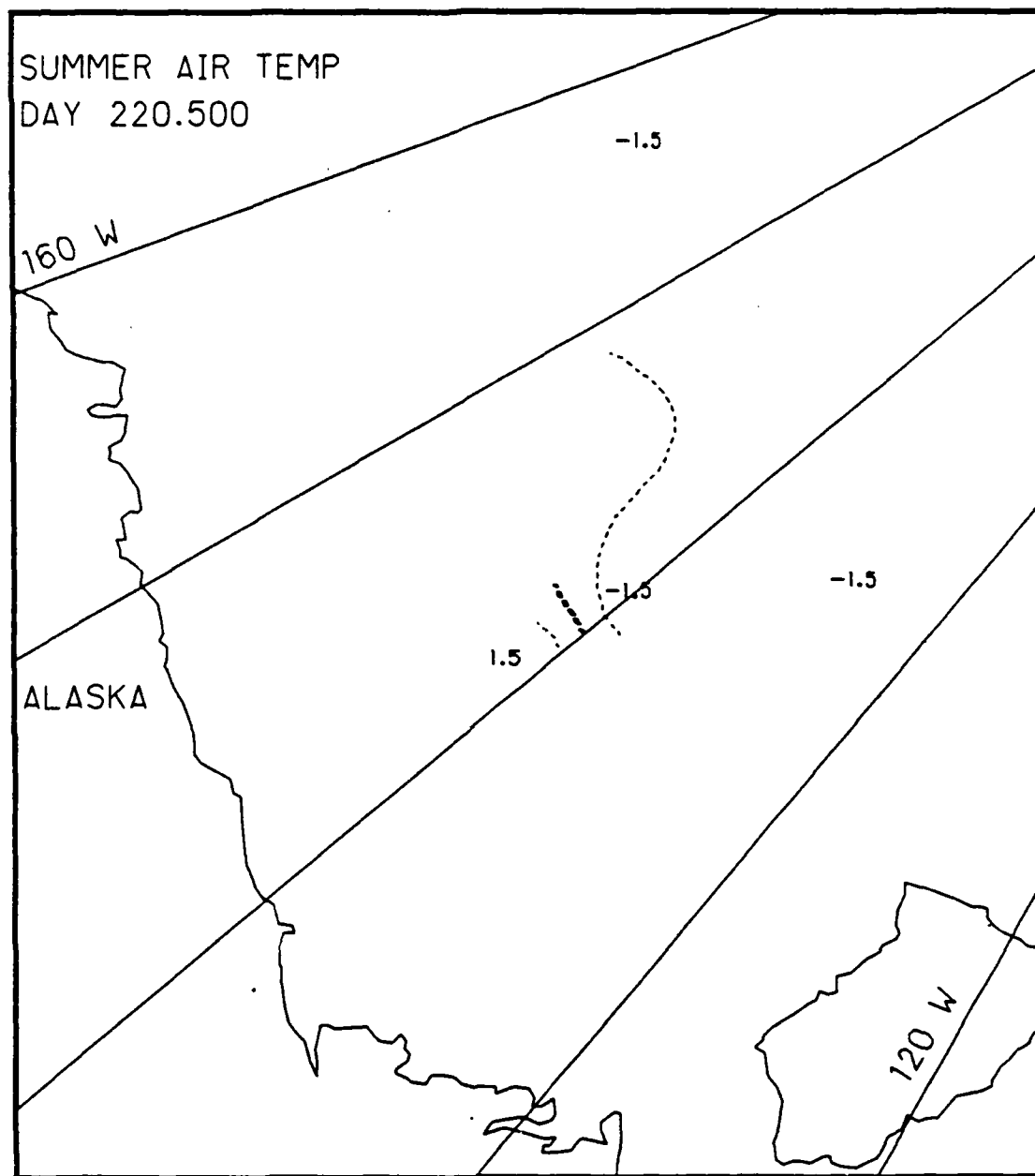


Fig. C.5. Spatial atmospheric temperature variations, day 220.5, based on the AIDJEX data from stations with hydrophones, summer 1975.

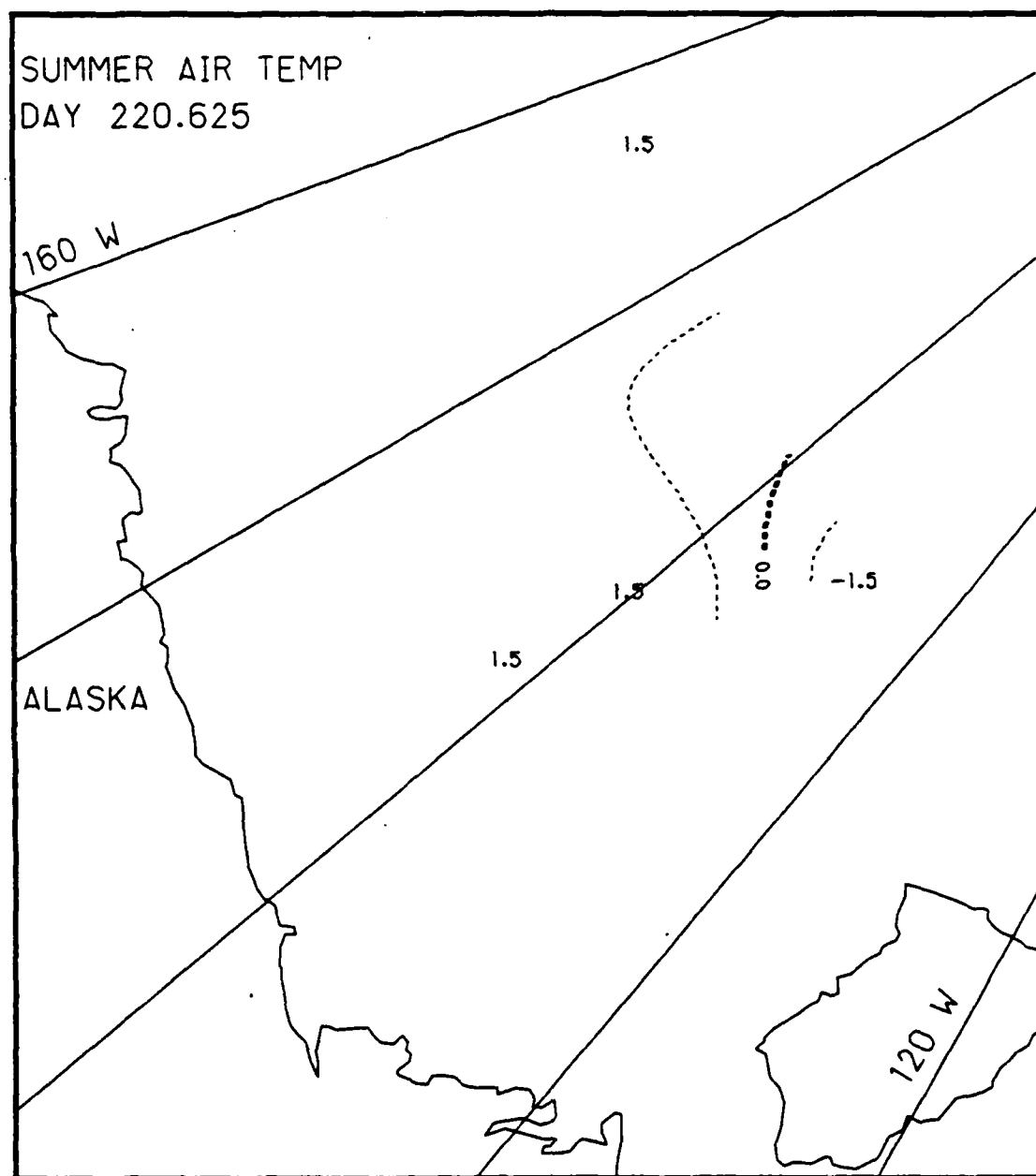


Fig. C.6. Spatial atmospheric temperature variations, day 220.625, based on the AIDJEX data from stations with hydrophones, summer 1975.

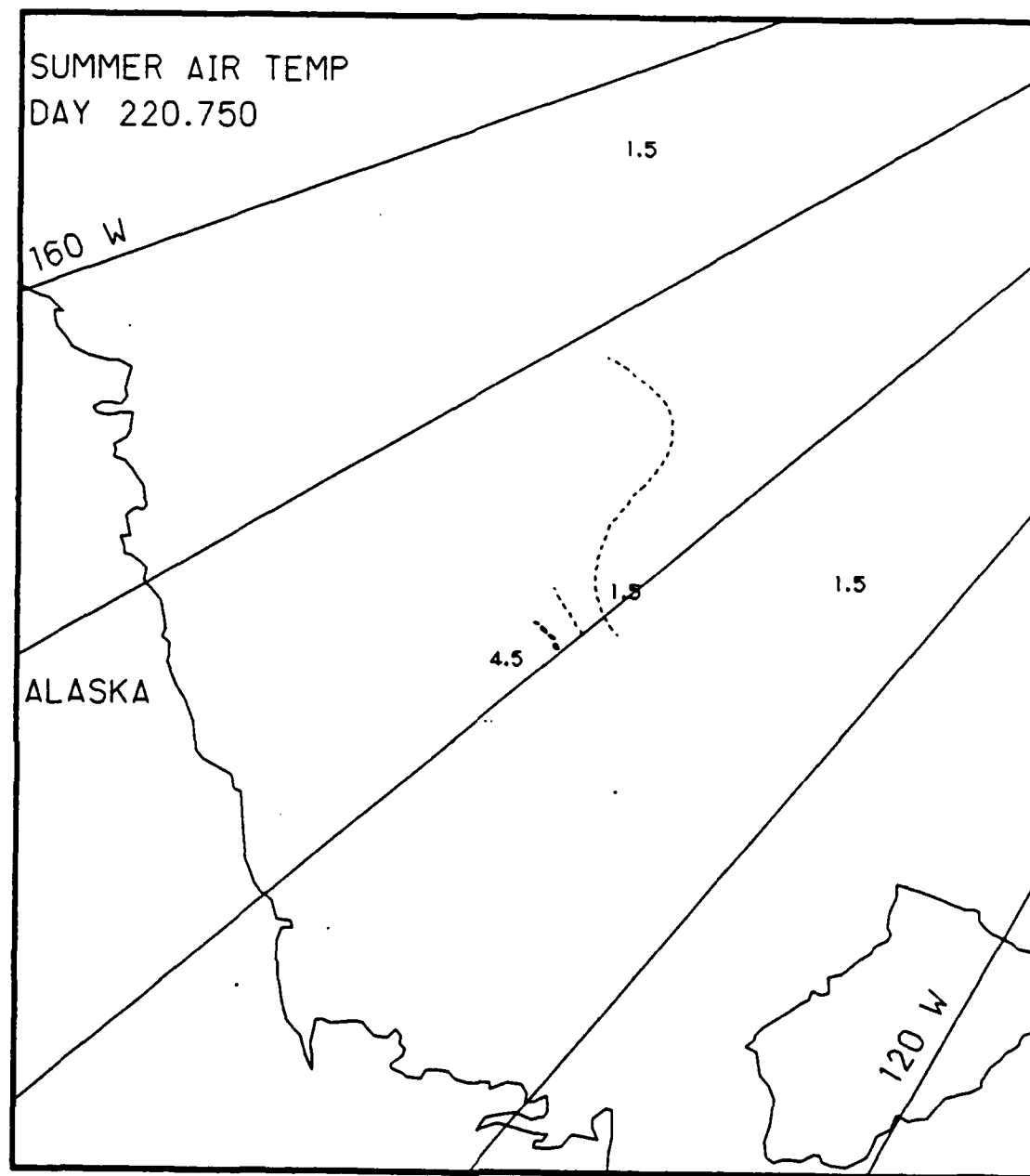


Fig. C.7. Spatial atmospheric temperature variations, day 220.75, based on the AIDJEX data from stations with hydrophones, summer 1975.

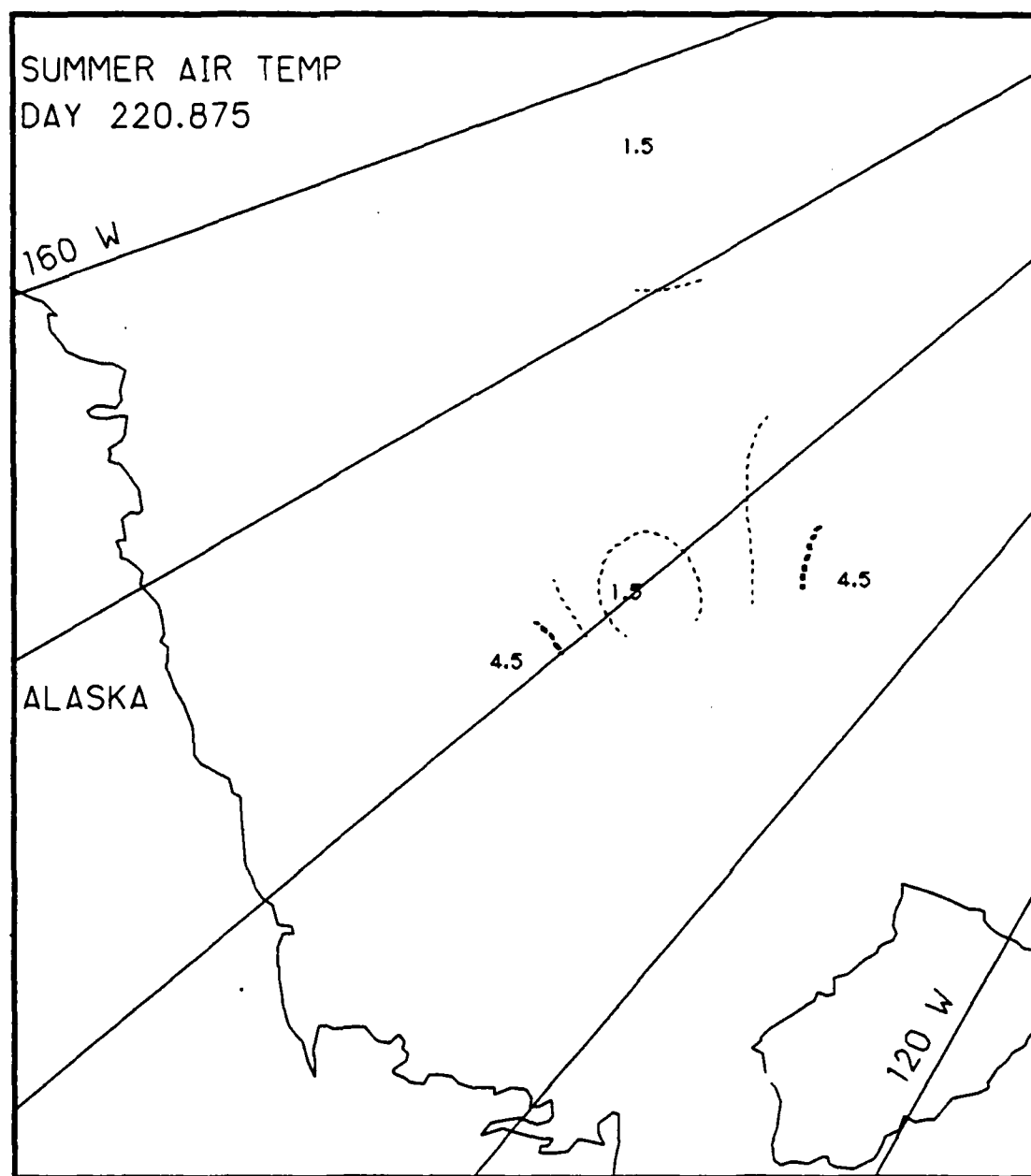


Fig. C.8. Spatial atmospheric temperature variations, day 220.875, based on the AIDJEX data from stations with hydrophones, summer 1975.

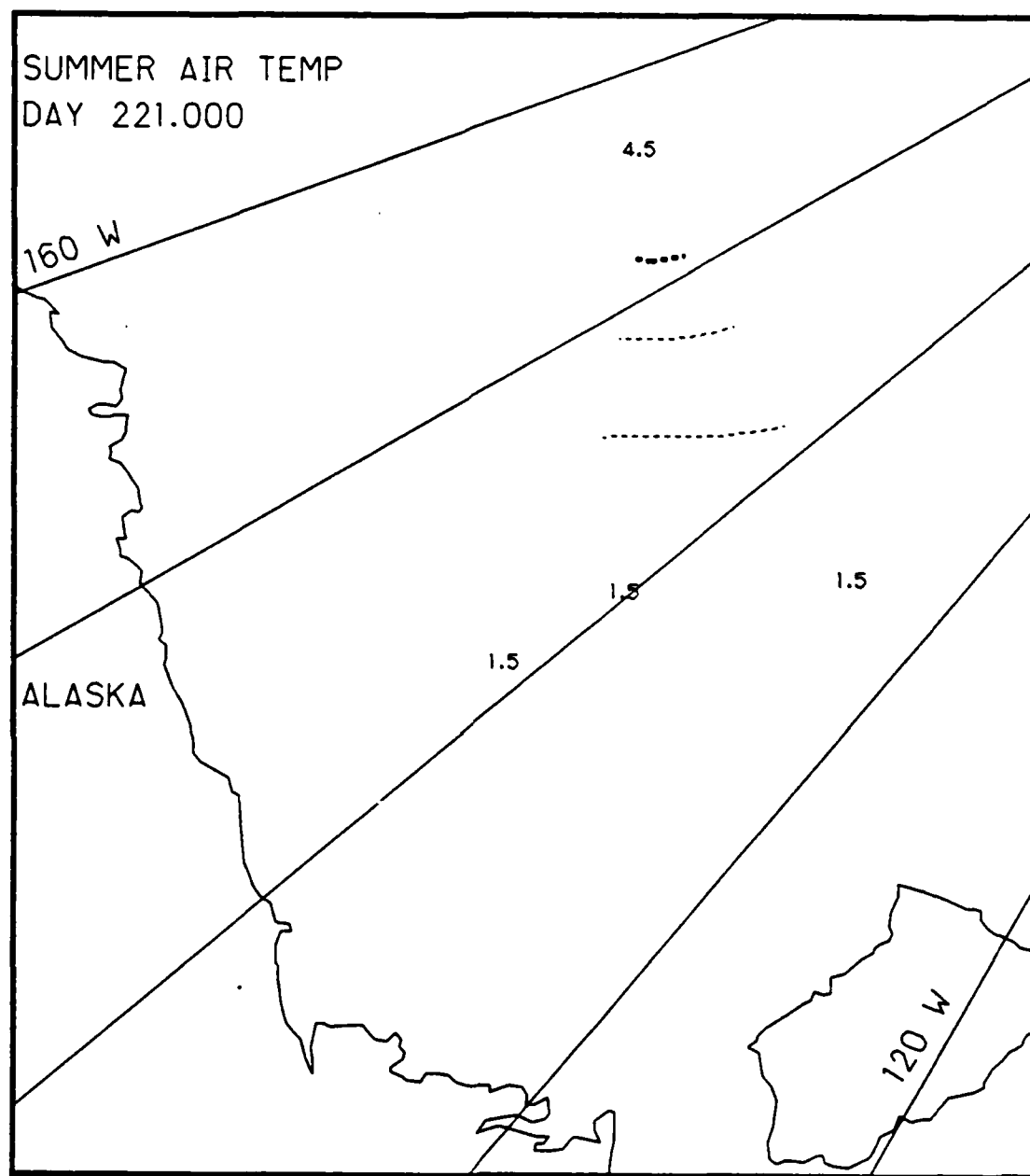


Fig. C.9. Spatial atmospheric temperature variations, day 221.0, based on the AIDJEX data from stations with hydrophones, summer 1975.

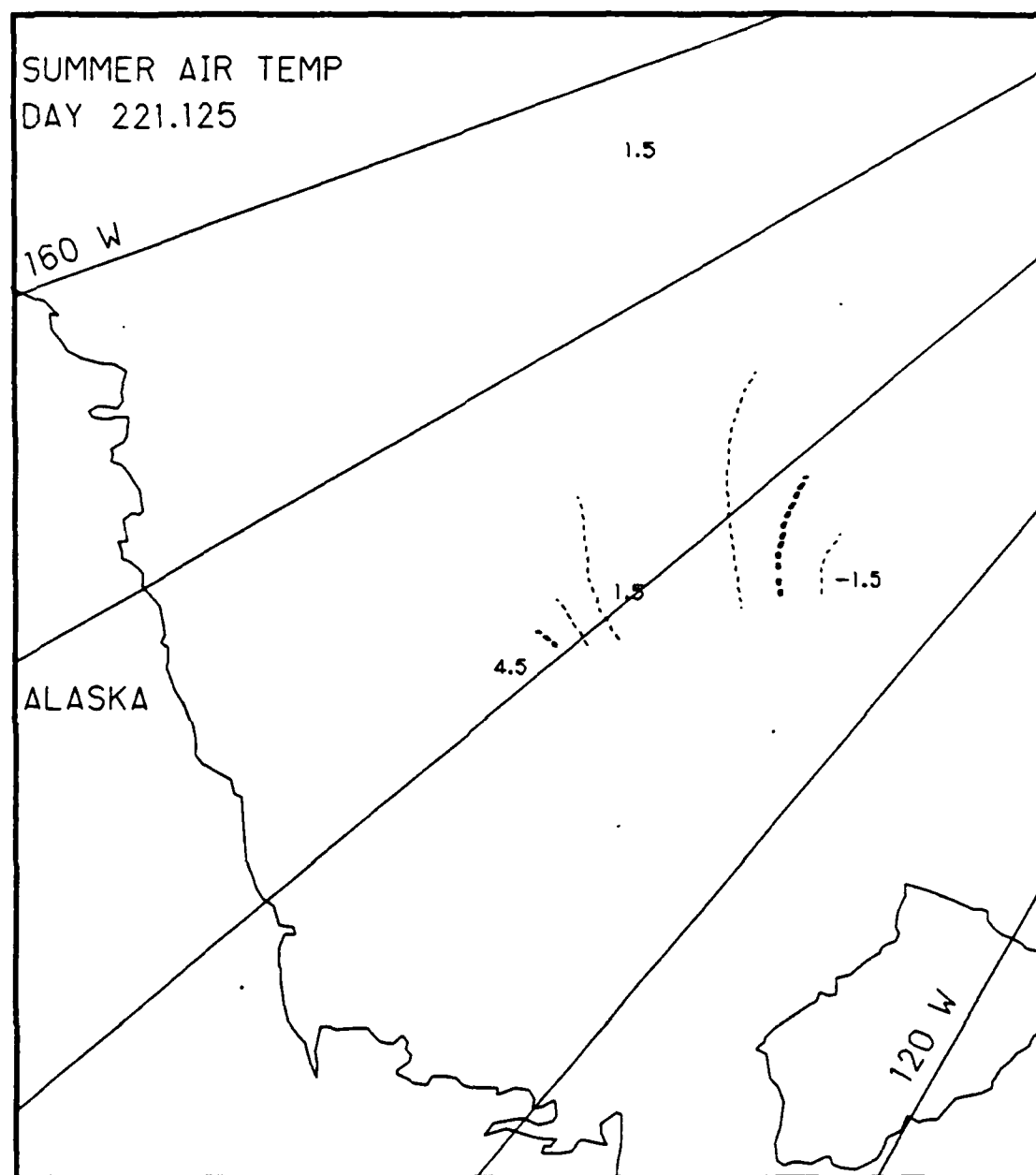


Fig. C.10. Spatial atmospheric temperature variations, day 221.125, based on the AIDJEX data from stations with hydrophones, summer 1975.

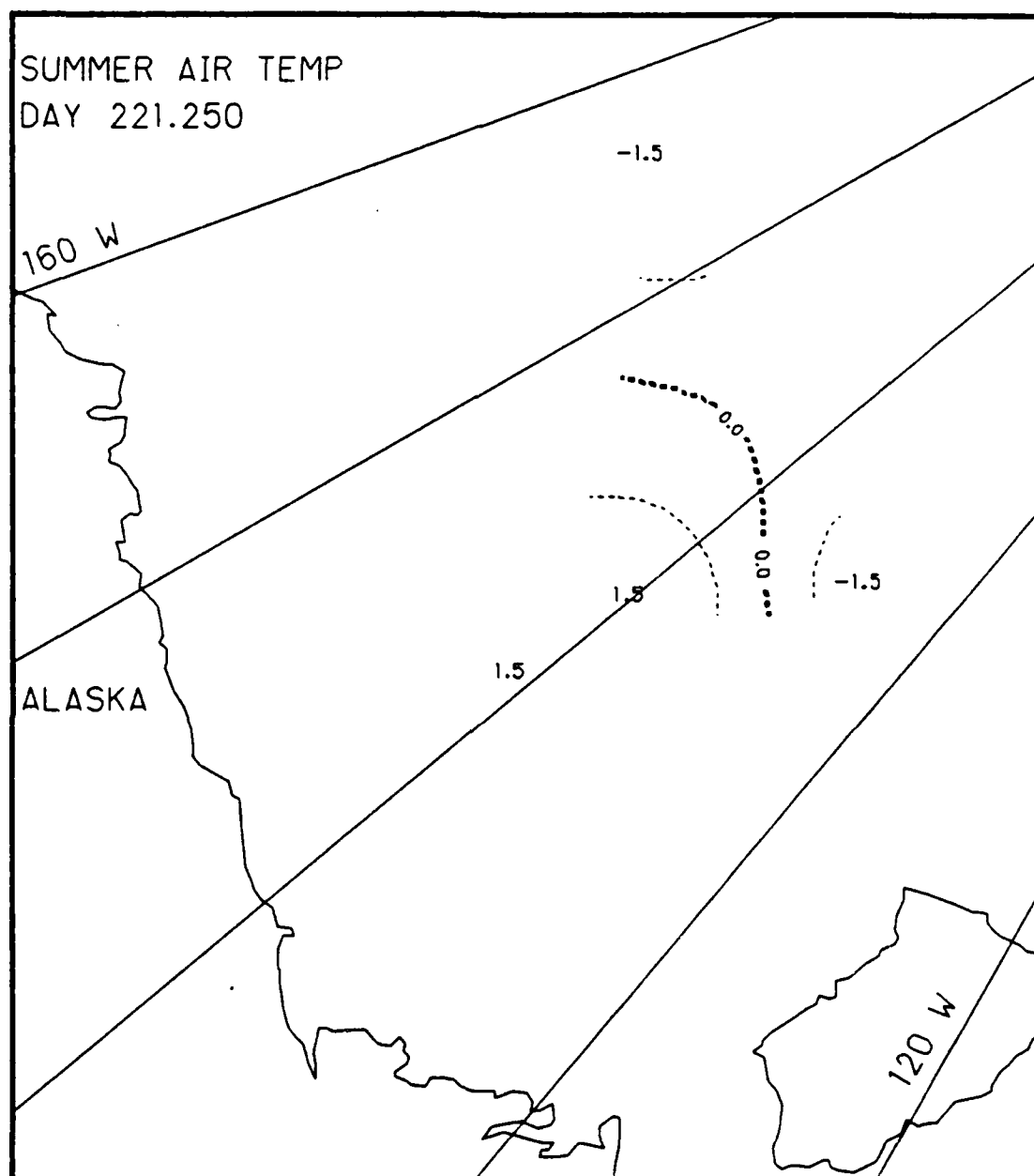


Fig. C.11. Spatial atmospheric temperature variations, day 221.25, based on the AIDJEX data from stations with hydrophones, summer 1975.

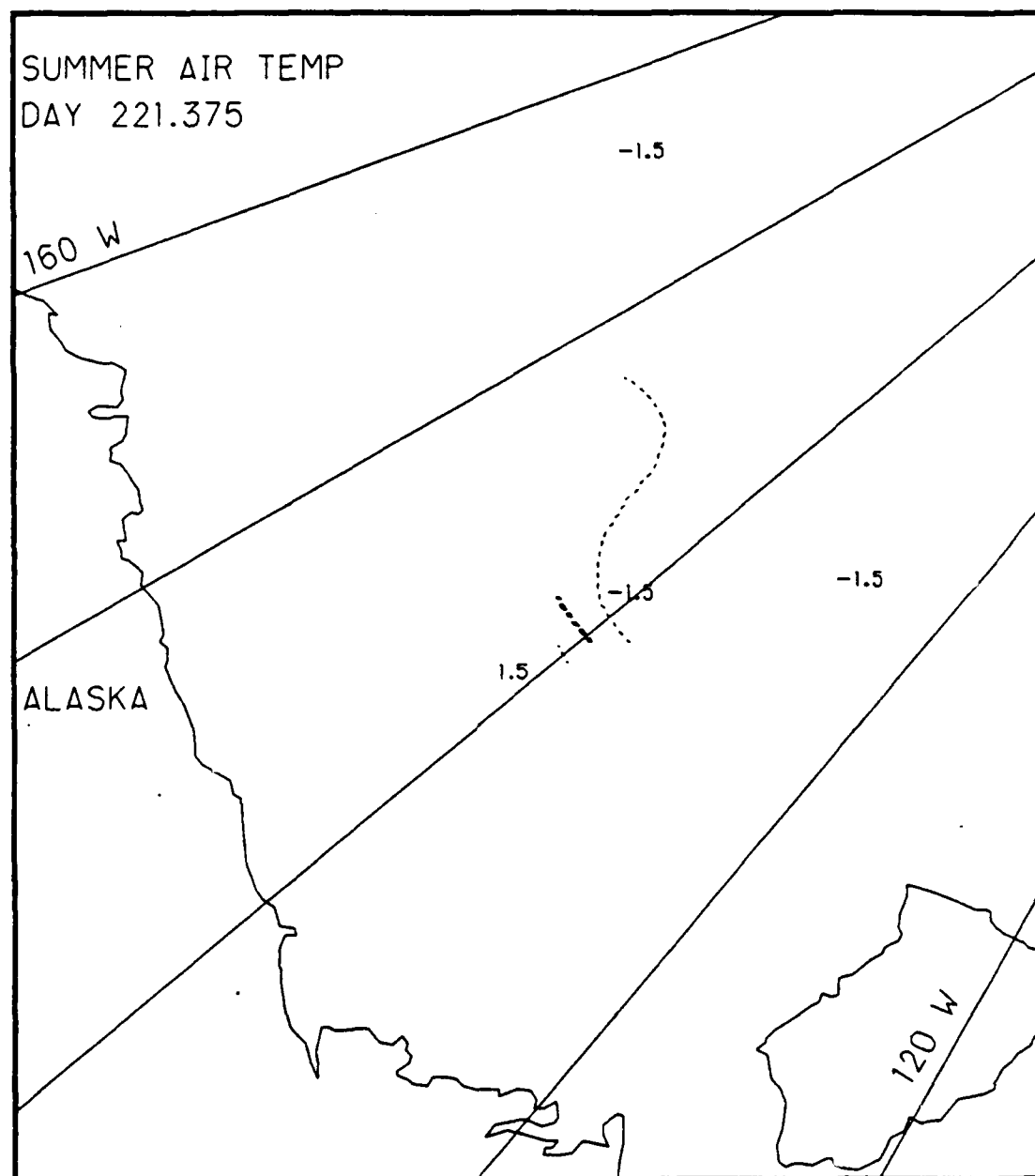


Fig. C.12. Spatial atmospheric temperature variations, day 221.375, based on the AIDJEX data from stations with hydrophones, summer 1975.

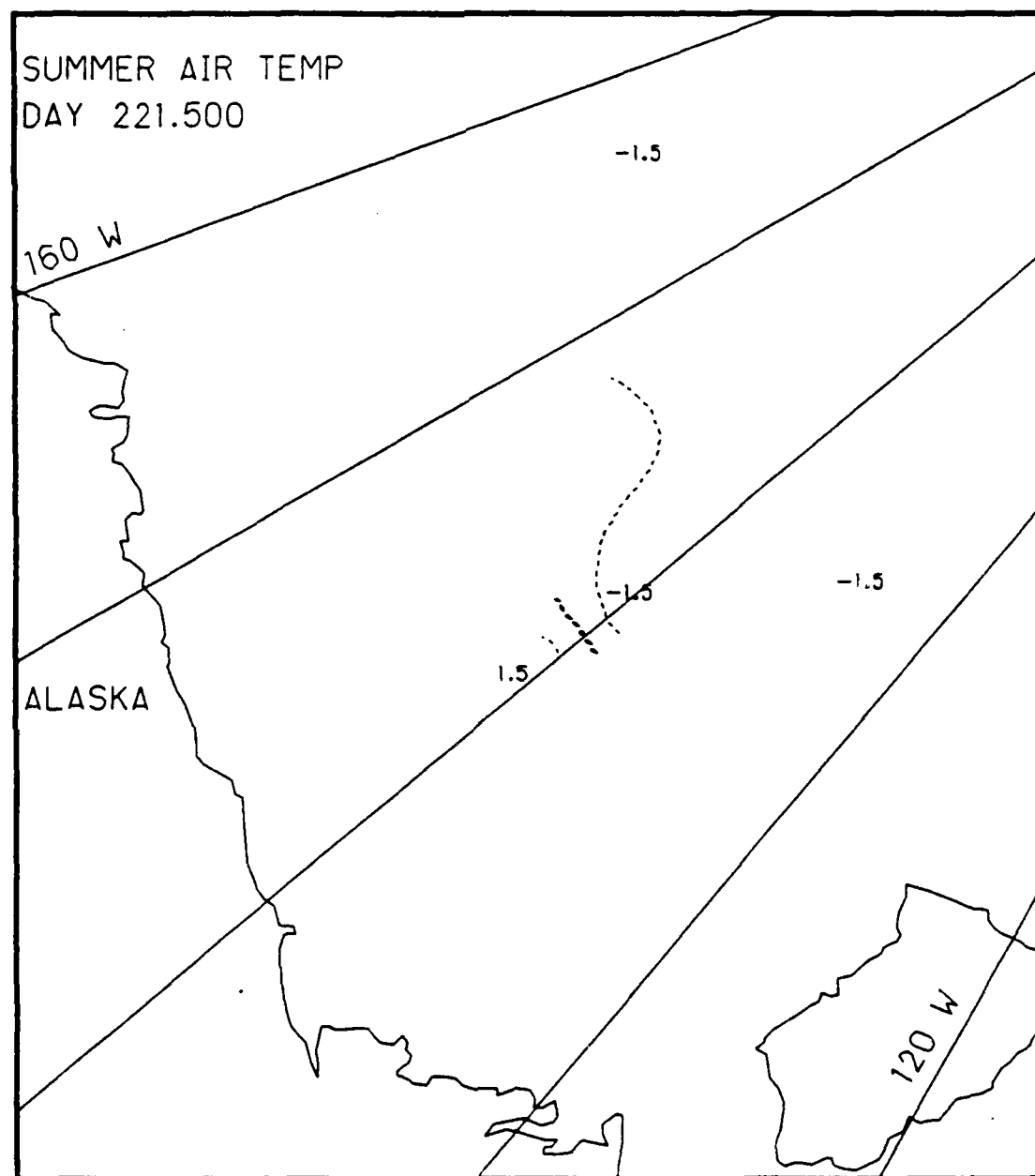


Fig. C.13. Spatial atmospheric temperature variations, day 221.5, based on the AIDJEX data from stations with hydrophones, summer 1975.

AD-A165 303

A STUDY OF SEA ICE KINEMATICS AND THEIR RELATIONSHIP TO

3/4

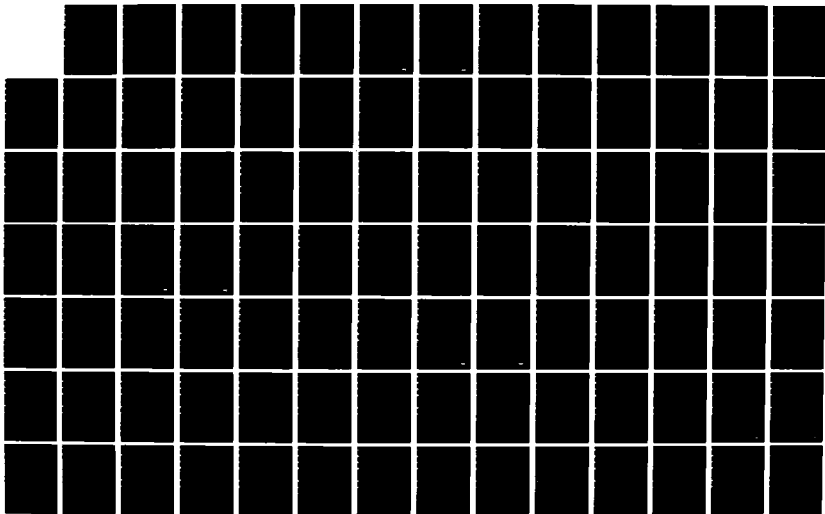
ARCTIC AMBIENT NO. (U) SCIENCE APPLICATIONS

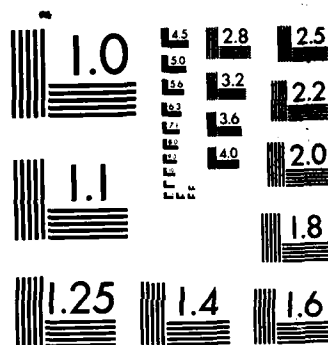
INTERNATIONAL CORP COLLEGE STATION TX J K LEWIS ET AL.

UNCLASSIFIED

FEB 86 SAIC-85/1950-PT-1/2 N00014-85-C-0531 F/G 8/12

NL





MICROCOPY RESOLUTION TEST CHART
NATIONAL BUREAU OF STANDARDS-1963-A

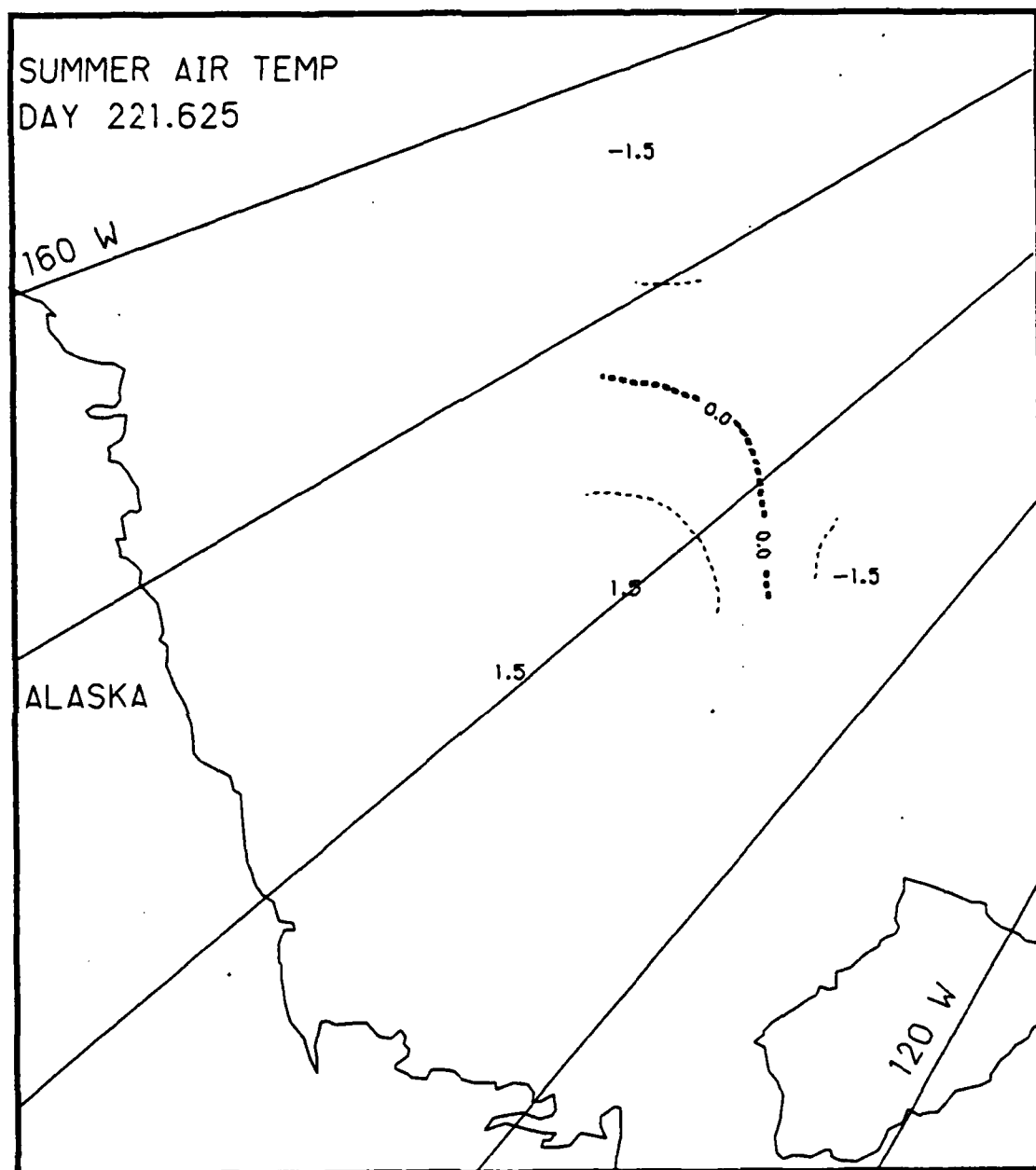


Fig. C.14. Spatial atmospheric temperature variations, day 221.625, based on the AIDJEX data from stations with hydrophones, summer 1975.

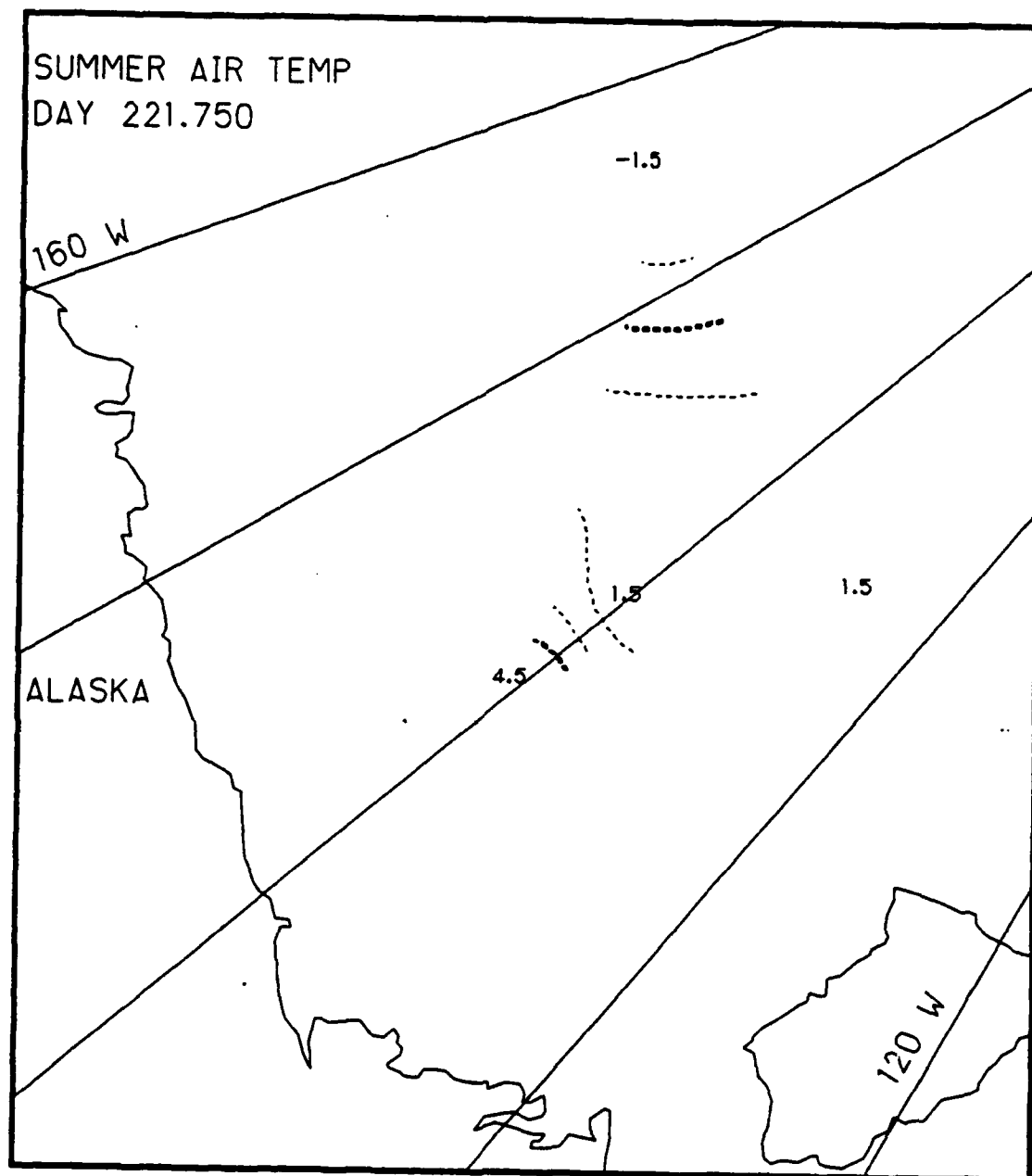


Fig. C.15. Spatial atmospheric temperature variations, day 221.75, based on the AIDJEX data from stations with hydrophones, summer 1975.

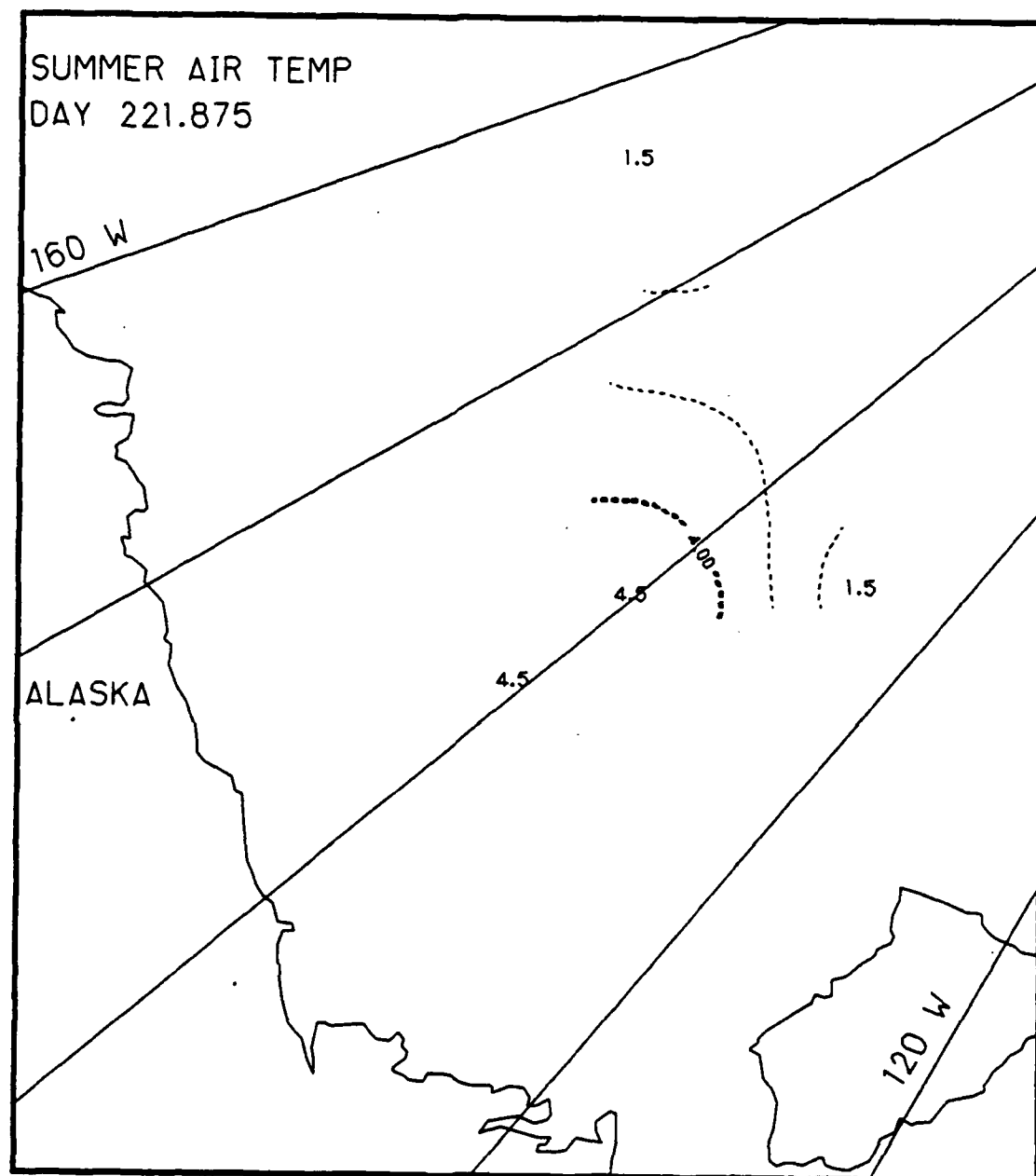


Fig. C.16. Spatial atmospheric temperature variations, day 221.875, based on the AIDJEX data from stations with hydrophones, summer 1975.

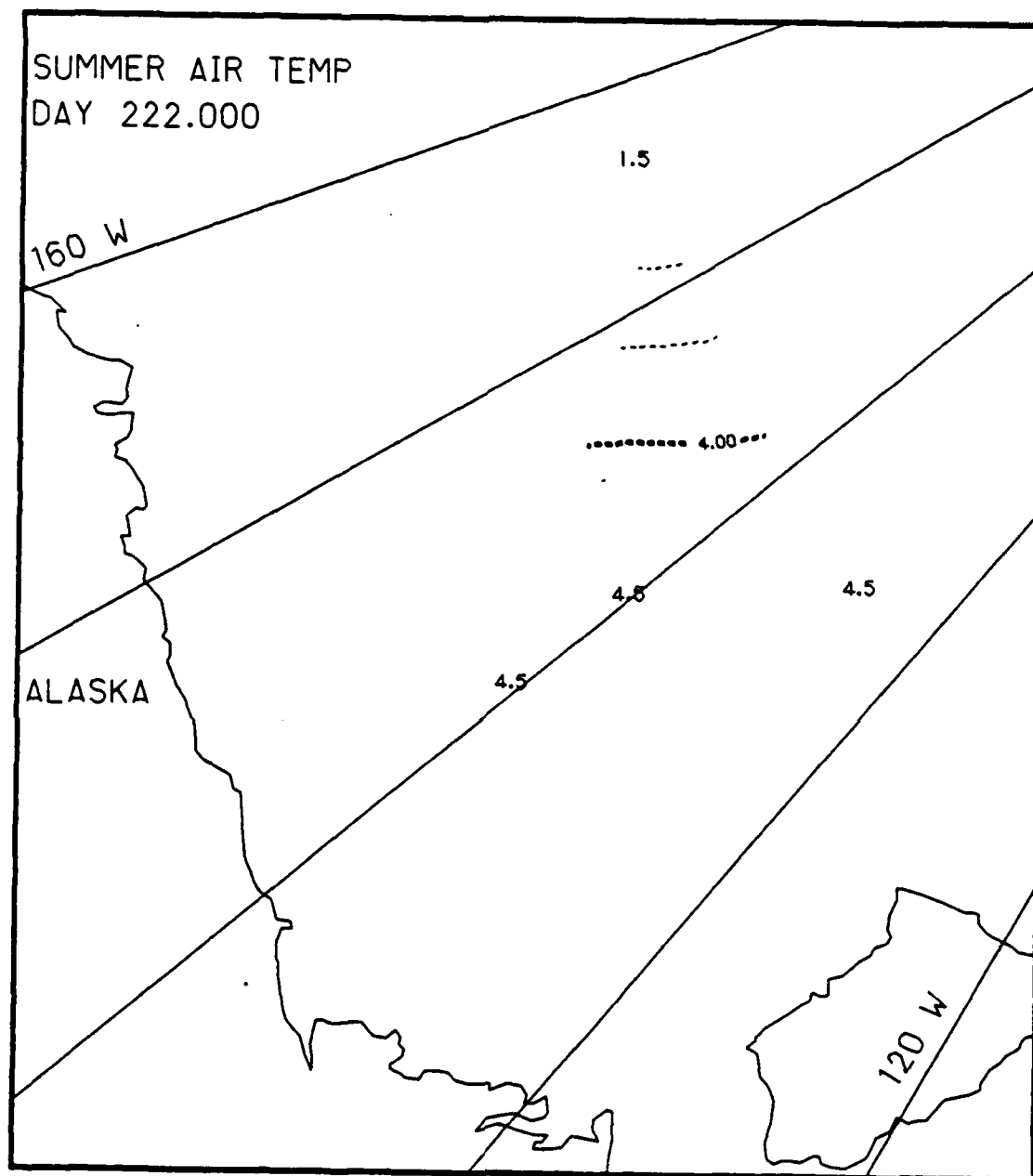


Fig. C.17. Spatial atmospheric temperature variations, day 222.0, based on the AIDJEX data from stations with hydrophones, summer 1975.

Appendix D

Two-Dimensional Contour Maps of Arctic Atmospheric Pressure Variations, 16-17 November 1975 (Fall)

This appendix contains the two-dimensional contour maps of the AIDJEX atmospheric pressure data collected at those stations with hydrophones during the 48 hour period of 16-17 November 1975. The contour maps show the spatial variations of atmospheric pressure (millibars) at 3 hr intervals.

List of Figures
Appendix D

2-62

	<u>Page</u>
Fig. D.1. Spatial atmospheric pressure variations, day 320.0	2-63
Fig. D.2. Spatial atmospheric pressure variations, day 320.125	2-64
Fig. D.3. Spatial atmospheric pressure variations, day 320.25	2-65
Fig. D.4. Spatial atmospheric pressure variations, day 320.375	2-66
Fig. D.5. Spatial atmospheric pressure variations, day 320.5	2-67
Fig. D.6. Spatial atmospheric pressure variations, day 320.625	2-68
Fig. D.7. Spatial atmospheric pressure variations, day 320.75	2-69
Fig. D.8. Spatial atmospheric pressure variations, day 320.875	2-70
Fig. D.9. Spatial atmospheric pressure variations, day 321.0	2-71
Fig. D.10. Spatial atmospheric pressure variations, day 321.125	2-72
Fig. D.11. Spatial atmospheric pressure variations, day 321.25	2-73
Fig. D.12. Spatial atmospheric pressure variations, day 321.375	2-74
Fig. D.13. Spatial atmospheric pressure variations, day 321.5	2-75
Fig. D.14. Spatial atmospheric pressure variations, day 321.625	2-76
Fig. D.15. Spatial atmospheric pressure variations, day 321.75	2-77
Fig. D.16. Spatial atmospheric pressure variations, day 321.875	2-78
Fig. D.17. Spatial atmospheric pressure variations, day 322.0	2-79

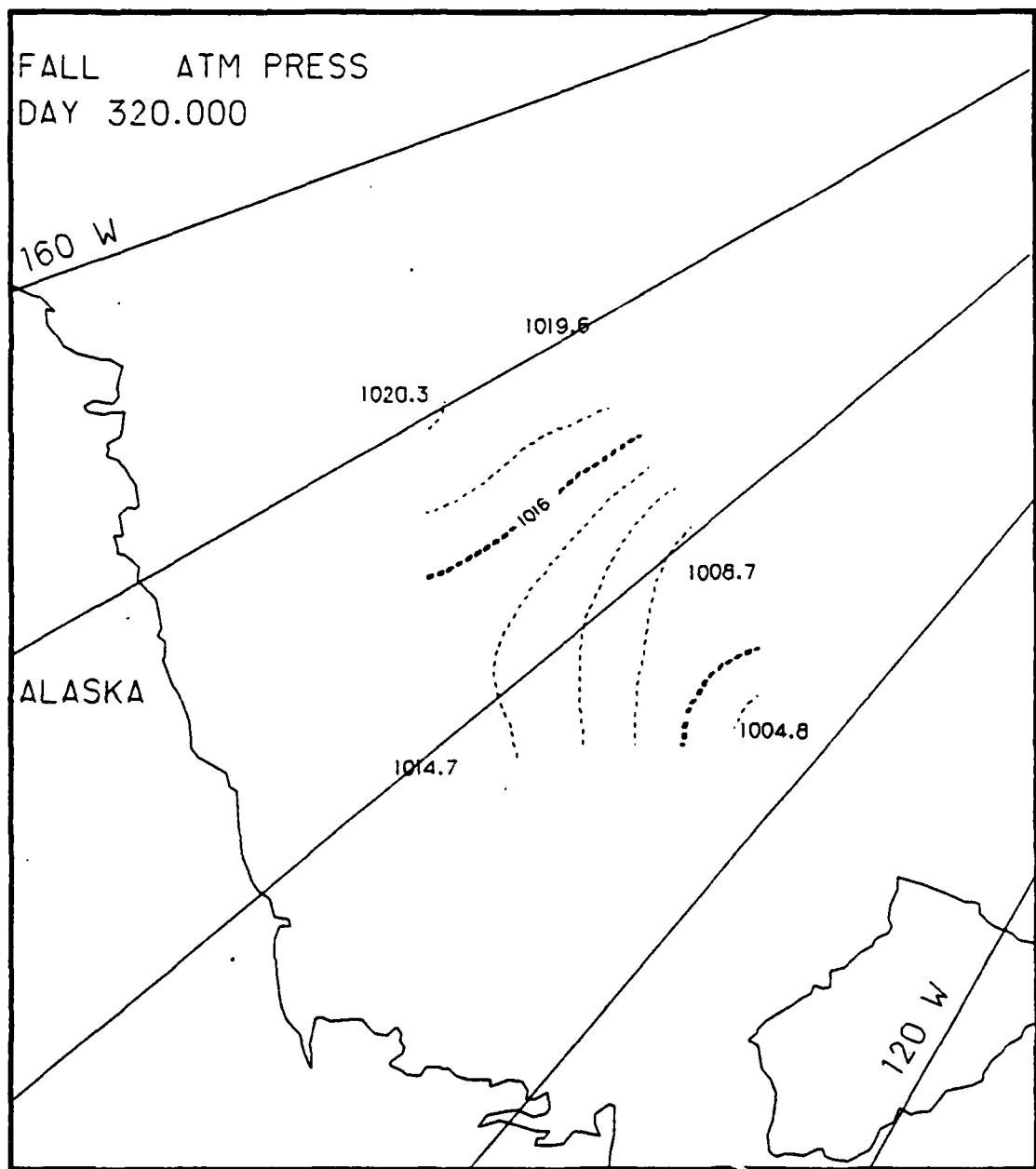


Fig. D.1. Spatial atmospheric pressure variations, day 320.0, based on the AIDJEX data from stations with hydrophones, fall 1975.

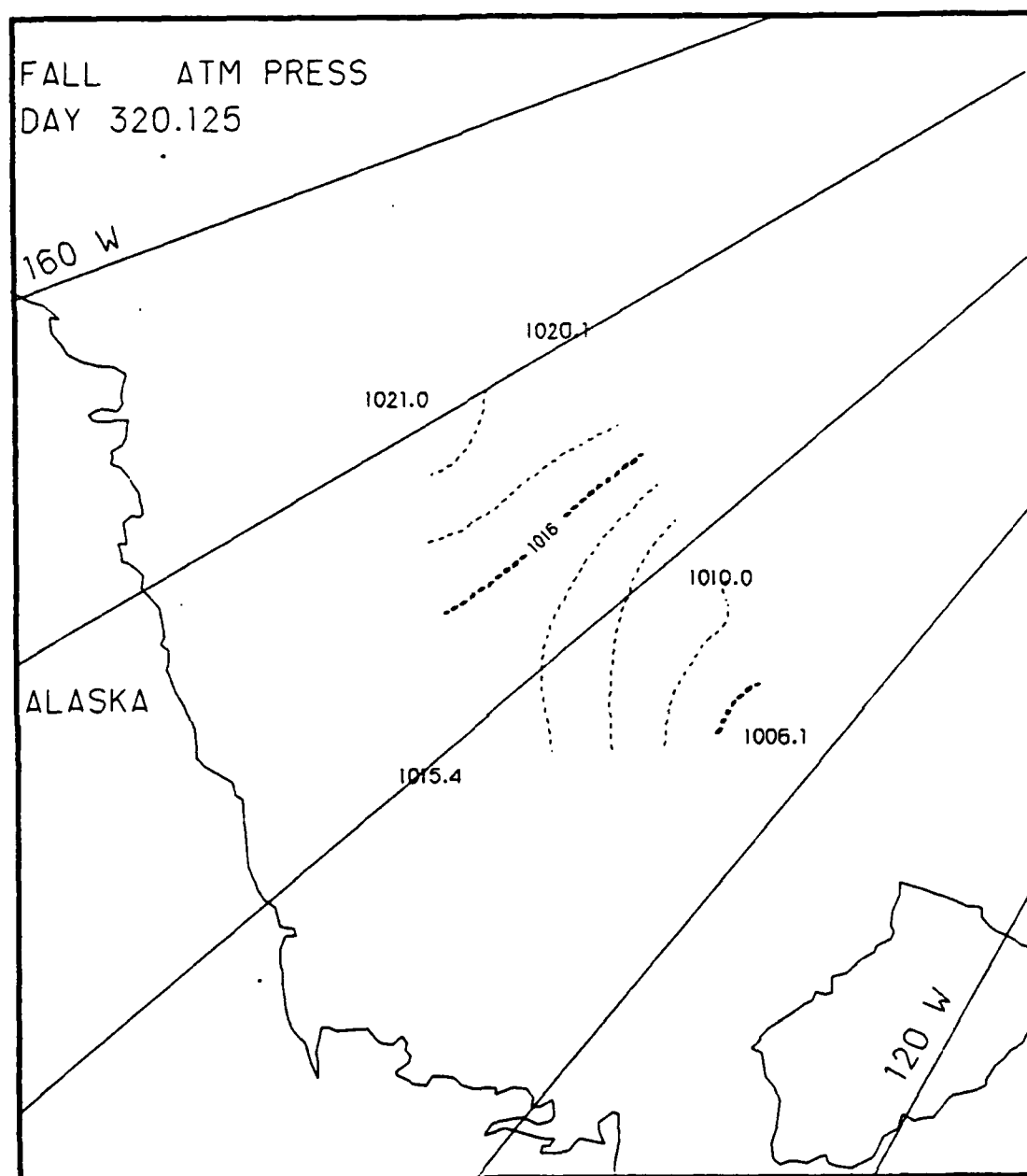


Fig. D.2. Spatial atmospheric pressure variations, day 320.125, based on the AIDJEX data from stations with hydrophones, fall 1975.

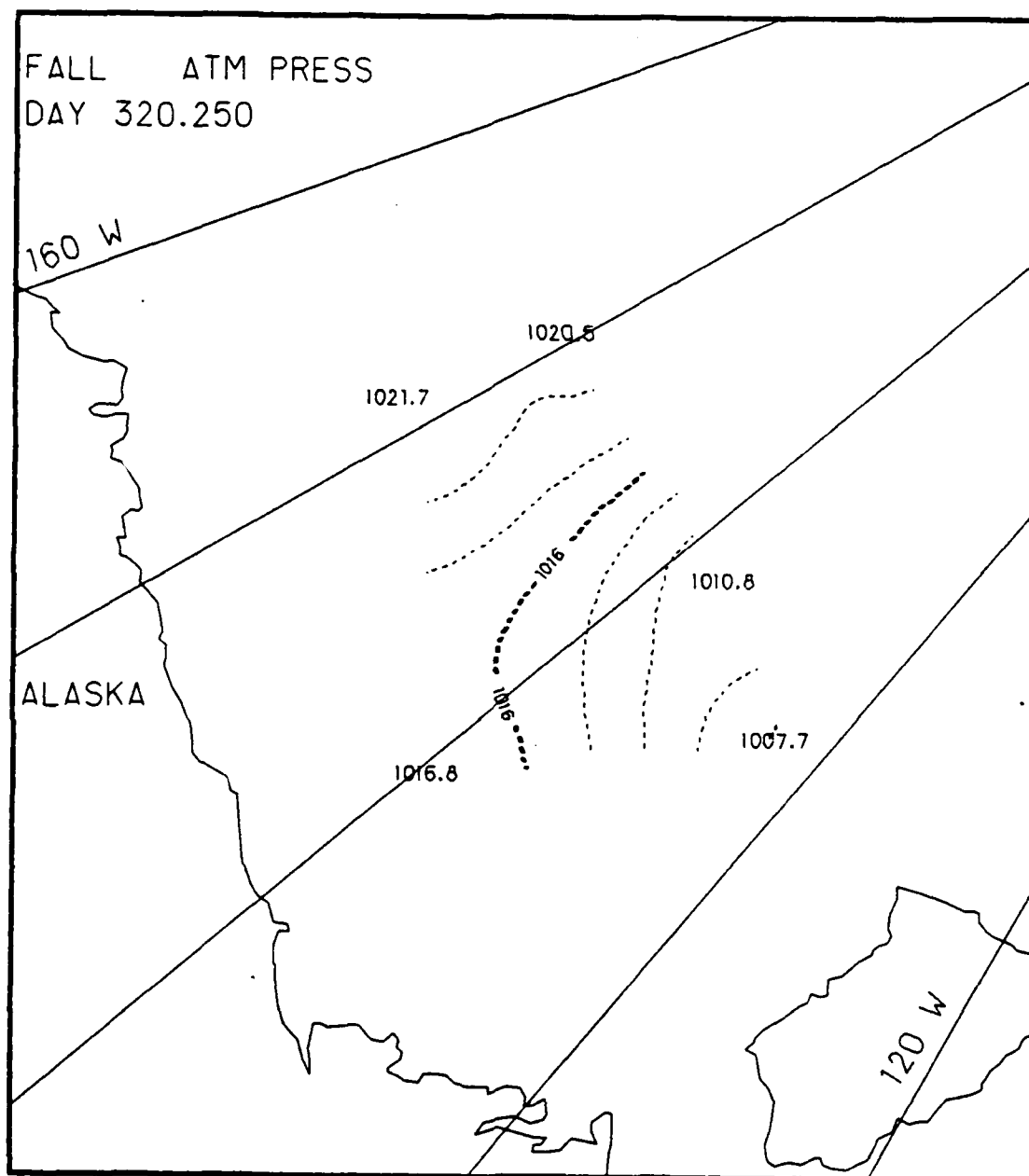


Fig. D.3. Spatial atmospheric pressure variations, day 320.25, based on the AIDJEX data from stations with hydrophones, fall 1975.

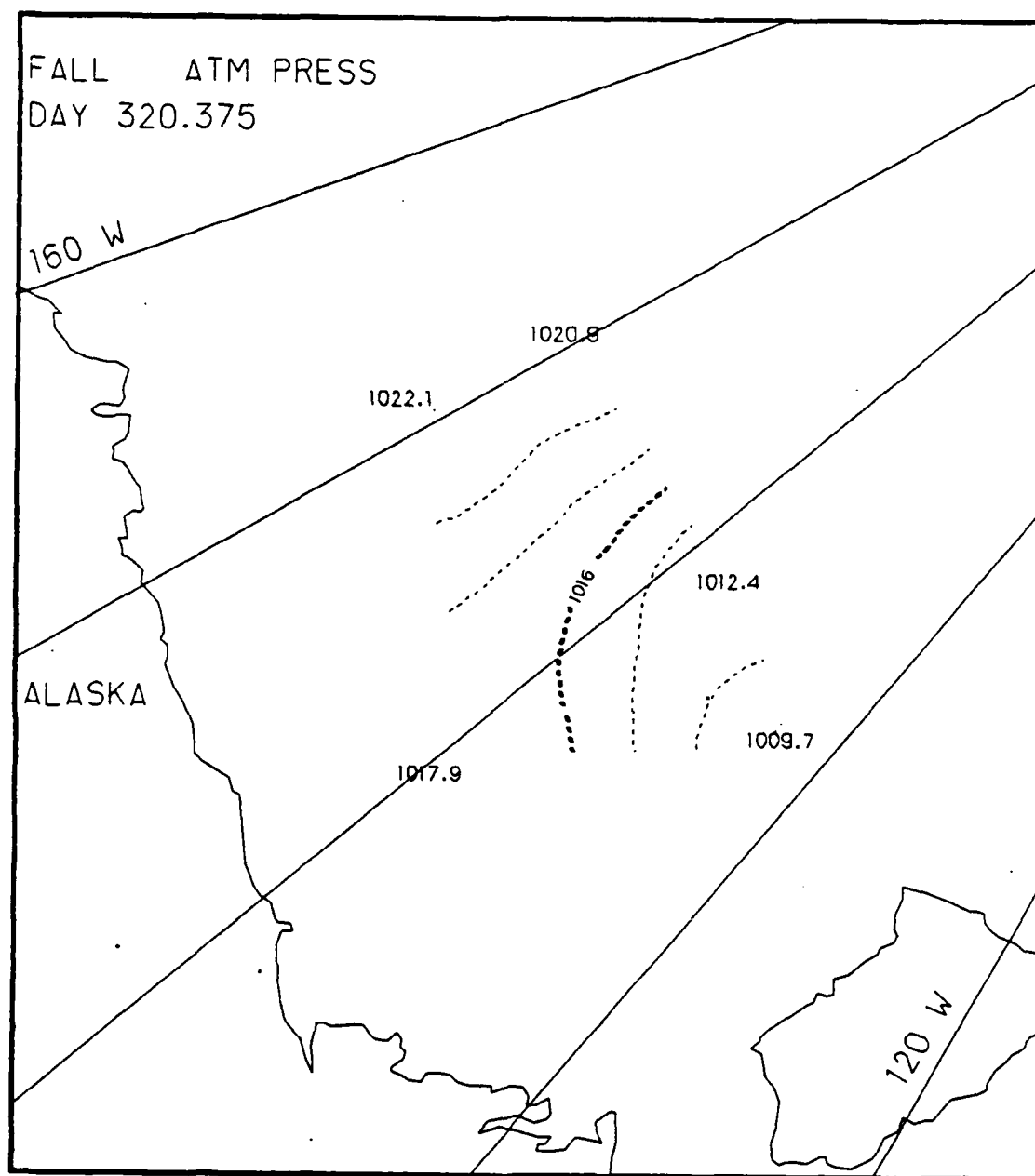


Fig. D.4. Spatial atmospheric pressure variations, day 320.375, based on the AIDJEX data from stations with hydrophones, fall 1975.

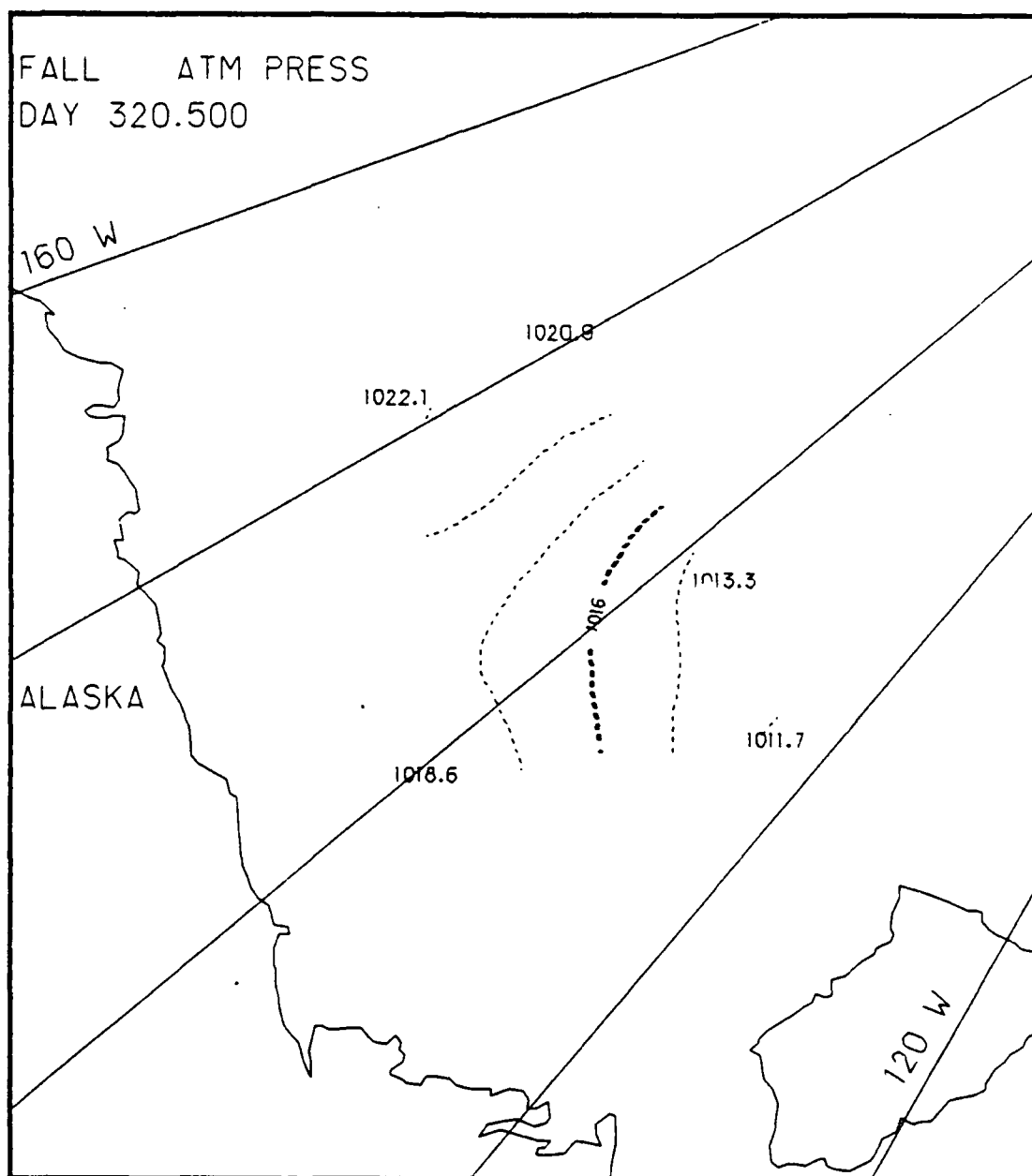


Fig. D.5. Spatial atmospheric pressure variations, day 320.5, based on the AIDJEX data from stations with hydrophones, fall 1975.

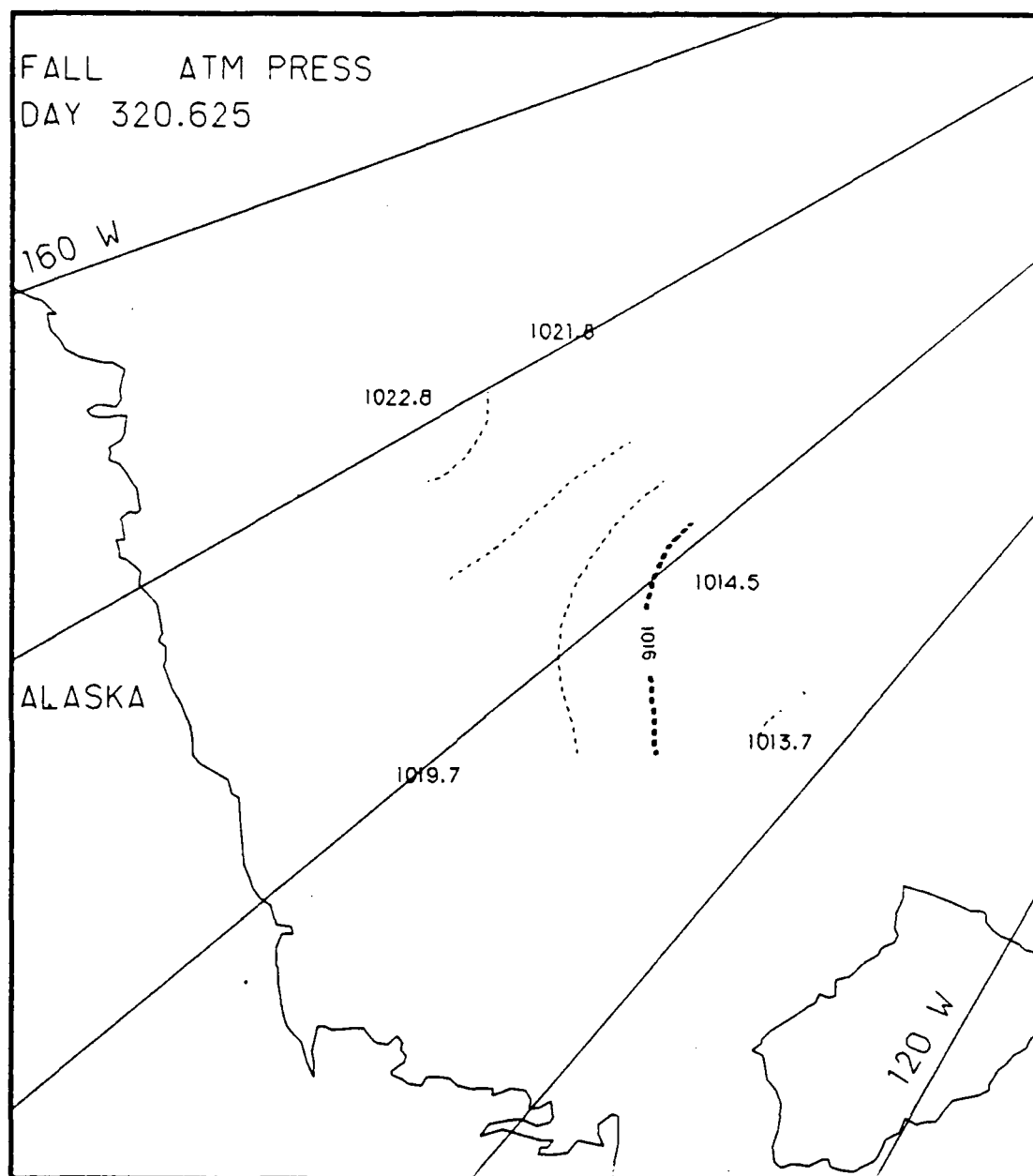


Fig. D.6. Spatial atmospheric pressure variations, day 320.625, based on the AIDJEX data from stations with hydrophones, fall 1975.

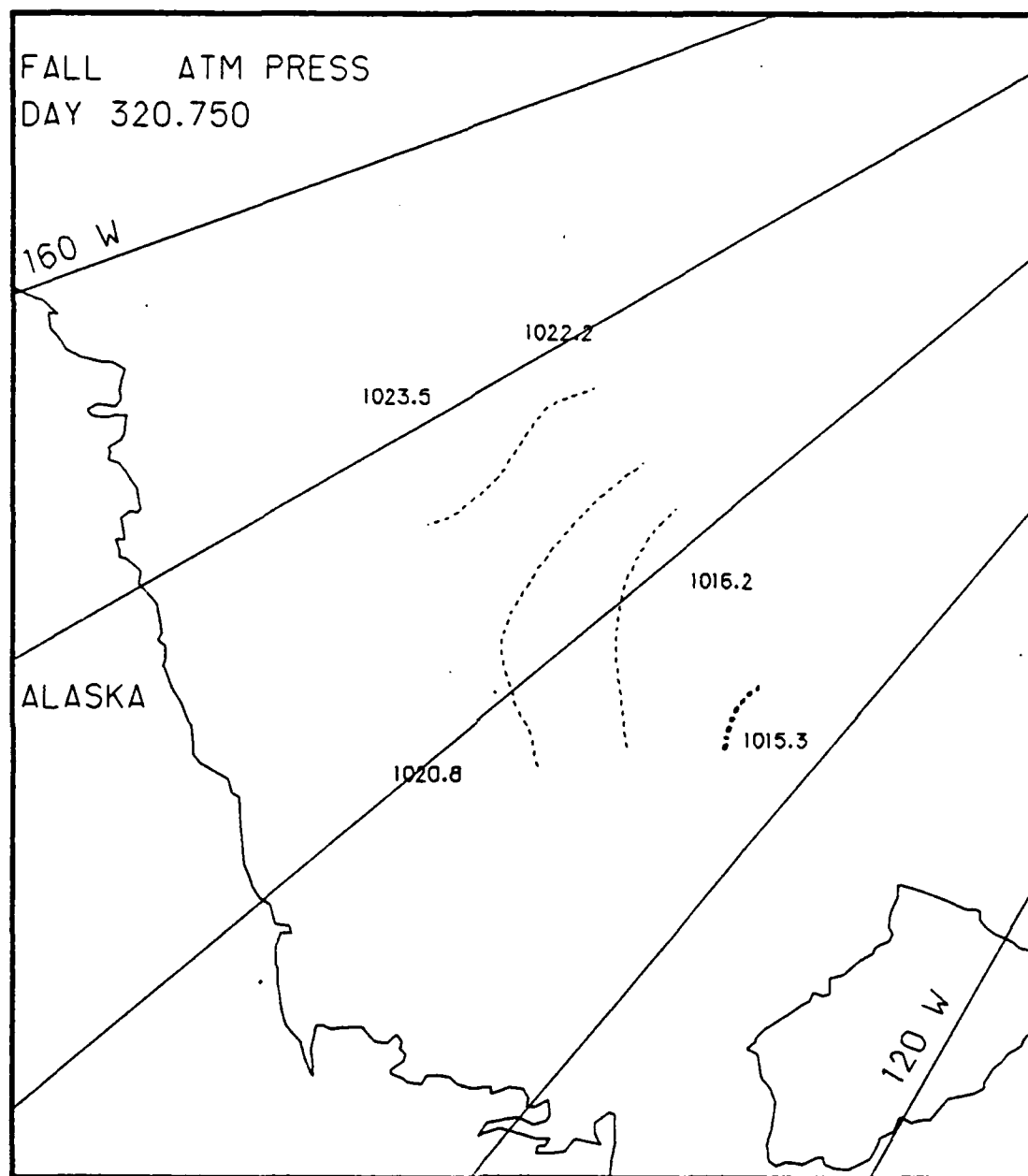


Fig. D.7. Spatial atmospheric pressure variations, day 320.75, based on the AIDJEX data from stations with hydrophones, fall 1975.

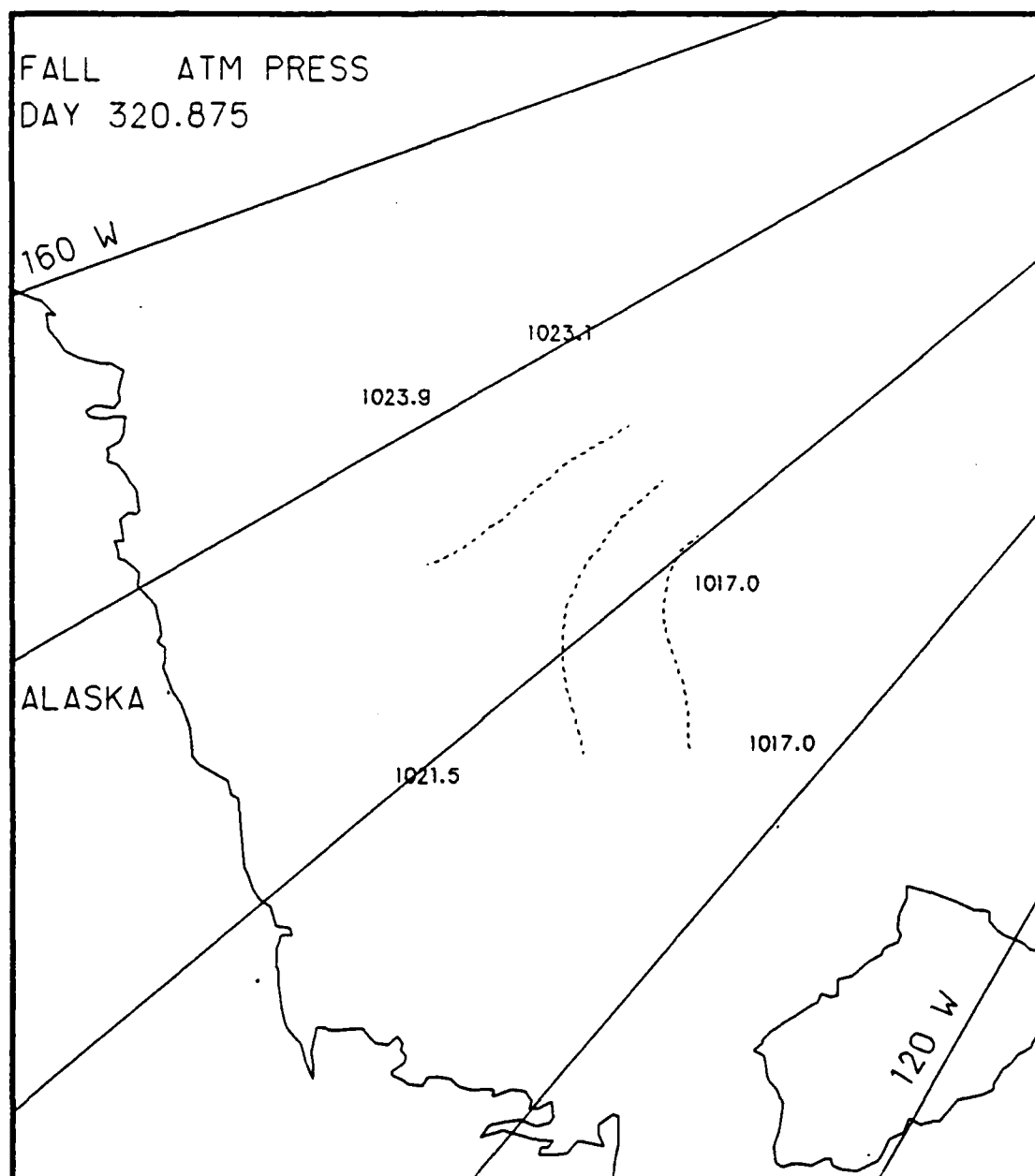


Fig. D.8. Spatial atmospheric pressure variations, day 320.875, based on the AIDJEX data from stations with hydrophones, fall 1975.

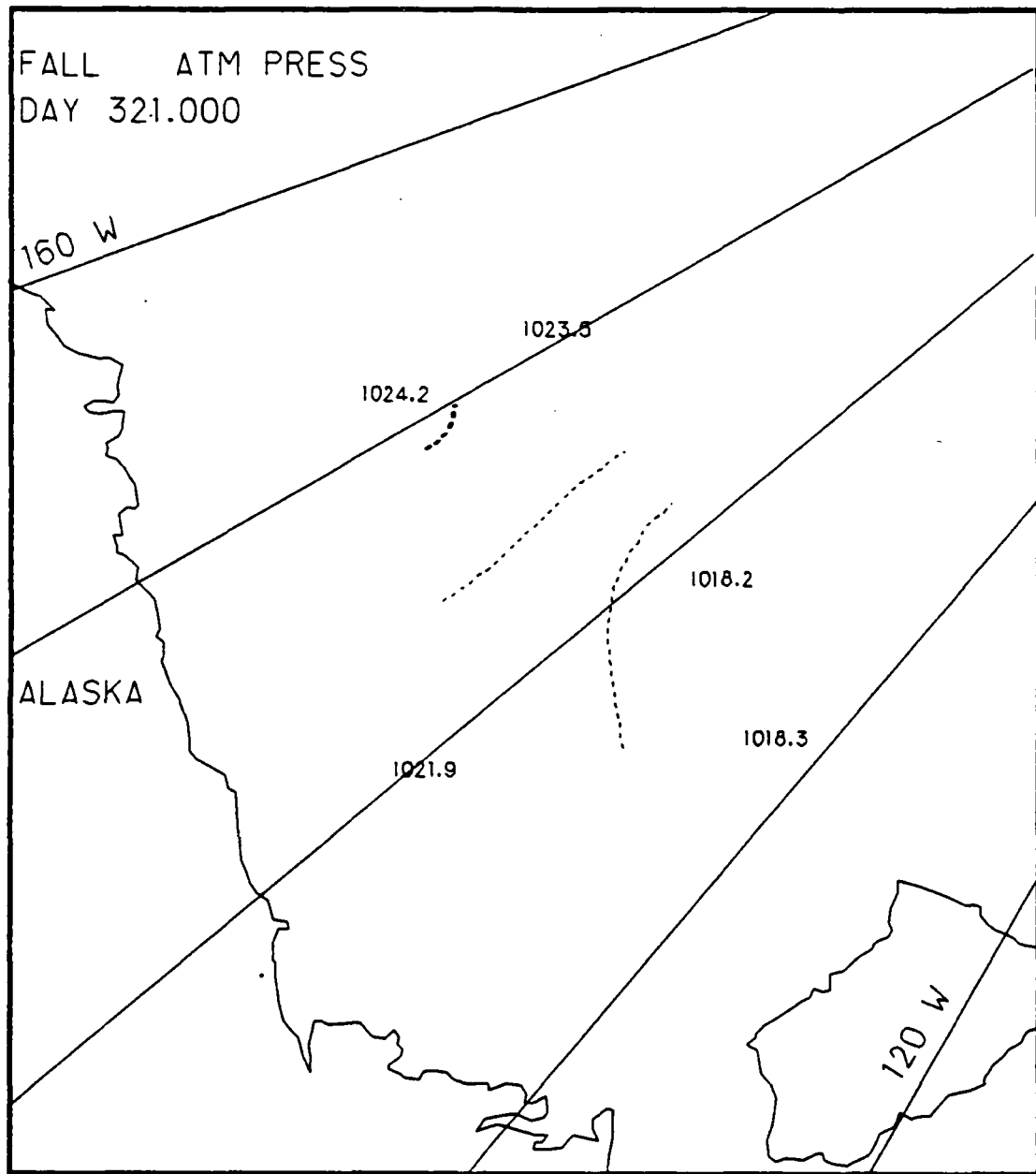


Fig. D.9. Spatial atmospheric pressure variations, day 321.0, based on the AIDJEX data from stations with hydrophones, fall 1975.

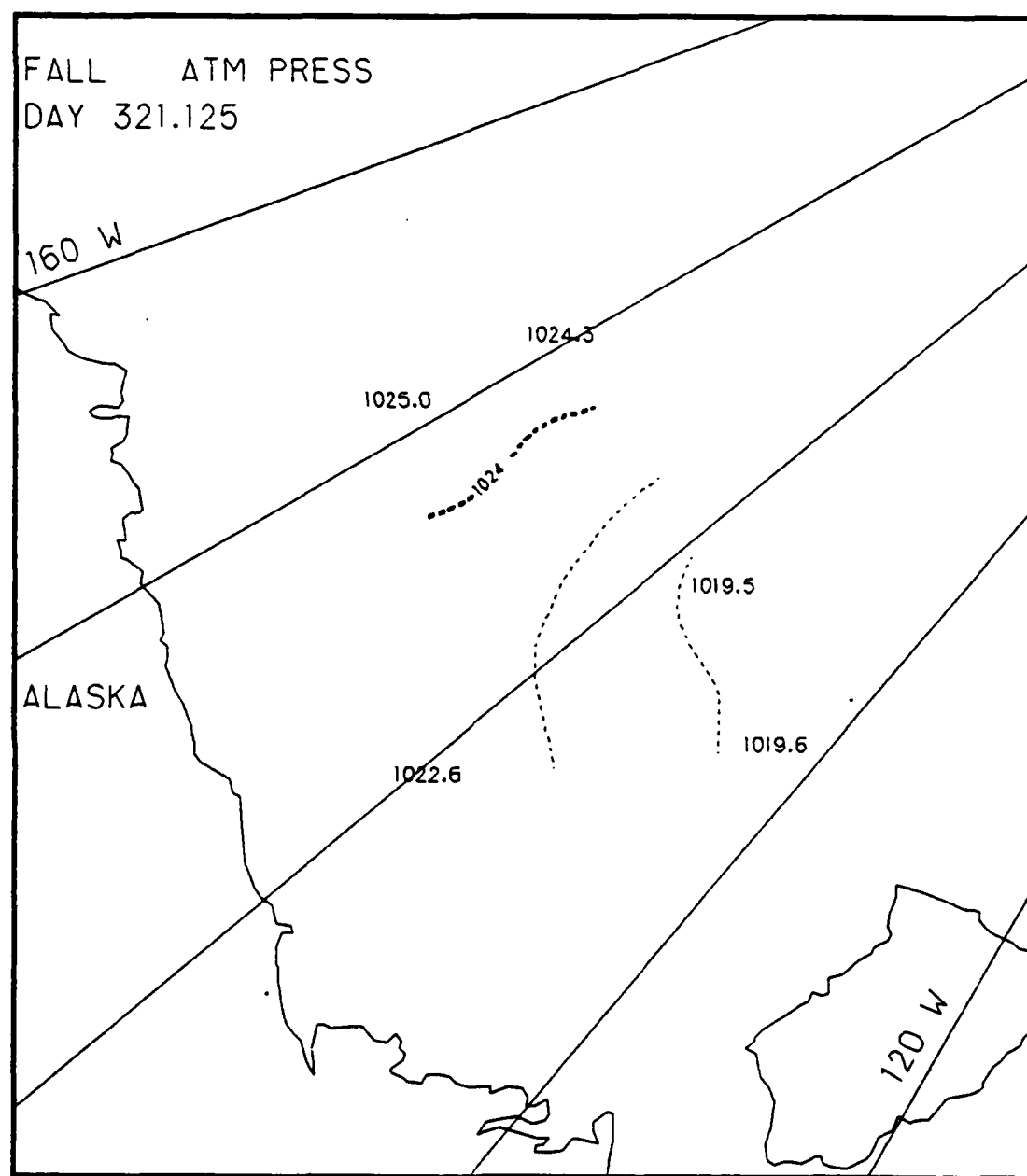


Fig. D.10. Spatial atmospheric pressure variations, day 321.125, based on the AIDJEX data from stations with hydrophones, fall 1975.

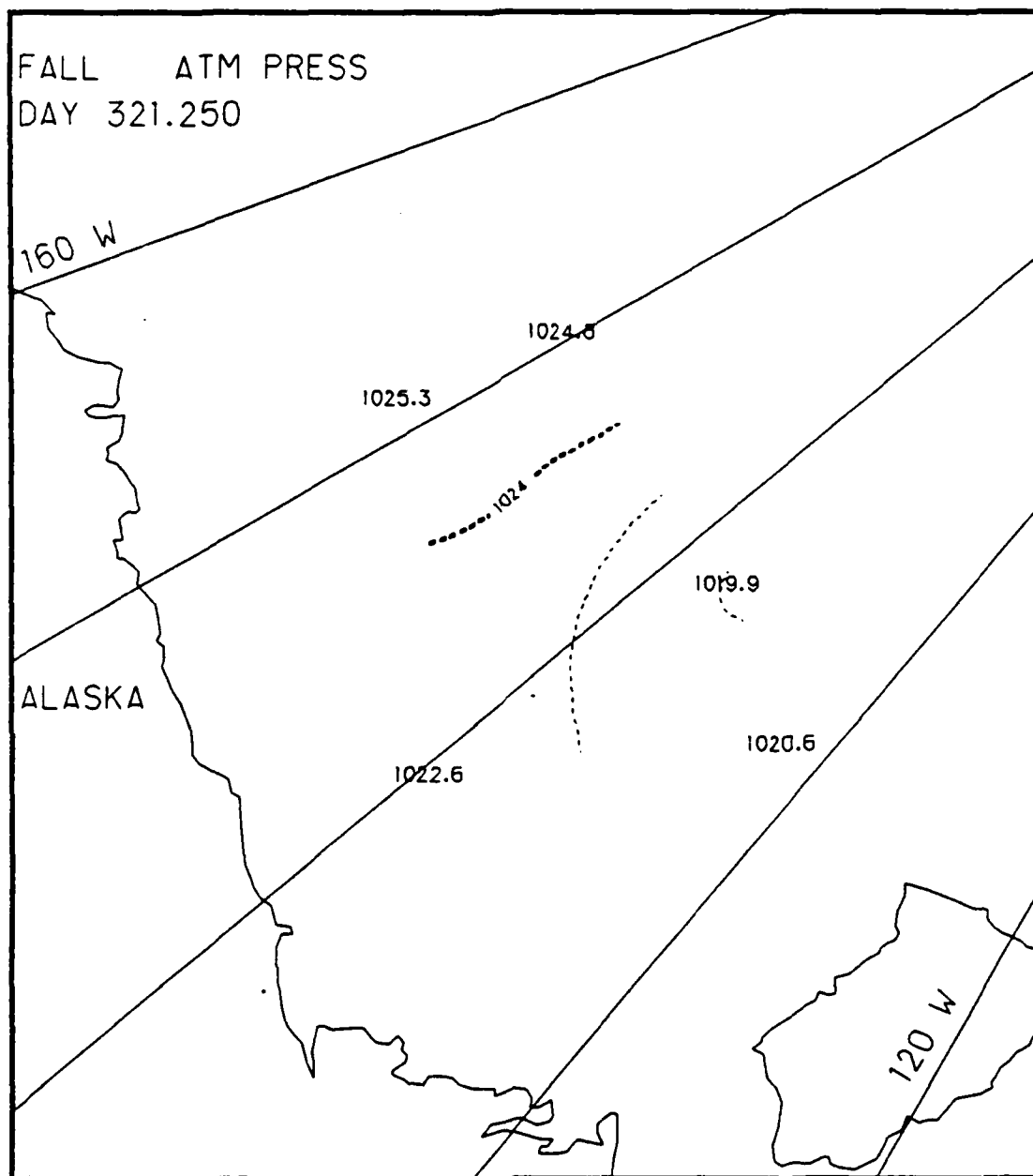


Fig. D.11. Spatial atmospheric pressure variations, day 321.25, based on the AIDJEX data from stations with hydrophones, fall 1975.

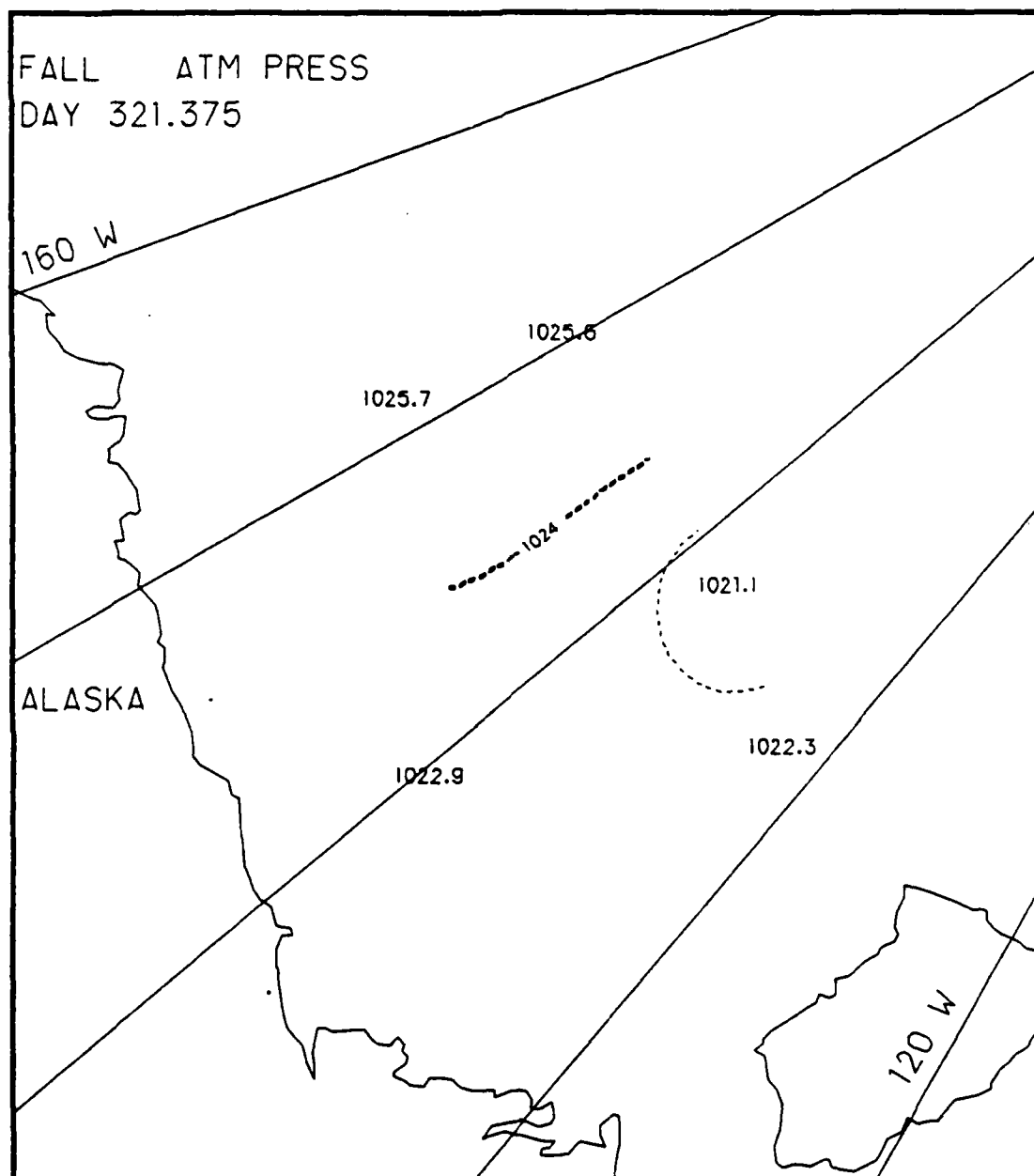


Fig. D.12. Spatial atmospheric pressure variations, day 321.375, based on the AIDJEX data from stations with hydrophones, fall 1975.

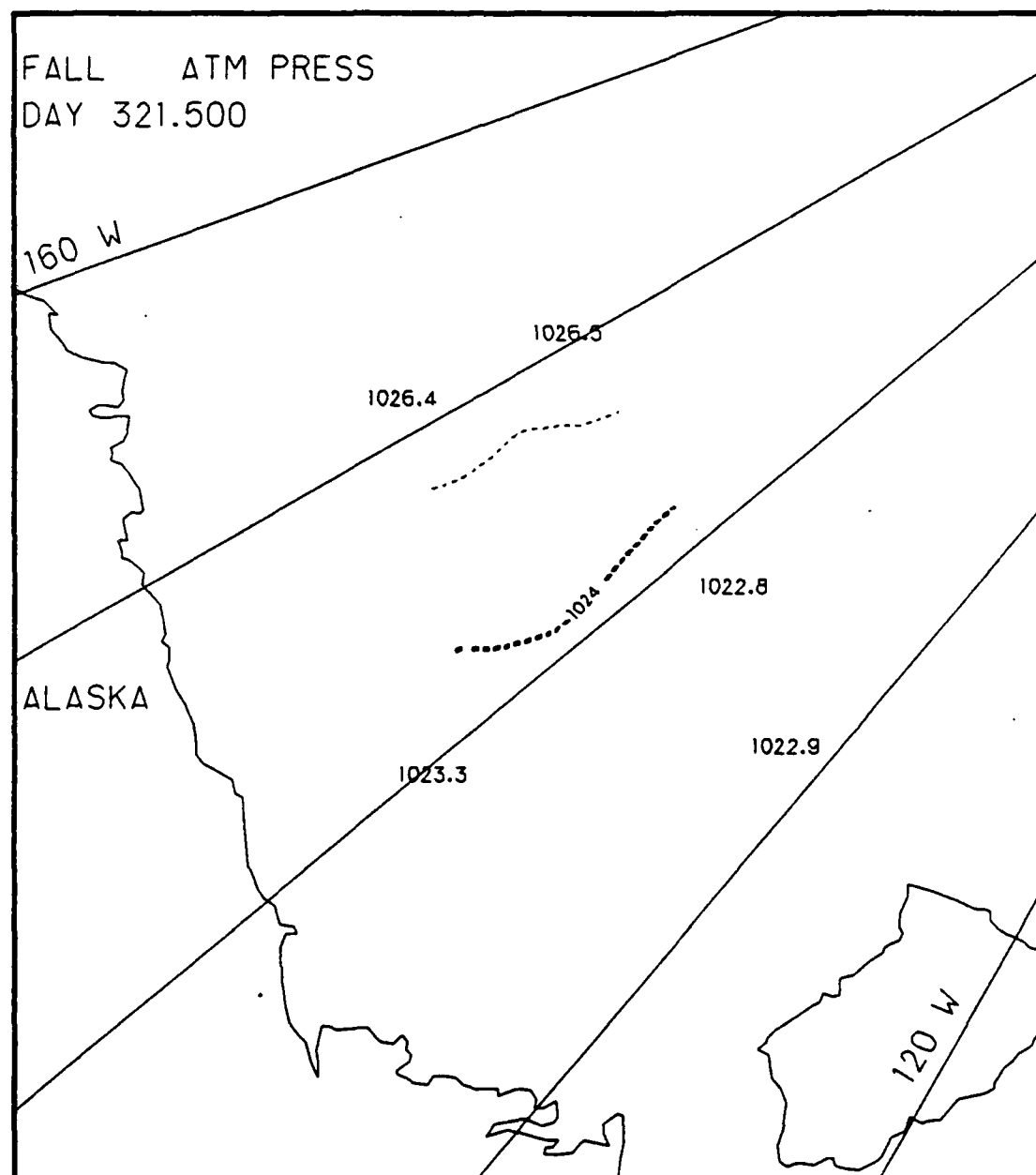


Fig. D.13. Spatial atmospheric pressure variations, day 321.5, based on the AIDJEX data from stations with hydrophones, fall 1975.

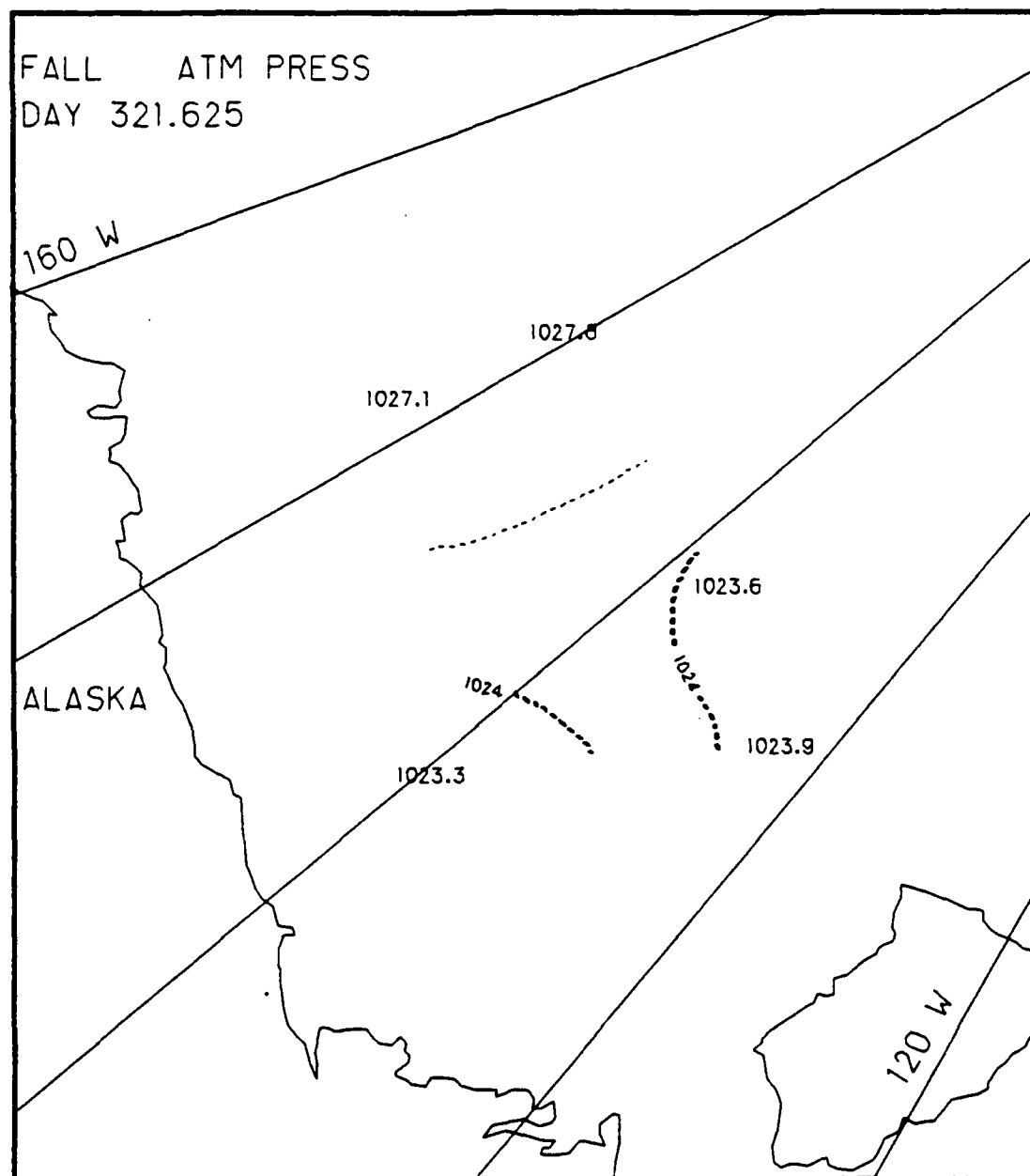


Fig. D.14. Spatial atmospheric pressure variations, day 321.625, based on the AIDJEX data from stations with hydrophones, fall 1975.

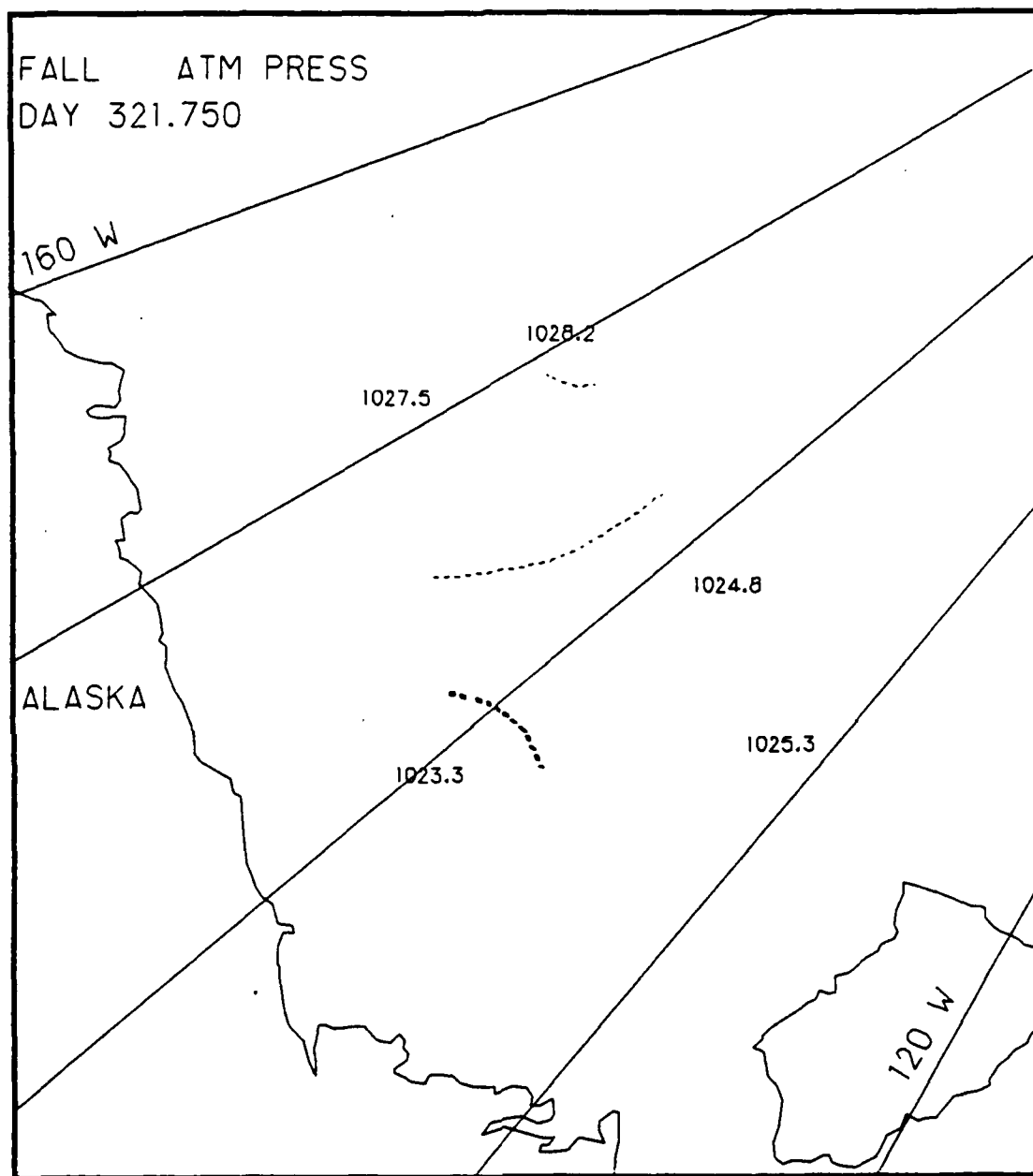


Fig. D.15. Spatial atmospheric pressure variations, day 321.75, based on the AIDJEX data from stations with hydrophones, fall 1975.

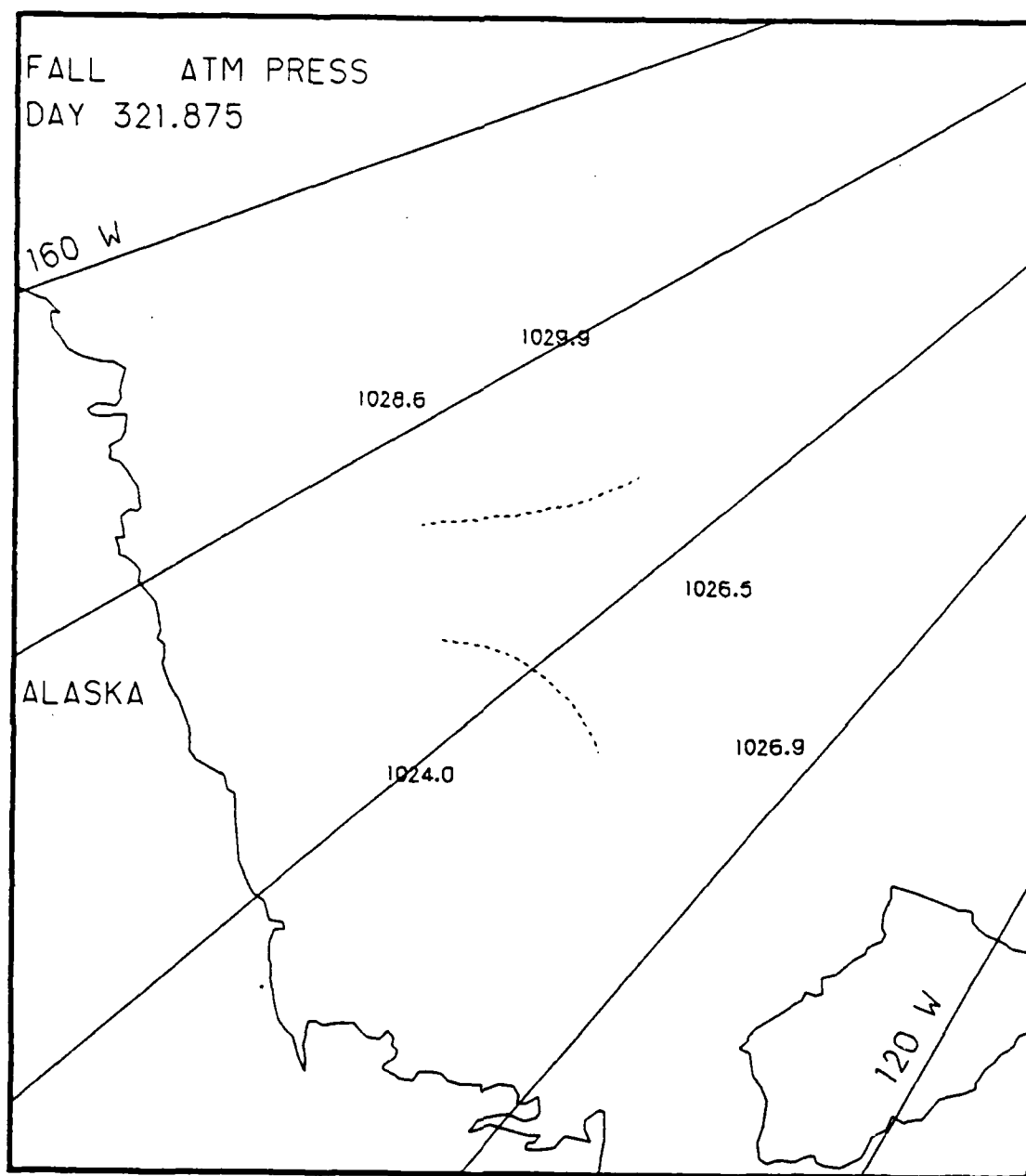


Fig. D.16. Spatial atmospheric pressure variations, day 321.875, based on the AIDJEX data from stations with hydrophones, fall 1975.

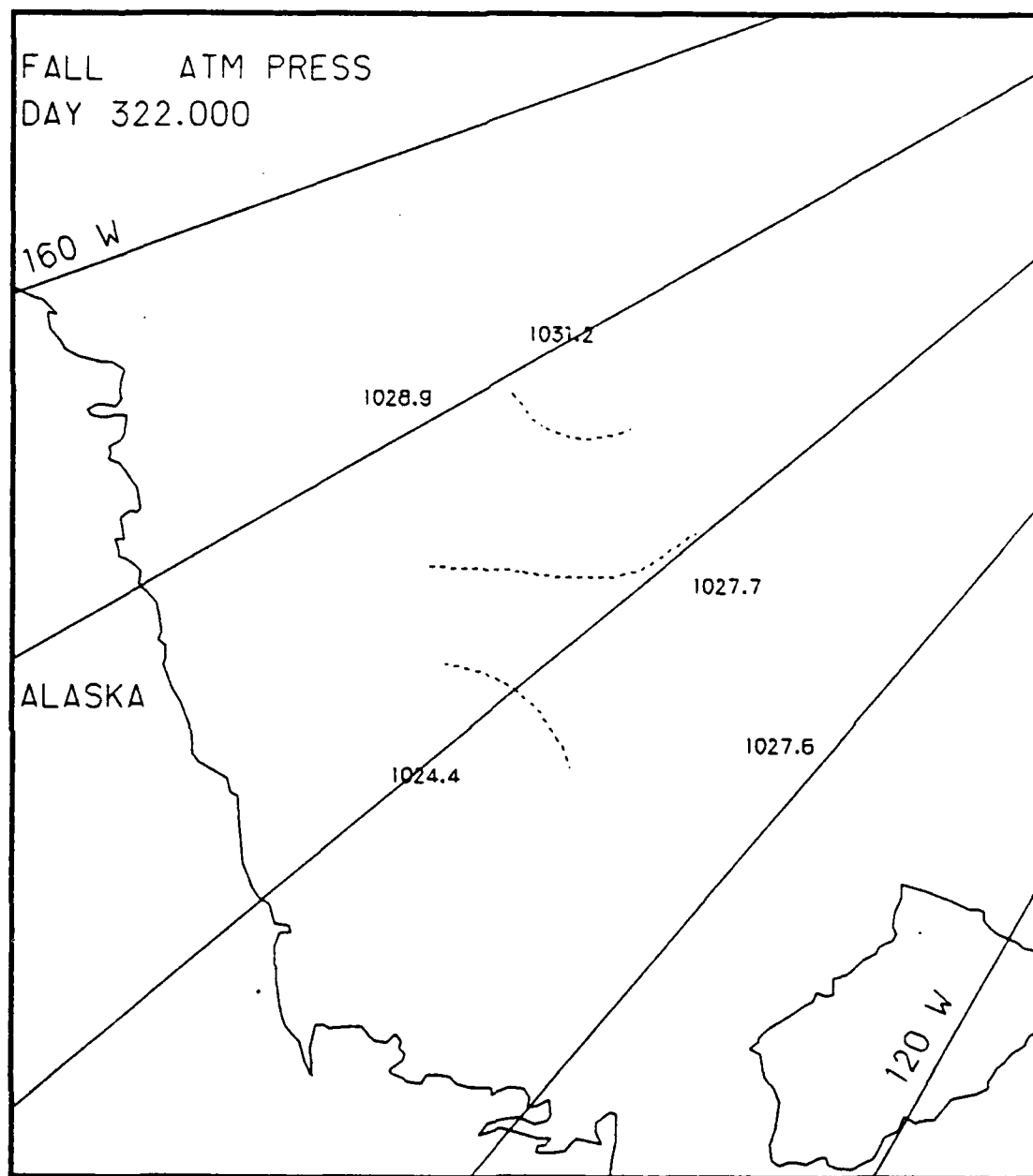


Fig. D.17. Spatial atmospheric pressure variations, day 322.0, based on the AIDJEX data from stations with hydrophones, fall 1975.

Appendix E

Two-Dimensional Contour Maps of Arctic Atmospheric Temperature Variations, 16-17 November 1975 (Fall)

This appendix contains the two-dimensional contour maps of the AIDJEX atmospheric temperature data collected at those stations with hydrophones during the 48 hour period of 16-17 November 1975. The contour maps show the spatial variations of atmospheric temperature ($^{\circ}\text{C}$) at 3 hr intervals.

List of Figures
Appendix E

2-81

	<u>Page</u>
Fig. E.1. Spatial atmospheric temperature variations, day 320.0	2-82
Fig. E.2. Spatial atmospheric temperature variations, day 320.125	2-83
Fig. E.3. Spatial atmospheric temperature variations, day 320.25	2-84
Fig. E.4. Spatial atmospheric temperature variations, day 320.375	2-85
Fig. E.5. Spatial atmospheric temperature variations, day 320.5	2-86
Fig. E.6. Spatial atmospheric temperature variations, day 320.625	2-87
Fig. E.7. Spatial atmospheric temperature variations, day 320.75	2-88
Fig. E.8. Spatial atmospheric temperature variations, day 320.875	2-89
Fig. E.9. Spatial atmospheric temperature variations, day 321.0	2-90
Fig. E.10. Spatial atmospheric temperature variations, day 321.125	2-91
Fig. E.11. Spatial atmospheric temperature variations, day 321.25	2-92
Fig. E.12. Spatial atmospheric temperature variations, day 321.375	2-93
Fig. E.13. Spatial atmospheric temperature variations, day 321.5	2-94
Fig. E.14. Spatial atmospheric temperature variations, day 321.625	2-95
Fig. E.15. Spatial atmospheric temperature variations, day 321.75	2-96
Fig. E.16. Spatial atmospheric temperature variations, day 321.875	2-97
Fig. E.17. Spatial atmospheric temperature variations, day 322.0	2-98

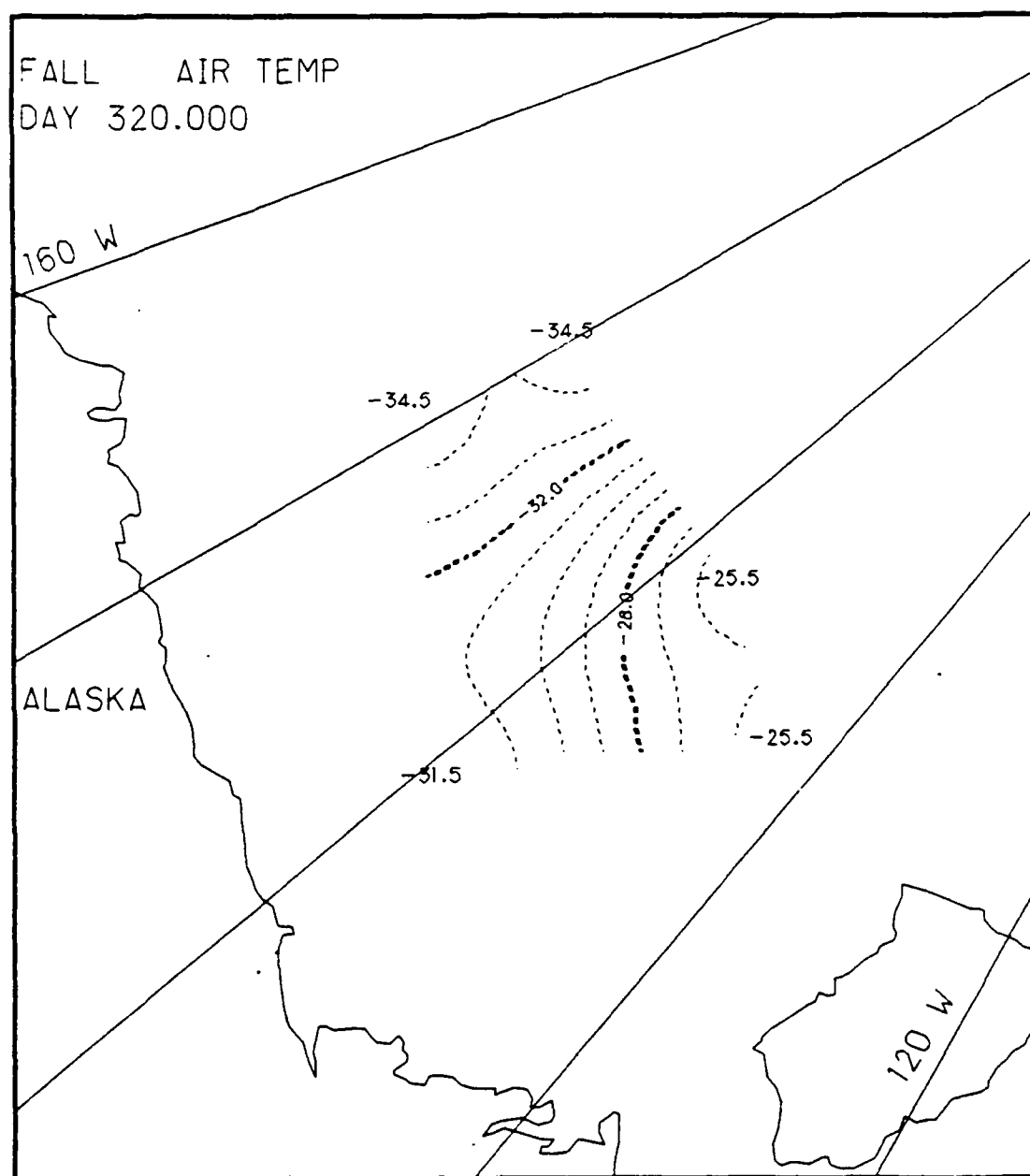


Fig. E.1. Spatial atmospheric temperature variations, day 320.0, based on the AIDJEX data from stations with hydrophones, fall 1975.

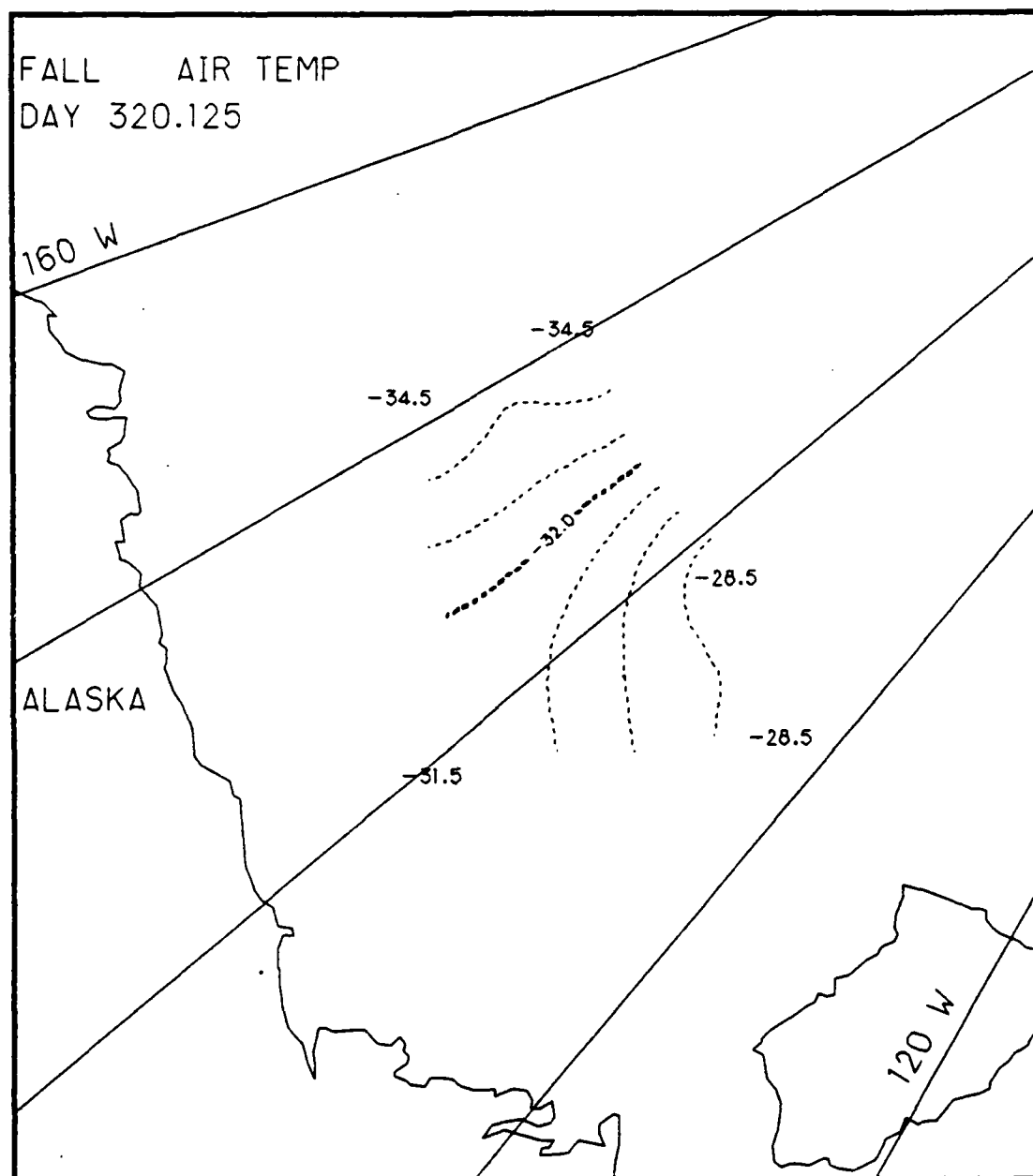


Fig. E.2. Spatial atmospheric temperature variations, day 320.125, based on the AIDJEX data from stations with hydrophones, fall 1975.

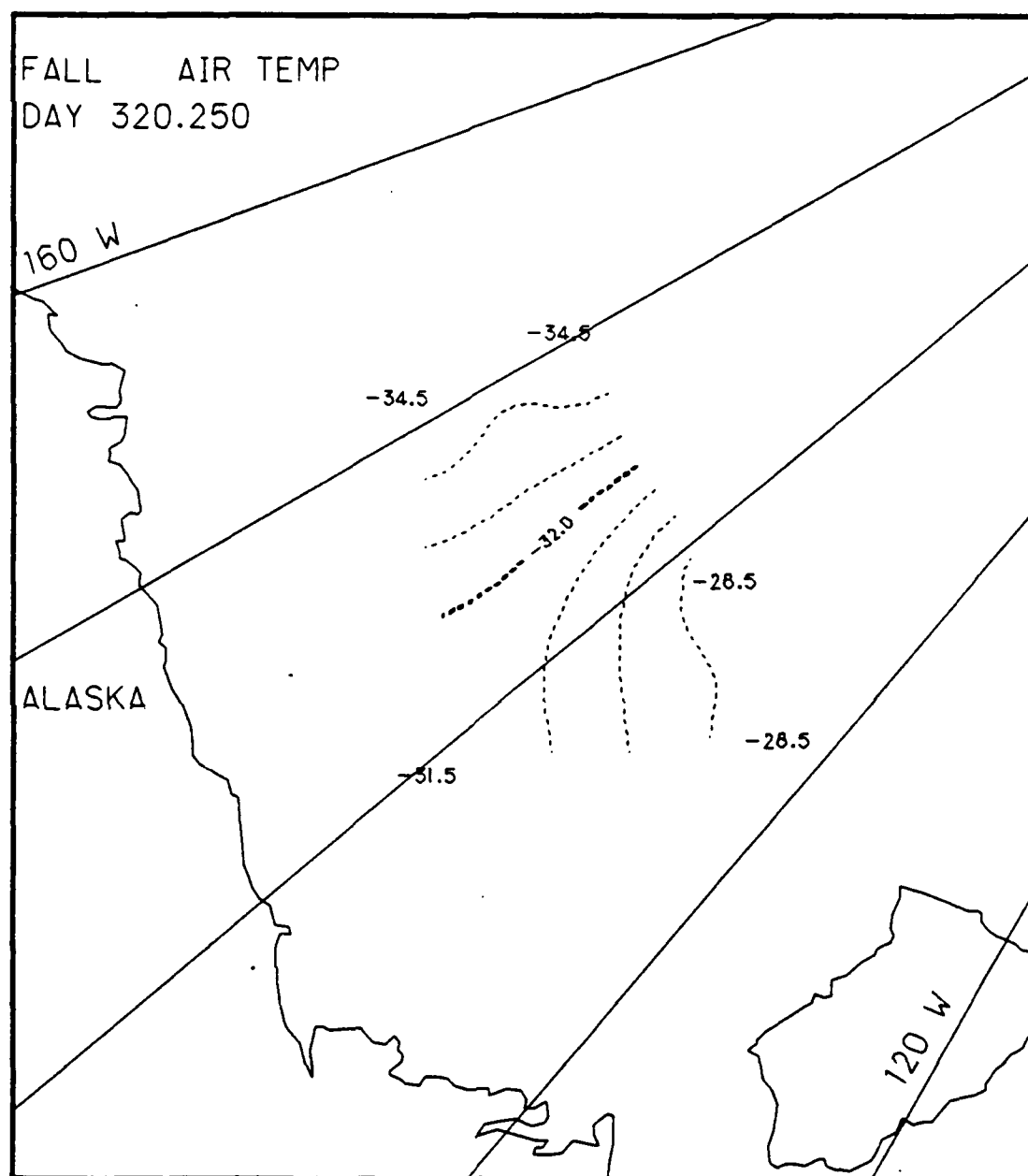


Fig. E.3. Spatial atmospheric temperature variations, day 320.25, based on the AIDJEX data from stations with hydrophones, fall 1975.

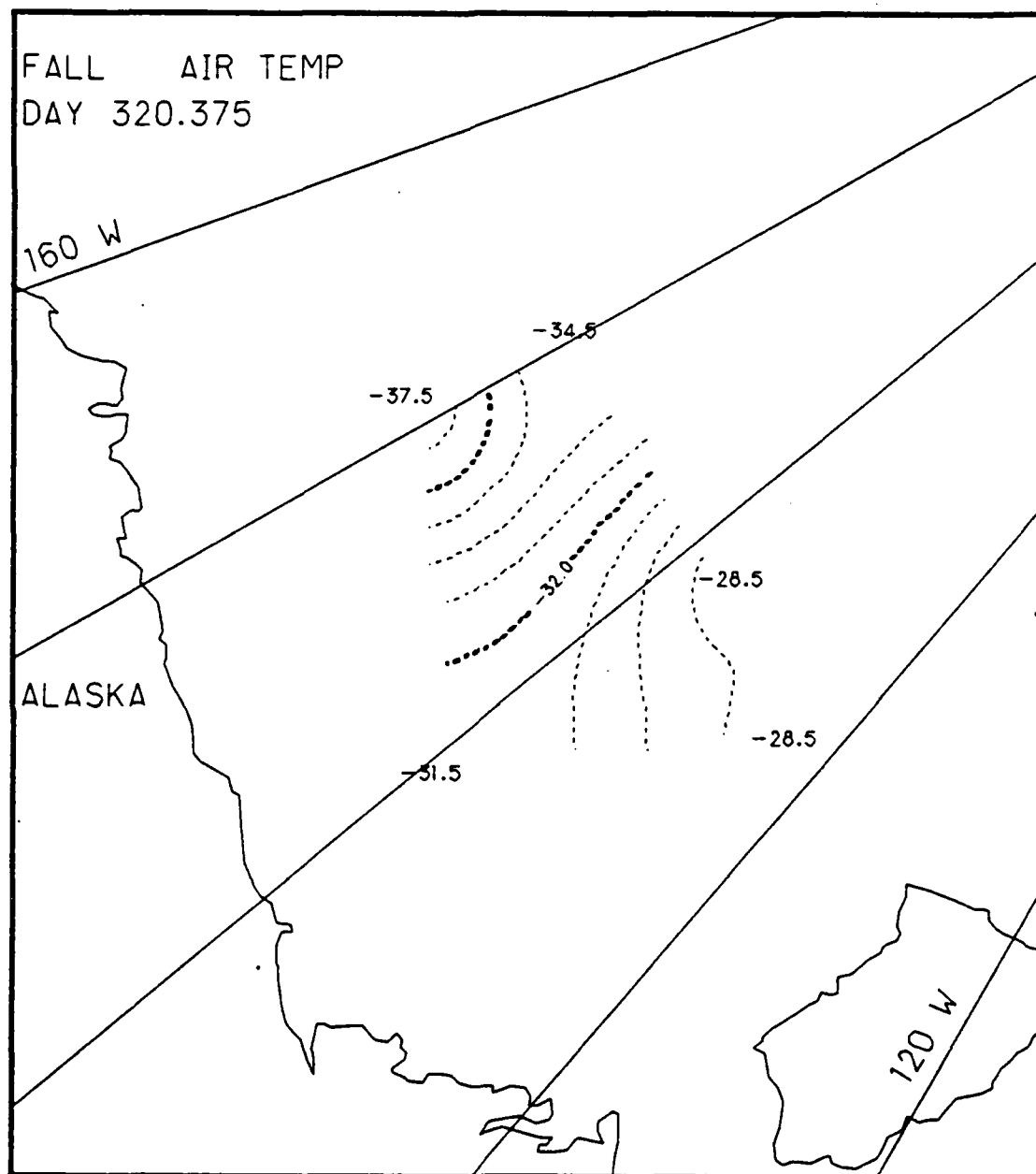


Fig. E.4. Spatial atmospheric temperature variations, day 320.375, based on the AIDJEX data from stations with hydrophones, fall 1975.

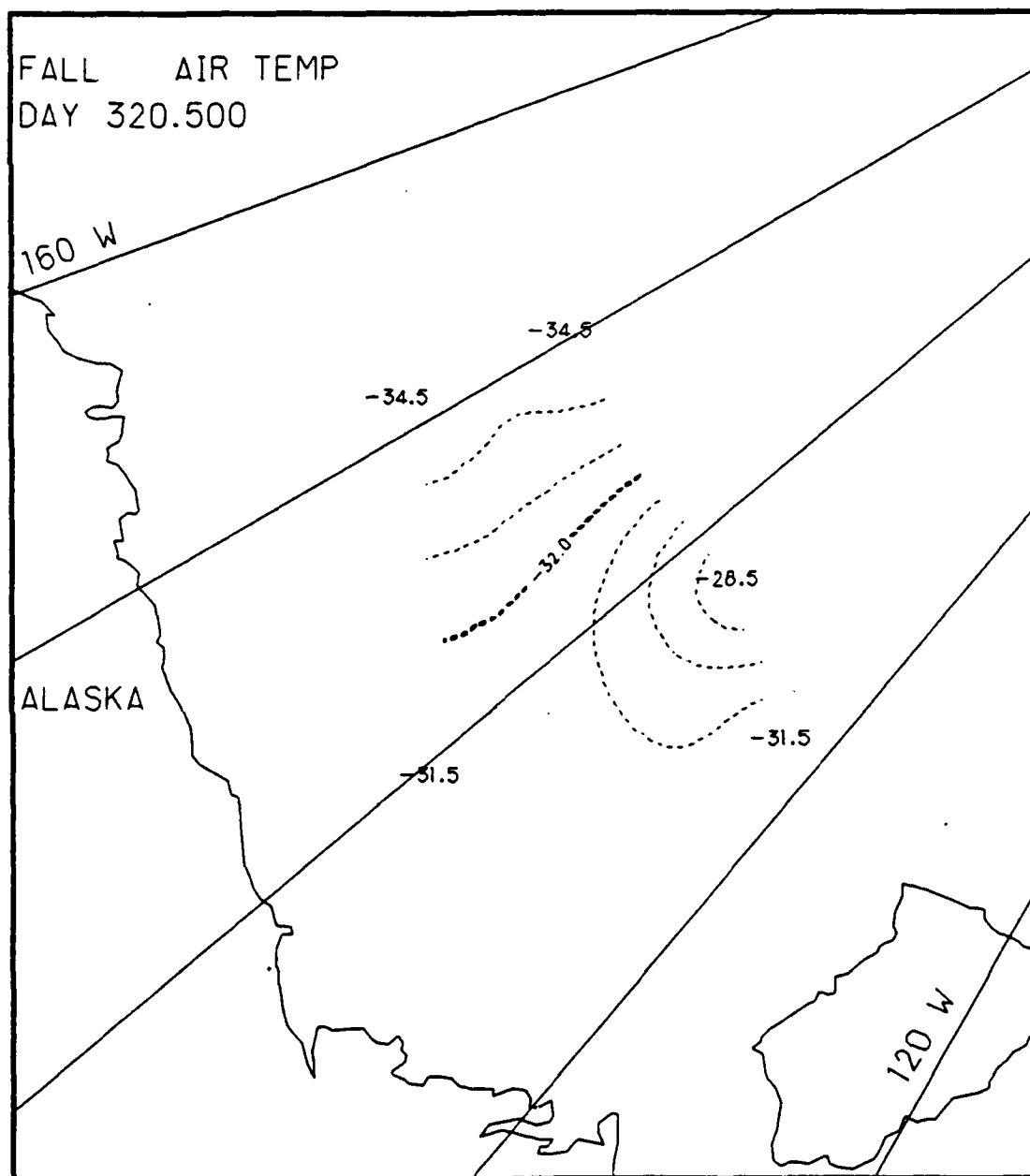


Fig. E.5. Spatial atmospheric temperature variations, day 320.5, based on the AIDJEX data from stations with hydrophones, fall 1975.

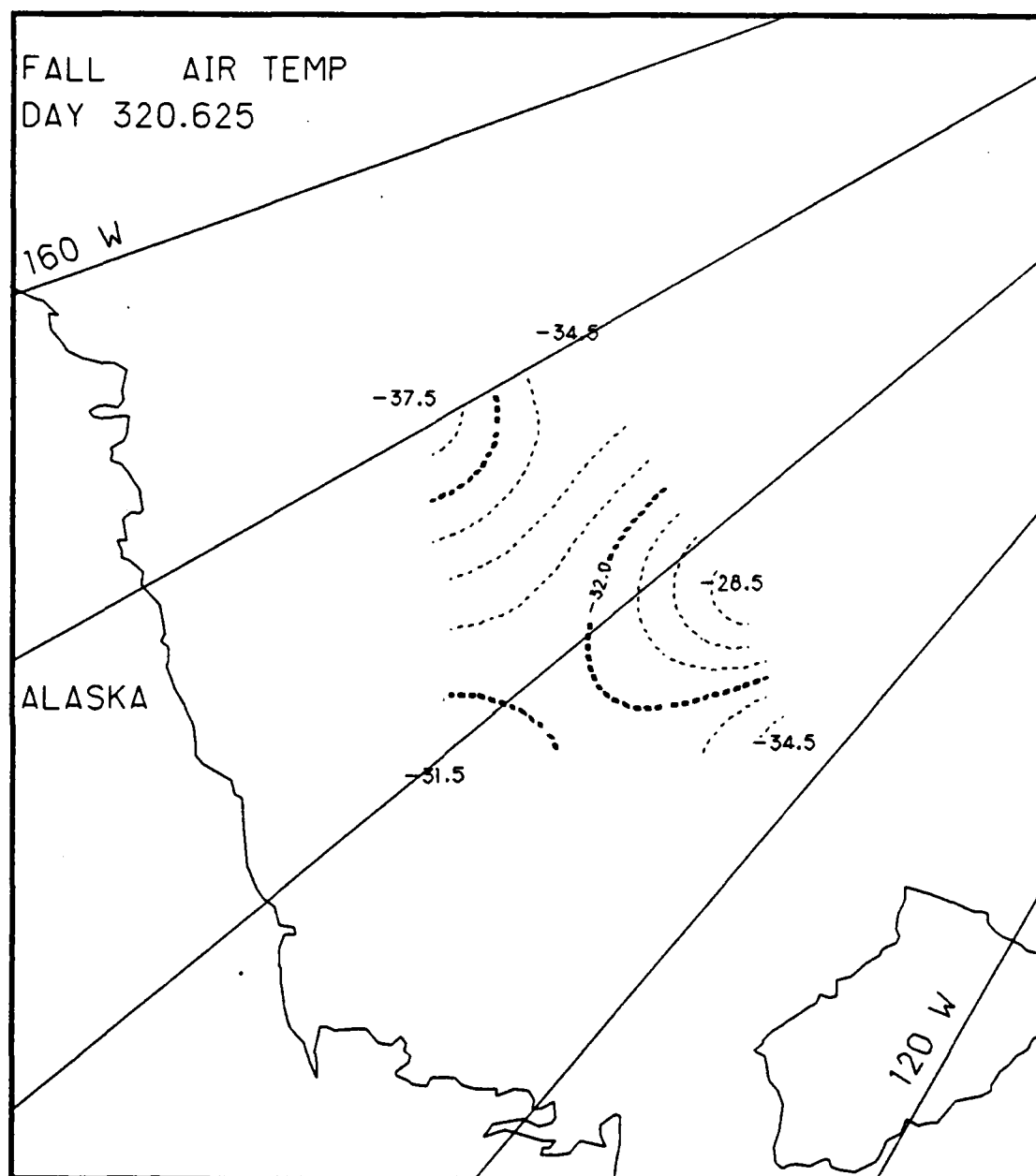


Fig. E.6. Spatial atmospheric temperature variations, day 320.625, based on the AIDJEX data from stations with hydrophones, fall 1975.

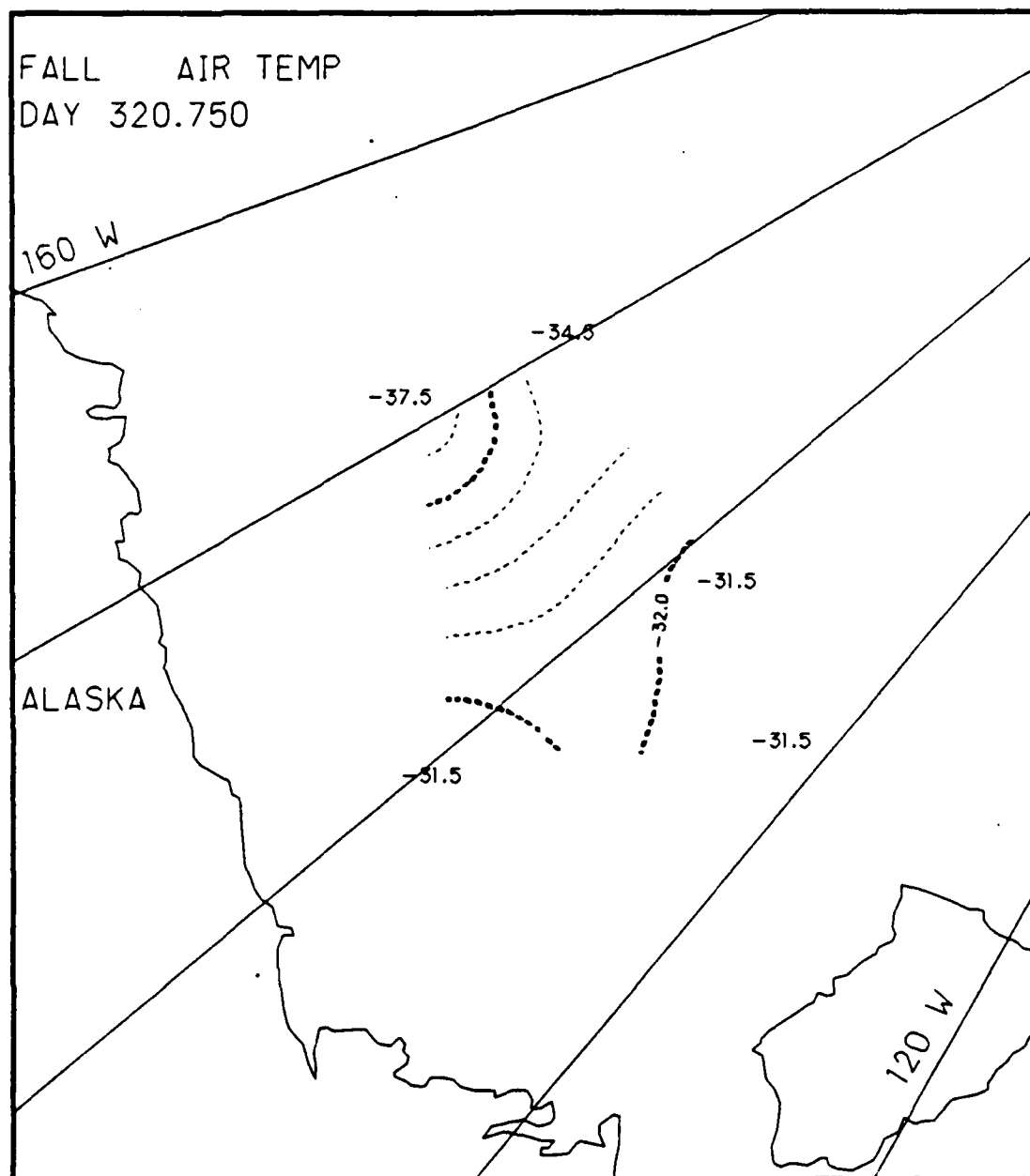


Fig. E.7. Spatial atmospheric temperature variations, day 320.75, based on the AIDJEX data from stations with hydrophones, fall 1975.

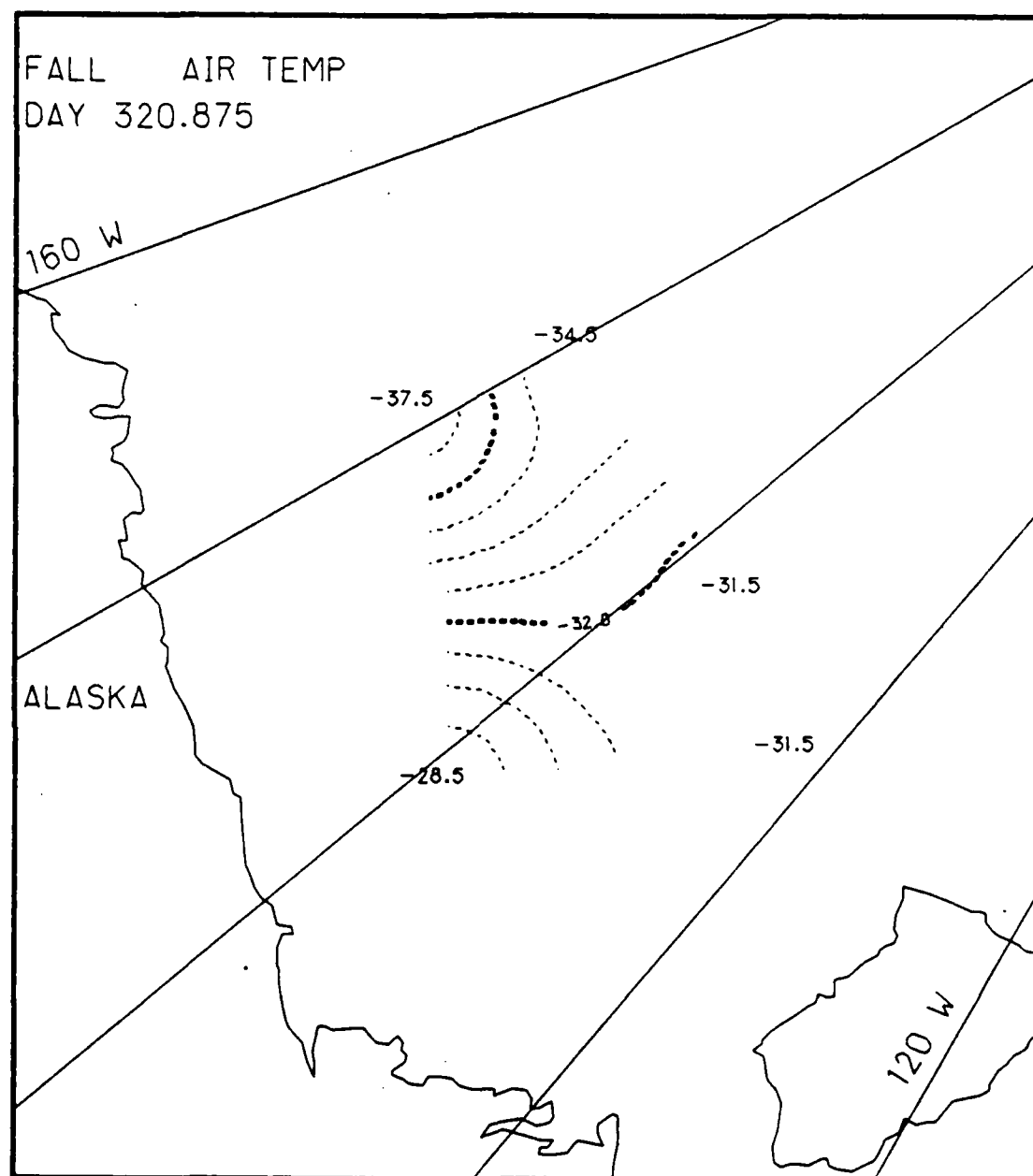


Fig. E.8. Spatial atmospheric temperature variations, day 320.875, based on the AIDJEX data from stations with hydrophones, fall 1975.

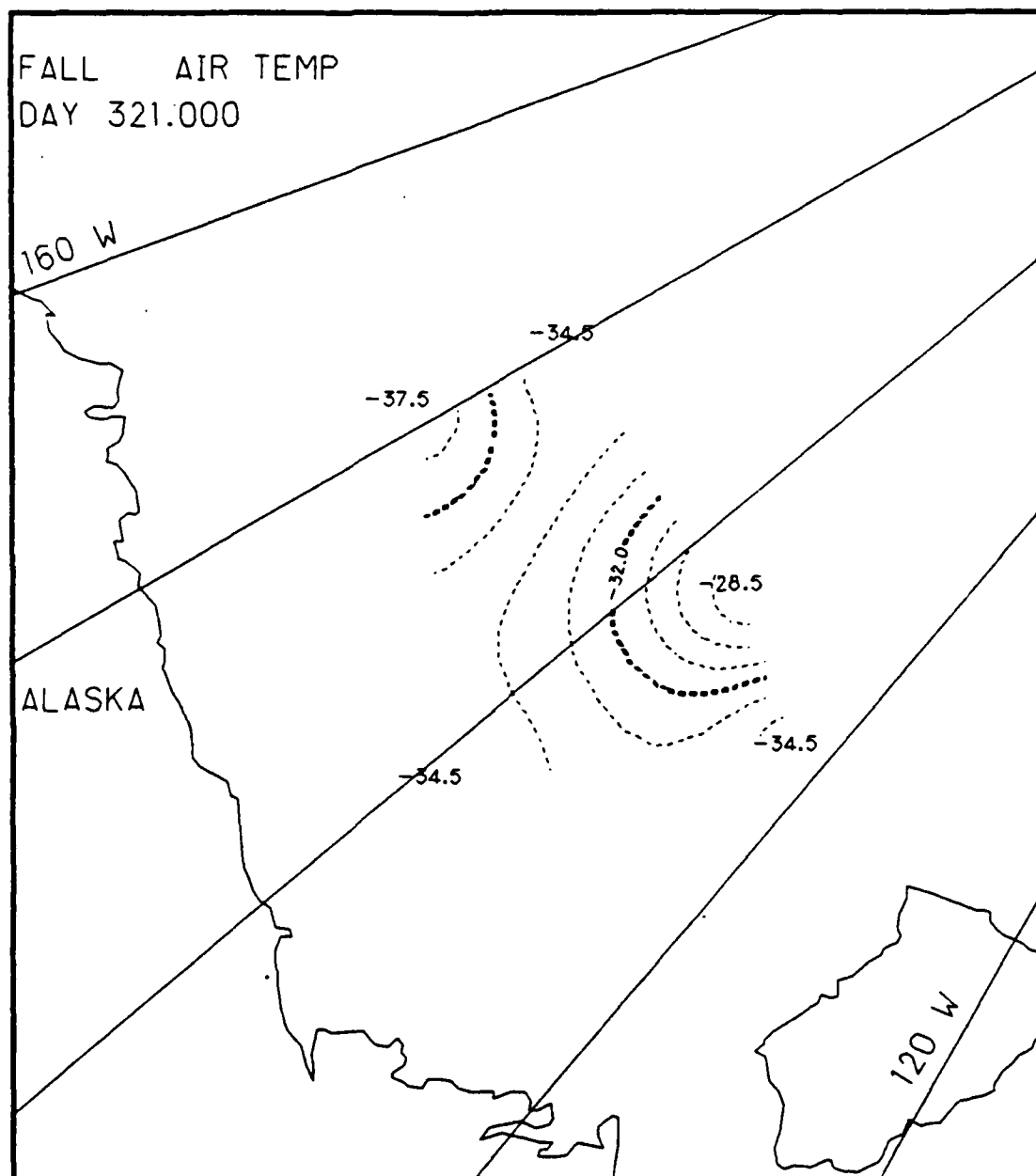


Fig. E.9. Spatial atmospheric temperature variations, day 321.0, based on the AIDJEX data from stations with hydrophones, fall 1975.

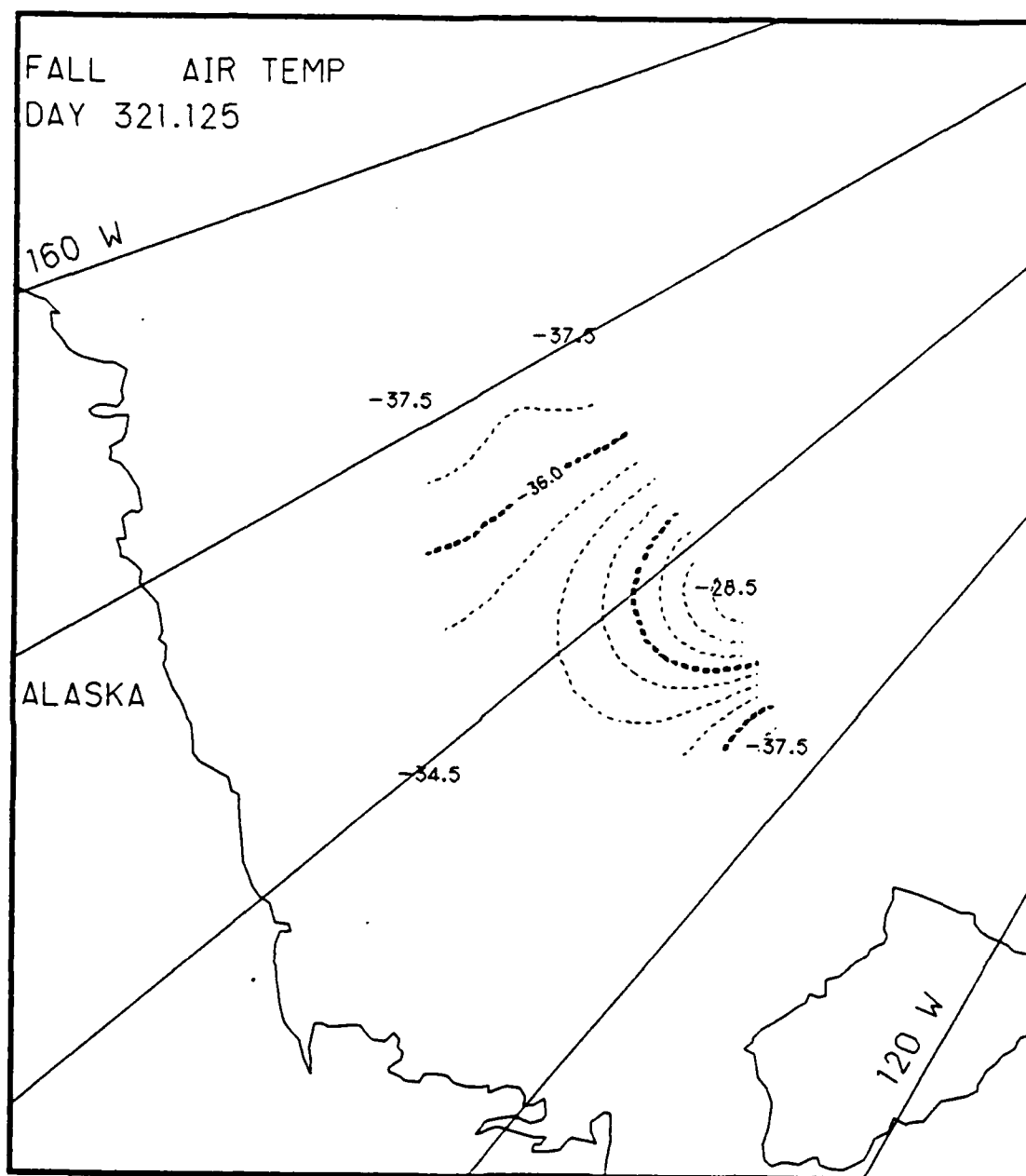


Fig. E.10. Spatial atmospheric temperature variations, day 321.125, based on the AIDJEX data from stations with hydrophones, fall 1975.

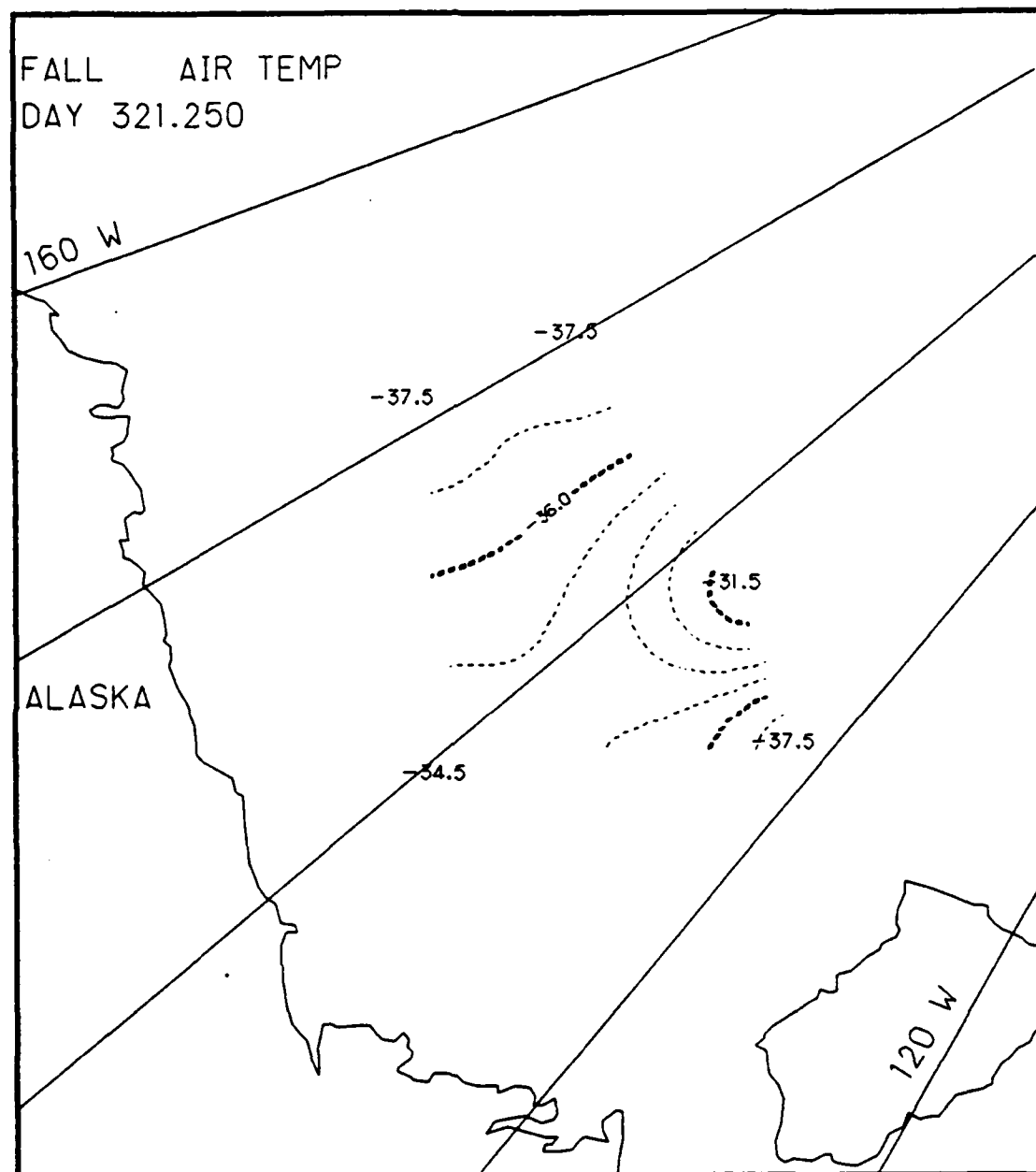


Fig. E.11. Spatial atmospheric temperature variations, day 321.25, based on the AIDJEX data from stations with hydrophones, fall 1975.

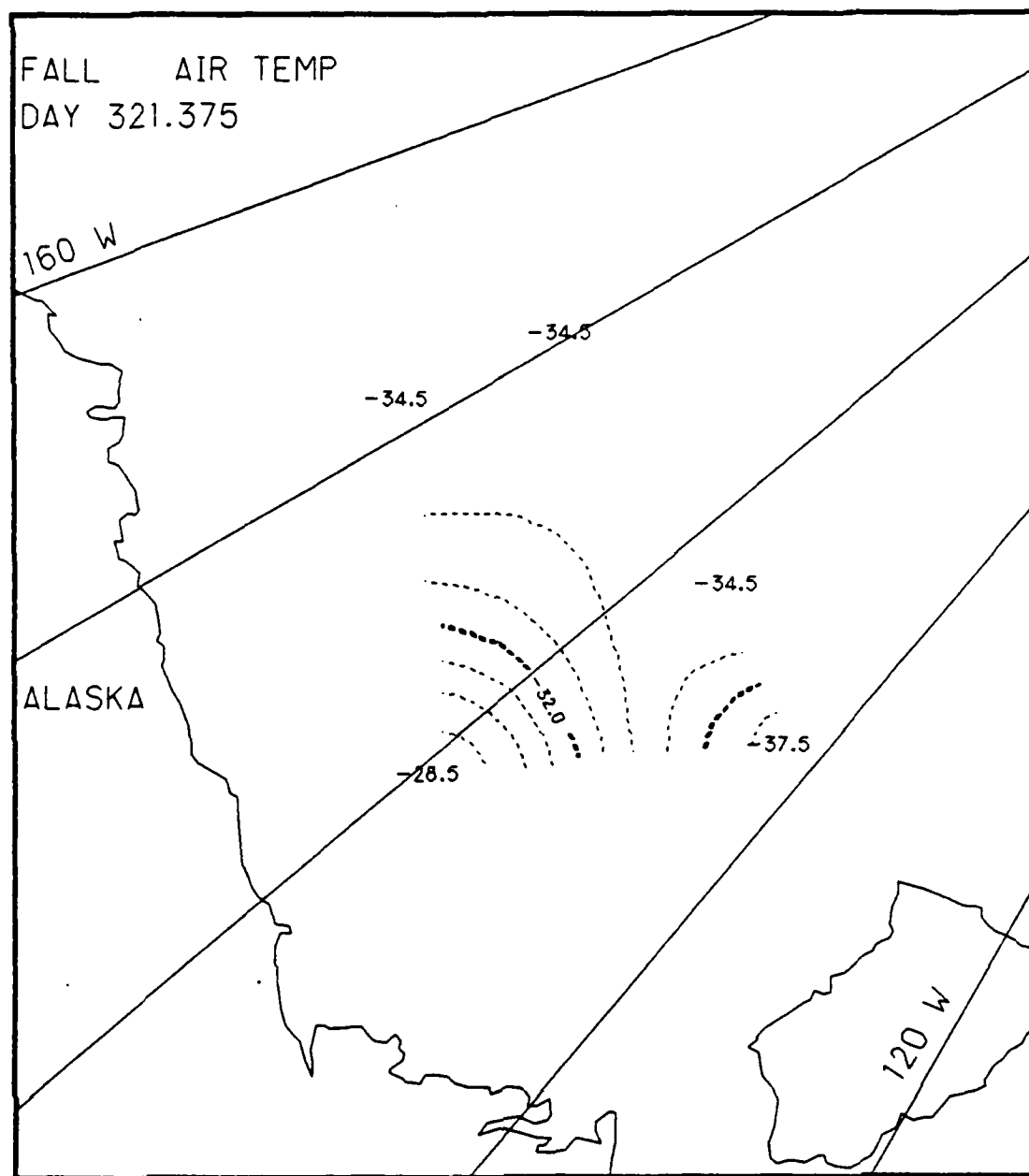


Fig. E.12. Spatial atmospheric temperature variations, day 321.375, based on the AIDJEX data from stations with hydrophones, fall 1975.

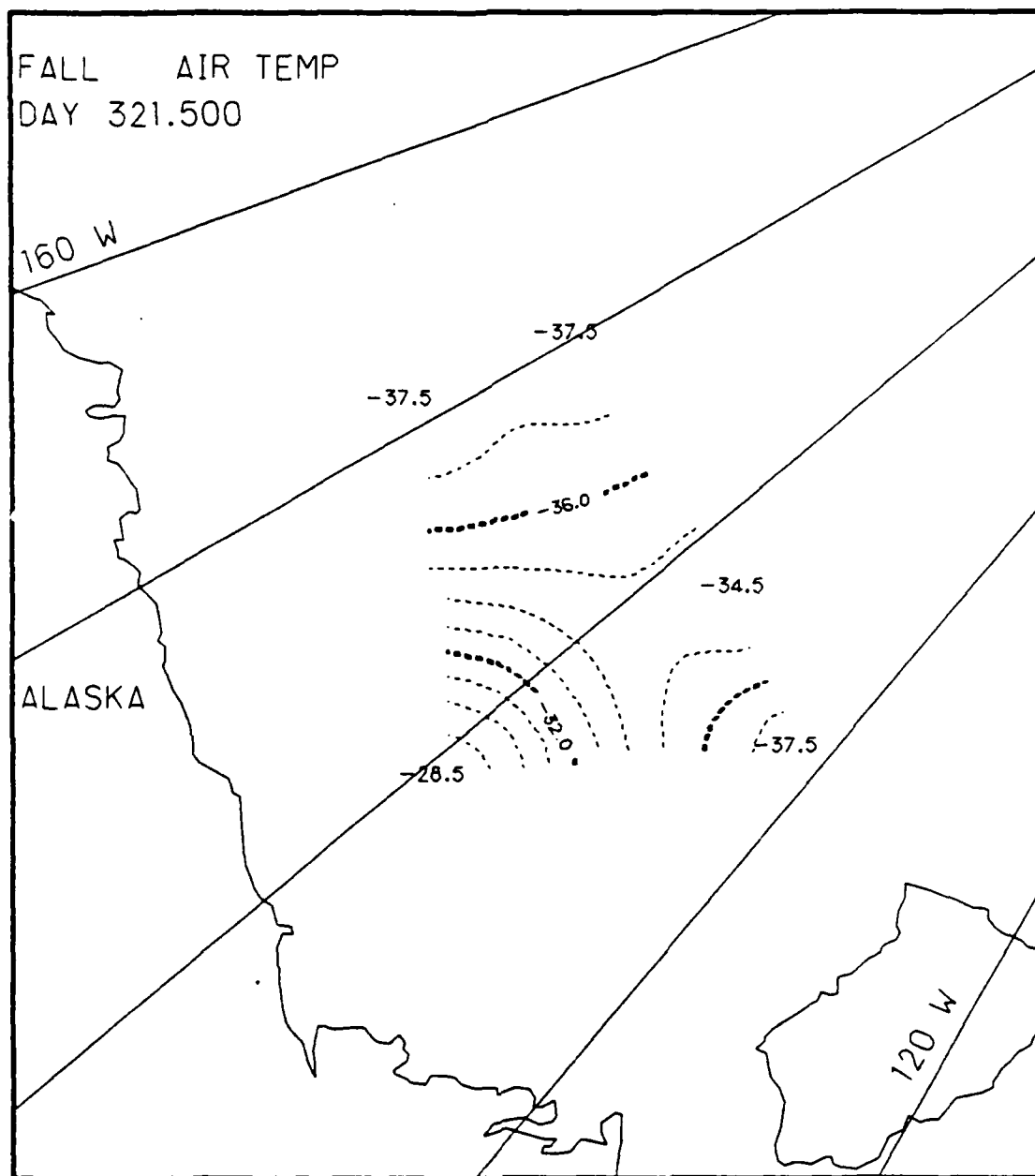


Fig. E.13. Spatial atmospheric temperature variations, day 321.5, based on the AIDJEX data from stations with hydrophones, fall 1975.

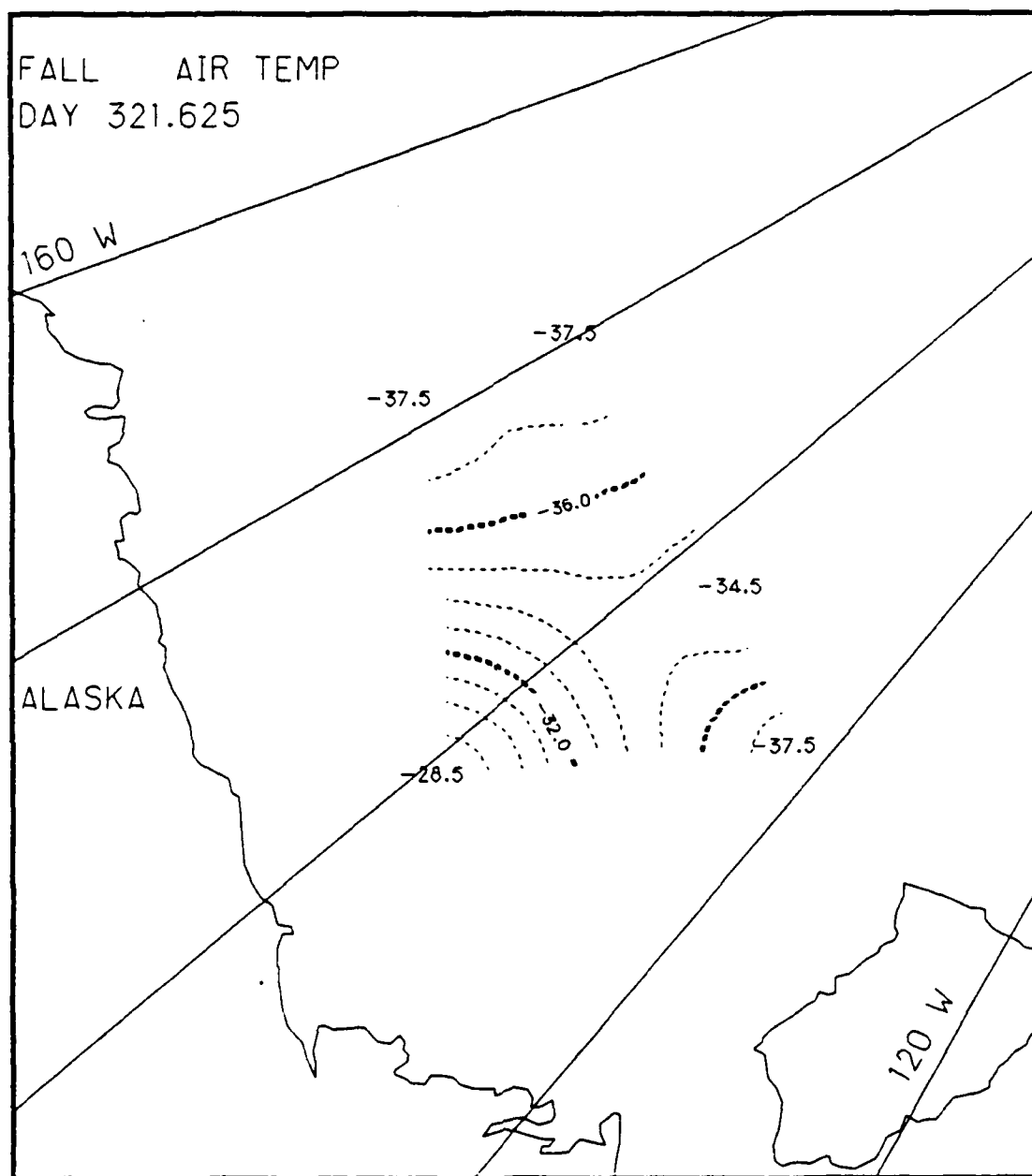


Fig. E.14. Spatial atmospheric temperature variations, day 321.625, based on the AIDJEX data from stations with hydrophones, fall 1975.

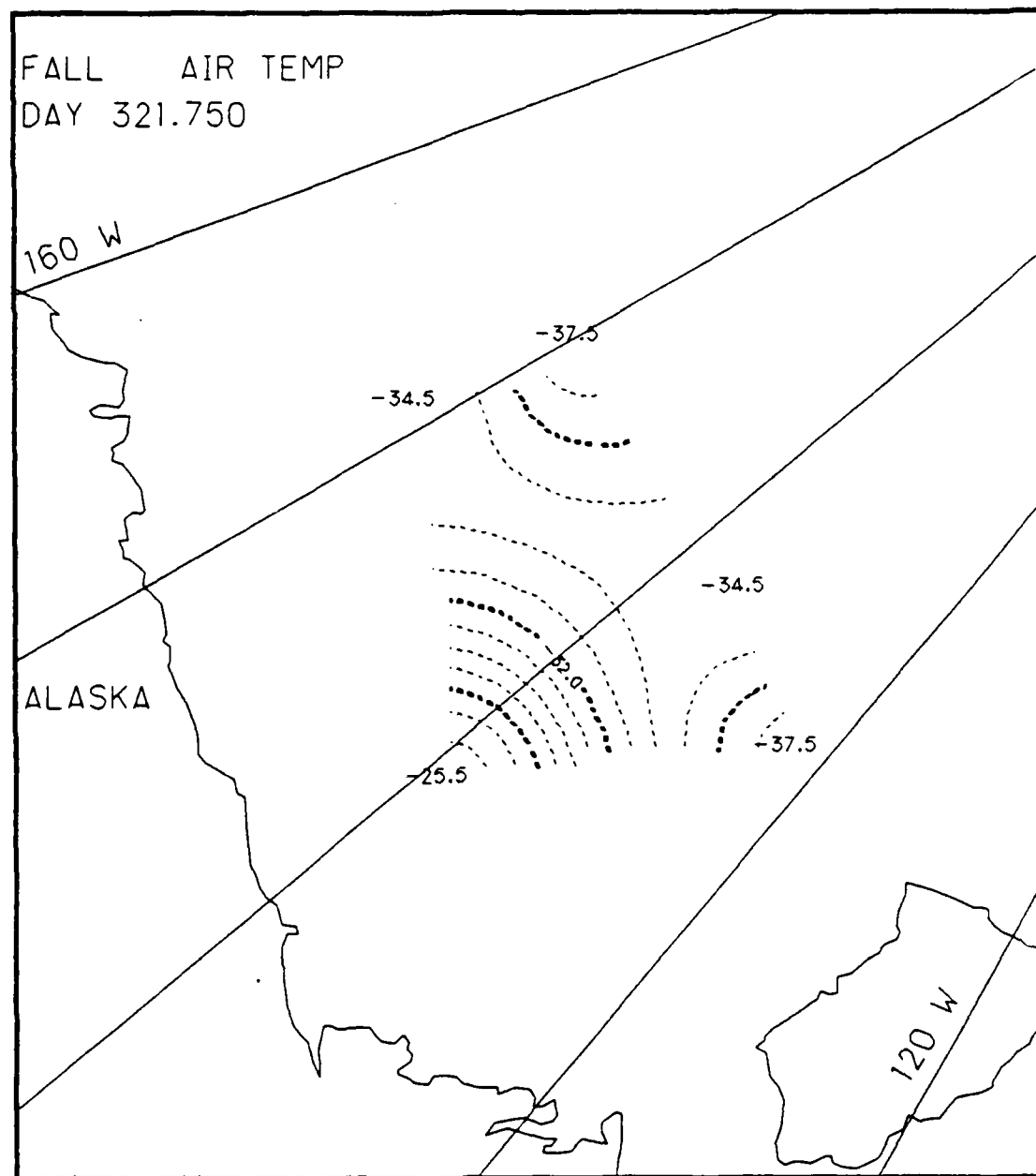


Fig. E.15. Spatial atmospheric temperature variations, day 321.75, based on the AIDJEX data from stations with hydrophones, fall 1975.

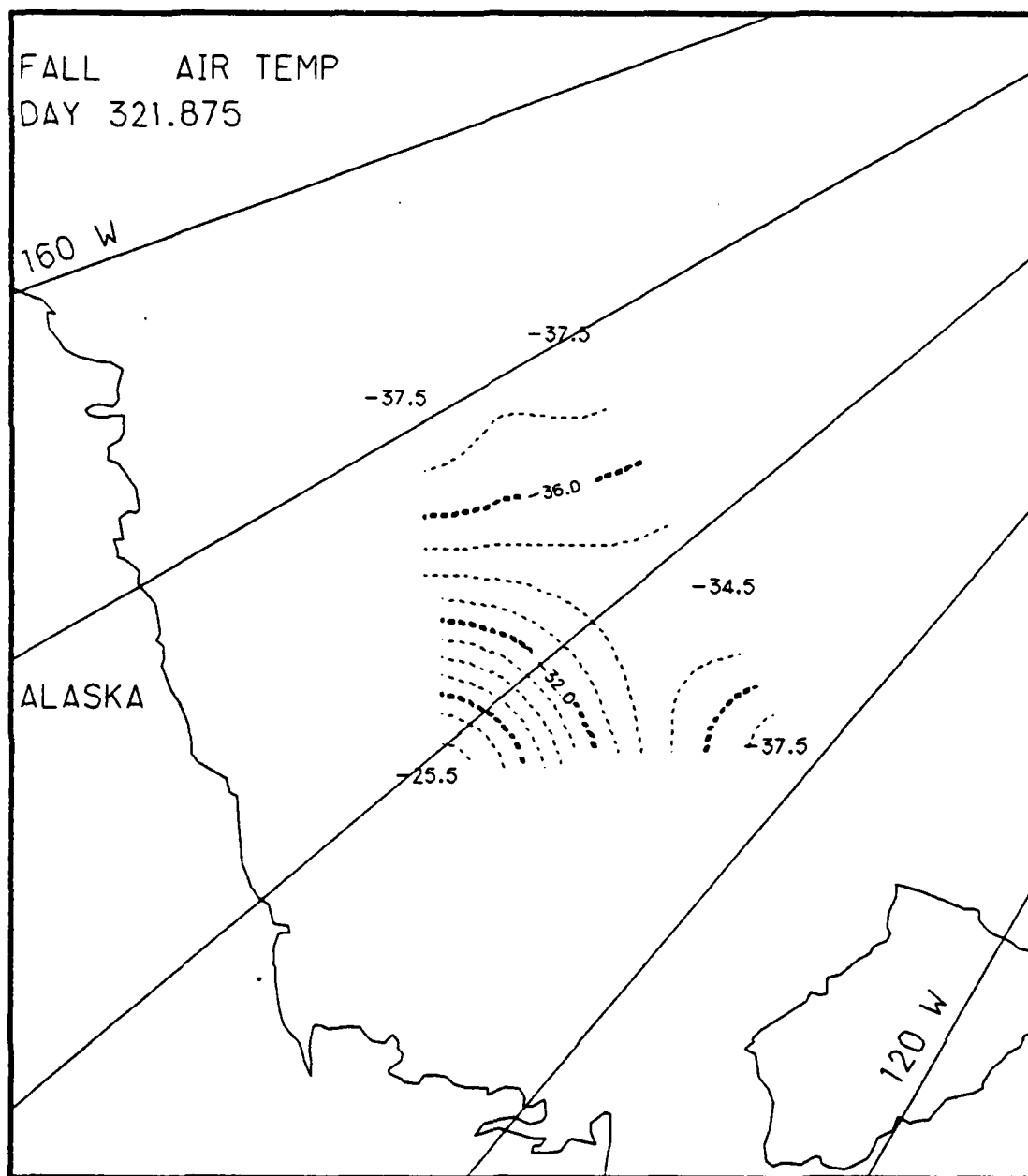


Fig. E.16. Spatial atmospheric temperature variations, day 321.875, based on the AIDJEX data from stations with hydrophones, fall 1975.

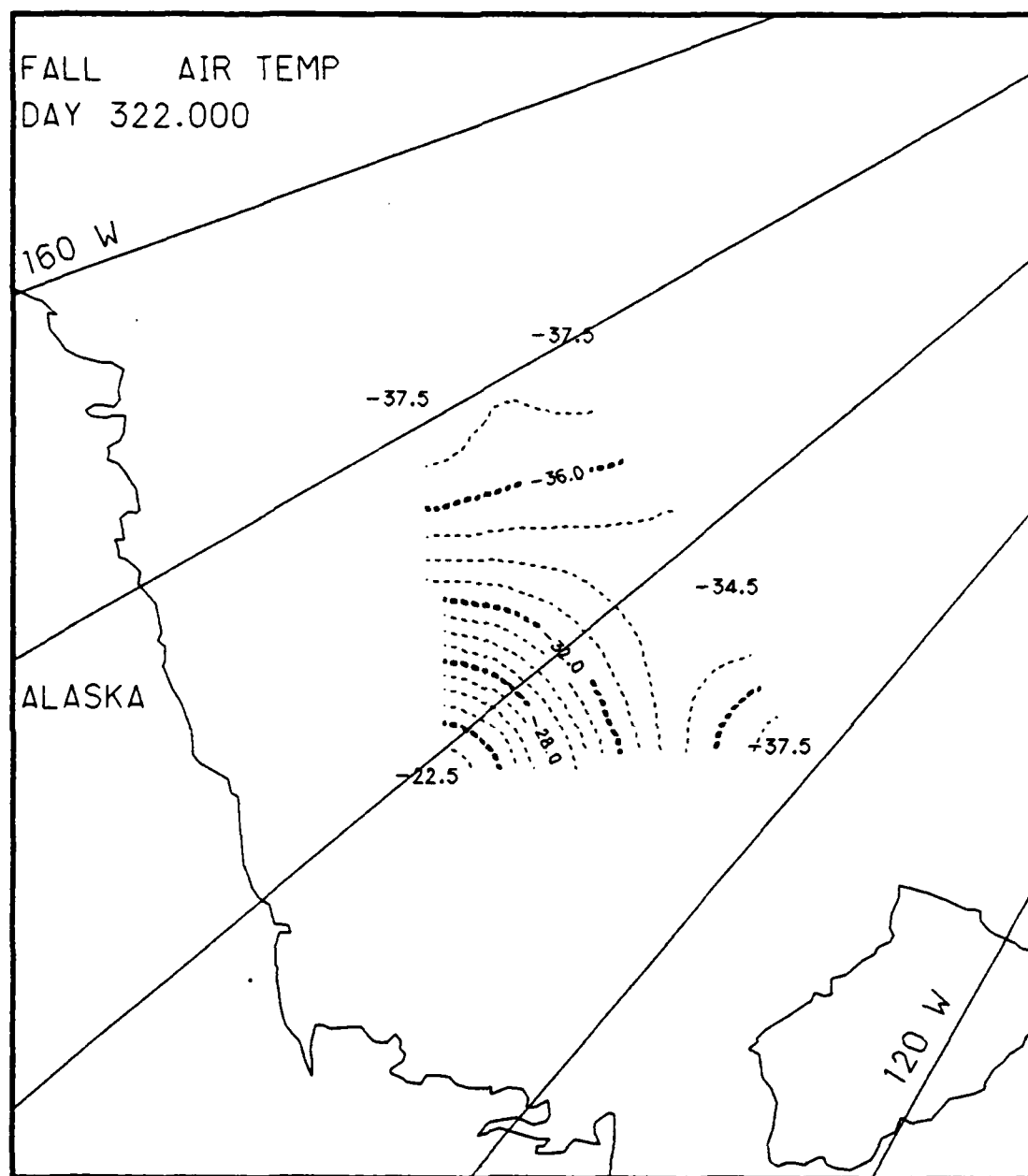


Fig. E.17. Spatial atmospheric temperature variations, day 322.0, based on the AIDJEX data from stations with hydrophones, fall 1975.

Appendix F

Two-Dimensional Contour Maps of Arctic Atmospheric Pressure Variations, 9-10 February 1976 (Winter)

This appendix contains the two-dimensional contour maps of the AIDJEX atmospheric pressure data collected at those stations with hydrophones during the 48 hour period of 9-10 February 1976. The contour maps show the spatial variations of atmospheric pressure (millibars) at 3 hr intervals.

List of Figures
Appendix F

2-100

	<u>Page</u>
Fig. F.1. Spatial atmospheric pressure variations, day 39.0	2-101
Fig. F.2. Spatial atmospheric pressure variations, day 39.125	2-102
Fig. F.3. Spatial atmospheric pressure variations, day 39.25	2-103
Fig. F.4. Spatial atmospheric pressure variations, day 39.375	2-104
Fig. F.5. Spatial atmospheric pressure variations, day 39.5	2-105
Fig. F.6. Spatial atmospheric pressure variations, day 39.625	2-106
Fig. F.7. Spatial atmospheric pressure variations, day 39.75	2-107
Fig. F.8. Spatial atmospheric pressure variations, day 39.875	2-108
Fig. F.9. Spatial atmospheric pressure variations, day 40.0	2-109
Fig. F.10. Spatial atmospheric pressure variations, day 40.125	2-110
Fig. F.11. Spatial atmospheric pressure variations, day 40.25	2-111
Fig. F.12. Spatial atmospheric pressure variations, day 40.375	2-112
Fig. F.13. Spatial atmospheric pressure variations, day 40.5	2-113
Fig. F.14. Spatial atmospheric pressure variations, day 40.625	2-114
Fig. F.15. Spatial atmospheric pressure variations, day 40.75	2-115
Fig. F.16. Spatial atmospheric pressure variations, day 40.875	2-116
Fig. F.17. Spatial atmospheric pressure variations, day 41.0	2-117

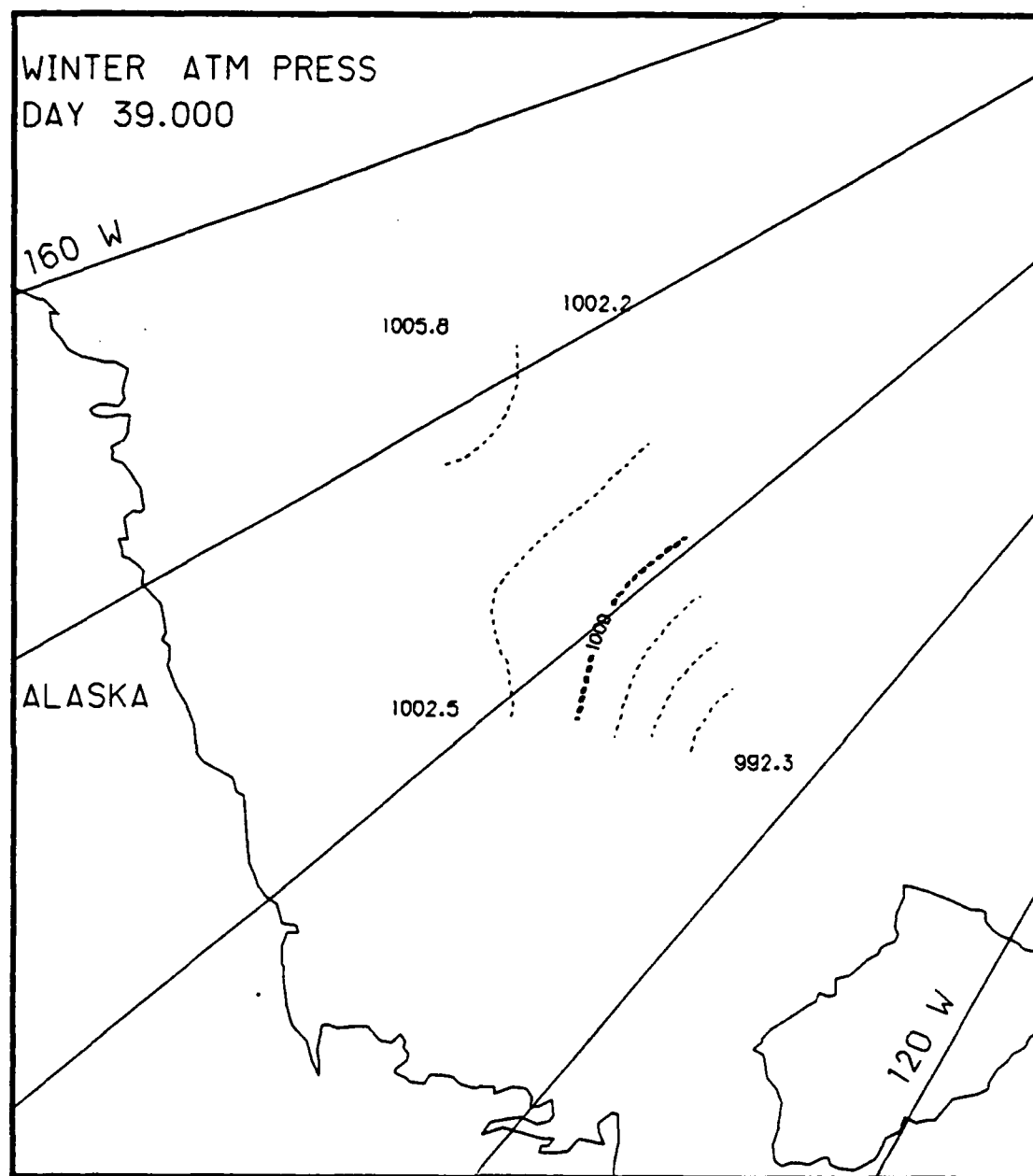


Fig. F.1. Spatial atmospheric pressure variations, day 39.0, based on the AIDJEX data from stations with hydrophones, winter 1976.

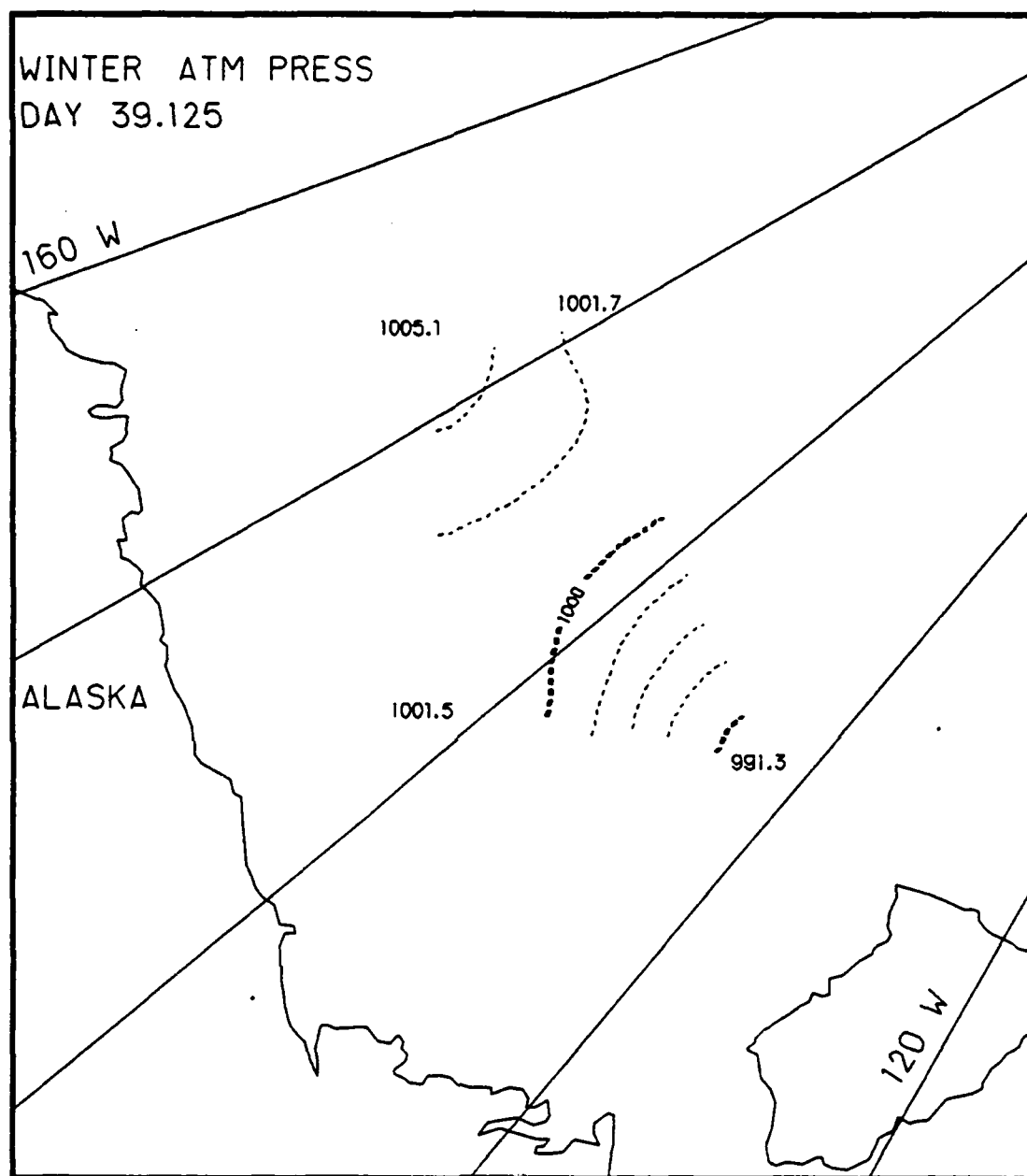


Fig. F.2. Spatial atmospheric pressure variations, day 39.125, based on the AIDJEX data from stations with hydrophones, winter 1976.

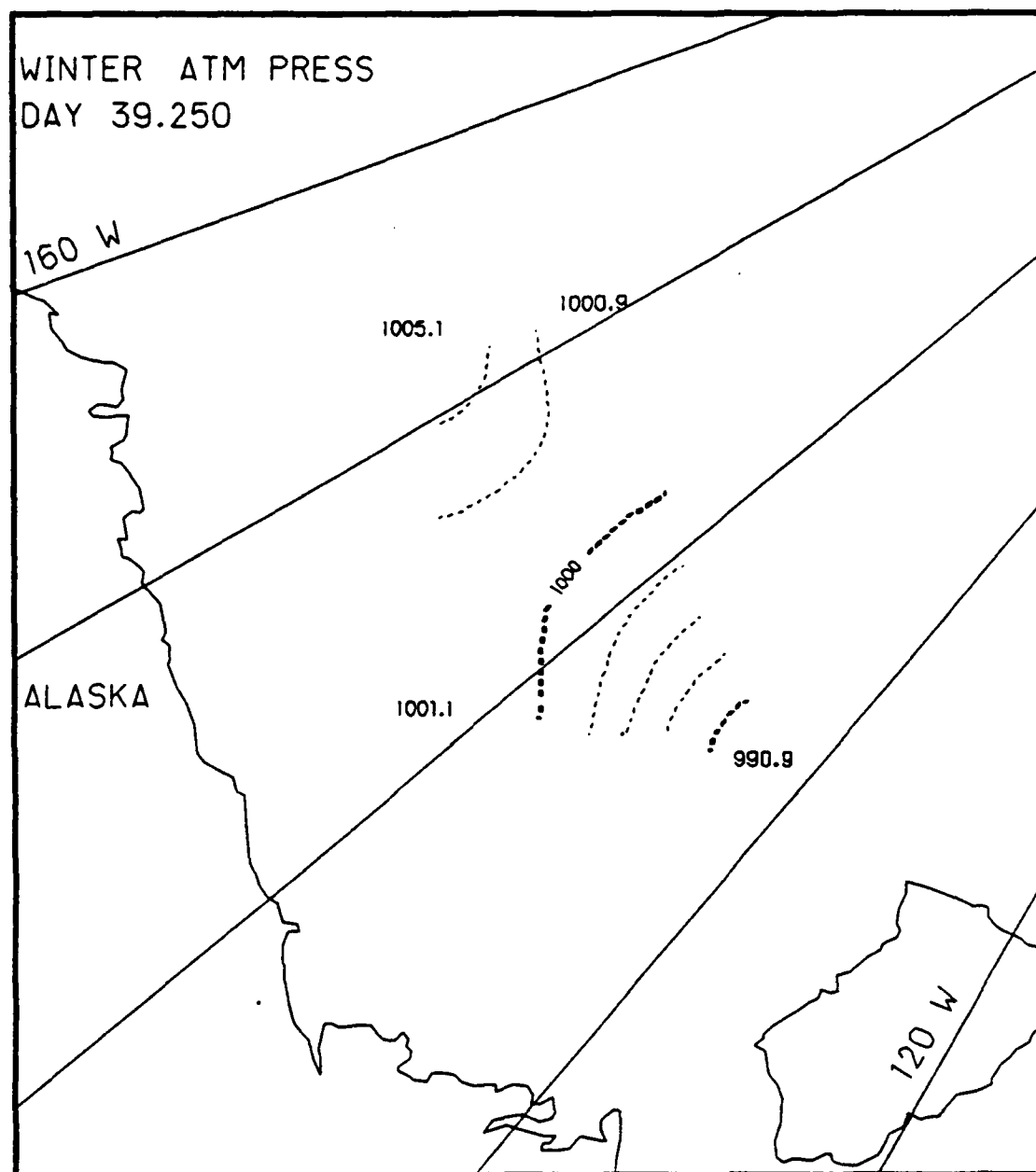


Fig. F.3. Spatial atmospheric pressure variations, day 39.25, based on the AIDJEX data from stations with hydrophones, winter 1976.

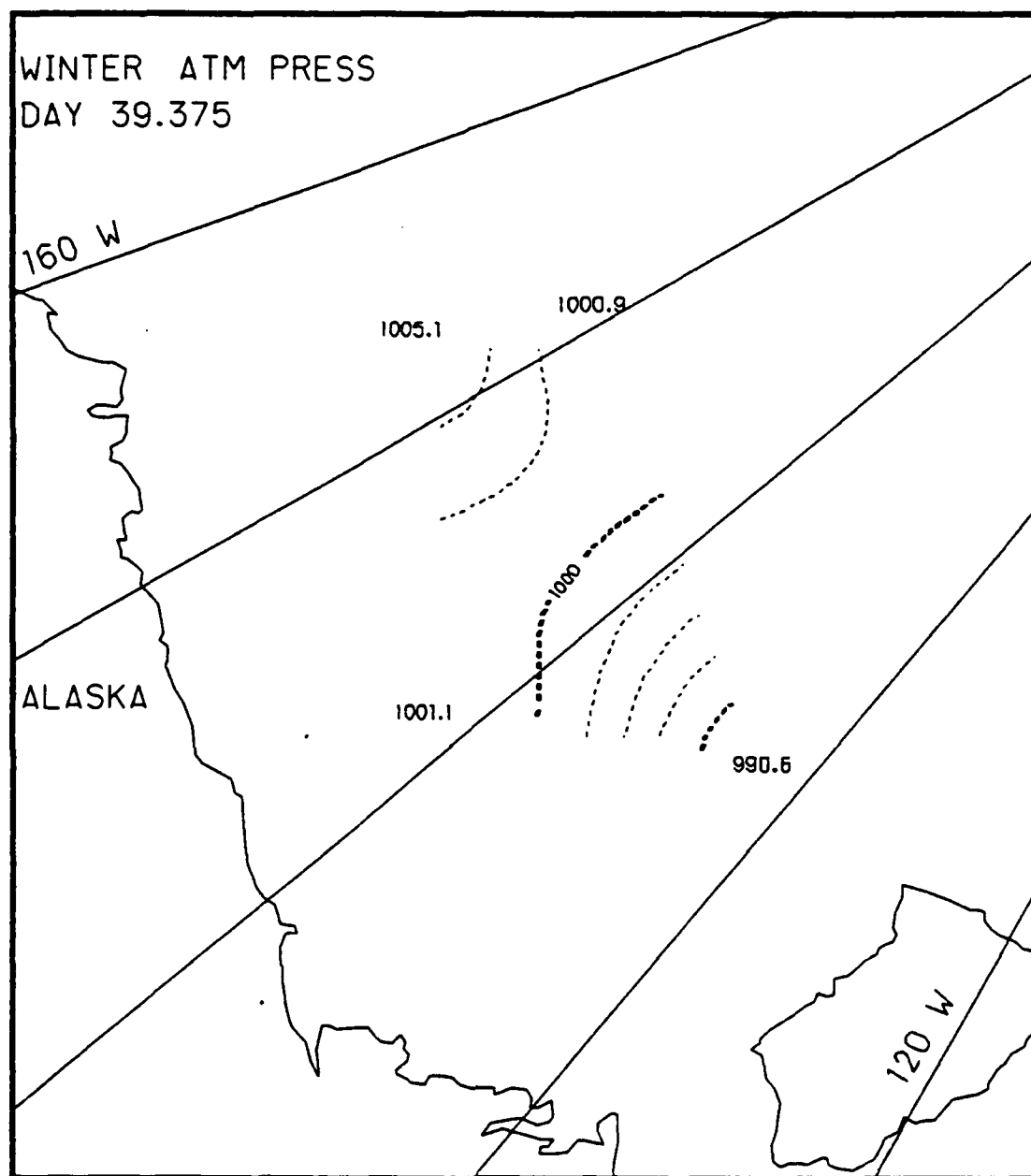


Fig. F.4. Spatial atmospheric pressure variations, day 39.375, based on the AIDJEX data from stations with hydrophones, winter 1976.

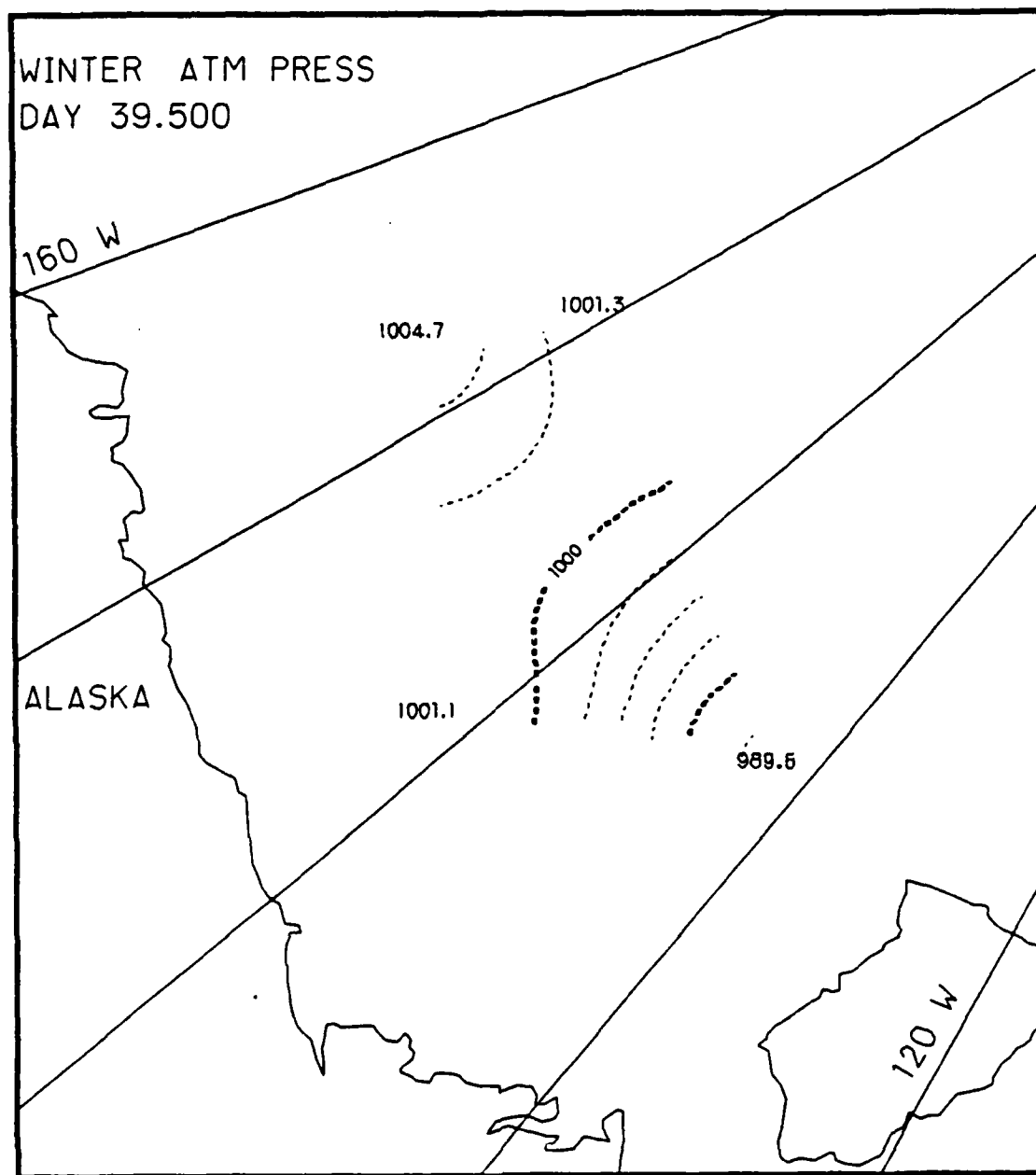


Fig. F.5. Spatial atmospheric pressure variations, day 39.5, based on the AIDJEX data from stations with hydrophones, winter 1976.

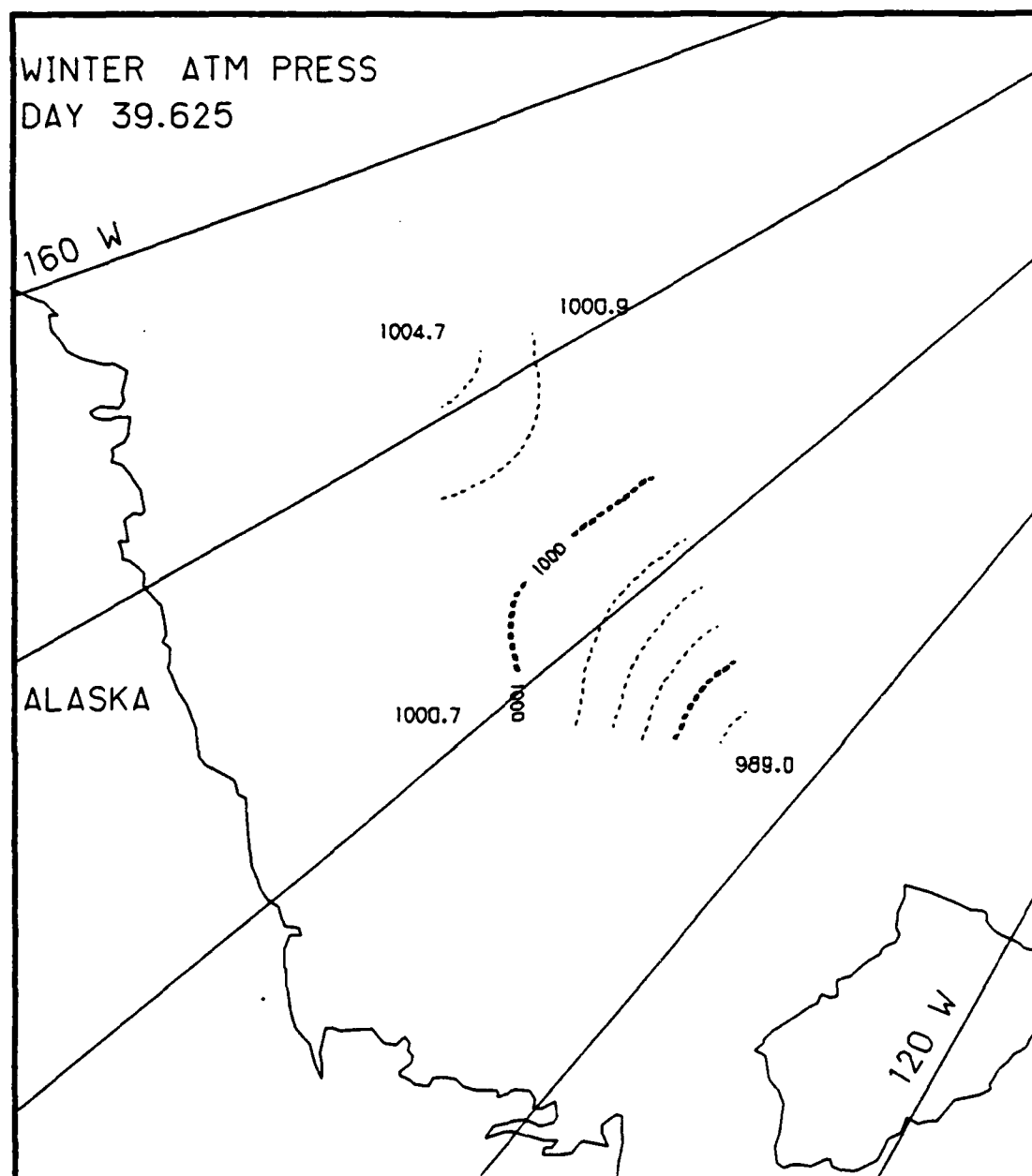


Fig. F.6. Spatial atmospheric pressure variations, day 39.625, based on the AIDJEX data from stations with hydrophones, winter 1976.

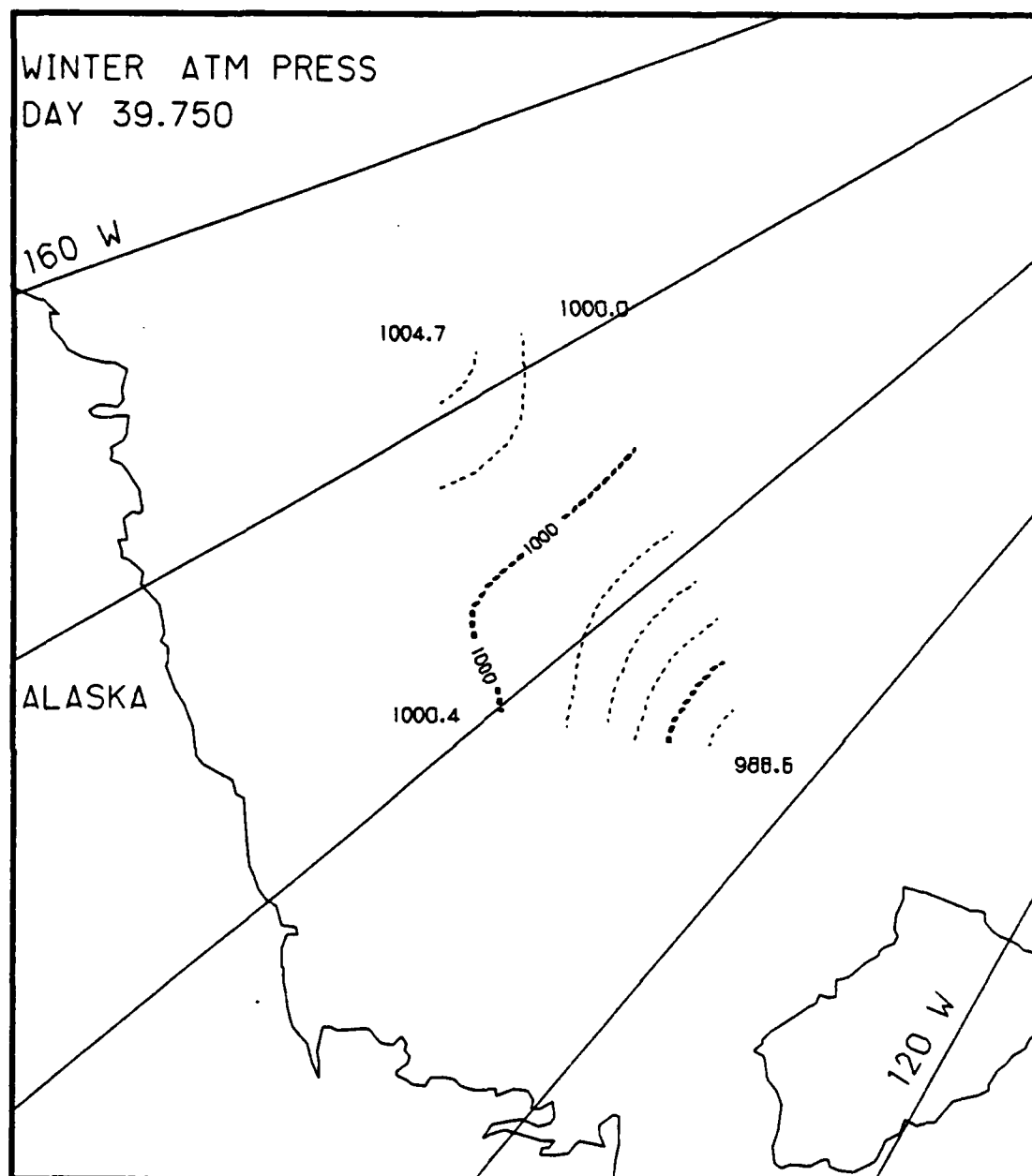


Fig. F.7. Spatial atmospheric pressure variations, day 39.75, based on the AIDJEX data from stations with hydrophones, winter 1976.

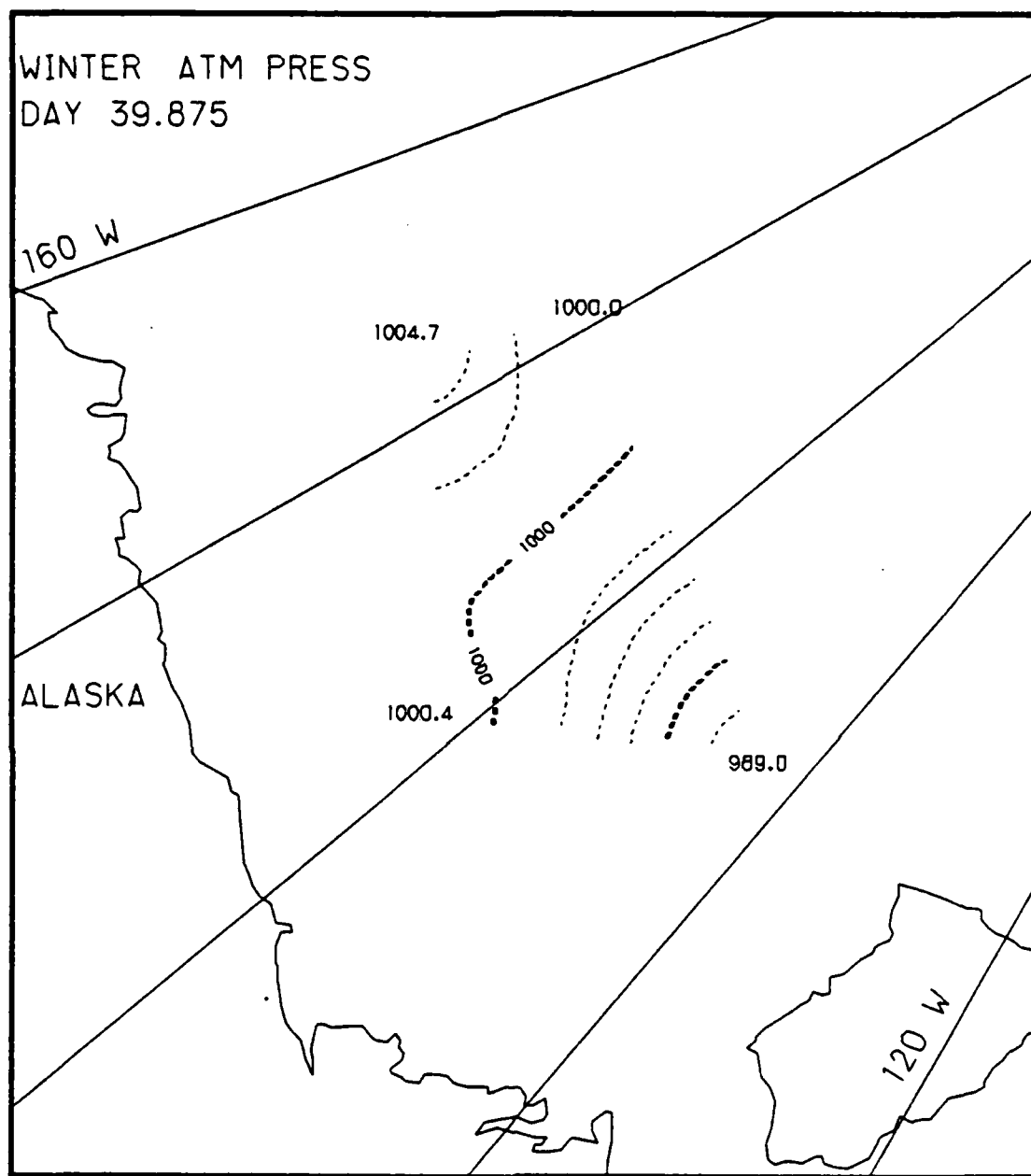


Fig. F.8. Spatial atmospheric pressure variations, day 39.875, based on the AIDJEX data from stations with hydrophones, winter 1976.

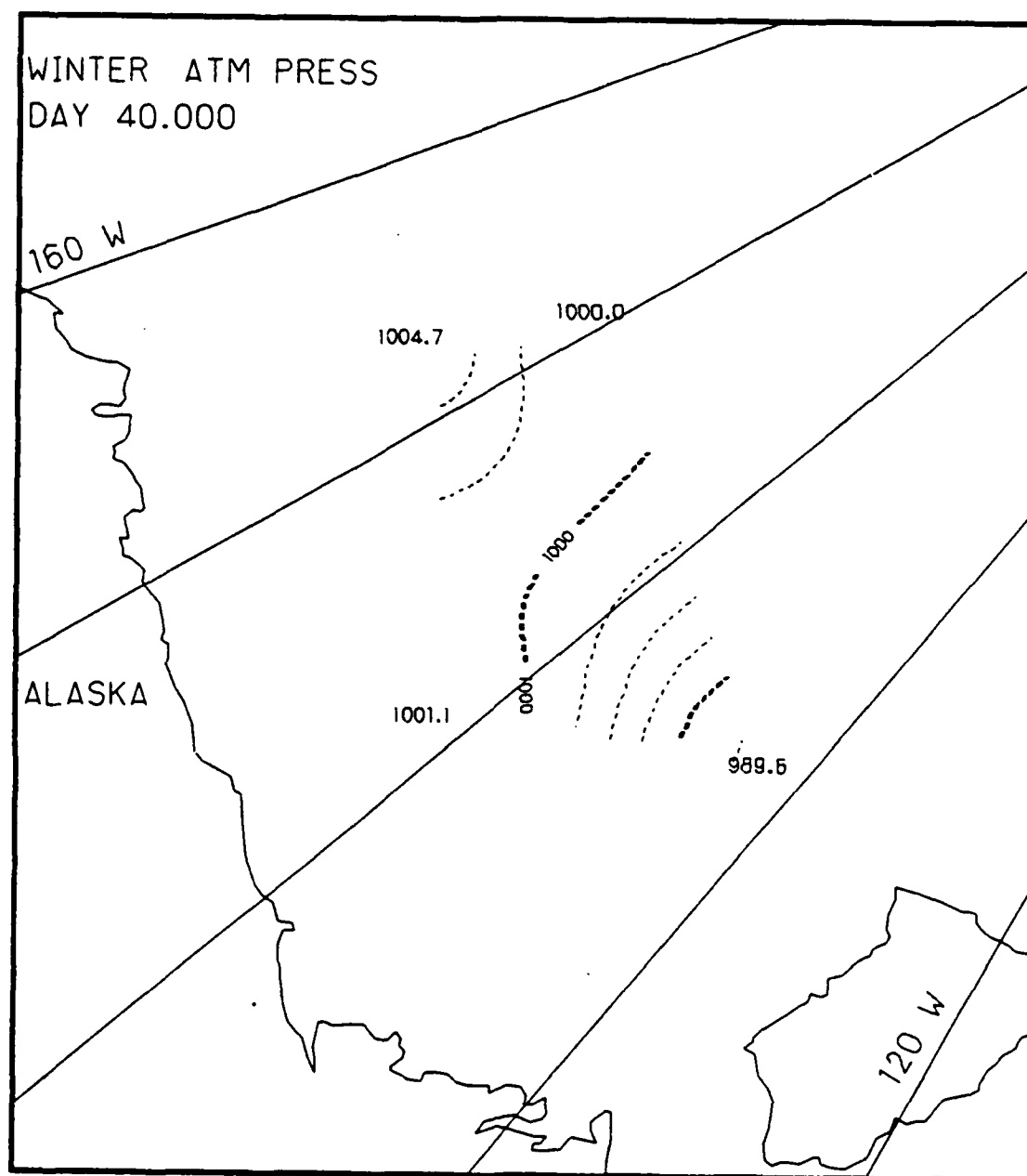


Fig. F.9. Spatial atmospheric pressure variations, day 40.0, based on the AIDJEX data from stations with hydrophones, winter 1976.

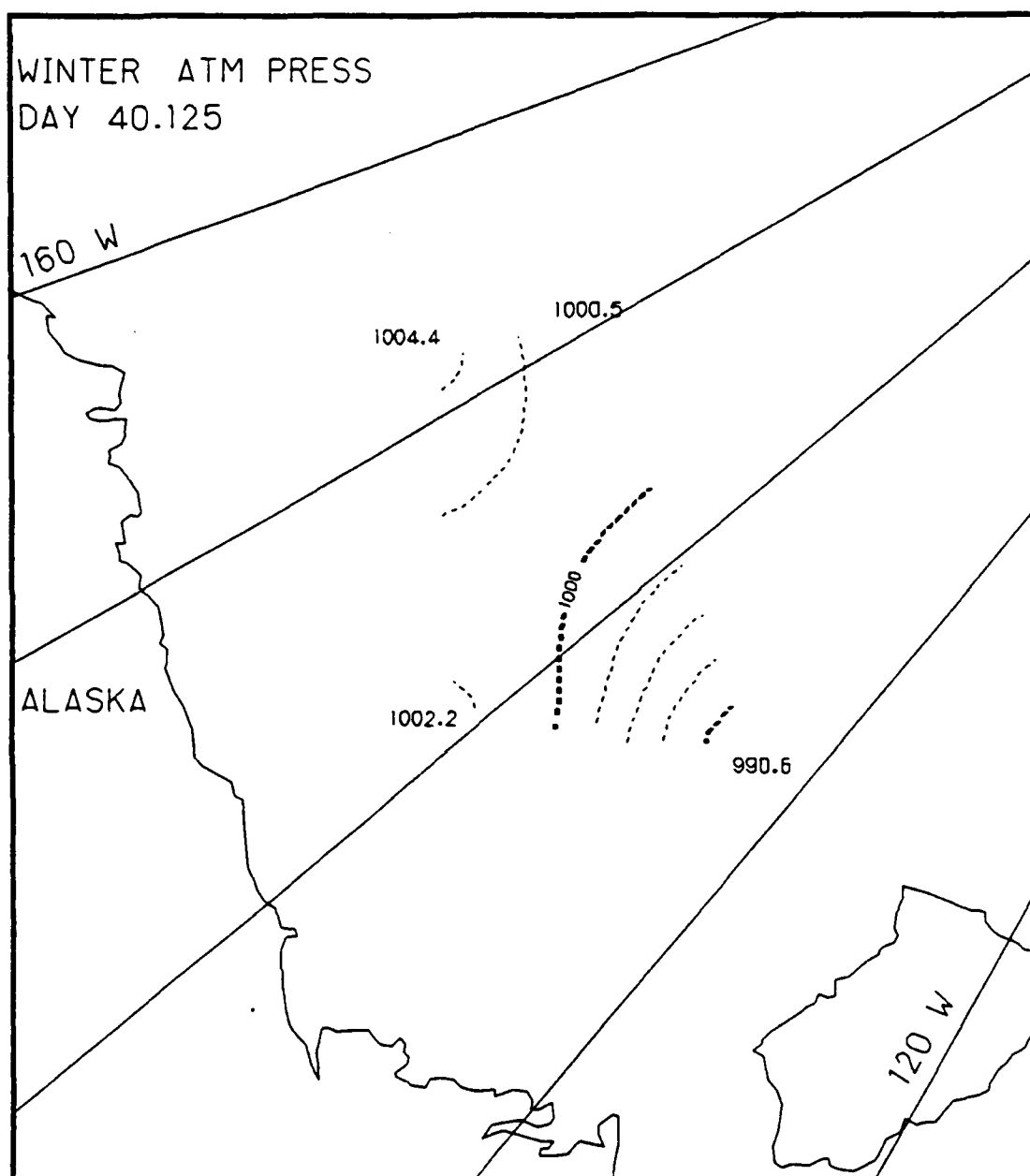


Fig. F.10. Spatial atmospheric pressure variations, day 40.125, based on the AIDJEX data from stations with hydrophones, winter 1976.

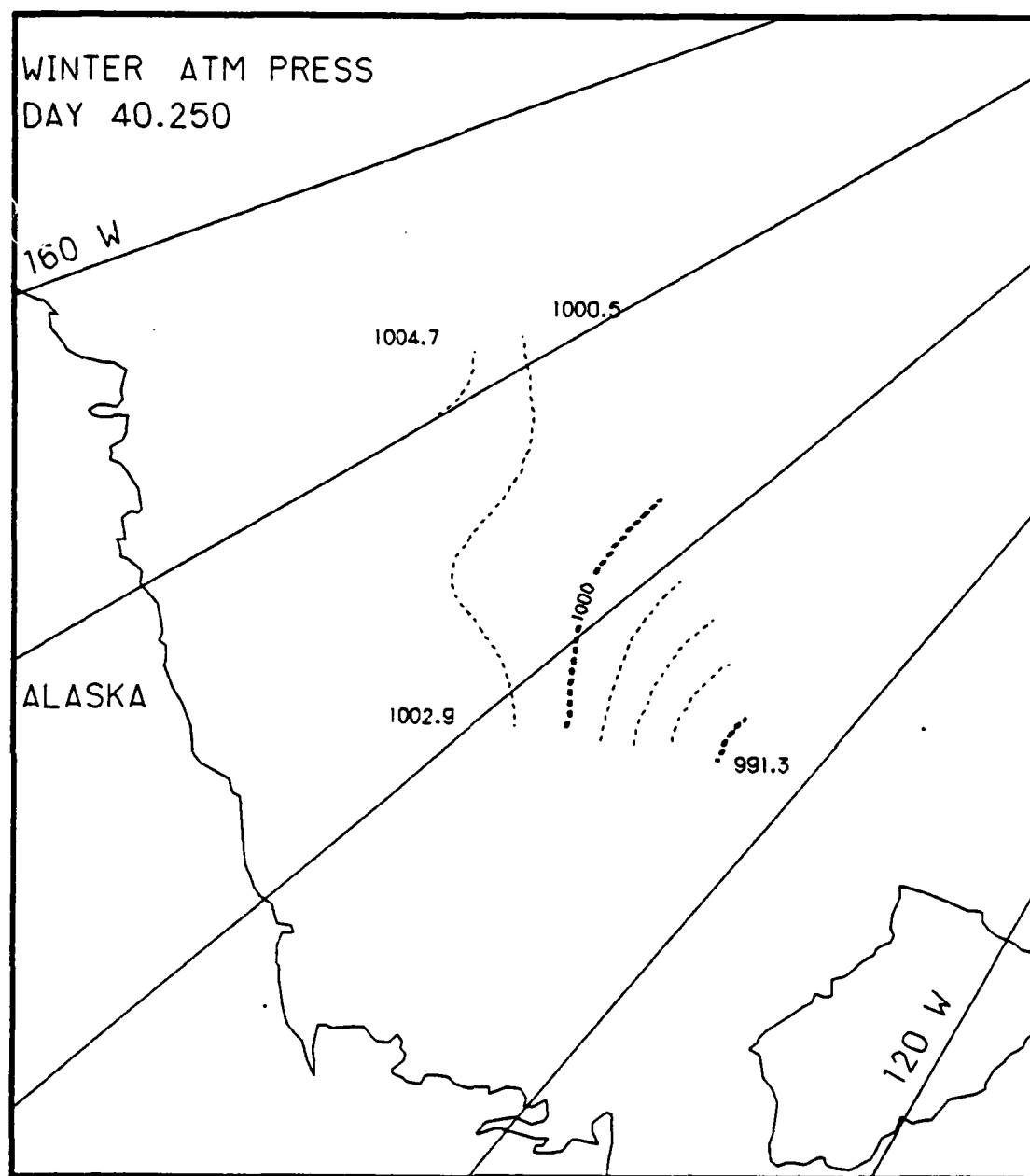


Fig. F.11. Spatial atmospheric pressure variations, day 40.25, based on the AIDJEX data from stations with hydrophones, winter 1976.

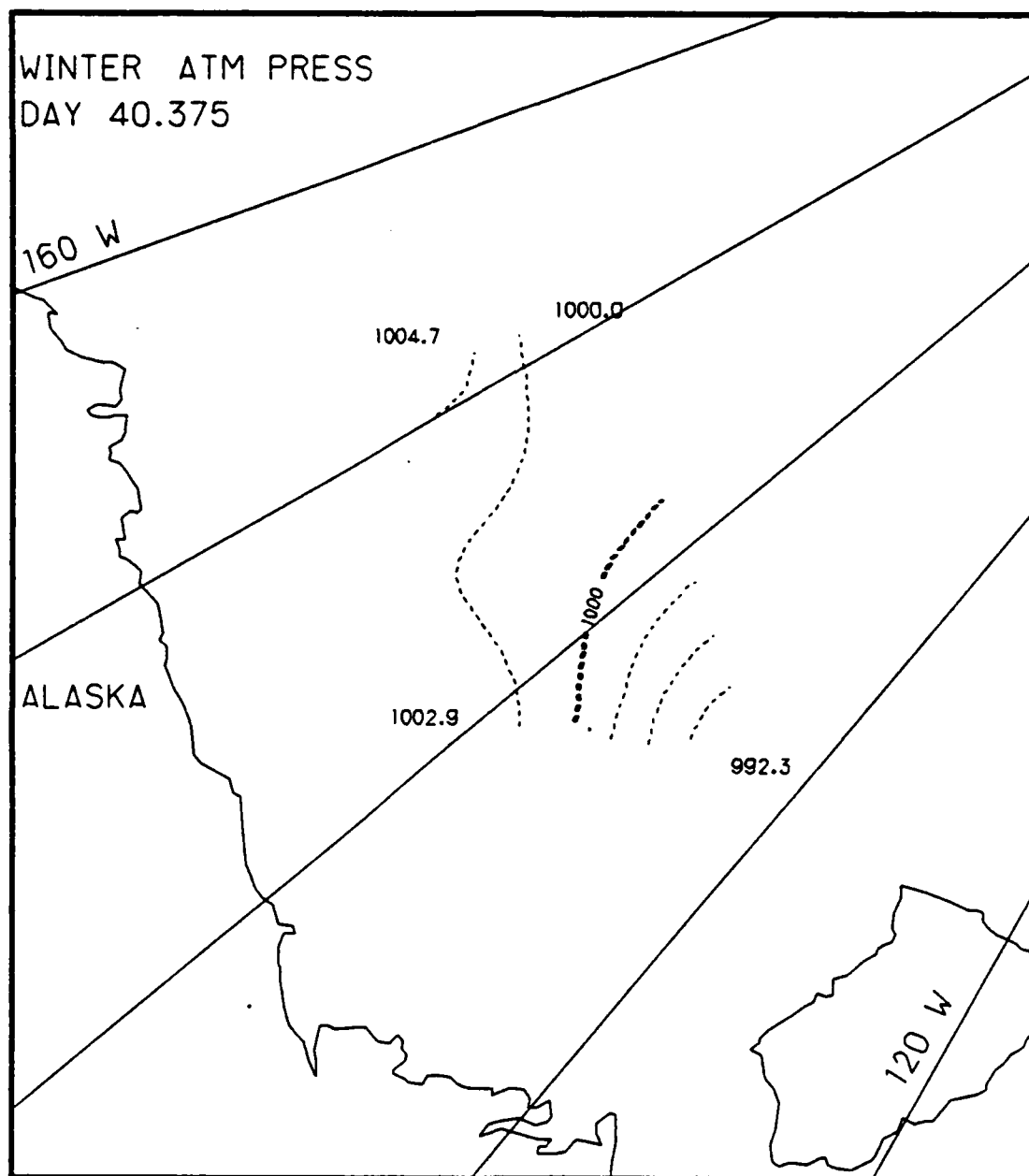


Fig. F.12. Spatial atmospheric pressure variations, day 40.375, based on the AIDJEX data from stations with hydrophones, winter 1976.

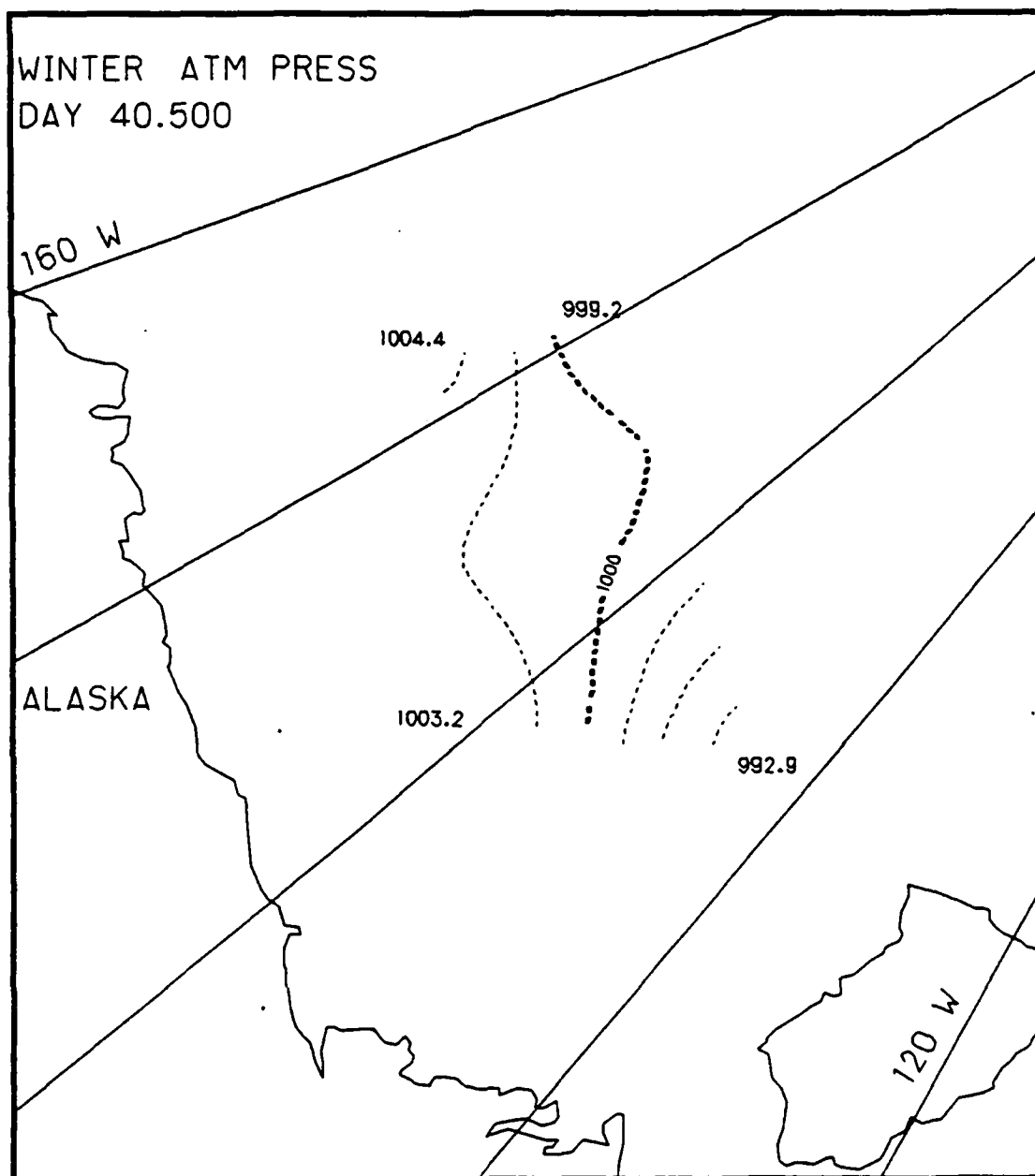


Fig. F.13. Spatial atmospheric pressure variations, day 40.5, based on the AIDJEX data from stations with hydrophones, winter 1976.

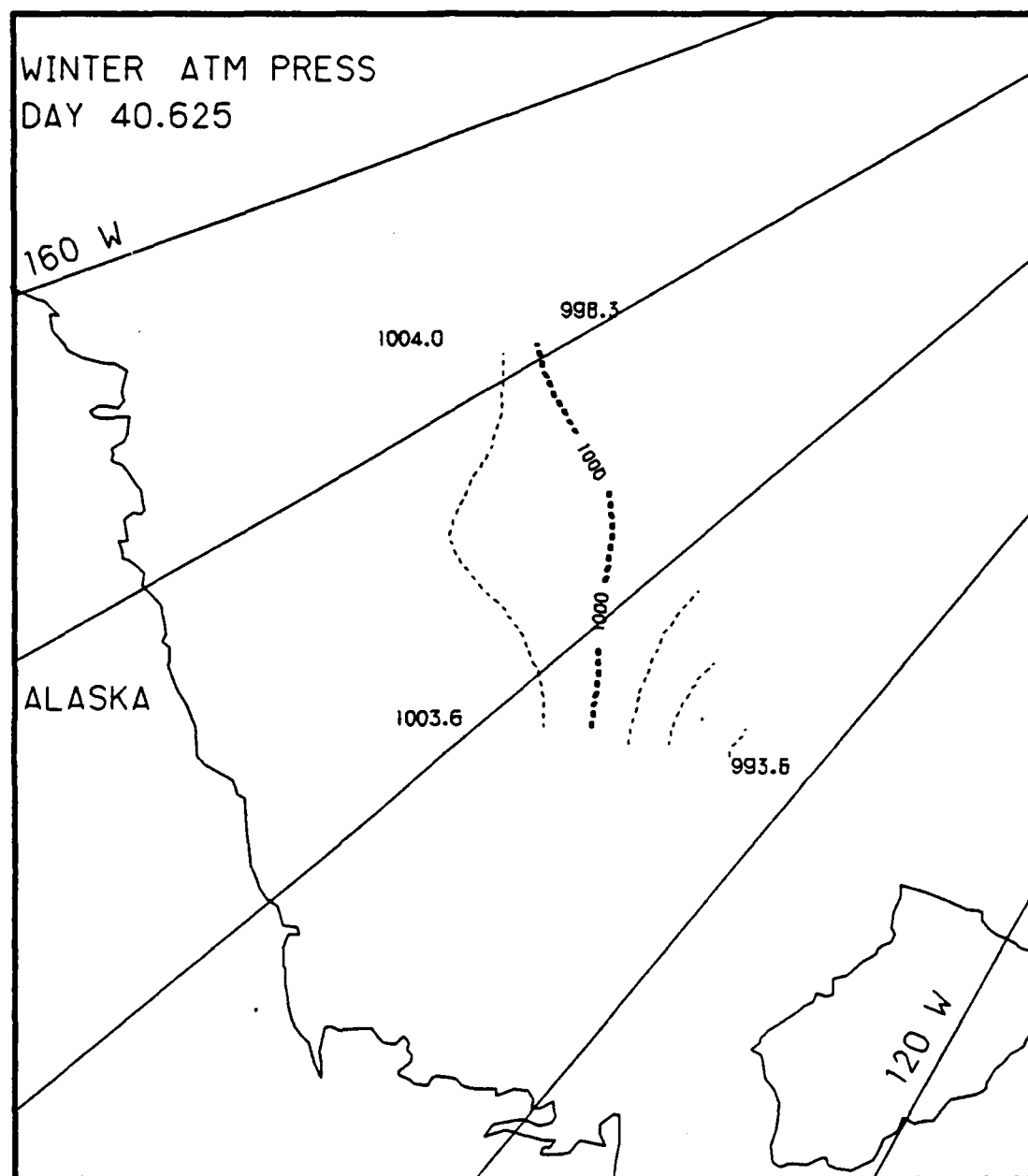


Fig. F.14. Spatial atmospheric pressure variations, day 40.625, based on the AIDJEX data from stations with hydrophones, winter 1976.

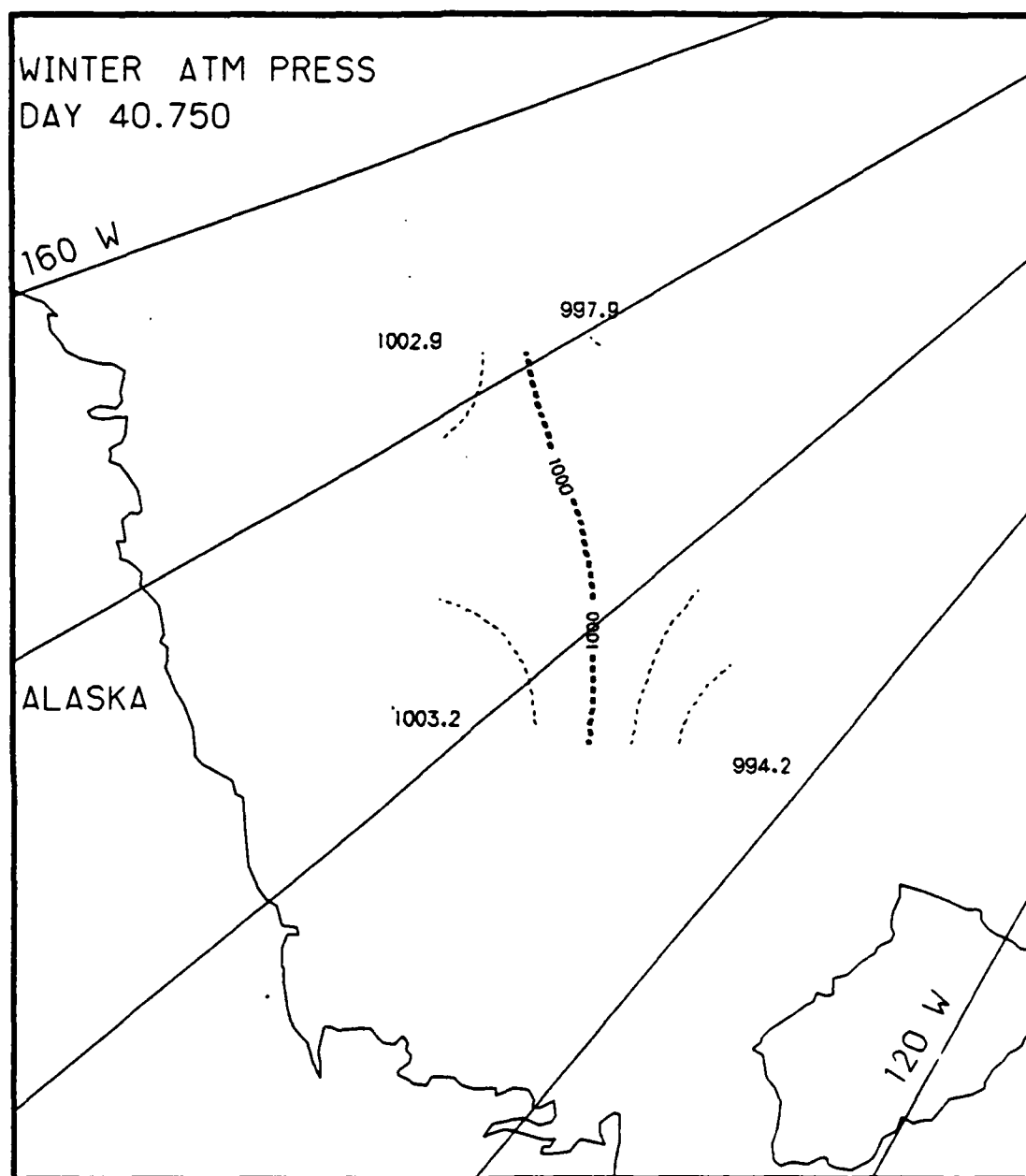


Fig. F.15. Spatial atmospheric pressure variations, day 40.75, based on the AIDJEX data from stations with hydrophones, winter 1976.

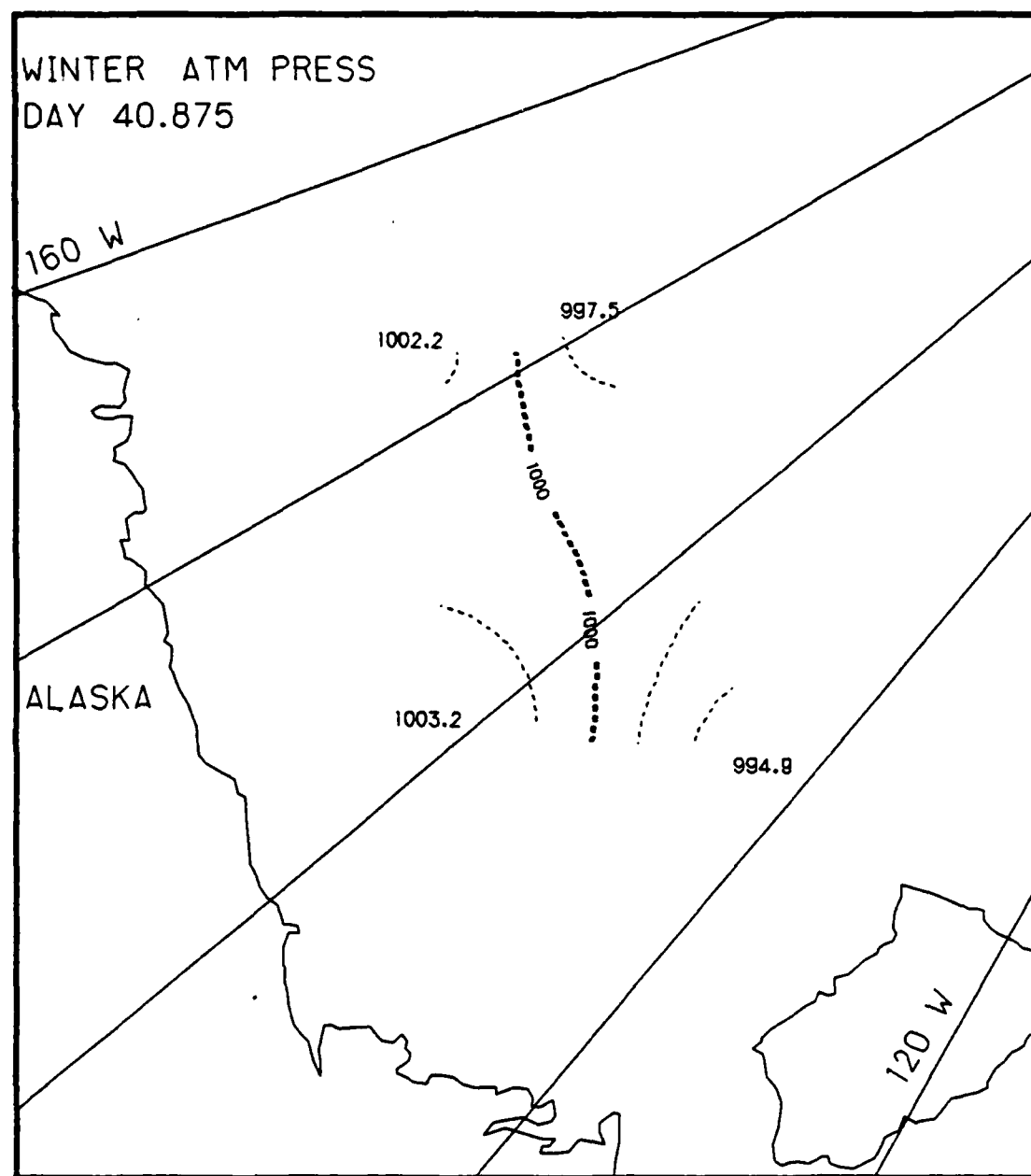


Fig. F.16. Spatial atmospheric pressure variations, day 40.875, based on the AIDJEX data from stations with hydrophones, winter 1976.

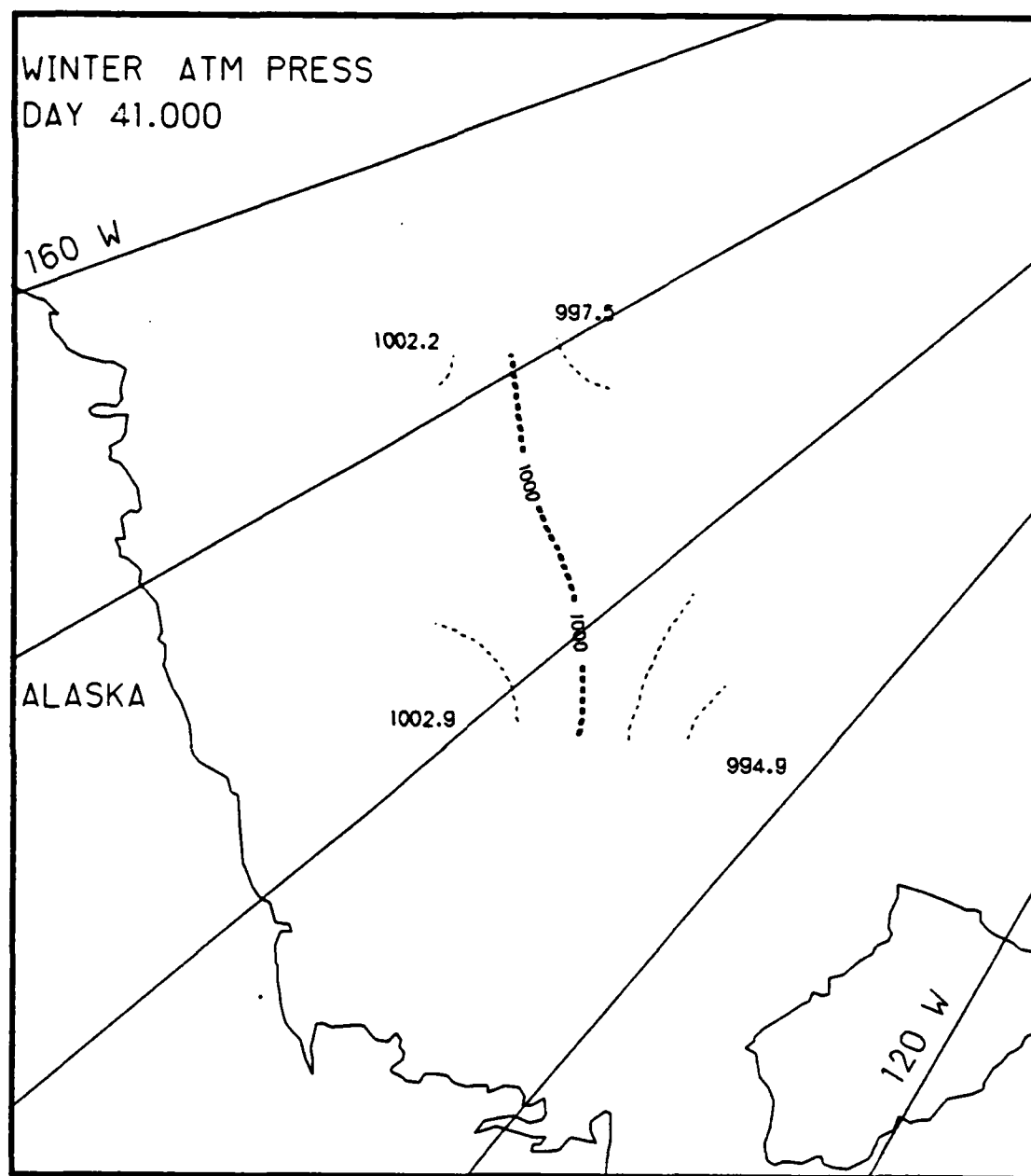


Fig. F.17. Spatial atmospheric pressure variations, day 41.0, based on the AIDJEX data from stations with hydrophones, winter 1976.

Appendix G

Two-Dimensional Contour Maps of Arctic Atmospheric Temperature Variations, 9-10 February 1976 (Winter)

This appendix contains the two-dimensional contour maps of the AIDJEX atmospheric temperature data collected at those stations with hydrophones during the 48 hour period of 9-10 February 1976. The contour maps show the spatial variations of atmospheric temperature ($^{\circ}\text{C}$) at 3 hr intervals.

List of Figures
Appendix G

2-119

	<u>Page</u>
Fig. G.1. Spatial atmospheric temperature variations, day 39.0	2-120
Fig. G.2. Spatial atmospheric temperature variations, day 39.125	2-121
Fig. G.3. Spatial atmospheric temperature variations, day 39.25	2-122
Fig. G.4. Spatial atmospheric temperature variations, day 39.375	2-123
Fig. G.5. Spatial atmospheric temperature variations, day 39.5	2-124
Fig. G.6. Spatial atmospheric temperature variations, day 39.625	2-125
Fig. G.7. Spatial atmospheric temperature variations, day 39.75	2-126
Fig. G.8. Spatial atmospheric temperature variations, day 39.875	2-127
Fig. G.9. Spatial atmospheric temperature variations, day 40.0	2-128
Fig. G.10. Spatial atmospheric temperature variations, day 40.125	2-129
Fig. G.11. Spatial atmospheric temperature variations, day 40.25	2-130
Fig. G.12. Spatial atmospheric temperature variations, day 40.375	2-131
Fig. G.13. Spatial atmospheric temperature variations, day 40.5	2-132
Fig. G.14. Spatial atmospheric temperature variations, day 40.625	2-133
Fig. G.15. Spatial atmospheric temperature variations, day 40.75	2-134
Fig. G.16. Spatial atmospheric temperature variations, day 40.875	2-135
Fig. G.17. Spatial atmospheric temperature variations, day 41.0	2-136

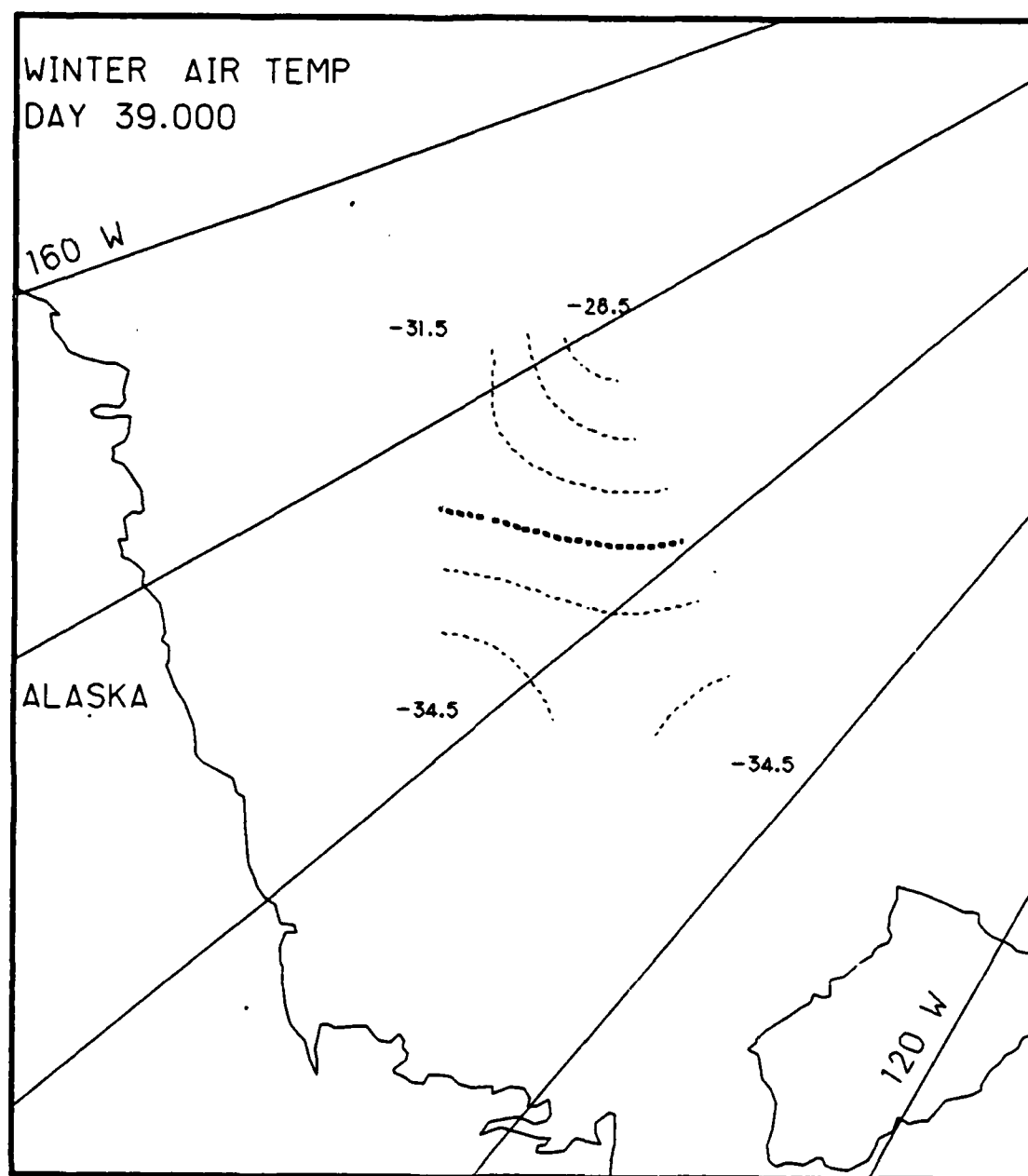


Fig. G.1. Spatial atmospheric temperature variations, day 39.0, based on the AIDJEX data from stations with hydrophones, winter 1976.

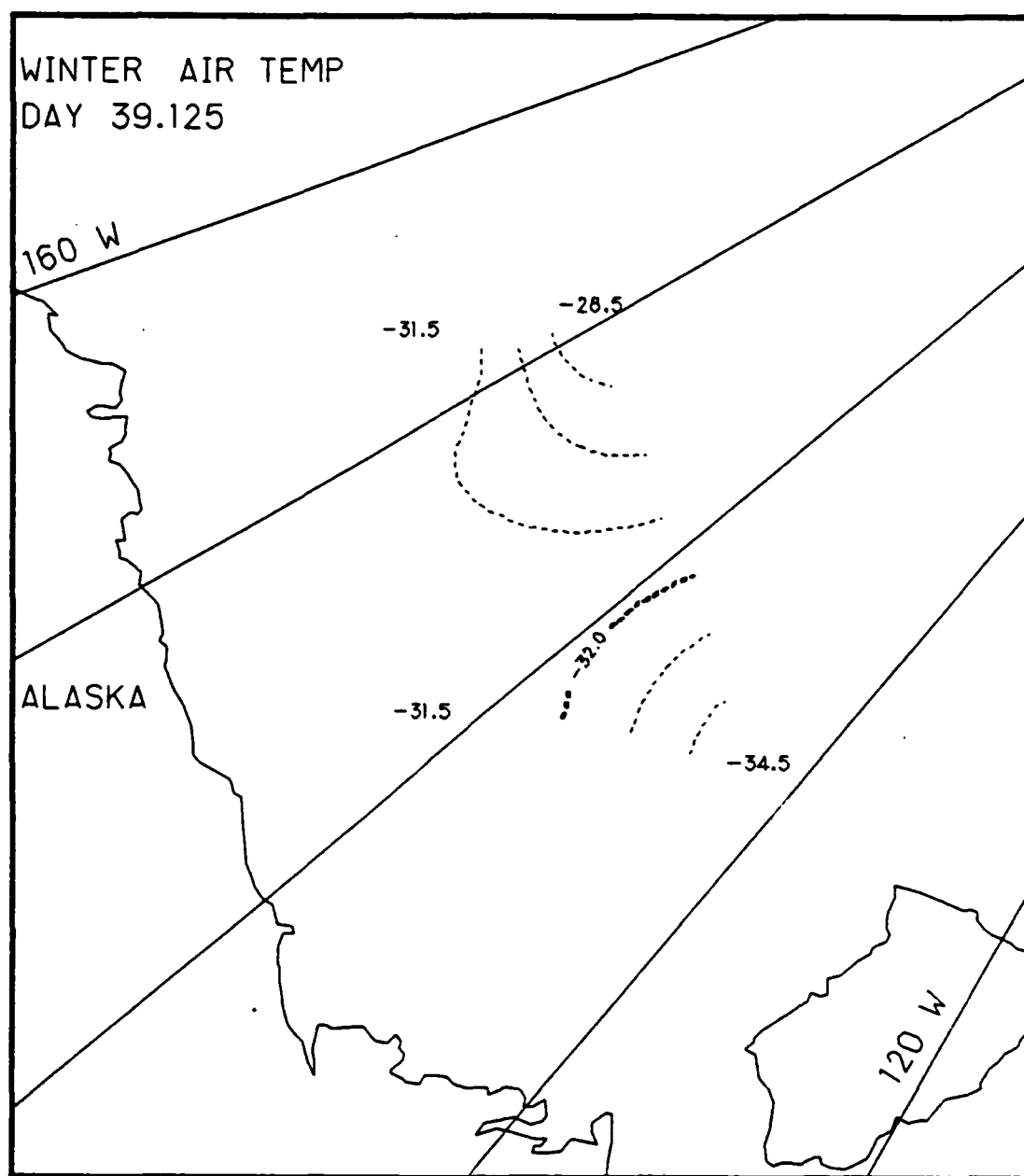


Fig. G.2. Spatial atmospheric temperature variations, day 39.125, based on the AIDJEX data from stations with hydrophones, winter 1976.

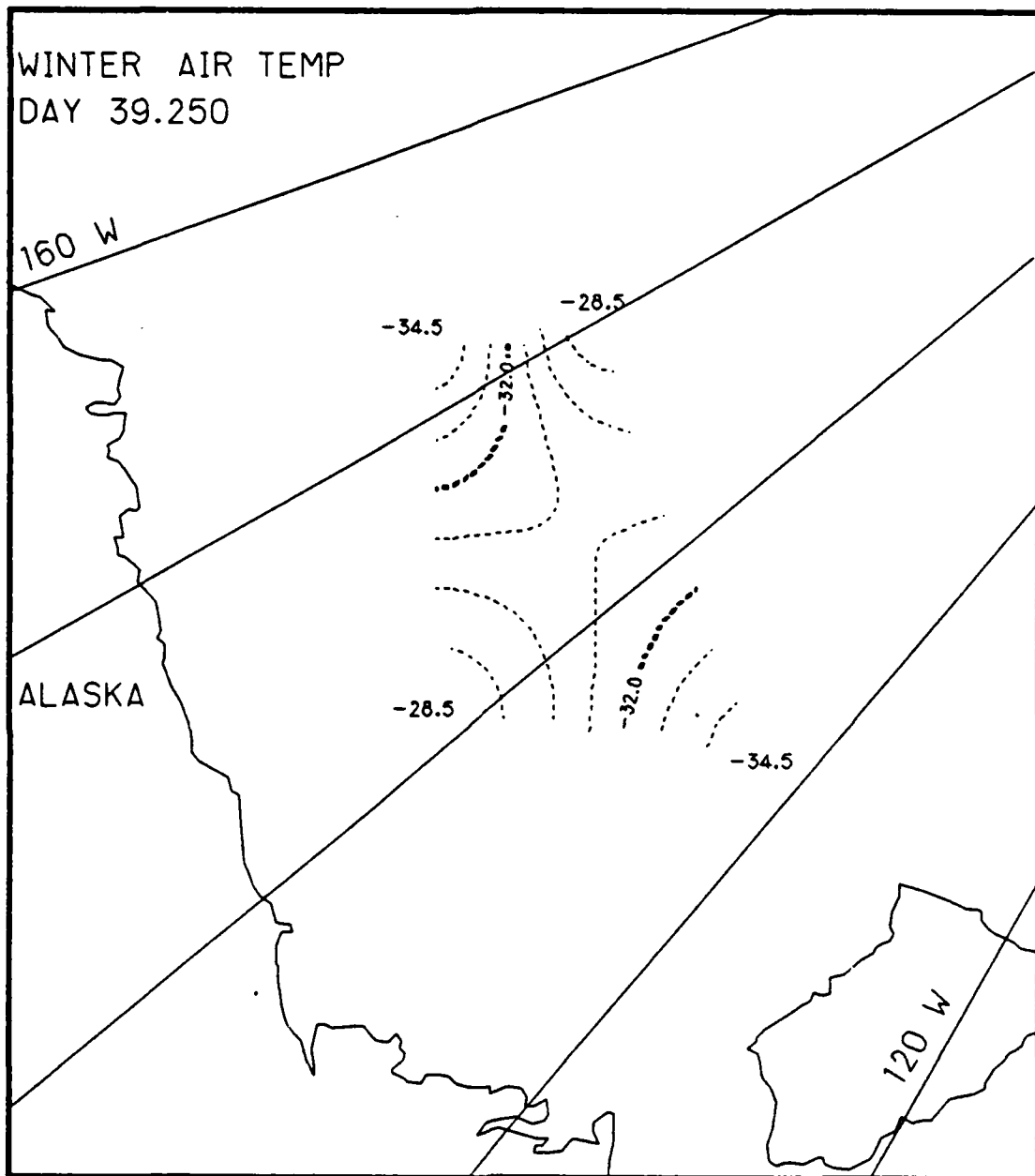


Fig. G.3. Spatial atmospheric temperature variations, day 39.25, based on the AIDJEX data from stations with hydrophones, winter 1976.

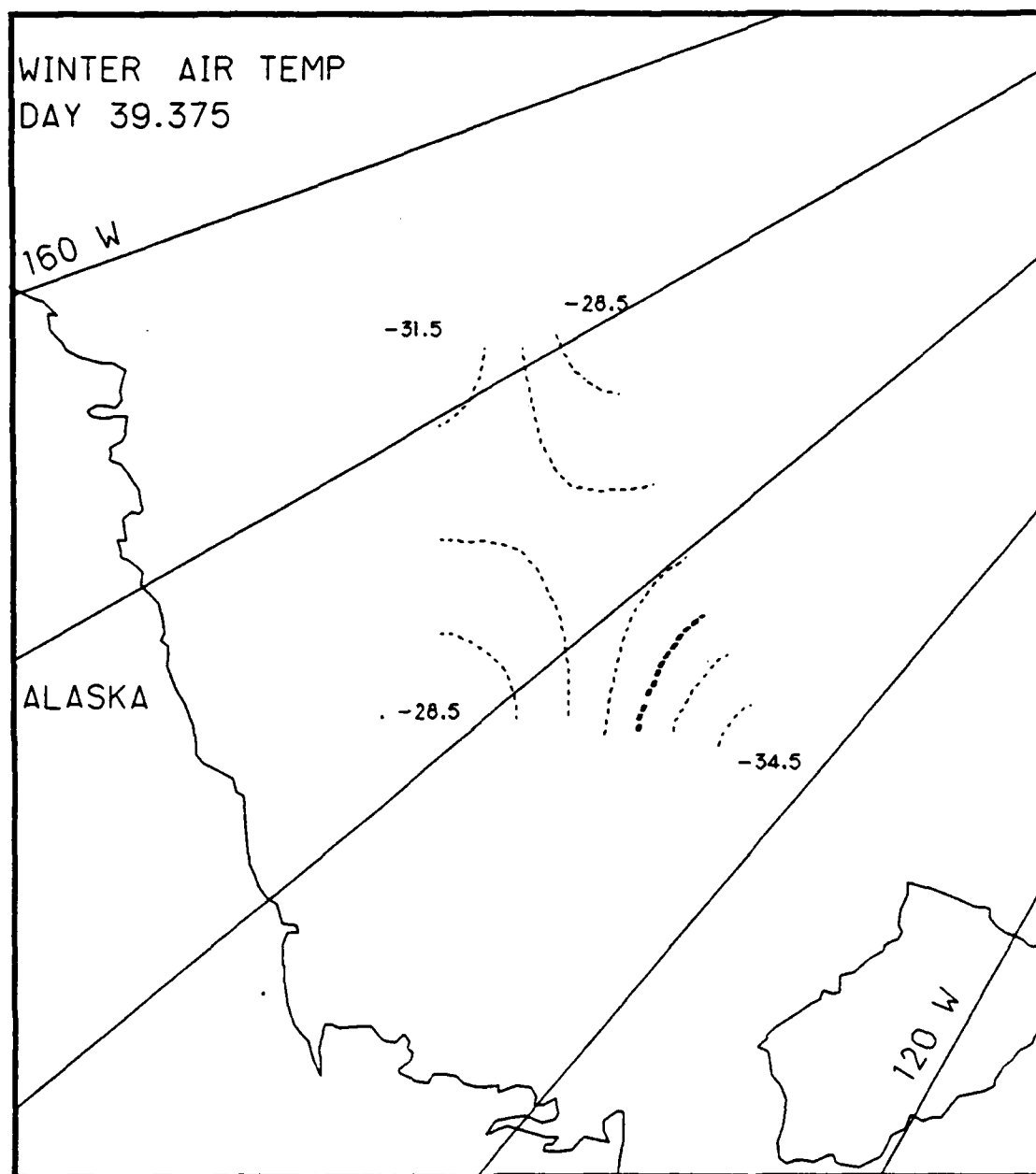


Fig. G.4. Spatial atmospheric temperature variations, day 39.375, based on the AIDJEX data from stations with hydrophones, winter 1976.

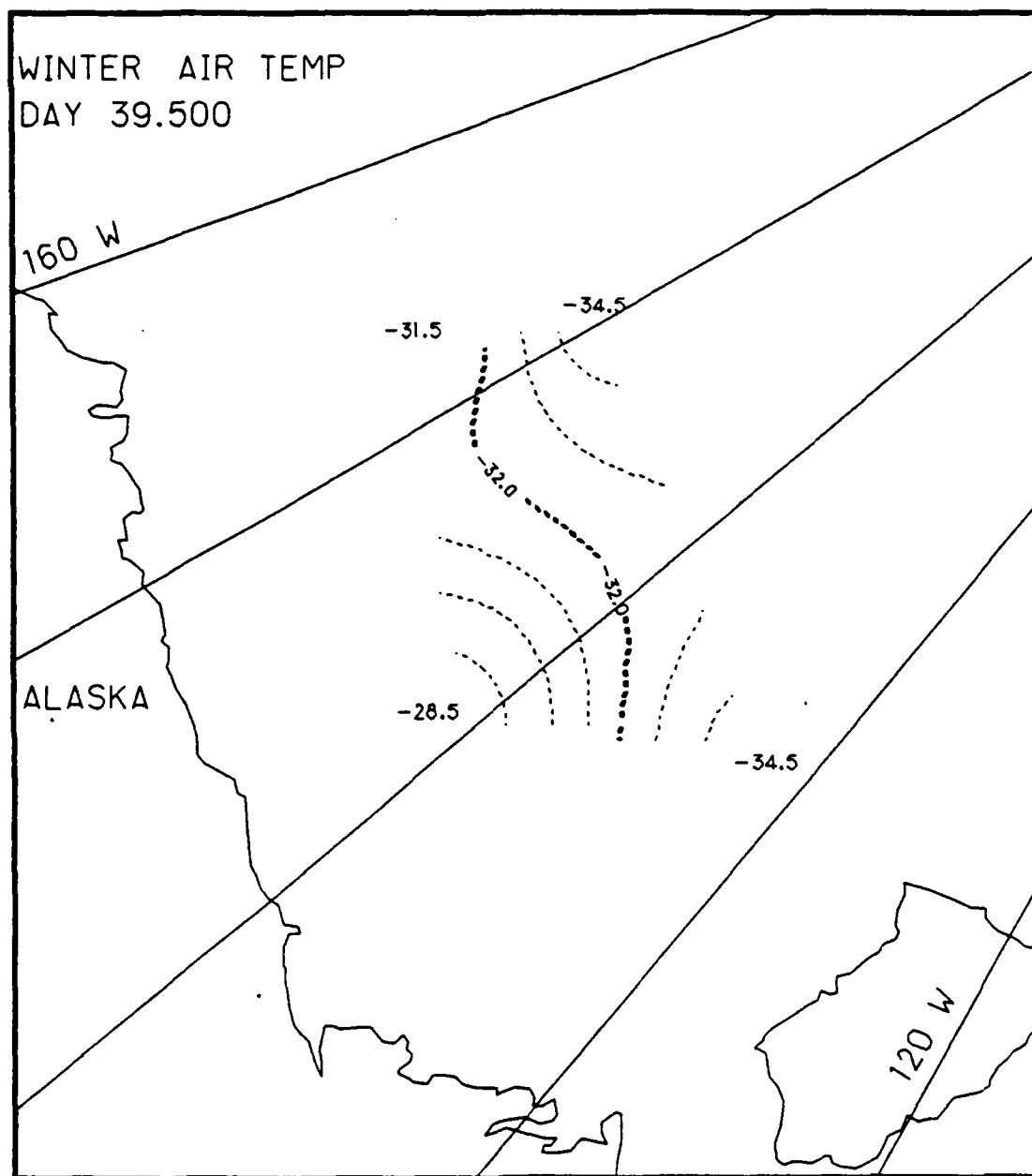


Fig. G.5. Spatial atmospheric temperature variations, day 39.5, based on the AIDJEX data from stations with hydrophones, winter 1976.

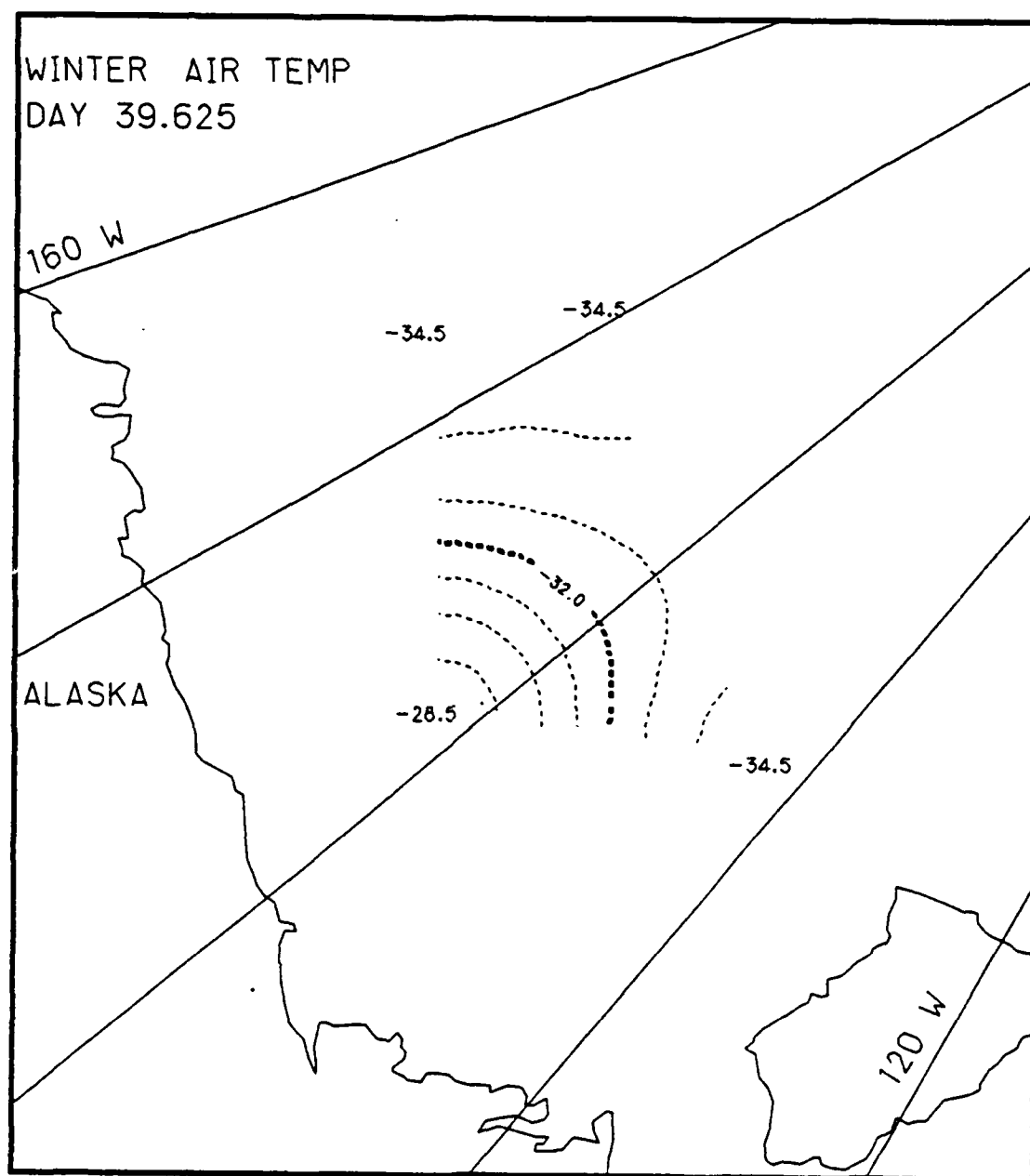


Fig. G.6. Spatial atmospheric temperature variations, day 39.625, based on the AIDJEX data from stations with hydrophones, winter 1976.

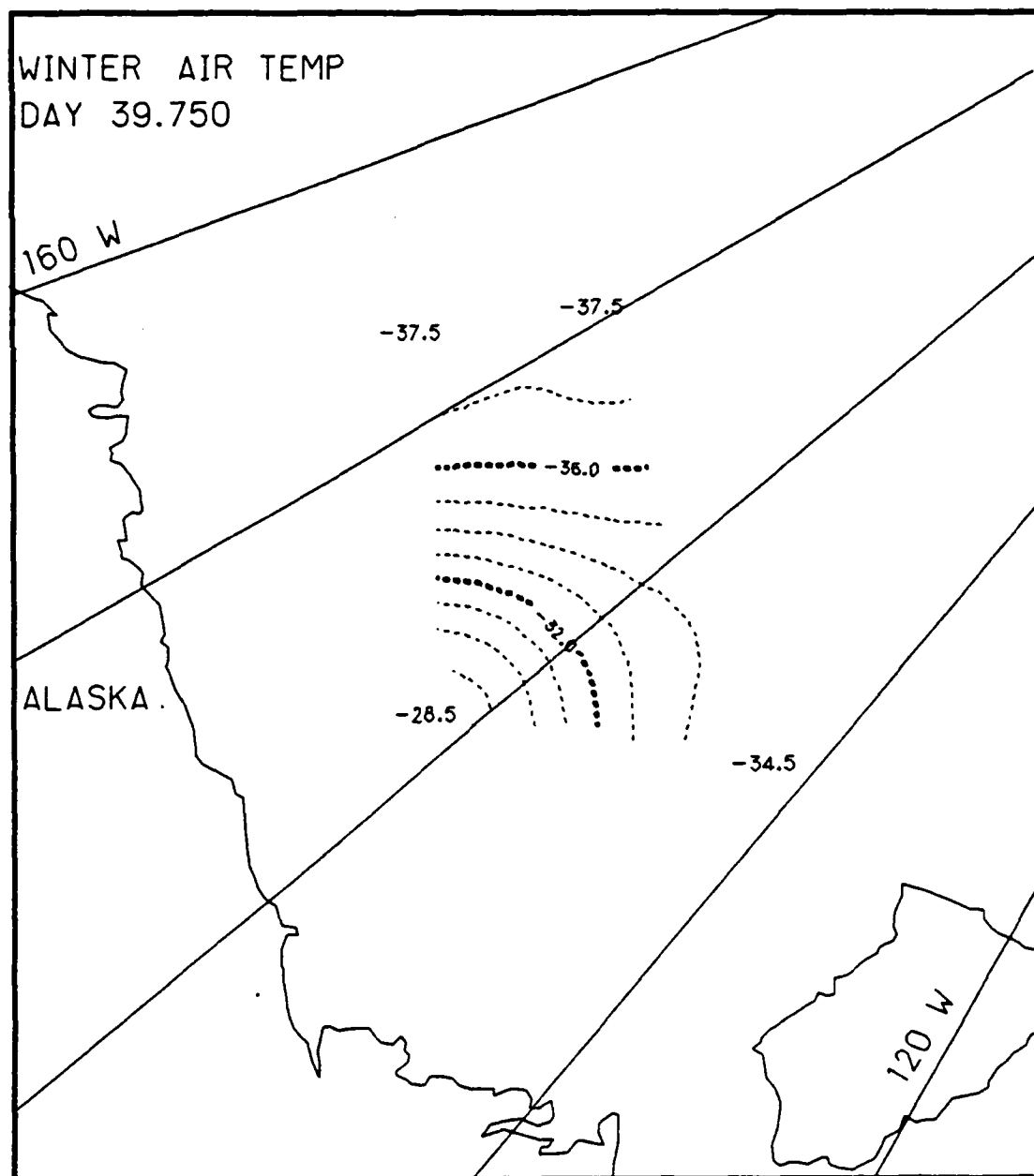


Fig. G.7. Spatial atmospheric temperature variations, day 39.75, based on the AIDJEX data from stations with hydrophones, winter 1976.

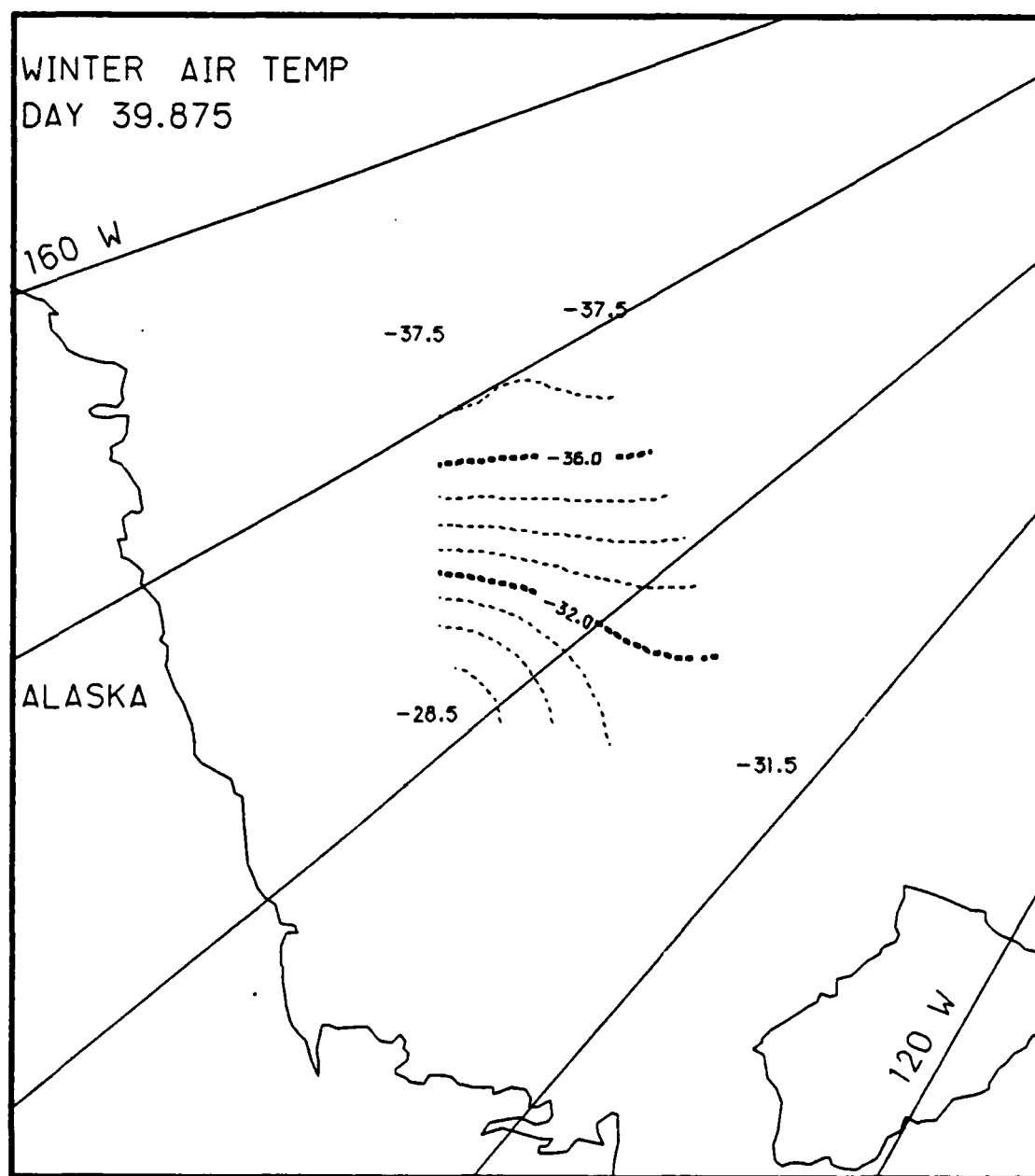


Fig. G.8. Spatial atmospheric temperature variations, day 39.875, based on the AIDJEX data from stations with hydrophones, winter 1976.

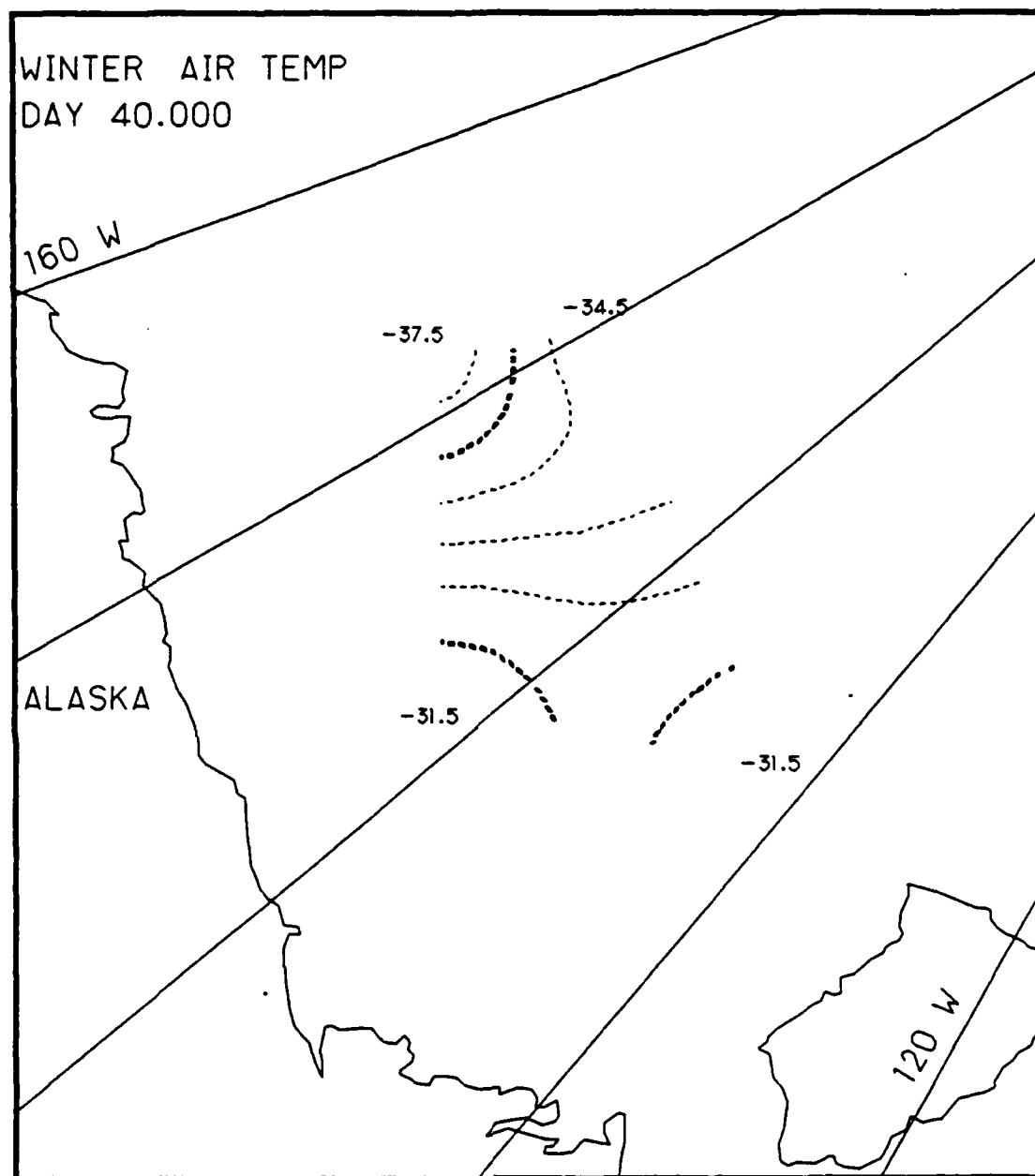


Fig. G.9. Spatial atmospheric temperature variations, day 40.0, based on the AIDJEX data from stations with hydrophones, winter 1976.

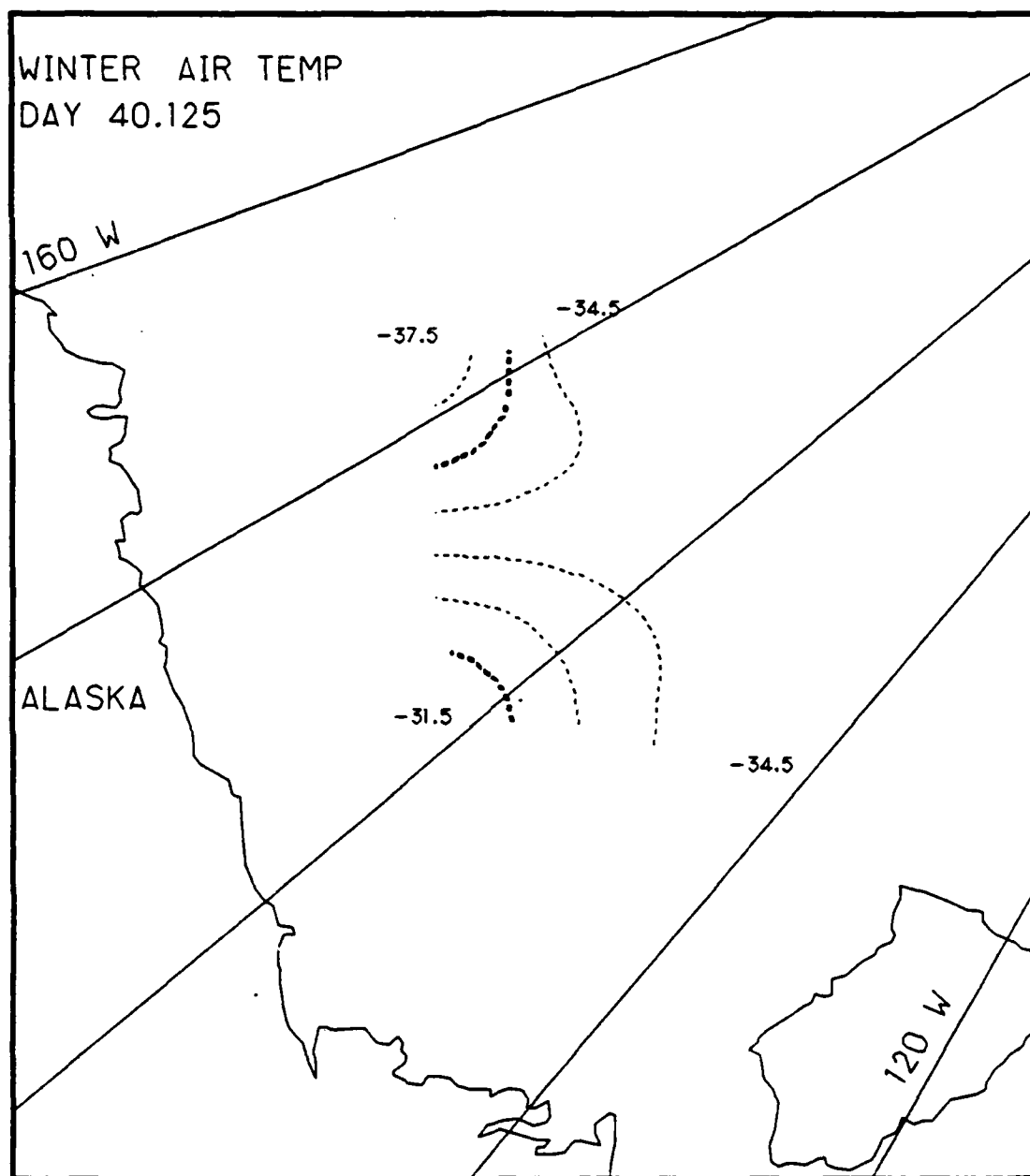


Fig. G.10. Spatial atmospheric temperature variations, day 40.125, based on the AIDJEX data from stations with hydrophones, winter 1976.

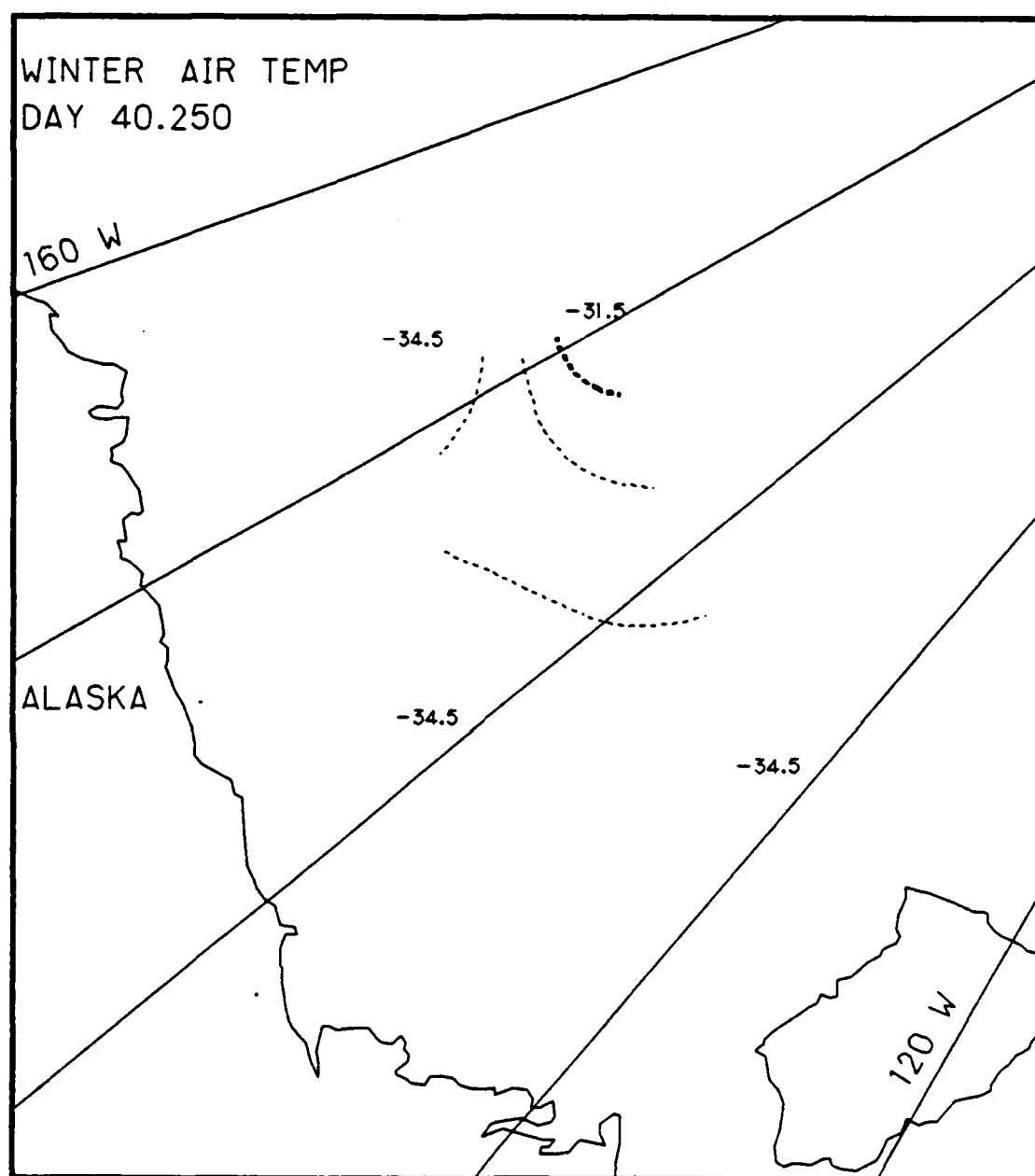


Fig. G.11. Spatial atmospheric temperature variations, day 40.25, based on the AIDJEX data from stations with hydrophones, winter 1976.

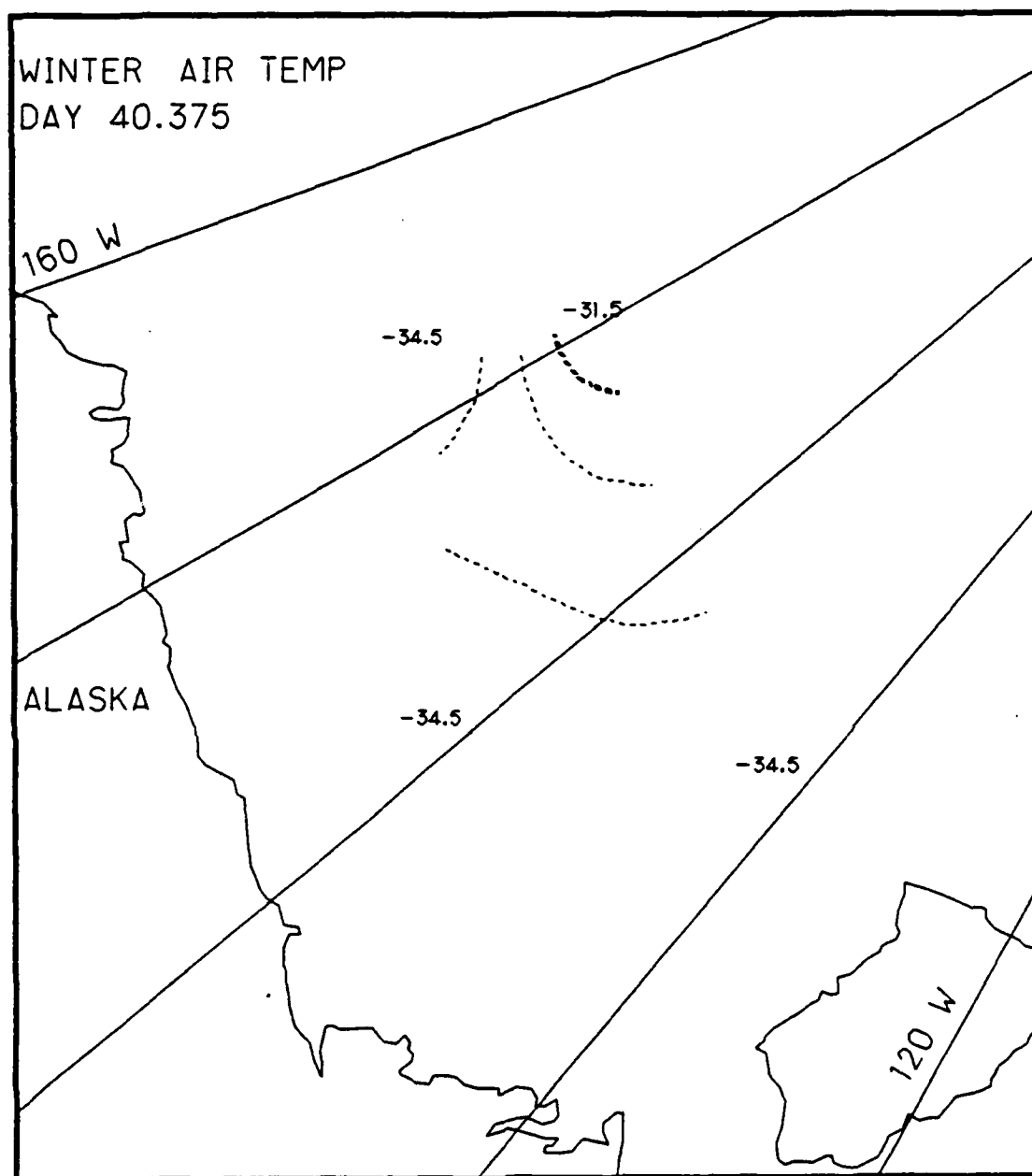


Fig. G.12. Spatial atmospheric temperature variations, day 40.375, based on the AIDJEX data from stations with hydrophones, winter 1976.

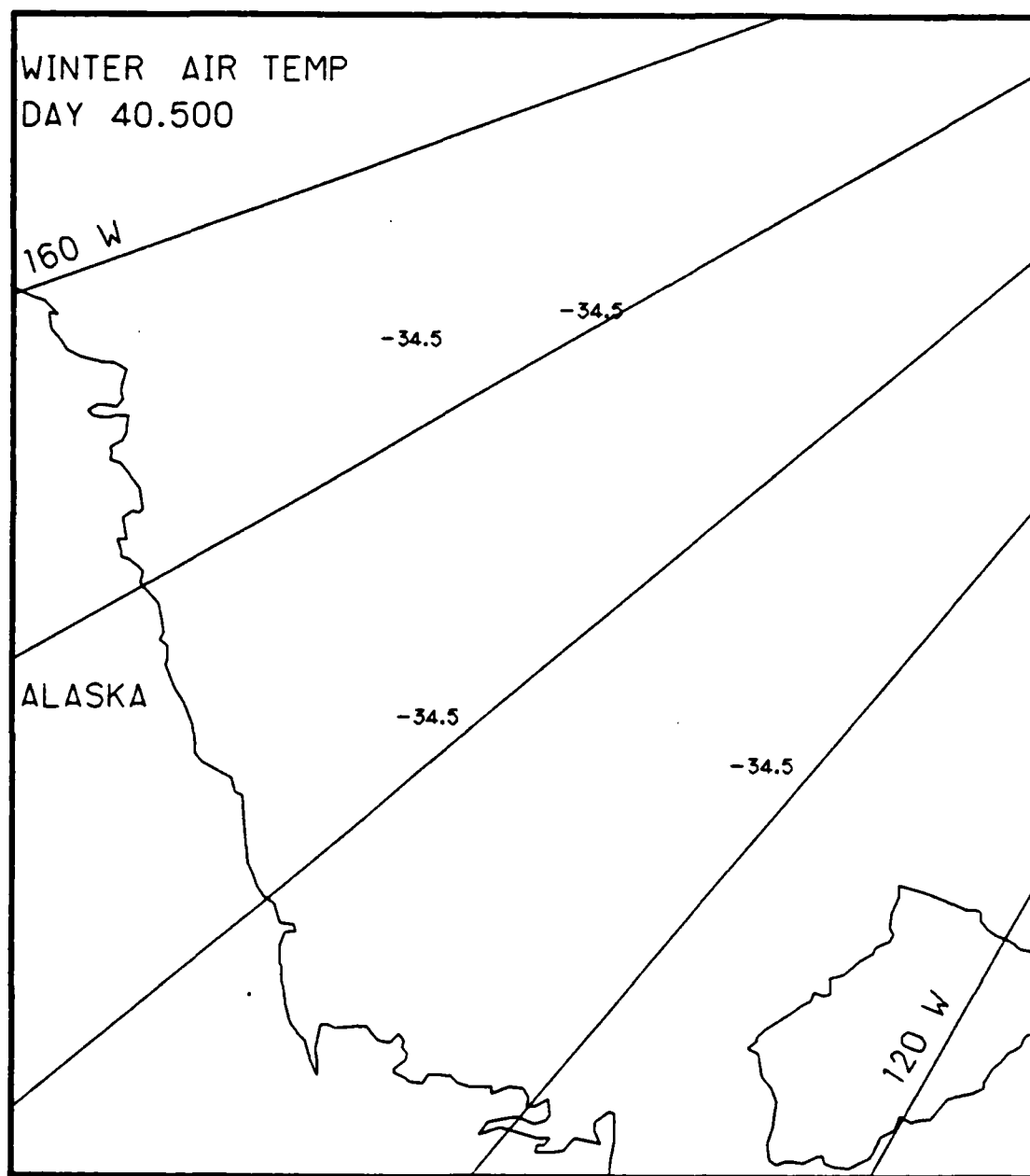


Fig. G.13. Spatial atmospheric temperature variations, day 40.5, based on the AIDJEX data from stations with hydrophones, winter 1976.

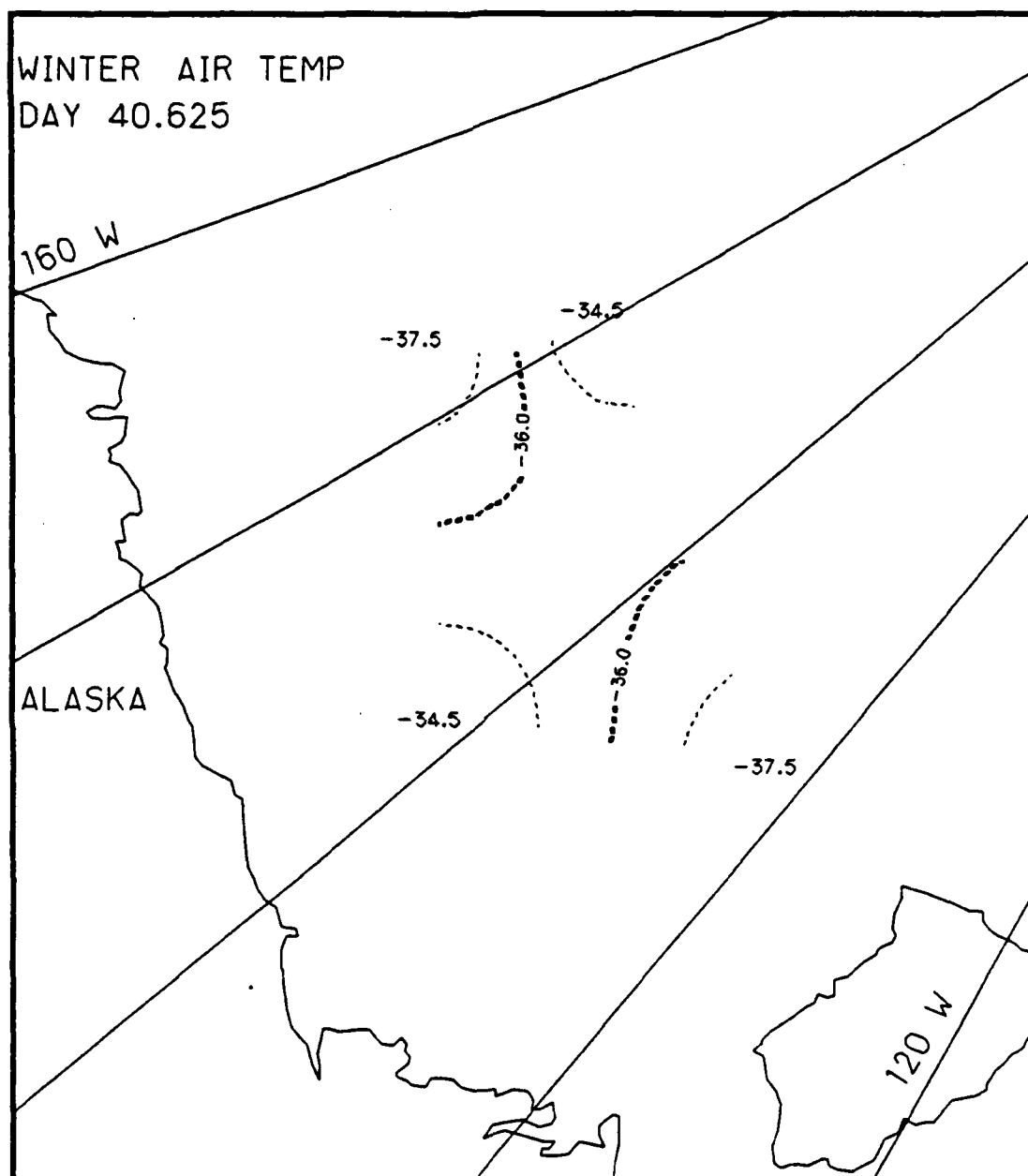


Fig. G.14. Spatial atmospheric temperature variations, day 40.625, based on the AIDJEX data from stations with hydrophones, winter 1976.

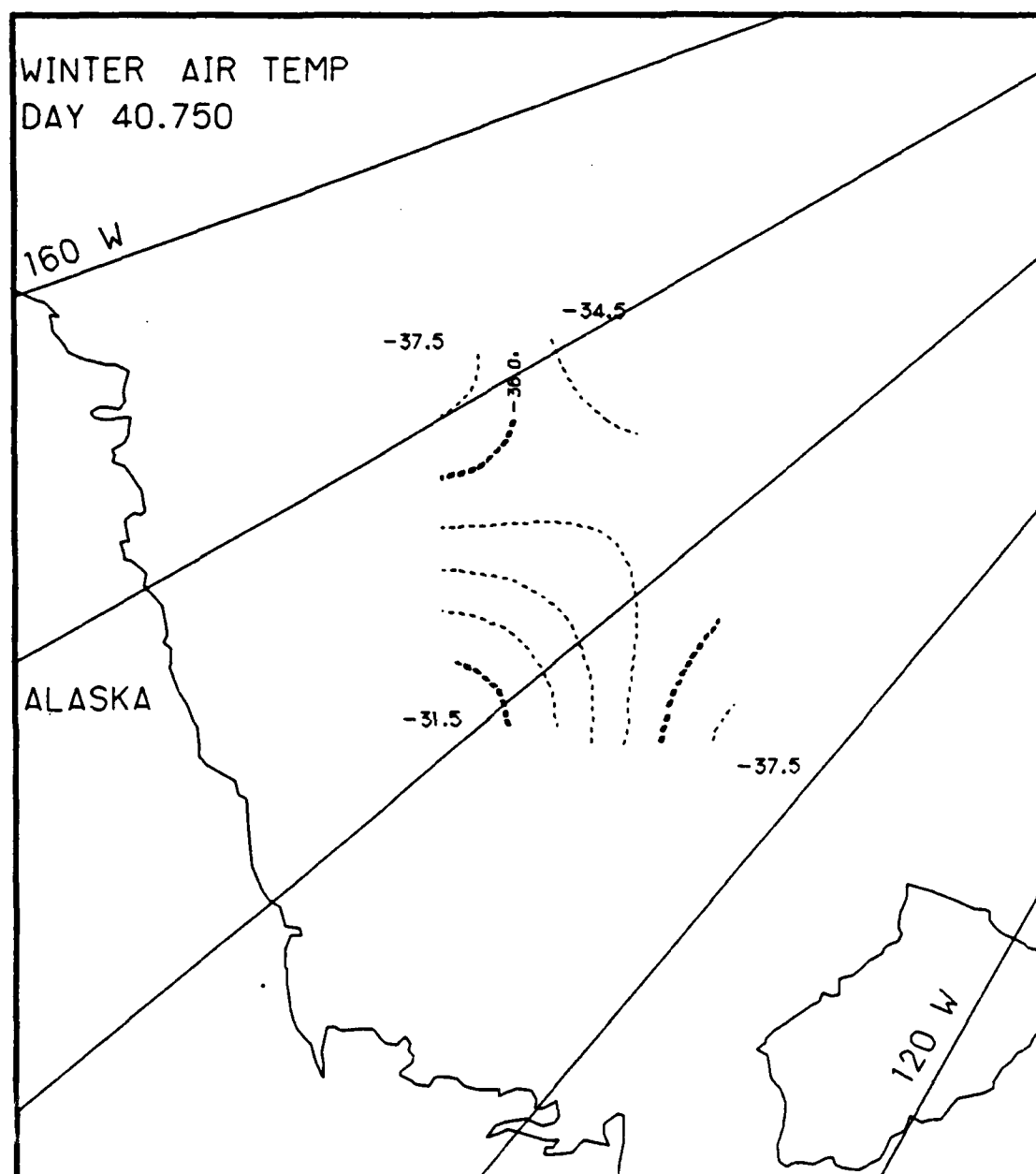


Fig. G.15. Spatial atmospheric temperature variations, day 40.75, based on the AIDJEX data from stations with hydrophones, winter 1976.

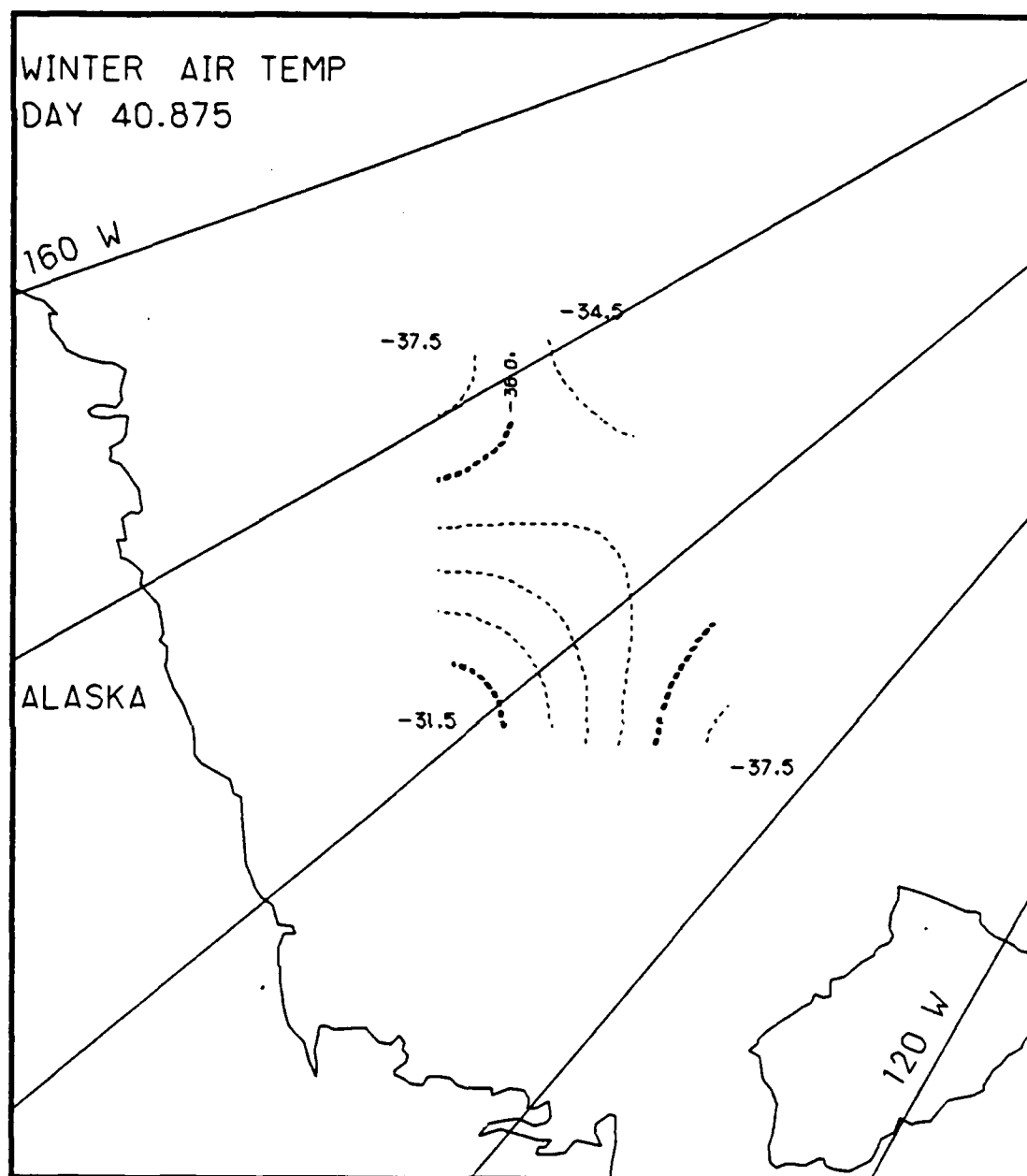


Fig. G.16. Spatial atmospheric temperature variations, day 40.875, based on the AIDJEX data from stations with hydrophones, winter 1976.

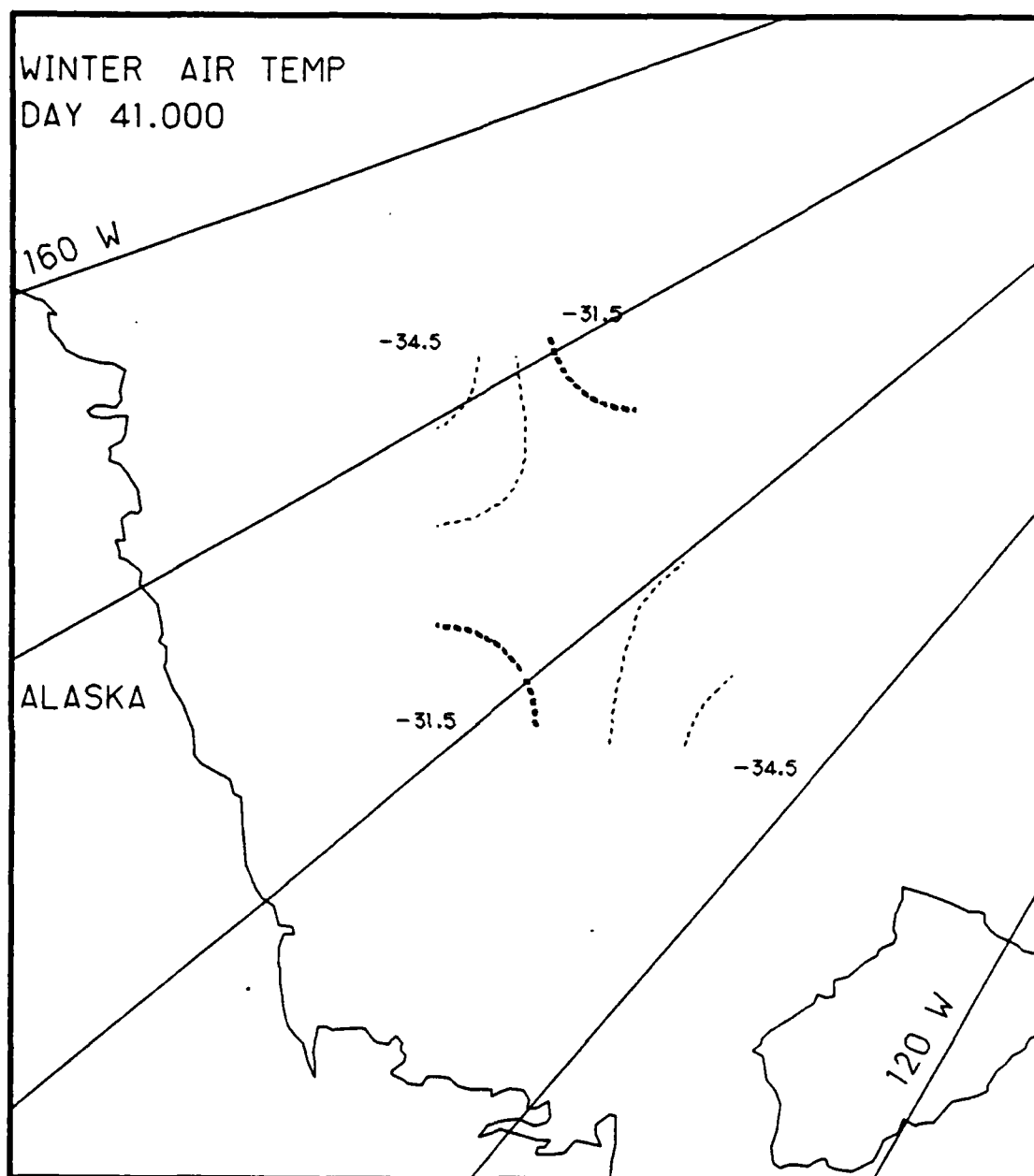


Fig. G.17. Spatial atmospheric temperature variations, day 41.0, based on the AIDJEX data from stations with hydrophones, winter 1976.

Appendix H

Two-Dimensional Contour Maps of Arctic Atmospheric Pressure Variations, 21-22 February 1976 (Winter)

This appendix contains the two-dimensional contour maps of the AIDJEX atmospheric pressure data collected at those stations with hydrophones during the 48 hour period of 21-22 February 1976. The contour maps show the spatial variations of atmospheric pressure (millibars) at 3 hr intervals.

List of Figures
Appendix H

2-138

	<u>Page</u>
Fig. H.1. Spatial atmospheric pressure variations, day 51.0	2-139
Fig. H.2. Spatial atmospheric pressure variations, day 51.125	2-140
Fig. H.3. Spatial atmospheric pressure variations, day 51.25	2-141
Fig. H.4. Spatial atmospheric pressure variations, day 51.375	2-142
Fig. H.5. Spatial atmospheric pressure variations, day 51.5	2-143
Fig. H.6. Spatial atmospheric pressure variations, day 51.625	2-144
Fig. H.7. Spatial atmospheric pressure variations, day 51.75	2-145
Fig. H.8. Spatial atmospheric pressure variations, day 51.875	2-146
Fig. H.9. Spatial atmospheric pressure variations, day 52.0	2-147
Fig. H.10. Spatial atmospheric pressure variations, day 52.125	2-148
Fig. H.11. Spatial atmospheric pressure variations, day 52.25	2-149
Fig. H.12. Spatial atmospheric pressure variations, day 52.375	2-150
Fig. H.13. Spatial atmospheric pressure variations, day 52.5	2-151
Fig. H.14. Spatial atmospheric pressure variations, day 52.625	2-152
Fig. H.15. Spatial atmospheric pressure variations, day 52.75	2-153
Fig. H.16. Spatial atmospheric pressure variations, day 52.875	2-154
Fig. H.17. Spatial atmospheric pressure variations, day 53.0	2-155

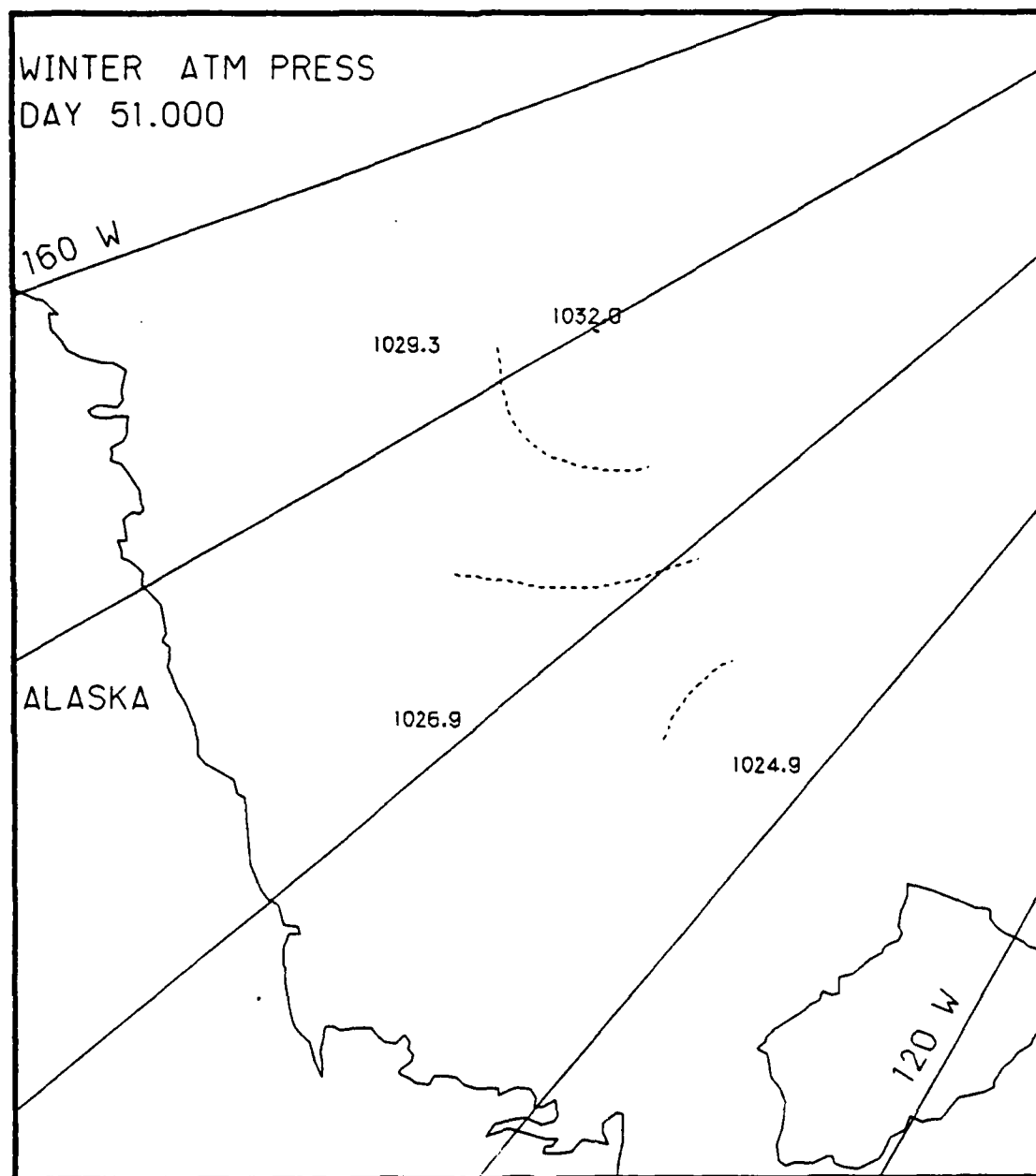


Fig. H.1. Spatial atmospheric pressure variations, day 51.0, based on the AIDJEX data from stations with hydrophones, winter 1976.

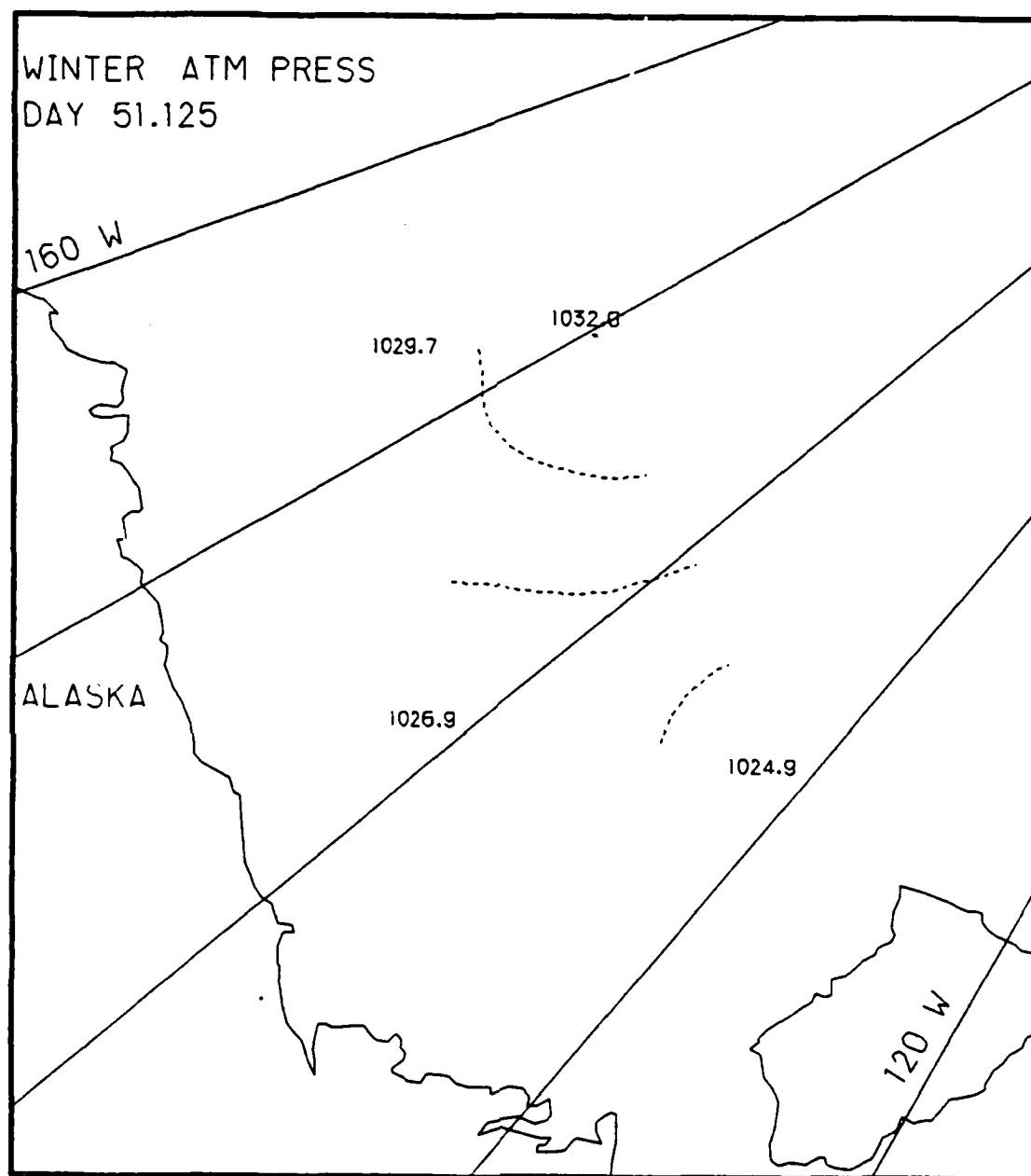


Fig. H.2. Spatial atmospheric pressure variations, day 51.125, based on the AIDJEX data from stations with hydrophones, winter 1976.

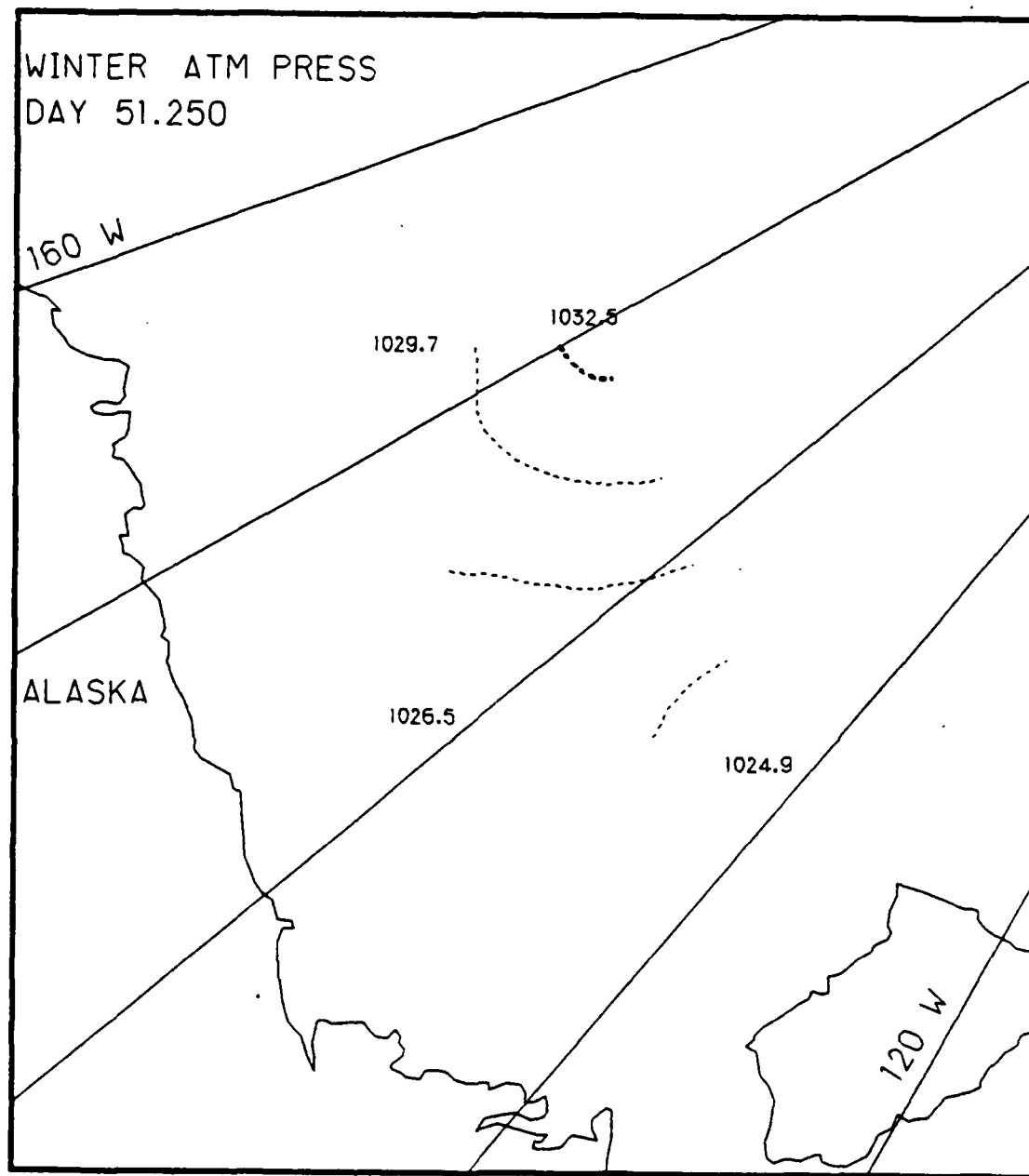


Fig. H.3. Spatial atmospheric pressure variations, day 51.25, based on the AIDJEX data from stations with hydrophones, winter 1976.

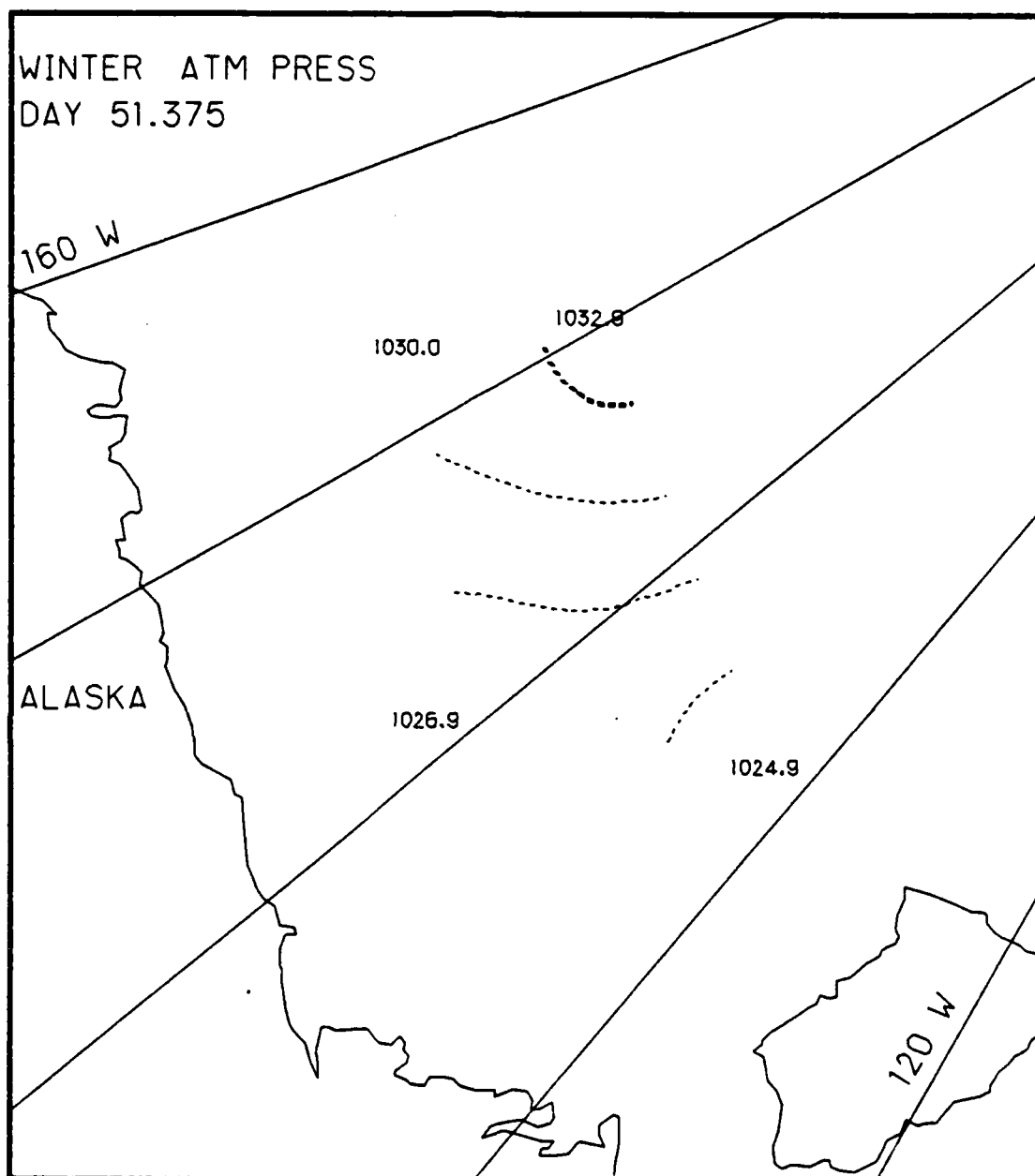


Fig. H.4. Spatial atmospheric pressure variations, day 51.375, based on the AIDJEX data from stations with hydrophones, winter 1976.

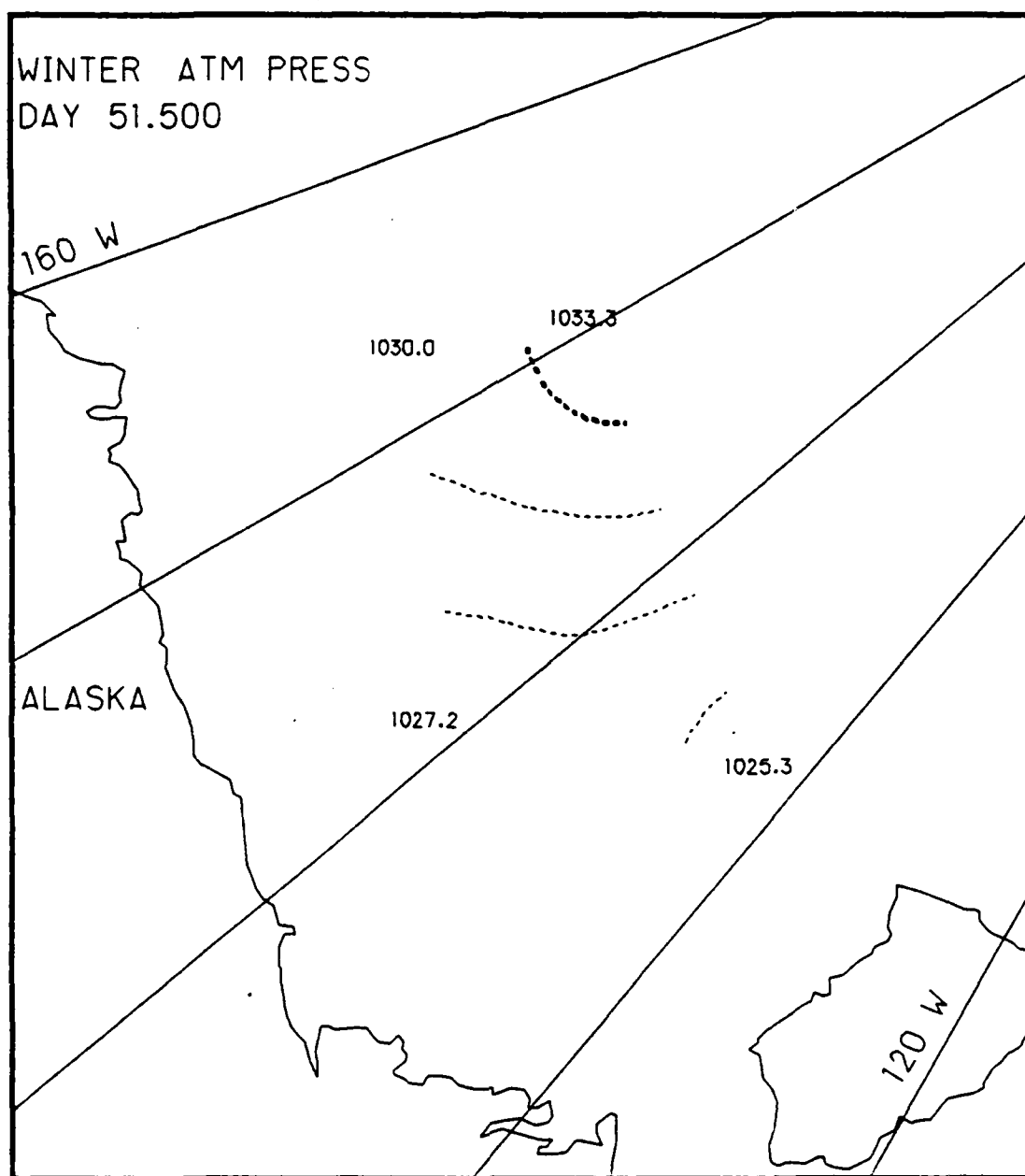


Fig. H.5. Spatial atmospheric pressure variations, day 51.5, based on the AIDJEX data from stations with hydrophones, winter 1976.

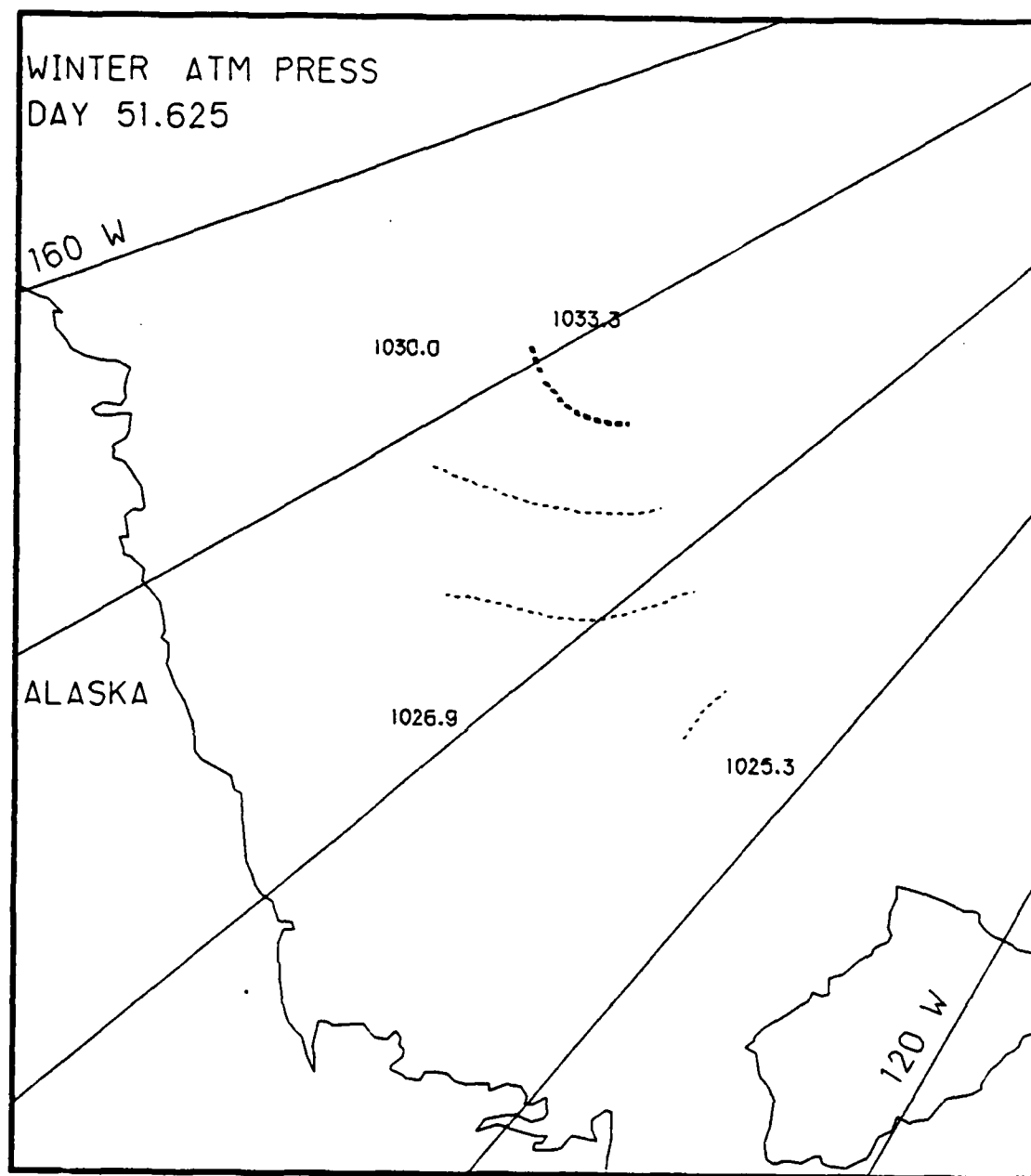


Fig. H.6. Spatial atmospheric pressure variations, day 51.625, based on the AIDJEX data from stations with hydrophones, winter 1976.

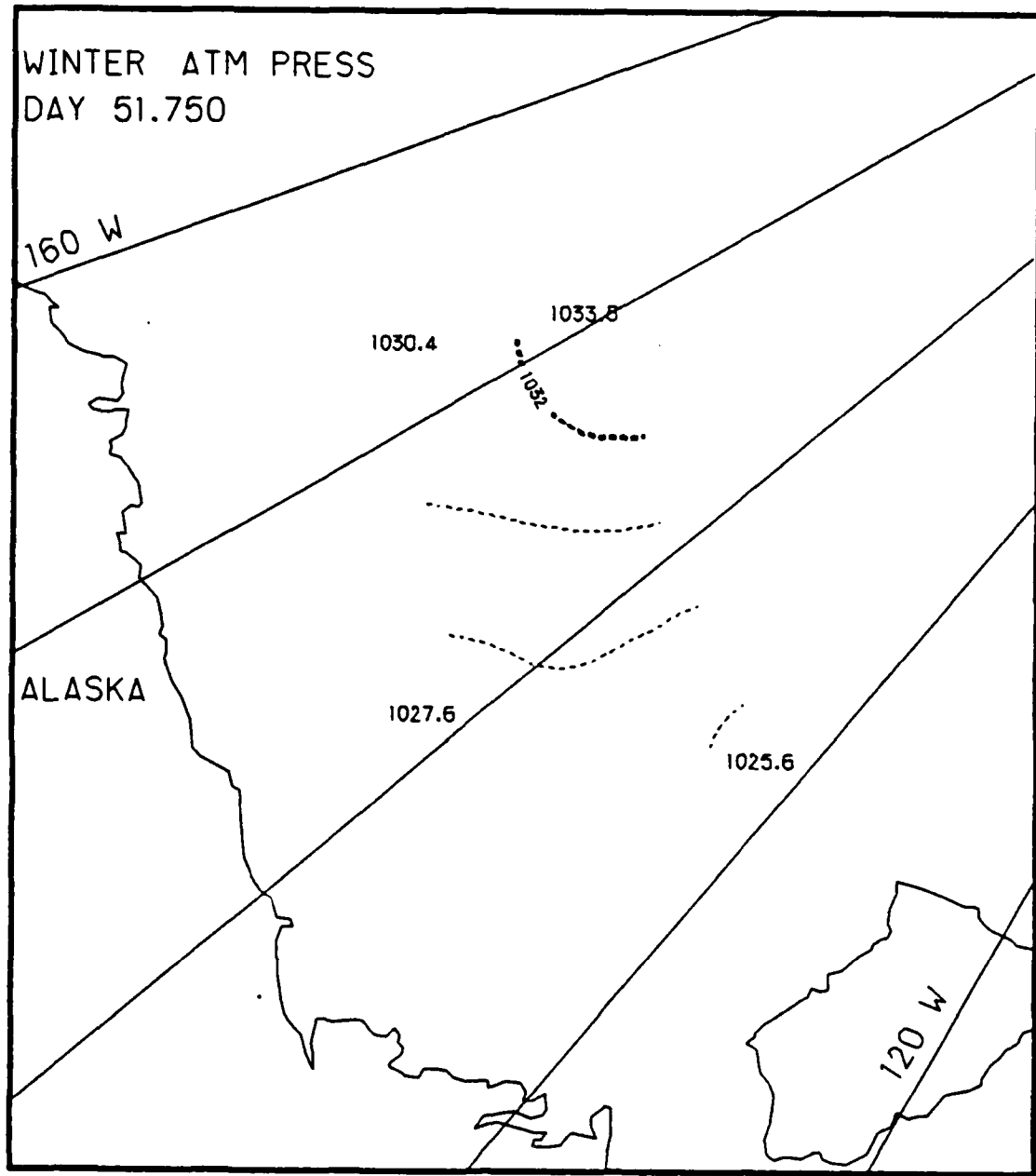


Fig. H.7. Spatial atmospheric pressure variations, day 51.75, based on the AIDJEX data from stations with hydrophones, winter 1976.

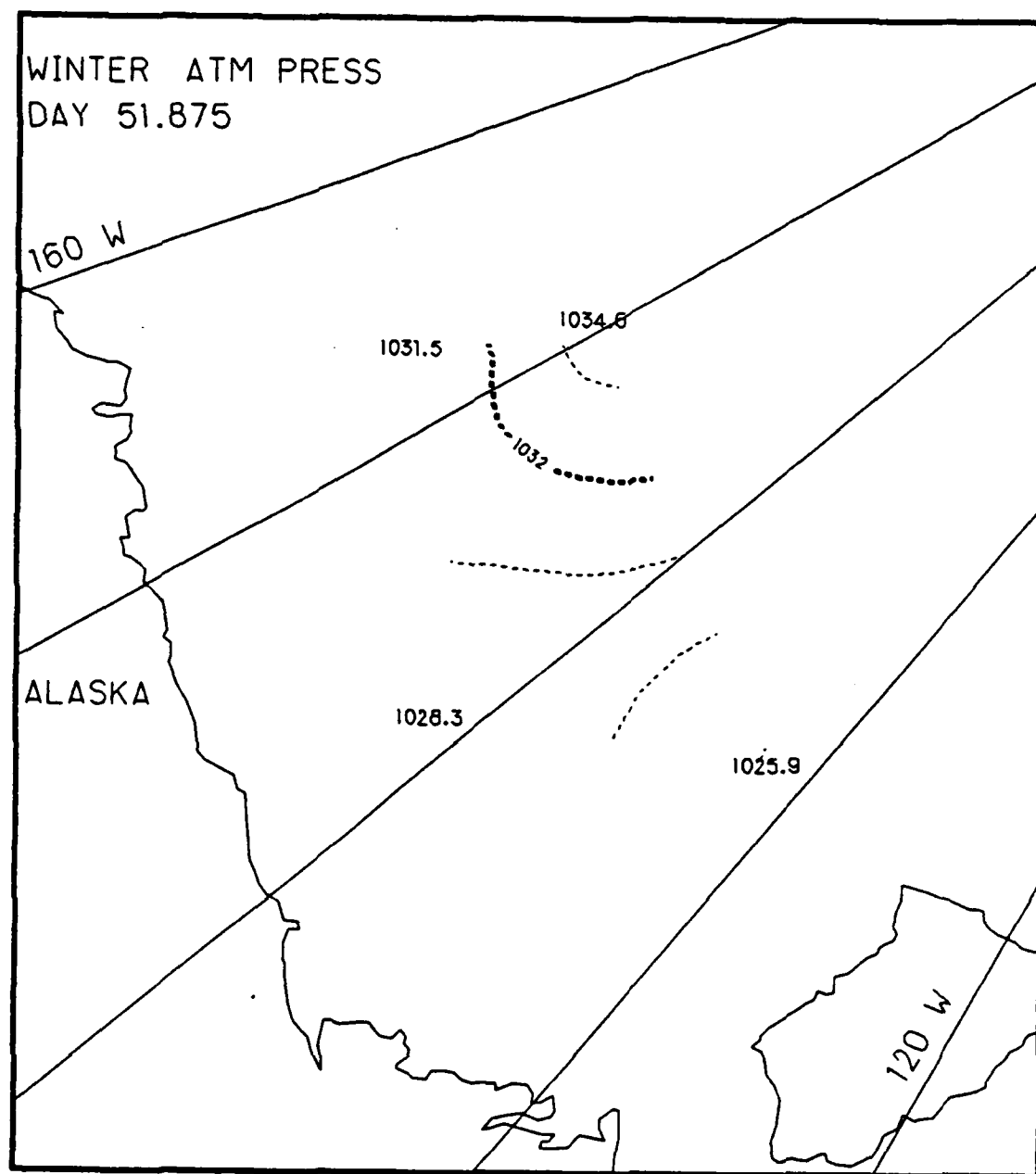


Fig. H.8. Spatial atmospheric pressure variations, day 51.875, based on the AIDJEX data from stations with hydrophones, winter 1976.

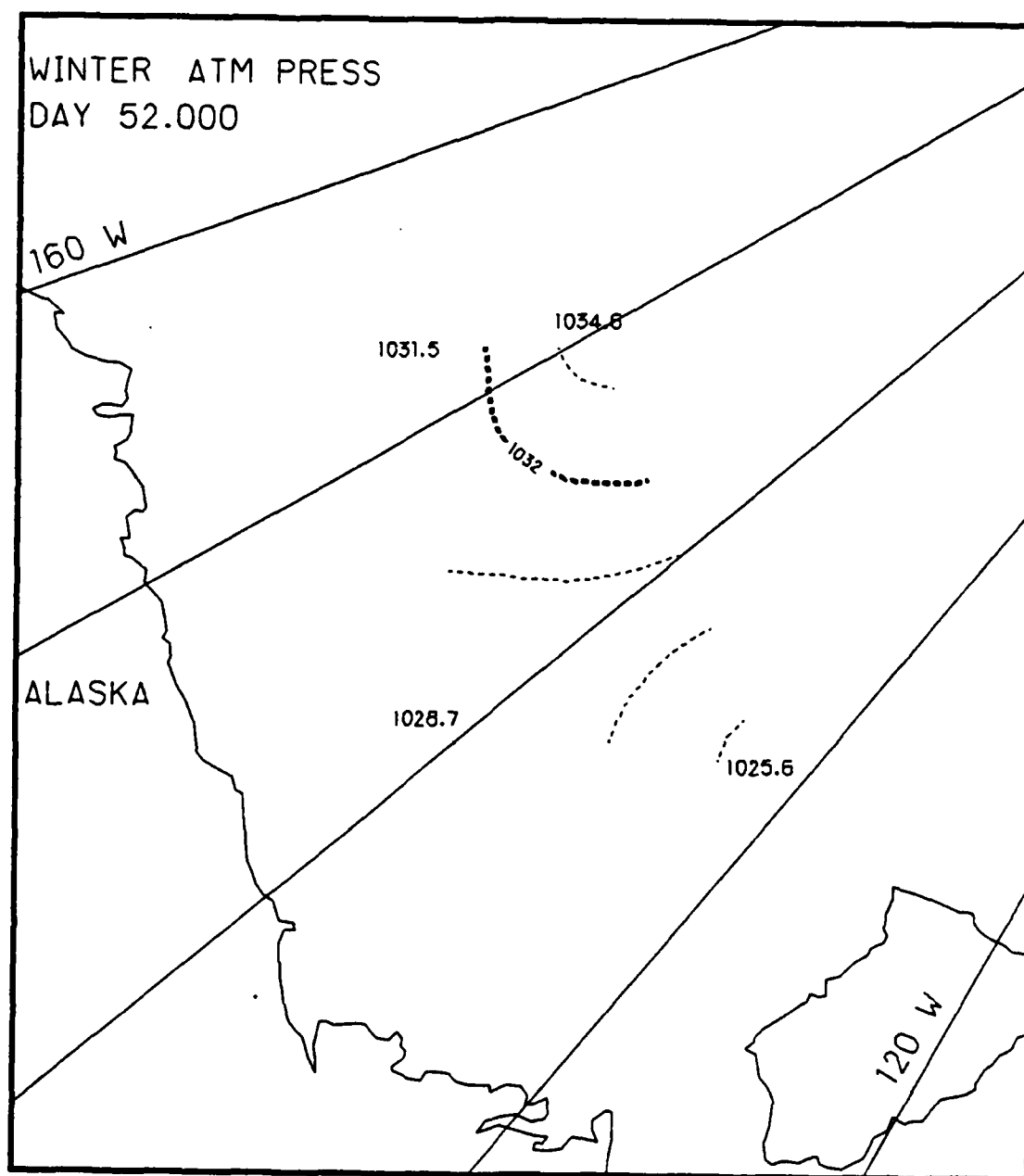


Fig. H.9. Spatial atmospheric pressure variations, day 52.0, based on the AIDJEX data from stations with hydrophones, winter 1976.

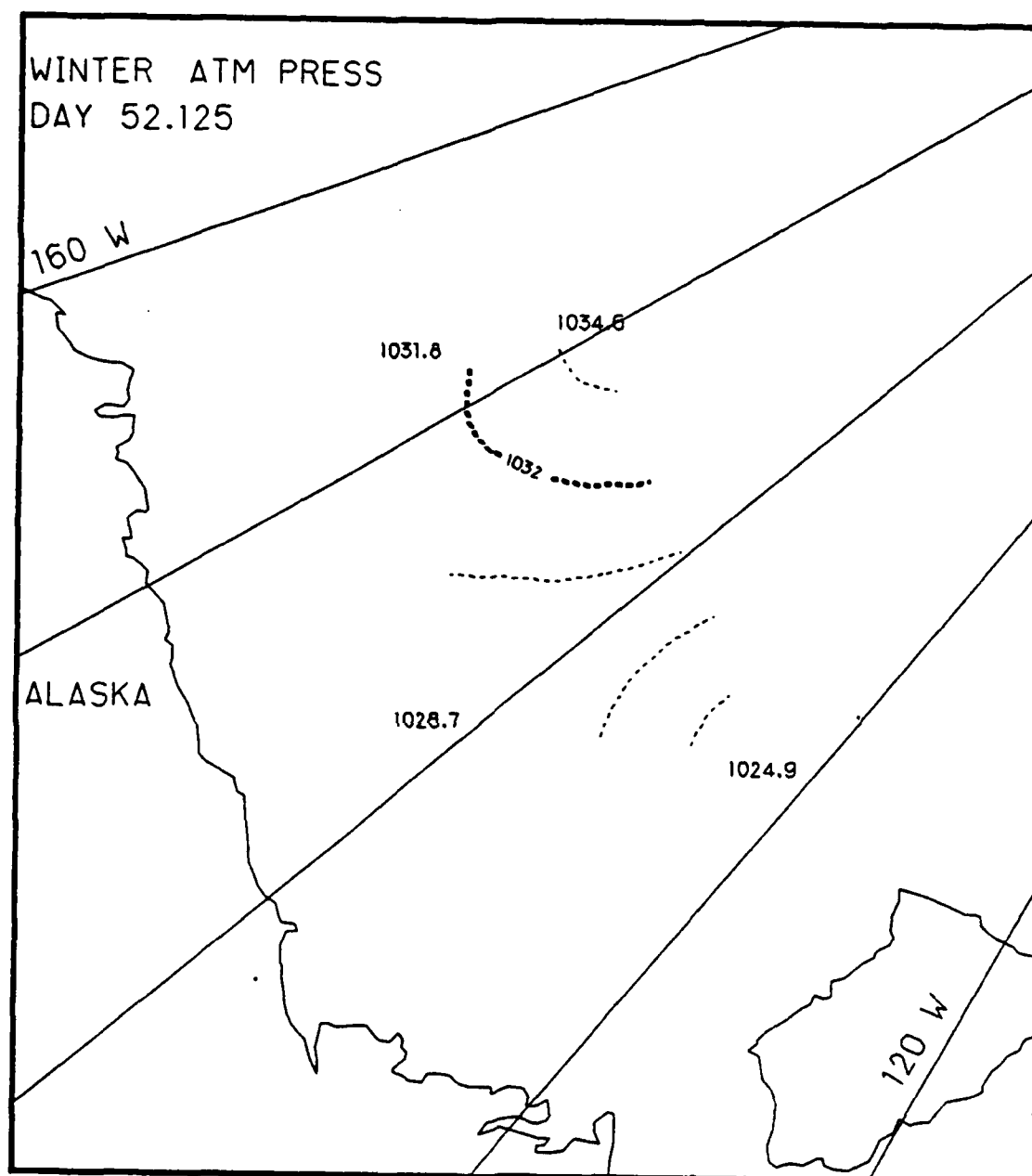


Fig. H.10. Spatial atmospheric pressure variations, day 52.125, based on the AIDJEX data from stations with hydrophones, winter 1976.

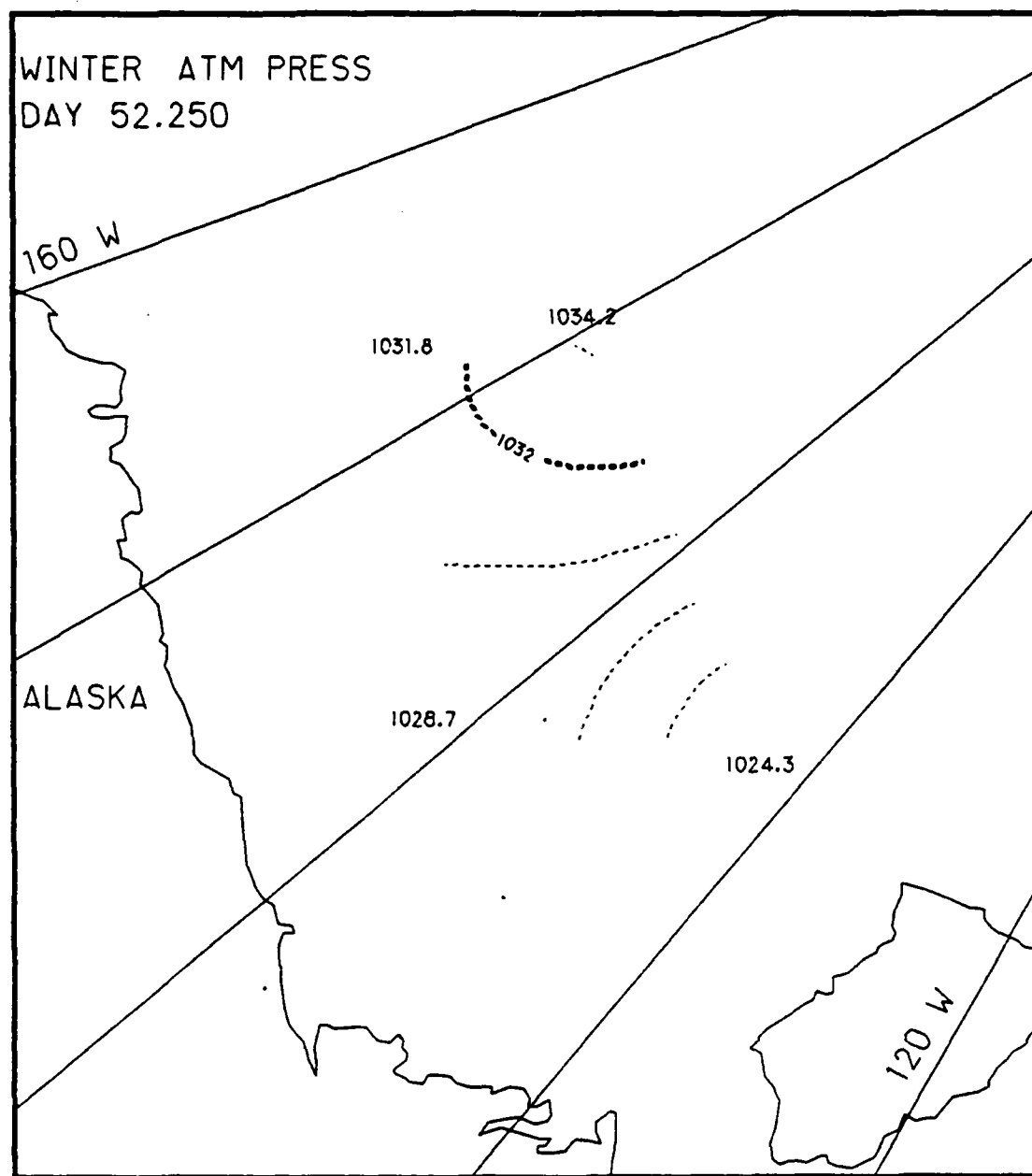


Fig. H.11. Spatial atmospheric pressure variations, day 52.25, based on the AIDJEX data from stations with hydrophones, winter 1976.

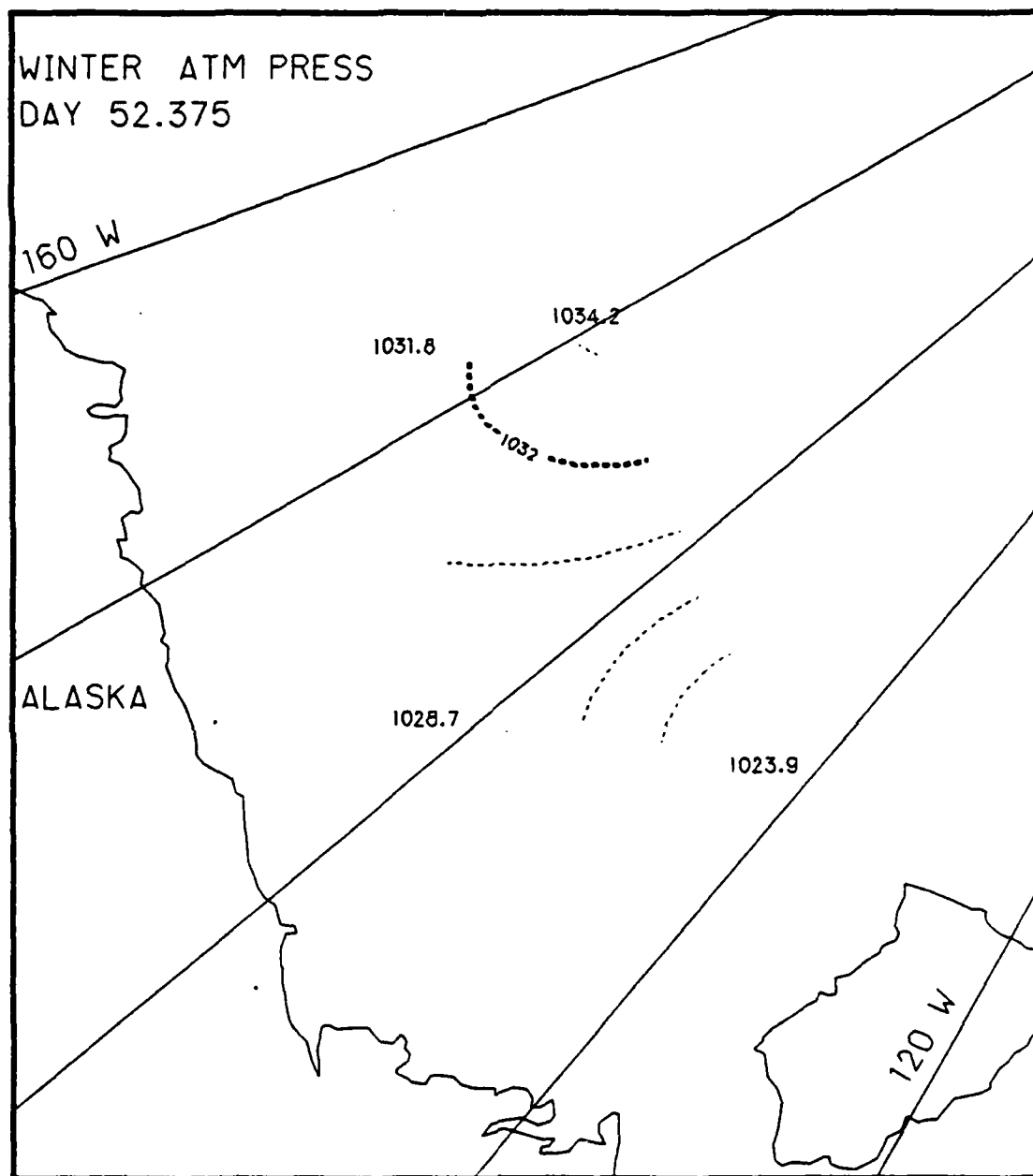


Fig. H.12. Spatial atmospheric pressure variations, day 52.375, based on the AIDJEX data from stations with hydrophones, winter 1976.

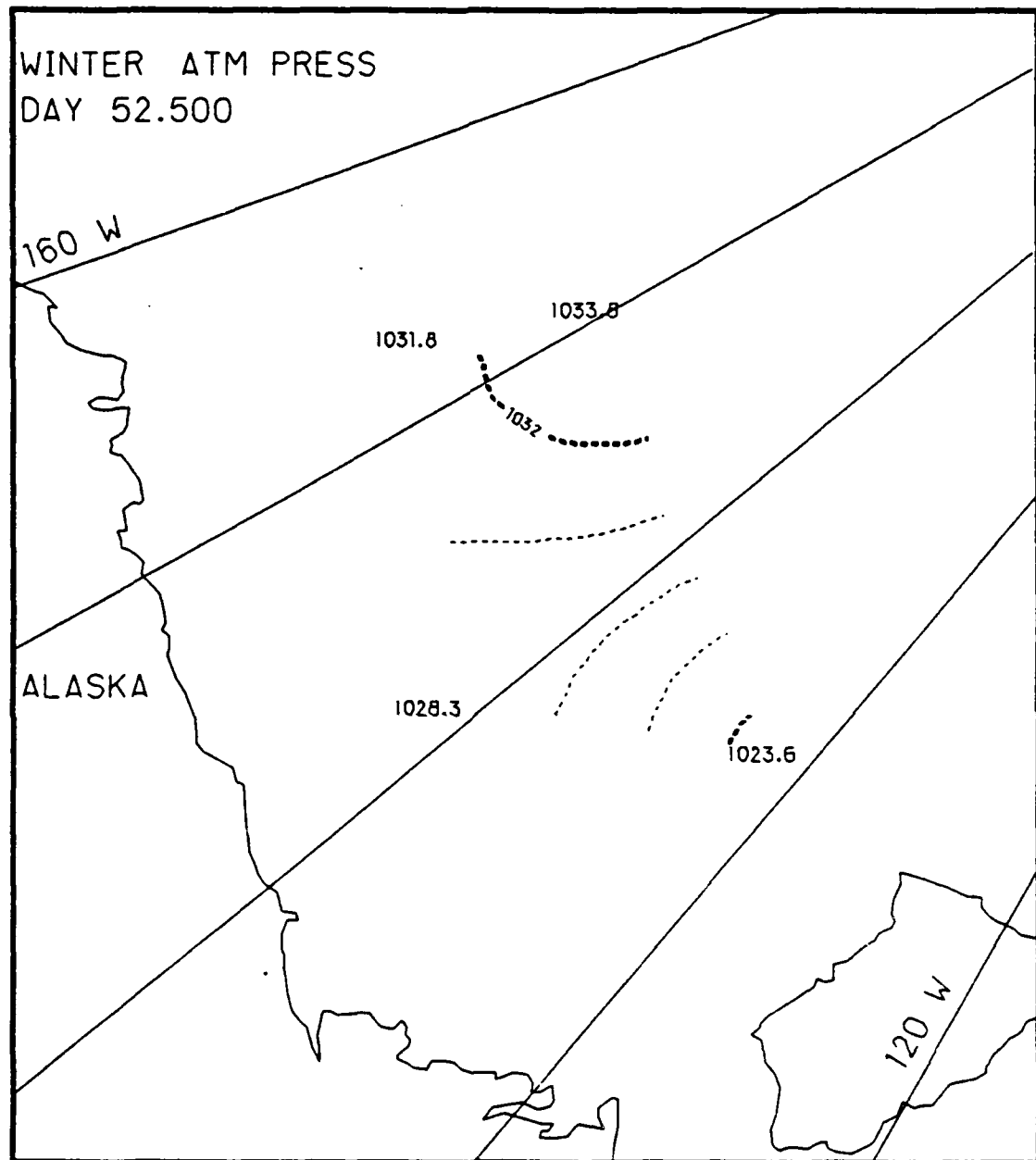


Fig. H.13. Spatial atmospheric pressure variations, day 52.5, based on the AIDJEX data from stations with hydrophones, winter 1976.

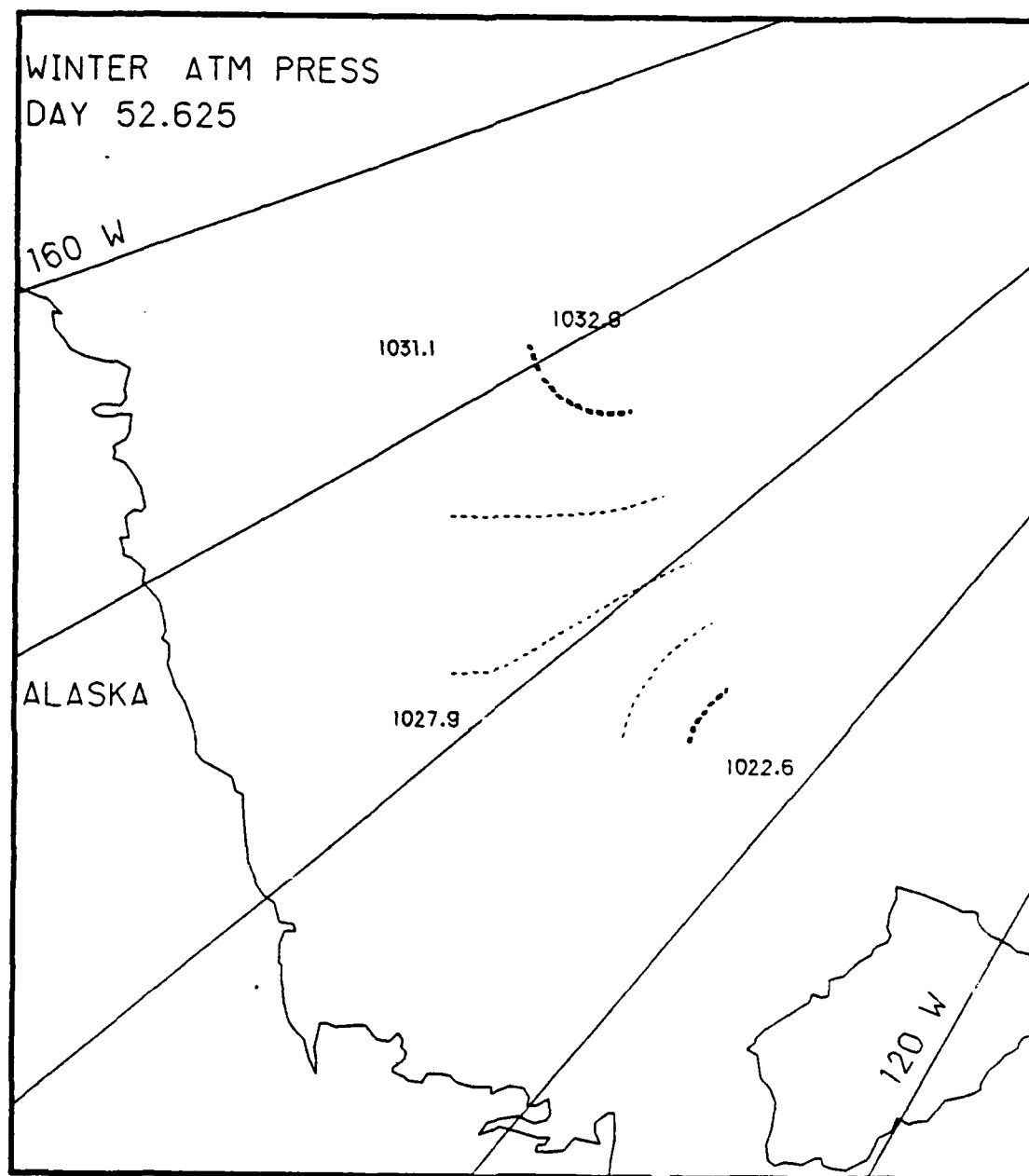


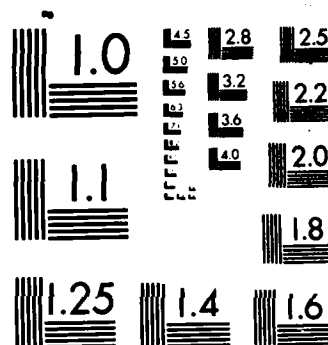
Fig. H.14. Spatial atmospheric pressure variations, day 52.625, based on the AIDJEX data from stations with hydrophones, winter 1976.

UNCLASSIFIED

ARCTIC AMBIENT NO. (U) SCIENCE APPLICATIONS
INTERNATIONAL CORP COLLEGE STATION TX J K LEWIS ET AL
FEB 86 SAIC-85/1950-PT-1/2 N00014-85-C-0531 F/G 8/12

MI

ENI
4.86



MICROCOPY RESOLUTION TEST CHART
NATIONAL BUREAU OF STANDARDS-1963-A

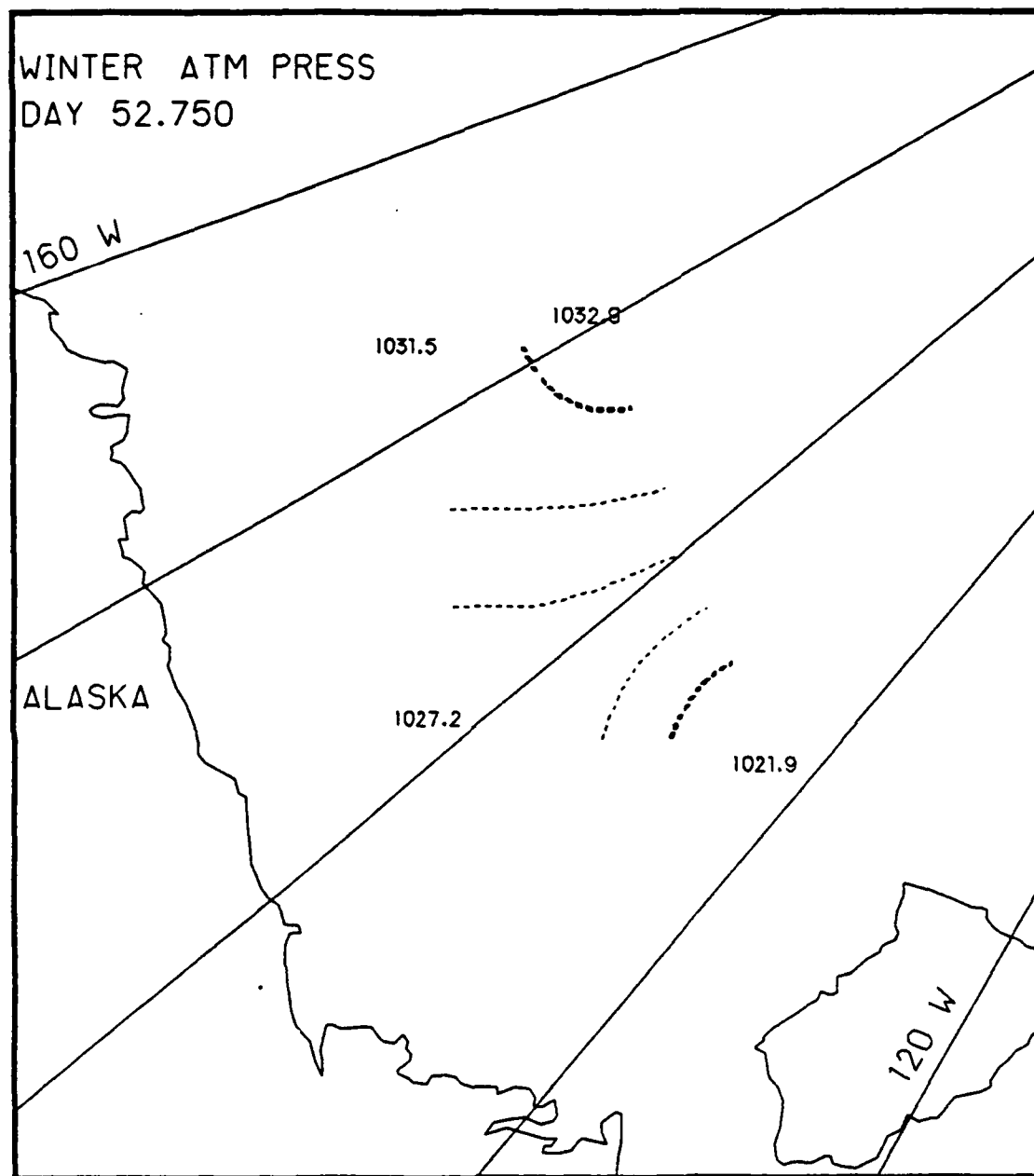


Fig. H.15. Spatial atmospheric pressure variations, day 52.75, based on the AIDJEX data from stations with hydrophones, winter 1976.

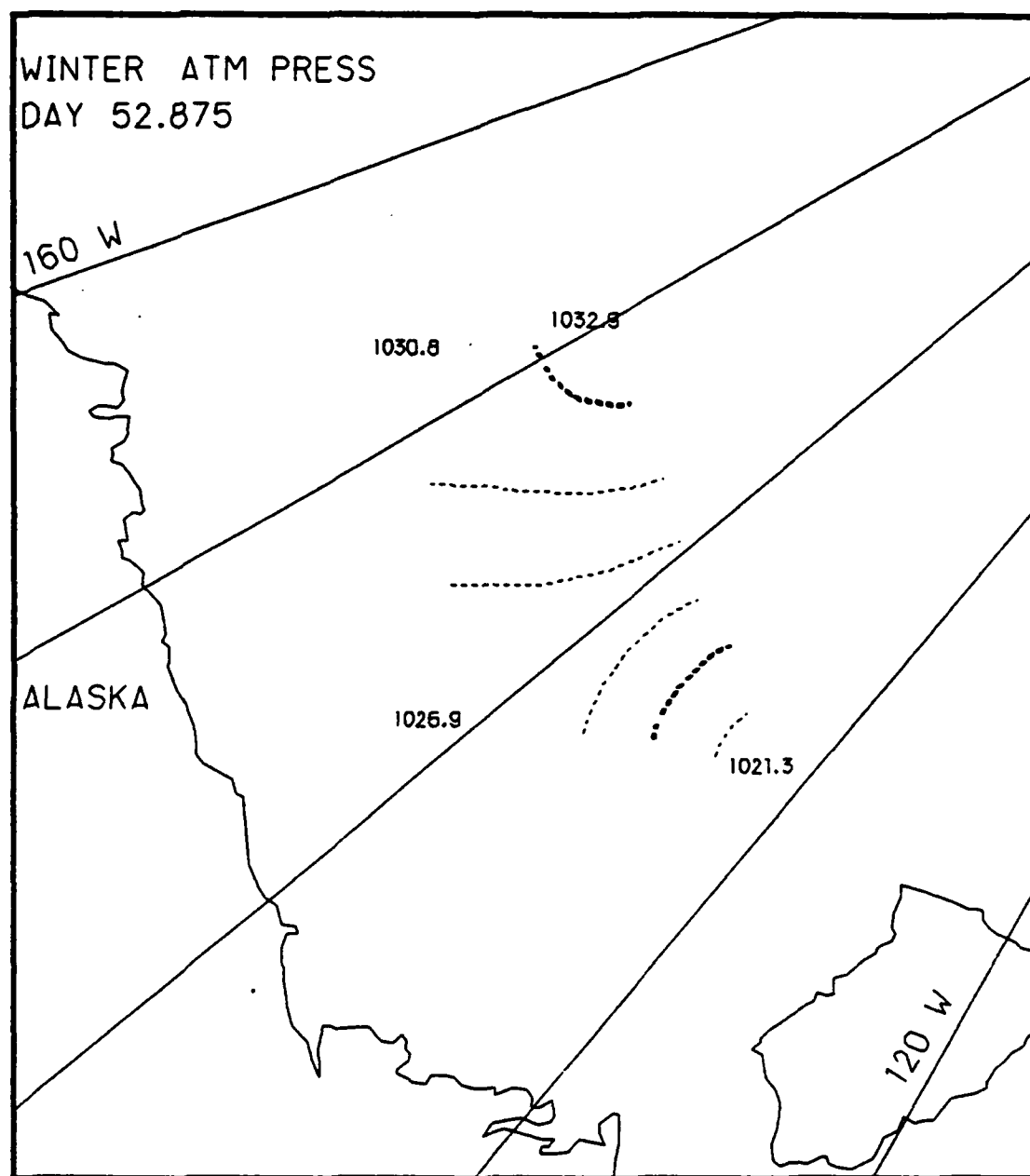


Fig. H.16. Spatial atmospheric pressure variations, day 52.875, based on the AIDJEX data from stations with hydrophones, winter 1976.

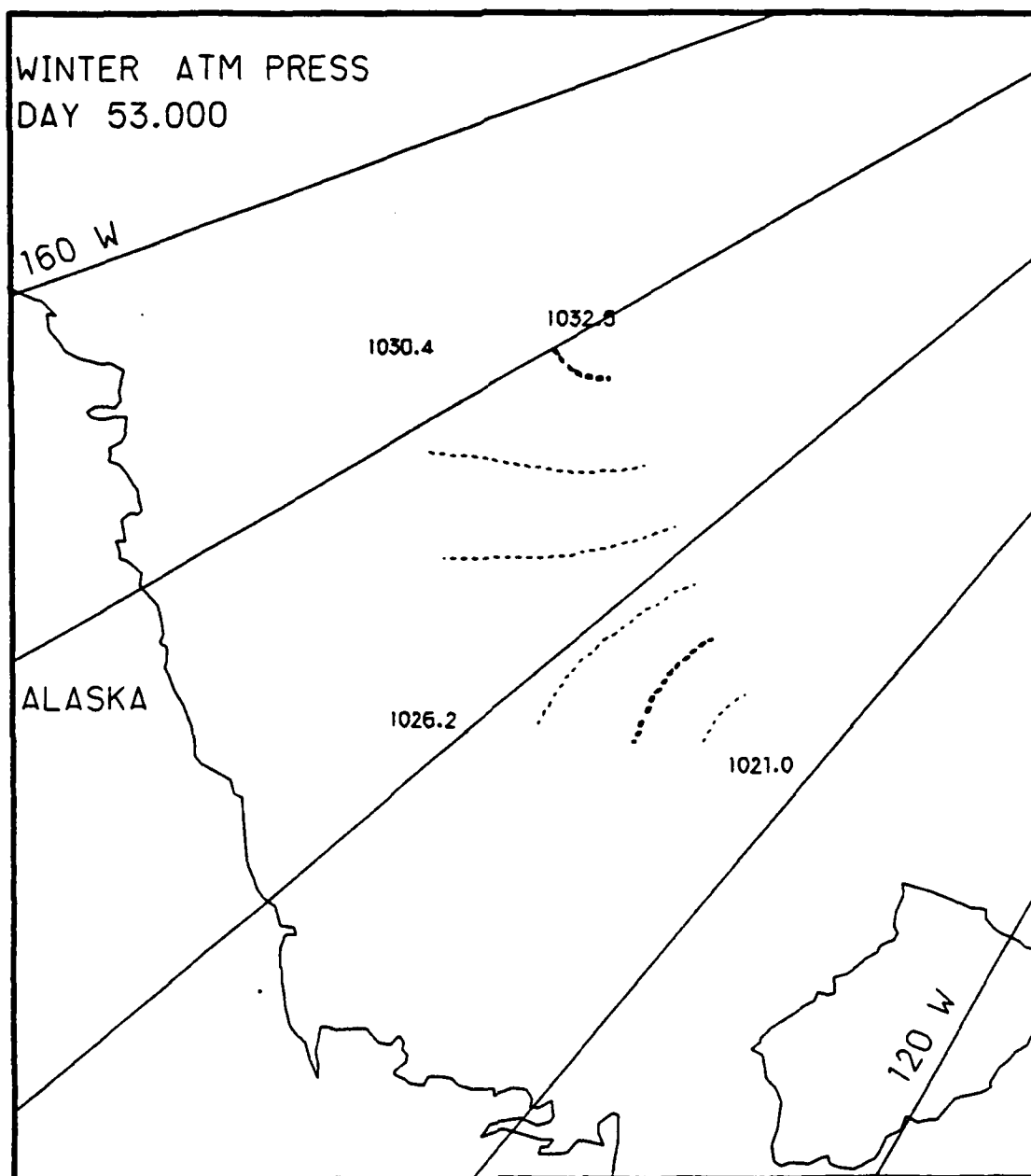


Fig. H.17. Spatial atmospheric pressure variations, day 53.0, based on the AIDJEX data from stations with hydrophones, winter 1976.

Appendix I

Two-Dimensional Contour Maps of Arctic Atmospheric Temperature Variations, 21-22 February 1976 (Winter)

This appendix contains the two-dimensional contour maps of the AIDJEX atmospheric temperature data collected at those stations with hydrophones during the 48 hour period of 21-22 February 1976. The contour maps show the spatial variations of atmospheric temperature ($^{\circ}\text{C}$) at 3 hr intervals.

List of Figures
Appendix I

	<u>Page</u>
Fig. I.1. Spatial atmospheric temperature variations, day 51.0	2-158
Fig. I.2. Spatial atmospheric temperature variations, day 51.125	2-159
Fig. I.3. Spatial atmospheric temperature variations, day 51.25	2-160
Fig. I.4. Spatial atmospheric temperature variations, day 51.375	2-161
Fig. I.5. Spatial atmospheric temperature variations, day 51.5	2-162
Fig. I.6. Spatial atmospheric temperature variations, day 51.625	2-163
Fig. I.7. Spatial atmospheric temperature variations, day 51.75	2-164
Fig. I.8. Spatial atmospheric temperature variations, day 51.875	2-165
Fig. I.9. Spatial atmospheric temperature variations, day 52.0	2-166
Fig. I.10. Spatial atmospheric temperature variations, day 52.125	2-167
Fig. I.11. Spatial atmospheric temperature variations, day 52.25	2-168
Fig. I.12. Spatial atmospheric temperature variations, day 52.375	2-169
Fig. I.13. Spatial atmospheric temperature variations, day 52.5	2-170
Fig. I.14. Spatial atmospheric temperature variations, day 52.625	2-171
Fig. I.15. Spatial atmospheric temperature variations, day 52.75	2-172
Fig. I.16. Spatial atmospheric temperature variations, day 52.875	2-173
Fig. I.17. Spatial atmospheric temperature variations, day 53.0	2-174

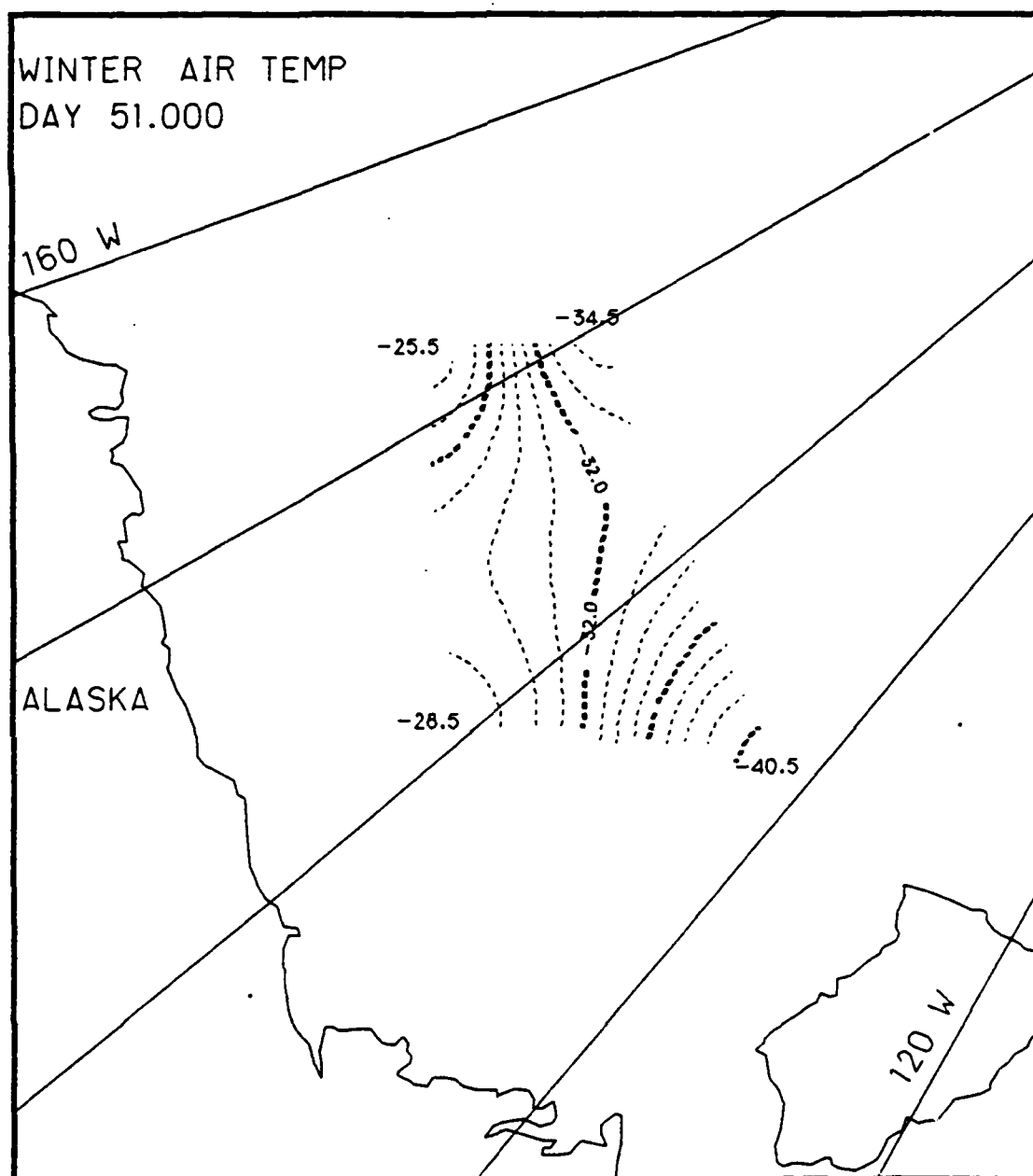


Fig. I.1. Spatial atmospheric temperature variations, day 51.0, based on the AIDJEX data from stations with hydrophones, winter 1976.

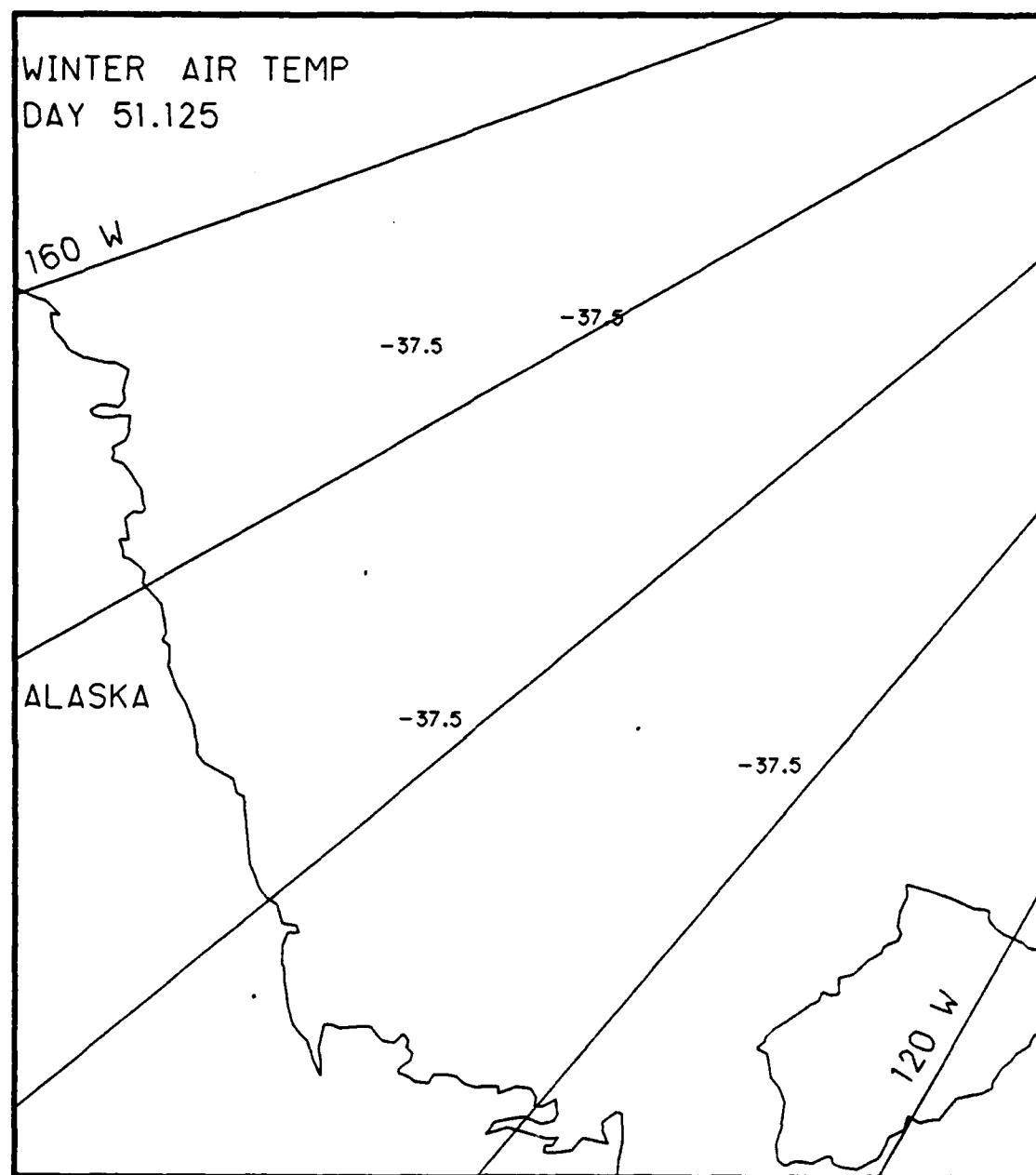


Fig. I.2. Spatial atmospheric temperature variations, day 51.125, based on the AIDJEX data from stations with hydrophones, winter 1976.

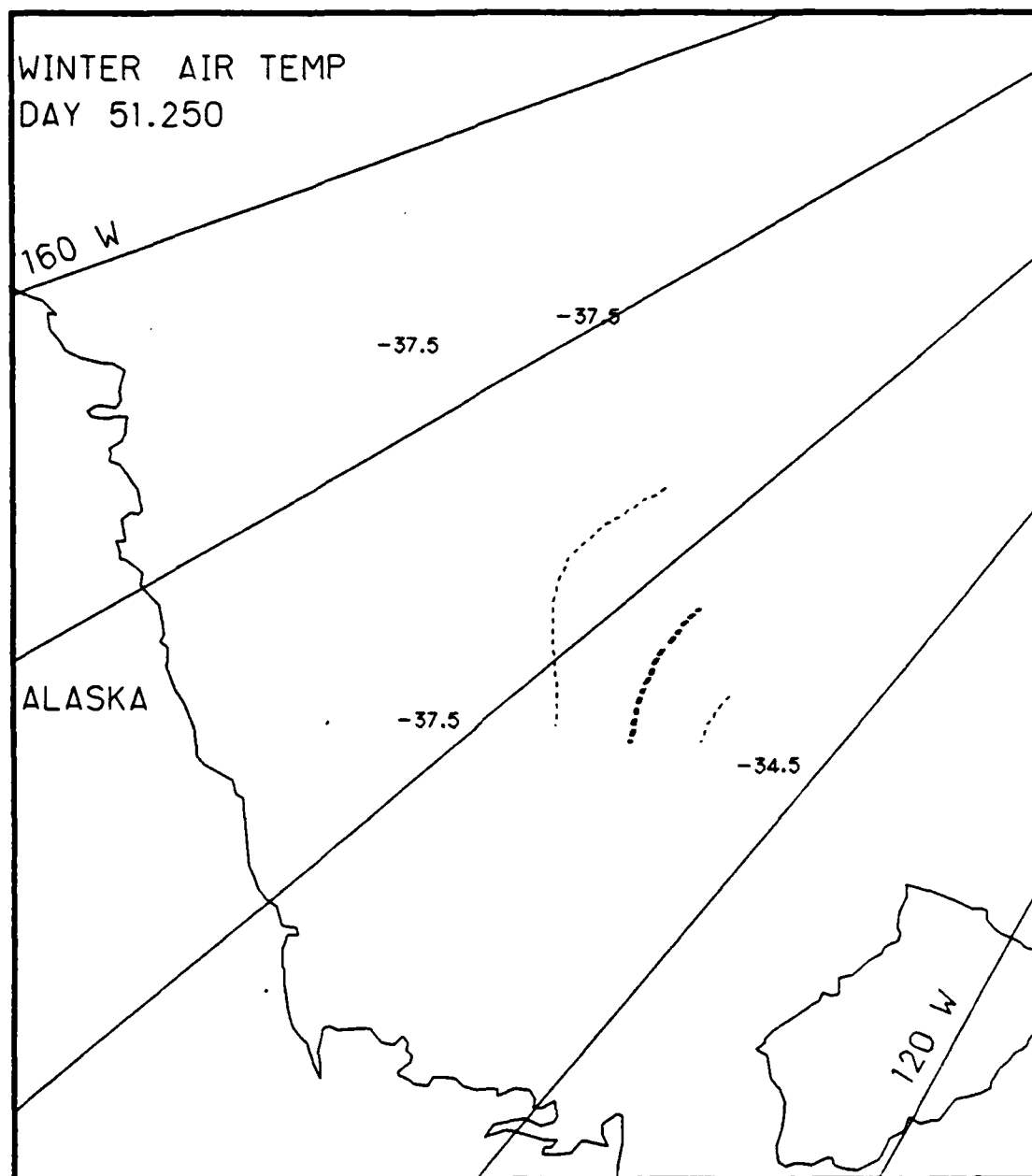


Fig. I.3. Spatial atmospheric temperature variations, day 51.25, based on the AIDJEX data from stations with hydrophones, winter 1976.

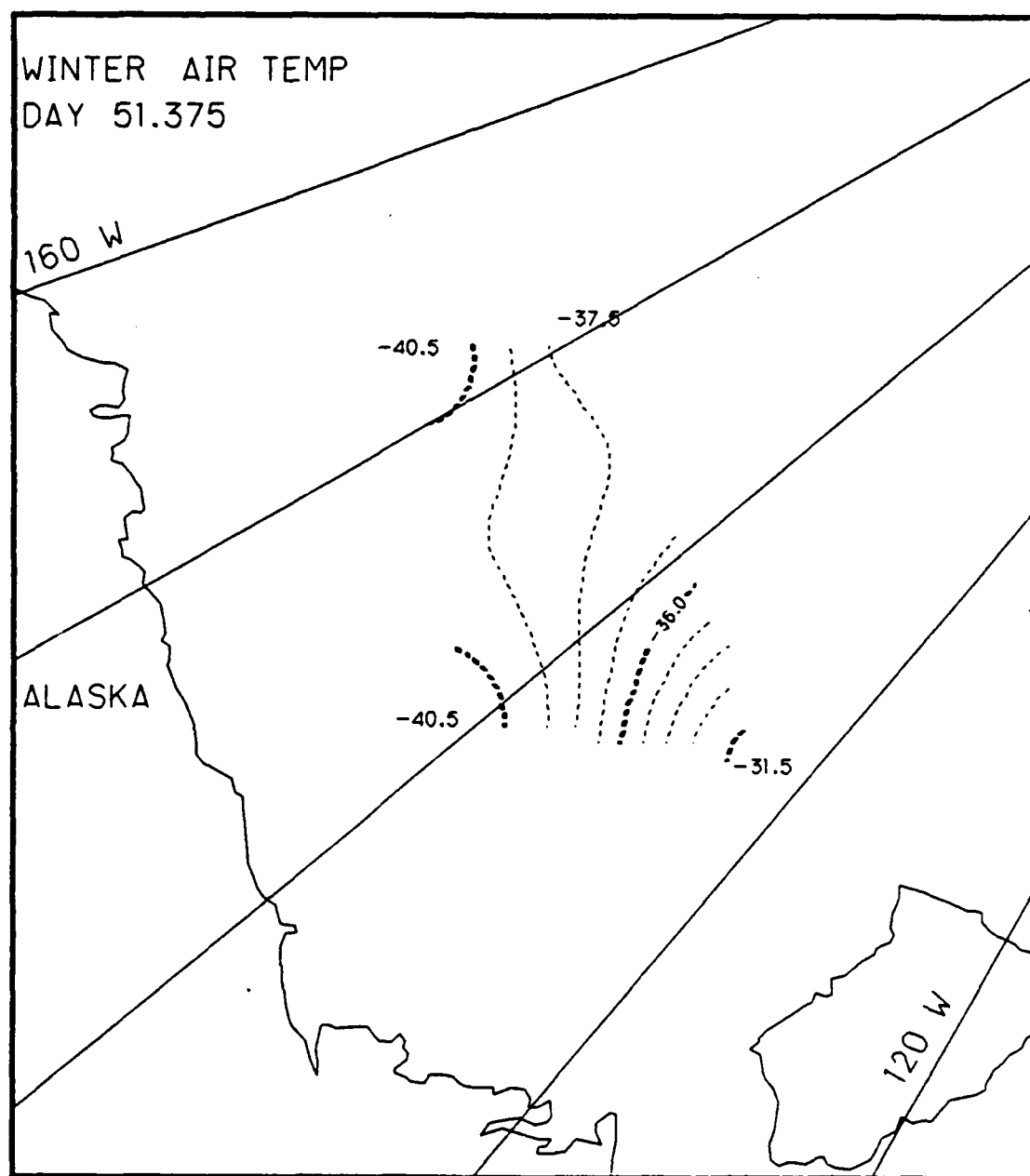


Fig. I.4. Spatial atmospheric temperature variations, day 51.375, based on the AIDJEX data from stations with hydrophones, winter 1976.

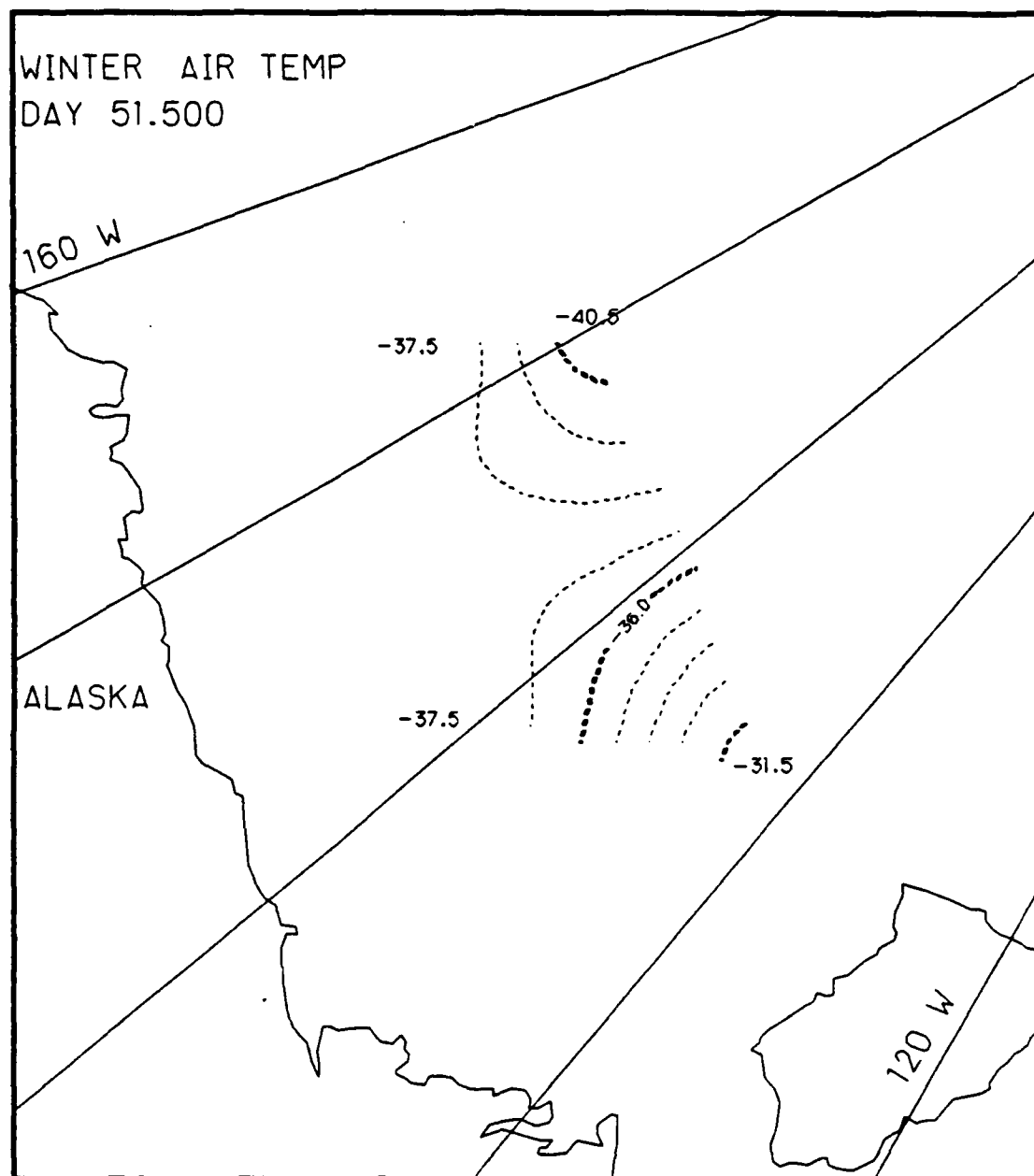


Fig. I.5. Spatial atmospheric temperature variations, day 51.5, based on the AIDJEX data from stations with hydrophones, winter 1976.

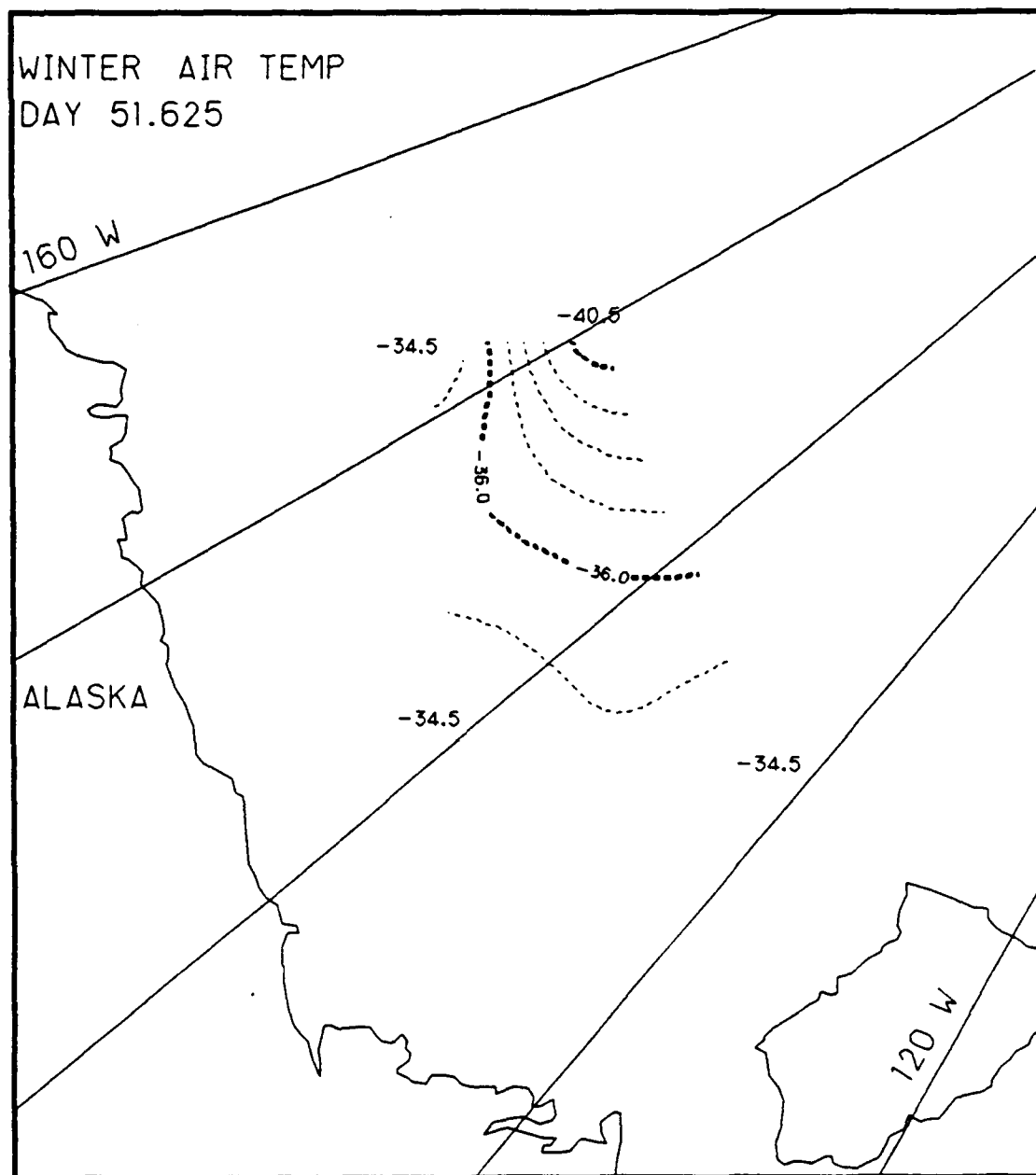


Fig. I.6. Spatial atmospheric temperature variations, day 51.625, based on the AIDJEX data from stations with hydrophones, winter 1976.

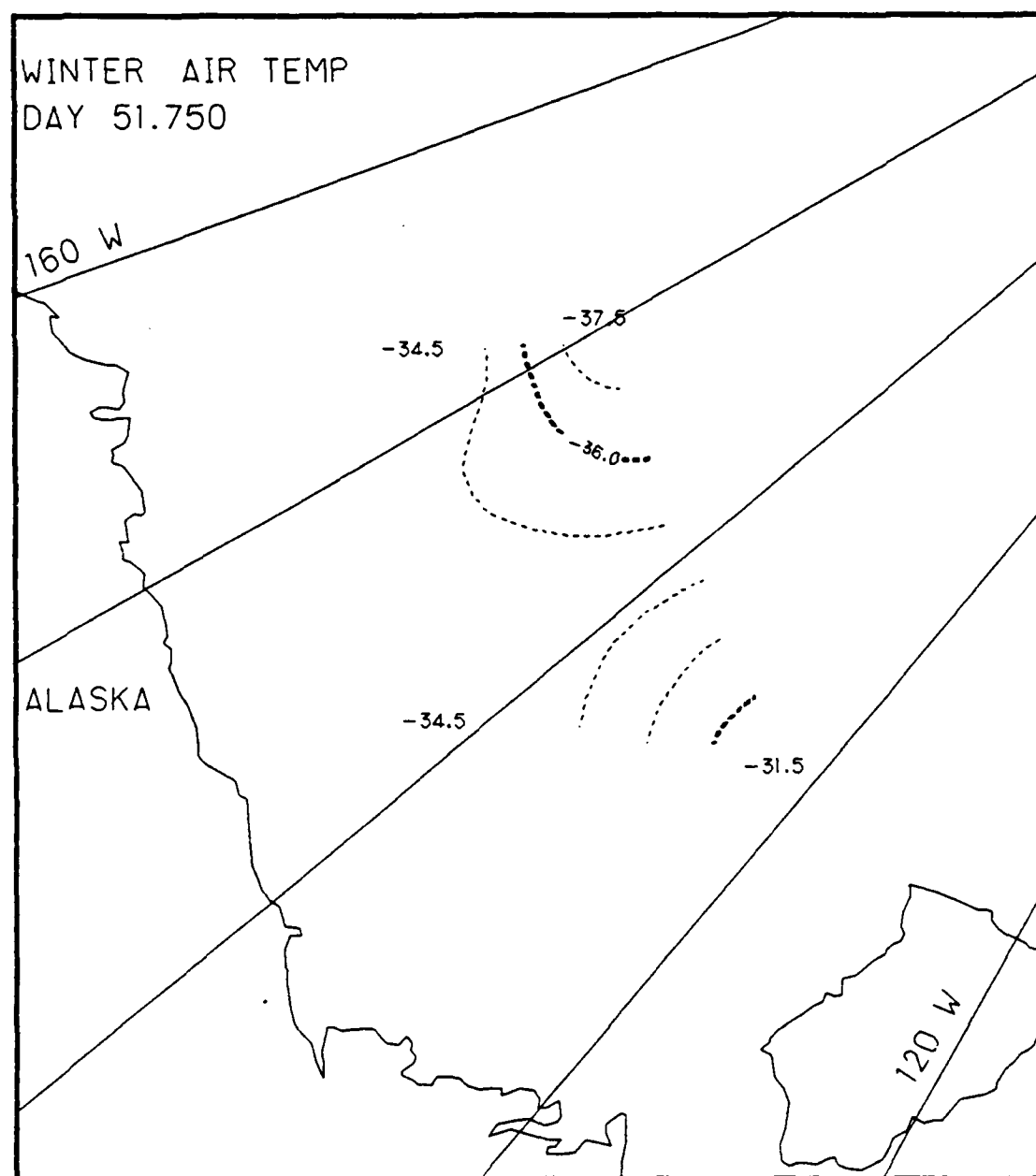


Fig. I.7. Spatial atmospheric temperature variations, day 51.75, based on the AIDJEX data from stations with hydrophones, winter 1976.

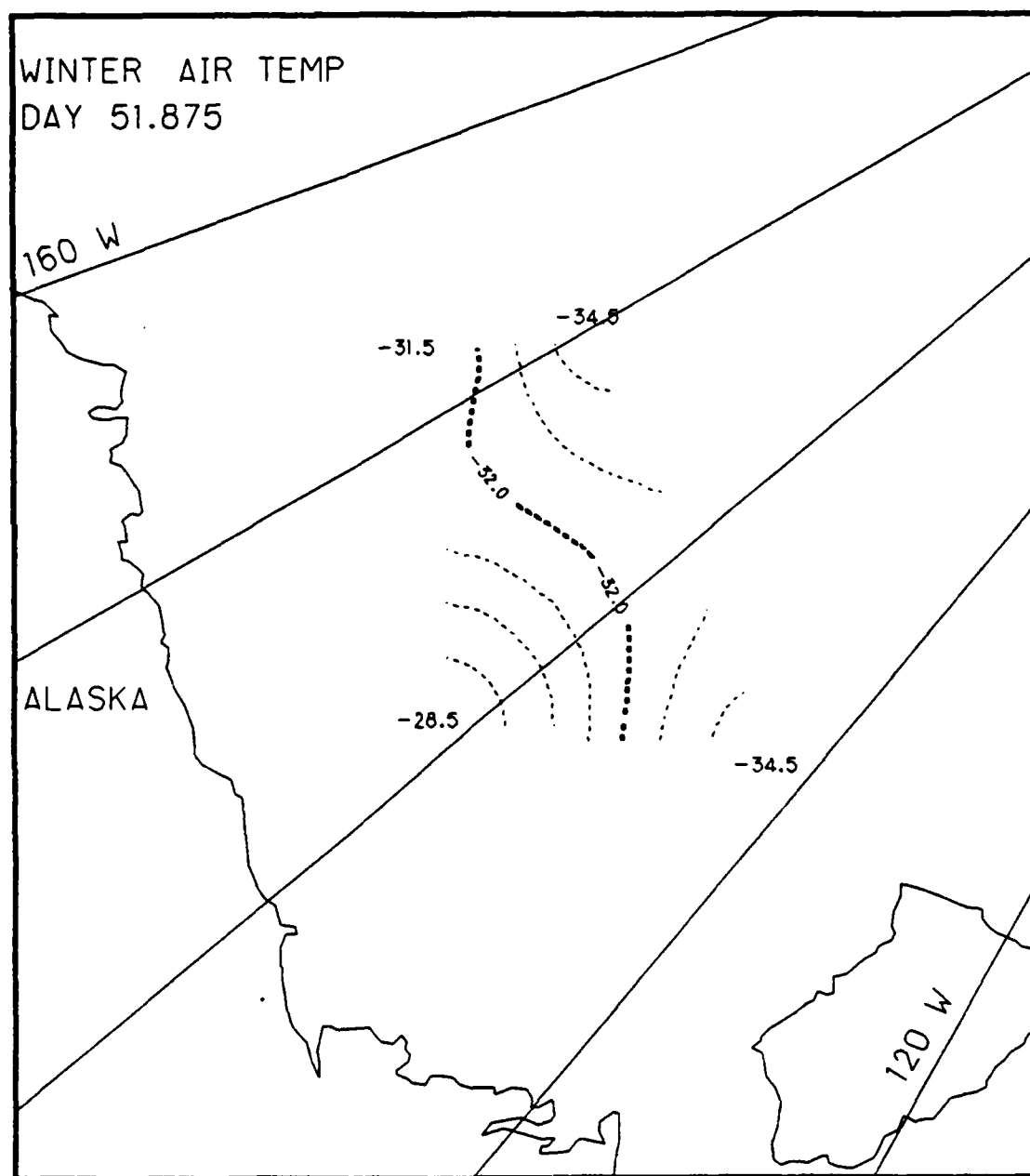


Fig. I.8. Spatial atmospheric temperature variations, day 51.875, based on the AIDJEX data from stations with hydrophones, winter 1976.

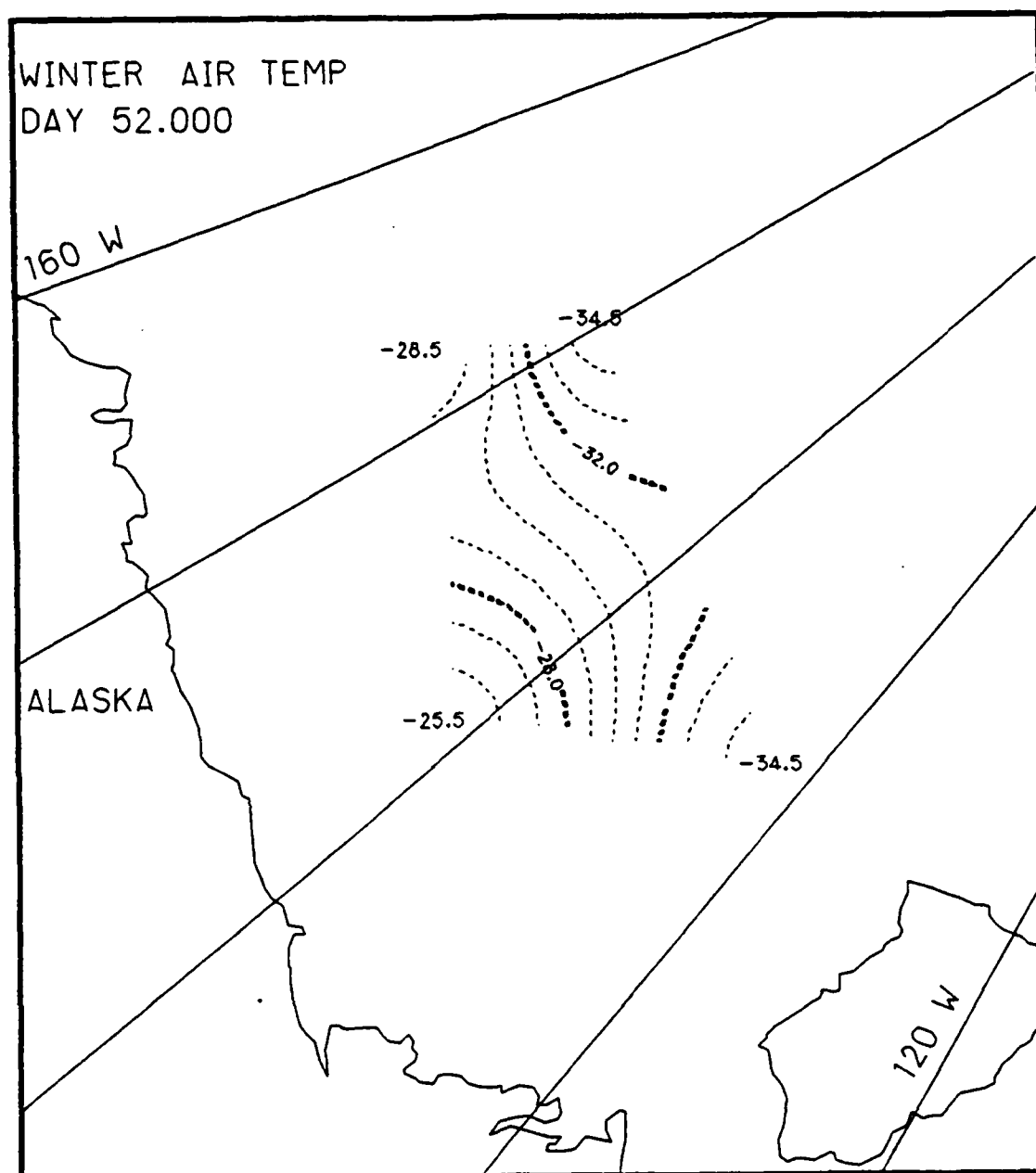


Fig. I.9. Spatial atmospheric temperature variations, day 52.0, based on the AIDJEX data from stations with hydrophones, winter 1976.

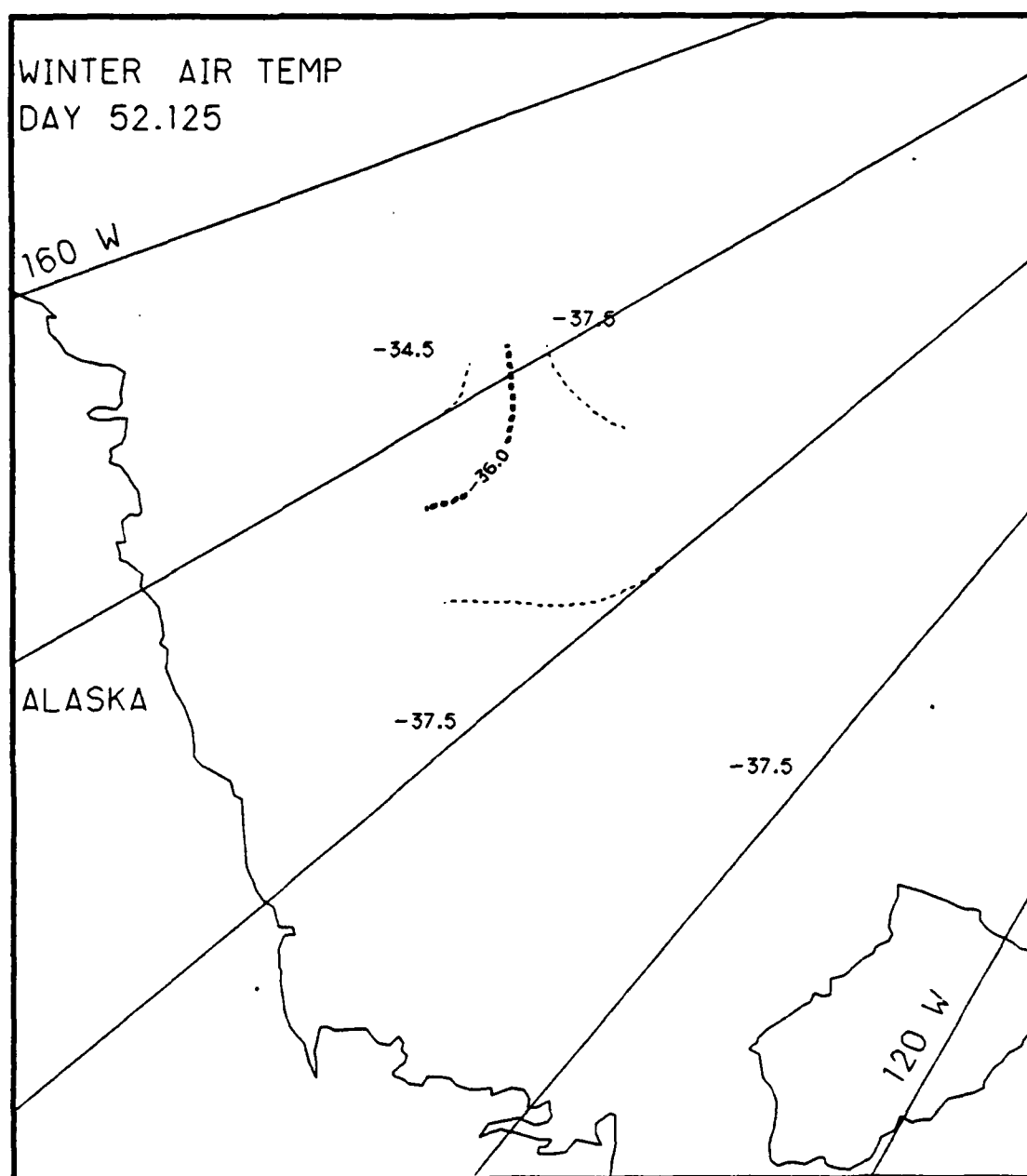


Fig. I.10. Spatial atmospheric temperature variations, day 52.125, based on the AIDJEX data from stations with hydrophones, winter 1976.

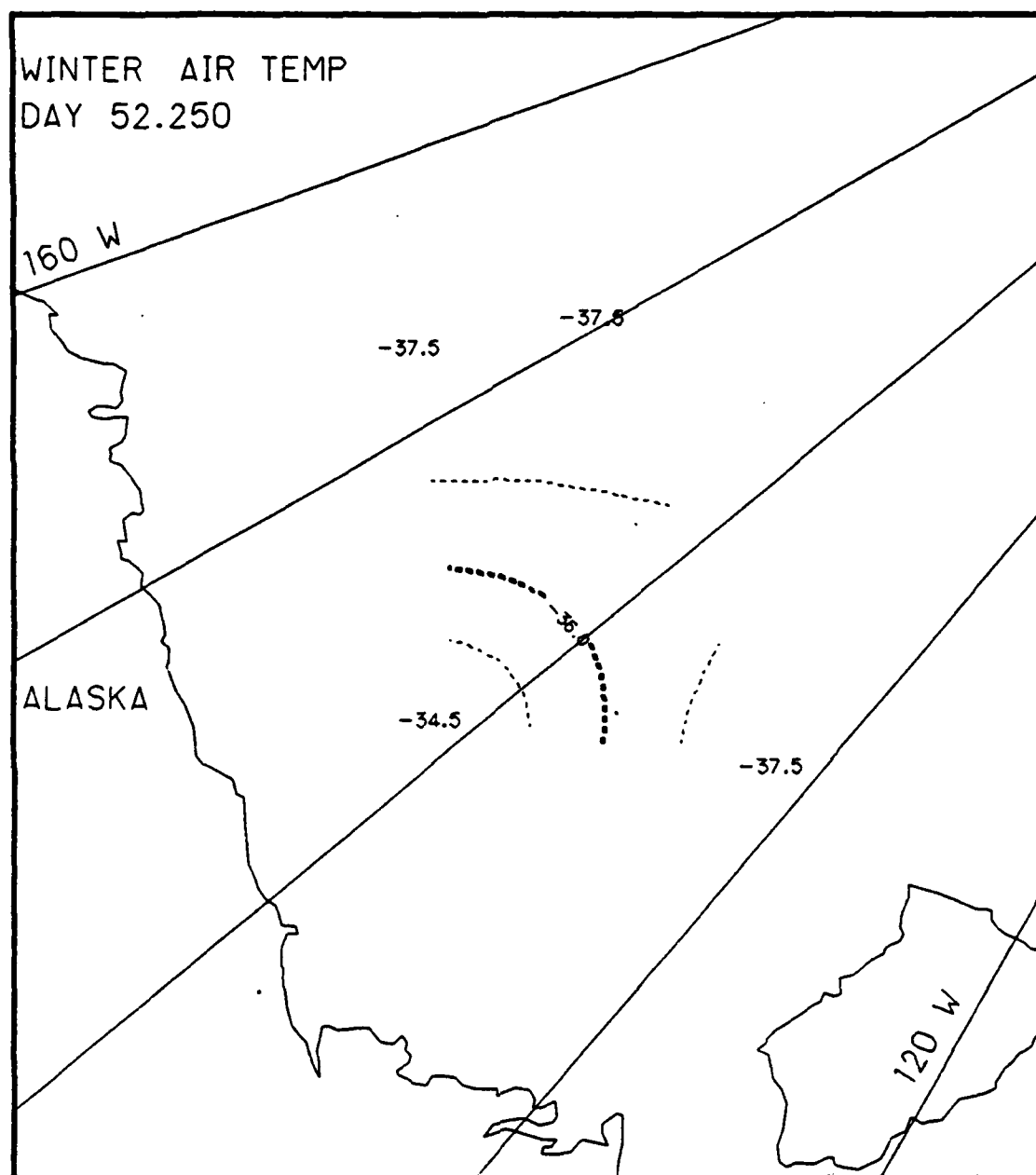


Fig. I.11. Spatial atmospheric temperature variations, day 52.25, based on the AIDJEX data from stations with hydrophones, winter 1976.

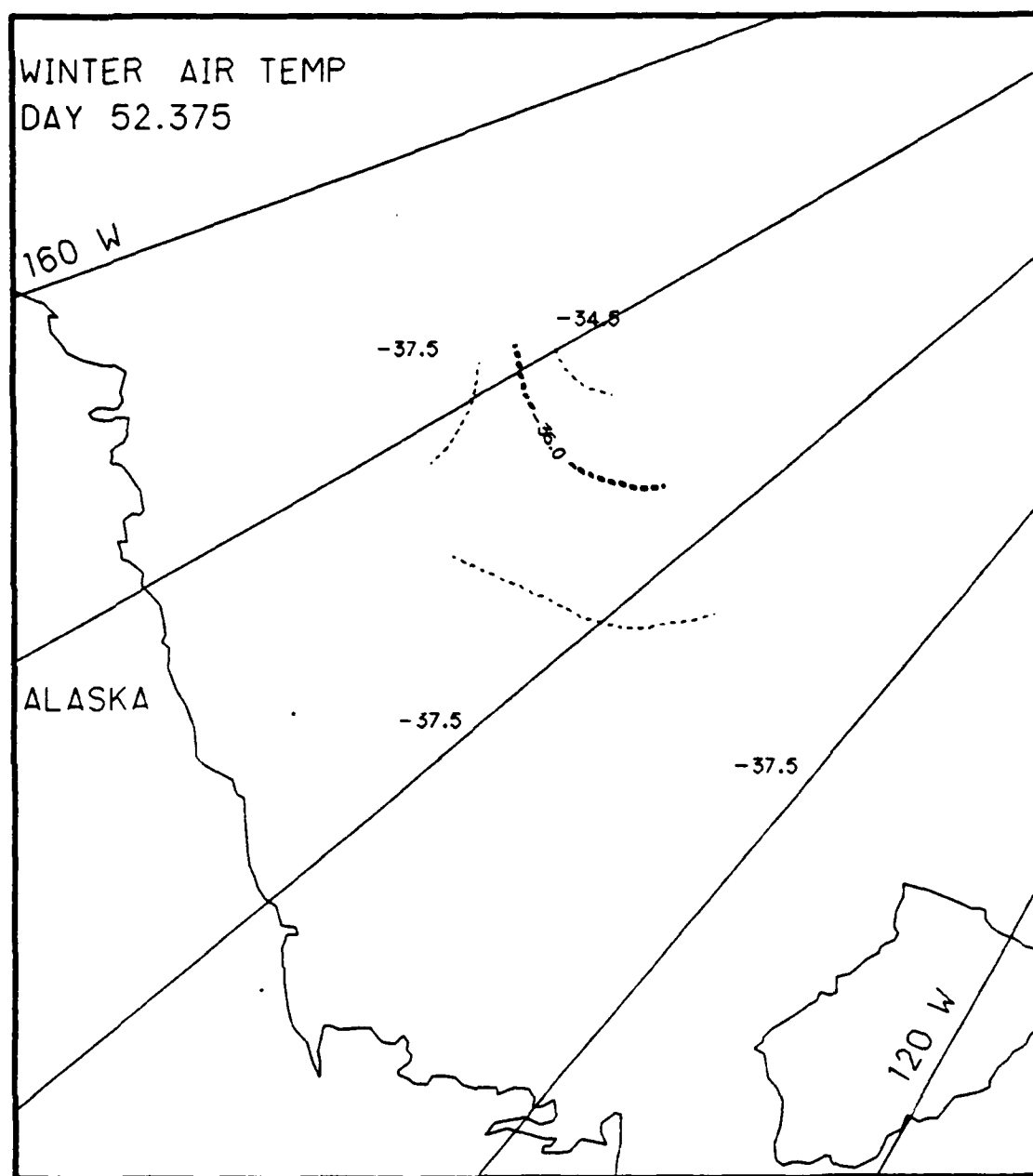


Fig. I.12. Spatial atmospheric temperature variations, day 52.375, based on the AIDJEX data from stations with hydrophones, winter 1976.

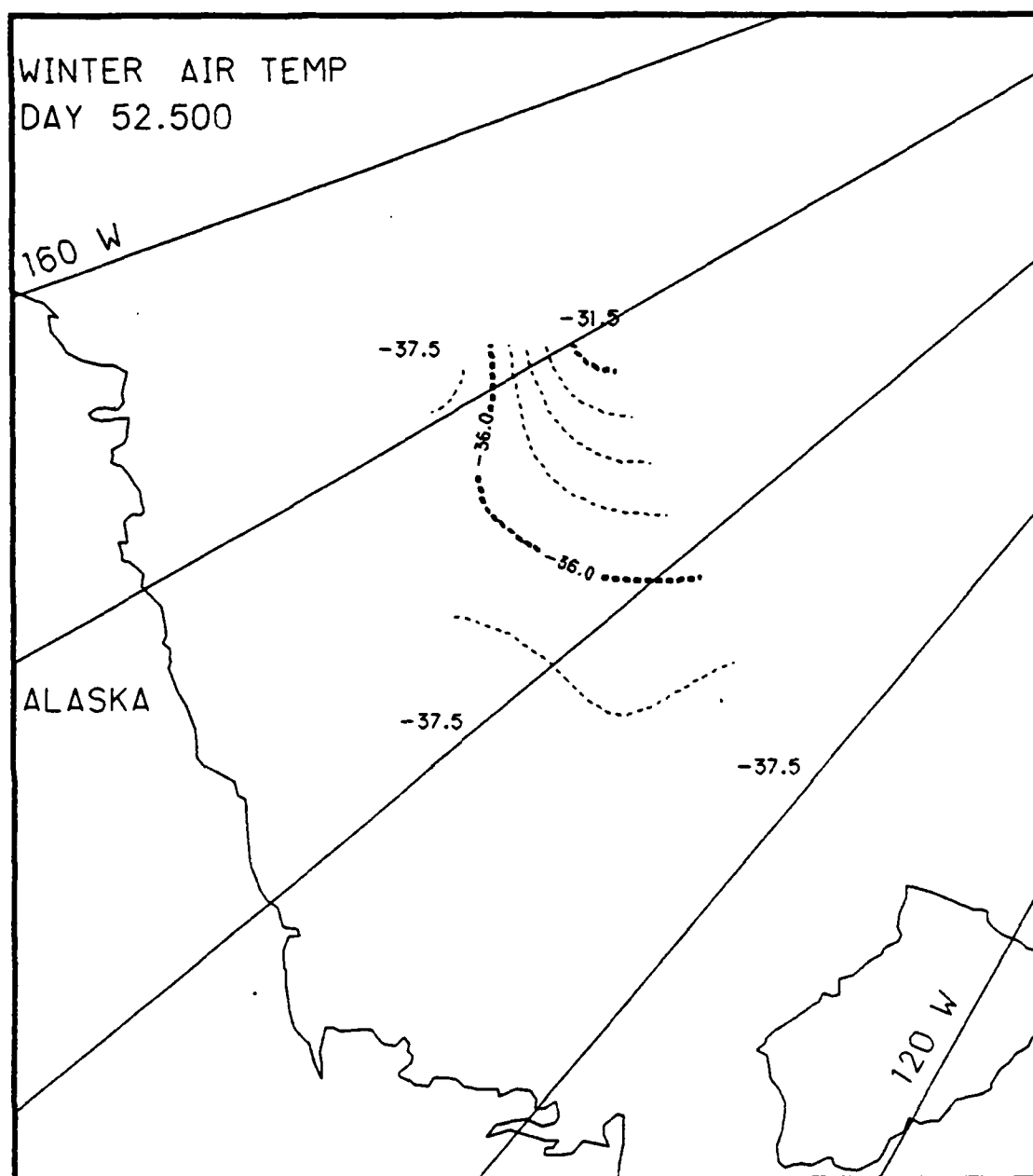


Fig. I.13. Spatial atmospheric temperature variations, day 52.5, based on the AIDJEX data from stations with hydrophones, winter 1976.

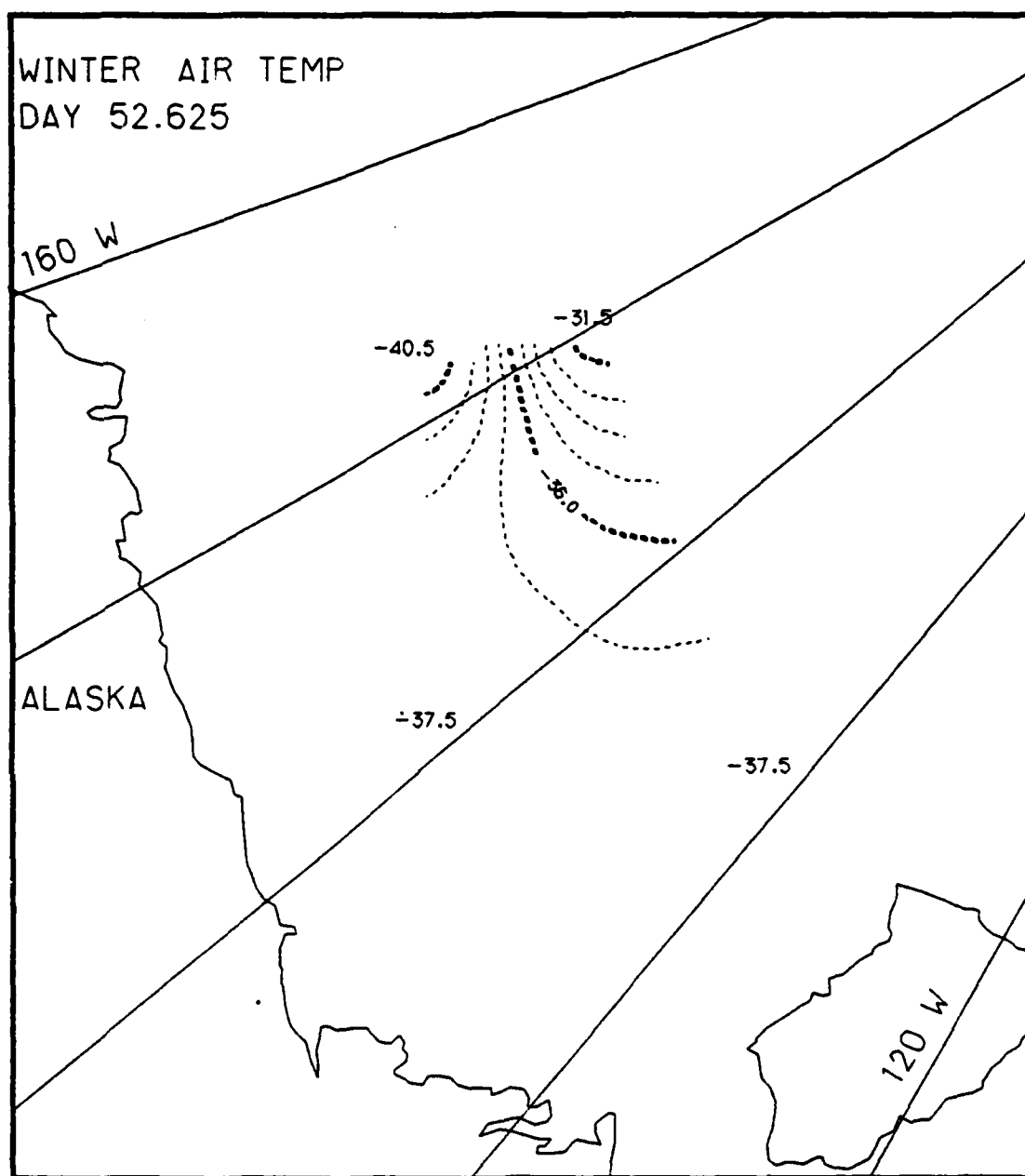


Fig. I.14. Spatial atmospheric temperature variations, day 52.625, based on the AIDJEX data from stations with hydrophones, winter 1976.

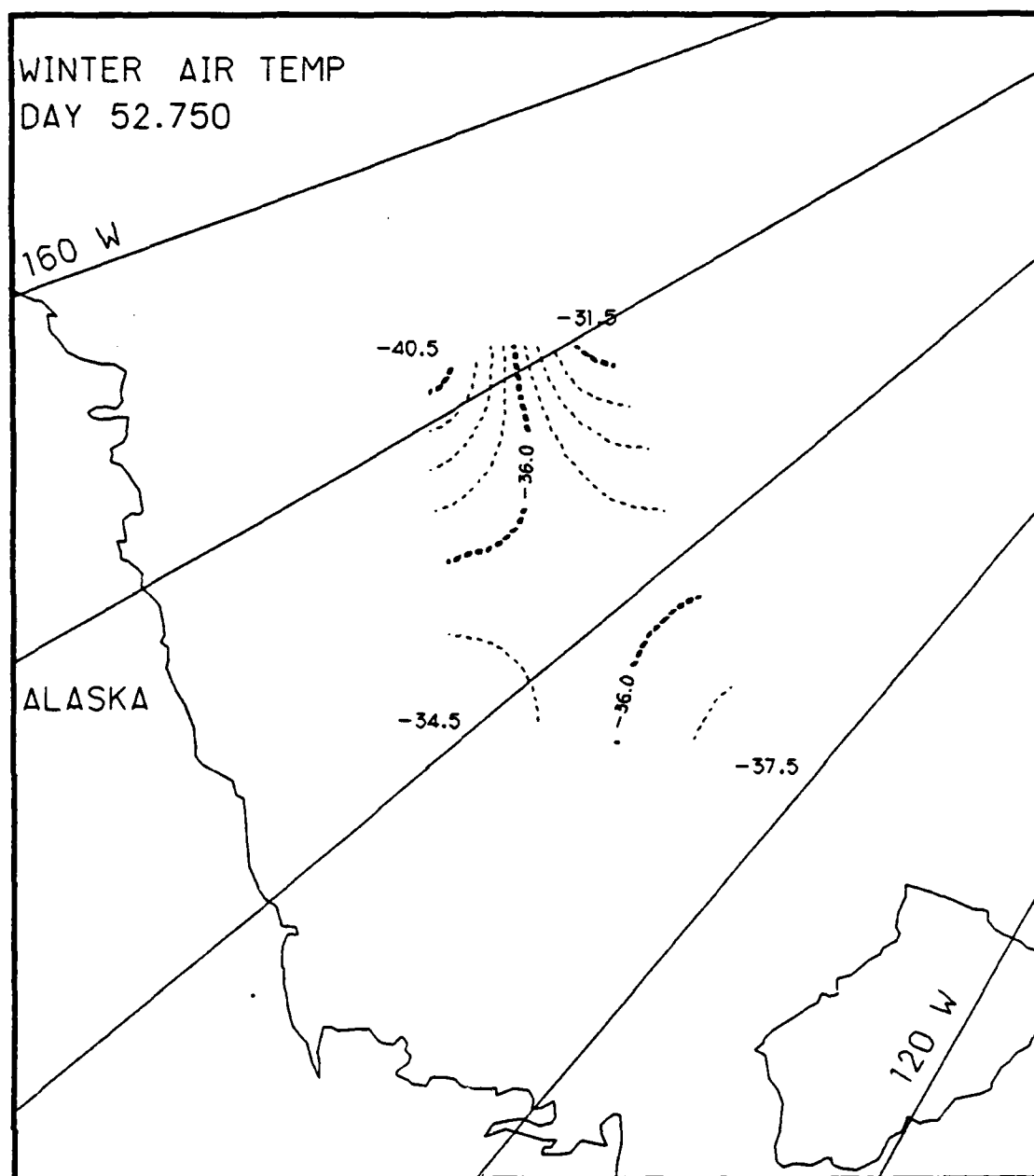


Fig. I.15. Spatial atmospheric temperature variations, day 52.75, based on the AIDJEX data from stations with hydrophones, winter 1976.

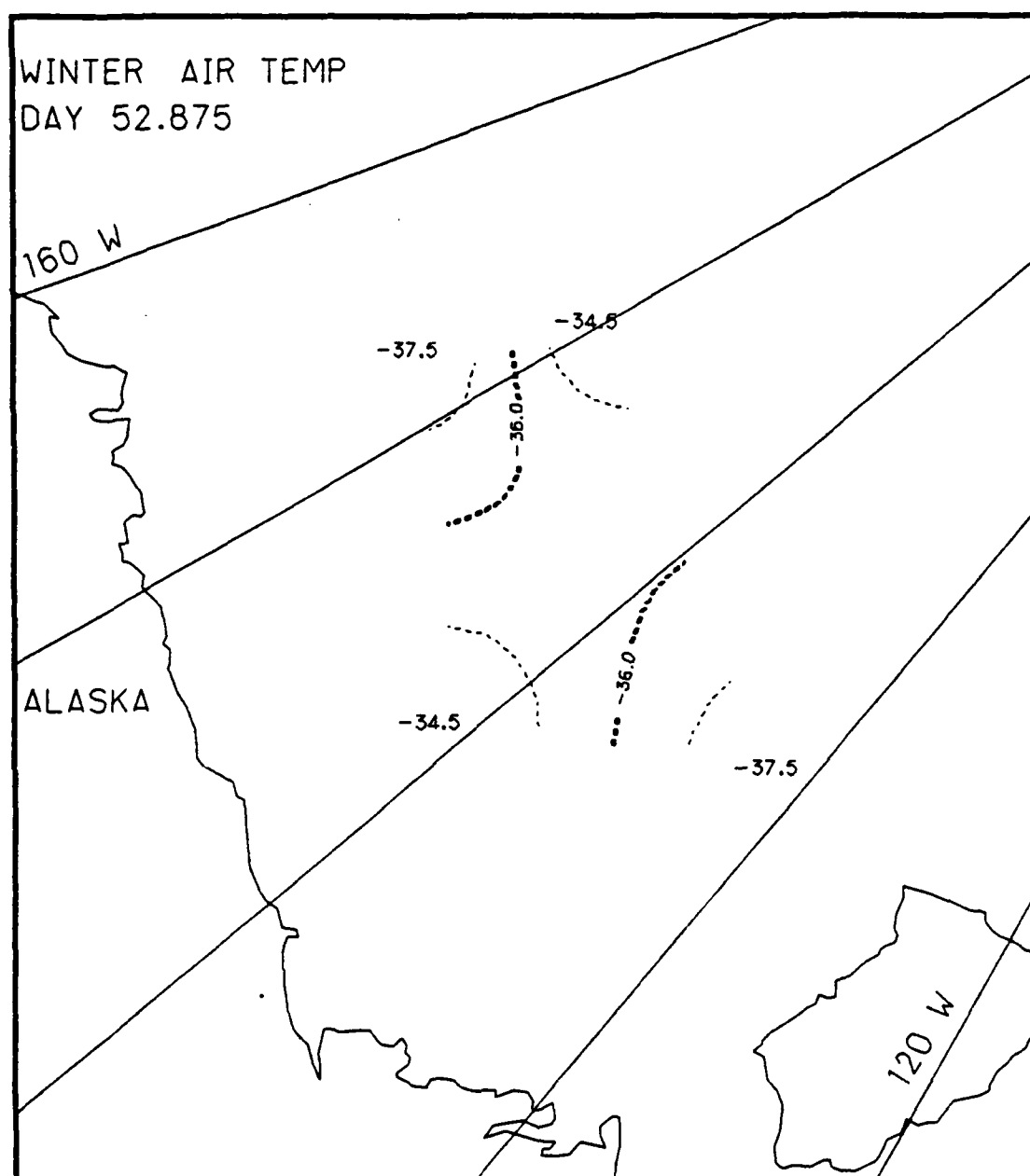


Fig. I.16. Spatial atmospheric temperature variations, day 52.875, based on the AIDJEX data from stations with hydrophones, winter 1976.

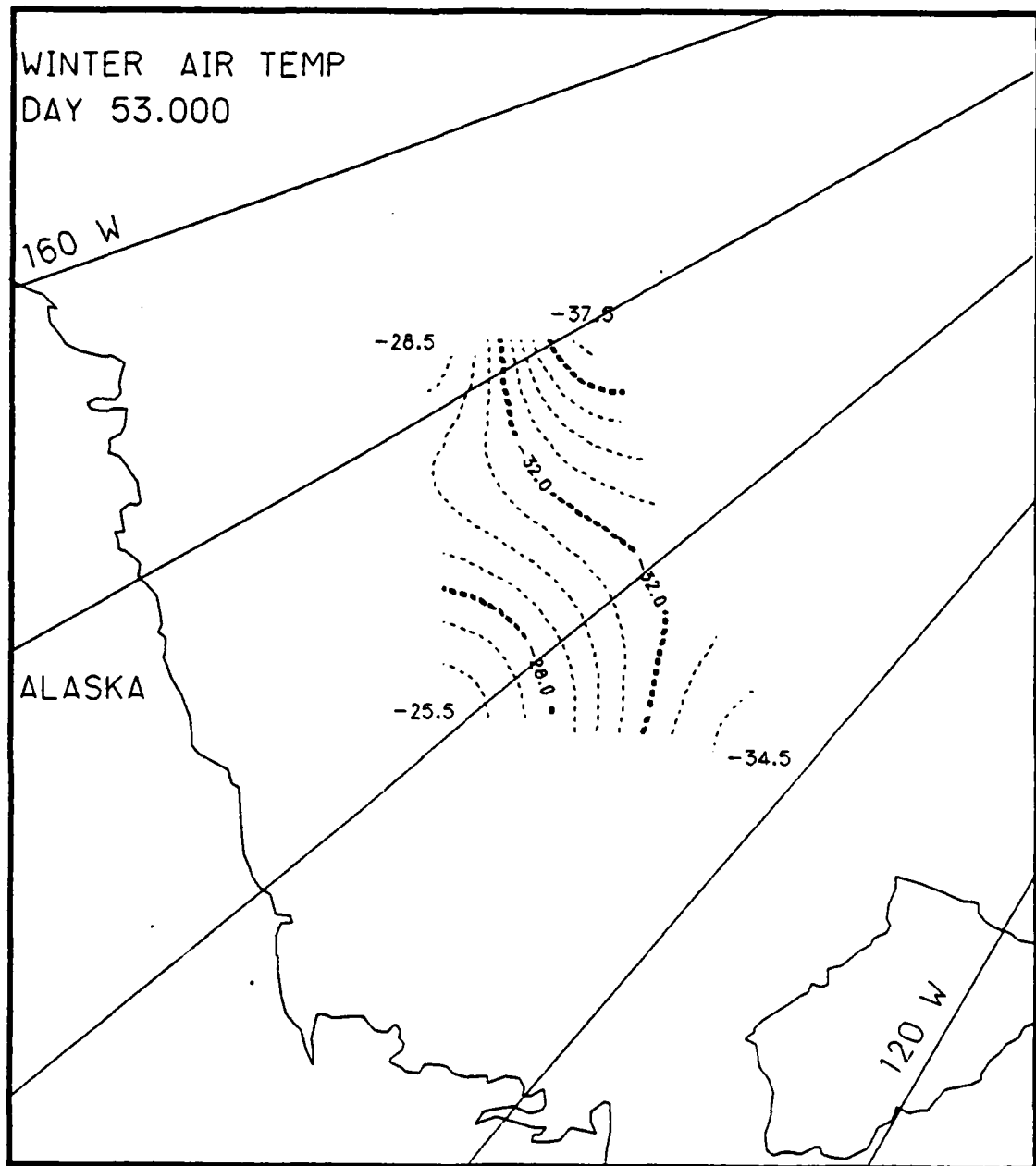


Fig. I.17. Spatial atmospheric temperature variations, day 53.0, based on the AIDJEX data from stations with hydrophones, winter 1976.

Appendix J

Two-Dimensional Contour Maps of
Arctic Atmospheric Pressure Variations,
16-17 May 1976 (Spring)

This appendix contains the two-dimensional contour maps of the AIDJEX atmospheric pressure data collected at those stations with hydrophones during the 48 hour period of 16-17 May 1976. The contour maps show the spatial variations of atmospheric pressure (millibars) at 3 hr intervals. The contour map for day 135.75 was not generated as a result of a lack of data.

List of Figures
Appendix J

2-176

	<u>Page</u>
Fig. J.1. Spatial atmospheric pressure variations, day 135.0	2-177
Fig. J.2. Spatial atmospheric pressure variations, day 135.125	2-178
Fig. J.3. Spatial atmospheric pressure variations, day 135.25	2-179
Fig. J.4. Spatial atmospheric pressure variations, day 135.375	2-180
Fig. J.5. Spatial atmospheric pressure variations, day 135.5	2-181
Fig. J.6. Spatial atmospheric pressure variations, day 135.625	2-182
Fig. J.7. Spatial atmospheric pressure variations, day 135.875	2-183
Fig. J.8. Spatial atmospheric pressure variations, day 136.0	2-184
Fig. J.9. Spatial atmospheric pressure variations, day 136.125	2-185
Fig. J.10. Spatial atmospheric pressure variations, day 136.25	2-186
Fig. J.11. Spatial atmospheric pressure variations, day 136.375	2-187
Fig. J.12. Spatial atmospheric pressure variations, day 136.5	2-188
Fig. J.13. Spatial atmospheric pressure variations, day 136.625	2-189
Fig. J.14. Spatial atmospheric pressure variations, day 136.75	2-190
Fig. J.15. Spatial atmospheric pressure variations, day 136.875	2-191
Fig. J.16. Spatial atmospheric pressure variations, day 137.0	2-192

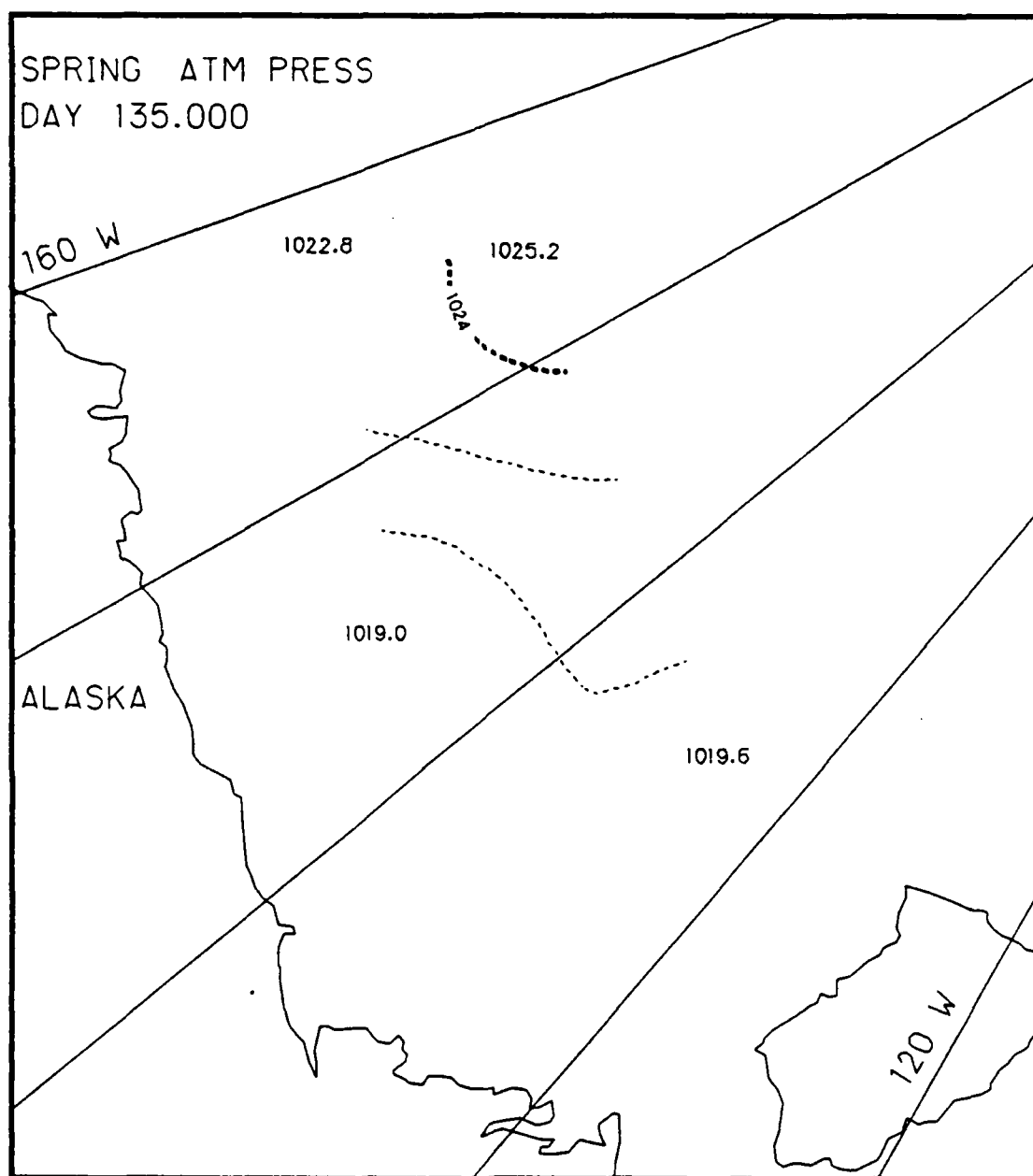


Fig. J.1. Spatial atmospheric pressure variations, day 135.0, based on the AIDJEX data from stations with hydrophones, spring 1976.

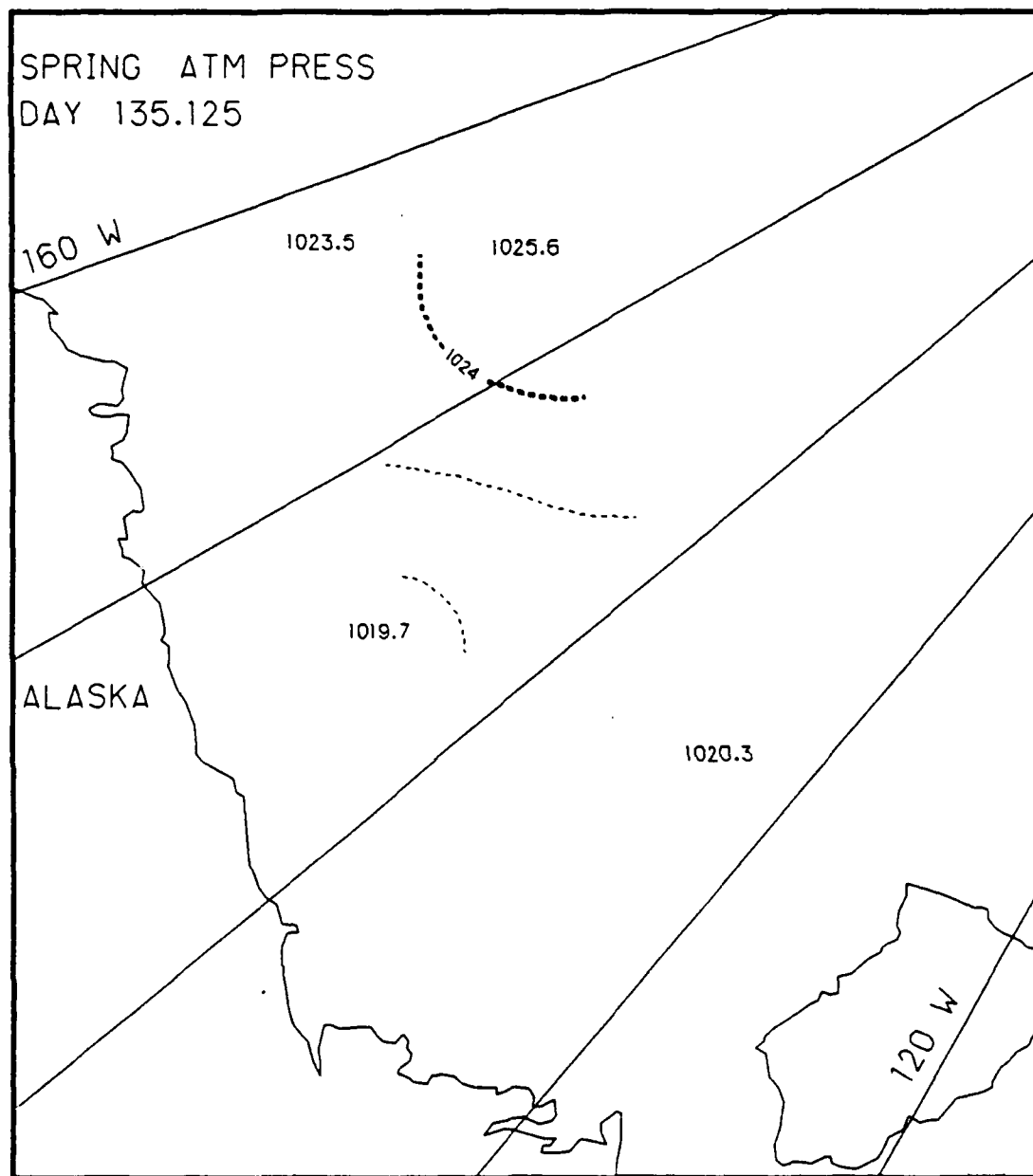


Fig. J.2. Spatial atmospheric pressure variations, day 135.125, based on the AIDJEX data from stations with hydrophones, spring 1976.

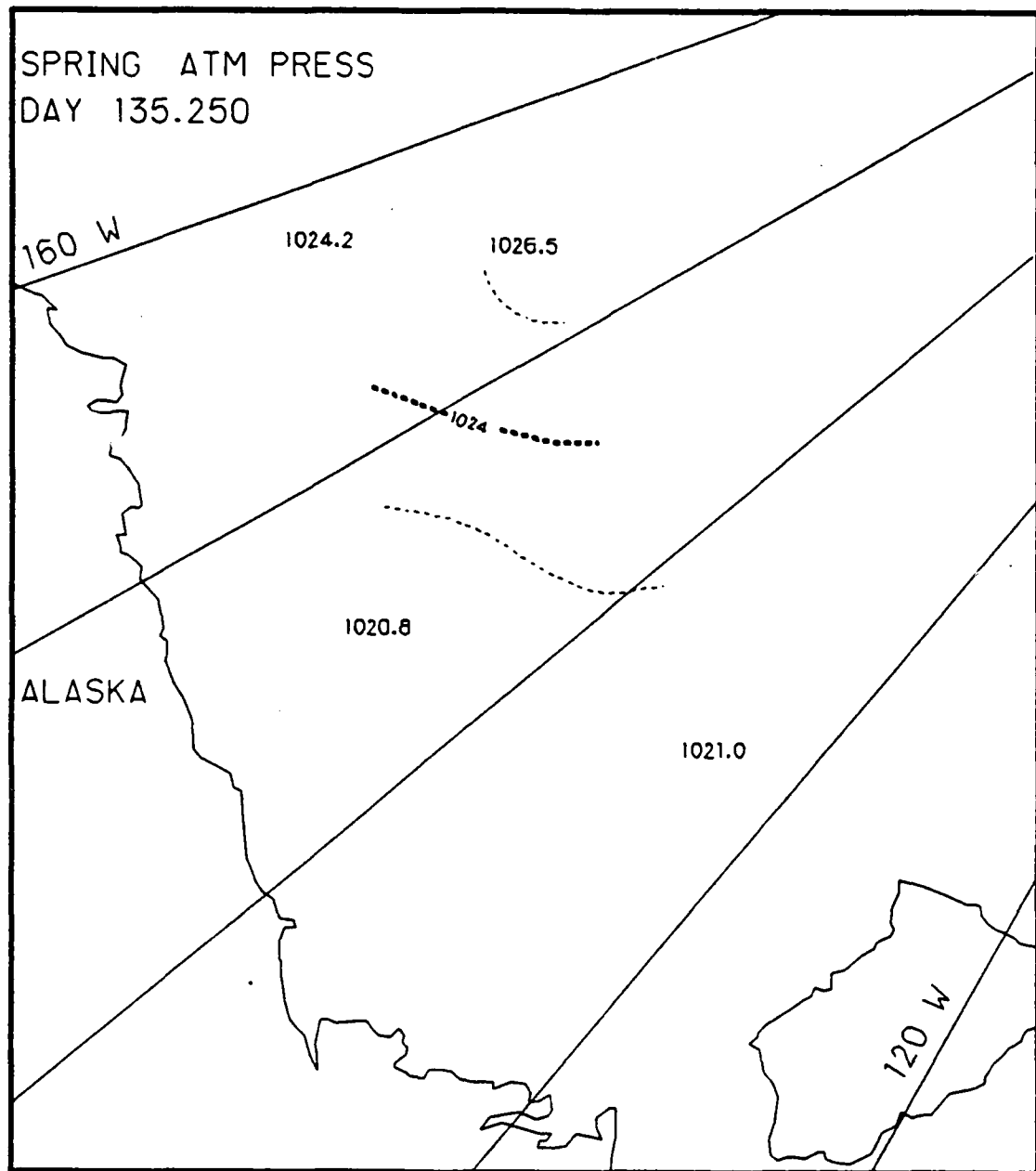


Fig. J.3. Spatial atmospheric pressure variations, day 135.25, based on the AIDJEX data from stations with hydrophones, spring 1976.

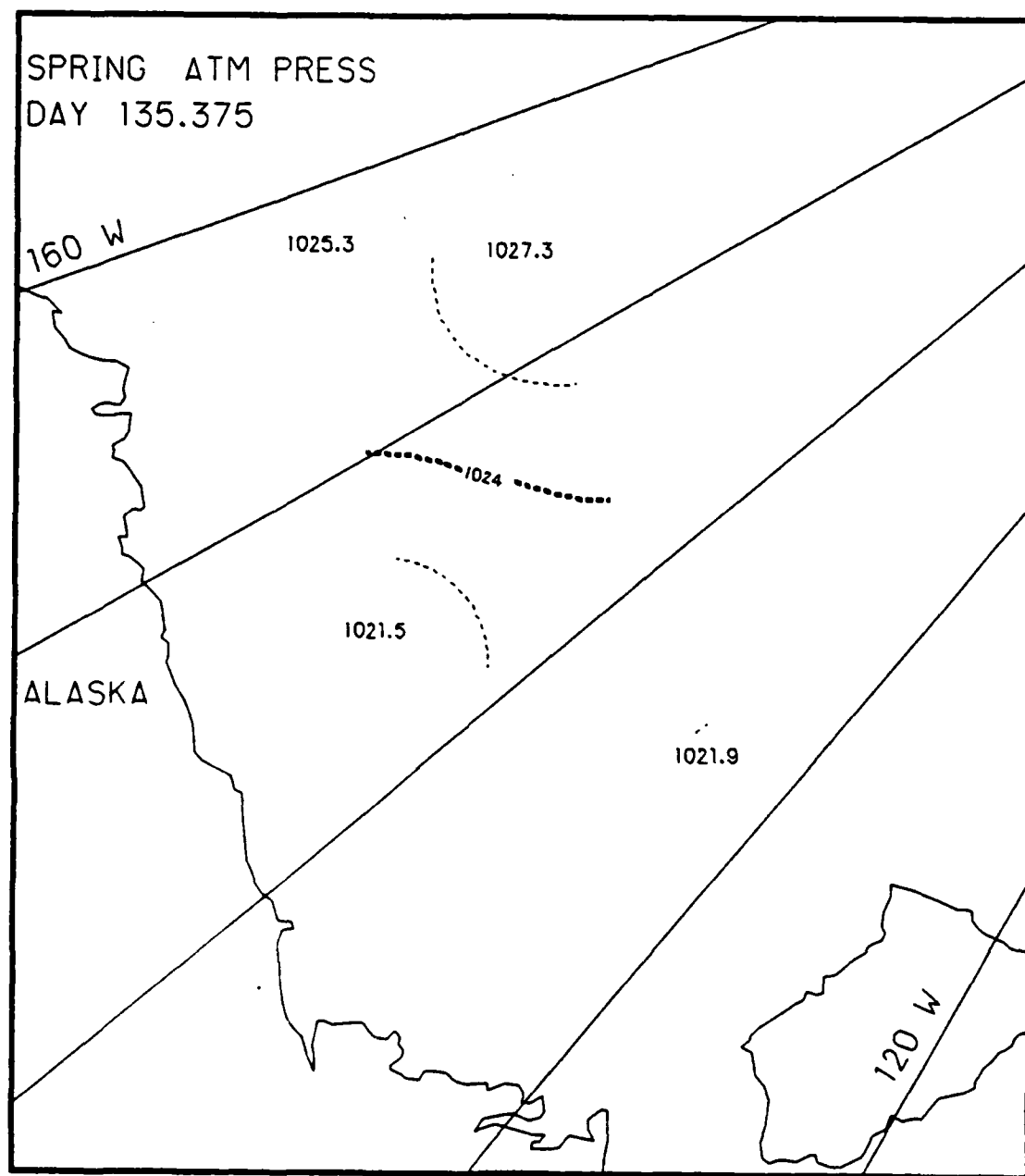


Fig. J.4. Spatial atmospheric pressure variations, day 135.375, based on the AIDJEX data from stations with hydrophones, spring 1976.

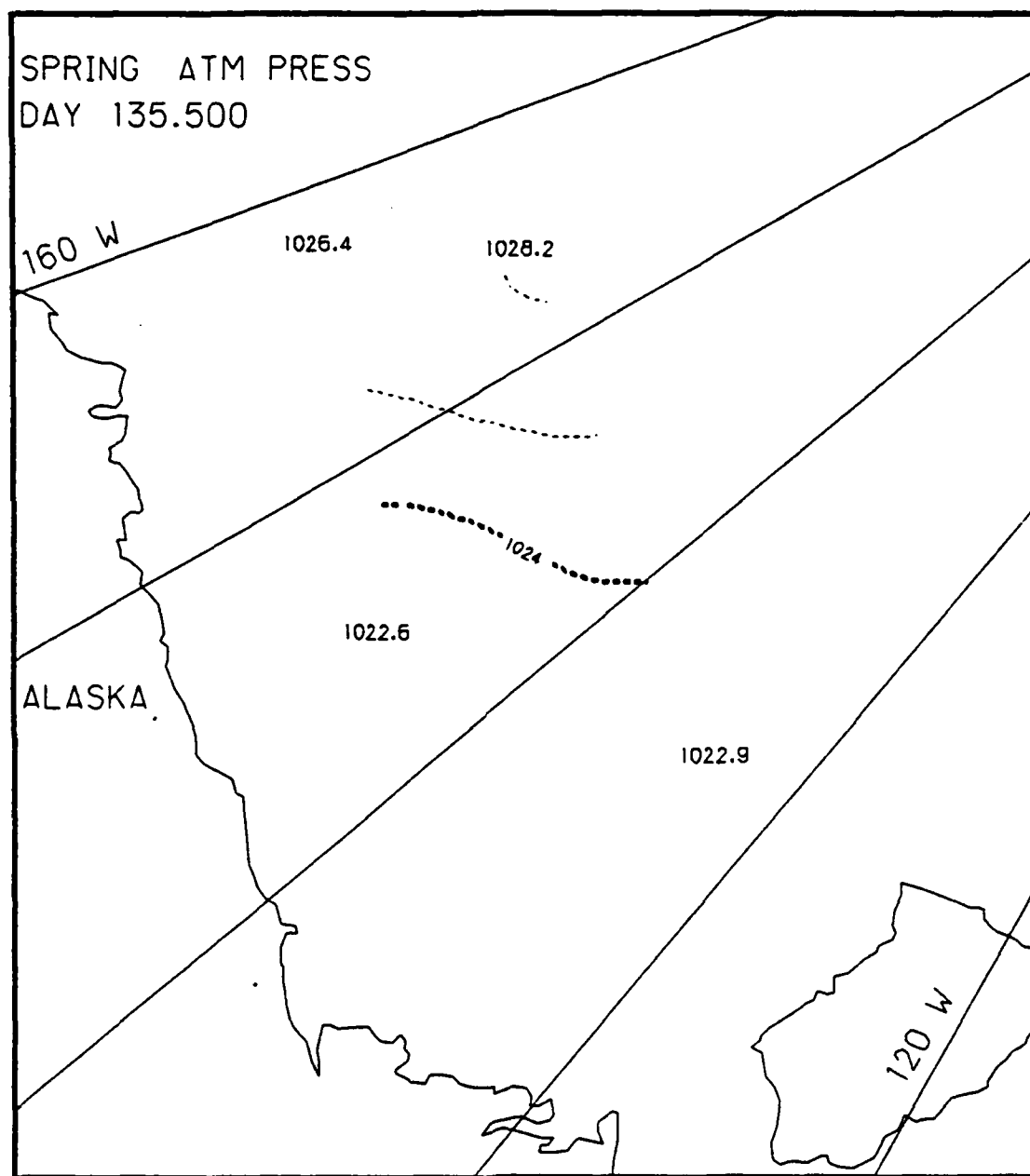


Fig. J.5. Spatial atmospheric pressure variations, day 135.5, based on the AIDJEX data from stations with hydrophones, spring 1976.

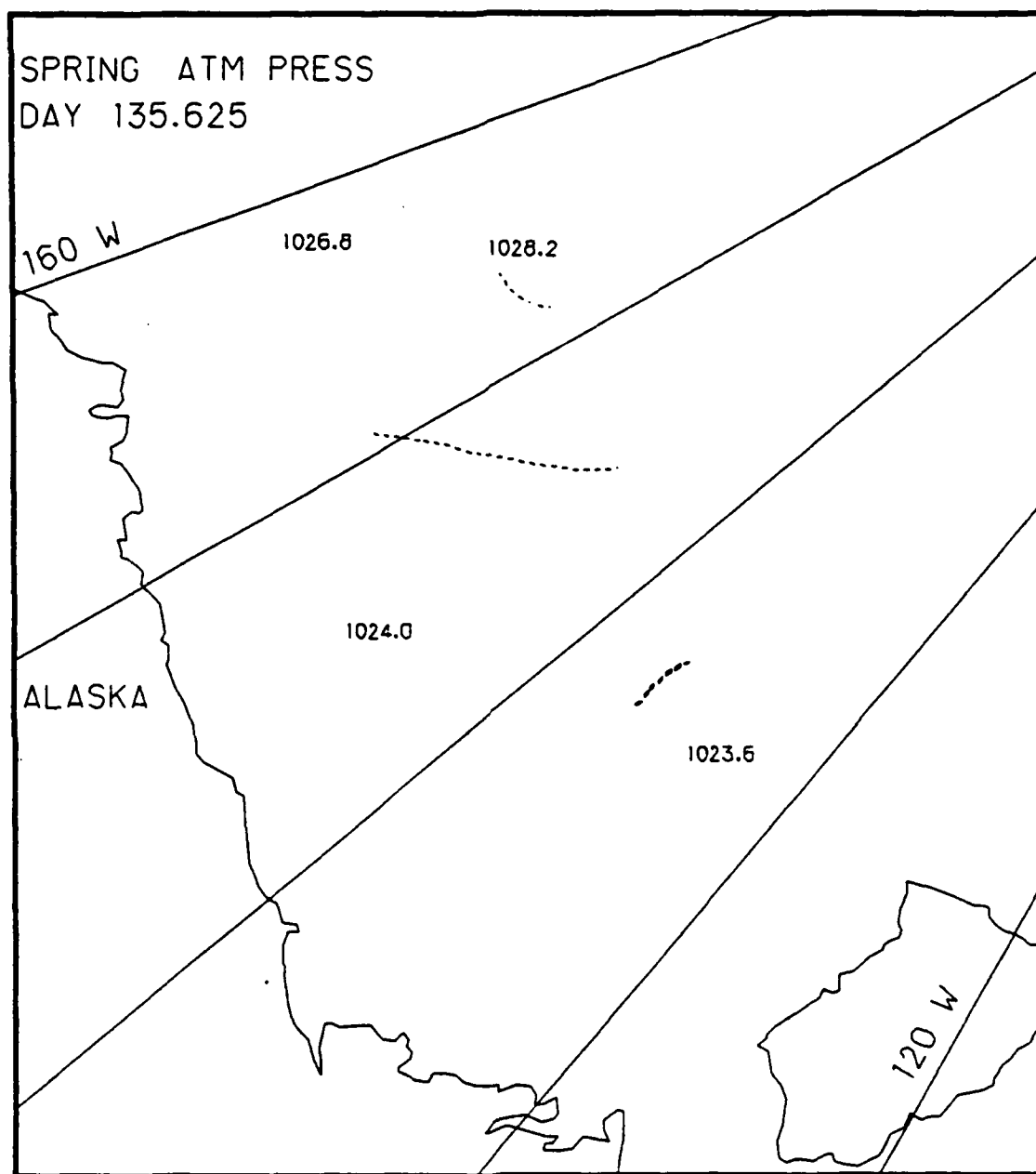


Fig. J.6. Spatial atmospheric pressure variations, day 135.625, based on the AIDJEX data from stations with hydrophones, spring 1976.

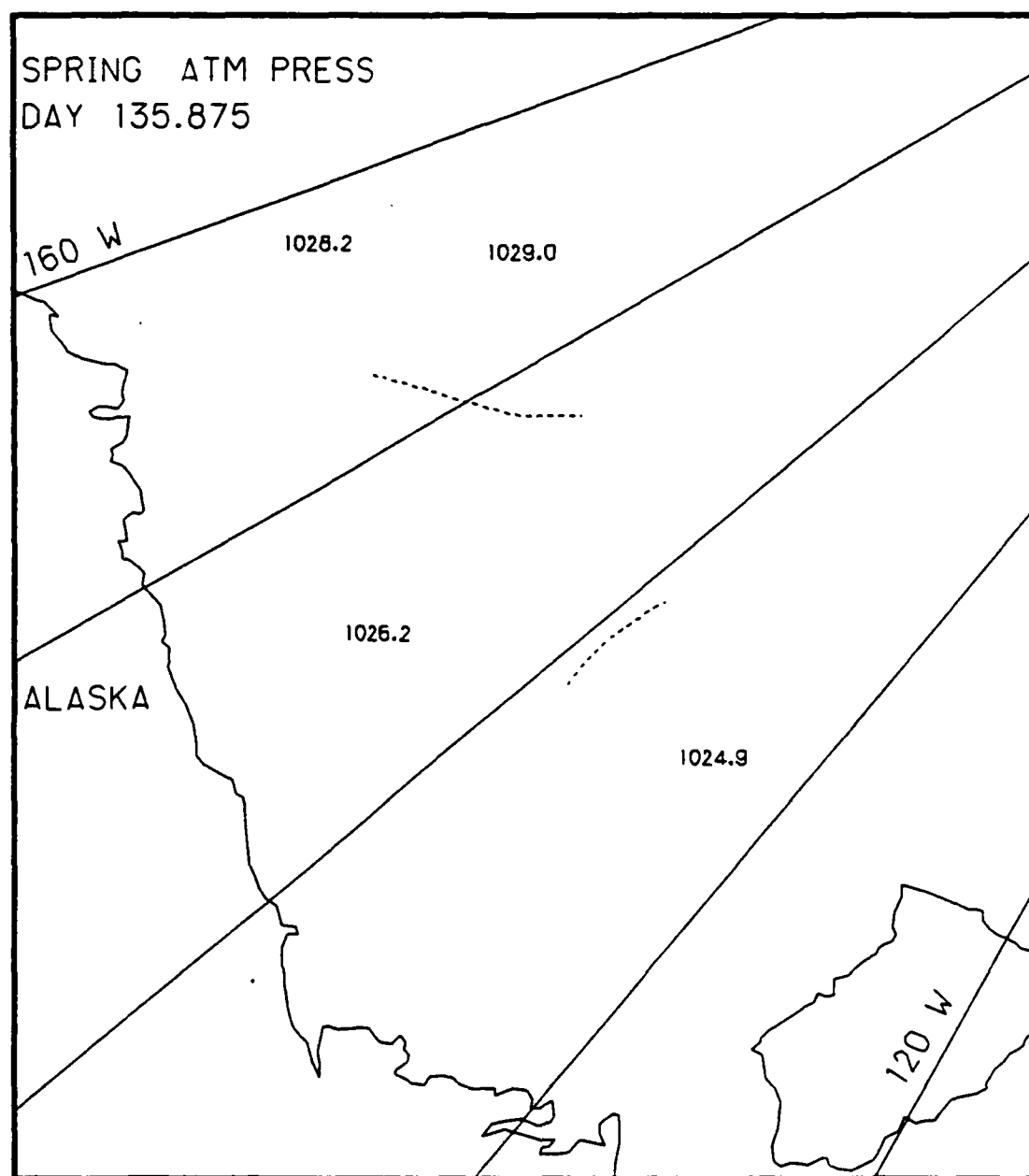


Fig. J.7. Spatial atmospheric pressure variations, day 135.875, based on the AIDJEX data from stations with hydrophones, spring 1976.

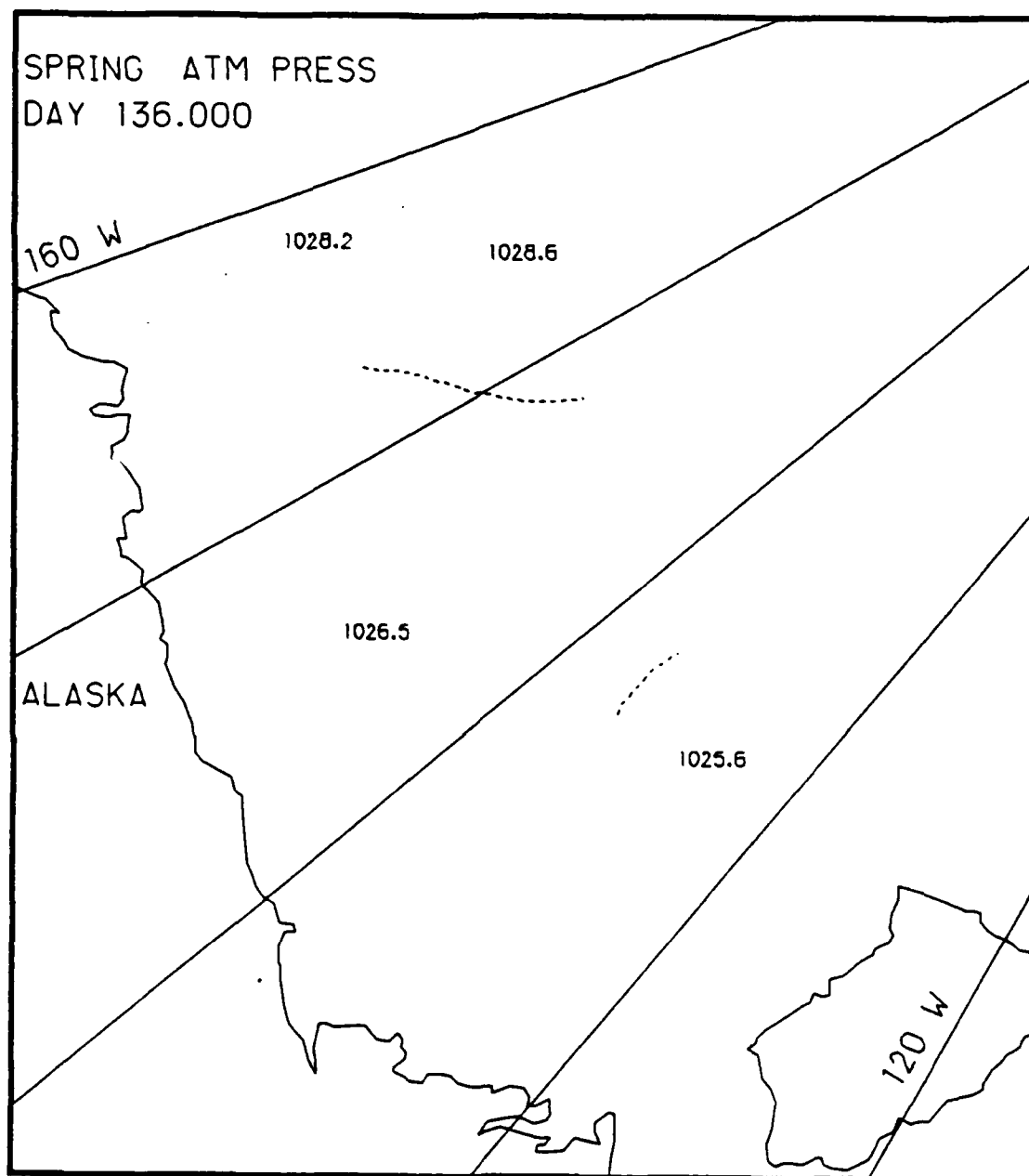


Fig. J.8. Spatial atmospheric pressure variations, day 136.0, based on the AIDJEX data from stations with hydrophones, spring 1976.

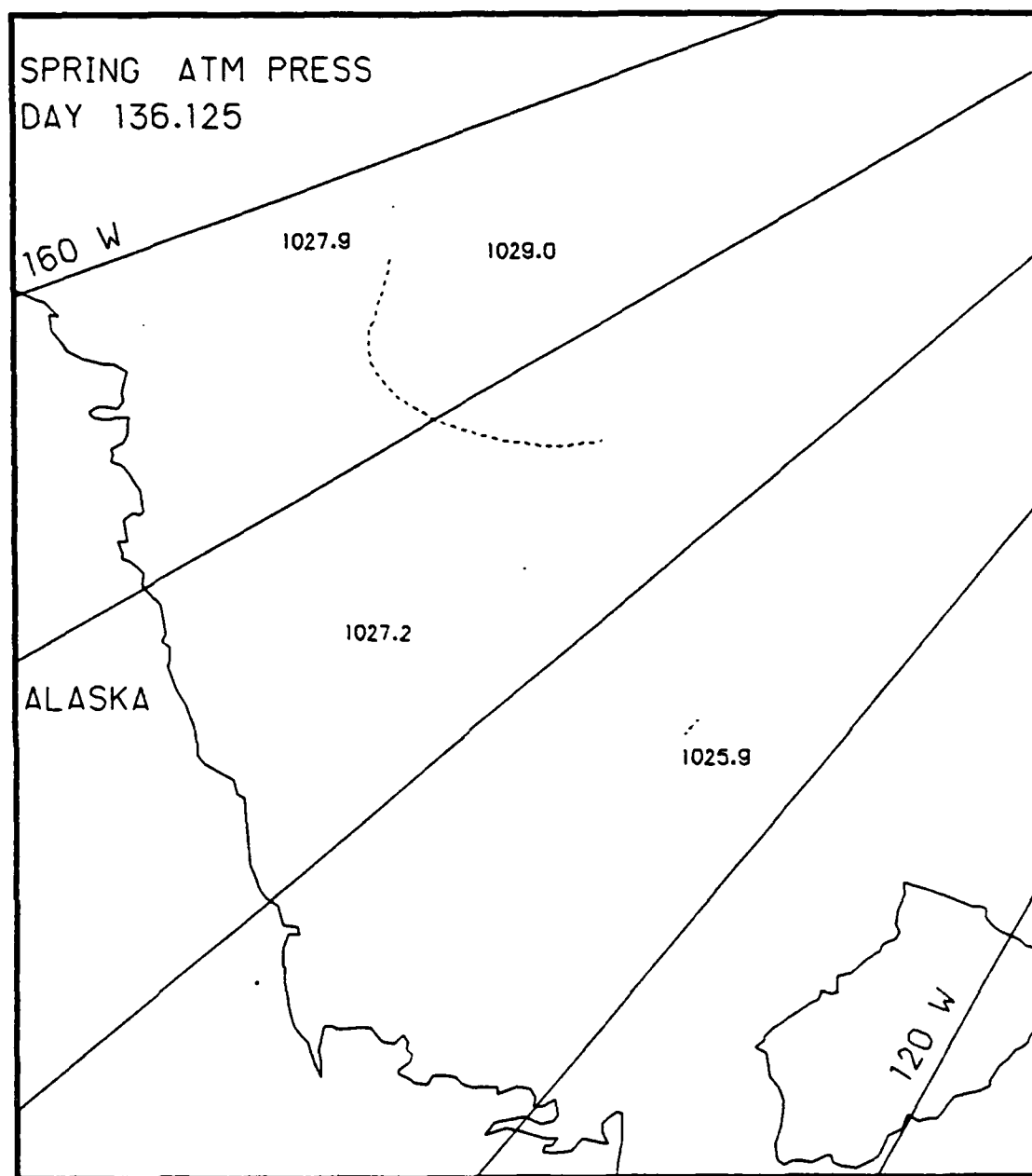


Fig. J.9. Spatial atmospheric pressure variations, day 136.125, based on the AIDJEX data from stations with hydrophones, spring 1976.

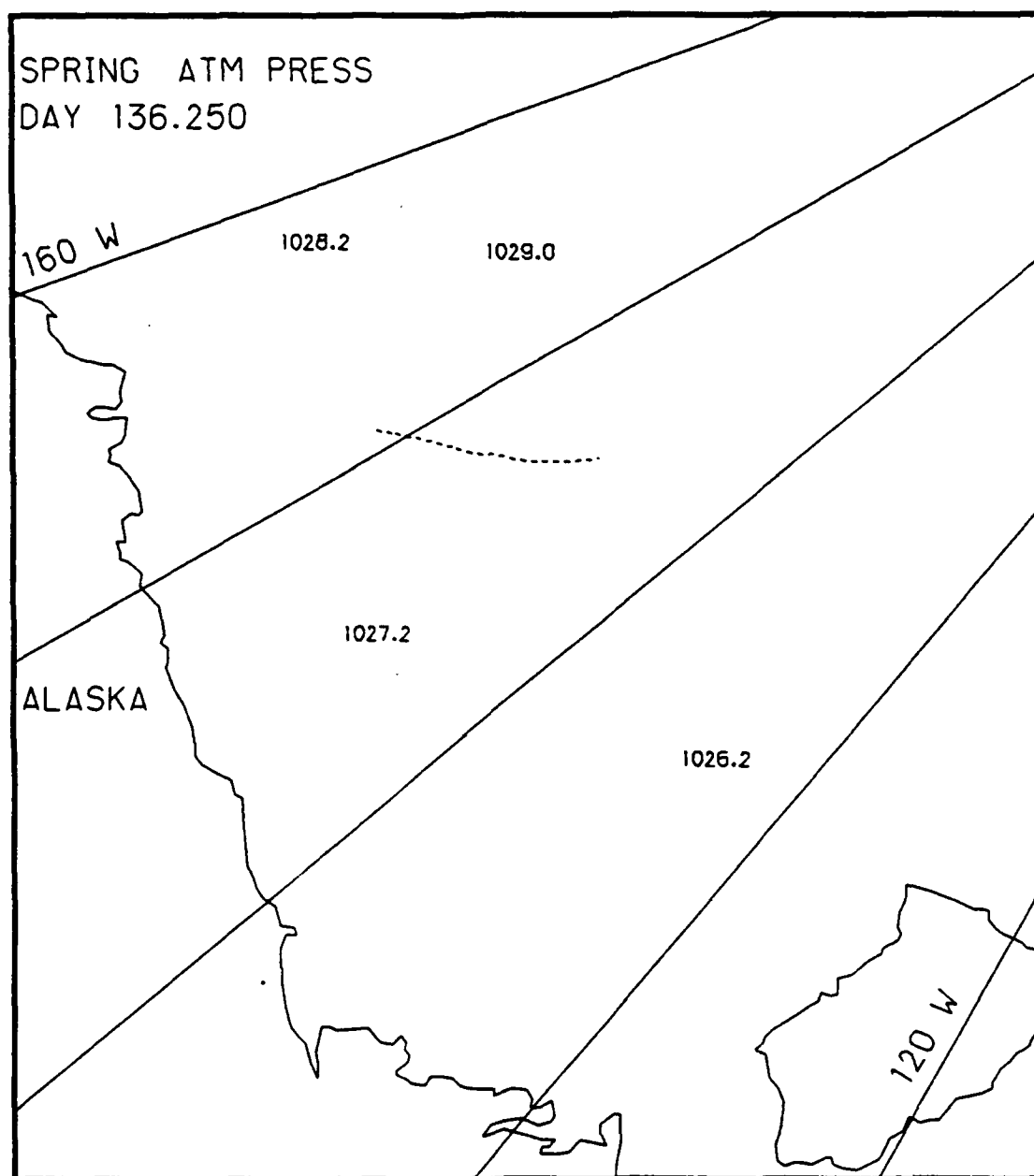


Fig. J.10. Spatial atmospheric pressure variations, day 136.25, based on the AIDJEX data from stations with hydrophones, spring 1976.

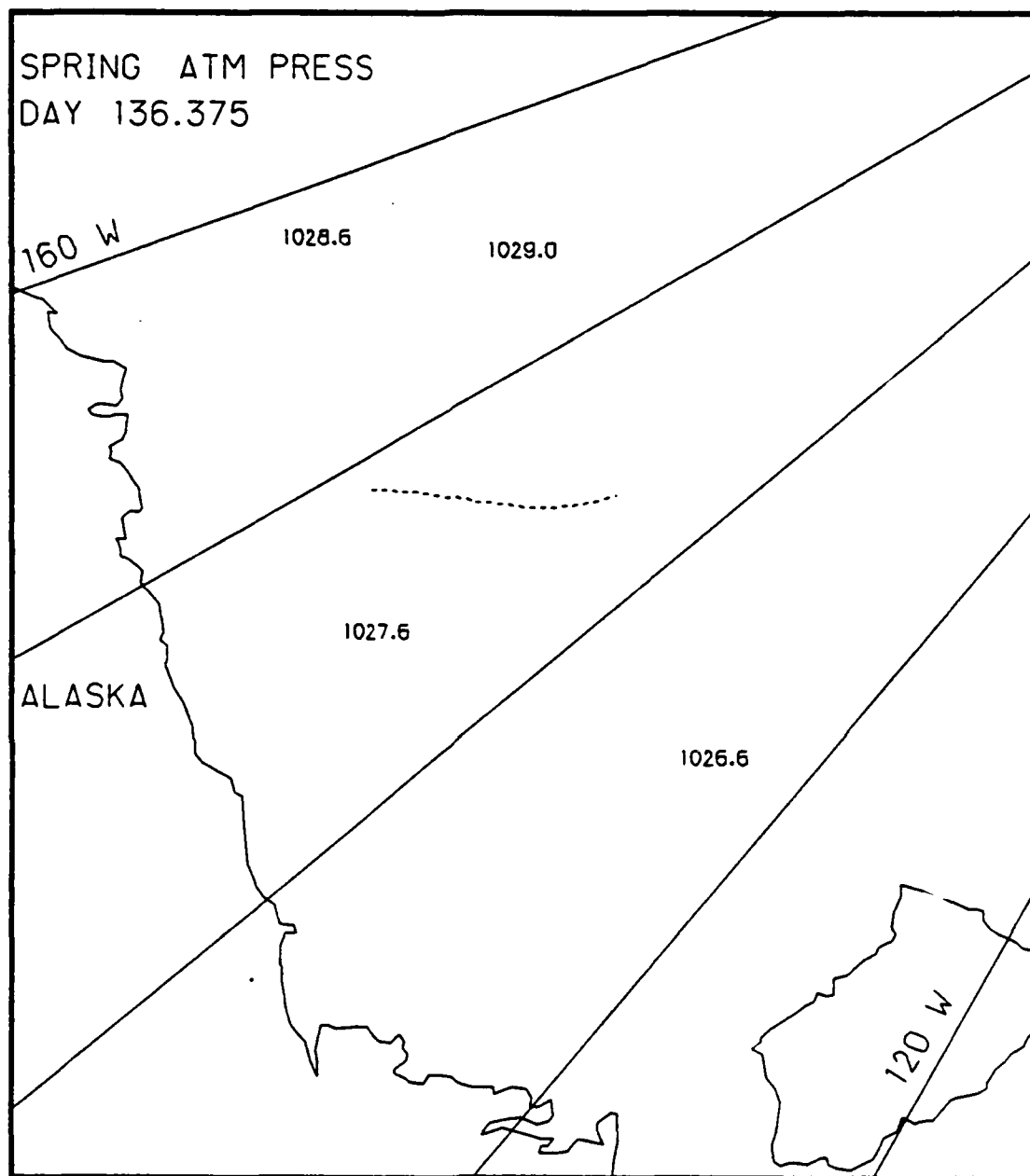


Fig. J.11. Spatial atmospheric pressure variations, day 136.375, based on the AIDJEX data from stations with hydrophones, spring 1976.

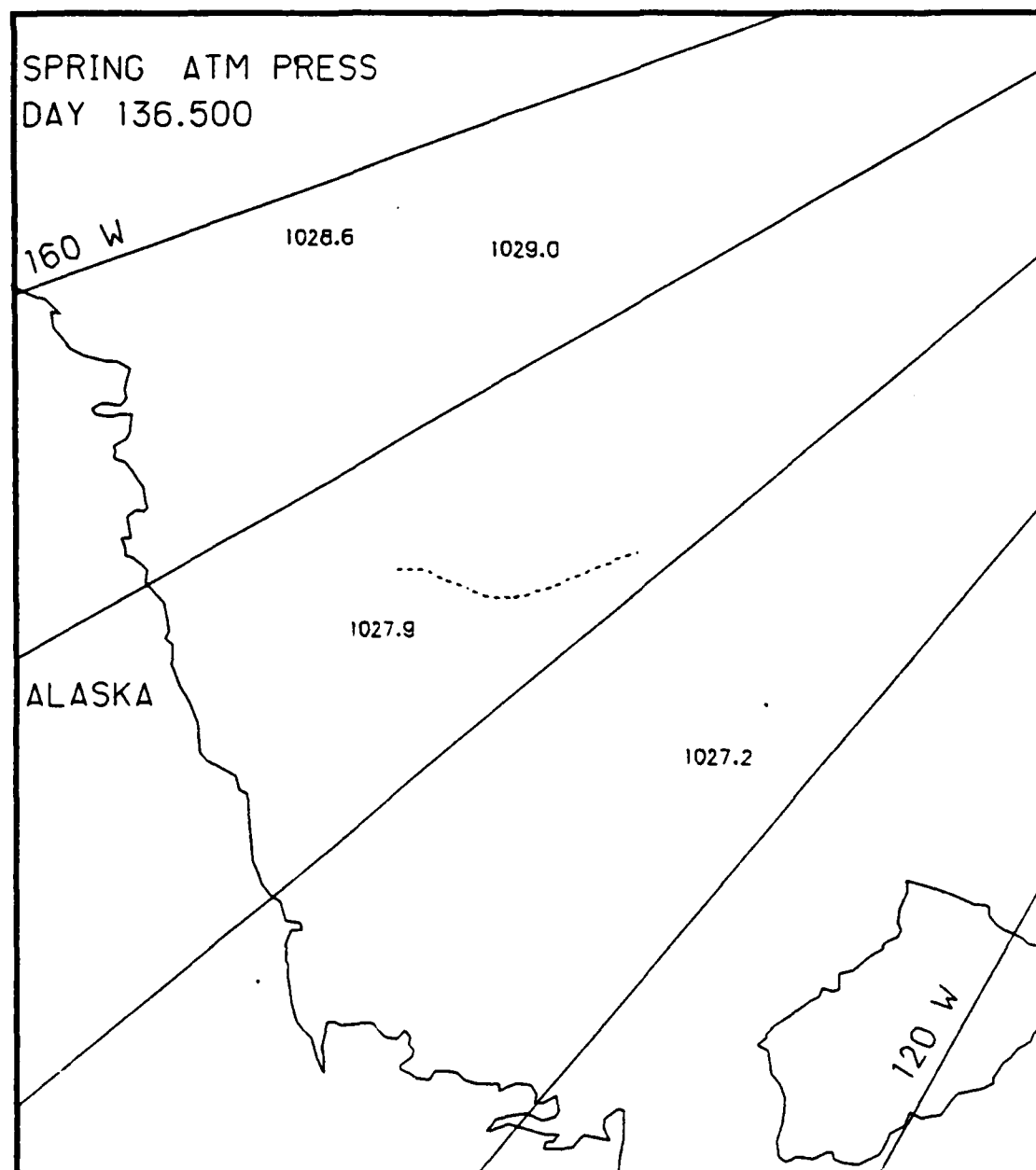


Fig. J.12. Spatial atmospheric pressure variations, day 136.5, based on the AIDJEX data from stations with hydrophones, spring 1976.

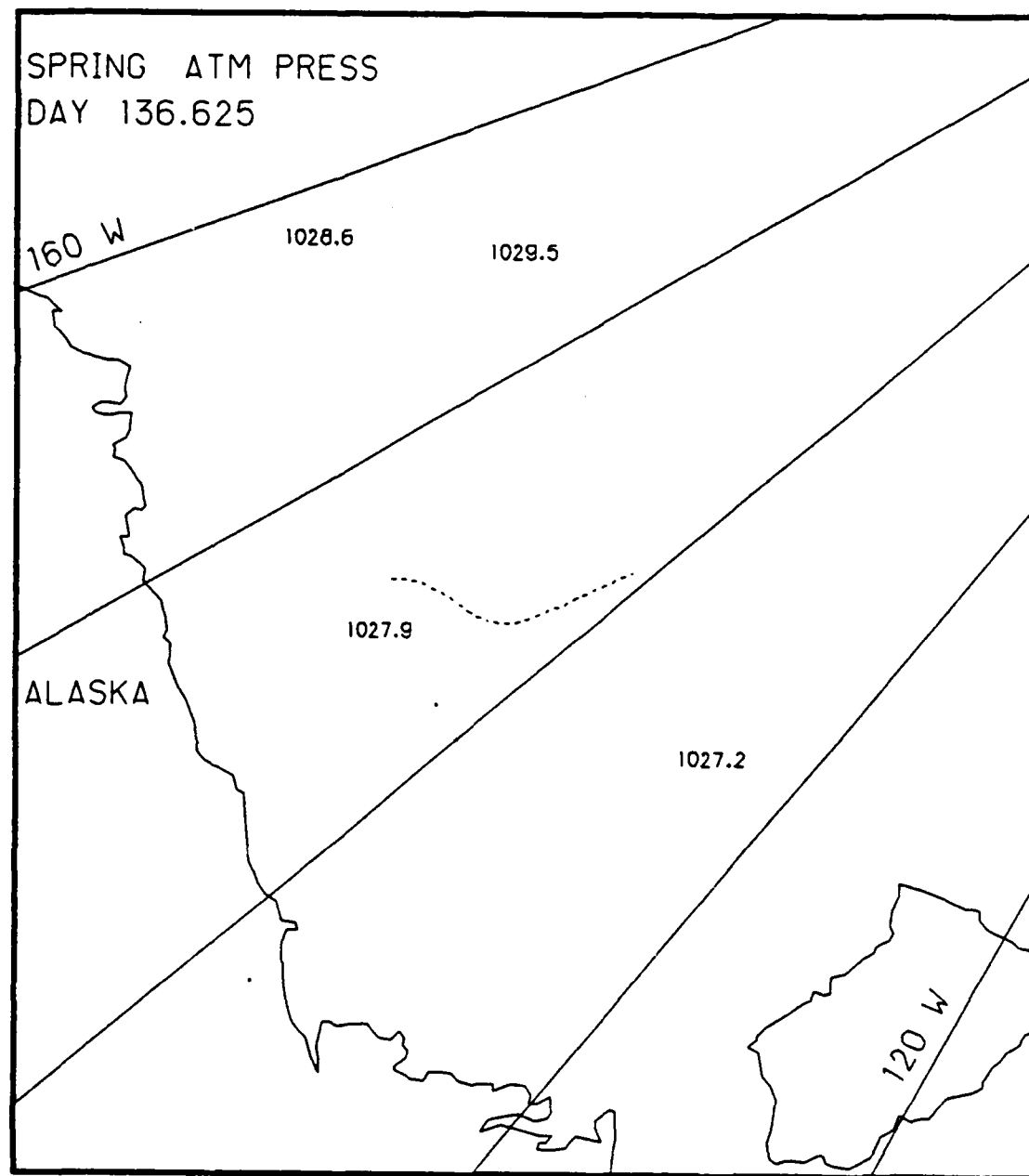


Fig. J.13. Spatial atmospheric pressure variations, day 136.625, based on the AIDJEX data from stations with hydrophones, spring 1976.

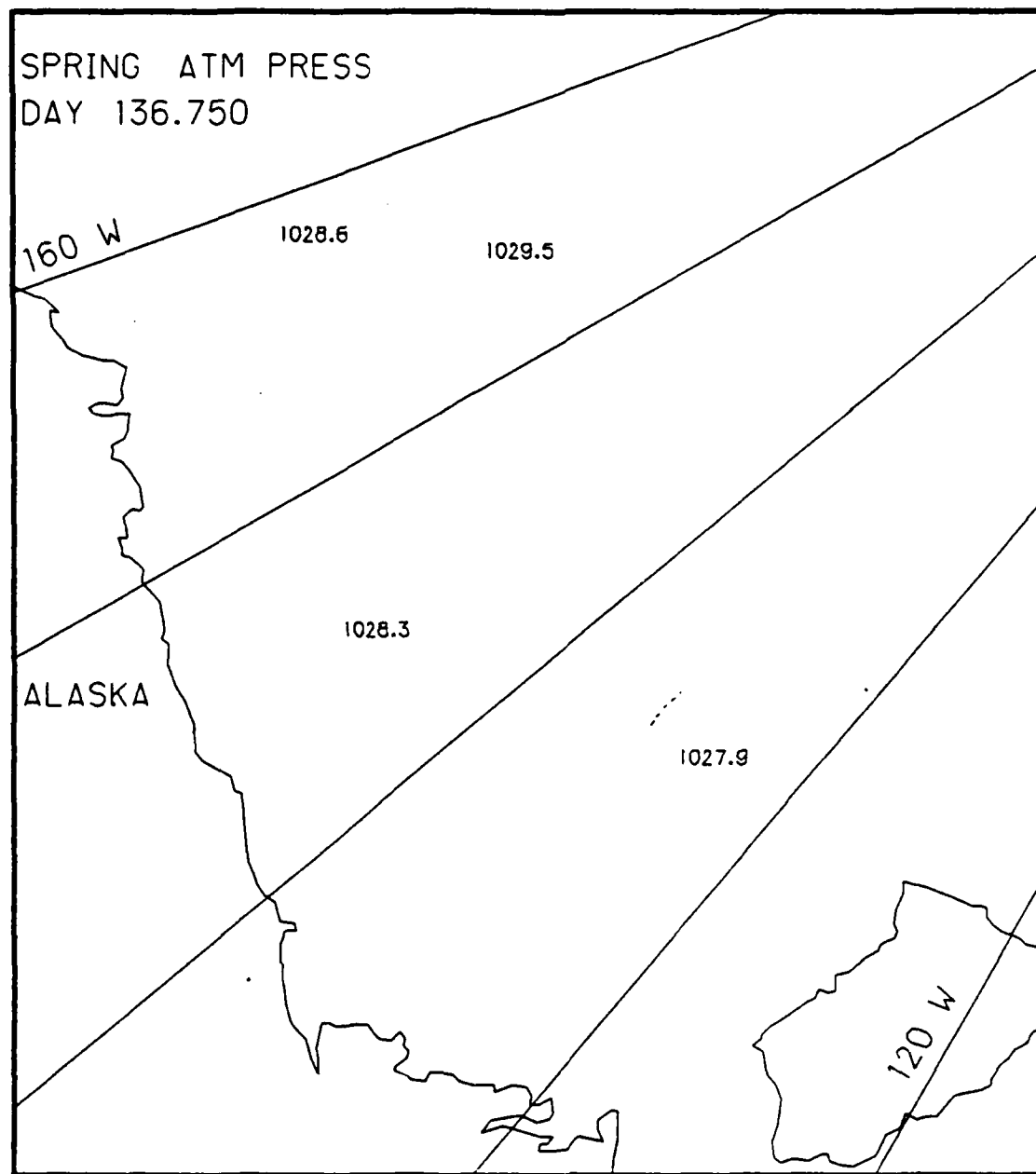


Fig. J.14. Spatial atmospheric pressure variations, day 136.75, based on the AIDJEX data from stations with hydrophones, spring 1976.

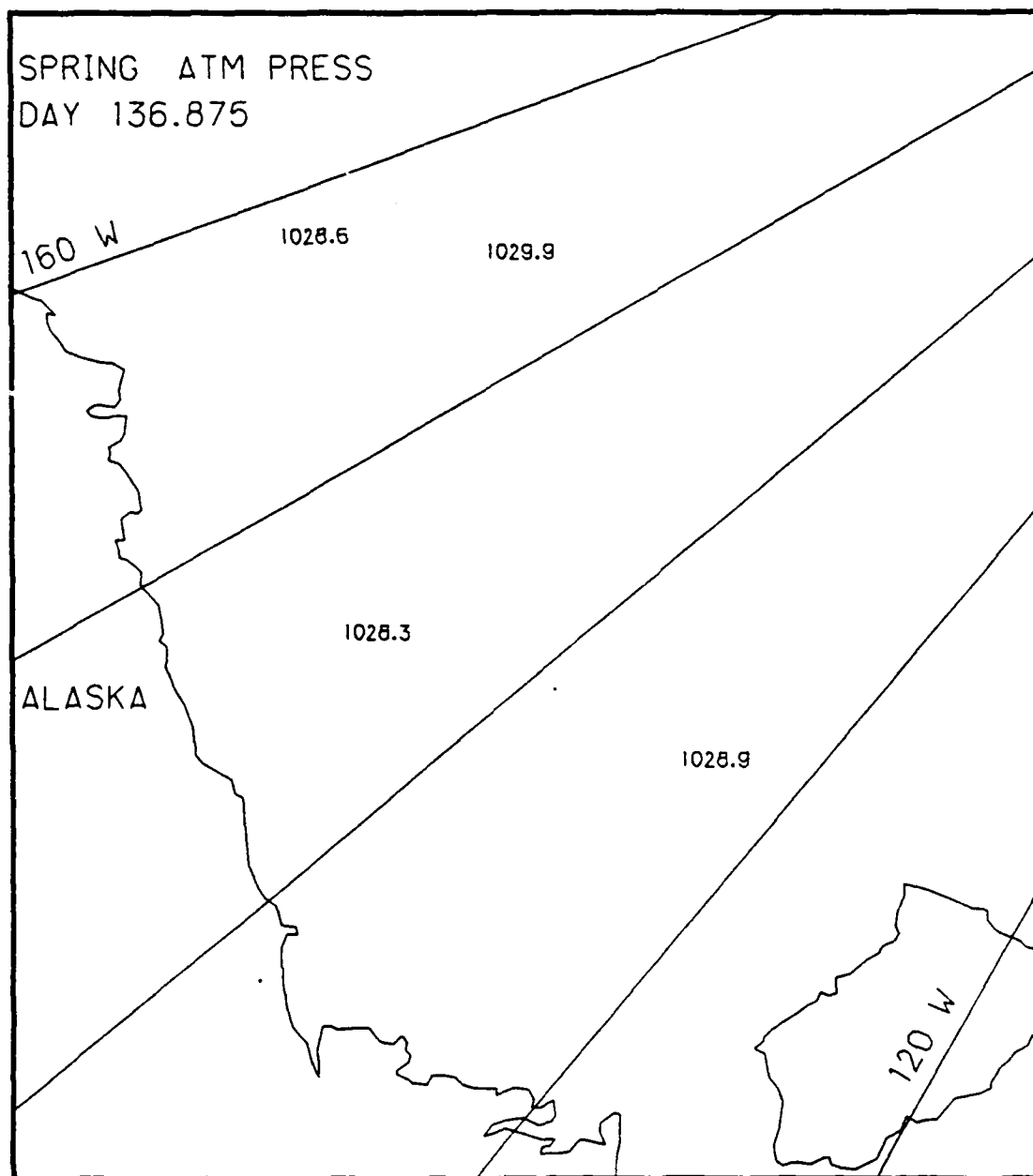


Fig. J.15. Spatial atmospheric pressure variations, day 136.875, based on the AIDJEX data from stations with hydrophones, spring 1976.

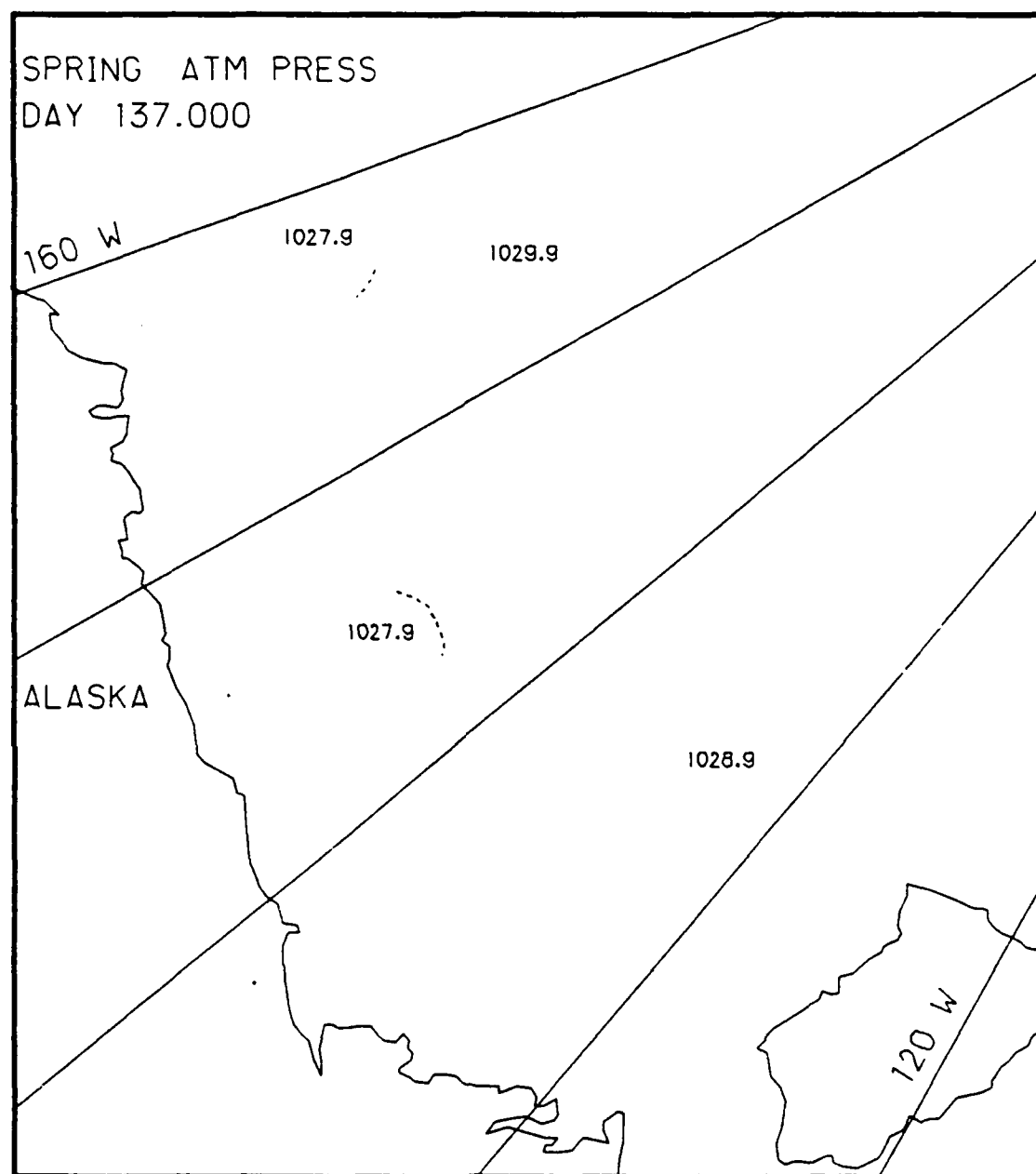


Fig. J.16. Spatial atmospheric pressure variations, day 137.0, based on the AIDJEX data from stations with hydrophones, spring 1976.

Appendix K

Two-Dimensional Contour Maps of
Arctic Atmospheric Temperature Variations,
16-17 May 1976 (Spring)

This appendix contains the two-dimensional contour maps of the AIDJEX atmospheric temperature data collected at those stations with hydrophones during the 48 hour period of 16-17 May 1976. The contour maps show the spatial variations of atmospheric temperature ($^{\circ}\text{C}$) at 3 hr intervals. The contour map for day 135.75 was not generated as a result of a lack of data.

List of Figures
Appendix K

	<u>Page</u>
Fig. K.1. Spatial atmospheric temperature variations, day 135.0	2-195
Fig. K.2. Spatial atmospheric temperature variations, day 135.125	2-196
Fig. K.3. Spatial atmospheric temperature variations, day 135.25	2-197
Fig. K.4. Spatial atmospheric temperature variations, day 135.375	2-198
Fig. K.5. Spatial atmospheric temperature variations, day 135.5	2-199
Fig. K.6. Spatial atmospheric temperature variations, day 135.625	2-200
Fig. K.7. Spatial atmospheric temperature variations, day 135.875	2-201
Fig. K.8. Spatial atmospheric temperature variations, day 136.0	2-202
Fig. K.9. Spatial atmospheric temperature variations, day 136.125	2-203
Fig. K.10. Spatial atmospheric temperature variations, day 136.25	2-204
Fig. K.11. Spatial atmospheric temperature variations, day 136.375	2-205
Fig. K.12. Spatial atmospheric temperature variations, day 136.5	2-206
Fig. K.13. Spatial atmospheric temperature variations, day 136.625	2-207
Fig. K.14. Spatial atmospheric temperature variations, day 136.75	2-208
Fig. K.15. Spatial atmospheric temperature variations, day 136.875	2-209
Fig. K.16. Spatial atmospheric temperature variations, day 137.0	2-210

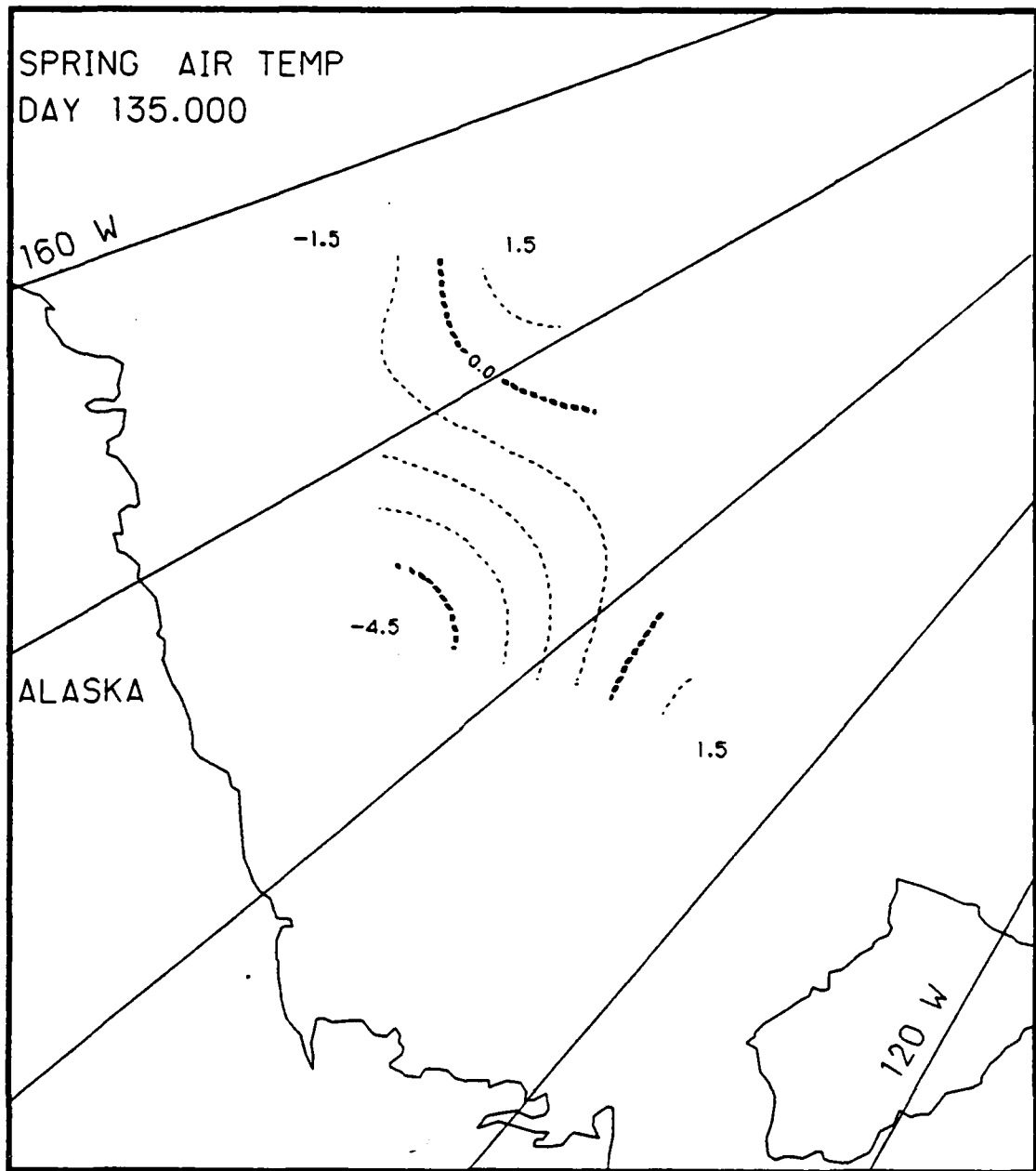


Fig. K.1. Spatial atmospheric temperature variations, day 135.0, based on the AIDJEX data from stations with hydrophones, spring 1976.

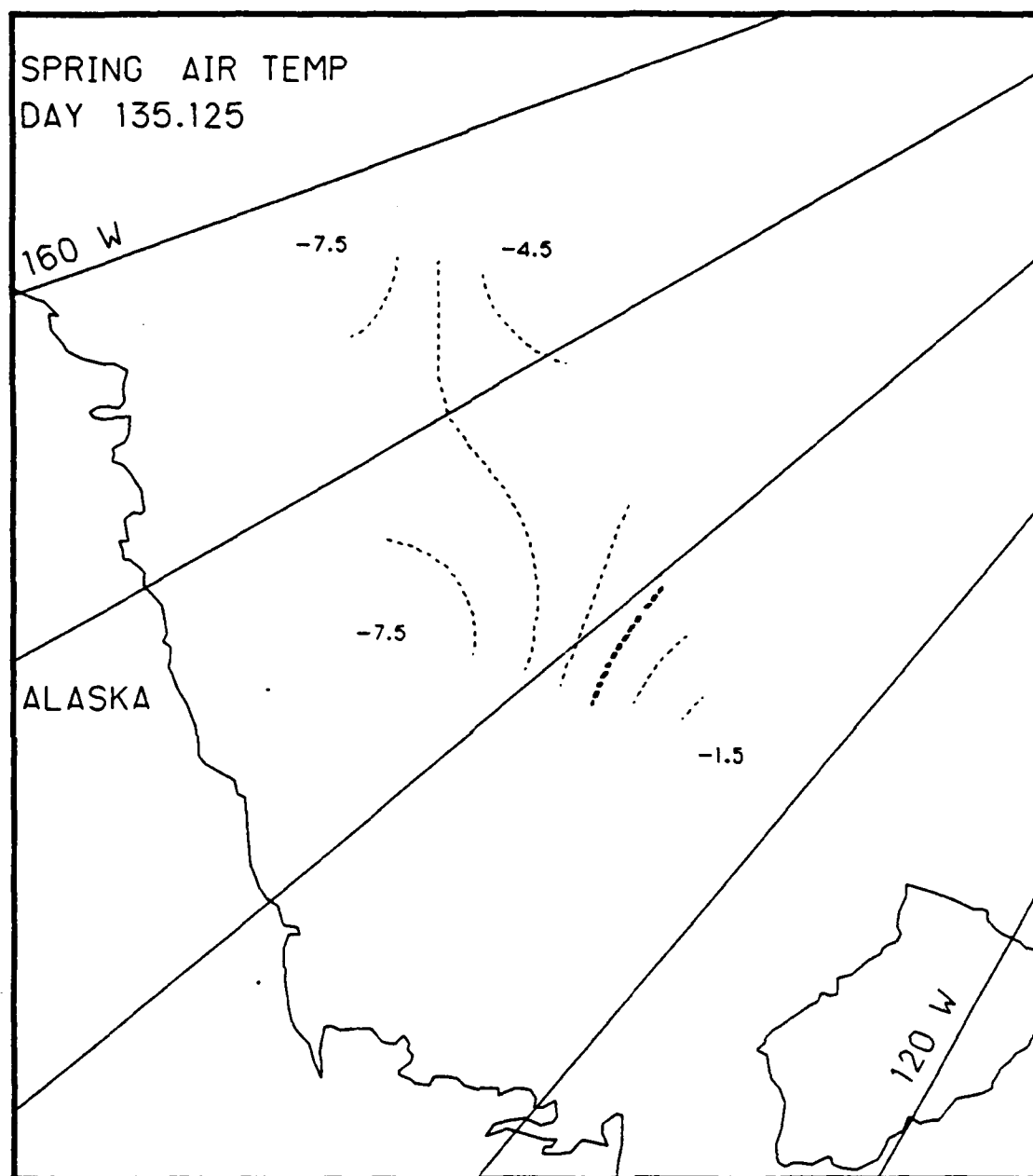


Fig. K.2. Spatial atmospheric temperature variations, day 135.125, based on the AIDJEX data from stations with hydrophones, spring 1976.

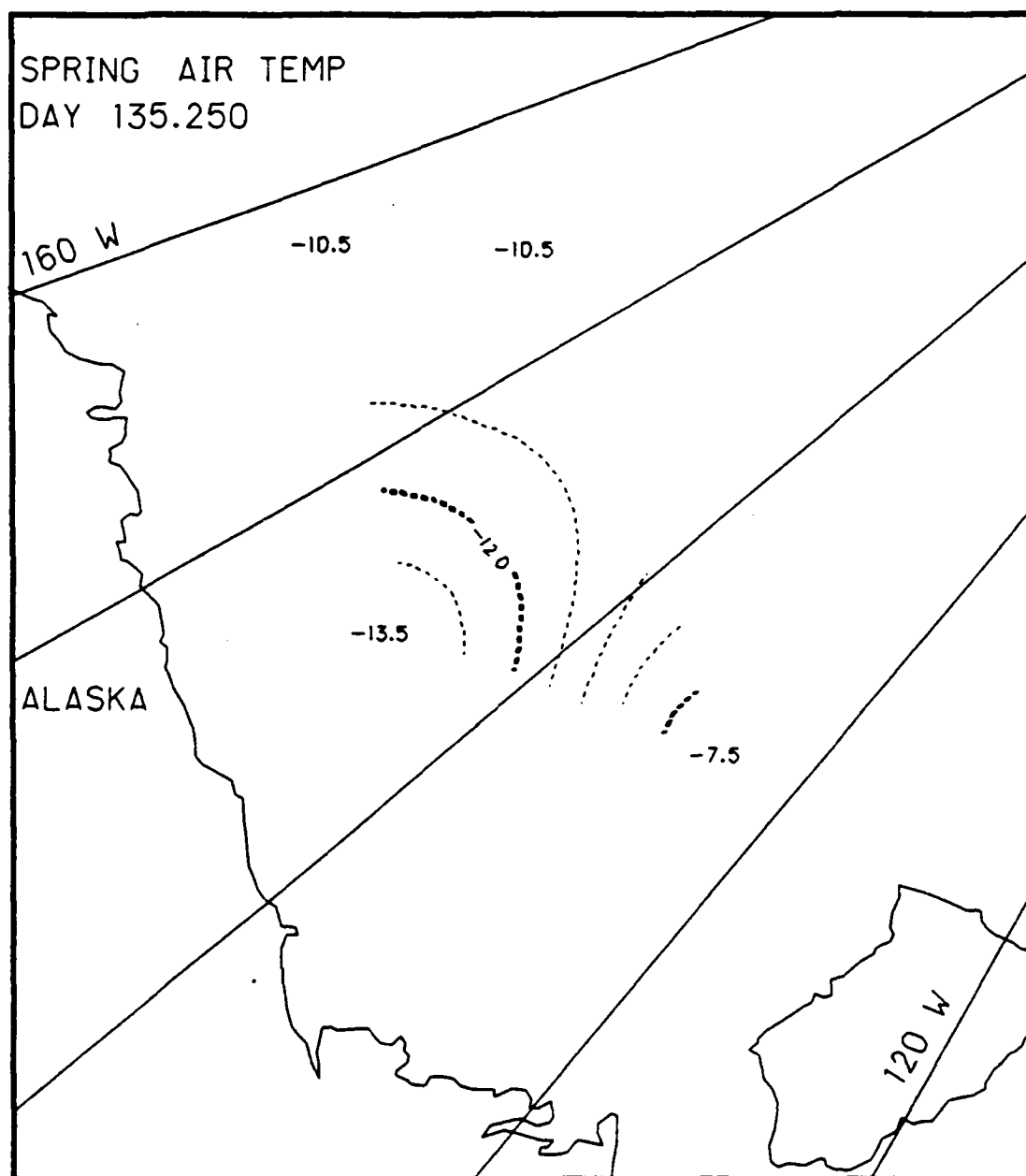


Fig. K.3. Spatial atmospheric temperature variations, day 135.25, based on the AIDJEX data from stations with hydrophones, spring 1976.

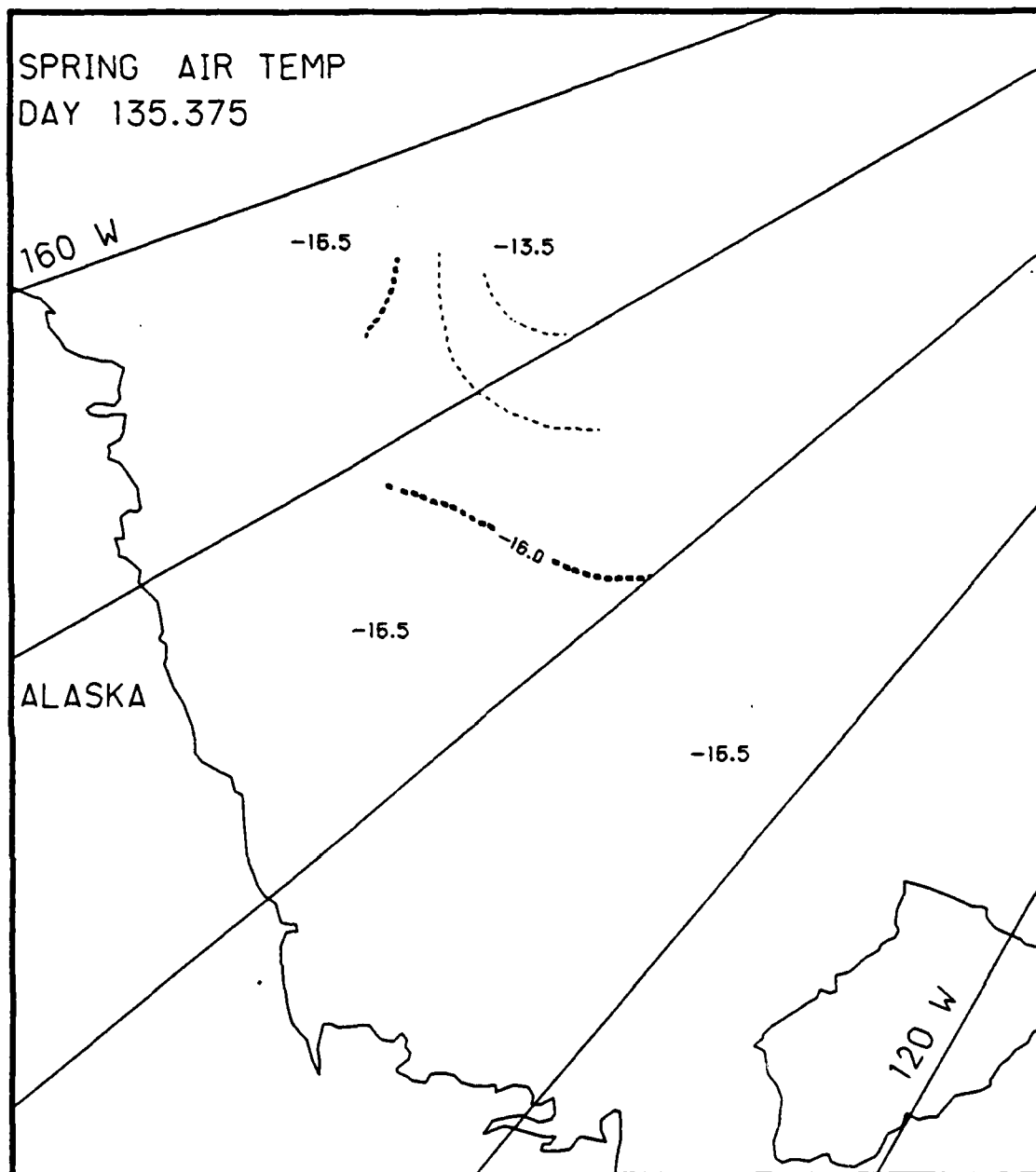


Fig. K.4. Spatial atmospheric temperature variations, day 135.375, based on the AIDJEX data from stations with hydrophones, spring 1976.

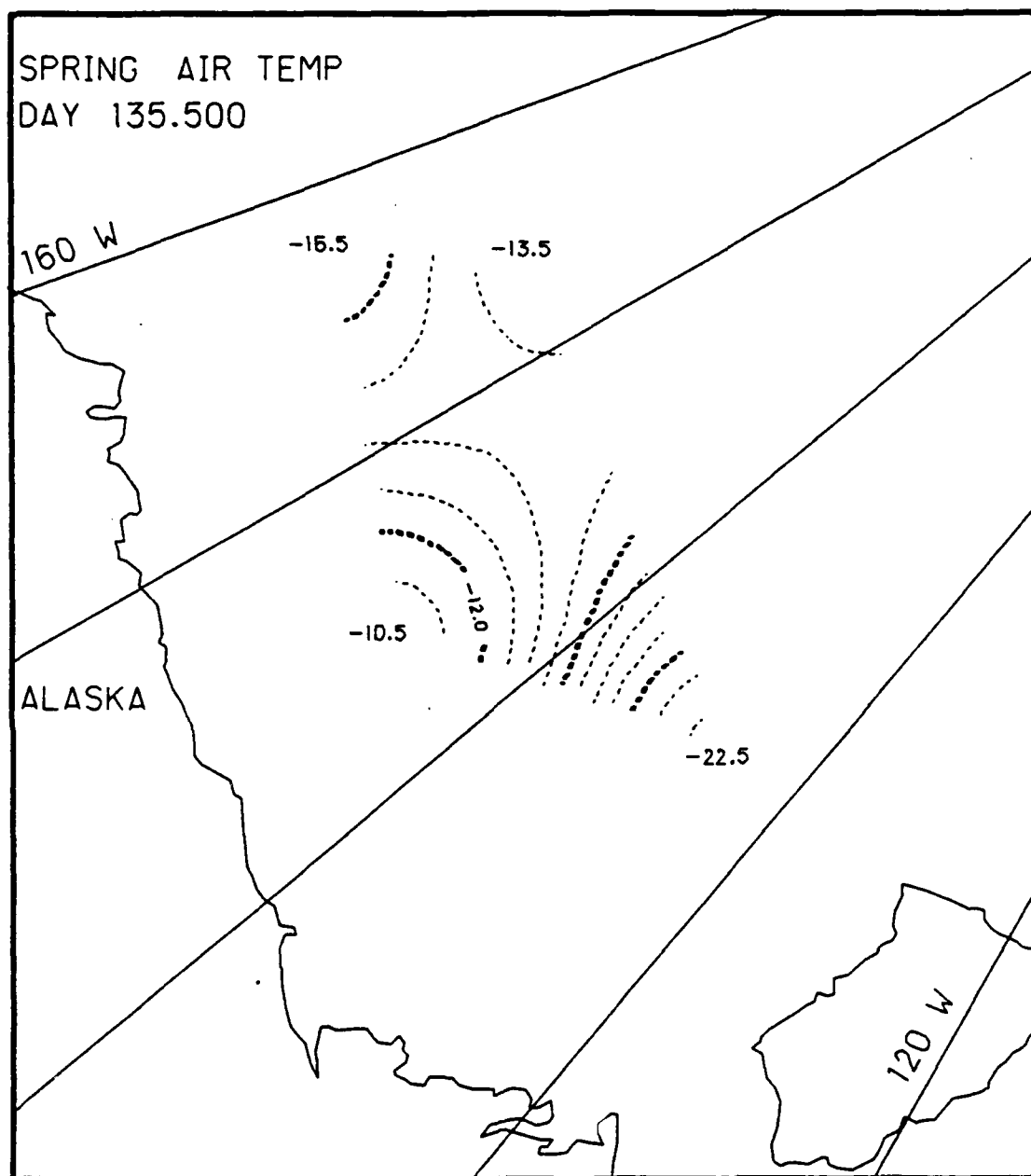


Fig. K.5. Spatial atmospheric temperature variations, day 135.5, based on the AIDJEX data from stations with hydrophones, spring 1976.

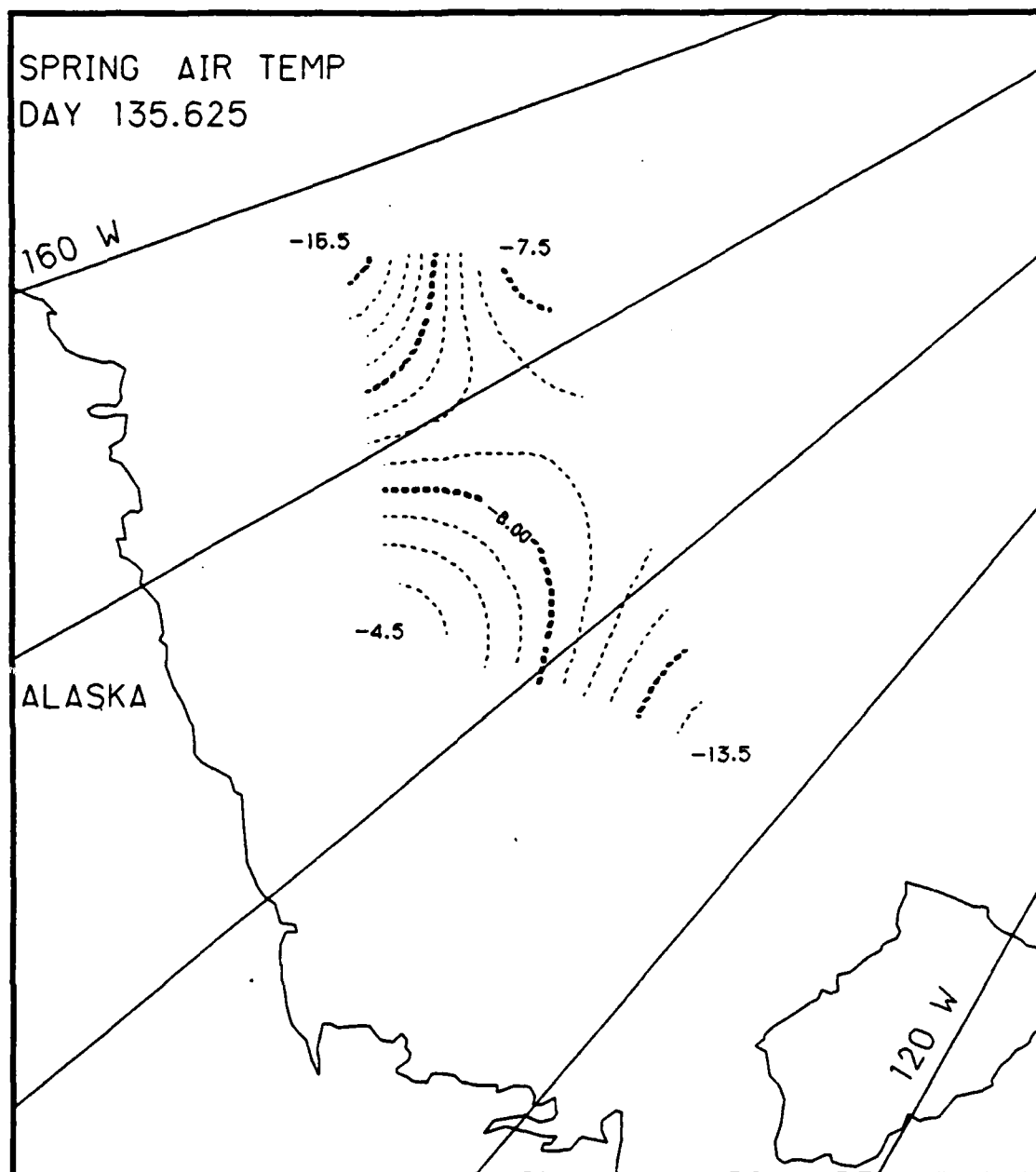


Fig. K.6. Spatial atmospheric temperature variations, day 135.625, based on the AIDJEX data from stations with hydrophones, spring 1976.

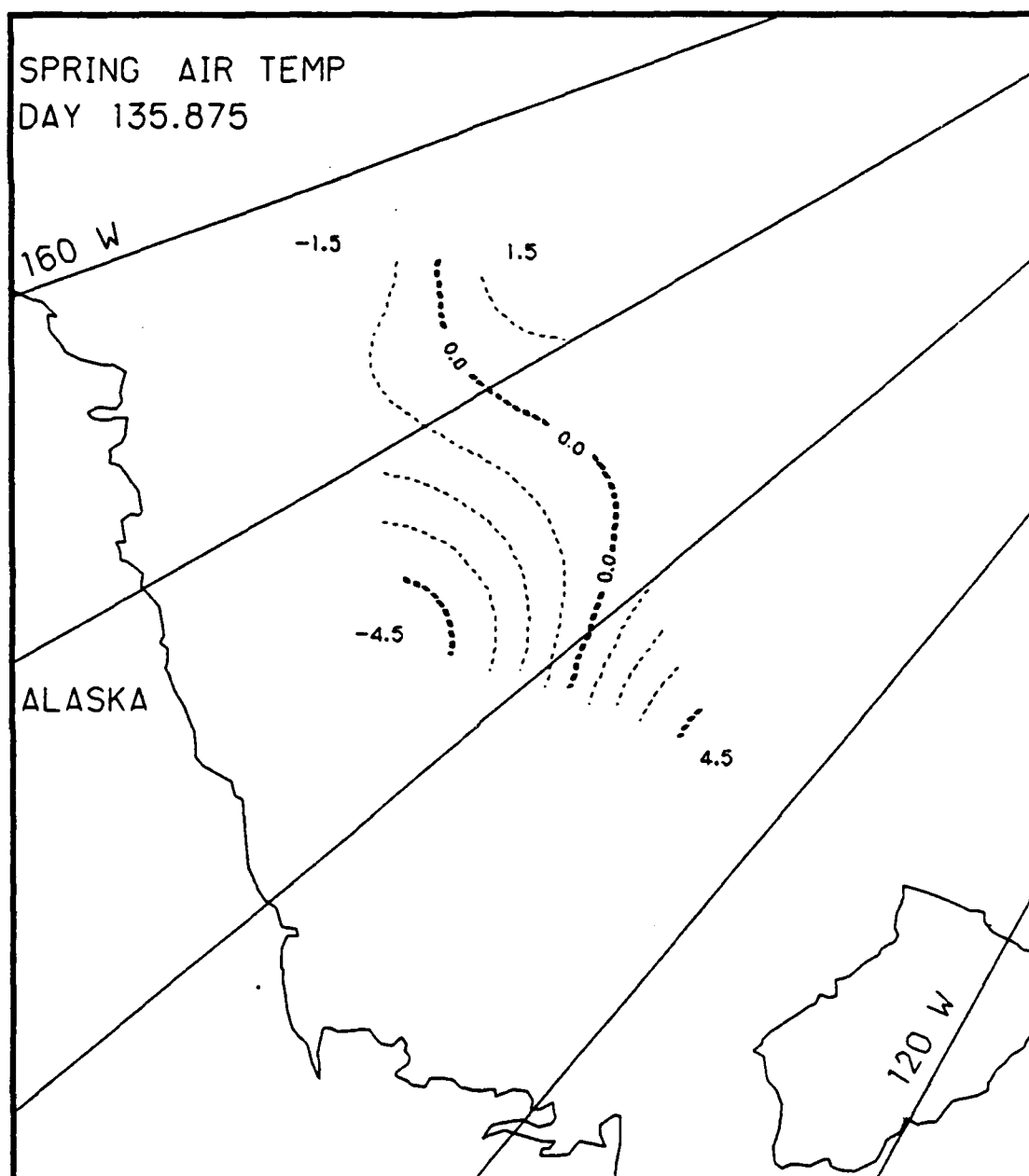


Fig. K.7. Spatial atmospheric temperature variations, day 135.875, based on the AIDJEX data from stations with hydrophones, spring 1976.

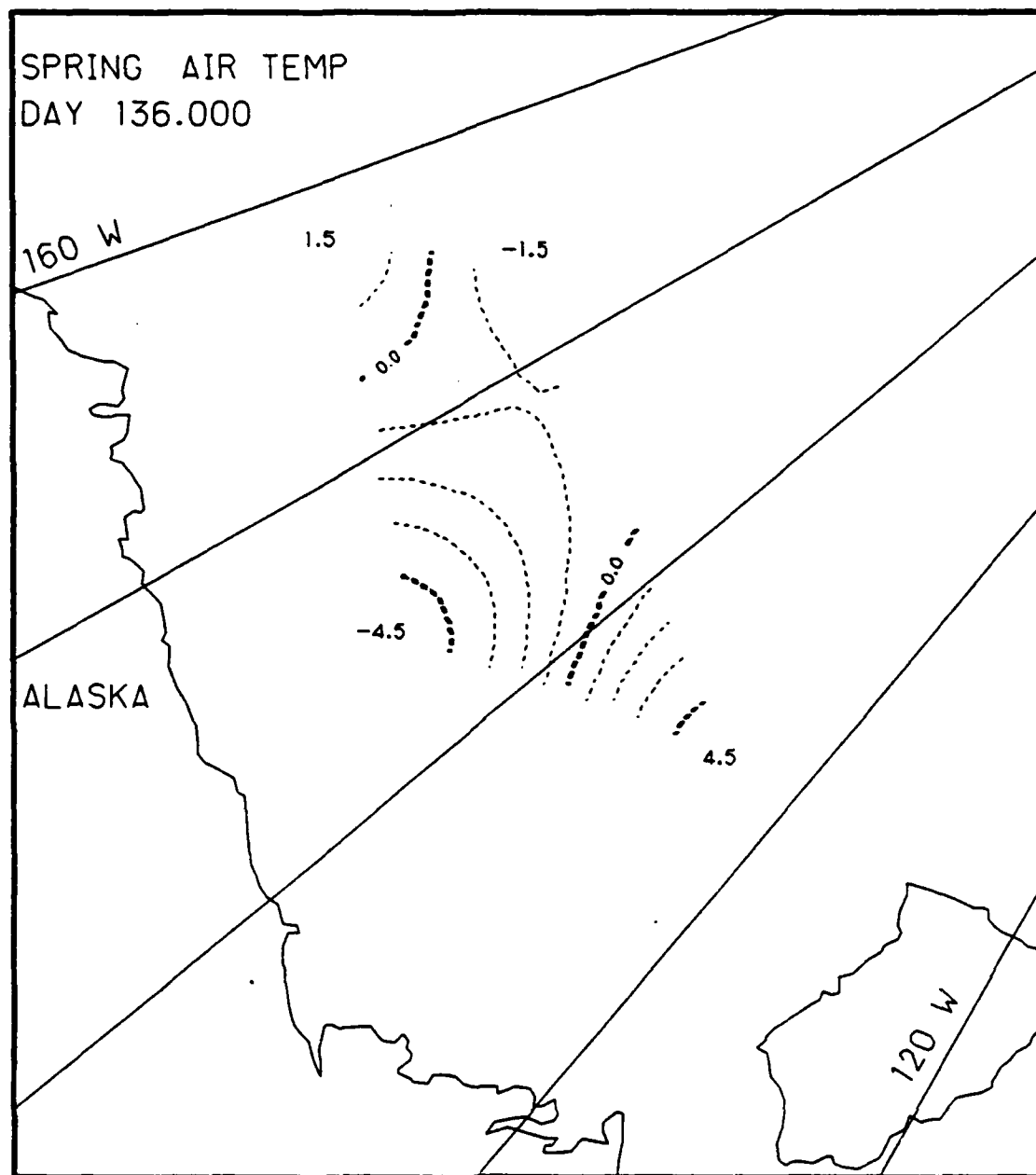


Fig. K.8. Spatial atmospheric temperature variations, day 136.0, based on the AIDJEX data from stations with hydrophones, spring 1976.

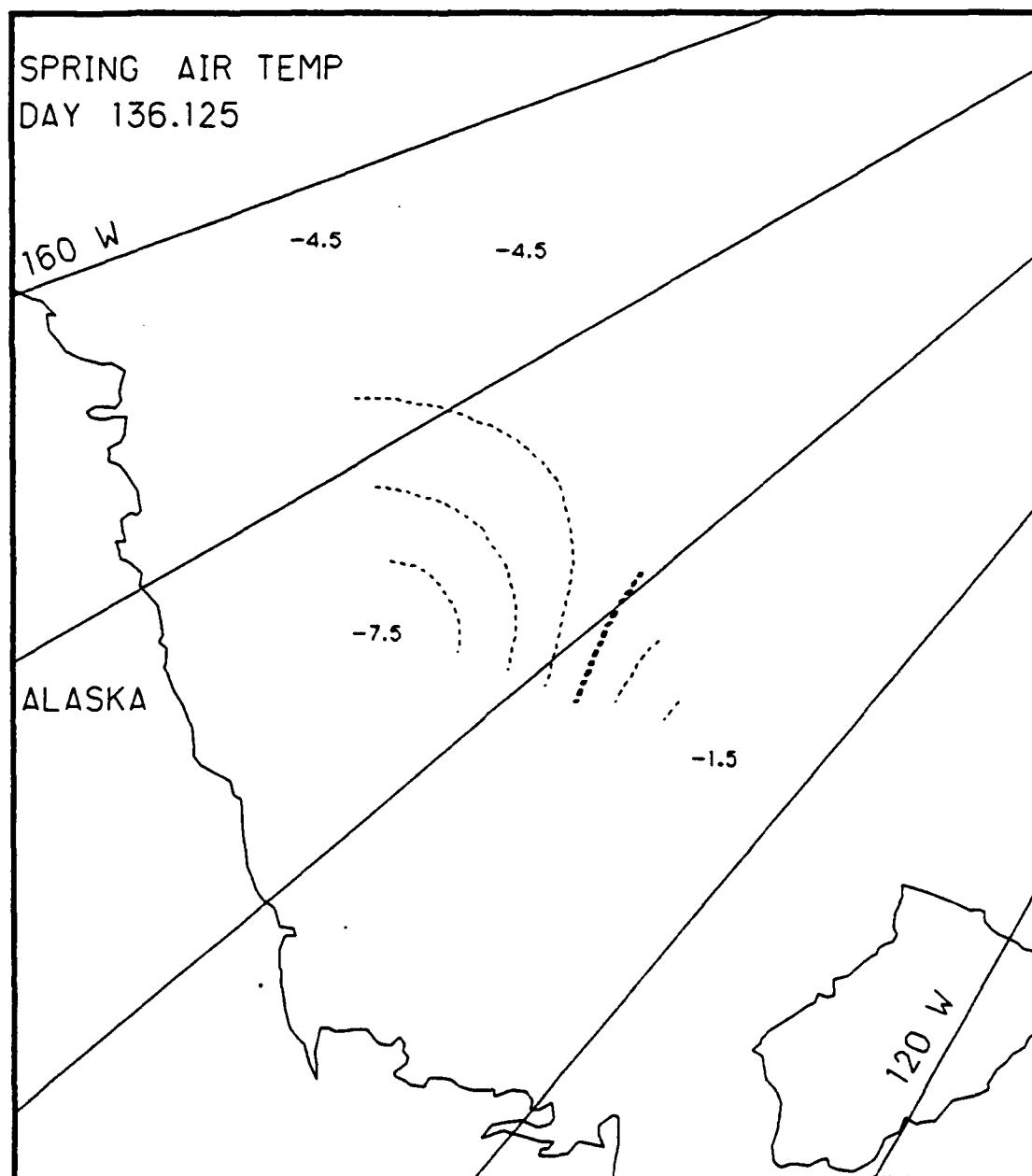


Fig. K.9. Spatial atmospheric temperature variations, day 136.125, based on the AIDJEX data from stations with hydrophones, spring 1976.

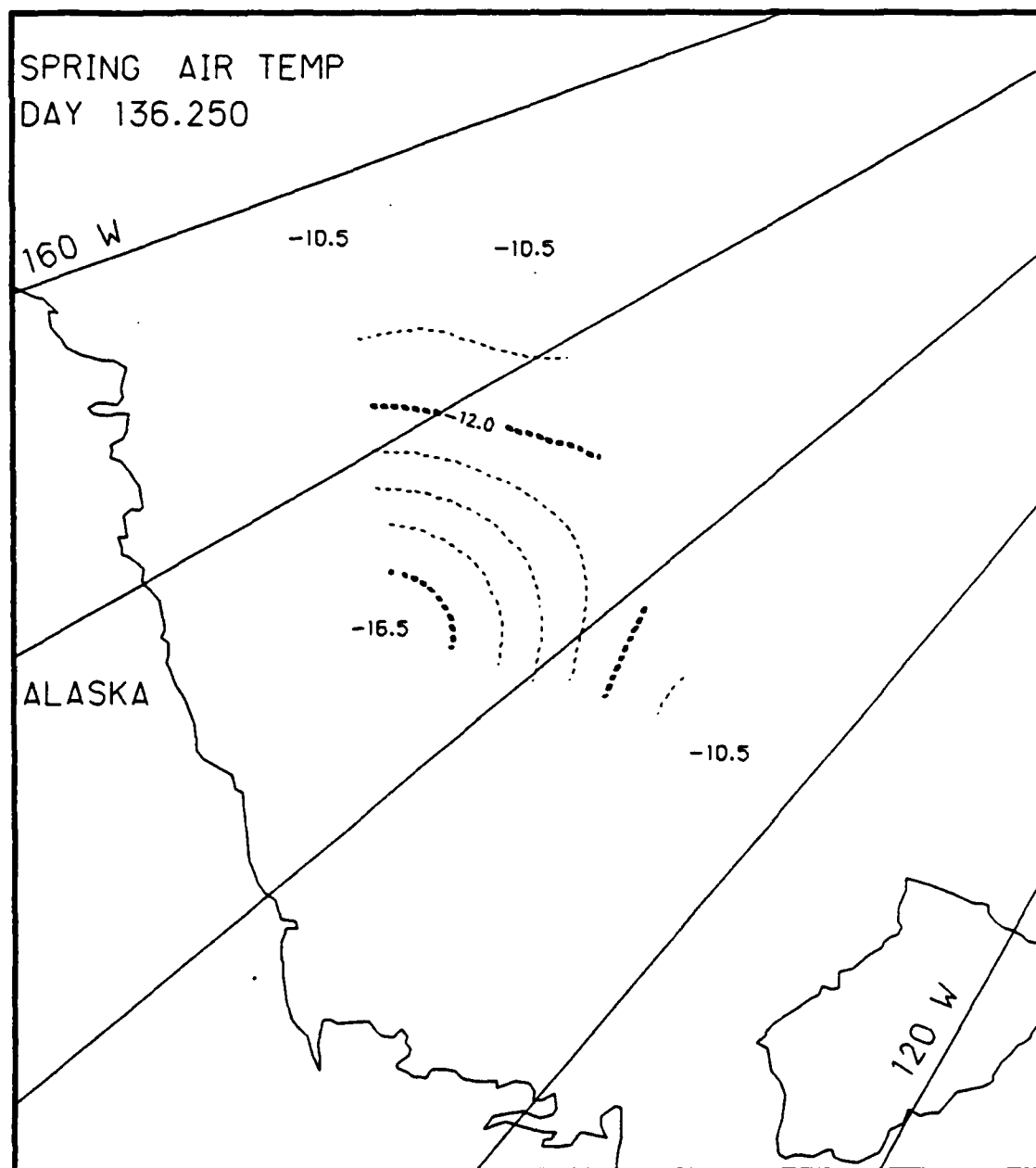


Fig. K.10. Spatial atmospheric temperature variations, day 136.25, based on the AIDJEX data from stations with hydrophones, spring 1976.

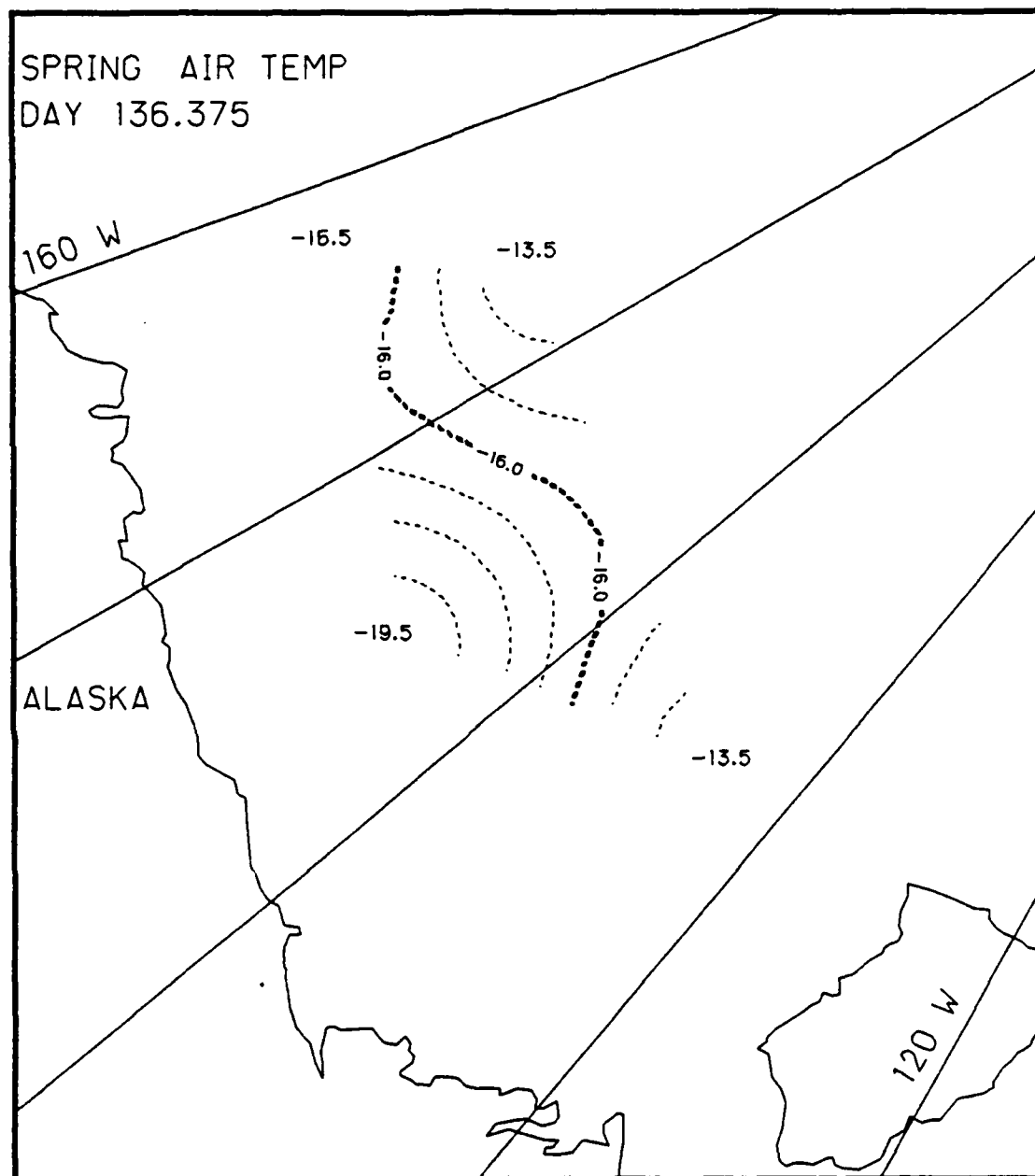


Fig. K.11. Spatial atmospheric temperature variations, day 136.375, based on the AIDJEX data from stations with hydrophones, spring 1976.

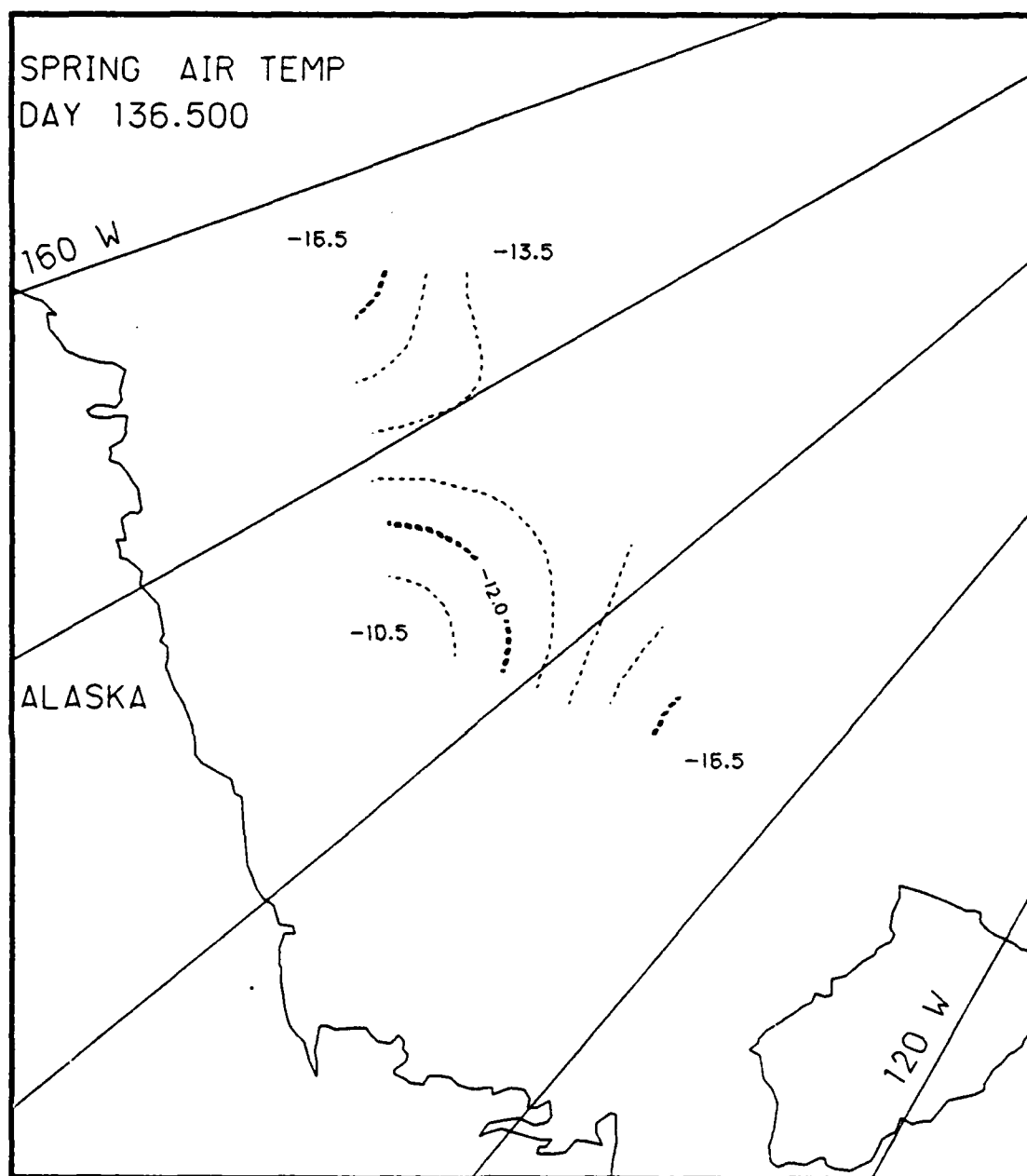


Fig. K.12. Spatial atmospheric temperature variations, day 136.5, based on the AIDJEX data from stations with hydrophones, spring 1976.

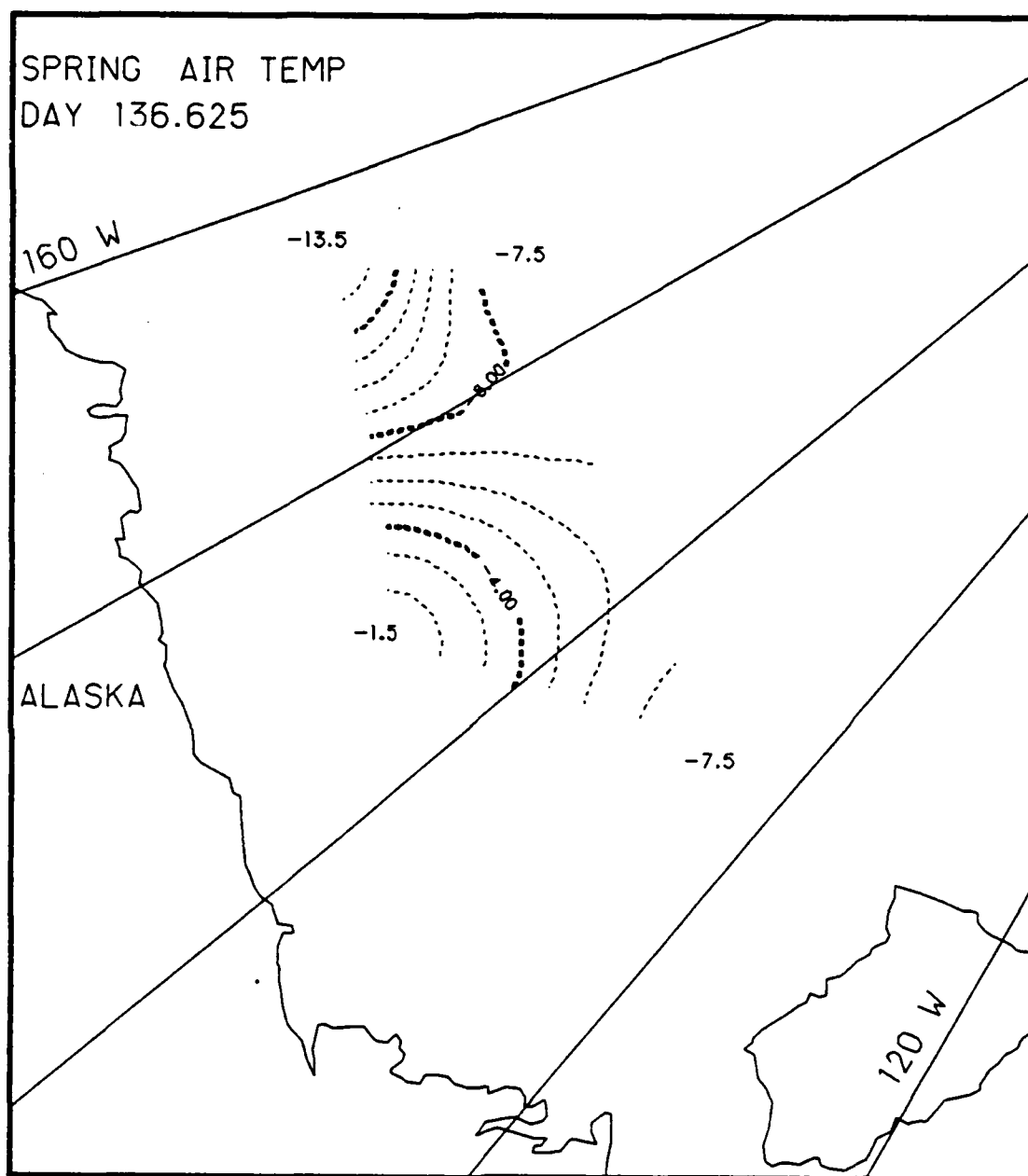


Fig. K.13. Spatial atmospheric temperature variations, day 136.625, based on the AIDJEX data from stations with hydrophones, spring 1976.

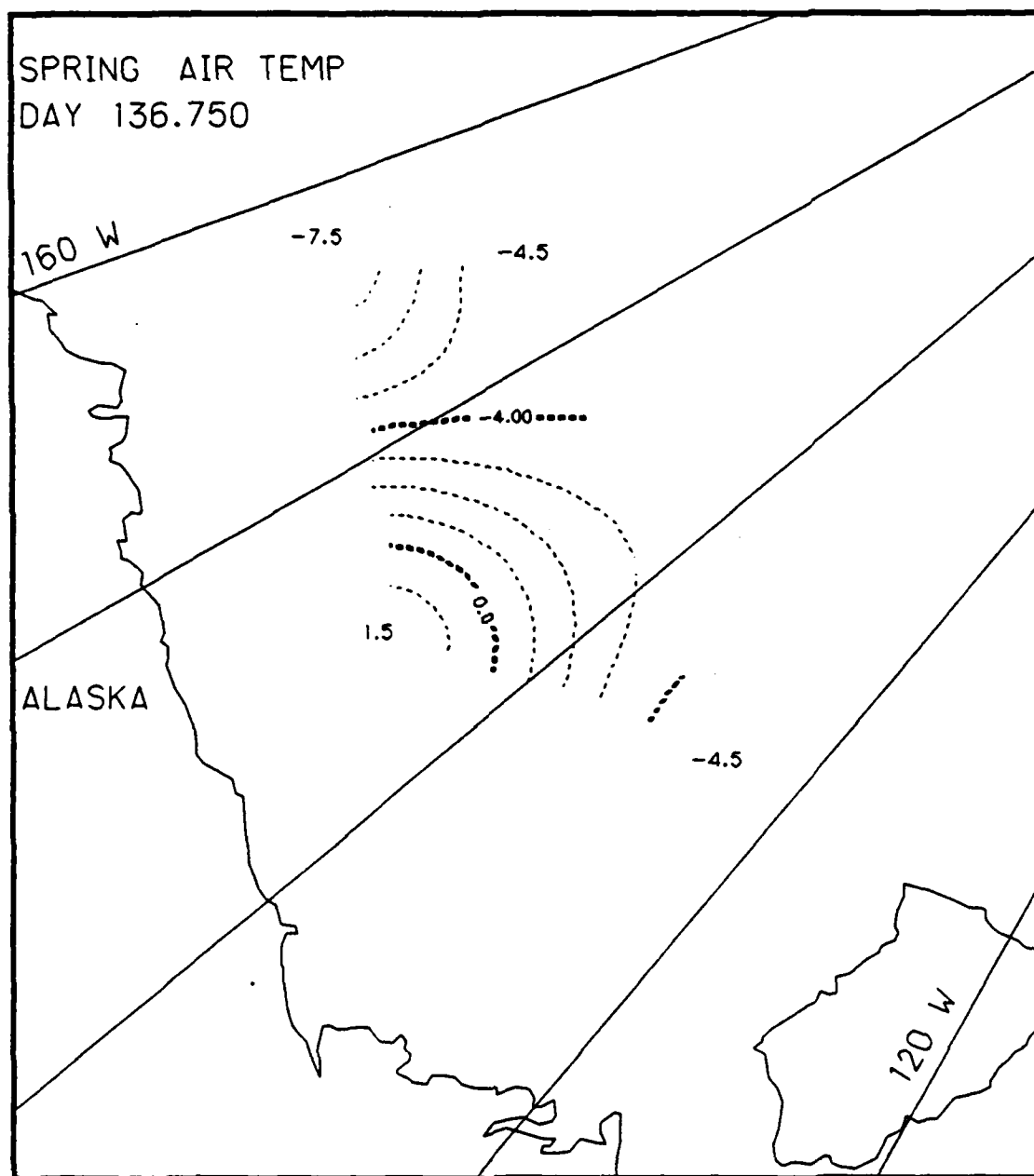


Fig. K.14. Spatial atmospheric temperature variations, day 136.75, based on the AIDJEX data from stations with hydrophones, spring 1976.

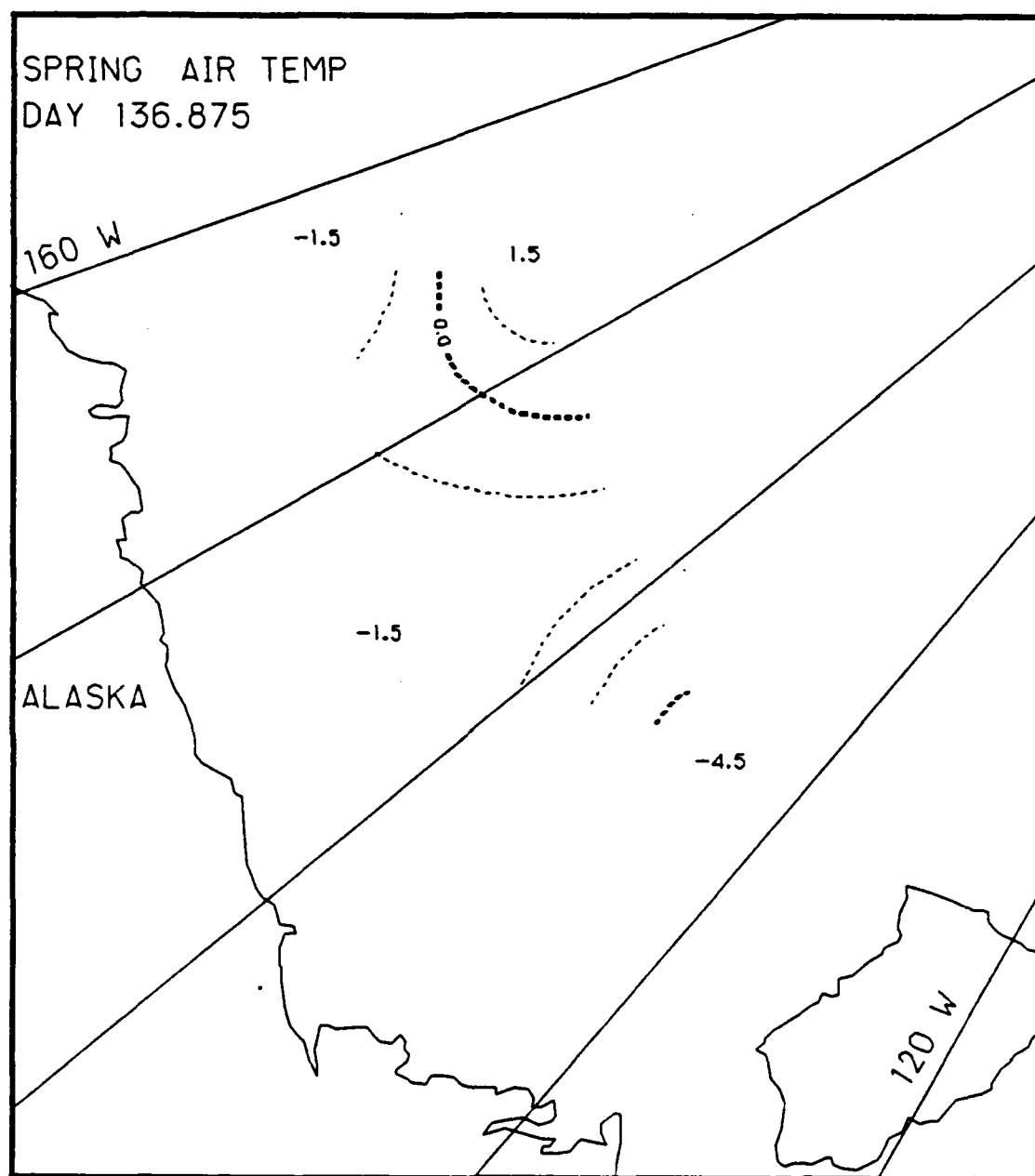


Fig. K.15. Spatial atmospheric temperature variations, day 136.875, based on the AIDJEX data from stations with hydrophones, spring 1976.

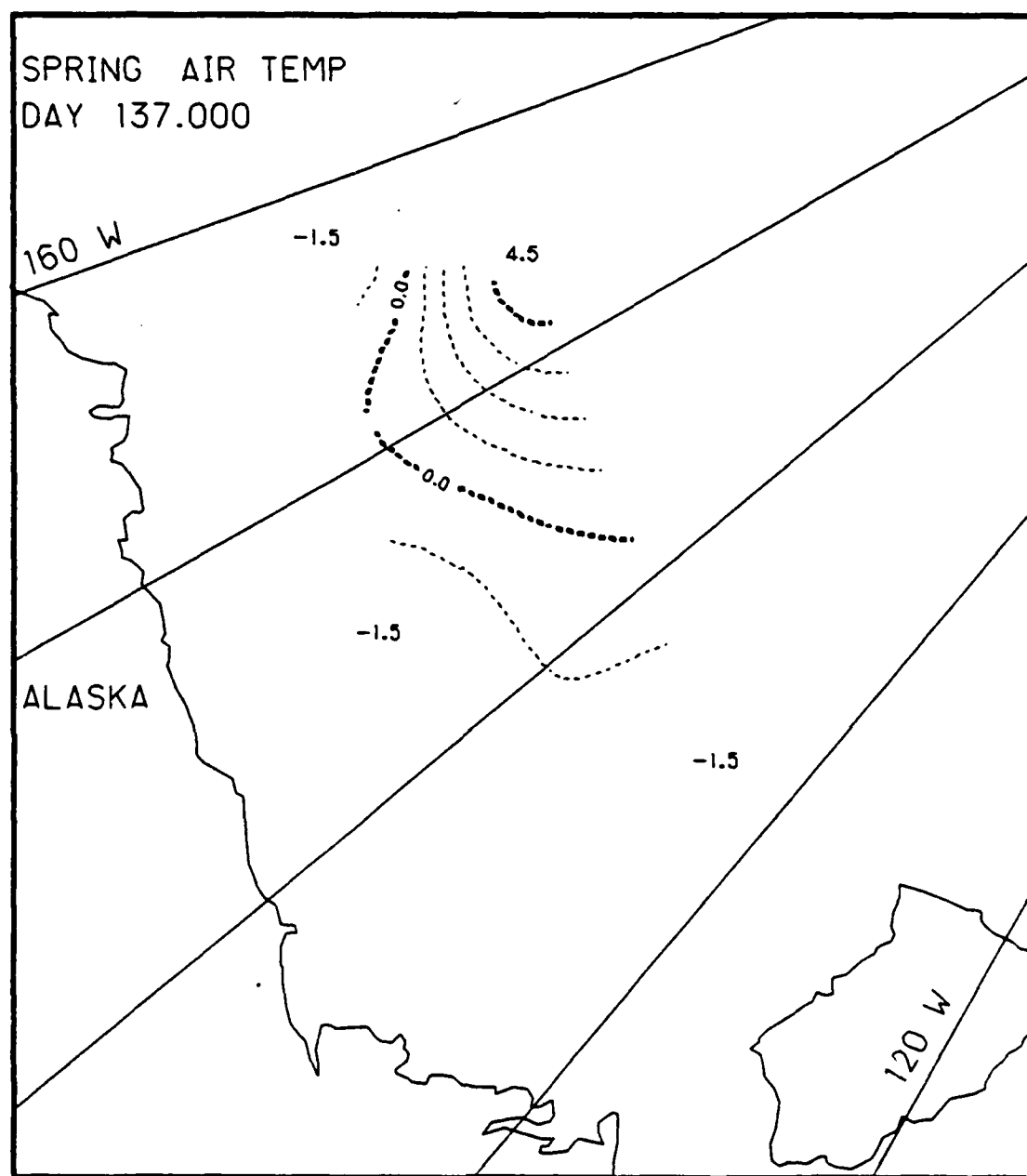


Fig. K.16. Spatial atmospheric temperature variations, day 137.0, based on the AIDJEX data from stations with hydrophones, spring 1976.

DTIC

END

4-86